

Development of a Low-Wearing Novel Hip Joint Prosthesis with a Longer Lifespan

Donald Dalli



University of Malta

Faculty of Engineering

Department of Metallurgy and Materials Engineering

Department of Mechanical Engineering

A dissertation submitted to the Faculty of Engineering in partial fulfilment of the requirements for the Degree of Doctor of Philosophy in Mechanical Engineering.

February 2021



L-Universit`
ta' Malta

University of Malta Library – Electronic Thesis & Dissertations (ETD) Repository

The copyright of this thesis/dissertation belongs to the author. The author's rights in respect of this work are as defined by the Copyright Act (Chapter 415) of the Laws of Malta or as modified by any successive legislation.

Users may access this full-text thesis/dissertation and can make use of the information contained in accordance with the Copyright Act provided that the author must be properly acknowledged. Further distribution or reproduction in any format is prohibited without the prior permission of the copyright holder.

Copyright Notice

1. Copyright in text of this dissertation rests with the Author. Copies (by any process) either in full, or of extracts, may be made **only** in accordance with regulations held by the Library of the University of Malta. Details may be obtained from the Librarian. This page must form part of any such copies made. Further copies (by any process) of copies made in accordance with such instructions may not be made without the permission (in writing) of the Author.
2. Ownership of the rights over any original intellectual property which may be contained in, or derived from, this dissertation is vested in the University of Malta and may not be made available for use by third parties without the written permission of the University, which will prescribe the terms and conditions of any such agreement.

In memory of my Grandfather,
Giuseppe Dalli
1936 – 2020

Abstract

The metal-on-polyethylene material combination has been the preferred choice amongst orthopaedic surgeons for artificial hip implants ever since its introduction in the clinical market by Sir John Charnley. In fact, metal-polyethylene hip implants account for the largest share (over one-third) of the global market. Their ubiquitous use has been driven by their ability to restore the biomechanics of the degenerated hip joint. Nonetheless, further improvements in the tribological performance of the polyethylene components are needed, since the average lifespan of these prostheses range between 15 to 25 years. The functionality of the hip joint can be once again restored using revision surgery; however, such procedures tend to be complicated, costly and have lower rates of success. The demand for such medical devices with an improved lifespan is continuously on the rise, due to the ever-increasing global population age and obesity.

In order to tackle the prevalent limited lifespan of primary hip joint replacements, research efforts in this work have been primarily focused on developing a new prosthesis design, hereinafter referred to as the MaltaHip, that exploits the molecular reorientation mechanism of the polyethylene material to reduce the extent of osteolysis. By producing uni-directional articulations, using multiple cylindrical joints that are orthogonal to each other, the surface molecules of the polyethylene components become highly aligned due to the molecular orientation hardening mechanisms, effectively producing highly wear resistant articulating surfaces. Further reductions in wear are also aided due to the increased contact area, provided by the cylindrical design of the articulation, which reduce the overall contact stresses. Therefore, the hypothesis that uni-directional cylindrical articulations consisting of polyethylene bearing surfaces provide reduced rates of wear, compared to the ball-and-socket articulation, was tested in this work.

A parametric CAD model of the MaltaHip has been developed to optimise the geometrical design of the cylindrical articulations. Finite element simulations were conducted to analyse the stresses that were produced on iterated designs of the prosthesis. The polyethylene components were simulated using an advanced viscoelastic-viscoplastic material model. Furthermore, comparisons of the generated stress were made to the conventional ball-and-socket prosthesis. The results produced from the finite element simulation were also used to predict the theoretical wear rates of the different prostheses designs, using various wear models which are available in literature.

Physical prototypes of the MaltaHip implant were fabricated based on the optimised design solution and then subjected to a series of physical tests. A single-station hip joint simulator was designed and built in parallel throughout this work that served as a testbed to validate the

functionality of the new mechanism of the MaltaHip implant. Furthermore, the simulator was used to provide initial indications regarding the tribological performance of the new prosthesis design. The test results also indicated that the newly designed prosthesis was able to achieve extreme joint angles with a reduced risk for dislocation. A mock surgery was conducted using the MaltaHip on a Thiel (soft) embalmed cadaver by orthopaedic surgeons, in order to gain insight on the practicality of implanting the new prosthesis. It was observed that the MaltaHip could be implanted with relative ease. Furthermore, the implanted prosthesis demonstrated that it could attain a wide range of motion with a high degree of stability.

After completion of the in-house tests, two sets of MaltaHip implants, each consisting of four prototypes, were produced. The first set of implants were produced out of UHMWPE (ultra-high molecular weight polyethylene) components, whereas the second set of implants were produced out of VEHXPE (Vitamin E-infused highly-crosslinked polyethylene) components. The eight implants were comprehensively wear tested according to ISO 14242-1:2014/Amd 1:2018 at Endolab® Mechanical Engineering GmbH, an accredited implant testing facility in Germany. Gravimetric measurements conducted on the tested specimens demonstrated that the MaltaHip implants produced lower wear rates than conventional ball-and-socket implants that were produced out of the same materials and wear tested under the same conditions. In fact, the MaltaHip implants made from UHMWPE components produced around a quarter of the wear produced by ball-and-socket implants. Furthermore, the MaltaHip implants made from VEHXPE resulted in a negative wear rate, implying that the rate of wear was lower than the rate of fluid lubricant absorption. The results of the study demonstrated that the reductions in the rate of wear were statistically significant, therefore supporting the research hypothesis that was tested in this work.

Optical microscopy images demonstrated that the machining marks on the polymeric components were preserved in most cases. This indicated that highly wear resistant surfaces, due to molecular orientation hardening effects, were indeed produced. A particle analysis conducted by Endolab® demonstrated that the produced wear particles ranged between 0.1 – 1.0 μm in size. Wear particles in this size range greatly contribute to the osteolysis effects. Nonetheless, due to the low volumes of wear that were generated by the prosthesis, the net osteolysis effect is postulated to be minimal, as indicated by a numerical method which is used to determine the extent of biological activity of the wear particles, as a function of particle sizes and the volumetric wear rate of the prosthesis. This result indicated that the MaltaHip could significantly reduce the extent of osteolysis, thereby potentially reducing the risk for revision surgery.

Acknowledgements

My sincere gratitude goes first to my project supervisors Prof. Ing. Joseph Buhagiar, Prof. Pierre Schembri Wismayer MD, and Prof. Ing. Pierluigi Mollicone for their continuous support, invaluable insight, and supervision throughout this doctoral study.

I would like to thank various members of the Faculty of Engineering from the University of Malta for their support throughout this work. Special thanks go to the technical staff of the Department of Metallurgy and Materials Engineering for their assistance on various aspects of the project, namely: Ing. James Camilleri, Ing. Mary Grace Micallef, Mr Nicholas Gingell, Mr Noel Tonna, Mr Daniel Dimech and Mr Andrew Agius. I would like to also thank the technical staff of the Department of Mechanical Engineering for their support related to the testing equipment, particularly: Mr Jean Paul Azzopardi, Mr Roberto Bonello and Mr Kevin Farrugia. I would like to also express my sincere appreciation towards the technical staff of the Department of Industrial and Manufacturing Engineering for manufacturing various components for the hip joint simulator, especially: Ing. John Paul Borg, Mr Jesmond Pace, Mr Joseph Curmi, and Mr Michael Curmi. Special thanks go to Dr. Ing Reiko Raute from the Department of Industrial Electrical Power Conversion, and Dr. Ing Marvin Bugeja from the Department of Systems & Control Engineering for their guidance related to the electrical actuation systems.

I wish to express my sincere gratitude towards orthopaedic surgeons Mr Ray Gatt MD FRCS MA, Mr Ryan Giordimaina MD FRCS, and theatre nurse Mr Herbert Doublet for performing the mock surgery on the cadaver and for their invaluable insight on the implantation of the prosthesis. Special thanks also go to Dr Ing. Anton Bartolo and Ing. Michelle Cortis from the Knowledge Transfer Office for their continuous support that enabled us to file a Patent Cooperation Treaty (PCT) to protect the invention that was developed in this work. I would like to also thank Dr Analise Cassar from the Anatomy Department from the Faculty of Medicine and Surgery for her support related to the preparation of the fluid test medium required for the experimental tests. I would like to also thank Ms Antoinette Bonello, Ms Antonella Sammut, Ms Vanessa Borg and Mr Sherif Suleiman for their administrative support throughout this work.

Special thanks go to Mr David Cole from David's Engineering Works Ltd for manufacturing various components for the hip joint simulator that was developed throughout this work. I would like to also thank Mr Matthias Goeke from IBG Automation GmbH for supplying various pneumatic and electrical components. I would like to also express my sincere gratitude towards Mr Manuel Pavia and his sons Mr Carl Pavia and Mr Mark Pavia from Empav Engineering Ltd., for undertaking the challenging task of fabricating the MaltaHip implants, successfully producing the implants to the highest machining standards, and also for their invaluable insight on various aspects of machining.

I would like to thank the researchers from the Office Room 217 for creating a supportive research atmosphere and sharing their experiences throughout my course of my study. Finally, I would also like to thank my parents, my grandmother and my girlfriend Laura Gretkowska for their continuous support and encouragement throughout the course of my study.

I would like to thank the Malta Council for Science and Technology for the funding scheme and for providing me the invaluable opportunity to work on the MaltaHip project. Project MaltaHip (Development of a Low-Wearing Novel Hip Joint Prosthesis for a Longer Lifespan) is a collaboration between the University of Malta and MCL Components Ltd. and is funded by the Malta Council for Science and Technology through Fusion: The R&I Technology Development Programme 2016 (R&I-2015-023T).

Accomplishments

Intellectual Property

- Initial filing of a UK patent application (1909181.8) with 26th June 2019 as the priority date.
- International Patent Cooperation Treaty (PCT) filing of “a prosthetic implant” (PCT/EP2020/067366) on the 22nd June 2020 with the European Patent Office (EPO), the Hague, as the receiving body.

Awards

- Awarded the Intellectual Property Organisation (WIPO) Medal for Inventors (December 2019).
- 1st Place – Malta Innovation Awards 2019 (Scientific Category), hosted by the Commerce Department of the Ministry of the Economy, Investment and Small Business (December 2019), for the MaltaHip implant design developed throughout this work.
- MaltaHip team nominated Empav Engineering Ltd. for the Industrial Excellence Award 2019 and was awarded by the Chamber of Engineers (November 2019).
- 2nd Place – Malta Innovation Awards 2017 (Scientific Category), hosted by the Commerce Department of the Ministry of the Economy, Investment and Small Business (March 2018), for the hip joint simulator developed throughout this work.
- 1st Place – Speak Out for Engineering (SOFE) in International Final held in Christchurch, New Zealand (February 2018), organised by the Institution of Mechanical Engineers (IMechE).

Table of Contents

Copyright Notice	ii
Abstract.....	iv
Acknowledgements.....	vi
Accomplishments	viii
Table of Contents.....	ix
List of Figures.....	xiv
List of Tables	xxiii
Glossary of Symbols.....	xxv
1. Introduction.....	1
1.1. Background and Motivation	1
1.2. Hypothesis Statement	3
1.3. Objectives	5
2. Literature Review	6
2.1. Introduction.....	6
2.1.1. Low-Friction Arthroplasty.....	6
2.1.2. Wear and Associated Clinical Complications.....	7
2.1.3. Developments in THR	8
2.2. Biomechanics of the Hip Joint.....	10
2.2.1. Introduction.....	10
2.2.2. Hip Joint Reaction Force	10
2.2.3. Factors Influencing Loads on the Hip.....	12
2.2.4. Comparison to the Ankle Joint	14
2.2.5. Comparison to the Knee Joint.....	16
2.3. Mechanics of UHMWPE.....	17
2.3.1. Introduction.....	17
2.3.2. Chemical Structure	18
2.3.3. Crystal Phases	19
2.3.4. Mechanical Properties.....	22
2.3.5. Creep Behaviour	24
2.3.6. Influence of Sterilization and Crosslinking on UHMWPE Mechanics	25
2.4. Modelling Mechanics of UHMWPE	27
2.4.1. Review of Models.....	27
2.4.2. Maxwell and Wiechert Material Models	29
2.4.3. Three Network Material Model	32

2.5.	Tribology and Degradation of UHMWPE.....	36
2.5.1.	Introduction.....	36
2.5.2.	Contact Mechanics in Tribology.....	36
2.5.3.	Plasticity-Induced Orientation	40
2.5.4.	Wear Mechanisms	44
2.5.5.	Wear Behaviour Dependence on Sliding Motion Direction	47
2.5.6.	Influence of Crosslinking.....	50
2.6.	Modelling Tribology of UHMWPE.....	53
2.6.1.	Review of Wear Models in Literature	53
2.6.2.	Archard’s Wear Law.....	53
2.6.3.	Saikko Model.....	54
2.6.4.	Liu Model	55
2.6.5.	Kang Model	56
2.6.6.	Petrella Model.....	57
2.7.	Wear Debris.....	59
2.7.1.	Overview.....	59
2.7.2.	Functional Biological Activity.....	61
2.8.	Conclusion	63
3.	Methodology.....	64
3.1.	Introduction.....	64
3.1.1.	MaltaHip Design Concept	64
3.1.2.	Materials	65
3.1.3.	Testing Conditions.....	66
3.2.	Mechanical Characterisation.....	68
3.3.	Parametric CAD Model	69
3.4.	Finite Element Simulations.....	74
3.4.1.	Overview.....	74
3.4.2.	Influence of Design Parameters	76
3.4.3.	Finalised Design	76
3.5.	Wear Modelling.....	80
3.5.1.	Overview.....	80
3.5.2.	Slide Track Modelling	81
3.5.3.	Wear Computation.....	82
3.6.	Fabrication of the MaltaHip Implant	83
3.6.1.	Machining.....	83
3.6.2.	Surface Finish and Polishing	84
3.7.	Hip Joint Simulation Testing	85

3.7.1.	Overview.....	85
3.7.2.	Implant Testing (In-house)	86
3.7.3.	Implant Testing (Endolab).....	89
3.8.	Wear Test Measurements	92
3.8.1.	Gravimetric Measurements.....	92
3.8.2.	Contact Area Inspection.....	94
3.9.	Analysis of Wear Particles.....	95
3.9.1.	Process Description	95
3.9.2.	Definitions of Morphological Characteristics.....	96
3.10.	Mock Surgery on Cadaver	97
4.	Experimental Setup.....	98
4.1.	Overview.....	98
4.2.	Motion Mechanism.....	99
4.3.	Loading Mechanism	102
4.4.	Lubrication System.....	104
5.	Results	105
5.1.	Introduction.....	105
5.2.	Material Model Results.....	106
5.2.1.	Material Model Calibration	106
5.2.2.	Material Model Validation.....	108
5.3.	Structural Model and Finite Element Results	111
5.3.1.	Introduction.....	111
5.3.2.	Mesh Sensitivity Analysis	111
5.3.3.	Influence of Design Parameters on Structural Integrity	112
5.3.4.	Interlocking Mechanism	120
5.3.5.	Structural Analysis of Finalised Design Solution.....	126
5.4.	Sliding Track Properties	150
5.4.1.	Cross-shear Ratio (CSR).....	150
5.4.2.	Sliding Distance.....	155
5.4.3.	Contact Area	157
5.5.	Wear Model Results	157
5.5.1.	Introduction.....	157
5.5.2.	Saikko Model.....	158
5.5.3.	Liu Model	159
5.5.4.	Kang Model	159
5.5.5.	Petrella Model.....	160
5.6.	The Fabricated Implant.....	161

5.6.1.	Machining Processes	161
5.6.2.	The Resultant Interlocking Mechanism	173
5.6.3.	Surface Roughness.....	178
5.7.	Experimental Wear Testing Results	187
5.7.1.	Implant Functionality (In-House Testing)	187
5.7.2.	Wear Performance (In-House Testing).....	189
5.7.3.	Wear Rate Results.....	191
5.7.4.	Contact Areas.....	206
5.7.5.	Optical Microscopy Images	220
5.7.6.	Wear Particles	244
5.8.	Mock Surgery on Cadaver	249
5.9.	Summary of Results.....	253
6.	Discussion.....	255
6.1.	Introduction.....	255
6.2.	Structural Model	256
6.2.1.	Material Characterisation and Modelling	256
6.2.2.	Component Design	262
6.2.3.	Comparison of Finalised MaltaHip and Ball-and-Socket Designs	264
6.3.	Wear Model Results	267
6.4.	Theoretical and Experimental Comparisons.....	270
6.4.1.	Contact Area	270
6.4.2.	Wear Results.....	272
6.5.	Analysis on Tribological Performance	273
6.5.1.	Physical Performance of Implants	273
6.5.2.	Analysis of MaltaHip UHMWPE Components.....	277
6.5.3.	Analysis of MaltaHip VEHXPE Components.....	280
6.5.4.	Analysis and Comparison of the MaltaHip Components	282
6.5.5.	Creep.....	283
6.5.6.	Lubrication.....	284
6.5.7.	Fluid Absorption.....	285
6.6.	Wear Particle Analysis	286
6.6.1.	Wear Particle Morphology.....	286
6.6.2.	Functional Biological Activity.....	289
6.7.	Implant Overview and Potential Improvements	290
6.7.1.	Implant Design and Materials.....	290
6.7.2.	Implant Interlocking Mechanism.....	292
6.8.	Summary.....	295

7. Conclusion.....	296
7.1. Work Contribution.....	296
7.2. Future Work.....	299
8. References.....	301
Appendix A: Material Certificates.....	319
A1. UHMWPE GUR 1050, Ram Extruded Bar – Ø 80 mm	319
A2. UHMWPE GUR 1050, Ram Extruded Bar – Ø 40 mm	322
A3. VEHXPE GUR 1020, Compression Moulding – Ø 60 mm	325
A4. High-N Austenitic Stainless Steel – Ø 50 mm.....	331
A5. High-N Austenitic Stainless Steel – Ø 30 mm.....	335

List of Figures

Figures	Description	Page
Fig. 1.1	Anatomy of the hip joint. Adapted from: [11].	2
Fig. 2.1	Illustration of the low-friction torque principle applied to hip arthroplasty as proposed by Charnley. Adapted from: [1].	6
Fig. 2.2	Hip dislocation dependent on femoral head size which dictates the ‘jump’ distance that is required. Adapted from: [60].	7
Fig. 2.3	Design variations of hip implants on the market.	9
Fig. 2.4	Anatomical directions relative to the hip. Adapted from: [11].	10
Fig. 2.5	Hip reaction forces on the hip during different loading conditions. Adapted from: [100].	11
Fig. 2.6	Reaction forces on the hip.	12
Fig. 2.7	Influence on the hip loading conditions, as a function of hip centre position varied along different dimensions. Adapted from: [102].	13
Fig. 2.8	Acetabular cup implantation angles. Source: [109].	13
Fig. 2.9	Natural ankle joint.	15
Fig. 2.10	Prosthetic ankle joint.	15
Fig. 2.11	Natural knee joint.	16
Fig. 2.12	Artificial knee implant.	17
Fig. 2.13	Basic chemical structures of ethylene and polyethylene. Source: [145].	18
Fig. 2.14	Structures in polyethylene at different levels.	20
Fig. 2.15	Crystal morphology of pristine UHMWPE.	21
Fig. 2.16	Deformations in the amorphous phase. Source [180].	24
Fig. 2.17	Schematic representation of crosslinking. Source: [202].	26
Fig. 2.18	Alpha-Tocopherol. Source: [212].	27
Fig. 2.19	Comparison between the stress-strain response obtained from experimental data, as compared to the linear elastic model. Source: [229].	29
Fig. 2.20	Schematic representation of the Generalized Maxwell material model.	29
Fig. 2.21	Weichert material model.	31
Fig. 2.22	Rheological representation of the Three Network (TN) Model. Source: [176].	33
Fig. 2.23	An example stress-strain curve produced by the TN model, separated into various domains, each produced by a different deformation mechanism controlled by the corresponding network in the model. Source: [31].	34
Fig. 2.24	The eight-chain model located in a unit cell, as proposed by Arruda and Boyce [237], which is used to model the length of the molecular chains upon being deformed. Source: [238].	34
Fig. 2.25	Contact mechanics of a micro-asperity. Adapted from: [243].	37
Fig. 2.26	Contact stress values on acetabular cup (22.225 mm femoral head diameter, 8.705 mm acetabular cup thickness), subjected to a load of 2500 N, inclined at 10° medially. Note that an elastic-plastic (multi-linear kinematic hardening) model was used. Source: [219].	39

Fig. 2.27	UHMWPE fibrils and the corresponding molecular structure, being subjected to an applied load σ_x that is inclined at an arbitrary angle α_f (represented by a unidirectional structure) with respect to the principal molecular chain orientation. The resolved stress components ($\sigma_l, \sigma_t, \tau_{lt}$) relative to the molecular polymer chain are shown. Adapted from: [152, 201, 243].	41
Fig. 2.28	Failure stress as a function of the off-axis loading angle. Adapted from: [243].	41
Fig. 2.29	Slide tracks due to multidirectional sliding motion of the hip. Source: [18].	42
Fig. 2.30	TEM images of wear tested UHMWPE and XPE samples. Source: [269].	44
Fig. 2.31	Wear mechanics. Representative topographic surfaces that are produced for UHMWPE on a microscopic scale following the wear processes are shown. Source: [273].	45
Fig. 2.32	Schematic illustration of the relative importance of abrasive wear, adhesive wear and surface fatigue wear for acetabular cups Source: [152].	45
Fig. 2.33	SN plot for conventional UHMWPE and XPE (100 kGy), illustrating the number of cycles required for the material to start yielding. Adapted from: [282].	47
Fig. 2.34	SEM images of worn surface topography of UHMWPE. Source: [245].	49
Fig. 2.35	Wear tested conventional UHMWPE acetabular cup.	50
Fig. 2.36	Optical microscope images of crosslinked UHMWPE.	52
Fig. 2.37	Retrieved crosslinked acetabular cup. Source: [291].	53
Fig. 2.38	Wear-factor k computed as a function based on the cross-shear ratio and contact pressure, as proposed by Kang et al. [303].	56
Fig. 2.39	An example of a slide track produced by node $j = 1$, with a sharp 90° curve, that has been divided into segments according to the distance covered in time increments i is illustrated. When mem is 1 (left), only one segment is penalised. When mem is 3 (right), three segments are penalised to represent the process of molecular reorientation that occurs during sliding motion. Source: [298].	58
Fig. 2.40	Particle size distribution with different sliding trajectories. Source: [245].	59
Fig. 2.41	Wear particles of UHMWPE subjected to different sterilization and crosslinking techniques. Source: [85].	60
Fig. 2.42	Biological activity $B(r)$ composed as a function of particle size derived from in vitro cell culture studies. Adapted from: [306].	62
Fig. 3.1	Degrees of freedom of the natural and artificial MaltaHip hip.	64
Fig. 3.2	Early concept of the MaltaHip, acting as the starting point for this doctoral work.	65
Fig. 3.3	Different phases during the gait cycle. Source: [314].	67
Fig. 3.4	Load and motion profiles specified for hip joint simulator testing, as specified by ISO 14242-1:2014/Amd 1:2018. Source: [315].	67
Fig. 3.5	Cylindrical test samples extracted from round bar for compression round bars.	69
Fig. 3.6	Compression cylindrical test samples of UHMWPE conducted inside a temperature-controlled bath at 37°C .	69
Fig. 3.7	Developed design of the MaltaHip used for the parametric CAD modelling.	70
Fig. 3.8	Design parameters of the abductor component, and their corresponding range of tested values.	72
Fig. 3.9	Design parameters of the rotator component, and their corresponding range of tested values.	72
Fig. 3.10	Design parameters of the flexor component, and their corresponding range of tested values.	73
Fig. 3.11	Design parameter of the MaltaHip cup component, and its corresponding range of tested values.	73

Fig. 3.12	Design parameters of the clearance values of the articulations, and their corresponding range of tested values.	74
Fig. 3.13	Designations for the finalised design of the MaltaHip implant used throughout this work.	77
Fig. 3.14	Designations for the ball-and-socket implant used throughout this work.	77
Fig. 3.15	Designations used throughout this work for the final version of the MaltaHip.	78
Fig. 3.16	Boundary conditions applied to finalised design of the MaltaHip.	80
Fig. 3.17	General flowchart of the wear rate computation using finite element (FE) and slide track data.	81
Fig. 3.18	Features produced by 5-Axis CNC Machine are marked in red. Remaining features were produced using a CNC Lathe.	83
Fig. 3.19	Equipment and consumables used during polishing of external surfaces of the metallic components.	84
Fig. 3.20	Equipment and consumables used during polishing of internal surface of the flexor component.	85
Fig. 3.21	In-house developed hip joint simulator. Flexible enclosure which contains the fluid during testing is not shown in the photo.	87
Fig. 3.22	Fixation of the prosthesis in the hip joint simulator.	88
Fig. 3.23	Endolab® Mechanical Engineering GmbH six-station hip joint simulator according to ISO 14242-1:2014/Amd 1:2018. Source: Endolab® report (unpublished).	90
Fig. 3.24	Single test station of the Endolab® hip joint simulator (1: Upper implant holder containing the polyurethane resin cast holding the acetabular cup, 2: Cone adapter, 3: Lower implant holder, 4: Temperature and fluid level sensor, 5: Heating, and 6: Arrangement to exclude contaminating particles to prevent interference with the wear test). Source: Endolab® report (unpublished).	91
Fig. 3.25	Schematic illustration of the contact area inspection process at 1.0 and 5.0 million cycles.	94
Fig. 3.26	Filtration system used for the particle analysis preparation according to ISO 17853:2011. Source: Endolab® report (unpublished).	96
Fig. 3.27	Particle measurements indicating the maximum and minimum Feret diameters. Source: [328]	97
Fig. 4.1	Overview of the hip joint simulator.	98
Fig. 4.2	Schematic illustration of the motion mechanism, showing the rotation frames and their corresponding actuators. Note: The pelvic and femoral bone are not used in the actual test setup.	99
Fig. 4.3	Motion mechanism of the hip joint simulator.	100
Fig. 4.4	Abduction/Adduction motion theoretical requirements.	100
Fig. 4.5	Flexion/Extension motion theoretical requirements.	101
Fig. 4.6	Internal/External motion theoretical requirements.	101
Fig. 4.7	Pneumatic circuit for the loading mechanism of the hip joint simulator.	103
Fig. 4.8	Lubrication system of the hip joint simulator. Note: The pelvic and femoral bone are not used in the actual test setup.	104
Fig. 5.1	Experimental and theoretical engineering stress-strain curves of UHMWPE and VEHXPE. Experimental results are based on compression tests. Theoretical results are based on the Three Network model (calibrated from the same experimental data). A strain rate of 0.03 s ⁻¹ was used in all tests.	107
Fig. 5.2	Boundary conditions applied on the cylindrical test samples.	109
Fig. 5.3	The true stress-strain relationships of (a) UHMWPE and (b) VEHXPE obtained from the finite element models, being compared to the results obtained from the compressions tests.	110

Fig. 5.4	Plot for mesh sensitivity analysis using the normalised maximum contact pressure as the metric for determining the optimised element size.	112
Fig. 5.5	Influence of the MaltaHip design parameters on the maximum contact stresses for each component.	116
Fig. 5.6	Influence of the MaltaHip design parameters on the von Mises stresses of the components.	119
Fig. 5.7	Short ‘jump’ distance with the early version of the MaltaHip as no geometrical features are available to prevent dislocation.	121
Fig. 5.8	The conversion from the simplified to the finalised MaltaHip. The former (left) illustrates the major bearing surfaces that were used for the parametric study, and the latter (right) illustrates the finalised MaltaHip design which includes the interlocking mechanism.	122
Fig. 5.9	Assembly steps involved to interlock the components of the MaltaHip prosthesis.	125
Fig. 5.10	Von Mises stresses on the hemispherical cup during gait cycle, at 0.1 s time intervals.	128
Fig. 5.11	Total strain on the hemispherical cup during gait cycle at 0.1 s time intervals.	129
Fig. 5.12	The contact stress values of hemispherical cup during gait cycle at 0.1 s time intervals.	130
Fig. 5.13	Contact status of the hemispherical cup during gait cycle at 0.1 s time intervals.	131
Fig. 5.14	Edge-loading exhibited in the hemispherical cup.	132
Fig. 5.15	Von Mises stresses on the MaltaHip cup (interior view) during gait cycle at 0.1 s time intervals.	135
Fig. 5.16	Von Mises stresses on the MaltaHip rotator (superior view) during gait cycle at 0.1 s time intervals.	136
Fig. 5.17	Von Mises stresses on the MaltaHip rotator (medial view) during gait cycle at 0.1 s time intervals.	137
Fig. 5.18	Total strain on the MaltaHip cup during gait cycle at 0.1 s time intervals.	138
Fig. 5.19	Total strain on the MaltaHip rotator (superior view) during gait cycle at 0.1 s time intervals.	139
Fig. 5.20	Total strain on the MaltaHip rotator (medial view) during gait cycle at 0.1 s time intervals.	140
Fig. 5.21	Contact stress on the MaltaHip cup during gait cycle at 0.1 s time intervals.	141
Fig. 5.22	Contact stress on the MaltaHip rotator (superior view) during gait cycle at 0.1 s time intervals.	142
Fig. 5.23	Contact stress on the MaltaHip rotator (medial view) during gait cycle at 0.1 s time intervals.	143
Fig. 5.24	Contact status of the MaltaHip cup (interior view) during gait cycle at 0.1 s time intervals.	144
Fig. 5.25	Contact status of the MaltaHip rotator (interior view) during gait cycle at 0.1 s time intervals.	145
Fig. 5.26	Contact status of the MaltaHip rotator (interior view) during gait cycle at 0.1 s time intervals.	146
Fig. 5.27	Von Mises stresses on the MaltaHip flexor (superior view) during gait cycle at 0.1 s time intervals.	148
Fig. 5.28	Von Mises stresses on the MaltaHip flexor (inferior view) during gait cycle at 0.1 s time intervals.	149
Fig. 5.29	Anterolateral view: Typical slide tracks of a ball-and-socket implant resulting in cross-shear ratio values ranging between 0.08 and 0.89.	151
Fig. 5.30	Anteromedial view: Typical slide tracks of a ball-and-socket implant resulting in cross-shear ratio values ranging between 0.08 and 0.89.	152

Fig. 5.31	Variation of the CSR values of slide tracks during the gait cycle.	153
Fig. 5.32	Slide tracks of the MaltaHip components. All components possess a cross-shear ratio of 0. The different colouring schemes are only used to distinguish between the different components of the MaltaHip. Note that all axes are in mm.	154
Fig. 5.33	Comparison of the sliding distances of the ball-and-socket and MaltaHip implants.	156
Fig. 5.34	Contacting areas of the articulations of the ball-and-socket and MaltaHip implant designs.	157
Fig. 5.35	Predicted cumulative wear during a gait cycle for UHMWPE ball-and-socket and MaltaHip implants using the Saikko wear model [18].	158
Fig. 5.36	Predicted cumulative wear during a gait cycle for UHMWPE ball-and-socket and MaltaHip implants using the Liu wear model [267].	159
Fig. 5.37	Predicted cumulative wear during a gait cycle for UHMWPE ball-and-socket and MaltaHip implants using the wear model proposed by Kang et al. [303].	160
Fig. 5.38	Overestimation of the wear factor values for UHMWPE at low values of cross-shear ratio, due to the high discrepancy between the experimental and modelled values. Adapted from: [303].	160
Fig. 5.39	Predicted cumulative wear during a gait cycle for UHMWPE ball-and-socket and MaltaHip implants using the wear model proposed by Petrella et al. [303].	161
Fig. 5.40	The direction of the polymer chains on the surface of the MaltaHip cup is dependent on the mounting orientation of the ram extruded bar.	164
Fig. 5.41	Turning processes on the MaltaHip cup using a CNC lathe.	165
Fig. 5.42	The unique geometry of the outer profile of the MaltaHip components was machined using a 5-Axis CNC milling using the swarf milling technique (as opposed to surface milling) to obtain a smooth and continuous surface.	166
Fig. 5.43	Machining procedure used for the fabrication of the flexor component.	167
Fig. 5.44	Machining processes involved in the rotator component.	169
Fig. 5.45	Flat side machined in the taper of the abductor used for alignment.	169
Fig. 5.46	The MaltaHip implant with UHMWPE polymeric components.	170
Fig. 5.47	The MaltaHip implant with VEHXPE polymeric components.	171
Fig. 5.48	The MaltaHip implants that were fabricated and wear tested in the Endolab® hip joint simulator.	172
Fig. 5.49	Assembly of initial version of the MaltaHip implant design which did not include the interlocking mechanism.	173
Fig. 5.50	Assembly of the MaltaHip components.	177
Fig. 5.51	MaltaHip cup, internal superior surface (curved).	180
Fig. 5.52	Range of surface roughness values produced by the MaltaHip cups.	180
Fig. 5.53	MaltaHip rotator, external superior surface (flat).	181
Fig. 5.54	Range of surface roughness values produced by the MaltaHip rotators external flat surfaces.	181
Fig. 5.55	MaltaHip rotator, external superior surface (taper).	182
Fig. 5.56	Range of surface roughness values produced by the MaltaHip rotators external taper surfaces.	182
Fig. 5.57	MaltaHip flexor, external medial surface (flat).	183
Fig. 5.58	Range of surface roughness values produced by the MaltaHip flexors (external taper surfaces).	183
Fig. 5.59	MaltaHip abductor, external superior surface (curved).	184

Fig. 5.60	Range of surface roughness values produced by the MaltaHip abductors (external superior surface).	184
Fig. 5.61	Ball-and-socket hemispherical cup, internal superior pole.	185
Fig. 5.62	Range of surface roughness values produced by the ball-and-socket hemispherical cups (internal superior pole). The surface roughness of the hemispherical cup F2 is still below the 2000 μm threshold as stipulated by the ISO 7206-2. The high discrepancy is likely to be attributed due to different machining techniques that might have been employed as both components were produced from different batches.	185
Fig. 5.63	Ball-and-socket femoral head, external superior pole.	186
Fig. 5.64	Range of surface roughness values produced by the ball-and-socket femoral heads (external superior pole).	186
Fig. 5.65	Flexion/Extension (FE). Minimum FE ROM requirement: 100°. MaltaHip FE ROM result: 235° (130° + 105°).	188
Fig. 5.66	Internal/External (IE) rotation. Minimum IE ROM requirement: 90°. MaltaHip IE ROM result: 145° (75° + 70°).	188
Fig. 5.67	Abduction/Adduction (AA). Minimum AA ROM requirement: 60°. MaltaHip AA ROM result: 90° (50° + 40°).	188
Fig. 5.68	Fluid uptake during the initial soaking and wear testing (500k cycles) of the ball-and-socket and MaltaHip, as produced from the in-house built hip joint simulator.	190
Fig. 5.69	Mean gravimetric wear rates \overline{W}_G of the ball-and-socket, and MaltaHip implants that were wear tested at Endolab® Mechanical Engineering GmbH. Standard error (SE) values are also shown in the bar charts.	192
Fig. 5.70	The t -distribution (left-tailed test) used for the small sample size to determine whether H_0 should be rejected or not, for the case investigating $H_a: \mu < \mu_0$	193
Fig. 5.71	Wear vs. number of cycles of the MaltaHip UHMWPE cup components.	195
Fig. 5.72	Wear vs. number of cycles of the MaltaHip UHMWPE rotator components.	196
Fig. 5.73	Wear vs. number of cycles of the MaltaHip UHMWPE cup and rotator components.	197
Fig. 5.74	Wear vs. number of cycles of the MaltaHip high-N austenitic stainless steel flexor components.	198
Fig. 5.75	Wear vs. number of cycles of the MaltaHip high-N austenitic stainless steel abductor components.	199
Fig. 5.76	Wear vs. number of cycles of the MaltaHip VEHXPE cup components.	201
Fig. 5.77	Wear vs. number of cycles of the MaltaHip VEHXPE rotator components.	202
Fig. 5.78	Wear vs. number of cycles of the MaltaHip VEHXPE cup and rotator components.	203
Fig. 5.79	Wear vs. number of cycles of the MaltaHip high-N stainless steel flexor components.	204
Fig. 5.80	Wear vs. number of cycles of the MaltaHip high-N stainless steel abductor components.	205
Fig. 5.81	Load bearing surface of the UHMWPE MaltaHip cups showing extensive contact (inferior view).	207
Fig. 5.82	Load bearing surface of the VEHXPE MaltaHip cups showing extensive contact (inferior view).	207
Fig. 5.83	Non-load bearing surface of the UHMWPE MaltaHip cups showing minimal contact (lateral view).	208
Fig. 5.84	Non-load bearing surface of the VEHXPE MaltaHip cups showing minimal contact (lateral view).	208
Fig. 5.85	Load bearing surface of the UHMWPE rotator illustrate extensive contact with the internal surface of the flexor (superior view).	210
Fig. 5.86	Load bearing surface of the VEHXPE rotator illustrate nearly complete contact with the internal surface of the flexor (superior view).	210

Fig. 5.87	Medial view of the UHMWPE rotator illustrating extensive contact at the tapered section (load bearing surface) with the internal surface of the flexor, and minimal contact at the cylindrical section (non-load bearing surface) with the internal surface of the flexor.	211
Fig. 5.88	Medial view of the VEHXPE rotator illustrating extensive contact at the tapered section (load bearing surface) with the internal surface of the flexor, and minimal contact at the cylindrical section (non-load bearing surface) with the internal surface of the flexor.	211
Fig. 5.89	Possible abduction rotation, causing contacting and non-contacting regions (Scale of abduction rotation effect is exaggerated for ease of visualisation).	212
Fig. 5.90	Anterior view of the UHMWPE rotator component illustrating extensive contact at the taper section (load bearing surface) and minimal contact at the cylindrical section (non-load bearing surface) with the internal surface of the flexor.	213
Fig. 5.91	Anterior view of the VEHXPE rotator component illustrating extensive contact at the tapered section (load bearing surface) and minimal contact at the cylindrical section (non-load bearing surface) with the internal surface of the flexor.	213
Fig. 5.92	Posterior view of the UHMWPE rotator component illustrating extensive contact at the taper (load bearing surface) and moderate contact at the cylindrical section (non-load bearing surface) with the internal surface of the flexor.	214
Fig. 5.93	Posterior view of the VEHXPE rotator component illustrating extensive contact at the taper (load bearing surface) and moderate contact at the cylindrical section (non-load bearing surface) with the internal surface of the flexor.	214
Fig. 5.94	Internal surface of the UHMWPE rotator illustrating extensive contact with the abductor component (inferolateral view).	216
Fig. 5.95	Internal surface of the VEHXPE rotator illustrating extensive contact with the abductor component (inferolateral view).	216
Fig. 5.96	Internal load bearing surface of the UHMWPE rotator illustrating full contact with the abductor component (inferior view).	217
Fig. 5.97	Internal load bearing surface of the VEHXPE rotator illustrating full contact with the abductor component (inferior view).	217
Fig. 5.98	Anterolateral view of the UHMWPE rotator component illustrating extensive contact at the tapered section (load bearing surface) with the internal surface of the flexor, and moderate contact at its internal section (non-load bearing surface) with the abductor component. Contact area for 1.0 million cycles is not available.	218
Fig. 5.99	Anterolateral view of the VEHXPE rotator component illustrating extensive contact at the tapered section (load bearing surface) with the internal surface of the flexor, and moderate contact at its internal section (non-load bearing surface) with the abductor component. Contact area for 1.0 million cycles is not available.	218
Fig. 5.100	Posterolateral view of the UHMWPE rotator component illustrating extensive contact at the tapered section (load bearing surface) with the internal surface of the flexor, and moderate contact at its internal section (non-load bearing surface) with the abductor component. Contact area for 1.0 million cycles is not available.	219
Fig. 5.101	Posterolateral view of the VEHXPE rotator component illustrating extensive contact at the tapered section (load bearing surface) with the internal surface of the flexor, and moderate contact at its internal section (non-load bearing surface) with the abductor component. Contact area for 1.0 million cycles is not available.	219
Fig. 5.102	Microscopic images of the MaltaHip UHMWPE cup at the internal superior surface.	222
Fig. 5.103	Microscopic images of the MaltaHip UHMWPE cup at the internal medial surface.	223
Fig. 5.104	Microscopic images of the MaltaHip UHMWPE rotator at the external superior surface. ...	224
Fig. 5.105	Microscopic images of the MaltaHip UHMWPE rotator at the external anterior and posterior non-load bearing surfaces.	225
Fig. 5.106	Microscopic images of the MaltaHip UHMWPE rotator at the internal surface.	226
Fig. 5.107	Microscopic images of the MaltaHip VEHXPE cup at the internal superior surface.	229
Fig. 5.108	Microscopic images of the MaltaHip VEHXPE cup at the internal medial surface.	230

Fig. 5.109	Microscopic images of the MaltaHip VEHXPE rotator at the external superior surface.	231
Fig. 5.110	Microscopic images of the MaltaHip VEHXPE rotator at the external anterior and posterior surfaces.	232
Fig. 5.111	Microscopic images of the MaltaHip VEHXPE rotator at the internal surface.	233
Fig. 5.112	External superior load bearing surface of the flexor.	236
Fig. 5.113	External load bearing surfaces of the flexor (regions D and E).	237
Fig. 5.114	External load bearing surfaces of the flexor (regions F and G).	238
Fig. 5.115	Internal surfaces of the flexor (regions H and I).	239
Fig. 5.116	Load bearing surface of the abductor.	240
Fig. 5.117	External surface of the abductor.	241
Fig. 5.118	Load bearing surface of the abductor.	242
Fig. 5.119	External surface of the abductor.	243
Fig. 5.120	Representative boxplot, illustrating the statistical mean, median and the different zones of the percentiles used in this work. Source: Endolab® report (unpublished).	246
Fig. 5.121	Box plot illustrating the equivalent circle diameter (ECD) of the UHMWPE (1.1) and VEHXPE (2.1) wear particles.	246
Fig. 5.122	Frequency and cumulative frequency of the equivalent circle diameter (ECD) for the two main type of polymers being investigated in this work.	247
Fig. 5.123	FE-SEM images of (a) UHMWPE and (b) VEHXPE wear particles generated by the MaltaHip implants between 4.5 and 5.0 million cycles.	248
Fig. 5.124	Total hip replacement using the MaltaHip implant.	249
Fig. 5.125	Preparation of the femur bone and insertion of the femoral implant.	251
Fig. 5.126	Implantation of the MaltaHip cup and reduction of the hip.	252
Fig. 6.1	Comparison of contact stress values of the MaltaHip components using elastic linear model and the Three Network model. The elastic linear model overestimates the actual stress values.	260
Fig. 6.2	Comparison of von Mises stress values of the MaltaHip components using elastic linear model and the Three Network model.	261
Fig. 6.3	Thickness profile of the MaltaHip polymeric components.	263
Fig. 6.4	Comparison of wear models on conventional ball-and-socket and MaltaHip implants.	269
Fig. 6.5	Comparison of the theoretical contact area based on finite element analysis and experimental testing. Note: yellow area indicates that surfaces are near. Light orange area indicates sliding contact. Dark orange area indicates sticking contact.	271
Fig. 6.6	Comparison between the volumetric wear rates obtained in this work using the theoretical wear models (Liu and Petrella), and experimental results (produced by Endolab® hip joint simulator).	273
Fig. 6.7	Variation of volumetric wear rates across different hip joint simulators obtained during wear testing with the same metal-on-polyethylene implant design. Adapted from: [324].	274
Fig. 6.8	Steady-state wear rates of commonly used material couples in hip implant bearings as tested using the Endolab® hip joint simulator. Each dot represents the average of three bearing couples of the same design. Adapted from: [66].	275
Fig. 6.9	Postulated abrasion wear due to different slide tracks being generated as a consequence of an embedded hard particle (represented by the black dot) with different activities performed by the implant-bearer.	277
Fig. 6.10	Hemispherical cup is prone to high rates of wear during running-in due to orientation softening as a consequence of the machining process.	278

Fig. 6.11	Box plot illustrating the statistical data concerning the equivalent circle diameter (ECD) of the particles produced by the MaltaHip and the ball-and-socket design. See the representative boxplot in Fig. 5.120 (p. 246) for an explanation of the statistical mean, median and the different zones of the percentiles used in these box plots. Source: Endolab® report (unpublished).	288
Fig. 6.12	Articulations of the dual-mobility hip implant. Adapted from: [368].	292
Fig. 6.13	Different assembly methods used of dual-mobility implant. Source: [369].	293
Fig. 6.14	Activities requiring extreme joint angles.	294

List of Tables

Table	Description	Page
Table 1.1	Classification of hip implant with different material combinations.	1
Table 2.1	Three Network Model material parameters. Source: [235].....	32
Table 2.2	Tested slide tracks (Load: Sinusoidal dynamic contact pressure: 15 MPa, Cycles: 10k). Adapted from: [245].	48
Table 2.3	Specific Biological Activity (<i>SBA</i>) and Functional Biological Activity (<i>FBA</i>). Source: [306].	62
Table 3.1	Mathematical functions defining the angular motions of the hip, as specified by ISO 14242-1:2014/Amd 1:2018. Source: [315].	67
Table 3.2	Mathematical functions defining the load profile of the hip, as specified by ISO 14242- 1:2014/Amd 1:2018. Source: [315].	68
Table 3.3	Range of values tested for each design parameter.	71
Table 3.4	Summary of the variables required to computed the parameters of each wear model.	82
Table 4.1	Specifications of the selected motors for the motion mechanism.	102
Table 5.1	Calibrated material model parameters of UHMWPE and VEHXPE using MCalibration. ..	108
Table 5.2	Optimised principal design parameters of the MaltaHip.....	120
Table 5.3	Comparison in stress values between the ball-and-socket and MaltaHip implants.	132
Table 5.4	Summary of surface roughness values (R_a) of the MaltaHip implant.	179
Table 5.5	Summary of surface roughness values (R_a) of the ball-and-socket implant.	179
Table 5.6	The minimum range of motion (ROM) required by ISO 21535:2007/Amd 1:2016, and the results produced by the MaltaHip.	187
Table 5.7	Summary of steady-state gravimetric wear rates using UHMWPE bearing components. The steady-state gravimetric wear rate results of the individual polymeric components of the MaltaHip, as well as their combined effect (considered as a whole implant) are presented. All values have been corrected by the fluid absorption data obtained from the loaded soak control.	192
Table 5.8	Summary of steady-state gravimetric wear rates using VEHXPE bearing components. The steady-state gravimetric wear rate results of the individual polymeric components of the MaltaHip, as well as their combined effect (considered as a whole implant) are presented. All values have been corrected by the fluid absorption data obtained from the loaded soak control.	192
Table 5.9	Summary of the statistical data used to compute the test statistic T_{st}	193
Table 5.10	The mean gravimetric wear rate (mg/million cycles) is computed during the running-in and steady-state periods, and the overall duration, based on linear regression results of MaltaHip UHMWPE cups 1.1 – 1.3. The rate of fluid absorption (mg/million cycles) is also presented based on the loaded soak control MaltaHip UHMWPE cup 1.4.	195
Table 5.11	The mean gravimetric wear rate (mg/million cycles) is computed during the running-in and steady-state periods, and the overall duration, based on linear regression results of MaltaHip UHMWPE rotators 1.1 – 1.3. The rate of fluid absorption (mg/million cycles) is also presented based on the loaded soak control MaltaHip UHMWPE rotator 1.4. Note that R^2 represents the regression coefficient, whereas SE represents the standard error.	196
Table 5.12	The mean gravimetric wear rate (mg/million cycles) is computed during the running-in and steady-state periods, and the overall duration, based on linear regression results of MaltaHip UHMWPE cups and rotators 1.1 – 1.3. The rate of fluid absorption (mg/million cycles) is also presented based on the loaded soak control MaltaHip UHMWPE cup and rotator 1.4. Note that R^2 represents the regression coefficient, whereas SE represents the standard error.	197

Table 5.13	The mean gravimetric wear rate (mg/million cycles) is computed based on linear regression results of MaltaHip High-N stainless steel flexors 1.1 – 1.3.	198
Table 5.14	The mean gravimetric wear rate (mg/million cycles) is computed based on linear regression results of MaltaHip high-N stainless steel abductors 1.1 – 1.3.	199
Table 5.15	The mean gravimetric wear rate (mg/million cycles) is computed during the running-in and steady-state periods, and the overall duration, based on linear regression results of MaltaHip VEHXPE cups 2.1 – 2.3. The rate of fluid absorption (mg/million cycles) is also presented based on the loaded soak control MaltaHip VEHXPE cup 2.4. Note that R^2 represents the regression coefficient, whereas SE represents the standard error.	201
Table 5.16	The mean gravimetric wear rate (mg/million cycles) is computed during the running-in and steady-state periods, and the overall duration, based on linear regression results of MaltaHip VEHXPE rotators 2.1 – 2.3. The rate of fluid absorption (mg/million cycles) is also presented based on the loaded soak control MaltaHip VEHXPE rotator 2.4. Note that R^2 represents the regression coefficient, whereas SE represents the standard error.	202
Table 5.17	The mean gravimetric wear rate (mg/million cycles) is computed during the running-in and steady-state periods, and the overall duration, based on linear regression results of MaltaHip VEHXPE cups and rotators 2.1 – 2.3. The rate of fluid absorption (mg/million cycles) is also presented based on the loaded soak control MaltaHip VEHXPE cup and rotator 2.4. Note that R^2 represents the regression coefficient, whereas SE represents the standard error.	203
Table 5.18	The mean gravimetric wear rate (mg/million cycles) is computed based on linear regression results of MaltaHip High-N Stainless Steel Flexors 2.1 – 2.3.	204
Table 5.19	The mean gravimetric wear rate (mg/million cycles) is computed based on linear regression results of MaltaHip high-N stainless steel abductors 2.1 – 2.3.	205
Table 5.20	Morphological characterisation of the UHMWPE analysed particles generated between 4.5 and 5.0 million cycles.	245
Table 5.21	Morphological characterisation of the VEHXPE analysed particles generated between 4.5 and 5.0 million cycles.	245
Table 6.1	Specific Biological Activity (<i>SBA</i>) and Functional Biological Activity (<i>FBA</i>). Source:.....	289

Glossary of Symbols

Symbol	Description
<i>A</i>	Area
A	Matrix representing dimensions of the abductor
<i>a</i>	Pressure dependence of flow
A_c	Abductor clearance
A_f	Abductor exterior fillet
A_{t1}	Abductor internal thickness
A_{t2}	Abductor wall thickness
AA	Abduction/Adduction
AR	Aspect ratio
ASTM	American Society for Testing and Materials
<i>B</i>	Biological activity
BW	Body weight
<i>C</i>	Volumetric concentration
C	Matrix representing dimensions of the MaltaHip cup
C_t	Cup thickness
C_w	Wear coefficient
CNC	Computer numerical control
CoC	Ceramic-on-ceramic
COG	Centre of gravity
CoM	Ceramic-on-Metal
CoP	Ceramic-on-Polyethylene
CSR	Cross-shear ratio
d_{max}	Longest distance between any two points of the wear particle
d_{min}	Longest perpendicular distance to d_{max}
d_w	Linear wear depth
DOF	Degree of freedom
<i>E</i>	Elastic modulus
EC	Eight-Chain model
ECD	Equivalent circle diameter
EtO	Ethylene oxide
<i>F</i>	Normal force
F	Matrix representing dimensions of the flexor
F_c	Flexor clearance

F_f	Flexor fillet
F_M	Muscle force
F_{t1}	Flexor internal thickness
F_{t2}	Flexor external thickness
f_x	Sliding frequency in the x direction
f_y	Sliding frequency in the y direction
FBA	Functional biological activity
FE	Flexion/Extension
FF	Form factor
G	Shear modulus
HDPE	High density polyethylene
HXPE	Highly crosslinked polyethylene
i	Index of summation
j	Discretised locations on the wear surface corresponding to the nodes of the finite element model
I_2	An invariant representing a scalar value that is obtained from the stress tensor function
IE	Internal/External rotation
ISO	International Standards Organization
H_0	Null hypothesis
H_a	Alternative (research) hypothesis
k	Wear factor
k^*	Wear factor for the worst case scenario for cross-shear sliding motion
k_a	Experimentally-derived coefficient for the Kang model
k_b	Experimentally-derived coefficient for the Kang model
k_c	Experimentally-derived coefficient for the Kang model
k_o	Wear factor associated for unidirectional sliding motion
k_p	Constant related to the probability per unit encounter of production of a wear particle
L	Applied load
L_a	Long lever arm (perpendicular distance from the axis of rotation to the line of action of the partial body weight)
l_a	Short lever arm (perpendicular distance from the axis of rotation to the line of action of the muscle force)
LDPE	Low density polyethylene
LMC	Least material condition
LLDPE	Linear low density polyethylene
m_A	Stress exponential of network A
m_B	Stress exponential of network B

mc	Million cycles
$m_{i,j}$	Incremental weight factor that considers the material memory of the molecular chains
mem	Number of steps required to align the polymer chain according to direction of sliding motion
MMC	Maximum material condition
MoC	Metal-on-ceramic
MoM	Metal-on-metal
MoP	Metal-on-polyethylene
N	Upper bound of summation
n	Number of cycles
n_t	Temperature exponential
N_n	Number of contact nodes
P	Perimeter
p	Pressure
p_m	Flow pressure of the softer material
p_o	Maximum contact pressure
\vec{p}_o	Vector representing initial node position
\vec{p}_t	Vector representing transferred position
q	Relative contribution of modified eight-chain of network C
q_i	Discrete force
q_{ST}	Surface traction
R	Reaction force at the hip
\mathbf{R}	Matrix representing dimensions of the rotator
r	Size of the wear particle
R_a	Surface roughness
R_c	Rotator clearance
R_d	Rotator diameter
R_f	Rotator fillet
\mathbf{R}_t	Rotational matrix
R_{t1}	Rotator internal thickness
R_{t2}	Rotator height
R_1	Reaction force at hip 1 (during standing)
R_2	Reaction force at hip 2 (during standing)
R^2	Regression coefficient
S_n	average increase in mass of the control implant due to fluid absorption
SBA	Specific biological activity
SD	Standard deviation

SE	Standard error of mean
T	Stress relaxation time
T_{st}	Test statistic
t	Time
t_j	Discrete time steps
TN	Three Network model
T_g	Glass transition temperature
TAR	Total ankle replacement
THR	Total hip replacement
UHMWPE	Ultra-high molecular weight polyethylene
VEHXPE	Vitamin E-infused highly crosslinked polyethylene
XPE	Crosslinked polyethylene
W	Upper body weight (trunk, head and arms)
W'	Partial body weight (trunk, head, arms and lifted leg)
W_{an}	Average uncorrected mass
W_G	Gravimetric wear rate
$\overline{W_G}$	Mean gravimetric wear rate
W_l	Longitudinal frictional work
W_N	Gravimetric wear at N cycles
W_t	Transverse frictional work
W_V	Volumetric wear rate
x	Sliding distance
α	Thermal expansion coefficient
α_f	Angle of applied stress relative to the molecular chain direction
β	Evolution rate of shear modulus of network B
γ	Elastic shear strain
$\dot{\gamma}_v$	Viscous shear rate
ϵ	Strain
ϵ_1	Strain of the spring
ϵ_2	Strain of the damper
η	Viscosity of the dashpot
θ	Working temperature
$\hat{\theta}$	Temperature factor
θ_0	Thermal expansion reference temperature
θ_a	Angle between partial body weight W' and muscle force F_M
$\theta_{i,j}$	Angle of the segment during the current time increment
κ	Bulk modulus

λ_L	Locking stretch
μ	Coefficient of friction
μ_0	Population mean
μ_A	Shear modulus of network A
μ_{Bi}	Initial shear modulus of network B
μ_{Bf}	Final shear modulus of network B
μ_U	Mean gravimetric wear rate of population of UHMWPE ball-and-socket implants
μ_C	Shear modulus of network C
μ_V	Mean gravimetric wear rate of population of XPE ball-and-socket implants
σ	Stress
σ_l	Longitudinal stress
σ_t	Transverse stress
$\hat{\tau}_A$	Flow resistance of network A
$\hat{\tau}_B$	Flow resistance of network B
τ_e	Elastic shear stress
τ_{lt}	Shear stress
τ_v	Viscous shear stress

1. Introduction

1.1. Background and Motivation

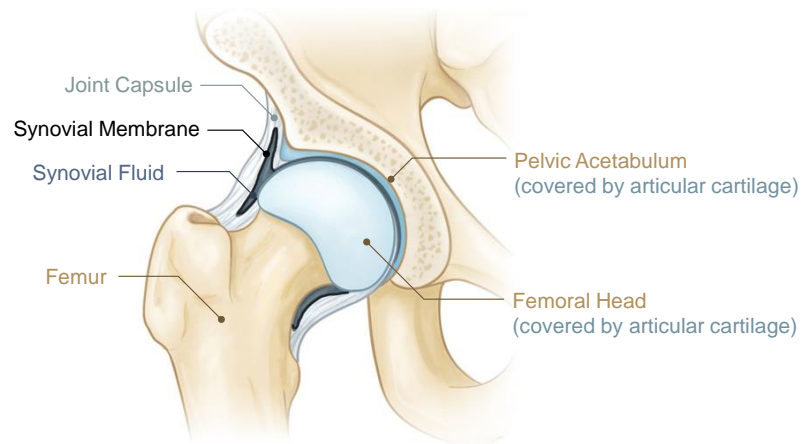
The natural hip joint is formed at the junction of the pelvic acetabulum and the femoral head, forming a synovial ball-and-socket joint. It serves as a load bearing joint, provides a wide range of motion, and maintains the stability of the body [1–4]. The ball-and-socket geometry enables the joint to articulate about three orthogonal anatomical axes, which are referred to as the flexion/extension (FE), abduction/adduction (AA) and internal/external rotation (IE) [2]. The stability of the joint is maintained by the ligamentous capsule that surrounds the joint, thus limiting the extent of disengagement between the two opposing surfaces [3]. Despite the demanding conditions, the functional longevity of the natural joint is maintained by the articular cartilage, a continuously growing tissue, which prevents the direct contact of the bone surfaces, as illustrated in Fig. 1.1a. The articular cartilage is continuously lubricated by the synovial fluid which is produced by the synovial membrane and encapsulated in the joint [2].

Prolonged life expectancy and obesity are amongst the common factors that compromise the integrity of the articular cartilage [5, 6]. This forms part of a condition, known as osteoarthritis, which compromises the protective joint space as it exposes the bone surfaces, limiting the motion of the joint and inducing pain [7]. In chronic situations, a total hip replacement (THR) is conducted to restore the functionality of the hip. THR is also required to help remedy other diseases, including rheumatoid arthritis (whereby the autoimmune system mistakenly attacks the body’s own tissue), avascular necrosis of the hip (a condition which hinders the blood flow to the bones), and any other condition which compromises the functionality of the hip [8].

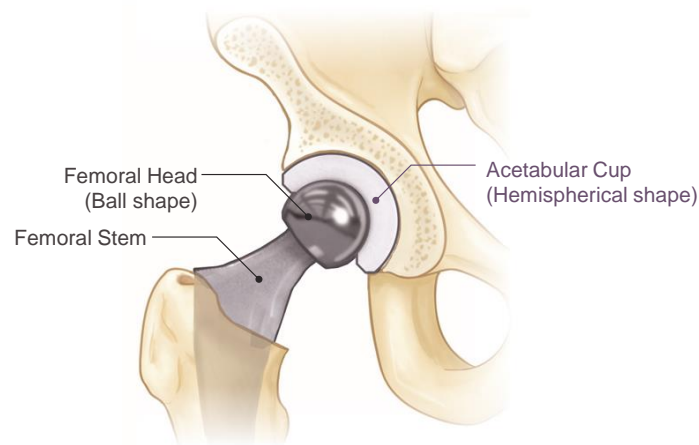
The artificial hip prosthesis consists mainly of a femoral head which articulates against a hemispherical acetabular cup, as shown in Fig. 1.1b. Commercial hip implants come in a range of material combinations, which are classified under hard-on-soft [9], and hard-on-hard bearing materials [10], as shown in Table 1.1.

Table 1.1: Classification of hip implant with different material combinations.

Hard-on-soft	Hard-on-hard
<ul style="list-style-type: none">• Metal-on-polyethylene (MoP)• Ceramic-on-polyethylene (CoP)	<ul style="list-style-type: none">• Metal-on-metal (MoM)• Ceramic-on-metal (CoM)• Ceramic-on-ceramic (CoC)



(a) Natural hip joint.



(b) Artificial hip joint.

Fig. 1.1: Anatomy of the hip joint. Adapted from: [11].

The MoP hip implant is the most used type of prosthesis by orthopaedic surgeons. In fact, MoP implants account for over one-third of all hip implants sales worldwide [12]. The acetabular cups are produced from either ultra-high molecular-weight polyethylene (UHMWPE, specified by ASTM F648) or highly crosslinked polyethylene (HXPE, specified by ASTM F2565). The latter can be blended with alpha-tocopherol (Vitamin E) for improved oxidation resistance (VEHXPE, specified by ASTM F2695). Both types of polyethylene can be produced from different powder grades (GUR 1020 or GUR 1050). The metallic femoral head in MoP implants is usually produced from 316LVM stainless steel (ASTM F138), high-nitrogen austenitic stainless steel (ASTM F1586), or cobalt-chromium-molybdenum alloy (ASTM F75). The ubiquitous use of MoP implants is attributed to their relatively low cost of raw materials, compared to prostheses produced out of ceramic materials, and their low severity of clinical complications, compared to hard-on-hard implants with metallic components which can induce nanotoxicity effects.

Despite the successful recovery of hip joint function, MoP implants have a limited lifespan which require the patient to undergo revision surgery after 15 – 25 years [13]. Unfortunately, revision surgery tends to be more complicated, costly, and possesses lower rates of success [14]. The main reason for the limited lifespan of MoP implants is mostly attributed to the compromised tribological performance of the polyethylene component. It has been observed that the strength of the polyethylene surface molecules is diminished due to multi-directional sliding motion which occurs due to molecular orientation softening mechanisms [15–17]. Furthermore, contact stress concentrations promote the liberation of wear particles [18–20]. Both of these factors are enhanced by the ball-and-socket geometry of the articulation.

Research efforts have been focussed on improving the wear resistance of the polyethylene components [21–24]. Despite of the numerous prosthetic hip joints are available on the market, their geometrical design has remained practically the same since their inception. Inspired by the low rates of osteoarthritis of the ankle joints (being 9 to 10 fold lower than those exhibited in hip and knee joints [25]), this work exploits the biomimetics of the ankle joint to provide a unique artificial articulation that is essentially based on the cylindrical (hinge) joint [2]. The geometrical design of the articulation is intended to produce uni-directional sliding motion (to promote molecular orientation hardening mechanisms in polyethylene), under distributed contact stress conditions (to minimize the volume of wear particles that are liberated). The flexible motion of the ball-and-socket is reproduced by using three cylindrical articulations that are aligned orthogonal to each other. The molecular orientation hardening mechanisms were observed in both UHMWPE and VEHXPE materials, and thus both materials will be applied to the new design of the prosthetic hip.

1.2. Hypothesis Statement

Considering that polyethylene is prone to orientation hardening mechanisms (which drastically improve its wear resistance), together with its potential application to a prosthetic hip, the research hypothesis statement is formulated in this section. The MoP hip implant with a ball-and-socket design is currently regarded as the gold standard in the industry. Hence, any other hip implant design, such as the one consisting of three orthogonal cylindrical articulations being proposed, is regarded to provide inferior performance, and hence is not exploited in the field. In relation to the new articulation mechanism being proposed in this work, the null hypothesis H_0 statement is formulated as follows:

H_0 : An artificial hip consisting of three metal-on-polyethylene cylindrical articulations, aligned perpendicular to each other, produces at least equal or higher rate of gravimetric wear than that produced in an artificial hip consisting of a metal-on-polyethylene ball-and-socket articulation.

Gravimetric wear rate data was obtained from Endolab® Mechanical Engineering GmbH and is used to represent the population means¹ for the two polymeric materials (UHMWPE and VEHXPE) being investigated in this work. Therefore, the null hypothesis H_0 for the new prosthetic hip consisting of UHMWPE components can be mathematically expressed as follows,

$$H_0: \mu_U \geq 29.1 \text{ mg/mc} \quad \text{Eq. 1.1}$$

where, μ_U represents the mean gravimetric wear rate of UHMWPE components, and mg/mc denotes milligrams per million cycles. Similarly, the null hypothesis H_0 for the new prosthetic hip consisting of VEHXPE components can be mathematically expressed as follows,

$$H_0: \mu_V \geq 4.5 \text{ mg/mc} \quad \text{Eq. 1.2}$$

where, μ_V represents the mean gravimetric wear rate of XPE components. It is postulated that an artificial hip that exploits such mechanism could potentially produce lower rates of wear than a conventional ball-and-socket implant.

Given the observations made regarding the reduced wear rate with uni-directional sliding articulations, the alternative (research) hypothesis H_a statement to be investigated (i.e. the claim to be tested in this work) is formulated as follows,

H_a : An artificial hip consisting of three metal-on-polyethylene cylindrical articulations, aligned perpendicular to each other, produces lower rate of gravimetric wear than that produced in an artificial hip consisting of a metal-on-polyethylene ball-and-socket articulation.

Therefore, the alternative hypothesis H_a for the new prosthetic hip consisting of UHMWPE components can be mathematically expressed as follows,

$$H_a: \mu_U < 29.1 \text{ mg/mc} \quad \text{Eq. 1.3}$$

Similarly, the alternative hypothesis H_a for the new prosthetic hip consisting of VEHXPE components can be mathematically expressed as follows,

$$H_a: \mu_V < 4.5 \text{ mg/mc} \quad \text{Eq. 1.4}$$

The possible outcome for the hypothesis testing is to either ‘reject’ or ‘fail to reject’ the null hypothesis H_0 . Hypothesis testing in this work was conducted at 99% confidence interval. If the null hypothesis H_0 is rejected, this implies that H_a is more accurate, based on the data obtained

¹ It should be noted that gravimetric wear rates produced by different hip joint simulators and experimental setups are incomparable, due to specific machine factors which induce discrepancies in the results. Hence, in this work, the mean gravimetric wear rates obtained from Endolab® Mechanical Engineering GmbH will be regarded to represent the mean gravimetric wear rate of the population.

from this work. It should be noted that rejection of the null hypothesis H_0 does not prove that the H_a is true, but rather implies that the observations made in this work conform to the research hypothesis statement that was put forward in this study.

1.3. Objectives

A provisional design for a prosthetic hip, hereinafter referred to as the MaltaHip, that is based on the biomimicry of the natural ankle joint, was developed throughout this work. Therefore, the design leverages on the enhanced wear resistance of the polyethylene materials when subjected to uni-directional sliding motion and reduced levels of contact stress. Hence, the main objectives of this work were as follows:

1. Design the new prosthesis, hereinafter referred to as the MaltaHip, consisting of cylindrical articulations that can reproduce the 3 degrees-of-freedom (DOFs) of the hip.
2. Perform finite element simulations to analyse the structural integrity of the MaltaHip implant.
3. Predict the wear rate of the MaltaHip implant based on theoretical wear models that are available in literature.
4. Fabricate the MaltaHip implants using clinically-approved materials whilst abiding to the design standards in the field.
5. Develop an experimental test rig (hip joint simulator) to verify the functionality of the new articulation mechanism of the MaltaHip concept and to provide initial indications on its tribological performance.
6. Perform a comprehensive wear testing regime using hip joint simulation according to ISO 14242-1:2014/Amd 1:2018 at an accredited implant testing facility.
7. Perform a morphological analysis on the generated wear particles according to ISO 17853:2011 at an accredited implant testing facility.
8. Perform a mock surgery on a cadaver to assess the ease of implantation, range of motion, and stability inside the body.
9. Compare the tribological performance of the tested MaltaHip implants to the performance of other ball-and-socket hip implants that were subjected to the same wear testing conditions.

2. Literature Review

2.1. Introduction

2.1.1. Low-Friction Arthroplasty

The design of the most commonly used contemporary hip implant is based on the *low-friction arthroplasty* principle, as pioneered by Sir John Charnley in the early 1960s [26, 27]. The paradigm-shifting design was developed after Charnley observed that hard-on-hard artificial hips succumbed to failure as a consequence of high frictional effects [26]. Metal-on-metal artificial hips failed due to high frictional effects caused by poor machining tolerances, resulting in deterioration of the cement bonds [28], followed by loosening of the implants [29]. On the other hand, first-generation alumina components used in ceramic-on-ceramic hip implants were prone to high fracture rates [30].

The notion of low-frictional torque arthroplasty was embodied through the use of a small-diameter femoral head coupled with a soft ultra-high molecular weight polyethylene (UHMWPE) acetabular cup, as illustrated in Fig. 2.1. The introduction of an intrinsically self-lubricating material was fundamental to the low-friction arthroplasty principle [28]. Sir John Charnley observed that UHMWPE was the ideal candidate material, not only for its relatively high abrasion resistance [31, 32] and low-frictional effects [33], but also for its excellent impact [34, 35], fracture [36, 37], and chemical resistance [38]. In addition, Charnley postulated that a small-diameter ball could further minimize the generation of free wear particles by burnishing the particulate matter into the polymer surface, as opposed to large diameter counterface, such as in the case of the knee, which promotes rolling and sliding motion that sets polymer wear particles free [28].

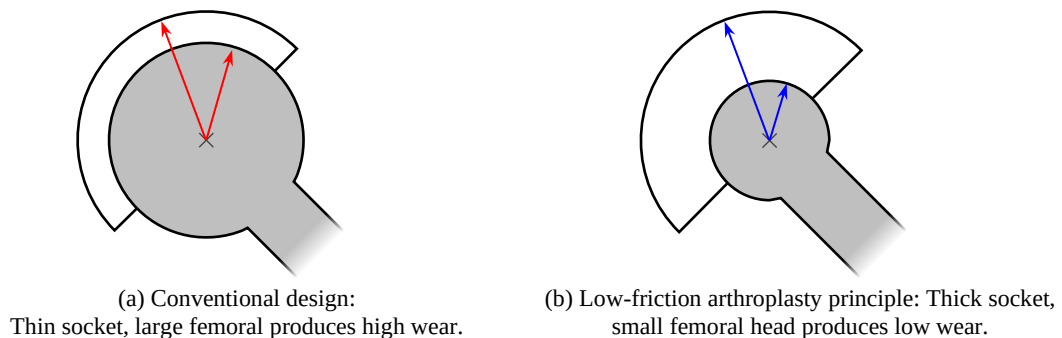


Fig. 2.1: Illustration of the low-friction torque principle applied to hip arthroplasty as proposed by Charnley.
Adapted from: [1].

2.1.2. Wear and Associated Clinical Complications

Aseptic loosening² is the leading cause of metal-on-polymer hip implant failure, accounting to 47.2%³ of all revision surgeries [39]. Unfortunately, this phenomenon induces pain and hinders hip functionality [40–43]. This phenomenon is initiated through exposure of the joint to polymeric wear debris generated at the articulation of the prosthesis, which activates the macrophages found in the bone tissue causing osteolysis⁴ [44–48]. It is not the wear volume on its own that determines the biological response to the debris, but rather the concentration of the wear volume that is within the critical size range (0.1 – 1.0 μm) for bone tissue destruction [43, 49].

Another clinical complication of the artificial hip that leads to revision surgery is dislocation secondary to prosthesis malposition⁵ [50]. The risk for dislocation decreases with increasing head diameters⁶ [51–53], as shown in Fig. 2.2. Hip dislocation is highly dependent on the specific geometry of the prosthesis and independent of the materials that are used [51]. A larger prosthetic head offers enhanced stability over a smaller one, as it requires greater displacement to ‘jump’ from the cup [52, 54]. Despite these anti-dislocation benefits, larger femoral heads have been associated with increased polyethylene wear rates, thus accelerating osteolysis and subsequent loosening of the prosthetic implant [55, 56]. Other causes leading to revision surgery include periprosthetic fracture and infection [57, 58]. The latter is the leading cause for the low success rate of revision surgery. Clinical complications associated with removal of primary implant and fixation of the newer prosthesis to the compromised bone stock further hinder the lifespan of the revised prosthesis [59].

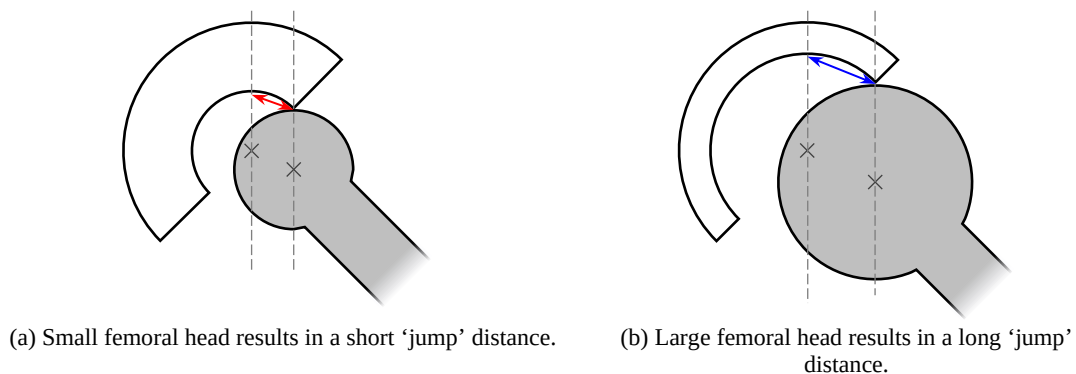


Fig. 2.2: Hip dislocation dependent on femoral head size which dictates the ‘jump’ distance that is required. Adapted from: [60].

² Aseptic loosening: Lack of implant stability leading to its mobilization.

³ Based on data between 1 April 2003 and 31 December 2019 [39].

⁴ Osteolysis: Erosive bone resorption.

⁵ Dislocation occurs between 2 – 5% of primary surgeries, and 5 – 10% of revision surgeries [50].

⁶ Typical range of femoral head diameters: 22 to 46 mm [53].

2.1.3. Developments in THR

Despite the ubiquitous use of UHMWPE as the principal load-bearing surface in artificial hip implants, accounting nearly 60% of the market⁷ [12], the relatively weak wear resistance of UHMWPE (as compared to metallic bearing surfaces) is partly responsible for the aseptic loosening mechanism, effectively limiting the operational lifetime of the prostheses [46, 61, 62]. This issue is further exacerbated by the growing demand as a consequence of increasing population age and weight, which escalates the incidence of intra-articular degenerative arthritis [63].

Efforts to improve wear have been largely focussed on improving the materials rather than the design, with emphasis being put on the UHMWPE components. Carbon fibre-reinforced polyethylene (Poly-II®, Zimmer)⁸ is an example of a novel biomaterial that was introduced in the clinical market, however failed clinically due to poor fibre-matrix adhesion [64–66]. Highly-crystalline polyethylene (Hylamer®, DuPuy/Du Pont)⁹ is another instance of an alternative cup material, which was attained using hot isostatic pressing processes involving higher process temperatures and pressures than conventional techniques [67]. Unfortunately, highly crystalline polyethylene succumbed to high wear rates, delamination and fractures [68–72], mainly attributed to formation of ill-defined orthorhombic or monoclinic crystal structures [67]. Both variants had been retracted from the market due to their poor clinical performance.

A major leap in the field of hip arthroplasty was achieved with the synthesis of crosslinked-polyethylene (XPE) as it was demonstrated to significantly limit the wear debris volume [73–77]. Nonetheless, this polyethylene variant was prone to oxidation causing the cup to undergo embrittlement [73, 78, 79].

During the oxidation process, macroalkyl free radicals are formed due to radiolytic cleavage of C-H bonds of the polyethylene [80]. Additionally, macroallyl free radicals are formed due to the migration of alkyl radicals next to a transvinylene group with diffused oxygen. The reaction of macroalkyl and macroallyl produces peroxy free radicals. The peroxy free radicals extract hydrogen atoms from the neighbouring -CH₂- units, producing hydroperoxides and further new macroalkyl radicals [81]. The decomposition of hydroperoxides to carbonyl species such as ketones, esters, and acids is used to determine the extent of oxidation in UHMWPE [82].

⁷ Data reported from studies conducted in 2019 [12]. Includes metal-on-polymer and ceramic-on-polymer hip implants.

⁸ Poly II®: Released in the 1976, discontinued in 1983 [22, 64].

⁹ Hylamer®: Released in the late 1980s, discontinued in the late 1990s [68, 71].

The detrimental effects of oxidation were circumvented by diffusing Vitamin E (alpha-tocopherol) into the polyethylene (VEHXPE) [83, 84]. Short to midterm follow-up studies demonstrated reduced rates of osteolysis and revision surgeries [85–88], even at up to 16 years follow-up [89]. On the other hand, other studies [90, 91] have highlighted that the reduced radiological wear¹⁰ of crosslinked-polyethylene did not directly correlate to reduced osteolysis or wear-related revision surgery. This could potentially limit the extent of perceived benefits attained using XPE over its conventional type. Since the diameters of the wear particulates of XPE are smaller than those produced by conventional UHMWPE, these can possibly cause higher inflammatory reactions in the long-run [92]. As a result of its recent introduction, long-term follow-up studies are still needed to scrutinize the biological effect of XPE wear debris [93].

Geometrical developments remained relatively modest since the inception of the artificial joint [50], as shown in Fig. 2.3. Designs that deviate from the conventional ball-and-socket design have been developed to target specific age groups with specific functions. These include the hip resurfacing implant [94, 95], a bone-preserving technique intended for young and active patients, and the dual-mobility hip implant [96, 97], which are more resistant to dislocation whilst permitting a wider range of motion. Nonetheless, the fundamental design of such implants still relies on the concept of the ball-and-socket joint.

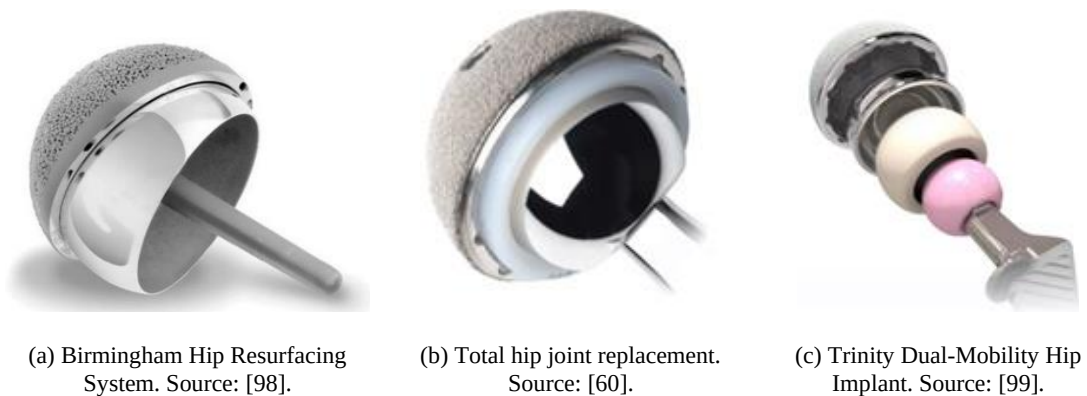


Fig. 2.3: Design variations of hip implants on the market.

¹⁰ Radiological wear: Wear measurement as interpreted from medical images which illustrate the femoral head penetration into the acetabular cup.

2.2. Biomechanics of the Hip Joint

2.2.1. Introduction

A biomechanical analysis of the hip joint is necessary to determine the reaction forces and the corresponding distribution of contact stresses [1]. The biomechanics of the hip are governed by the continuous action of the muscles which must adapt to the body weight and type of activity performed by the individual [2]. The magnitude and exposure time of these stresses dictate the lifespan of the natural and artificial hip joints [1, 2]. For ease of reference, the anatomical directions of the hip (medial/lateral, superior/inferior, anterior/posterior) are provided in Fig. 2.4, which will be used throughout the dissertation.

2.2.2. Hip Joint Reaction Force

Theoretical models have been developed in literature to determine the reaction forces at the hip joint [1, 100]. Anatomical variations can drastically influence the biomechanical response of the hip, and therefore influence the muscle tension as well as the contact stresses at the joint [101, 102]. To outline the mechanics principle involved in the hip joint system, all forces will be considered acting on a 2D plane. When standing erect on both legs, the weight of the upper body W (trunk, head and arms) is supported by the two hip joints, as shown in Fig. 2.5a. In this configuration, each hip carries 50% of the upper body weight (which corresponds to 31% of the total body weight) as represented by R_1 and R_2 [1, 2].

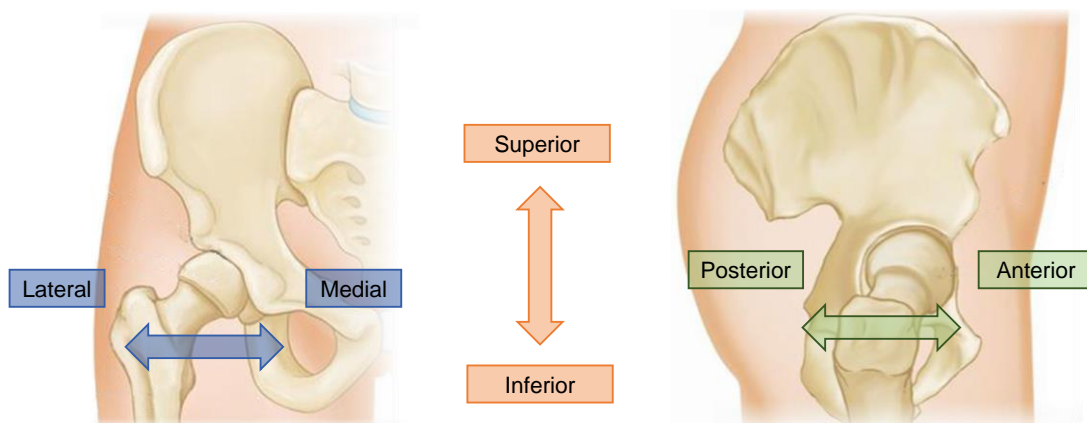


Fig. 2.4: Anatomical directions relative to the hip. Adapted from: [11].

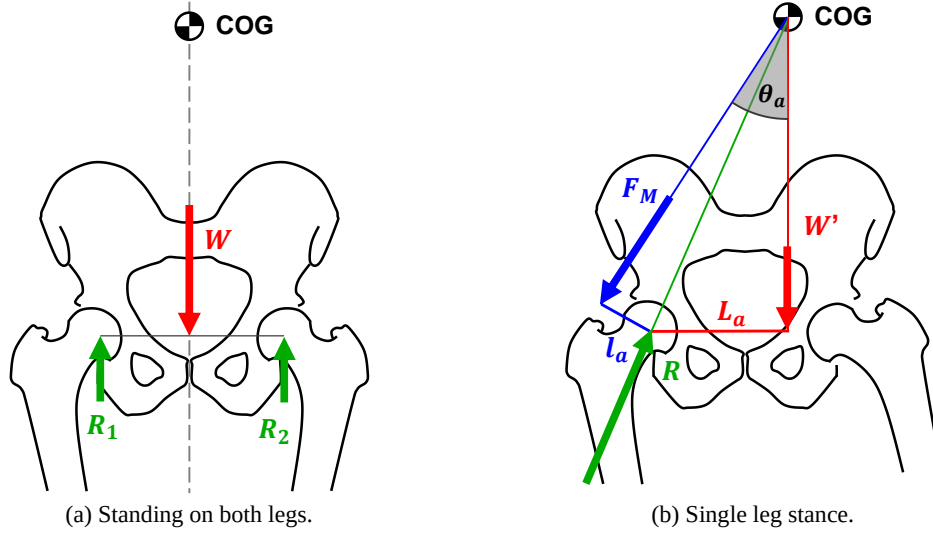


Fig. 2.5: Hip reaction forces on the hip during different loading conditions. Adapted from: [100].

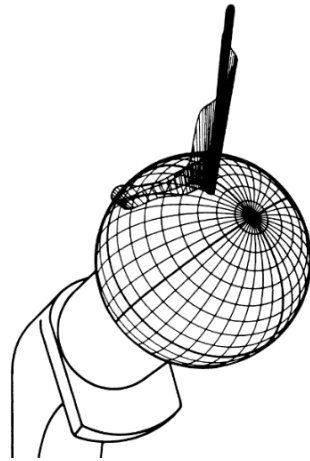
The instant the leg is lifted during walking represents a single leg stance, as shown in Fig. 2.5b. For the sake of simplification, it is assumed that the leg is lifted slowly, such that its acceleration is negligible, and therefore the static scenario can be assumed. The loaded hip must now support the combined weight of the upper body and the lifted leg (W'); equivalent to 81% of the total body weight (BW) [1]. The addition of the lifted leg weight shifts the centre of gravity (COG) towards the lifted leg. As the body is supported on only one leg, the hip acts as a pivot and the supported body generates a moment about this pivot in the adduction (clockwise) direction ($W' \times L_a$). Counterbalancing of the body system is achieved through an anticlockwise moment that is produced by the abductor muscles producing a force F_M . However, due to the short lever arm l_a at the greater trochanter, the abductor muscles must exert a significantly large force F_M , on the scale of 3 to 4 times the BW [1, 101, 103]. Hence, the balanced moments can be presented as follows:

$$W' L_a = F_M l_a \quad \text{Eq. 2.1}$$

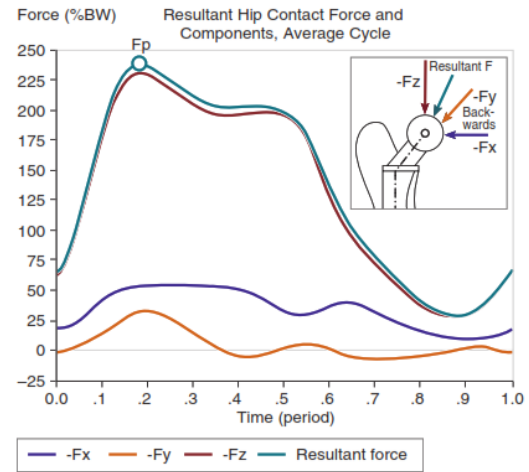
The downward forces are balanced by the reaction force R at the hip, and can be represented as follows [1]:

$$R = \sqrt{(W')^2 + F_M^2 + 2W'F_M \cos(\theta_a)} \quad \text{Eq. 2.2}$$

where, θ_a represents the angle between W' and F_M . Under dynamic conditions, as the leg pushes against the ground to cause the body to accelerate in an upward direction, the reaction force generated to the ground exacerbates the internal loading conditions on the hip (through load transfer), thus increasing the value of R . In fact, the reaction force at the hip that is generated is around 4 to 5 times greater than the BW. This peak load is achieved instantaneously and occurs periodically, and thus has been described to be analogous to a hammering effect [1, 100].



(a) Three-dimensional plot of resultant force during gait cycle obtained from telemetric prosthesis with crutches. Source: [104].



(b) Plot of typical hip reaction force and corresponding components developed during gait. Source: [105].

Fig. 2.6: Reaction forces on the hip.

Activities such as stair climbing, fast walking and stumbling, correspond to greater reaction forces at the hip, approximately 8 to 10 times BW [106]. Telemetric prostheses have been used to measure and verify the reaction forces at the hip joint (as shown in Fig. 2.6) [104].

2.2.3. Factors Influencing Loads on the Hip

As the hip joint acts as a mechanical pivot, the reaction force and contact stresses of the artificial hip joint are influenced by the position of the acetabular cup. It has been observed that an offset¹¹ of 10 mm in the lateral and inferior directions resulted an increase in the mean loads on the hip during the normal gait cycle by 8% and 1%, respectively, as shown in Fig. 2.7 [102], which consequently influences the lifespan of the prosthesis. In a retrospective study [107] constituting of 109 primary hip joint replacements, medialized acetabular cups, which were seen in 10 patients, were noted to produce lower wear rates ($0.077 \text{ mm}^3/\text{year}$), as compared to other malpositioned acetabular cups.

¹¹ Offset is the distance from the centre of rotation of the femoral head, to the longitudinal axis of the femur.

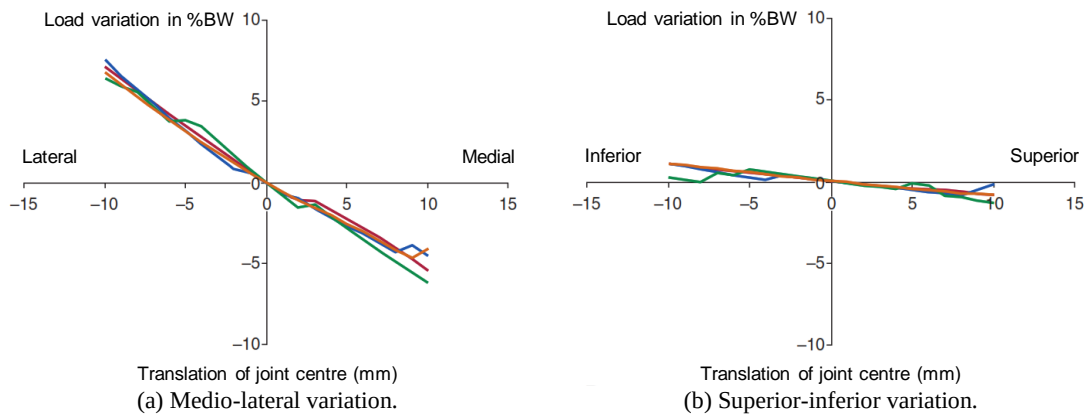


Fig. 2.7: Influence on the hip loading conditions, as a function of hip centre position varied along different dimensions. Adapted from: [102].

During surgical reconstruction, the acetabular cup should be positioned at 45° (Fig. 2.8a) and the joint centre should be at least restored to its anatomic position, particularly in the mediolateral direction, to prevent exacerbation of the loading conditions [66]. In some cases, alterations are made to the anatomic structure to improve the loading conditions on the hip by setting the joint centre towards the medial position, to reduce the moment arm of the body weight. This is achieved by setting the offset of the prosthesis which can be optimized by using modular femoral heads with different joint centre positions. This ensures that proper muscle tensioning is achieved in order to enhance the stability of the implant [101].

Femoral anteversion (Fig. 2.8b) also influences the load conditions on the hip, and thus dictates the outcome and longevity of the prosthesis. The effect of anteversion was negligible for joint angles below 15 degrees. The most pronounced effects were observed when anteversion exceeded 20 degrees, as this would cause increased stresses at the articulation [108].

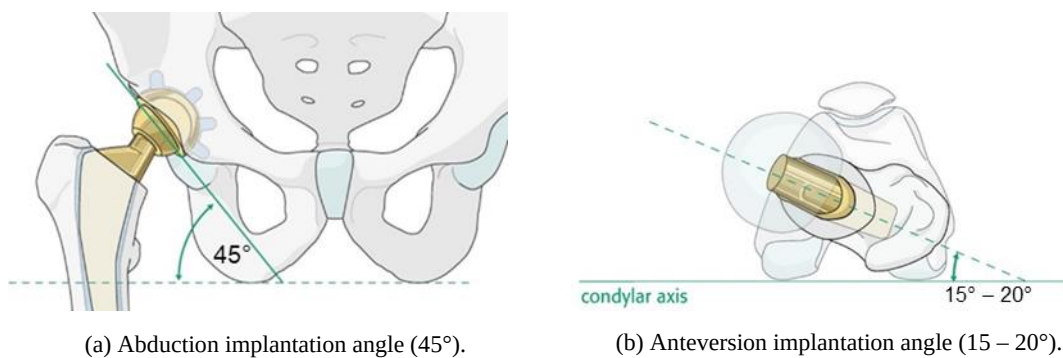


Fig. 2.8: Acetabular cup implantation angles. Source: [109].

2.2.4. Comparison to the Ankle Joint

The ankle joint shares the same anatomical functions of the hip in terms of providing load-bearing capabilities and stability to the lower limb. The joint primarily allows for plantar/dorsi flexion motion and is therefore described as a hinge joint. Other motions are permitted, being inversion/eversion and internal/external rotation, but with reduced range of mobility. This is attributed to its unique bone structure which consists of the tibia and fibula of the leg, and the talus of the foot (Fig. 2.9a). The talus possesses a half-cylinder surface and acts like a mechanical pivot [2]. The deep curvature that exists in the tibia and fibula highly contributes to the stability of the joint and could theoretically maintain its static position in the absence of the collateral ligaments [28]. During the stance phase, the ankle joint experiences forces of magnitude 5 to 7 times BW, as compared to the 4 to 5 BW in the hip joint [110], as shown in Fig. 2.9b. Although the natural ankle endures higher loads, it has been observed that the rate of osteoarthritis in ankle joints is much less; up to 9 to 10 times lower [25].

Despite the lower rates of osteoarthritis in the ankle joint, its artificial counterpart has demonstrated to be less successful than the artificial hip implant, as revision rates for total ankle replacements (TAR) are nearly twice as frequent [111, 112]. The first attempts at TAR were conducted in early 1970s. First generation TAR were prone to high failure rates due to instability, leading to subsidence at the bone-implant interface and excessive PE wear [113]. Other factors included subluxation¹², delayed wound healing, reflex sympathetic dystrophy¹³, deep infection, malleolar fracture, severe bearing wear, and osteolysis [114]. Consequently, TAR was overshadowed by more reliable procedures, such as arthrodesis¹⁴. However, it was also later observed that arthrodesis was causing further arthritis at the hindfoot, and thus interest was once again generated in TAR. Despite the relatively low occurrences of ankle arthritis, the absolute number of patients requiring the prosthesis is growing due to the increasing global population age and obesity [112]. In TARs, the peak contact stresses are located on the condyle edges, as shown in Fig. 2.10. TARs are subjected to high shear and compressive forces. Mechanisms that contribute to wear in liners are high contact and subsurface stresses that break down the material over time [115].

¹² Subluxation: Partial dislocation.

¹³ Reflex sympathetic dystrophy: A disorder that causes lasting pain due to the surgery.

¹⁴ Fusion of the ankle bones using plates, screws or pins resulting in increased stability at the expense of mobility.

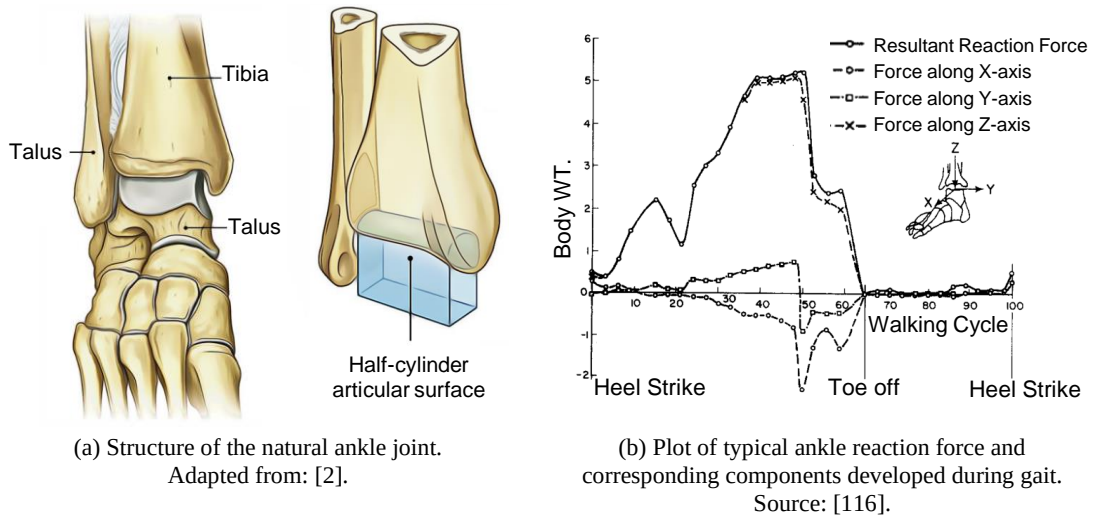


Fig. 2.9: Natural ankle joint.

Even though the ankle articulates similarly to a hinged joint (majority of motion occurs along the plane of dorsiflexion/plantar flexion), the polymer insert of the TAR still undergoes multidirectional due to its eversion/inversion motion. This type of wear is usually exhibited as scratches, shear bands, and adhesive wear, due to the generation of high contact stresses, which exceed the yield strength of the surface structure [113]. A slight misalignment was observed to exacerbate the compressive and shear stresses, leading to fracture of the polymeric component [117]. It is interesting to note that in general, the natural ankle joint exhibits higher average contact stress, but lower maximum contact stress than the natural hip joint, which is attributed to its cylindrical articular surface¹⁵ [118].

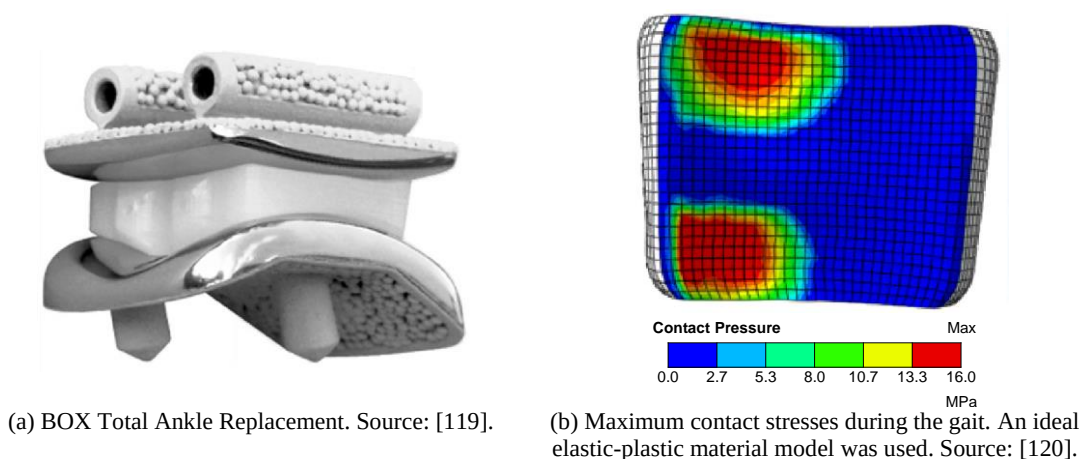


Fig. 2.10: Prosthetic ankle joint.

¹⁵ Direct quantitative comparisons are not made, due to differing methods which are reported in the studies. The statement is intended to provide a general indication of the type of stresses which are exhibited in both type of joints.

Ankle implants have been observed to produce submicron-sized particles, with round morphology, and larger particles possessing elongated and fibrillar morphology. In comparison, it was observed that hip implants produced a greater number of submicron-sized particles with rounder shape [121]. Schipper *et al.* [122] in their work compared the wear debris morphology of ankle implants consisting of conventional and crosslinked polyethylene inserts, and observed that the latter type produced particles with rounder morphology.

2.2.5. Comparison to the Knee Joint

The natural knee joint primarily consists of an articulation between the femur and tibia, and a secondary articulation that takes place between the patella and the femur (Fig. 2.11a) [2]. Motion of the primary articulation is one of the most complex in the body as it possesses 6 DOFs, although the majority of the motion occurs along the flexion/extension motion coupled with limited anterior-posterior motion as the motion of the other degrees of freedom are highly limited, and hence behaves similarly to a hinge joint [123]. The articular bone surfaces consist of two femoral condyles, which articulate against the adjacent surfaces of the tibial condyles. During flexion, the round sections of the femoral condyles are in contact with the superior tibia, whereas the flat sections of the femoral condyles are in contact with the superior tibia. The unique geometry of this articulation enables flexion/extension to possess a range of motion greater than 90° , causing drastic changes in the contact conditions of the articulation, as can be observed in Fig. 2.11b. Two menisci are located within the articulation, in the form of C-shaped cartilages, which improve the congruency of the joint during motion, and thus improve the distribution of contact stresses [2].

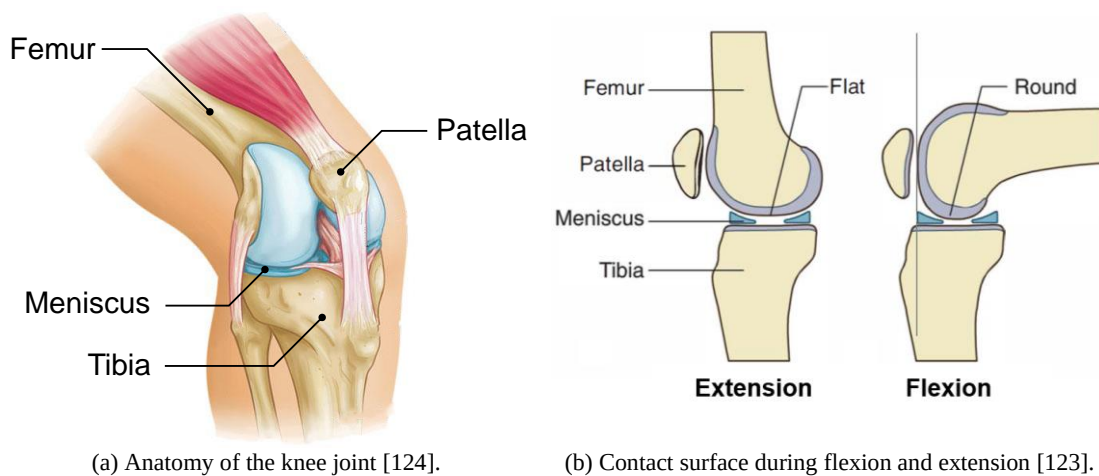


Fig. 2.11: Natural knee joint.

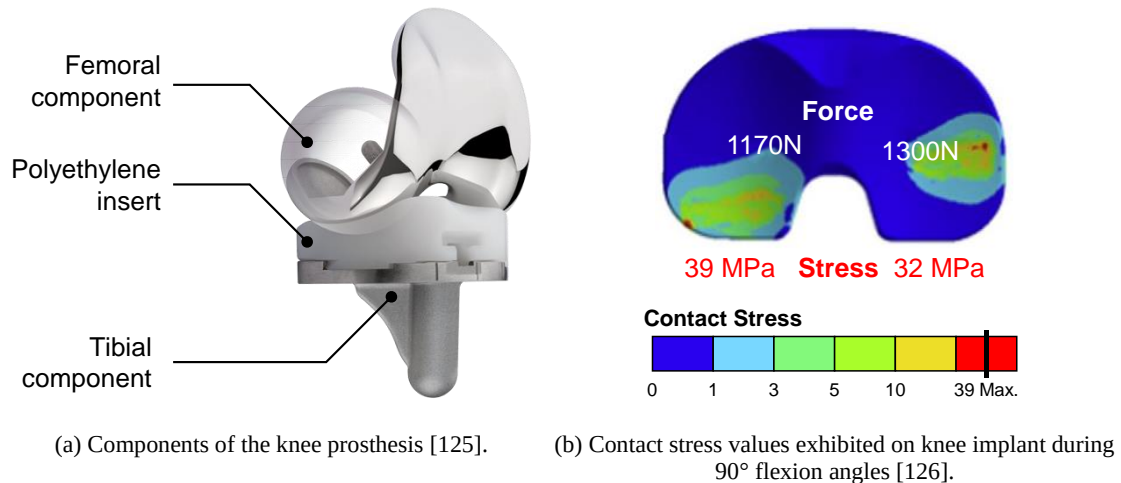


Fig. 2.12: Artificial knee implant.

Knee replacement involves the total reconstruction of the articulation, which reproduces the natural counterpart, consisting of a metallic femoral component, with two protruding condyles, that articulate against a polymeric tibial insert. The articulation results in a combination of oscillatory rolling and sliding motion [2]. Due to the wide range of knee implants designs that exists, the acting stresses differ significantly from one knee implant to another. However, in general, the design of the knee replacements is non-congruent, since the condyles of the femoral component rub against the polyethylene liner during use. Finite element analysis have indicated that knee tibial inserts exhibit highly localised von Mises stress (around 32 MPa) [127, 128] and contact stress values (around 39 MPa, see Fig. 2.12) [126, 129] greater than the yield strength of UHMWPE (21 – 25 MPa). The non-conforming geometry of the knee implant leads to the generation of high contact stresses at the tibial inserts and thus undergo fatigue wear, leading to delamination and thus structural failure of the component [71, 130–134]. In contrast, hip joint replacement possesses a conformal design, due to its ball-and socket geometry, therefore the acetabular cup exhibits lower contact stress values than the polymer tibial component in knee prostheses [135].

2.3. Mechanics of UHMWPE

2.3.1. Introduction

The mechanics of UHMWPE have an influence on the tribological performance of polyethylene [36, 136–138]. A qualitative review of the mechanical and deformation mechanisms is provided in this section. Mathematical models to predict the effect of load, geometry, and material properties on the stress and strain distributions occurring within joint replacement components are provided in Section 2.4.

2.3.2. Chemical Structure

UHMWPE is a linear semicrystalline homopolymer containing the repeat unit $[C_2H_4]_n$, and is terminated by methyl groups [139]. It is produced from ethylene $[C_2H_4]$ gas¹⁶ (Fig. 2.13a) that is the precursor of polymers residing to the polyethylene family, which also encompasses LDPE, LLDPE and HDPE¹⁷. The main difference between these types of polyethylenes lies in their molecular weights and chain structures [71]. The general chemical structure of the polyethylene is shown in Fig. 2.13b, illustrating the tetravalency of the carbon atoms, giving rise to the characteristic 112° bond angle [140, 141].

UHMWPE is mostly held together via covalent bonds which exist within the polymer chains. The adjacent polymeric chains are subjected to secondary forces (also referred to as van der Waal forces). Covalent bonds are characterised by short interatomic distances (1.54 and 1.09 Å¹⁸ for C-C and C-H, respectively [142]) and high bond energies (83 and 99 kcal/mol¹⁹ for C-C and C-H, respectively [143]), and thus dictate the thermal stability of the polymer [144]. The intermolecular bonds are characterized by longer interatomic distances and weaker bonding strengths, which are inversely proportional to the sixth power of the interatomic distance [144]. The secondary forces, which decrease in strength with increasing temperature, determine the extent of molecular chain mobility [144]. Above the glass transition temperature ($T_g = -150^\circ C$), the carbon backbone can move, rotate and even fold, whereas below T_g , the polymeric chains do not possess sufficient energy to move past one another [137]. The virgin UHMWPE is classified as a thermoplastic, due to the long-range linear bonding that is free from any intersecting covalent bonds between the molecular chains (i.e. crosslinks), and thus permitting the free motion of the chains [34].

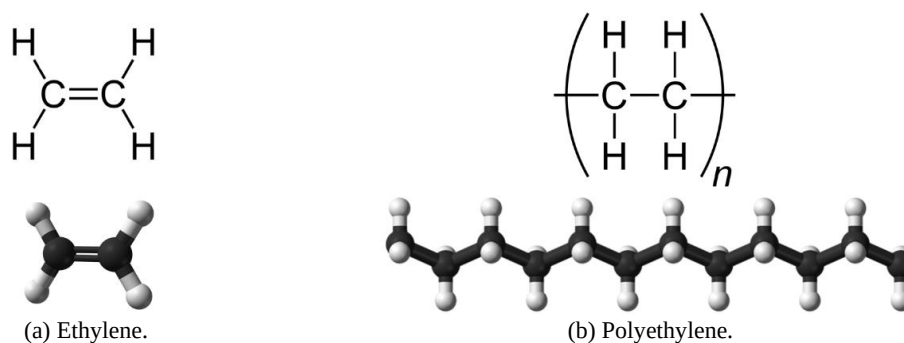


Fig. 2.13: Basic chemical structures of ethylene and polyethylene. Source: [145].

¹⁶ Ethylene gas has a molecular weight of 28.

¹⁷ Low density polyethylene (branched structure, <50,000 g/mol), linear low density polyethylene (linear structure, <50,000 g/mol) and high density polyethylene (linear structure, ~200,000 g/mol), respectively.

¹⁸ 1 Å is equivalent to 0.1 nm.

¹⁹ 1 kcal is equivalent to 4.185 kJ.

When untangled, a single molecular chain of UHMWPE can be imagined as a long molecule consisting of a carbon backbone being over a kilometre long [71]. The high molecular weight²⁰ of UHMWPE gives rise to high entanglement that is directly linked to its stellar macroscopic properties, including its superior resistance to wear and creep [27, 146]. Molecular weight influences the static fracture response, as well as mechanical behaviour (cold drawing, orientation hardening) at large strains beyond the yield strength [36]. Longer chain molecules serve to effectively transfer the load to the polymer backbone by strengthening the inter molecular interactions [27]. It was observed that the impact strength of UHMWPE saturates at average molecular weights between 2.4 and 3.3 million g/mol [71, 146–148]. The average molecular weight of UHMWPE for orthopaedic applications is 4.0 million g/mol. Two grades of UHMWPE resins are currently used in orthopaedic applications, being GUR 1020 (3.5 million g/mol) and GUR 1050²¹ (5.5 – 6.0 million g/mol) [71, 149].

2.3.3. Crystal Phases

The high packing efficiency of UHMWPE is a result of its achirality²² and the absence of functional groups [144], resulting in the polymer to possess a semicrystalline structure, composed of the crystalline and amorphous phases [139, 150]. The behaviour of the different phases is better described from a physical point-of-view, rather than from a chemical one, as the effect of an individual atom becomes negligible as compared to the gross effect of each molecular chain [144].

The crystalline phase is made up of structured macromolecules in lamellae, which follow an orthorhombic structure [151], although a monoclinic structure has been also observed to coexist [67]. In an orthorhombic structure, the carbon chains form a zigzag pattern, with their general direction being parallel to the *c*-axis and perpendicular to the lamellae axis [151], as shown in Fig. 2.14a. The spatial arrangement of the lamellae is due to rotations about C-C bonds that occur after hundreds of chain atoms have entered the phase. Other rotations are thus prevented due to the relatively strong intermolecular forces that are created in the crystalline domain [144]. The characteristic elongated lamellar shape of the crystallites is due to the high aspect ratio which exists between interface length, and the chain fold thickness [152]. In fact, these lamellae are approximately 10 – 50 nm thick and 10 – 50 µm long, and the interlamellar

²⁰ ISO 11542 requirement: 1.0 million g/mol. ASTM D4020 requirement: 3.1 – 6.0 million g/mol.

²¹ GUR stands for ‘granular’. First digit indicates whether the resin was made in Germany (1) or United States (4). Second digit indicates the presence (1) or absence (0) of calcium stearate. Third digit indicates the approximate molecular weight in millions (2 or 5 million). The fourth digit is always 0, and its meaning is not generally known. Designation developed by Hoechst/Celanese [66].

²² Achiral: Symmetry in the molecular structure, such that part of it can be superimposed in its mirror image.

spacing is 50 nm, as measured by using the small-angle X-ray scattering technique [71, 153]. The GUR series of UHMWPE utilized for orthopaedic applications prevents the formation of spherulites (a semicrystalline structure which consists of lamella that form along the radial directions), which is attributed to its high molecular weight, and is in fact characterised by particle boundaries due to fusion defects [146, 154–158]. In contrast, spherulites have been observed with Himont 1900, an UHMWPE variant with lower molecular weight possessing approximately 2.0 – 4.0 million g/mol [155], produced via extrusion [157] and hot isostatic pressing techniques [146, 155]. No spherulites were observed with compression-moulded versions [157, 158], and hot isostatic pressing of GUR series [155]. The absence of a spherulitic structure in UHMWPE is attributed to its high molecular weight (being greater than other types of polyethylenes), resulting in a high-melt viscosity, therefore making it difficult for the crystallites to organise themselves [154, 159].

The amorphous phase consists of randomly oriented macromolecules, and its structure is usually compared to a bowl of spaghetti. The formation of the amorphous phase is due to the generation of defects in the crystal lattice occurring during synthesis [144]. Due to the low T_g of UHMWPE, the secondary forces in the amorphous phase are set free during *in vivo* conditions, enabling the individual bonds to move and rotate, and thus the polymer undergoes viscoelastic-viscoplastic behaviour [31, 160, 161]. The amorphous phase is found as an interphase between the crystalline phases and is linked via tie molecules, as shown in Fig. 2.14b. Tie molecules in UHMWPE play a critical role in transferring external stresses, thus contributing to its outstanding elasticity [144, 162, 163]. The crystalline regions can be viewed as anchor points to limit the mobility of the rest of the molecular chains [36].

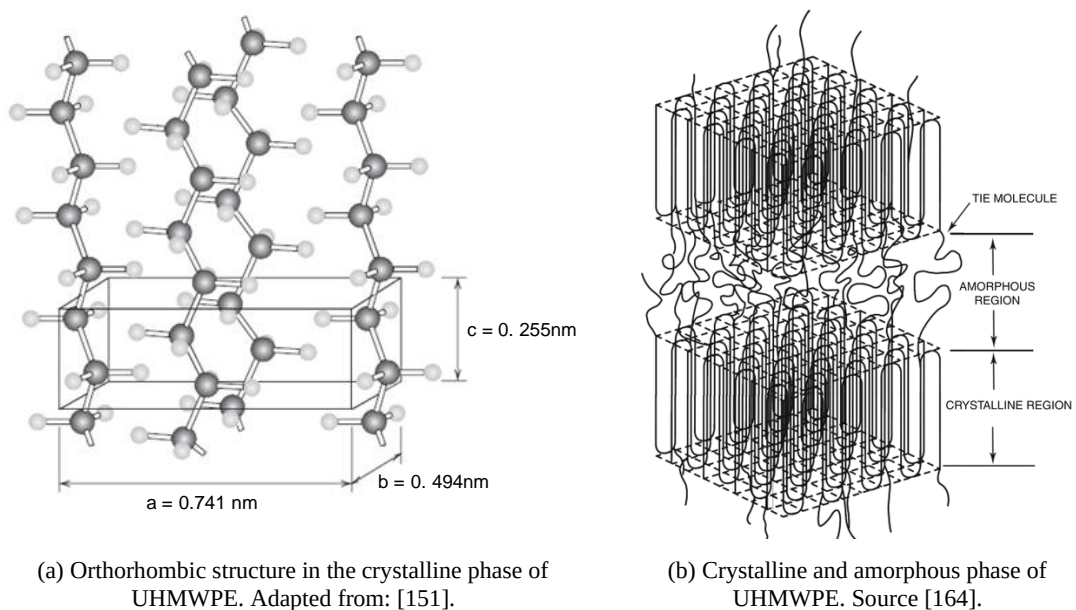
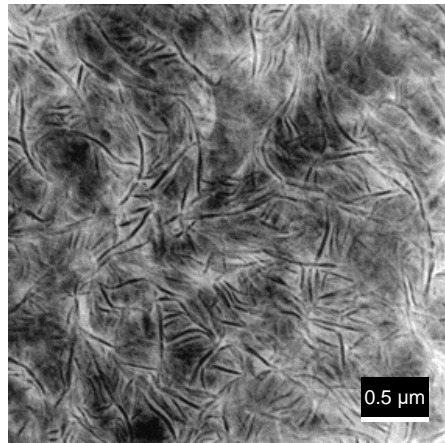
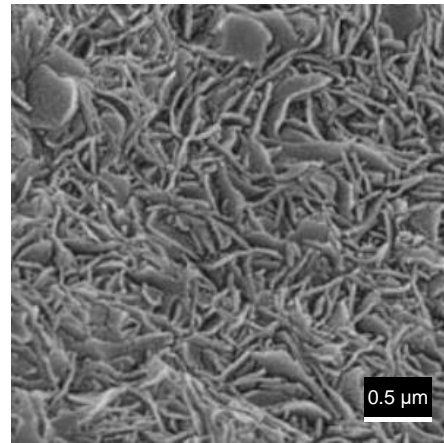


Fig. 2.14: Structures in polyethylene at different levels.



(a) TEM image of UHMWPE with darker regions indicating the lamellae. Source: [165].



(b) SEM image of lamellae following etching of the amorphous phase. Source: [166].

Fig. 2.15: Crystal morphology of pristine UHMWPE.

The percentage crystallinity in UHMWPE is dictated by the manufacturing process and is limited to approximately 50%, due to inevitable entanglements as a result of the long molecular chains [71]. In fact, the shorter molecular chains found in HDPE²³ are less prone to entanglements and thus achieve higher percentages of crystallinity, around 60 – 80% [71], [167]. The crystal structure can be observed using transmission electron microscopy (TEM), and its etched counterpart using scanning electron microscopy (SEM), as shown in Fig. 2.15. Etching is done using a permanganic solution²⁴ that selectively removes the amorphous phase [168], as it reacts at a significantly high rate than the crystalline phase, thus exposing the lamellae [169].

The mechanical response of UHMWPE is sensitive to temperature changes [170]. Below the glass transition temperature T_g , the polymer chains exhibit practically no motion [144, 170]. At elevated temperatures above T_g , the thermal energy causes segments of the long molecular chains in the amorphous phase to be highly agitated, which dictates the viscoelastic-viscoplastic behaviour of UHMWPE. At body temperature, the amorphous phase of UHMWPE becomes more mobile, resulting in a reduction in its yield strength of UHMWPE. At elevated temperatures, between 60 and 90 °C, only small crystallites undergo melting, whereas at further increased temperature, between 130 and 137 °C, the bulk UHMWPE undergoes melting, as indicated by differential scanning calorimetry (DSC) measurements [36, 71, 171]. The relatively high melting temperature of UHMWPE corresponds to thick and highly-aligned crystals [71, 171]. In fact, above the melting point, a UHMWPE component does not change shape, but instead changes its appearance from opaque to translucent, as a result of the disintegration of the crystalline phase [36].

²⁴ The etchant consists of 1.34 g potassium permanganate (KMnO₄), in a 100 mL mixture of 67 mL 98% sulphuric acid (H₂SO₄), 26 mL dried orthophosphoric acid (H₃PO₃), and 7 mL distilled water [168, 169].

2.3.4. Mechanical Properties

In the previous section, the behaviour of UHMWPE was described in terms of molecules which existed in two distinct types of phases: amorphous and crystalline [150]. However, modelling a system at the molecular-chain level for components such as a prosthetic hip, is not feasible as it would entail a high number of complex molecular interactions to be simulated. Although the true interacting forces (covalent and van der Waal) exist between the individual atoms inside the molecular chains, it is more feasible to consider UHMWPE as a bulk by idealizing it as a continuum model.

The mechanical properties of UHMWPE are influenced by the volume crystallinity and orientation of crystallites. Moreover, this is dependent on the number of tie molecules (which is inversely proportional to the thickness of the crystallite), the number and the nature of connections within the amorphous regions (i.e. degree of mechanical entanglements) [152, 171, 172]. The elastic modulus increases almost linearly with increasing crystallinity [36, 152], however, this has been demonstrated not to be beneficial to the wear resistance such as in the case of Hylamer® [68–72], owed to phase transformation from orthorhombic to a monoclinic structure [21, 69, 173, 174]. Therefore, the conventional UHMWPE represents the optimum case between elastic modulus and wear resistance [152]. Further details on the influence of mechanical properties and tribological behaviour of the polyethylene are given in Section 2.6.

The concept of viscoelasticity represents a molecular arrangement model for the consolidated mechanical behaviour of two ideal materials: elastic solid and viscous liquid. The former represents a material with a definite shape, and whose deformation is reversible under the application of an external force. The latter represents a material with no definite shape and flows irreversibly upon the application of a force. Upon the application of load onto a viscoelastic material, elastic deformation occurs instantaneously, whereas the viscous deformation occurs over a period of time [175, 176].

The viscoelastic behaviour of UHMWPE is dependent on its molecular weight, the structure of the repeating unit, their frequency, and the resultant intermolecular forces. The viscous part provides a measure of the energy dissipations that arise due to friction between the polymer chains as they slide against each other during flow [144]. In fact, the average molecular weight is usually measured indirectly from intrinsic viscosity measurements, which provides a picture of the mechanical behaviour of UHMPWE [36]. Intrinsic viscosity of PE increases non-linearly with increasing molecular weight [27]. UHMWPE is inherently viscous due to its high molecular-weight molecules configured in a semicrystalline structure that is densely populated with tie molecules, which enhances its internal resistance to flow, and thus gives rise to its

characteristic abrasive wear resistance and bulk impact strength [27, 36]. Furthermore, UHMWPE is nearly incompressible²⁵, due to its high Poisson's ratio of 0.46, as shown from experimental data [177].

Limited information is available in literature regarding the typical range of strain rates of *in vivo* UHMWPE cups. As correctly pointed out by Kurtz *et al.* [160] the elastic modulus, yield and ultimate tensile strength for UHMWPE are in most cases reported in terms of monotonic engineering stress and strain data that are strain rate-independent and/or temperature-independent, since these are the minimum values required to meet international standards. However, these values on their own do not reflect the actual viscoelastic-viscoplastic response of UHMWPE [160]. Hence, the entire stress-strain curve is needed to accurately characterize the yielding and plastic behaviour of UHMWPE, to accurately model fatigue and wear behaviour [160, 165]. Therefore, the polymer deformation and the resultant stress does not only depend on the applied strain (just as in the case of linear-elastic materials), but also on rate of strain that is applied, due to its viscoelastic-viscoplastic behaviour [178].

During monotonic loading, the stress-strain behaviour up to the yield point is noted to be similar during tension and compression loading [165]. Under applied stress, deformations initiate in the amorphous phase, due to their lower elastic modulus and the glass transition temperature being well below room temperature [179]. The main deformation mechanisms occurring in the amorphous phase are shearing, stretching (under tension) and breaking of bonds resulting in stack rotation of the crystal lamella (under compression) [180], as shown in Fig. 2.16. The activation energy needed to deform the amorphous phase is around 2 – 10% of the total energy required to initiate chain-dislocation-slip within the crystals [181]. Strains up to 0.4% permit reversible deformation in the amorphous phase, due to entropy-elastic behaviour of the molecules [179]. Butler *et al.* [182] reported that for slightly higher strains but below the yield point, (strains in the range of 0.11 – 0.14), plastic deformation is accommodated at the amorphous region. However, at larger strains, resistance to deformation is governed increasingly by the plasticity of the crystalline lamellae [160, 182].

²⁵ Incompressible implies that the volume remains nearly the same under applied loads. Poisson's ratio of 0.5 is used for incompressible materials.

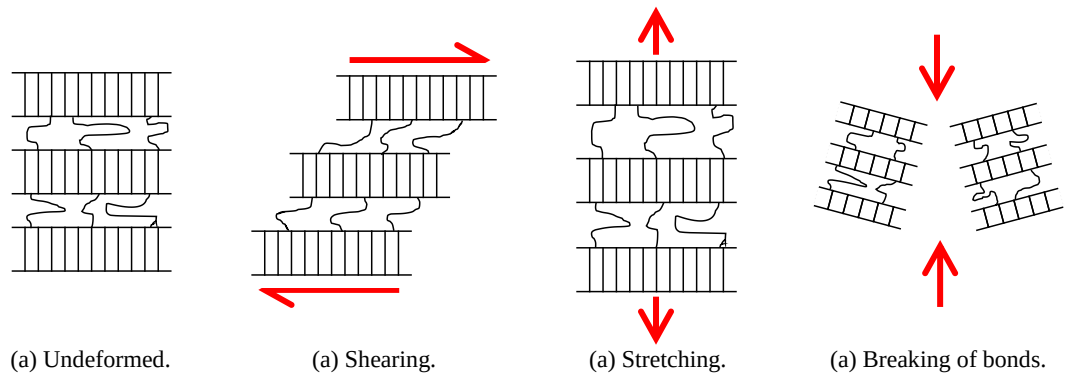


Fig. 2.16: Deformations in the amorphous phase. Source [180].

At higher strains exceeding the yield point, deformation mechanisms involve shearing of the amorphous part [183]. Lattice shearing from orthorhombic to monoclinic configuration takes place and this can also be complemented by mechanical twinning and dislocation motion [184]. Dislocation motion occurs via slip when the shear stress value is exceeded. Under such conditions, the crystal structure of the polyethylene undergoes deformation leading to induced orientation, without the polymer chain being broken [184, 185]. At high tension loads, UHMWPE is susceptible to crazing, that is the development of microvoids that are only held by molecular bridging, which break at sufficiently high tensile loads leading to cracking [186]. Hamilton *et al.* [187] determined that the ultimate response in tension was governed by microscopic flaws, rather than macroscopic flaws, such as intragranular fusion defects.

2.3.5. Creep Behaviour

Creep refers to the propensity of a material to deform as a monotonic function of time, temperature and the applied stress [36]. An acetabular UHMWPE cup undergoes creep due to molecular sliding (above T_g) being subjected to a load, resulting in time and temperature dependent bulk deformation [188, 189]. Upon the application of load, internal stress is generated due to the flow of molecules, referred to as back stress [175]. Strain is accumulated as a result of long-term stress. Polymers do not creep indefinitely, as they approach a steady-state when the applied stress becomes equal to the back stress. When the applied stress is released, back stress returns the molecules to their original structure and the accumulated strain (being a function of time and stress) returns to zero, given that enough time is provided. This phenomenon is termed as stress relaxation [175]. The dimensional changes that are induced due to creep are achieved without any loss of mass [190]. Despite its susceptibility to creep, UHMWPE suffers from minimal dimensional instability, due to its high crystallinity and the presence of long molecular chains that are prone to high entanglements, thus hindering their mobility [36, 191].

During loading of the hip, part of the deformations in UHMWPE are influenced by creep (increased strain due to long-term stress) and stress relaxation (decreased stress due to long-term

strain) mechanisms [71]. Creep deformations occur below the yield strength, and in fact, it is temporary and thus distinct from plasticity, since in theory creep deformations are recoverable, provided that the load is removed [192], as experimentally demonstrated in [193–195]. On the other hand, plastic deformation occurs immediately due to yielding as a result of joint loading [196]. Although creep is a recoverable process, the timeframes during which the implant is unloaded are very short compared to the rate of recovery, and thus creep can be regarded to effectively produce permanent deformation [192, 196]. Around 70 - 85% of creep deformation has been reported to occur during the initial 10% of the lifetime, after which a quasi-steady-state deformation is attained [196, 197]. Crosslinked polyethylene components have been also observed to exhibit creep deformation, however to a lower extent as compared to conventional polyethylene [198, 199].

Generic oversimplified creep models, based on logarithmic functions serve as initial approximations of UHMWPE behaviour [191, 192]. These logarithmic models that predict creep deformation of polymers are functions of time, and consider the component thicknesses and contact stresses to remain constant. Experimental tests on UHMWPE acetabular cups [200] and test samples [191, 195] demonstrated that the majority of the creep occurs during the early time period following application of the load. However, such models do not portray the actual mechanical behaviour of UHMWPE, as the contact stresses changes due to viscoelastic behaviour of UHMWPE. In fact, these may not be suitable to model the long-term creep deformation of prosthetic hips, due to the changing strain rates. Improved models are required in order to predict the stress as a function of the changing strain rate [192], as outlined later in Section 2.4.

2.3.6. Influence of Sterilization and Crosslinking on UHMWPE Mechanics

Sterilization of UHMWPE is achieved using high energy radiation (1) gamma or electron beam radiation, (2) ethylene oxide (EtO) or (3) gas plasma treatment. Steam sterilization is not suitable for polyethylene as it negatively influences the dimensional stability of the components. Gamma irradiation is preferred over other processes due to its deep penetration. Crosslinking (Fig. 2.17) has been observed to occur as a beneficial by-product of gamma and electron beam irradiation, resulting in enhanced wear resistance. In fact, the process was intentionally introduced in 1998 as an effective means to modify the crystalline structure and thus prolong the lifespan of the artificial hip implants [76, 160]. Crosslinking increases the number of covalent bonds between the molecular chains, thus hindering their general mobility. Thus, molecular orientation becomes harder to take place (but not eliminated), and therefore the extent of fibril rupturing contributing to adhesive wear is reduced [201].

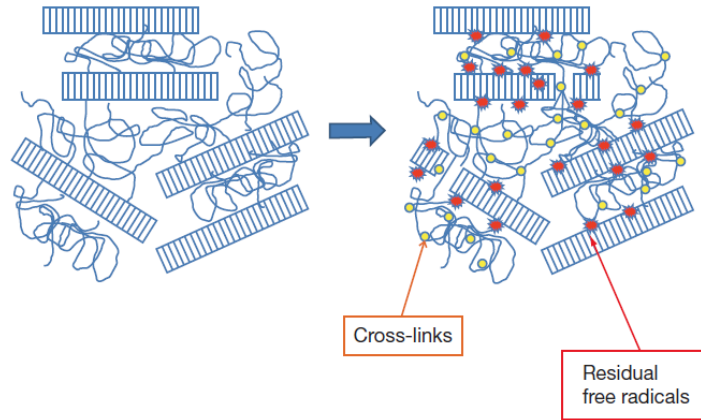


Fig. 2.17: Schematic representation of crosslinking. Source: [202].

Doses of 25 – 40 kGy are mostly intended for sterilization, although some crosslinking takes place. Higher doses are intentionally performed to increase the level of crosslinking to improve the wear rate, however, no further improvements are attained in wear resistance when the dosage exceeds 100 kGy [71, 203, 204]. Crosslinking is achieved at the cost of chain scission, and the generation of free radicals. The chain scission process results in the formation of shortened molecular chains, therefore facilitating the recrystallization process (i.e. realignment of the polymer chains) due to enhanced chain mobility [205]. The production of free radicals causes long-term oxidative degradation of the polyethylene, which effectively leads to embrittlement and reduced general structural integrity due to reduced molecular weight of the polymeric components [76, 84, 149, 206].

Post-irradiation, thermal processing on UHMWPE in the form of annealing or remelting is conducted to reduce the residual free radicals, enhance the oxidation resistance of UHMWPE [160], and to reduce residual stresses [207]. Annealing is done below the melting temperature to maintain the crystallinity and mechanical properties, whereas remelting is done above the melt temperature [208–210]. Although free radicals were not observed, this is achieved at the cost of altering the crystallinity which influences its mechanical properties, such as the yield strength, plastic flow and fracture behaviour [160, 211].

To counteract the problems associated with gamma sterilization followed by long-term shelf-storage that lead to oxidative chain scission and degradation, sterilization protocols shifted towards gamma radiation sterilization in vacuum-packaging or inert-gas packaging and gas plasma [150]. Even though the gamma treatment is done in an inert environment, the gamma irradiated polyethylene remains susceptible to oxidation following annealing due to the presence of free radicals.

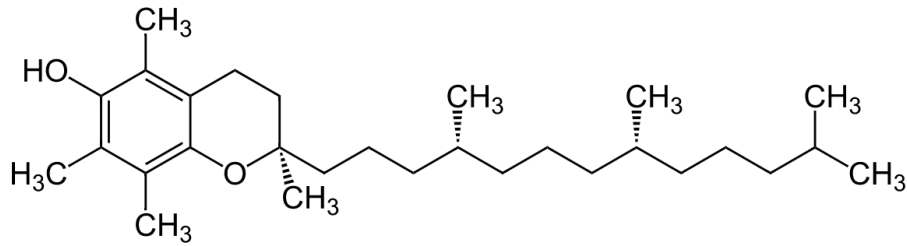


Fig. 2.18: Alpha-Tocopherol. Source: [212].

In order to minimise oxidation effects, whilst maintaining the high wear resistance of crosslinked polyethylene, antioxidants such as Vitamin E (alpha-tocopherol, shown in Fig. 2.18) have been introduced to further suppress the generation of free radicals [213]. Effectively, Vitamin E serves as a free radical scavenger and stabilizes the polyethylene. The introduction of Vitamin E prevents the loss in crystallinity, and thus the fatigue strength of the polyethylene is maintained. Vitamin E-infused highly crosslinked polyethylene (VEHXPE) cups enabled larger femoral heads with thinner acetabular cups to be produced to minimize the extent of dislocation [52, 54]. Vitamin E may be incorporated into the polyethylene either in the blend prior or post consolidation of the polyethylene [71]. It has been observed that the incorporation of Vitamin E in UHMWPE does not incur significant changes to the mechanical properties of the polyethylene [214]. One drawback of Vitamin E infused polyethylene is its increased resistance to post radiation crosslinking [215]. Therefore, the radiation dosage must be increased to compensate for the increased crosslinking resistance offered by Vitamin E. Nonetheless, the improved fatigue resistance attained due to the introduction of Vitamin E current studies have demonstrated that VEHXPE can be an ideal candidate material for young and active patients [216, 217].

2.4. Modelling Mechanics of UHMWPE

2.4.1. Review of Models

Theoretical models that predict the volumetric wear rely on the contact stress results that are produced by finite element models. Hence, this highlights the importance of implementing the correct material model to accurately reproduce the mechanical response of the material, as a function of the load and geometry, in order to provide reliable volumetric wear predictions [132]. In this section, the material models that are used for UHMWPE are reviewed. It should be noted that such models do not take into account the tribological behaviour of the material under consideration [130]. The wear models are separately reviewed in Section 2.5 (p. 36).

Early finite element analyses probing the structural integrity of total joint replacements implemented a rate-independent constitutive model, based on classical isotropic plasticity, to predict the behaviour of UHMWPE [218]. These models were based on linear elastic or elastic-plastic (bi-linear or multi-linear kinematic hardening models) approximations of the stress-strain behaviour of polyethylene, which did not take into account the effect of unloading, and thus assume monotonic loading conditions [132, 165, 226–228, 192, 219–225]. Fig. 2.19 illustrates that linear elastic models (indicated by the green and blue plots) oversimplify the actual stress-strain behaviour of UHMWPE (as indicated by the red plot), resulting in significant discrepancies. The linear elastic models do not consider the viscoelastic-viscoplastic behaviour of the polyethylene material, and therefore neglect the load rate dependency and creep effects that are induced by the material.

The stress-strain behaviour of UHMWPE has been incorporated into previous finite element simulations of THR using classical isotropic, rate-independent plasticity to approximate the nonlinear mechanical response of the polymer. Bowden and Bergström [229], outlined that such model is only suitable to predict the behaviour of the polymer for strain values of up to approximately 0.01, as indicated in Fig. 2.19 by the grey dashed line. Investigations of the unloading behaviour and permanent plastic deformations in polyethylene have shown that classical plasticity theory greatly overpredicts the permanent strains on unloading, leading to inflated residual strains and stresses [165, 229]. It has been observed that the use of elastic or elastic-plastic models could result in overestimating the component stresses [192]. Therefore, the change in contact pressure values due to the viscoelastic-viscoplastic behaviour of the polyethylene are not taken into consideration during the prediction of the wear volume.

Considering the discrepancies between the experimental and the elastic model results, an accurate representation of the biomechanical properties of the orthopaedic devices necessitates viscoelastic-viscoplastic modelling of polyethylene components under transient conditions, which takes into account the recoverable and irrecoverable deformations occurring, during the loading and unloading phases, to reproduce the time-variant dynamic behaviour [132, 192]. The true physical stress-strain curve is of considerable practical interest for the development of finite element models to accurately predict the multiaxial stress state at the articulating surfaces of the UHMWPE components. The true stress-strain curve provides useful information about the yielding behaviour, the true rate of strain hardening, and the stress-induced transformations of crystalline texture [165]. Therefore, when characterizing the mechanical behaviour of UHMWPE at large deformation, it is useful to adopt a description of the stress-strain curve in terms of the true stress and true strain.

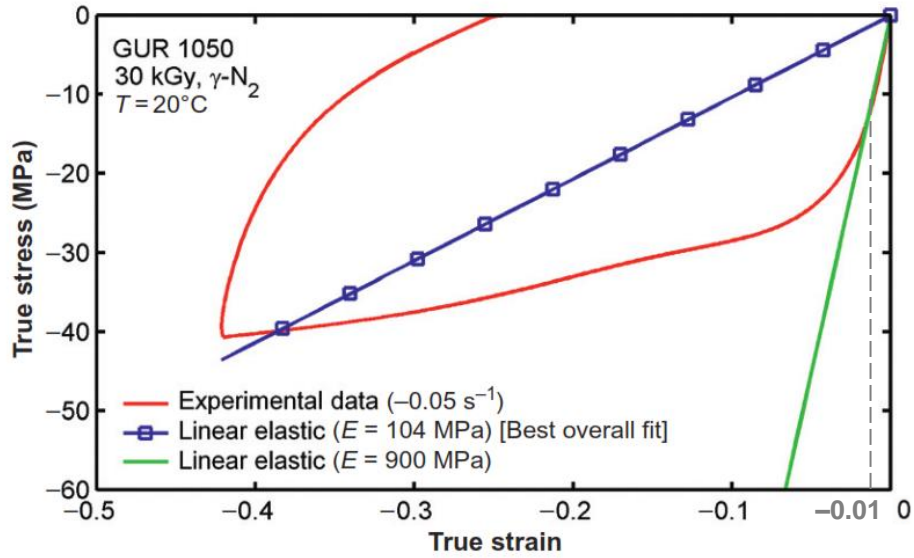


Fig. 2.19: Comparison between the stress-strain response obtained from experimental data, as compared to the linear elastic model. Source: [229].

Material creep and relaxation during periods of relative inactivity may influence accumulated stresses and could contribute to some of the discrepancies between *in vitro* wear simulations and *in vivo* results [192]. Due to the inability of elastic models to capture the creep behaviour of polyethylene, some of the works reported in literature have based their computations on a simplified creep law that is based on a basic logarithmic relationship using empirical data. This creep law is usually computed at specific intervals, independently of the material model and independently of the transient part of the model. As a consequence, the computational expense is drastically reduced [191, 227].

2.4.2. Maxwell and Wiechert Material Models

Viscoelastic material behaviours are often based on the Maxwell material model. The model uses a Hookean elastic spring and a Newtonian viscous dashpot in series (Fig. 2.20) [178, 230], which can mathematically represent the system under tension as shown by Eq. 2.3:

$$\sigma = E\epsilon_1 \Rightarrow \epsilon_1 = \frac{1}{E}\sigma \quad \text{Eq. 2.3}$$

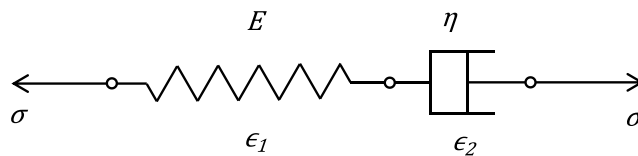


Fig. 2.20: Schematic representation of the Generalized Maxwell material model.

where, σ is the tensile stress, E is the elastic modulus, and ϵ_1 is the tensile strain. Similarly, the above model can be used to represent the shear stress, τ_e is the elastic shear stress, G is the shear modulus and γ the elastic shear strain [231].

$$\tau_e = G\gamma_e \quad \text{Eq. 2.4}$$

Similarly, the viscous shear stress τ_v can be related to the viscous shear rate $\dot{\gamma}_v$ and by Newton's law of viscosity. Therefore, the dashpot (damper) can be mathematically represented by,

$$\tau_v = \eta\dot{\gamma}_v \quad \text{Eq. 2.5}$$

where, η is the viscosity of the dashpot. From Eq. 2.5 and using the relationship between shear and tensile stress, the following equation can be obtained,

$$\sigma = \eta\dot{\epsilon}_2 \Rightarrow \dot{\epsilon}_2 = \frac{1}{\eta}\dot{\sigma} \quad \text{Eq. 2.6}$$

Since the Generalized Maxwell model consists of the elastic and viscous parts in series, under the application of stress $\sigma(t)$, the strain of the spring (ϵ_1) and the damper (ϵ_2) can thus be represented by,

$$\epsilon = \epsilon_1 + \epsilon_2 \quad \text{Eq. 2.7}$$

Differentiation produces the following equation,

$$\dot{\epsilon} = \dot{\epsilon}_1 + \dot{\epsilon}_2 \quad \text{Eq. 2.8}$$

Substituting Eq. 2.6 and the differential of Eq. 2.3 both in Eq. 2.8 and rearranging the terms, the standard form of the Maxwell material model is obtained as follows,

$$\dot{\epsilon} = \frac{\dot{\sigma}}{E} + \frac{\sigma}{\eta} \quad \text{or} \quad \sigma + \frac{\eta}{E}\dot{\sigma} = \eta\dot{\epsilon} \quad \text{Eq. 2.9}$$

Connecting several Maxwell models in parallel, the resulting model can be used to provide a more comprehensive view on the viscoelastic behaviour (elasticity, viscosity, creep, and stress relaxation). The generalized Maxwell material model [232] can be derived from Eq. 2.9 through the summation of elements as follows,

$$\frac{d\epsilon}{dt} = \frac{d\sigma}{dt} \sum_{i=1}^N \frac{1}{E_i} + \sigma \sum_{i=1}^N \frac{1}{\eta_i} \quad \text{Eq. 2.10}$$

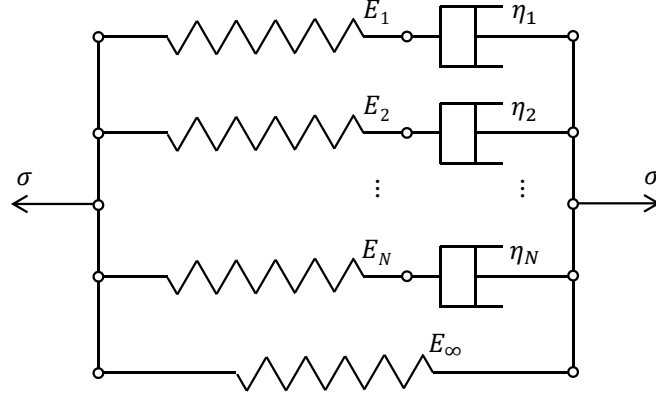


Fig. 2.21: Weichert material model.

A convenient implementation of the generalized Maxwell model is when the strain history (stress relaxation) is known, and thus the corresponding equation is given by,

$$\sigma(t) = \epsilon_0 \sum_{i=1}^N E_i e^{-\frac{t}{T_i}} \quad \text{Eq. 2.11}$$

where, t is time, T is the stress relaxation time. Adding one more spring to the generalized Maxwell material model, the Wiechert material model is produced (Fig. 2.21) [233]. Similar to the Maxwell material model, the spring and dashpot represent the elastic and viscous behaviours of the polymer, respectively. The springs and dashpots which are included in parallel to model the time-dependency of the relaxation processes as a result of molecular segments of different lengths which are found in viscoelastic polymers. This could be mathematically represented as,

$$\sigma(t) = \epsilon_0 \sum_{i=1}^N E_i e^{-\frac{t}{T_i}} + E_\infty \epsilon(t) \quad \text{Eq. 2.12}$$

where E_∞ is the equilibrium modulus, and E_i and T_i are the elastic components and relaxation time associated to the i^{th} Maxwell component. In order to obtain the tensile stress, $\sigma(t)$, the elastic modulus is multiplied by the uniaxial strain ϵ and applying the hereditary integral [234], as follows,

$$\sigma(t) = \int_0^t E(t-T) \frac{d\epsilon(T)}{dT} dT + E_\infty \epsilon(t) \quad \text{Eq. 2.13}$$

where σ is the stress, ϵ is the total strain, and t is the time. Creep and stress relaxation are observed in materials as a result of viscoelastic deformation.

Although this model describes qualitatively well the behaviour of a viscoelastic material, its simplistic nature is regarded inadequate to quantitatively correlate it the mechanical properties of the polymer. Having reviewed the fundamentals behind the Maxwell and Weichert model, a further advanced material model, referred to as the Three Network Model, is reviewed in the following section.

2.4.3. Three Network Material Model

The Three Network (TN) model, proposed by Bergström and Bischoff [31], is a material model intended to predict the macro-level mechanical response of a non-linear, time-dependant, viscoelastic-viscoplastic material, of semicrystalline material, such as UHMWPE. The TN model is composed of constitutive equations and the material parameters [176]. Hence, the material model is able to reproduce the linear viscoelasticity behaviour at small strain values, followed by distributed yielding, followed by non-linear viscoplastic flow, followed by material stiffening at extremely high strain values [31]. This section is intended to provide a descriptive high-level review of the constitutive equations of the material model. The actual mathematical formulae behind the material model are reported in [31]. The material parameters of the model are listed in Table 2.1.

Table 2.1: Three Network Model material parameters. Source: [235]

Symbol	Units	Description
μ_A	MPa	Shear modulus of network A
μ_{Bi}	Pa	Initial shear modulus of network B
μ_{Bf}	Pa	Final shear modulus of network B
μ_C	Pa	Shear modulus of network C
\hat{t}_A	Pa	Flow resistance of network A
\hat{t}_B	Pa	Flow resistance of network B
$\hat{\theta}$	K	Temperature factor
λ_L	-	Locking stretch
κ	MPa	Bulk modulus
a	-	Pressure dependence of flow
m_A	-	Stress exponential of network A
n_t	-	Temperature exponential
β	-	Evolution rate of μ_B
m_B	-	Stress exponential of network B
q	-	Relative contribution of modified eight-chain of network C
α	K ⁻¹	Thermal expansion coefficient
θ_0	K	Thermal expansion reference temperature (293 K)
θ	K	Current temperature

As the name suggests, the model consists of three molecular networks (denoted as A, B and C) that act in parallel to each other. In brief, the model consists of two distinct inelastic networks A and B, and a purely hyperelastic network C. Network A represents the elastic and viscoplastic deformation of the amorphous phase, whereas network B represents the elastic and

viscoplastic deformation of the semicrystalline domain of the polyethylene. Network C models the hyperelastic deformation of the material during large strain values (the entropic chain stretch hardening) [31, 236]. The material parameters must be specified for each network. A rheological representation of the model is shown in Fig. 2.22. The influence of the model the stress-strain curve of the material is shown in Fig. 2.23.

The total deformation occurring at each network is computed as function of the mechanical and thermal deformations. The mechanical deformations for each network are described further below. The thermal deformations are computed using a thermal expansion function which involves thermal expansion coefficient α , the thermal expansion reference temperature θ_0 , temperature factor $\hat{\theta}$ (which influences the material stiffness as a consequence of a change in temperature), and the current working temperature θ . By incorporating this function, the variation of the material stiffness can be reproduced over a wide range of temperatures. The temperature-dependence of the model can be disabled by setting the temperature factor $\hat{\theta}$ equal to zero.

The mechanical deformation in network A is computed as a function of the hyperelastic and viscoplastic deformations. The hyperelastic part is computed using the eight-chain (EC) material model, proposed by Arruda and Boyce [237], and therefore is used as a sub-components of the TN model.

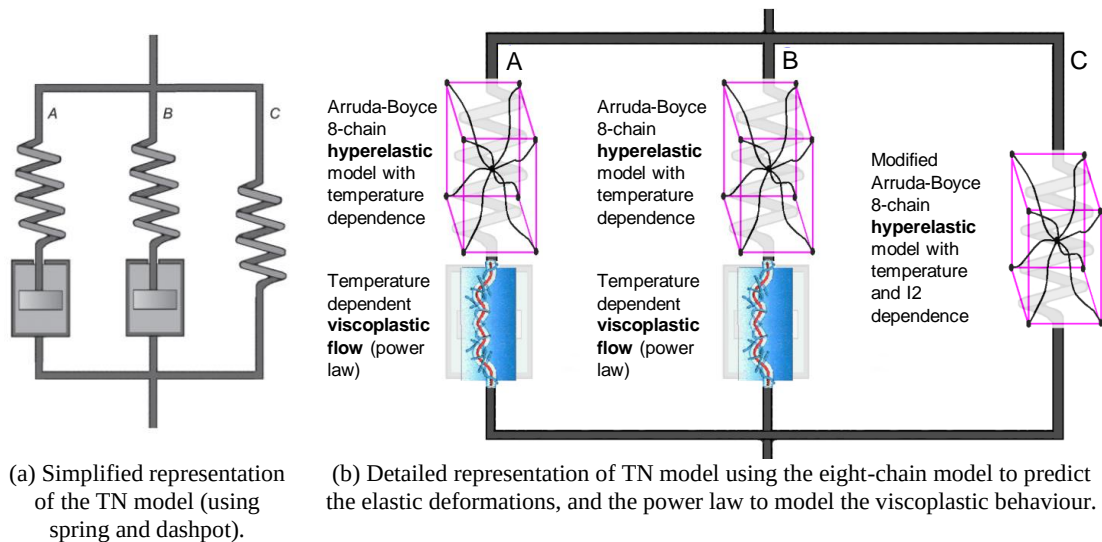


Fig. 2.22: Rheological representation of the Three Network (TN) Model. Source: [176].

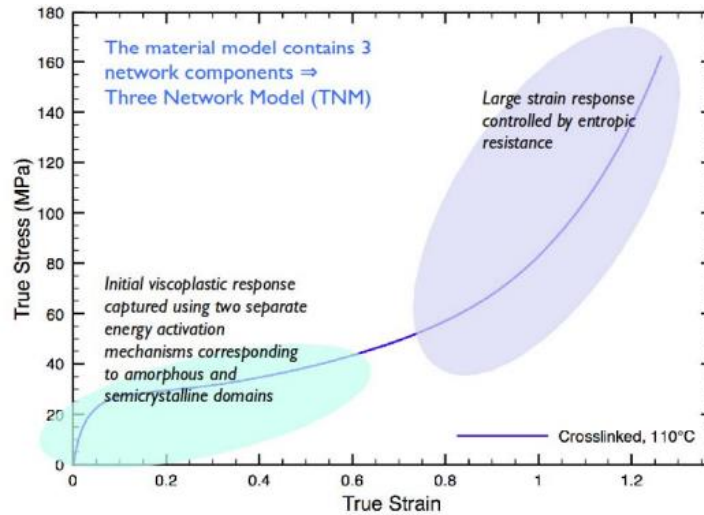


Fig. 2.23: An example stress-strain curve produced by the TN model, separated into various domains, each produced by a different deformation mechanism controlled by the corresponding network in the model. Source: [31].

The EC model depends on the current state of deformation, or more specifically, the energy that is stored in the material, rather than being dependent on the deformation history. The EC model does not capture yielding, viscoelasticity or time-dependant factors [229]. The EC model was originally intended to predict the response of elastomeric materials subjected to large strain multiaxial deformation. In brief, the hyperelastic EC model assumes that the macromolecules (or chain molecules) are on average located at the diagonals of a unit cell, as shown in Fig. 2.24. The deformation according to the EC model is computed using three material parameters, being the shear modulus (μ_A), bulk modulus (κ) and locking stretch (λ_L) [31]. The locking stretch (λ_L) represents a measure of the chain length when it becomes fully extended. These parameters are based on the physical micromechanics of chain molecules [237].

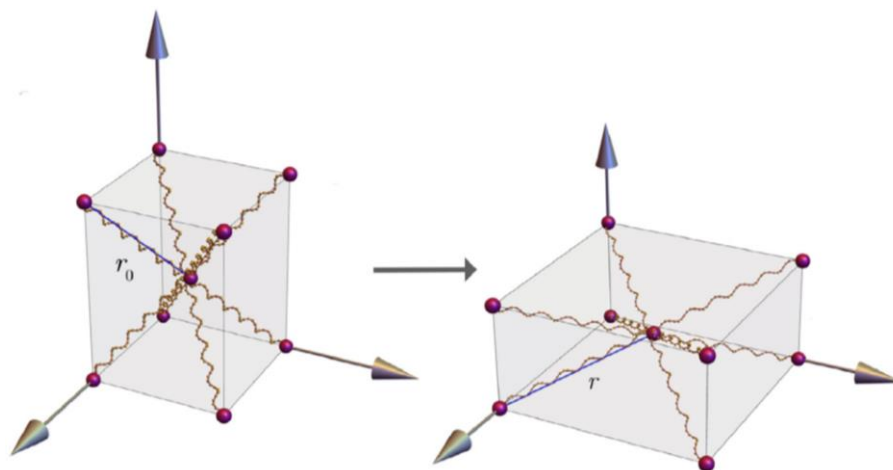


Fig. 2.24: The eight-chain model located in a unit cell, as proposed by Arruda and Boyce [237], which is used to model the length of the molecular chains upon being deformed. Source: [238].

The rate of viscoplastic flow of network A is computed using a power law function, which depends on the pressure dependence flow constant (a) and stress exponential of network A (m_A). In case that the temperature effects are included, the power law function is multiplied by a thermal power law function, constituted of θ , θ_o , and the temperature exponential (n_t).

Similarly, the deformation in network B is computed as a function of the hyperelastic and viscoplastic deformations. Network B is intended to model the characteristic distributed yielding of the semicrystalline domain, and therefore this requires that the molecular network A (which represents the initial mechanical response of the amorphous domain) to be stiffer and have a lower yield value than that network of B (distributed yielding occurs following the initial deformations taking place in network A). Similarly to network A, the hyperelastic part of network B is modelled using the eight-chain (EC) material model [237], which requires shear modulus (μ_B), bulk modulus (κ) and locking stretch (λ_L). However, network B considers that the shear modulus (μ_B) does not remain constant, but instead evolves according to the plastic strain that is generated. For this reason, the initial (μ_{Bi}) and final (μ_{Bf}) shear modulus of network B are specified, where μ_{Bi} should be larger than μ_{Bf} to simulate material softening. The rate at which μ_{Bi} progresses to μ_{Bf} is specified by an evolution rate parameter β . The change in the shear modulus models the distributed yielding of the material. Furthermore, the authors of the model [31] note that in order for the distributed yielding function to work, the stress resisting viscous flow of network A ($\hat{\tau}_A$) should be smaller than that of network B ($\hat{\tau}_B$).

The rate of viscoplastic flow of network B is computed in a similar fashion to that used for network A, and therefore depends on the pressure dependence flow constant (a) and stress exponential of network B (m_B). Once again, in case the temperature effects are considered, the power law function is multiplied by the same thermal power law function specified for network A (constituting of θ , θ_o , and the n_t).

The deformation of network C is computed by the EC hyperelastic deformation model which is modified such that it depends on the invariant I_2 . The invariant I_2 is basically a scalar value that is obtained from the stress tensor function, and its influence is computed using the relative contribution parameter q . Network C therefore depends on the shear modulus (μ_C), bulk modulus (κ) and locking stretch (λ_L). The stress at each network is computed as a function of the deformations that took place. The total stress is then calculated as the summation of the individual stress acting on each network.

2.5. Tribology and Degradation of UHMWPE

2.5.1. Introduction

An understanding of the tribological processes involved in a prosthetic implant due to wear of the acetabular cup is necessary for predicting its wear performance [44, 66, 132]. Despite the inherent low coefficient of friction and high wear resistance, its relatively low ultimate tensile strength and susceptibility to creep could pose clinical complications during *in vivo* conditions [210]. As reviewed throughout this section, the generation of submicron UHMWPE wear particles has been associated with multiaxial loading conditions that cause the local accumulated plastic strain to exceed the ultimate strength [165].

2.5.2. Contact Mechanics in Tribology

2.5.2.1. Overview

Contact mechanics concerns the study of the complex stress and strain conditions of the surfaces which are tangential to each other, subjected to an applied load, as a function of the material properties and their geometry [239, 240]. Hertz [241] developed the foundations of contact mechanics of two solids, which remain relevant to this field up to today [240]. Nonetheless, the Hertz contact model analyses the contact stress condition as a macroscopic effect and is intended for non-conformal designs²⁶. The Hertz contact theory is subject to several assumptions which idealise the properties of the contacting bodies. It is assumed that the contacting bodies follow a linear-elastic stress-strain relationship and must also be homogeneous and isotropic. Contact is assumed to be frictionless and that all strains are assumed to be small, such that these do not create significant deformations [240, 242]. Due to the intrinsic low wettability of UHMWPE, metal-on-polymer hip implants are prone to boundary lubrication conditions, resulting in a high number of micro-asperities coming in contact with one another. Therefore, the tribological processes can be better described by confining the Hertzian contact model to the local asperities of the surface, as proposed by Wang *et al.* [243]. Hence, by assuming a spherical contact at the tip of the micro-asperity, the stresses imposed during sliding motion are the normal pressure $p(x)$ and the surface traction $q_{ST}(x)$, which is necessary to overcome frictional effects (see Fig. 2.25). These are related by,

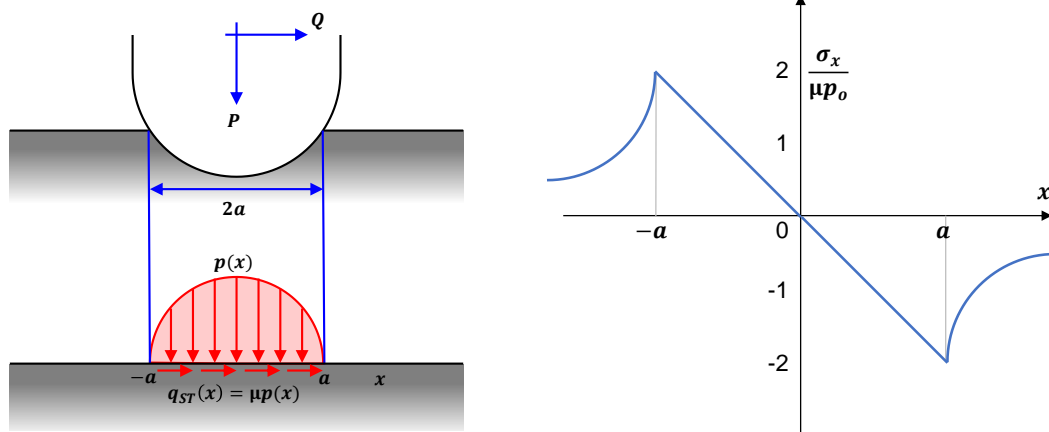
$$q_{ST}(x) = \mu p(x) \tag{Eq. 2.14}$$

²⁶ The Hertzian contact model is more suitable to ‘a ball pressed against a flat surface’ scenario, rather than to ‘a ball pressed against a highly-conformal cup’ (i.e. difference between the ball and the cup diameters is very small, as in the case of the prosthetic hip).

where, μ is the coefficient of friction. According to the contact mechanics theory [244], the maximum tensile stresses at the surface due to traction are exhibited at the trailing edge with a magnitude equivalent to $\sigma_x = 2\mu p_o$, where p_o is the maximum contact pressure.

When the acetabular cup and femoral head are put into contact, the contacting micro-asperities undergo plastic deformation. The plastic strain is accumulated at the asperity due to cyclic loading, that subsequently exceed the yield strength of the material. The critical strain criterion model stipulates that the wear particle is released when the accumulated plastic strain exceeds the critical strain [245]. However, this theory was only reproduceable in experimental setups involving linear motion [246, 247]. Although the relevance of contact load on the wear performance of the acetabular cup remains a key factor, it later transpired that the contribution of the sliding motion direction imparted a greater impact on the wear performance of the acetabular cup [15, 248].

Friction, in the context of tribology, is the resistance to relative motion and has a great influence on the stability of the implant and wear performance. Friction is a complex function of surface roughness, mechanical properties and electrostatic interactions [249]. Frictional effects at the acetabular cup introduce torque loads that lead to significant shear stresses at the bone-implant interface that may cause the fixation to fail by fatigue [26, 250]. Furthermore, frictional effects increase the temperature of the contacting surfaces (43 – 60 °C), which can negatively influence the mechanical performance of UHMWPE [251, 252]. Wear performance is diminished as the resistance to plastic deformation is lowered [160] and creep rates are accelerated as a consequence of increased temperatures [253].



(a) Distribution of normal and tangential forces in an asperity contact represented by sphere model.

(b) Principal stresses of the contact surface whereby the maximum stress occurs at the trailing contact edge.

Fig. 2.25: Contact mechanics of a micro-asperity. Adapted from: [243].

Under *in vivo* conditions, the continuously varying compressive loads on the hip greatly influence the deformation of the UHMWPE components. Hence, a more accurate representation would indeed be one which incorporates the non-linear behaviour of polyethylene [31]. The load magnitude and loading rate dictate the viscoelastic-viscoplastic effects and thus produce the temporary (recoverable) and permanent deformations, coupled with creep [192], which are critical in determining the contact pressure. If the load on the polyethylene is significant enough to exceed the elastic limit, the viscoelastic deformation is combined with permanent plastic deformation resulting in material flow and increased contact areas. Post-yield deformation of UHMWPE entails the fragmentation of the crystalline regions in conjunction with chain alignment in the amorphous and crystalline regions [38].

Plastically deformed regions are susceptible to low cycle fatigue failure, promoting the liberation of wear debris [133]. Quinci *et al.* [192], compared the different contact pressure values obtained when modelling UHMWPE as linear elastic, plastic and time-varying visco-dynamic model, against results in literature, and observed that the linear elastic model tends to overestimate the actual contact stresses. In view of the susceptibility to plastic flow, it is recommended that the maximum contact stress should be maintained below the linear elastic limit of UHMWPE.

Due to its inherent conformal contact²⁷ design, coupled the intrinsic low stiffness of the polyethylene, acetabular cups usually exhibit contact stresses which are below the compressive distributed yield strength (21 – 25 MPa) [152, 254], as can be shown by the example in Fig. 2.26. The generation of low contact stresses implies elastic contact and low articular frictional stresses, thus minimizing the effects of surface traction. The bulk of the material is likely to exhibit elastic deformation, with only confined regions of the surface layer undergo extensive plastic flow [152]. In contrast, the knee replacement represents the case that consists of a non-conformal contact²⁸ design, as the femoral component presses against the polyethylene spacer during motion, generating highly localized contact areas and thus leading to high rates of structural failures and fatigue delamination [130, 133].

²⁷ Conformal contact: Difference between the bearing and counterface radii is small, as in the case of the cup and femoral head of the prosthetic hip, leading to distributed contact stresses.

²⁸ Non-conformal contact: Difference between the bearing and counterface radii is large, as in the case of the plastic insert and femoral component of the prosthetic knee, lead to concentrated contact stresses.

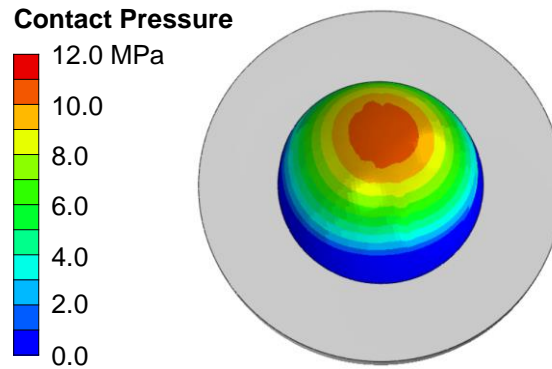


Fig. 2.26: Contact stress values on acetabular cup (22.225 mm femoral head diameter, 8.705 mm acetabular cup thickness), subjected to a load of 2500 N, inclined at 10° medially. Note that an elastic-plastic (multi-linear kinematic hardening) model was used. Source: [219].

2.5.2.2. Design Optimisation

Design optimization techniques are conducted to maximize the performance of the implant device under consideration whilst conforming to the constraints of the system (geometrical limitations, and mechanical loads). Finite element analysis is usually used as a tool to perform the design optimization process to provide a clear picture of the influence of the dimensions with respect to the physical attribute being inspected. This enables the identification of the ideal set of dimensions to meet the required performance of the device [255, 256].

Jin *et al.* [257] in their work have inspected the resultant contact stress value, as a function of acetabular cup thickness, femoral head diameter and radial clearances. The results of the study enabled the authors to identify the required acetabular cup thickness and radial clearances for different femoral head diameters. Goebel *et al.* [258] in their work performed a parametric study by varying the cup thickness, and femoral head diameter to analyse the deformations in UHMWPE liners using finite element techniques. Design optimisation techniques have been also implemented to analyse the relationship between the dimensions and geometry of the prosthesis components, and their influence on hip dislocation [259]. It should be noted that careful consideration must be given to the set of conditions which are tested during the identification of the ideal set of dimensions in such studies, since some features may be overlooked (e.g. use of linear-elastic model for modelling the mechanical response of UHMWPE) and not studied in detailed during the design optimisation processes. As a consequence, the proposed optimised solutions found in literature cannot be directly applied to new designs, but instead must be regarded with great care and considered within their limitations.

2.5.3. Plasticity-Induced Orientation

The knowledge gap between the mechanical properties and wear resistance was fulfilled by the discovery of stress-induced anisotropy as a result of molecular orientation during multi-direction joint articulation [15, 46, 152, 243, 248, 260–262]. Wear of UHMWPE is primarily influenced by the so-called slide track patterns, which resemble quasi-elliptical shapes in a normal ball-and-socket prosthesis [261, 263]. The type and magnitude of the load is somewhat (counterintuitively) less prominent than the direction of sliding motion [243].

In 1998, Wang *et al.* [152] reported the discovery of friction-induced molecular orientation in UHMWPE as a consequence of multi-directional sliding involved in UHMWPE, and its influence on the wear behaviour. The molecular chain of the articulating surface of polyethylene undergoes a restructuring process due to the accumulation of strain, which is caused by surface traction. Friction-induced microstructural changes act as wear precursors [166], with the prerequisite for molecular orientation being plasticity-inducing sliding motion. Plasticity-induced damage layer at the articulating surface precedes wear in acetabular components [160]. The association of cross-shear kinematics with polyethylene wear provides a better understanding of the influence of the mechanical properties on the wear performance of polyethylene. Only the energy released in the perpendicular direction to the principal molecular orientation directly influences the liberation of wear debris [201]. Studies of molecular reorientation in worn surfaces were confirmed in conventional UHMWPE as a result of plasticity-induced damage layer [264].

The motion-dependent behaviour of UHMWPE is attributed to its unique molecular structure, whose lamellar crystals orient preferentially to the direction of the sliding motion [265]. As UHMWPE is subjected to multidirectional motion, both tensile and shear stresses act in various directions (Fig. 2.27) [201]. In case the tensile stresses at the trailing edge of the asperity contact acts at an angle α_f (which is the typical case in a ball-and-socket configuration), the stresses can be transformed into their components: longitudinal stress σ_l , transverse stress σ_t , and shear stress τ_{lt} , as shown in Fig. 2.27. Therefore, the longitudinal stress σ_l and the transverse stress σ_t become aligned parallel and perpendicular, respectively, to the principal orientation of the polymer chain. Due to the anisotropy of the UHMWPE, the failure strength is highly dependent on the sliding motion direction as shown in Fig. 2.28 [243]. As the transverse strength is lower than the longitudinal strength, failure is more likely to occur at the inter-fibre section due to the weak van der Waal bonds [265], [266].

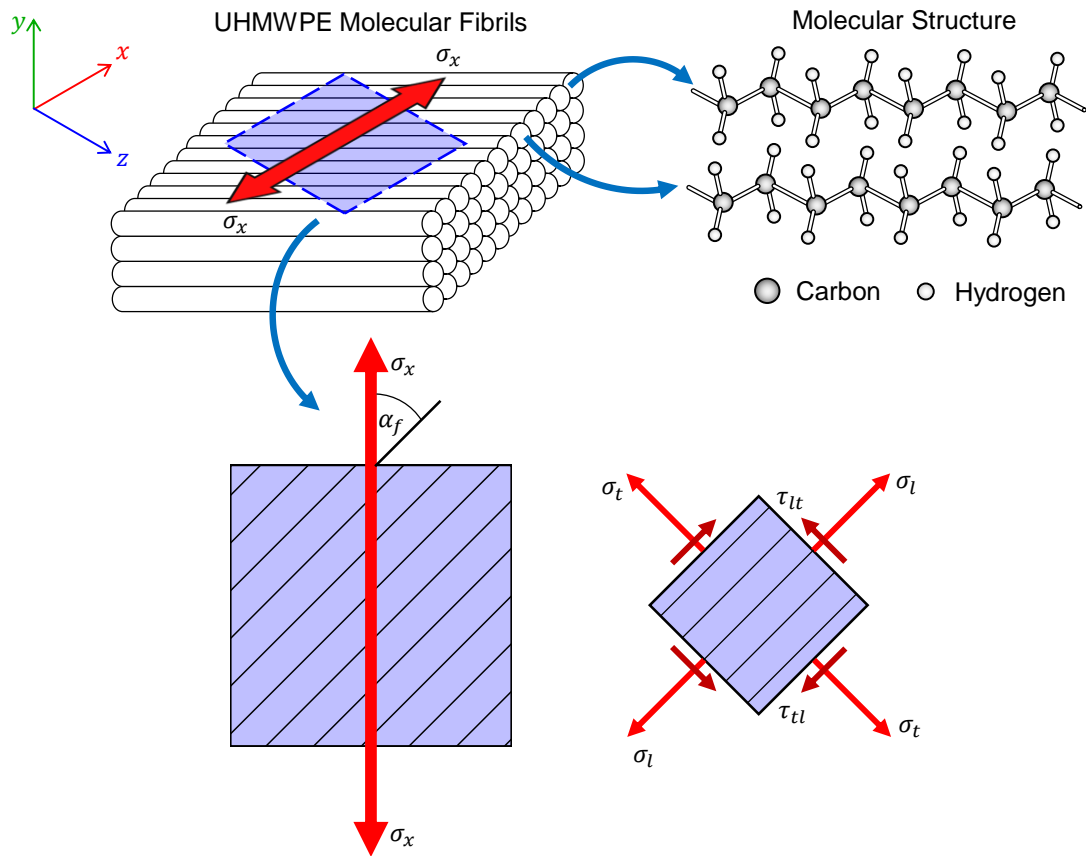


Fig. 2.27: UHMWPE fibrils and the corresponding molecular structure, being subjected to an applied load σ_x that is inclined at an arbitrary angle α_f (represented by a unidirectional structure) with respect to the principal molecular chain orientation. The resolved stress components (σ_l , σ_t , τ_{lt}) relative to the molecular polymer chain are shown. Adapted from: [152, 201, 243].

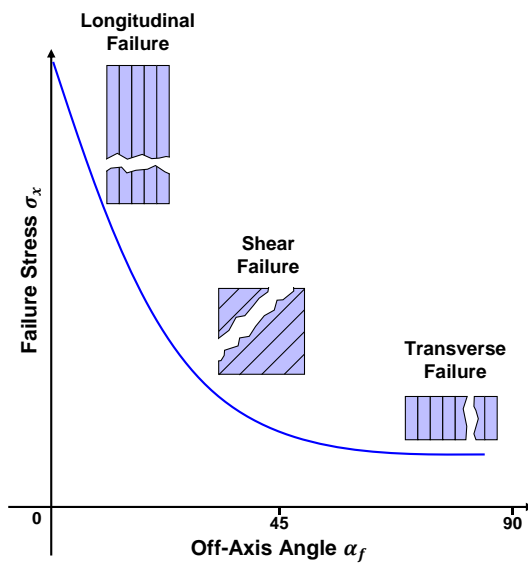


Fig. 2.28: Failure stress as a function of the off-axis loading angle. Adapted from: [243].

The trajectory of an arbitrary point in an acetabular cup, produced by the motion of the counterface, is referred to as a slide track [33]. For ease of visualisation, the slide tracks of arbitrary (but equally-spaced) points produced on the femoral head are shown in Fig. 2.29a. Furthermore, the load profile associated with an individual slide track is shown in Fig. 2.29b. The slide tracks produced on the acetabular cup would resemble the inverted shape of those produced by the femoral head, due to the relative motion between the hemispherical cup and femoral head. The orientation of the slide track relative to the principle molecular orientation is described by a cross-shear ratio [267]. The cross-shear ratio considers the direction of the sliding motion relative to the longitudinal axis of the UHMWPE molecular chain composing micro-fibrils. The cross-shear ratio is represented as a decimal value ranging from 0 to 1 (inclusive). A value of 0 represents no cross-shear motion, therefore sliding motion occurs parallel to the principal molecular orientation, whereas a value of 1 represents maximum cross-shear motion, therefore sliding motion occurs perpendicular to the principal molecular orientation.

Due to the small size of the asperity contact spots (possessing relatively short molecular chains), as opposed to the long molecular chains which are found in the bulk of the material, Wang *et al.* [243] postulated that the shear force applied to these asperities is likely to be less than that required to shear the long molecular chains found in the bulk of the material. Therefore, the asperities facilitate the liberation of wear particles. In this regard, the strength of the molecular chain can be regarded to be a function of the density of molecules inside the chains, and their alignment relative to the principal molecular orientation [201, 243]. Stretching of the molecular chains results in the breakage of the van der Waal forces that are adjacent to the microfibrils [166]. Hence, as abduction/adduction and internal/external rotation motion occurs at an angle to the principal directions of the flexion/extension motion, sub-micron wear particles are released [34].

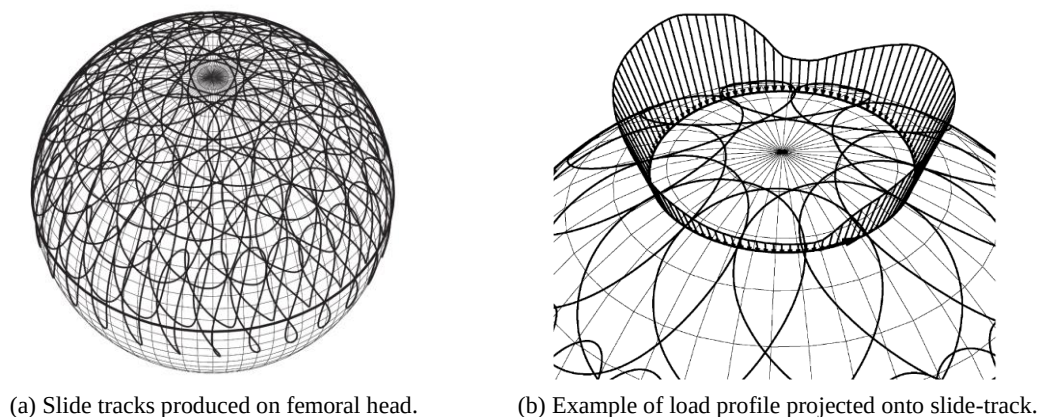
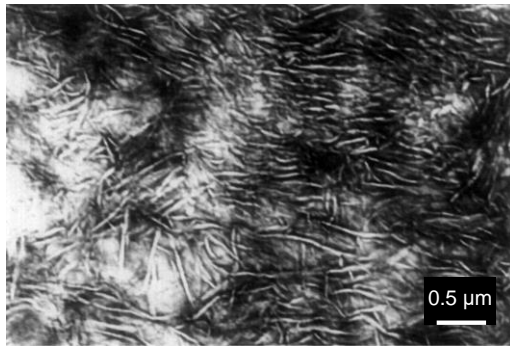


Fig. 2.29: Slide tracks due to multidirectional sliding motion of the hip. Source: [18].

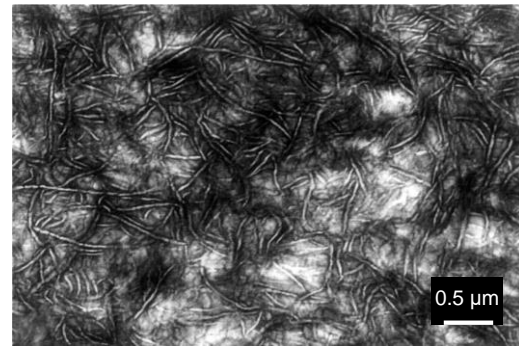
Under multi-directional sliding conditions, extensive wear damage was observed as a result of plasticity-induced orientation, both in clinically retrieved and experimentally wear tested UHMWPE cups [15, 166, 268]. Wear of UHMWPE was attributed to the transverse stress that was imposed on the plastically deformed surface molecular structures leading to the surface fibrils to be ruptured [15, 243, 269]. Molecular reorientation of the polymer is aided by increased temperatures due to frictional effects [166, 270]. Galetz and Glatzel [166] observed that surface areas of UHMWPE samples subjected to high speed multidirectional sliding (118 – 132 mm/s) and high normal loads (producing a maximum pressure value of 14.5 MPa) were most prone to microstructural changes, acting as sources of debris generation. On the other hand, it was observed that the subsurface microstructure remains unaltered, when compared to samples that have been subjected to unidirectional sliding.

Under unidirectional sliding conditions, the accumulation of plastic strain at the surface causes a disruption in the lamellar crystals forming a fibre-like structure [152], thus enhancing its mechanical properties anisotropically (Fig. 2.30a). These anisotropic improvements include orientation hardening, reduced frictional effects, and enhanced wear resistance [172, 271]. The failure strength along the molecular orientation becomes significantly greater due to the alignment of the C-C bonds [265]. Thus, the wear resistance of linear UHMWPE is attributed to its long and entangled chains, resulting in a highly anisotropic structure [152]. UHMWPE can carry greater loads in the fibre direction, but the least loads can be carried in the direction that is across the fibre direction. It was noted that at the deeper regions below the surface, UHMWPE was not influenced by the plasticity-inducing mechanism as an isotropic and random morphological structure was observed (Fig. 2.30b) [269].

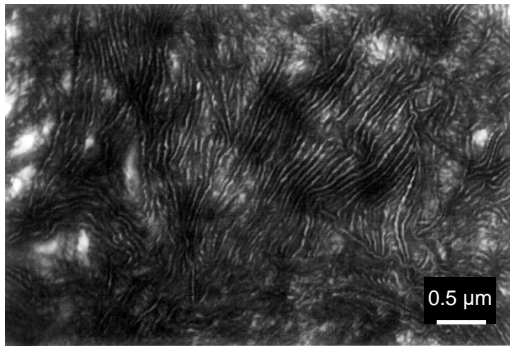
The phenomenon of plasticity-induced orientation was also confirmed in XPE (Fig. 2.30c). As crosslinks are generated between the randomly oriented polymer chains, the molecular strength is enhanced isotropically, higher interfacial stress is required to liberate the wear particles and thus adhesive wear is minimised. Abrasive wear is also drastically reduced when the polyethylene components are crosslinked, due to the improved strength of the surface. Nonetheless, it should be noted that the crystalline lamellae in XPE are still prone to plasticity-induced orientation, however to a lower extent, as greater surface stresses would be required compared to uncrosslinked UHMWPE [269]. In fact, the plasticity-induced orientation effect did not penetrate deeply into the polymer, as randomly oriented morphology was observed relatively close to the surface layer (Fig. 2.30d) [269]. Hence, multi-directional motion on XPE surface still undergoes molecular disruptions, leading to the formation of the plasticity-induced damaged layer, which acts as a precursor to wear [269].



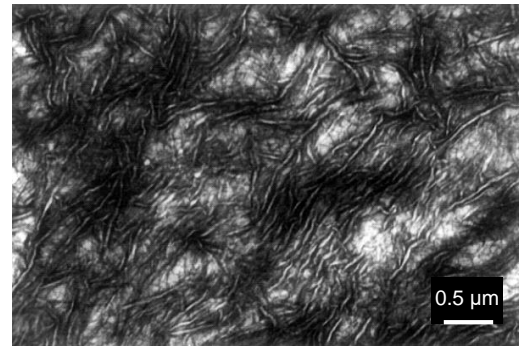
(a) UHMWPE: Lamellae alignment at the near-surface layer (depth: 1.3 – 2.0 μm).



(b) UHMWPE: Isotropic and random orphology at the subsurface (depth: 9.0 μm).



(c) XPE: Lamellae alignment at the near-surface layer (depth: 1.3 – 2.0 μm).



(d) XPE: Isotropic and random morphology at the subsurface (depth: 3.3 – 3.9 μm).

Fig. 2.30: TEM images of wear tested UHMWPE and XPE samples. Source: [269].

2.5.4. Wear Mechanisms

Wear mechanisms determine the type of damage, volume of wear, wear rate, particle size, and overall trends, such as steady-state behaviour and run-in, and can be sensitive to test conditions [86]. Adhesive, abrasive and surface fatigue (Fig. 2.31) wear have been all associated with wear of hemispherical acetabular cups. Wang *et al.* [15] suggests that these traditional concepts of wear mechanisms on their own are not sufficient to describe the actual wear process of UHMWPE, as these concepts do not take into account the structural anisotropy of the material. Wang *et al.* [152] have qualitatively illustrated the relative contribution of the different wear mechanisms in UHMWPE hemispherical cups, as shown in Fig. 2.32.

The wear mode in the human hip joint can be described as multidirectional sliding wearing due to the formation of quasi-elliptical paths, that cross each other during cycling motion of the gait [272]. As discussed earlier, the submicron wear particles in acetabular cups are the result of the interfacial friction produced by multiaxial loading and motion resulting in a reoriented crystalline lamella in the polyethylene molecular structure. On a macro level, localized plastic strain exceeds the ultimate strain value and results in the release of the wear debris [132, 152].

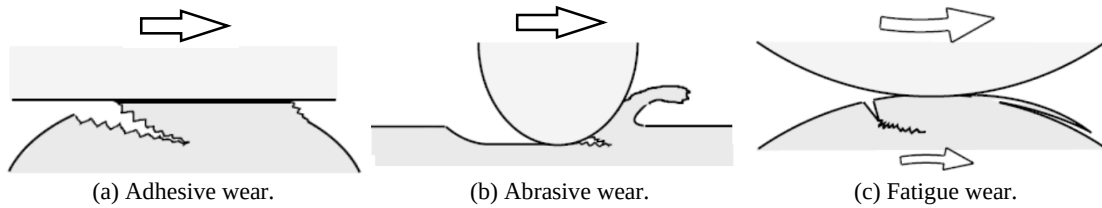


Fig. 2.31: Wear mechanics. Representative topographic surfaces that are produced for UHMWPE on a microscopic scale following the wear processes are shown. Source: [273].

Adhesive wear (Fig. 2.31a) is regarded to be the prominent type of wear mechanism in acetabular cups. The material surfaces subjected to load possess molecular forces greater than the inherent material properties of either surface. During relative motion of the two surfaces, the surface asperities undergo bonding. Further motion entails breaking of the bond junction, usually producing a wear particle from the weaker material and thus resulting in pits and voids. The adhesive wear process is accelerated by (1) the roughened hard counterface (either due to a poor surface finish or abrasion) as it acts as a base for UHMWPE film transfer, and (2) through oxidation (e.g. aging) which weakens the polymer at the subsurface, reducing its strength and facilitating its liberation from the bulk and transfer to the hard counterface [274, 275]. A glossy and polished smooth surface is usually produced in UHMWPE following adhesive wear processes [54, 210, 276–278].

Abrasive wear (Fig. 2.31b) may occur due to a roughened counterface or due to third-body particles that are released from the bone cement. The infiltration of loose third-body particles (e.g. PMMA cement debris, metallic debris and hydroxyapatite particles, ceramic debris) at the articular interface can become embedded in the polyethylene and cause ploughing and scratches to the surfaces [132]. Both the polyethylene bearing surface and the metallic alloy femoral bearing counterface are prone to the detrimental abrasive effects of hard third-body particles [243, 279].

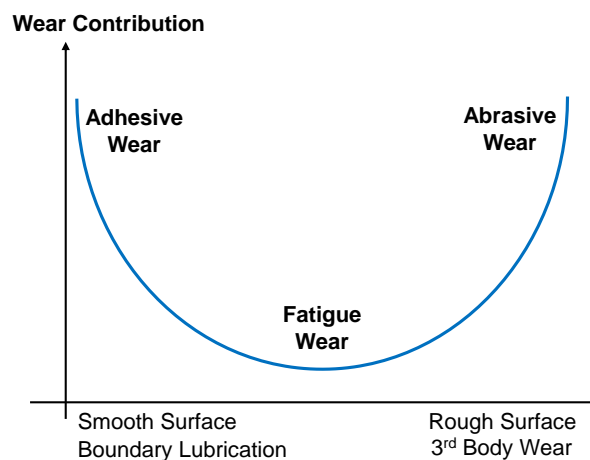


Fig. 2.32: Schematic illustration of the relative importance of abrasive wear, adhesive wear and surface fatigue wear for acetabular cups Source: [152].

Fatigue wear (Fig. 2.31c) occurs when UHMWPE component is subjected to high contact stresses, resulting in a profile of high shear stresses along the cross-section of the component. Fatigue damage is exhibited in various modes, including pitting, and surface and subsurface microcracks [243, 280], leading to the release of polyethylene particles [132]. The shear stress profile along the cross-section of the component peaks below the surface, and thus promotes the delamination of UHMWPE [130]. Fatigue wear is dominant in knee tibial inserts [71, 131, 132], as high contact stresses, which are generated due to their non-conforming geometry [130], exceed the fatigue limit of the material. Crosslinking and subsequent remelting (thermal processing) reduce the fatigue strength, as well as the mechanical properties, as a result of reduced crystallinity [281]. This effect is suppressed by diffusing Vitamin E to the crosslinked UHMWPE to maintain its fatigue strength [83].

Fatigue damage is usually evaluated in two approaches. The first approach evaluates the resistance of the material to initiate any cracks, assuming that the starting component is free of any defects. The second approach evaluates the ability of the material to resist crack propagation when defects are already present in the starting material [20]. Conventional UHMWPE possesses excellent fatigue resistance to crack initiation and propagation. The SN curve shown in Fig. 2.33 provides an indication of the number of cycles that are needed to initiate material yielding. It can be observed that the XPE (100kGy) exhibits a lower yield strength, and thus it is susceptible to undergo yielding at earlier stages of its lifespan when compared to UHMWPE [20, 35]. Furthermore, Baker *et al.* [20] outlined that the susceptibility to crack propagation of XPE is 51% higher, than that exhibited by UHMWPE. The increased susceptibility to crack propagation of XPE is attributed to its brittle-like nature, which prevents the material from generating plasticised regions at the crack tips, which is highly beneficial in attenuating the crack propagation effects.

Initiation of subsurface cracks and their subsequent propagation is the precursor for the liberation of large flakes, otherwise referred to as delamination [53]. Crack initiation is induced following cyclic stresses exhibited below any stress levels which could cause immediate fracture [53]. Muratoglu *et al.* [53] notes that the contact area is subjected to continuous alternating cycles of compressive and tensile stresses, hence creating the necessary mechanical conditions for fatigue to take place. The amalgamation of surface or subsurface microcracks promotes the formation of pitting [53]. Loss of geometric conformance accelerates delamination due to increased contact pressures. Delamination is enhanced by oxidation embrittlement as a by-product of crosslinking through the use of gamma-in-air sterilisation.

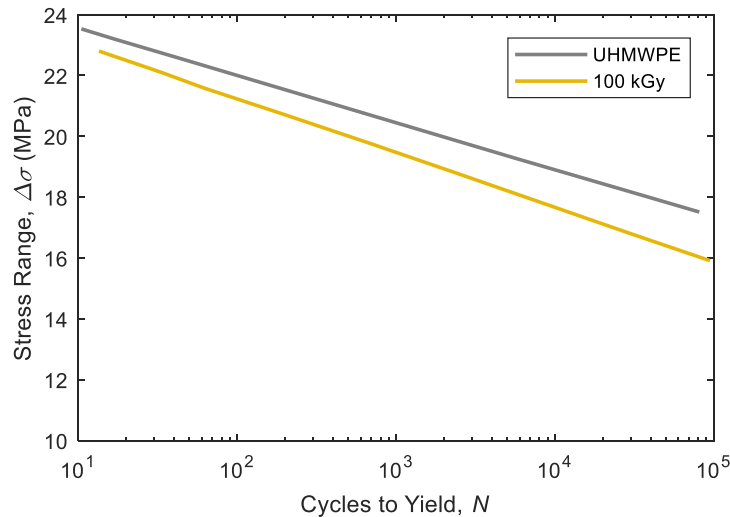


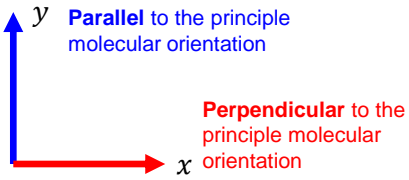
Fig. 2.33: SN plot for conventional UHMWPE and XPE (100 kGy), illustrating the number of cycles required for the material to start yielding. Adapted from: [282].

2.5.5. Wear Behaviour Dependence on Sliding Motion Direction

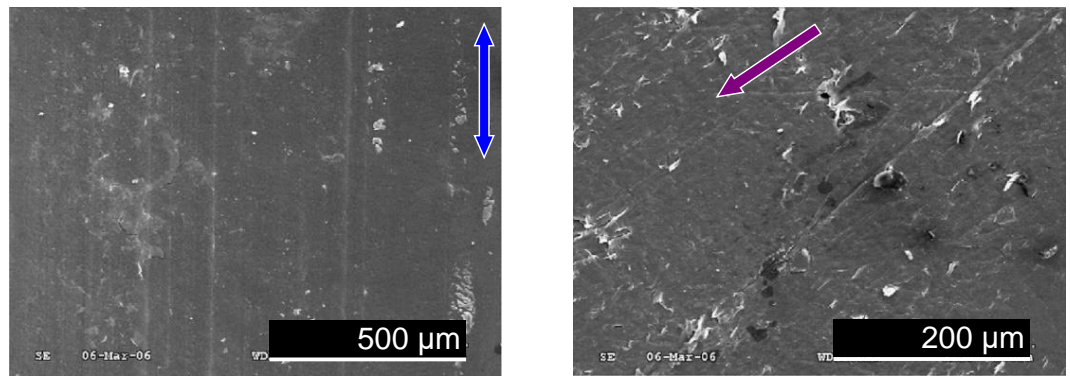
Ge *et al.* [245] analysed the wear behaviour of UHMWPE as a result of wear tracks with different trajectories. The tested trajectories include unidirectional, single-elliptical and double-elliptical patterns, as illustrated in Table 2.2 (the vertical y -axis represents the direction that is parallel to the principal molecular orientation), all of which emulate the different slide tracks exhibited in the conventional cup (as can be seen by the example slide tracks shown in Fig. 2.29, p. 42), when subjected to a contact stress value of 15 MPa, representative of the peak contact stress that is usually exhibited in acetabular cups.

Unidirectional sliding motion, being absent from cross-directional motion and cross-points, produced the least amount of wear after 10k cycles (0.30 mg), and also the least amount of wear per unit of sliding distance (1.25 mg/km). The single- and double-elliptical sliding motion trajectories were observed to produce plastic deformation, leading to adhesive and fatigue wear. The single-elliptical sliding trajectory produced the highest wear after 10k cycles (1.83 mg), and the highest amount of wear per unit of sliding distance (5.03 mg/km). Interestingly, the double-elliptical trajectory produced 0.93 mg of wear, that is half of the wear produced by the elliptical trajectory that is equal to 1.83 mg. Furthermore, the double-elliptical slide track produced a low gravimetric wear per unit of sliding distance (1.66 mg/km), which is one-third of that produced by the single-elliptical slide track. This is attributed to the higher proportion of linear motion that occurred along the direction of the principle molecular chain orientation [245].

Table 2.2: Tested slide tracks (Load: Sinusoidal dynamic contact pressure: 15 MPa, Cycles: 10k). Adapted from: [245].

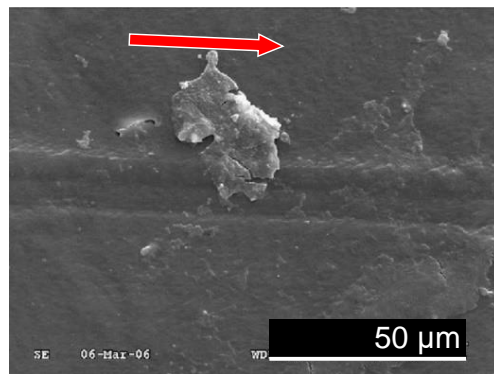
Sliding Motion Trajectory	Uni-Directional	Single-Elliptical	Double-Elliptical
Sliding frequency	$f_x = 0.0, f_y = 0.5$	$f_x = 0.5, f_y = 0.5$	$f_x = 1.0, f_y = 0.5$
Track pattern reference frame			
Sliding distance per cycle (mm)	24.0	36.4	56.1
Wear at 10k cycles (mg)	0.30	1.83	0.93
Wear per km of sliding distance (mg/km)	1.25	5.03	1.66

SEM images of the worn surfaces based on the different slide trajectories outlined in Table 2.2, are shown in Fig. 2.34. A smooth topographical surface can be observed to have been produced under uni-directional sliding conditions, as shown in Fig. 2.34a. Very light signs of ploughs are observed, which may be attributed to minor abrasion effects. However, the authors of the study did not specify what might have induced this effect [245]; whether this was attributed due to a roughened counterface or three-body wear. On the other hand, the single-elliptical trajectory shown in Fig. 2.34b is likely to have been attributed to adhesive wear due to the formation of ruptured fibrils, cavities, and shredded regions. Ge *et al.* [245] have also noted the presence of fatigue cracks. The sliding motion of the double-elliptical trajectory in the perpendicular direction has produced minor ploughing, as seen in Fig. 2.34c. Pits can also be observed in the sample, which may be attributed to fatigue. Fig. 2.34d represents the intersection point of the double-elliptical sliding trajectory, as evident from the change of direction of the coarse surface ripples. These ripples are easily detached from the bulk material, and thus contribute to the high wear rate of the polyethylene [245].

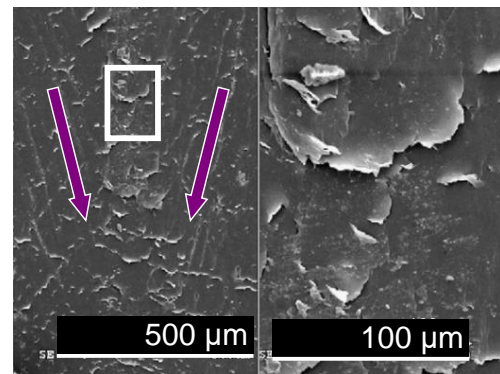


(a) Uni-directional sliding (motion occurred parallel to the principal molecular orientation).

(b) Single-elliptical sliding (motion is at an angle to the principal molecular orientation).



(c) Double-elliptical sliding (motion occurred perpendicular to the principal molecular orientation).



(d) Double-elliptical sliding (motion occurred at the cross-point of the double-elliptical trajectory).

Fig. 2.34: SEM images of worn surface topography of UHMWPE. Source: [245].

In various hip joint simulator studies [54, 210, 276–278], the appearance of wear tested conventional UHMWPE after 5 million cycles was observed to be glossy and polished, with the original machining marks being worn out (see example in Fig. 2.35a and b). In fact, this was reflected in a drastic decrease in the surface roughness (R_a) from just over $2 \mu\text{m}$ to nearly zero in less than 2 million cycles. On a microscopic level, at a very low number of wear testing cycles (250k cycles), the surface asperities are governed by the machining marks. Their initial flattening and detachment can be observed, attributing to the higher wear rates that occur during the running-in process, as can be seen in Fig. 2.35c. At 5 million cycles (Fig. 2.35d), the characteristic surface ripples can be seen which are likely to be attributed to the accumulation of plastic strain. Fibrils can also be observed to be protruding out perpendicularly to the surface ripples and in some instances, cracks were also noticed between the adjacent surface ripples. The fine scale of the surface ripples may suggest that micro-contact of the asperities behaved inelasticity as it exceeded the yield strength. Furthermore, the material yield strength is decreased due to strain softening as a consequence of multidirectional sliding motion [276].

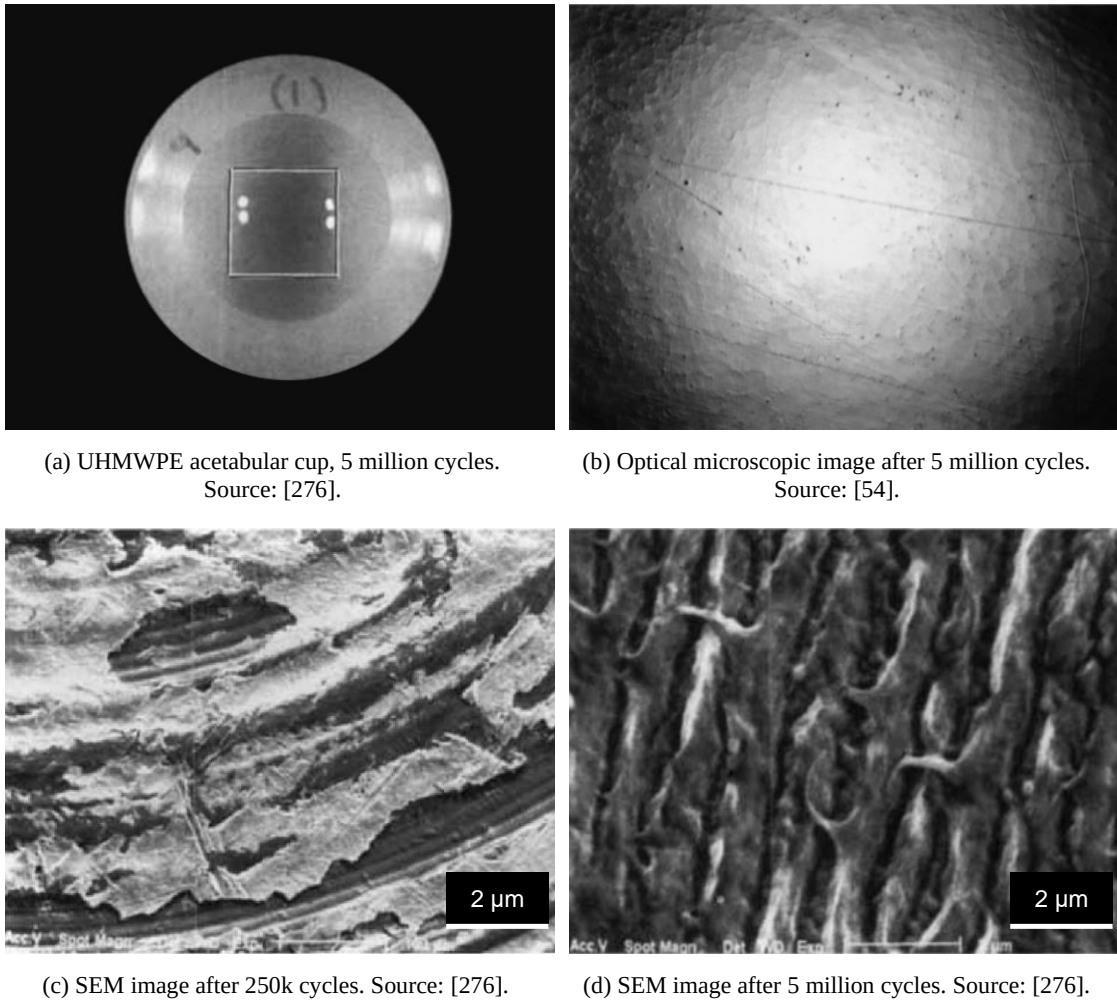


Fig. 2.35: Wear tested conventional UHMWPE acetabular cup.

2.5.6. Influence of Crosslinking

Acknowledging that the wear resistance of conventional linear polyethylene is dependent on the direction of sliding, research efforts were focussed towards enhancing its wear resistance isotropically to circumvent the orientation softening mechanisms due to cross-shear motion. Crosslinking increases the number of C-C bonds across the polymer chains and thus retards chain mobility and molecular rearrangement during sliding, hence enhancing the wear resistance of polyethylene in the lateral direction [201, 203]. Improved wear resistance results were observed during multi-axial motion in the first generation crosslinked cups, as opposed to non-crosslinked [27, 76, 283, 284].

The reduced ability of the molecules in XPE to reorient themselves results in the fibre strength being lower than in unirradiated UHMWPE when subjected to uniaxial motion. Wang *et al.* [15] have noted that under linear motion, conventional UHMWPE outperformed its

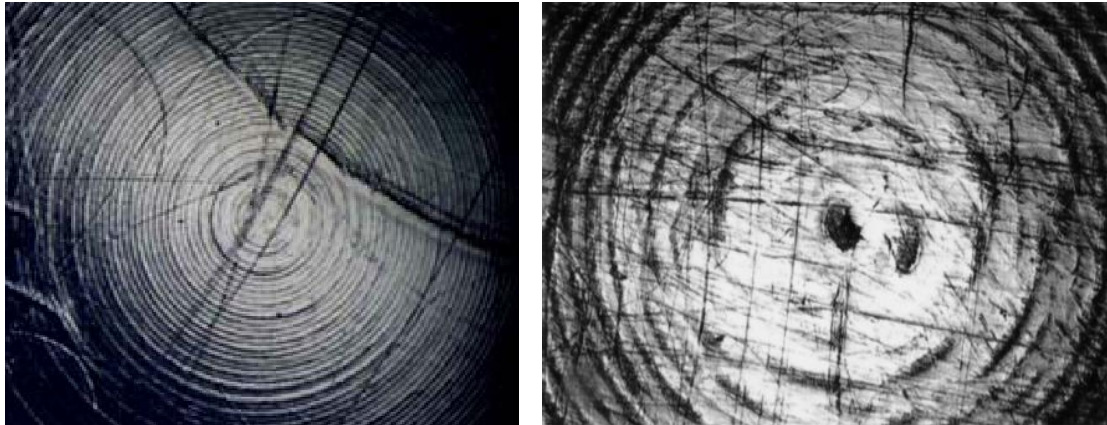
crosslinked counterpart by an approximately 30% in reduced wear. In addition, it has been demonstrated that the wear produced from XPE is independent from the slide track pattern.

Oxidative degradation of PE components during *in vivo* service has been observed following gamma radiation of the first generation acetabular cups [73, 285]. When implants are inserted into the living tissue, superoxide and hydrogen peroxide are released in the extracellular space as an inflammatory response resulting from surgical trauma [286]. Ambrosio *et al.* [285] postulated that hydroxyl (ROH) radicals that are produced *in vivo* are the main source of surface degradation. Long-term shelf aging has also been observed as an accelerator for oxidation [76].

Oxygen diffuses more rapidly in the amorphous phase than in the crystalline domains [71, 287]. Oxidation causes a reduction in molecular weight and occurs due to chain scission. The scission process is highly detrimental to the structural integrity of the polymer, as short chains are able to pack together more easily, leading to a lower molecular weight material with higher crystallinity and density and thus diminishes the abrasive wear resistance [73, 285, 288]. Oxidation stiffens the molecular chains leading to embrittlement and causes a reduction in fatigue strength. Peak oxidation was observed at around 1-2 mm below the surface, and in fact it has been correlated with the generation of cracks and delamination in retrieved acetabular liners [173]. This structural evolution may be responsible for the limited lifespan of this type of polymer component [288].

The level of oxidation was minimized with the introduction of second-generation crosslinked cups, which involved antioxidant enriched polymers. The inclusion of additives such as Vitamin E limits the liberation of the free radicals. Such a procedure eliminates the need for further thermal processing at elevated temperatures, which would otherwise degrade the strength of the polymer [66]. The elimination of free radicals minimizes oxidation rate, and consequently embrittlement of the crosslinked polyethylene. Modern crosslinking techniques involve having the polyethylene component subjected to ionizing radiation, during which crosslinking and generation of free radicals take place simultaneously. The latter are trapped in the crystalline domain. This procedure is usually followed by a remelting cycle (>137 °C), which in turn causes high chain mobility and converts the crystalline phase to an amorphous one, permitting the free radicals to be recombined [196].

Younger patients are more active, hence may be susceptible to a higher risk for dislocation. To minimize the risk of dislocation, larger femoral heads are used to increase its jump distance out of the acetabular cup (Fig. 2.2, p. 7) [27]. However, this is achieved at the expense of reduced cup thickness, which may cause the component to become prone to fracture failure which could pose serious clinical complications. Nonetheless, no statistically significant differences with crosslinked acetabular cups of different thicknesses have been observed [54].



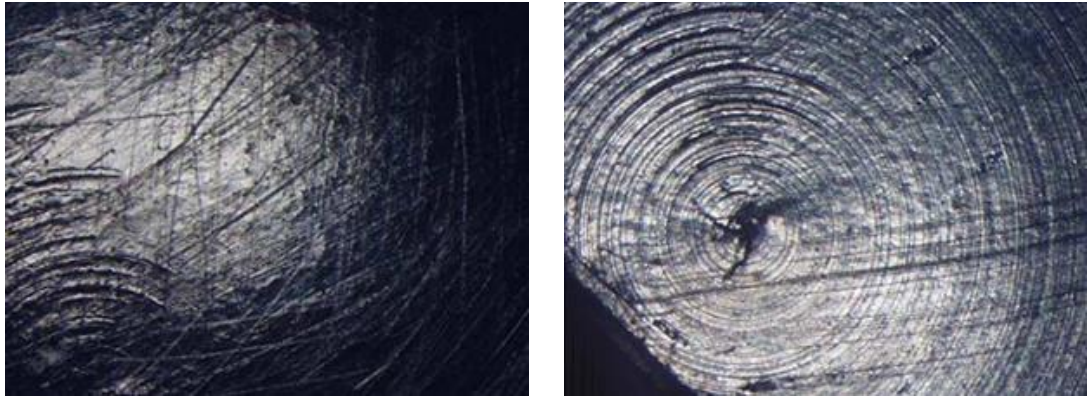
(a) Retrieved acetabular cups after 18 months *in vivo* service. Source: [289]. (b) Wear tested cup after 5 million cycles. Source: [210].

Fig. 2.36: Optical microscope images of crosslinked UHMWPE.

It is clearly agreed upon that the extent of osteolysis is a function of both size and volume of the wear particulates [91, 290]. The consensus on crosslinked polyethylene cups is that these components do not induce aseptic loosening on short-term basis, as demonstrated by early clinical data. Significant reductions were observed from gravimetric wear rates based on recently developed crosslinked polyethylene (45 – 87%) [27, 76, 283, 289]. Ongoing concerns regarding the fatigue resistance of XPE still prevail [27], and the level of gamma-irradiation dose for optimal crosslinking still remains widely debated amongst researchers [66, 91, 150].

The reduction of wear in crosslinked cups was evident from the persistence of machining marks which were retained following millions of cycles of wear testing [53, 54]. Optical microscopy images shown in Fig. 2.36 display signs of multidirectional scratches overlaid over the machining marks. Several authors postulated that these scratches were attributed to wear processes, such as third-body wear [54, 282]. This contrasts with the highly polished appearance of conventional UHMWPE which is usually achieved in less than a million cycle. No evidence of pitting, cracking and delamination was reported in this specific study [53, 289].

However, other studies [289, 291] have used retrieved HXPE acetabular cups and heated them to temperatures above their melt value. Following the heat process, most of the machining marks have resurfaced and at the same time most of the scratches disappeared. This implies that any deformation processes occurring during *in vivo* conditions have been recovered. The surface of the same acetabular cup before and after the heat cycle can be observed in Fig. 2.37a and b, respectively. This implies that the scratches were not attributed to material loss but were temporarily removed due to extensive local deformation. Only a small number of scratches have been retained, which are likely to be caused by third-body wear processes [289, 291].



(a) Surface topography of retrieved acetabular cup.

(b) Surface topography of the same area after heating above the melt temperature. Majority of machine marks have visibly resurfaced.

Fig. 2.37: Retrieved crosslinked acetabular cup. Source: [291].

2.6. Modelling Tribology of UHMWPE

2.6.1. Review of Wear Models in Literature

Wear studies are pivotal in evaluating and determining the performance of bearing surfaces [292]. Due to the complex nature involved in the physical wear processes, theoretical models are usually complemented by empirical data retrieved from experimental wear results [33]. As reviewed further below in this section, the inclusion of multi-directional motion effect exhibited in acetabular cups provides a better prediction of the wear debris generation.

2.6.2. Archard's Wear Law

Early computational models [18, 293] developed to predict the volumetric wear rate made use of Archard's wear law [294],

$$W_V = \frac{k_p L x}{p_m} \quad \text{Eq. 2.15}$$

where, W_V is the volumetric wear, k_p is a constant related to the probability per unit encounter of production of a wear particle (dimensionless), L is the applied load and x is the sliding distance, and p_m is the flow pressure of the softer material. The original Archard wear law did not take into consideration changes in contact area as it was based on pin-on-disc experimental setups, whereby the sacrificial pin retained the same contacting area [295, 296]. This implied a different k_p value had to be experimentally derived for different contacting areas. An improved equation was developed which was adapted to the local changing area based on the contact pressure [296–298], as follows,

$$W_V = k p x A \quad \text{Eq. 2.16}$$

where, k is the wear factor, p is the contact stress, and A is the contact area. The principle behind this wear law is quite straightforward as the volumetric wear W_V is directly proportional to contact pressure p and the sliding distance x . Theoretical studies to predict the volumetric wear based on Archard's wear law made use of linear-elastic and time-invariant material constitutive equations in their finite element models to identify the local contact stresses [294]. However, a sharp discrepancy was observed between the modelled rates and the wear rates obtained from retrieved acetabular cups, since the model did not consider the direction of sliding motion [18, 19, 299–301].

2.6.3. Saikko Model

Saikko and Caloni [18] point out that Archard's law (Eq. 2.15) [302] oversimplifies the force-track component, as it only takes into account the resultant force and its produced path. This scenario does not depict the actual contact conditions exhibited on a localised-level, and thus the model is likely to produce errors. Hence, Saikko and Caloni [18] propose a method that computes the volumetric wear W_V at discretized force-tracks located at different locations on the femoral head, using an adapted version of Archard's wear law (Eq. 2.16), by introducing the surface integral as follows,

$$W_V = nk \int_A L dx \quad \text{Eq. 2.17}$$

where, n is the number of cycles, k is the wear factor, A is the contact area, L is the applied load and dx represents the change in the sliding distance. The surface integral can be estimated as follows,

$$\int_A L dx \equiv \sum_{i=1}^{N_n} \sum_{j=1}^N q_i(t_j) \Delta x_i(t_j) \quad \text{Eq. 2.18}$$

where q_i is the discrete force, Δx_i is the discrete incremental displacement, t_j is the discrete time step, N_n is the number of contact nodes, N is the number of time steps, i is the index for contact nodes and discrete forces, and j is the time index.

However, as noted in Section 2.5.2.2 (p. 39), the actual volumetric wear is highly dependent on the level of cross-shear produced by the trajectory. As can be seen from Eq. 2.18, the Saikko model does not taken consider the volumetric wear W_V as a function of the amount of cross-shear taking place.

2.6.4. Liu Model

As wear of UHMWPE is dependent on the direction of sliding, several theoretical models based on the cross-shear ratio have been developed to better predict the wear. The theoretical wear model proposed by Liu *et al.* [267] is reviewed in this section. The model starts off by presenting the volumetric wear (W_V) which is proportional to the product of the contact area and sliding distance, as shown,

$$W_V = C_w Ax \quad \text{Eq. 2.19}$$

where, C_w is the wear coefficient, A is the contact area and x is the sliding distance. The linear wear depth (d_w) is obtained by dividing Eq. 2.19 by the contact area A ,

$$\frac{W_V}{A} = \frac{C_w Ax}{A} \Rightarrow d_w = C_w x \quad \text{Eq. 2.20}$$

In the conventional wear models, such as in [294], the wear coefficient is assumed to be constant. However, Liu *et al.* [267] postulate that this value is a function of the cross-shear ratio. The cross-shear ratio (CSR) is quantified as,

$$CSR = \frac{\Sigma W_t}{\Sigma(W_t + W_l)} \quad \text{Eq. 2.21}$$

where, W_t and W_l are the respective discretized frictional work values resolved in the transverse (t) and longitudinal (l) directions with reference to the principal molecular orientation. The generic form of the frictional work can be expressed as follows:

$$W_i(t) = \mu_i F_i(t) x_i(t) \quad \text{Eq. 2.22}$$

where, i specifies the direction, μ_i is the coefficient of friction, and F_i and x_i represent the normal force and sliding increment, respectively, at time t . The wear coefficient was empirically derived as a function of the cross-shear ratio for non-crosslinked UHMWPE (GUR 1050) [29] as shown,

$$C_w = (32.0CSR + 0.3) \times 10^{-9} \text{ when } CSR \leq 0.04 \quad \text{Eq. 2.23}$$

$$C_w = (1.9CSR + 1.6) \times 10^{-9} \text{ when } 0.04 < CSR \leq 0.5 \quad \text{Eq. 2.24}$$

Hence, by calculating the motion-dependent C_w , the corresponding linear (d_w) and volumetric (W_V) wear can be computed.

2.6.5. Kang Model

Kang *et al.* [303] propose a wear factor that is computed as a function of both the cross-shear motion and the contact pressure. The empirical data was derived experimentally using multi-directional pin-on-plate wear testers. The pins were produced from GUR 1050 UHMWPE, whereas the plates were produced from CoCr (cobalt-chromium) alloy. The cross-shear ratio (*CSR*) was varied from 0.0 to 0.25, whereas the contact pressure was varied from 1 to 10 MPa. Combinations of pin rotations and stroke lengths were used to generate the trajectories with a range of *CSRs*. The lubricant consisted of 25% (by volume) bovine serum diluted in sterile water. The experimentally derived wear factor k from this work is equal to,

$$k(CSR, \sigma_{ave}) = e^{(k_a + k_b \ln(C_0) + k_c \sigma_{ave})} \quad \text{Eq. 2.25}$$

where, k_a , k_b and k_c are coefficients, and their experimentally derived values are equal to -13.1, 0.19 and -0.29, respectively. The corresponding plot is shown in Fig. 2.38. The average contact pressure is calculated as follows,

$$\sigma_{ave} = \frac{\sum_{i=1}^N p_i}{t_j} \quad \text{Eq. 2.26}$$

where, p_i is the instantaneous contact pressure, t_j is the number of timesteps during one motion cycle. The computed wear factor is then plugged in Archard's adapted wear equation (Eq. 2.17) to predict the volumetric wear.

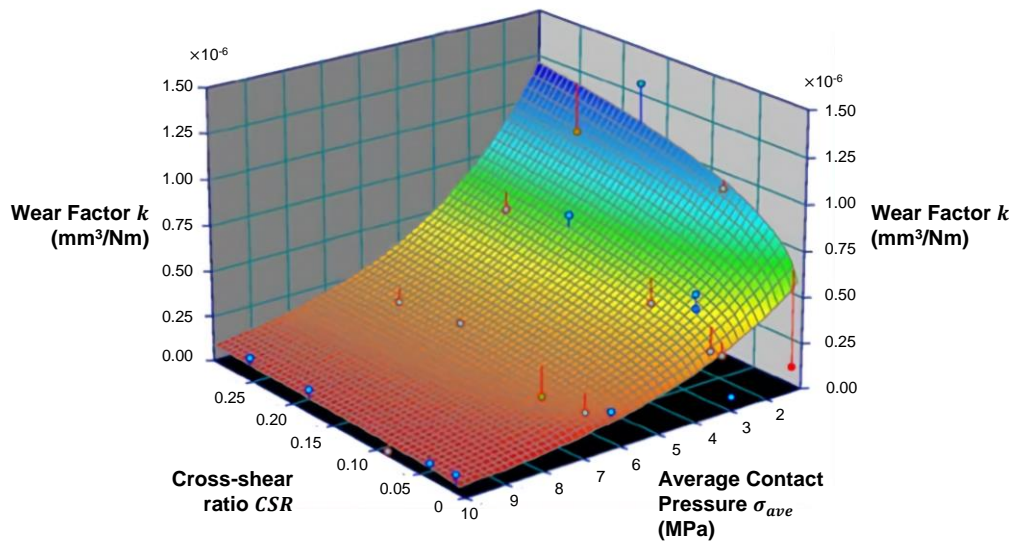


Fig. 2.38: Wear-factor k computed as a function based on the cross-shear ratio and contact pressure, as proposed by Kang *et al.* [303].

2.6.6. Petrella Model

Previous wear models that predict the volumetric wear have been significantly improved with the introduction of the cross-shear parameter [267, 303]. Nonetheless, such models assume that the orientation of the molecular chains remains aligned to the initial fibre orientation when in use, irrespective of the changing direction of sliding motion of the counterface (i.e. cross-shear ratio values are calculated relative to the principal fibre orientation, for ease of computation). However, it is well-known that this is not the case, since the orientation of the molecular chains is subject to reorientation according the direction of the sliding motion. The wear model proposed by Petrella *et al.* [298] does not only take into account the cross-shear effects, but also considers the incremental orientational changes on the molecular chains that occur within every incremental step for every sliding motion cycle. This is achieved by introducing an incremental weight factor m_{ij} that considers the material memory²⁹ ($m_{ij}=1$ implies sharp angles between slide track segments, $m_{ij}=0$ implies slide track segments have the same orientations), which is defined as follows,

$$m_{ij} = \sum_{s=1}^{mem} \frac{1}{mem} |\sin(\theta_{i,j} - \theta_{i-s,j})| \text{ where } i > mem \quad \text{Eq. 2.27}$$

where, mem represents the number of steps required to align the polymer chain according to direction of sliding motion, s is the mem incremental step, i represents the time increments, and j represents the discretised locations on the wear surface (which corresponds to the nodes in the finite element model), $\theta_{i,j}$ represents the angle of the segment during the current time increment, whereas $\theta_{i-s,j}$ represents the angle of the segment during the previous time increment. The sine function is used to penalise slide tracks with sharp angles (i.e. $\sin(90^\circ)=1$), therefore assigning the highest value to m_{ij} . An example illustrating the computation of the m_{ij} is shown in Fig. 2.39. The above function penalises any deviations that are done from the current incremental step as compared to the previous incremental step. Nonetheless, the function rewards segments of the slide tracks which possess the same orientation as the previous segment, by assigning the value of m_{ij} to 0. The volumetric wear W_V from the Petrella model is computed from the adapted Archard's wear law (Eq. 2.17) as follows [298],

$$W_V = k_o \sum_{j=1}^N \sum_{i=1}^n p_{ij} x_{ij} A_j + k^* \sum_{j=1}^N \sum_{i=1}^n p_{ij} x_{ij} m_{ij} A_j \quad \text{Eq. 2.28}$$

²⁹ The term material memory is used by Petrella *et al.* [298] to refer to the dependence upon the past sliding motion of the slide track produced on the polyethylene component.

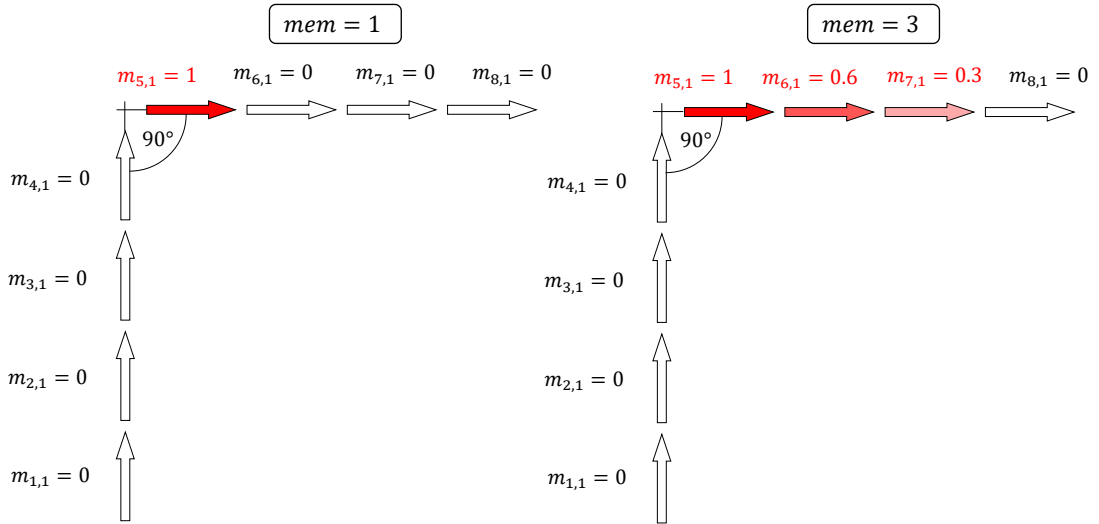


Fig. 2.39: An example of a slide track produced by node $j = 1$, with a sharp 90° curve, that has been divided into segments according to the distance covered in time increments i is illustrated. When mem is 1 (left), only one segment is penalised. When mem is 3 (right), three segments are penalised to represent the process of molecular reorientation that occurs during sliding motion. Source: [298]

which can be simplified as follows,

$$W_V = \sum_{j=1}^N \sum_{i=1}^n p_{ij} x_{ij} A_j (k_o + k^* m_{ij}) \quad \text{Eq. 2.29}$$

where, p_{ij} is the incremental node pressure, x_{ij} is the scalar distance of the incremental step, A_j is the local surface area under consideration, k_o is the wear factor associated for unidirectional sliding motion, and k^* is the wear factor for the worst case scenario for cross-shear sliding motion.

By considering Eq. 2.27, it can be observed that in this model, the wear is computed mainly in two parts. The first part idealises the sliding motion as unidirectional, and therefore the amount of wear under these ideal conditions is computed. The second part of the equation calculates the amount of wear due to deviations that occur in the sliding motion. The m_{ij} acts as a penalty for deviations done in the sliding motion. The value of the cross-shear ratio CSR is not required for the computation of the volumetric wear, since it exploits the concept of the material memory. The final volumetric wear can be computed by using Eq. 2.29.

2.7. Wear Debris

2.7.1. Overview

Apart from the volumetric wear, the long-term stability of the prosthesis is also highly dependent on particle size, shape and composition, and its concentration, which dictate the severity of the osteolysis effects [43, 49, 92]. Wear particles with different morphologies produce different biological reactions, thus leading to different degrees of osteolysis. The characterisation of the morphological parameters following the wear testing regime can be utilized to provide a quantitative indication of the potential biological reaction of the new hip implant design, as discussed below (Section 6.6.1, p. 286).

Ge *et al.* [245] in their study involving the analysis of conventional UHMWPE wear debris generated at different paths with varying levels of cross-shear (uni-directional, single-elliptical, and double-elliptical) identified that wear particles generated at the cross-points possessed smaller diameters. Referring back to Table 2.2 (p. 48) and Fig. 2.40, the distribution of the differently-sized particles according to the sliding trajectories can be observed [245]. Majority of the particles produced from unidirectional sliding produced particles with the largest diameters (range 10 – 270 μm), with only the 3% of the particles having diameters below 10 μm . The proportion of particles with diameters below 10 μm for the single-elliptical and double-elliptical trajectories increased to 16% and 27% respectively. As the inflammatory response has been associated with the small particle diameters (0.2 – 0.8 μm) [43, 49, 92], it is probable that the uni-directional motion test produced the lowest number of small-diameter particles and therefore can potentially produce the least severe biological reactions, as compared to the other trajectories.

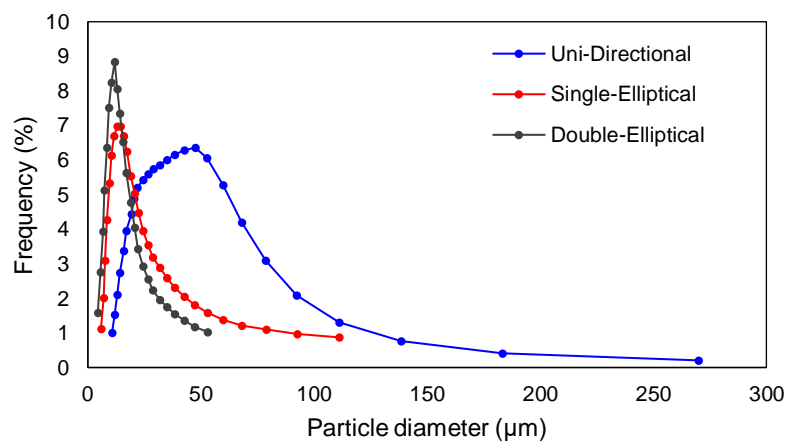


Fig. 2.40: Particle size distribution with different sliding trajectories. Source: [245].

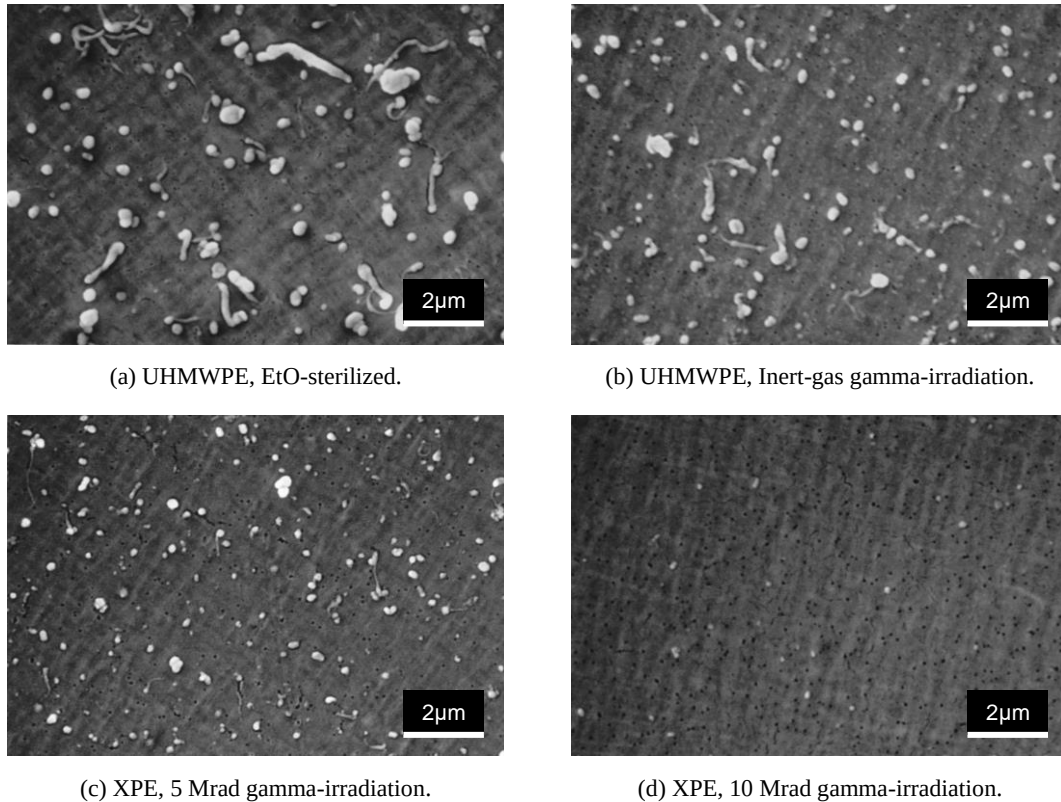


Fig. 2.41: Wear particles of UHMWPE subjected to different sterilization and crosslinking techniques. Source: [85].

The different types of polyethylene, conventional and crosslinked, used in orthopaedic applications also produce particles of different sizes at different rates [66]. UHMWPE wear particles sampled from periprosthetic tissue possessed varying geometry in the form of fibrous, dumbbell-shaped and particulates, signifying the different wear mechanisms that take place [276]. There is no clear consensus regarding the exact range of particles sizes which are responsible for osteolysis. However, it is generally accepted that particle sizes of 0.1 – 1.0 μm are mostly responsible for bone tissue destruction processes; the severity of which increases with decreasing particle sizes. On the other hand, wear particles measuring 10.0 μm or greater have not been associated with significant bone tissue destruction [43, 49, 304–306].

It is well established that increasing the irradiation dose results in a reduction in the gravimetric wear rate and the particulate diameters [85, 289], as can be observed in Fig. 2.41. Nonetheless, no statistically significant difference was produced in the number (quantity) of particles that were generated, as can be noted in Fig. 2.41a to c. At higher doses (Fig. 2.41d), a significant reduction in the quantity of wear particles was observed. Hence, Ries *et al.* [85] postulate that different morphologies are likely to prompt different cellular reactions, although their actual effects have not been studied in their work. Illgen *et al.* [91] also demonstrated that debris produced from 10 Mrad cross-linked polyethylene has smaller morphology and has been observed to be more inflammatory than its conventional type when tested in a murine model. In

fact, the individual crosslinked polyethylene particles resulted in higher osteolysis effects than conventional polyethylene particles [91, 307]. Consequently, researchers argue that the benefits of reduced wear owed to cross-linked polyethylene may, to some extent, be compromised by its higher inflammatory response.

2.7.2. Functional Biological Activity

Fischer *et al.* [306] provided a novel method for predicting the overall biological activity that induces osteolytic effects, as a function of the wear debris volume and particle sizes. This metric is intended to provide a quantitative index which can be used to perform relative comparisons.

The wear particles generated during wear accumulate at the bone tissue surrounding the implant, resulting in inflammation, bone resorption and subsequent loosening. Osteolysis is reduced by cytokines which are released by the activated macrophages. However, the amount of cytokines which are released is dependent on the size and volumetric concentration of the produced wear particles [43–49].

The adverse biological activity that inhibits the release of cytokines is denoted as $B(r)$, where r represents the size of the wear particle. The typical $B(r)$ values for different particle sizes as produced by a wide range of hip implants are shown in Fig. 2.42. The smallest particle sizes produce the most severe biological activity $B(r)$, and are represented by a normalised value of 1. The largest particles produce the least severe biological activity $B(r)$, and are assigned a value of 0.04 (as determined from cell culture studies by Fischer *et al.* [306]).

The percentage of particles found within a specific size range is described by the volumetric concentration and is denoted by $C(r)$, which is calculated by isolating the particles from the lubricant. The extent of a specific biological activity (*SBA*) of polyethylene wear debris is defined as the ‘relative biological activity per unit volume’ [306]. This is computed by integrating the biological activity $B(r)$, and the volumetric concentration $C(r)$, over the range of particle sizes, as shown,

$$SBA = \int_{0.1}^{100} C(r) B(r) dr \quad \text{Eq. 2.30}$$

The *SBA* value is highest ($SBA = 1$) if all the volume of the debris is in the range with the smallest particle diameters, and the *SBA* value is lowest ($SBA = 0.04$) if all the volume of the debris is in the range with the largest particle diameters. The overall biological activity attributed to a specific implant is computed by multiplying the *SBA* to the volumetric wear rate (W_V). This is referred to as the functional biological activity (*FBA*), and is computed as follows,

$$FBA = W_V \times SBA \quad \text{Eq. 2.31}$$

The typical *SBA* and *FBA* values for ball-and-socket implants, as presented by Fischer *et al.* [306], are shown in Table 2.3. From the produced results, it can be observed that the unirradiated cup (ref. 1) resulted in a lowest *SBA* value of 0.32. This is attributed to the generation of large particles, thus producing low values of $B(r)$. However, due to the high volumetric wear rates (W_V) which are typically produced by unirradiated UHMWPE cups, this resulted in a relatively high *FBA* value of 16.

Considering the moderately crosslinked cup (ref. 2), it can be observed that a higher *SBA* and *FBA* values have been produced, despite the lower volumetric wear rates which are typically produced by crosslinked cups. This case provides insight on instances that reported increased osteolysis effects with increased levels of crosslinking [308]. On the other hand, it can be observed that a highly crosslinked acetabular cup (ref. 5), produced a high *SBA* value of 0.83, but the overall osteolytic effects produced by the prosthesis are relatively low (*FBA* value being equal to 7), as a result of its low volumetric wear rate.

It should be noted that the presented results in Table 2.3 are meant to serve as quantitative indices to perform relative comparisons for implants that were tested under the exact same conditions. Due to the susceptibility of the polyethylene components to absorb the lubricant during use [309–311], accurate predictions of the *FBA* are difficult to achieve, as the gravimetric wear measurements do not take into consideration the amount of fluid absorb during sliding motion.

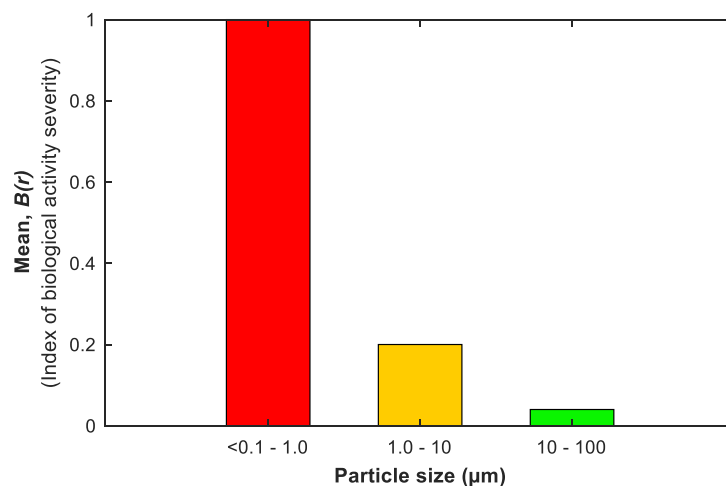


Fig. 2.42: Biological activity $B(r)$ composed as a function of particle size derived from *in vitro* cell culture studies. Adapted from: [306].

Table 2.3: Specific Biological Activity (*SBA*) and Functional Biological Activity (*FBA*). Source: [306].

Ref.	Implant	Material	Specific Biological Activity (<i>SBA</i>)	Functional Biological Activity (<i>FBA</i>)
1	Ball-and-Socket	GUR 1020, 0 kGy	0.32	16
2	Ball-and-Socket	GUR 1020, 40 kGy	0.50	18
3	Ball-and-Socket	GUR 1050, 0 kGy	0.96	43
4	Ball-and-Socket	GUR 1050, 25 kGy	0.89	41
5	Ball-and-Socket	GUR 1050, 100 kGy	0.83	7

2.8. Conclusion

Developments in the field of arthroplasty have been largely focussed on enhancing the wear resistance of the polyethylene components. Significant reductions in wear have been attained with the introduction of crosslinked polyethylene [160]. Nonetheless, hip implants on the market still possess a limited lifespan, ranging between 15 – 25 years [13], which is in most cases attributed to aseptic loosening [39].

It has been observed that the ball-and-socket design of the artificial hip has remained practically the same ever since its introduction in the clinical market. The inevitable multi-directional motion that is produced by the ball-and-socket articulation has been observed to be detrimental to the tribological performance of the prosthesis, as these types of motions weaken the molecular structure of the polyethylene surface due to molecular orientation softening effects [152]. Consequently, wear particles are liberated upon the application of contact stresses exhibited during the gait cycle [243].

To the best of the author's knowledge, no artificial hip implant design, which makes use of uni-directional articulations to exploit the molecular orientation hardening mechanisms of the polyethylene material, has been developed so far. Therefore, in this doctoral work, a novel hip implant design is developed which is constituted from cylindrical articulations, to promote uni-directional sliding motions. Accordingly, an improved wear resistant structure is produced, which could potentially minimize the effects of osteolysis.

3. Methodology

3.1. Introduction

3.1.1. MaltaHip Design Concept

In this work, a new hip implant design consisting of three uni-axially rotating cylindrical articulations, referred to as the MaltaHip, is developed. The novel articulating concept developed in this work leverages on the low contact stress and the orientation hardening effects (as discovered by Wang *et al.* [152]) that are produced by a metal-on-polyethylene cylindrical articulation. Since a cylindrical articulation enables only one rotational degree of freedom, a total of three cylindrical articulations are required, being orthogonally oriented to each other, to reproduce the flexion/extension (FE), internal/external rotation (IE), and abduction/adduction (AA) motions of the hip, as shown in Fig. 3.1a.

The kinematic sequence of the proposed MaltaHip concept is shown in Fig. 3.1b. The three pairs of cylindrical articulations can be realized with a minimum of four components, which are referred to as the acetabular cup, flexor, rotator and abductor, each intended to articulate independently of each other in their respective directions (initial concept design shown in Fig. 3.2). The MaltaHip cup and rotator components were assigned the soft bearing material, whereas the flexor and abductor were assigned the hard bearing material of the prosthesis.

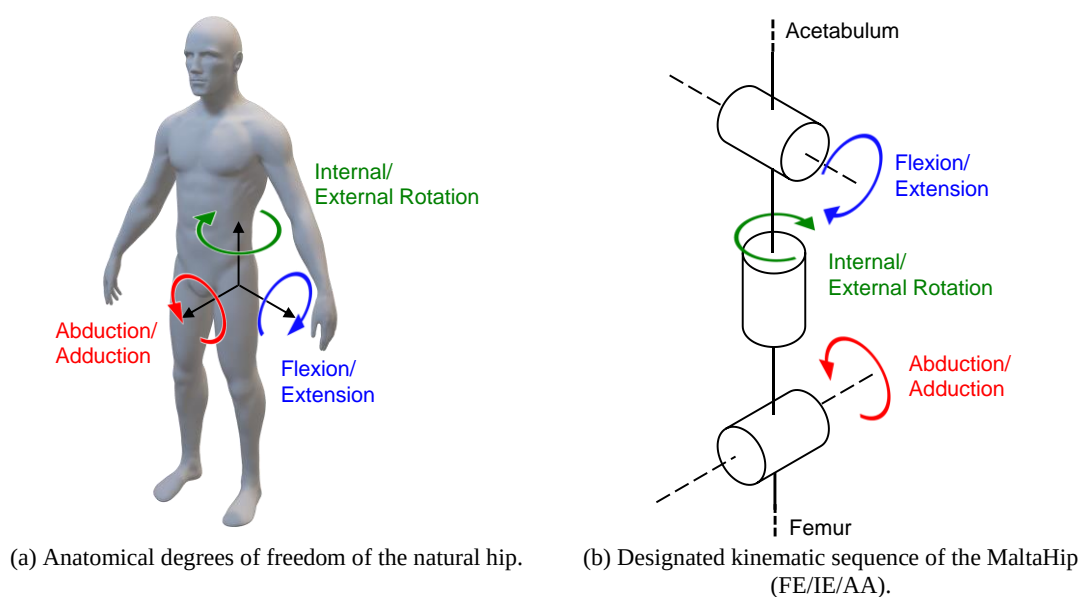


Fig. 3.1: Degrees of freedom of the natural and artificial MaltaHip hip.

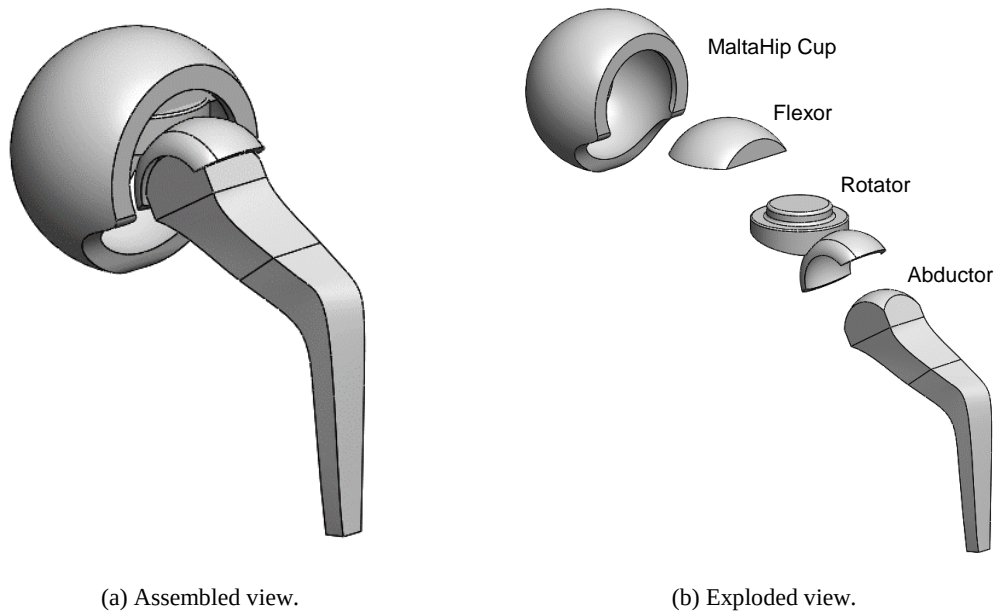


Fig. 3.2: Early concept of the MaltaHip, acting as the starting point for this doctoral work.

The original idea behind this concept was devised by Schembri Wismayer *et al.* [312] (unpublished), after observing that the natural ankle joints exhibit drastically lower rates of osteoarthritis (between 9 to 10 lower) than those exhibited in natural hip joints [25]. The initial concept design that was developed prior to this work (unpublished) is shown in Fig. 3.2. It served as the starting point for this doctoral work, which demonstrated the potential arrangement and kinematic sequence of the different components. The initial concept was based on a tri-cylindrical metal-on-metal articulations, designed to produce lower contact stresses than ball-and-socket articulations, due to the larger contact areas offered by the cylindrical geometry. However, after observing the potential improvements in the wear resistance that can be attained by the UHMWPE, when subjected to uni-directional sliding motion, this work focussed on developing a prosthesis which exploits molecular orientation hardening mechanisms of metal-on-polyethylene cylindrical articulations.

3.1.2. Materials

The MaltaHip concept is intended to demonstrate the potential reductions in wear that can be attained with a tri-cylindrical prosthesis design, when compared to its ball-and-socket counterpart. For this reason, clinically approved materials were selected for the MaltaHip implant design. Uncrosslinked and crosslinked polyethylene materials were tested in this work, representing the two main polyethylene types that are used in the field, and thus gain insight on their tribological response when subjected to uni-directional sliding motion in the tri-cylindrical MaltaHip prosthesis design.

For the MaltaHip implant with uncrosslinked polyethylene components, annealed and ram-extruded round bars of virgin UHMWPE with material grade of GUR 1050 according to ASTM F648-14³⁰ were used. Round bars with 80 mm and 40 mm diameters were used, and their corresponding material certificates can be found in Appendix A1 (p. 319) and A2 (p. 322), respectively. This material grade will be referred to as UHMWPE throughout the rest of this work. For the MaltaHip implant with crosslinked polyethylene components, annealed and compression moulded round bars of pre-irradiated (100kGy), Vitamin E-infused polyethylene with material grade of GUR 1020, according to ASTM F2695-12³¹ were used. A round bar with a 60 mm diameter was used, and the corresponding material certificate can be found in Appendix A3 (p. 325). This material grade will be referred to as VEHXPE (Vitamin E-infused highly-crosslinked polyethylene) throughout the rest of this work. All polyethylene round bars were supplied by Orthoplastics Ltd. (United Kingdom).

The metallic bearing components were produced out of annealed high-N austenitic stainless steel (ASTM 1586-13e1³²) due to its outstanding mechanical properties (high elastic modulus, high yield strength) and relative ease of machining, when compared to cobalt chromium molybdenum (CoCrMo) alloys. The high-N austenitic stainless steel was supplied by MetSuisse Distribution Ltd. (Switzerland). Round bars with 50 mm and 30 mm diameters were used, and their corresponding material certificates can be found in Appendix A4 (p. 331) and A5 (p. 335), respectively.

3.1.3. Testing Conditions

This work investigates the tribological performance of the MaltaHip prosthesis according to the walking gait cycle specified in ISO 14242-1:2014/AMD 1:2018³³. The standard specifies the angular movements of the joint, the load profile, and type of lubricant that must be used during the wear test to reproduce the *in vivo* conditions.

The one-second-long gait cycle, often expressed in percentage form, consists of a stance phase (between 0 – 60 %), and a swing phase (between 60 – 100 %), as shown in Fig. 3.3. The angular motions and load profile of the hip are shown in Fig. 3.4. The angular movements are

³⁰ ASTM F648-14 – Standard Specification for Ultra-High-Molecular-Weight Polyethylene Powder and Fabricated Form for Surgical Implants

³¹ ASTM F2695-12 – Standard Specification for Ultra-High Molecular Weight Polyethylene Powder Blended With Alpha-Tocopherol (Vitamin E) and Fabricated Forms for Surgical Implant Applications

³² ASTM F2695-12 – Standard Specification for Wrought Nitrogen Strengthened 21Chromium-10Nickel-3Manganese-2.5Molybdenum Stainless Steel Alloy Bar for Surgical Implants (UNS S31675)

³³ ISO 14242-1:2014/AMD 1:2018 – Implants for surgery – Wear of total hip-joint prostheses – Part 1: Loading and displacement parameters for wear-testing machines and corresponding environmental conditions for test.

based on sinusoidal functions, as defined in Table 3.1. The widest range of movement is produced by the flexion/extension motion ($-18^\circ < FE < 25^\circ$). Motions along the internal/external rotation ($-10^\circ < IE < 2^\circ$) and abduction/adduction ($-4^\circ < AA < 7^\circ$) directions are significantly shorter. The load profile is based on the double-peak curve proposed by Paul [313]. The curve of the load is mathematically defined in Table 3.2 and achieves a maximum force of 3000 N at 0.12 and 0.50 s during the stance phase, and maintains a minimum force of 300 N throughout the swing phase.

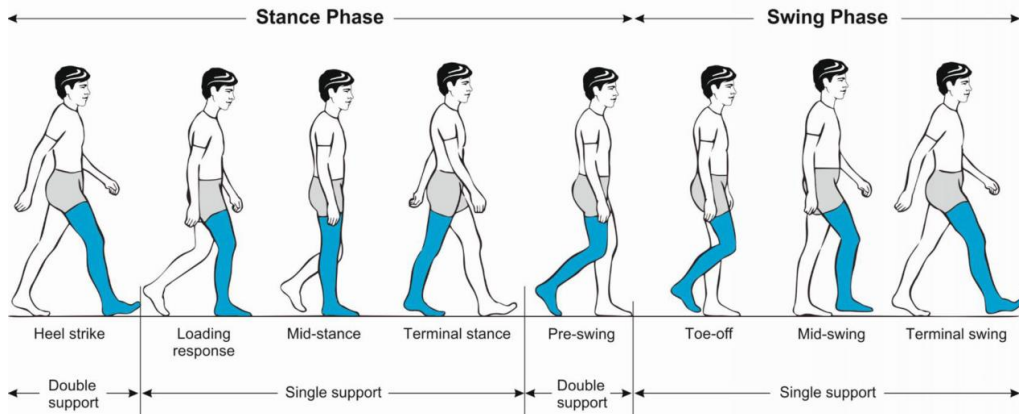


Fig. 3.3: Different phases during the gait cycle. Source: [314]

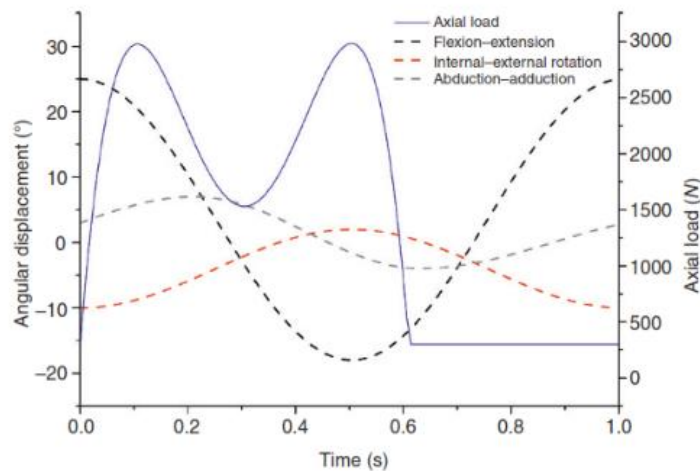


Fig. 3.4: Load and motion profiles specified for hip joint simulator testing, as specified by ISO 14242-1:2014/Amd 1:2018. Source: [315].

Table 3.1: Mathematical functions defining the angular motions of the hip, as specified by ISO 14242-1:2014/Amd 1:2018. Source: [315].

Gait cycle [%]	Abduction/adduction [degrees]	Flexion/extension [degrees]	Internal/external rotation [degrees]
$0 \leq t < 21$	$= 4.0 \sin(0.0748t) + 3$		
$21 \leq t < 62$	$= 5.5 \sin(0.0748t + 1.5)$	$= 21.5 \cos(0.0628t) + 3.5$	$= 6.0 \sin(1.5\pi + 0.0628t) - 4$
$62 \leq t \leq 100$	$= 4.0 \sin(0.26\pi + 0.0628t)$		

Table 3.2: Mathematical functions defining the load profile of the hip, as specified by ISO 14242-1:2014/Amd 1:2018. Source: [315].

Gait Cycle [%]	Load [kN]
$0 \leq t < 62$	$= L_1 t^4 + L_2 t^3 + L_3 t^2 + L_4 t + 0.3$ $L_1 = 9.30441236249746 \times 10^{-6}$ $L_2 = 1.13569119486952 \times 10^{-3}$ $L_3 = 4.46360765492253 \times 10^{-2}$ $L_4 = 6.09263366429307 \times 10^{-1}$
$63 \leq t < 100$	$= 0.3$

3.2. Mechanical Characterisation

The theoretical viscoelastic-viscoplastic behaviours of UHMWPE and VEHXPE were based on the Three Network material model which was developed by Bergstorm and Bischoff [31]. The parameters of the Three Network model for both polymers were calibrated to the specific materials that were used for the MaltaHip prosthesis. The calibration procedure was done in MCalibration Software (Veryst Engineering, United States) using stress-strain data obtained from uniaxial compression tests. The calibrated Three Network model was used for carrying out the finite element solutions. The samples used in the compression tests were extracted directly from the round bar materials used for the fabricated prosthesis (Fig. 3.5). The samples were cut into short columns having a diameter of 10 mm and a height of 5 mm.

Two sets of uniaxial compression tests containing three samples each (UHMWPE and VEHXPE) were conducted. The specimens were compressed at a constant engineering strain rate of 0.03 s^{-1} immersed in a temperature-controlled bath at 37°C . The first set of specimens were compressed to a maximum engineering strain value of 20 %, whereas the second set of specimens were compressed to a maximum engineering strain value of 60 %, intended to capture a wide range of strain values. Although the Three Network model considers the temperature-dependence effects of the material, the model was calibrated at a constant temperature of 37°C to reproduce the conditions exhibited at body temperature. The fluid was mechanically stirred to maintain a homogenous temperature throughout the bath. Every effort has been made to avoid barrelling³⁴ effects, mainly by ensuring that the contacting surfaces were polished to minimize frictional effects. Furthermore, frictional effects at the contacting surfaces were further reduced by the lubricity provided by the fluid inside the heated bath. Barrelling effects can negatively influence the stress-strain profile along the coupon during compression, and thus may decrease the accuracy of the results.

³⁴ Barrelling effect is induced when a high friction value (or bonding) is applied at the flat surfaces of the cylinder, causing the cylinder to expand unevenly, such that its mid-section would be wider than the top and bottom sections, resembling the geometry of a barrel.

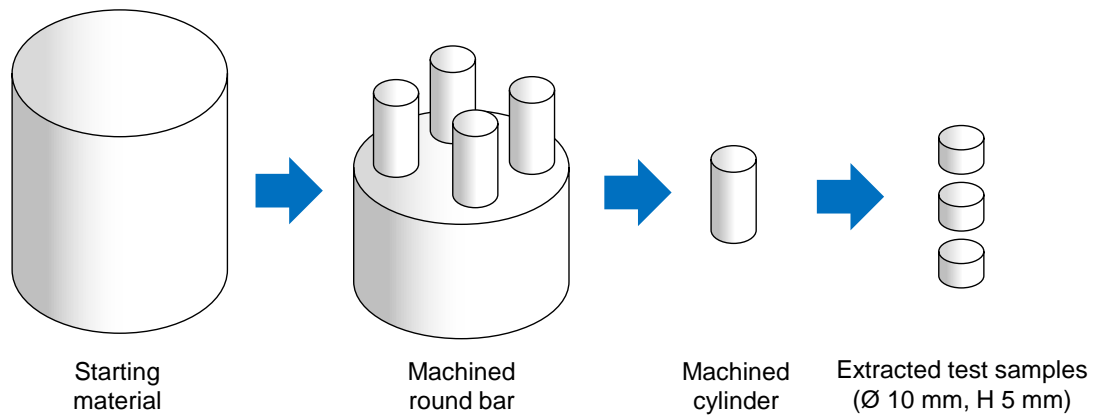


Fig. 3.5: Cylindrical test samples extracted from round bar for compression round bars.

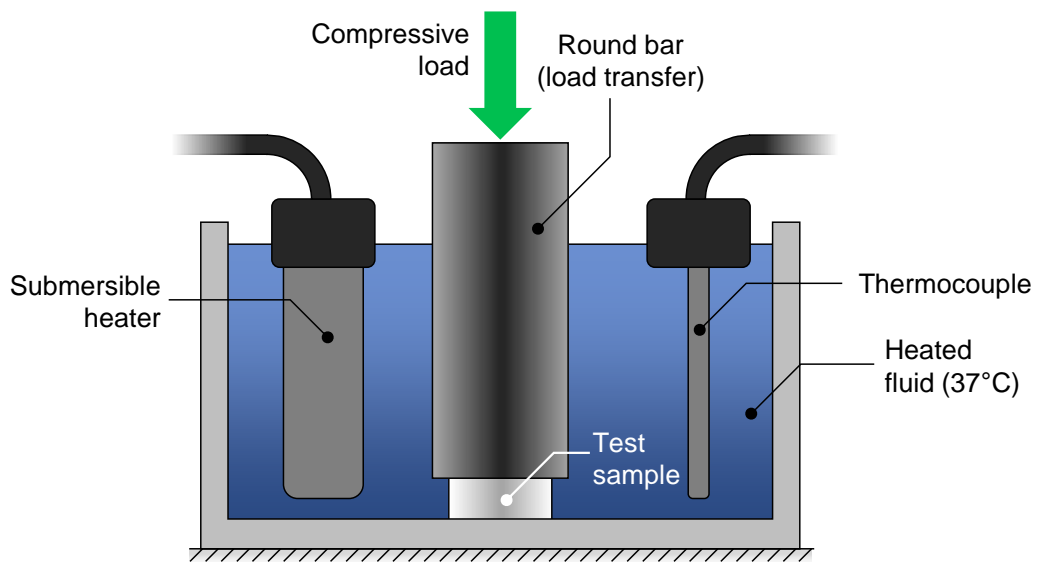


Fig. 3.6: Compression cylindrical test samples of UHMWPE conducted inside a temperature-controlled bath at 37°C

3.3. Parametric CAD Model

A parametric CAD model of the MaltaHip (Fig. 3.7) was developed using Dassault Systèmes SolidWorks 2018 [316], which served as a platform for optimizing the design of the prosthesis, by obtaining the correct size proportions of the components (cup, flexor, rotator and abductor). The MaltaHip parametric model was defined by a total of 14 design parameters, as presented in Table 3.3 and shown in Figs. 3.8 to 3.12, which consisted of component wall thicknesses, edge fillets (radii) and radial clearances, which are denoted by the subscripts t , f and c , respectively. The wall thicknesses were defined at the thinnest sections of the components due to their high influence on the structural integrity of the implant.

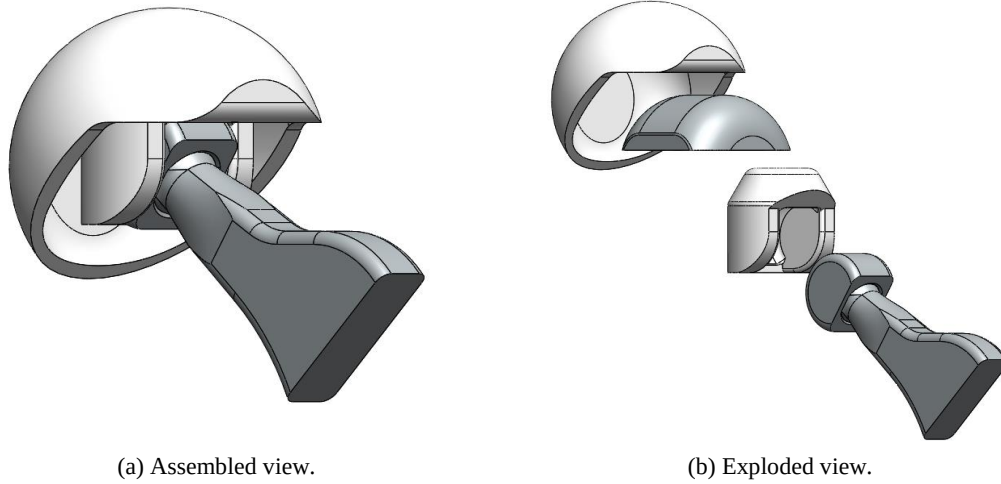


Fig. 3.7: Developed design of the MaltaHip used for the parametric CAD modelling.

It should be noted that for this study, a simplified version of the MaltaHip implant model was used. The model used during the parametric design study does not have any redundant surfaces which do not provide any load bearing capabilities. However, these surfaces are necessary for the final commercial version for practical purposes (e.g. grooves, overhang features that engage and interlock the components), to reduce the design complexity and the computational expense without compromising the accuracy of the results.

The parametric design was formulated in the following sequence: abductor, rotator, flexor and cup. Hence, a design change in the abductor component would influence the rotator design. Consequently, a design change in the rotator component would influence the flexor design. And lastly, design change in the flexor component would influence the acetabular cup design. However, a change in the acetabular cup design would not influence the abductor design. Furthermore, it should be noted that the abductor was mounted onto a stem. Therefore, the dimensions of the tapered neck of the abductor remained constant throughout the optimisation procedure. The design parameters ($A_{t1}, A_{t2}, A_f \dots C_t$) are designed to be independent of each other. All remaining non-parametric dimensions are designed to satisfy the conditions imposed on the parametric dimensions. The remaining dimensions of other non-parametric geometrical features of the abductor, rotator, flexor and cup are collectively represented by the matrices **A**, **R**, **F** and **C**, respectively, as shown in Eqs. 3.1 to 3.4. The actual dependencies between the parametric and non-parametric dimensions are generated by the CAD software.

$$\mathbf{A} = f(A_{t1}, A_{t2}, A_f, A_c) \quad \text{Eq. 3.1}$$

$$\mathbf{R} = f(\mathbf{A}, R_{t1}, R_{t2}, R_d, R_f, R_c) \quad \text{Eq. 3.2}$$

$$\mathbf{F} = f(\mathbf{A}, \mathbf{R}, F_{t1}, F_{t2}, F_f, F_c) \quad \text{Eq. 3.3}$$

$$\mathbf{C} = f(\mathbf{A}, \mathbf{R}, \mathbf{F}, C_t) \quad \text{Eq. 3.4}$$

The design parameters were varied through a range of values (as shown in Table 3.3) and their influence on the von Mises and contact stresses were analysed. Due to the great number of design parameters, only one parameter was varied and analysed at a time, which was then compared to the initial benchmark design. The parameterised CAD model enabled a unique hip implant design to be generated with each variation in the design parameters.

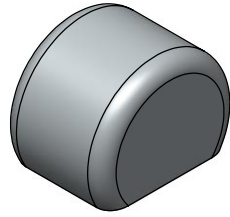
Table 3.3: Range of values tested for each design parameter.

Component	Design Parameters	Label	Range of Values [mm]
48 mm cup			
Abductor (A)	Min Internal Thickness	A_{t1}	2.0 – 4.0
	Min Width Thickness	A_{t2}	1.0 – 4.0
	Fillet	A_f	2.0 – 4.0
Rotator (R)	Min Thickness	R_{t1}	1.0 – 6.0
	Height	R_{t2}	6.0 – 9.0
	Diameter	R_d	16.5 – 18.0
	Fillet	R_f	1.0 – 6.0
Flexor (F)	Min Radial Thickness	F_{t1}	2.0 – 4.0
	Min Side Thickness	F_{t2}	1.0 – 3.0
	Fillet	F_f	6.0 – 12.0
Cup (C)	Min Thickness	C_t	2.0 – 8.0
Radial Clearances	Abductor Clearance	A_c	0.020 – 0.095
	Rotator Clearance	R_c	0.035 – 0.180
	Flexor Clearance	F_c	0.035 – 0.180

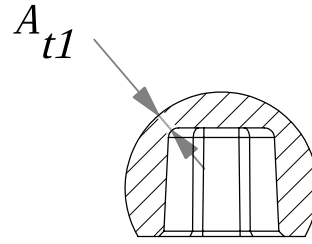
The outer dimensions of the MaltaHip cup are constrained by the diameter of the pelvic acetabulum. Hence, during this study it was imperative to identify the dimensions that provide the most beneficial effects in terms of reducing the von Mises and contact stresses, in order to optimise their effects whilst at the same time abiding by the imposed size limitations. For this study, an outer cup diameter of 48 mm was chosen, being the smallest diameter that could practically fit the mechanism of the MaltaHip. The small cup diameter enables design vulnerabilities related to mechanical stress to be immediately highlighted.

The radial clearance values for a ball and socket implant are specified by ISO 7206-2:2011/Amd 1:2016³⁵. The standard states that for femoral head diameters ranging between 28 to 36 mm, radial clearances at the maximum material condition (MMC) and the least material condition (LMC) should be 20 and 95 μm , respectively. For femoral head diameters over 36 mm, the radial clearances at the MMC and LMC should be 35 and 180 μm , respectively.

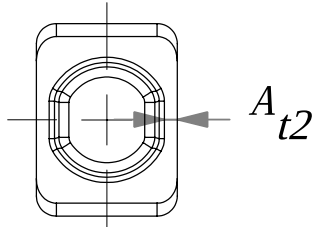
³⁵ ISO 7206-2/Amd 1:2016 – Implants for surgery – Partial and total hip joint prostheses – Part 2: Articulating surfaces made of metallic, ceramic and plastics materials – Amendment 1



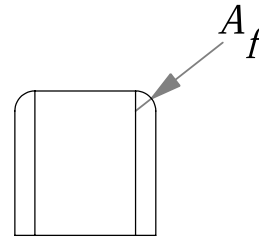
(a) Isometric view of the abductor component.



(b) Abductor internal thickness, A_{t1} [2.0 – 4.0 mm].

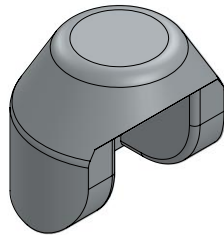


(c) Abductor wall thickness, A_{t2} [1.0 – 4.0 mm].

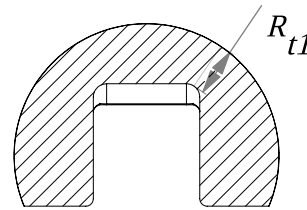


(d) Abductor exterior fillet, A_f [2.0 – 4.0 mm].

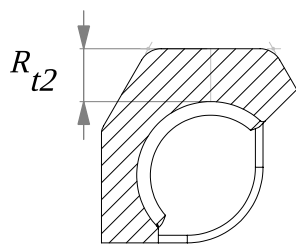
Fig. 3.8: Design parameters of the abductor component, and their corresponding range of tested values.



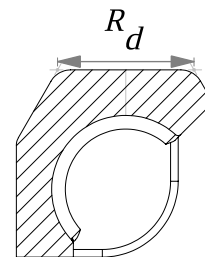
(a) Isometric view of the rotator component.



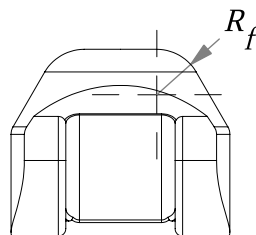
(b) Rotator internal thickness, R_{t1} [1.0 – 6.0 mm].



(c) Rotator height, R_{t2} [6.0 – 9.0 mm].



(d) Rotator diameter, R_d [16.5 – 18 mm].



(e) Rotator external fillet, R_f [1.0 – 6.0 mm].

Fig. 3.9: Design parameters of the rotator component, and their corresponding range of tested values.

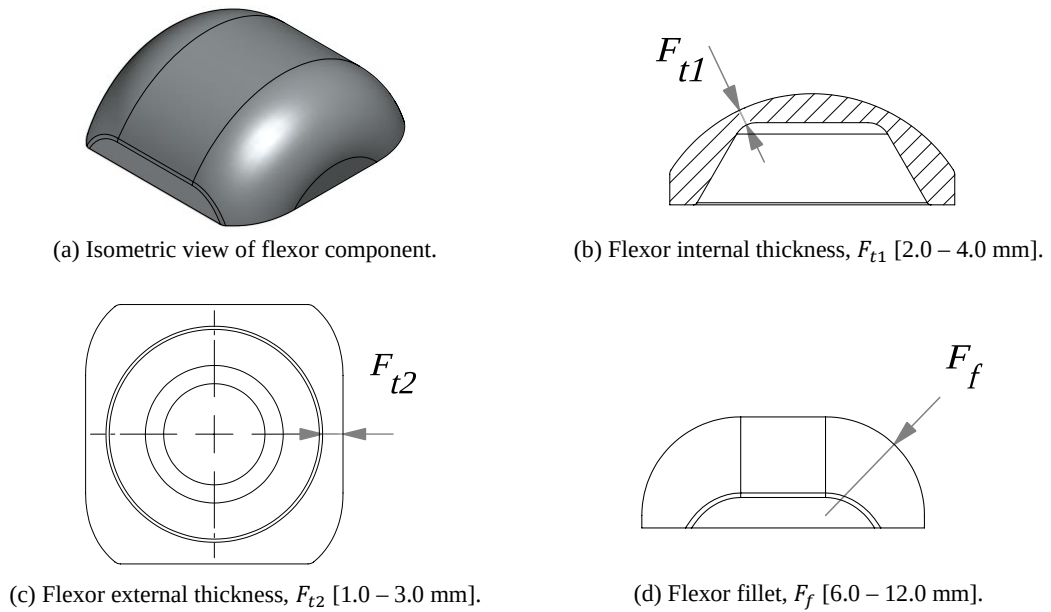


Fig. 3.10: Design parameters of the flexor component, and their corresponding range of tested values.

A manual iterative process was used in this work over an automated process to optimise the design. The manual process enables the generated stresses to be inspected after each iteration. Therefore, any results of interest could be easily analysed into further detail by performing smaller manual design variations. Furthermore, each manual iteration could be inspected in detail to ensure that a practical and sensible design was being produced. An automated process would have enabled all possible combinations to be tested, instead of testing one parameter at a time. However, if all possible combinations would have been tested, this would have resulted in an extremely large number of design combinations. The manual process provides a more practical approach for obtaining the initial critical dimensions of the designs.

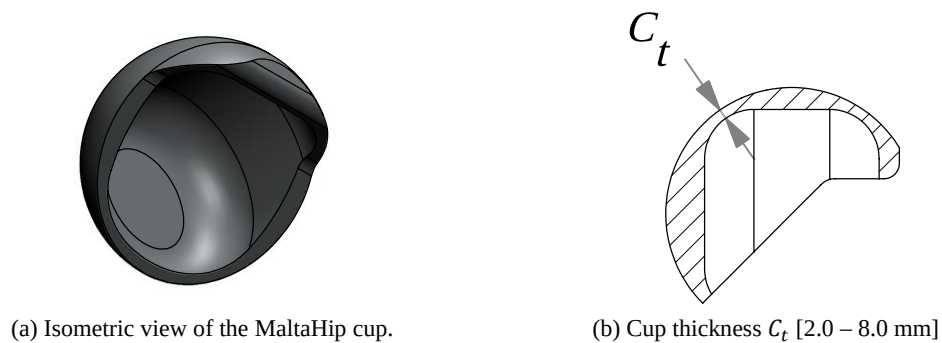


Fig. 3.11: Design parameter of the MaltaHip cup component, and its corresponding range of tested values.

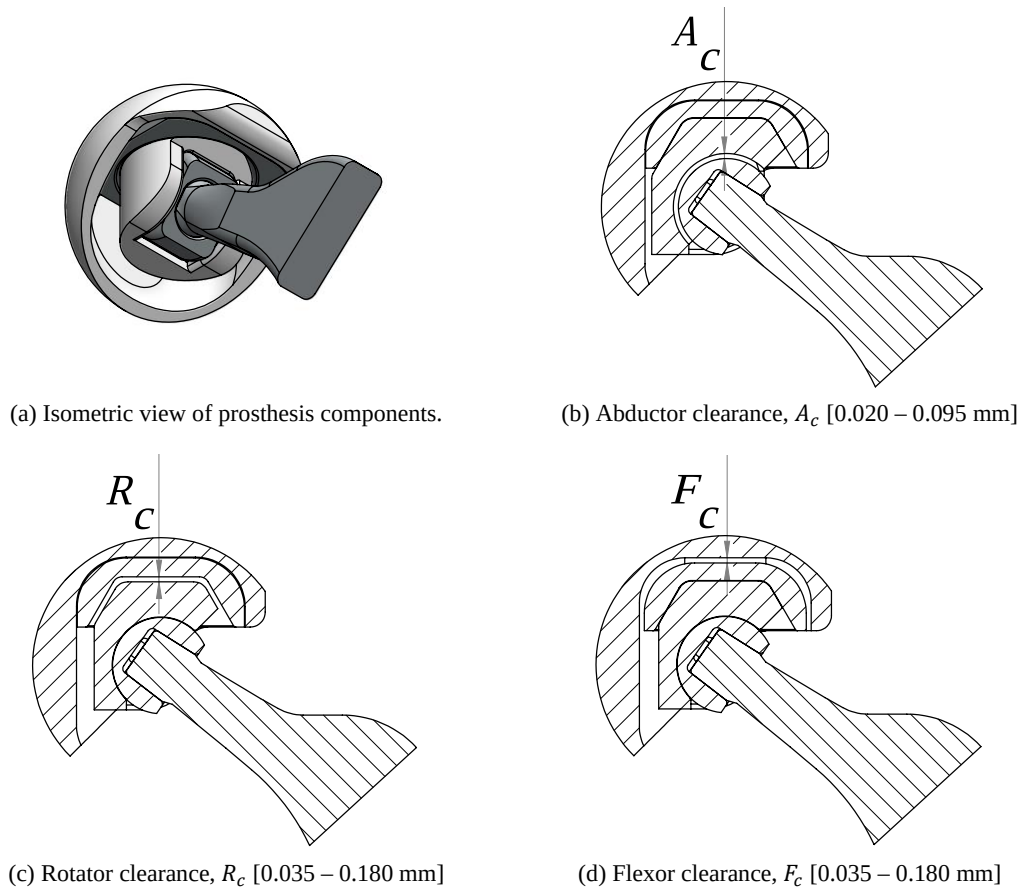


Fig. 3.12: Design parameters of the clearance values of the articulations, and their corresponding range of tested values.

3.4. Finite Element Simulations

3.4.1. Overview

Finite element simulations conducted in this work³⁶ were conducted using ANSYS Workbench 19.2 [317]. The simulations were primarily intended to evaluate the structural integrity of the bulk and surfaces of the MaltaHip components, through an analysis of the von Mises and contact stress values, respectively. The resultant contact stress values were also necessary for predicting the volumetric wear rate using the theoretical wear models.

³⁶ Specifications of the workstation used for the finite element simulations in this work:
 Central Processing Unit (CPU): Intel® Core™ i7-6700 CPU @ 3.40 GHz.
 Random-Access Memory (RAM): 32.0 GB.
 Graphics Processing Unit (GPU): NVIDIA GeForce GTX 1050 Ti (4.0 GB).

A mesh sensitivity analysis was conducted on a benchmark implant design, by varying element sizes between 0.4 to 1.5 mm in steps of 0.1 mm, which determined the mesh size to be used for all finite element studies conducted throughout this work. A mesh quality analysis was not conducted, due to the small size of the elements which was selected for the FE model, it was visibly noted that at the articulating surfaces elements with minimal element skewness, minimal size variations and low aspect ratios, all of which contribute to a high-quality mesh. In fact, the size of the elements was an order of magnitude smaller than the smallest feature of the implant, allowing them to easily occupy the smallest geometrical features of the implant. Finite element simulations performed in this work were divided into two main studies.

- The first study (Section 3.4.2, p. 76) was intended to analyse the influence of each design parameter on the stresses produced in the MaltaHip, which was crucial for optimising the dimensions of the components. The study was performed on the smallest acetabular cup (48 mm diameter) which could reasonably fit the MaltaHip mechanism. The small acetabular cup was selected for the parametric study so that vulnerabilities in design due to high stresses could be identified immediately.
- The second study (Section 3.4.3, p. 76) provides a complete finite element analysis on the finalised MaltaHip design, based on a 53 mm acetabular cup diameter. The finite element results produced on the finalised MaltaHip design were compared to that of a ball-and-socket prosthesis with the same outer dimensions.

The mechanical response of the polyethylene materials used to simulate the MaltaHip and ball-and-socket implants were based on the calibrated Three Network model, as outlined in Section 3.2. Comparisons were also made to finite element simulations which modelled the polyethylene material as a linear elastic model. The acetabular cup was placed in the anatomical position, inclined at 45 degrees.

It was not possible to pre-determine the exact value for the coefficient of friction before machining and testing the physical implants. This could only be measured and verified using specialised instrumentation (that must have been integrated to the hip joint simulator) to empirically measure the coefficient of friction of the different articulations. In addition, the coefficient of friction changes as the number of cycles increases (surfaces became smoother and therefore the coefficient of friction becomes lower). For this reason, a coefficient of friction of 0.1 was assumed at the metal-on-polyethylene articulations which represents the mixed lubrication condition [318].

3.4.2. Influence of Design Parameters

Finite element simulations conducted in the first study were done on a wide range of iterated MaltaHip designs, that were generated by varying each of the 14 design parameters specified in Section 3.3 (p. 69). Each MaltaHip design was generated by varying one design parameter at a time. Due to the high number of designs iterations that needed to be tested, simulations conducted in this study were based on a static structural analysis at 0.12 s of the gait cycle (which represent the case-scenario with the highest loads, and extreme joint angles, as shown in Fig. 3.4, p. 67).

The resultant von Mises and contact stress values, produced by each MaltaHip design, were compared to the benchmark design. This systematic approach enabled the characterisation of the mechanical response imparted by each design parameter on the MaltaHip design. The set of parameters that promoted the lowest stress values on the polyethylene components, whilst following the design constraints imposed by an implant with a 53 mm outer diameter cup, were selected for the final design of the contacting surfaces.

3.4.3. Finalised Design

Once the final dimensions of the MaltaHip were determined, additional geometrical features contributing to the interlocking mechanism were introduced. The interlocking mechanism enables the components to engage with each other, whilst at the same time minimizing the incidence of dislocation. Such design features did not contribute to significant changes to the stress values produced by the MaltaHip, as these were mostly comprised of non-load-bearing surfaces. The finalised design of the MaltaHip, and the designations used throughout this work for the different component of the MaltaHip are shown in Fig. 3.13. Furthermore, comparisons were made to a ball-and-socket implant consisting of a 53 mm outer diameter cup and a 28 mm femoral head diameter, as shown in Fig. 3.14. For clarity purposes, the acetabular cup of the MaltaHip will be referred to as the ‘MaltaHip cup’ and acetabular cup of the ball-and-socket implant will be referred to as the ‘hemispherical cup’ hereinafter. The designations that are used throughout this work for the external, internal and articulation surfaces of the MaltaHip are presented in Fig. 3.15.

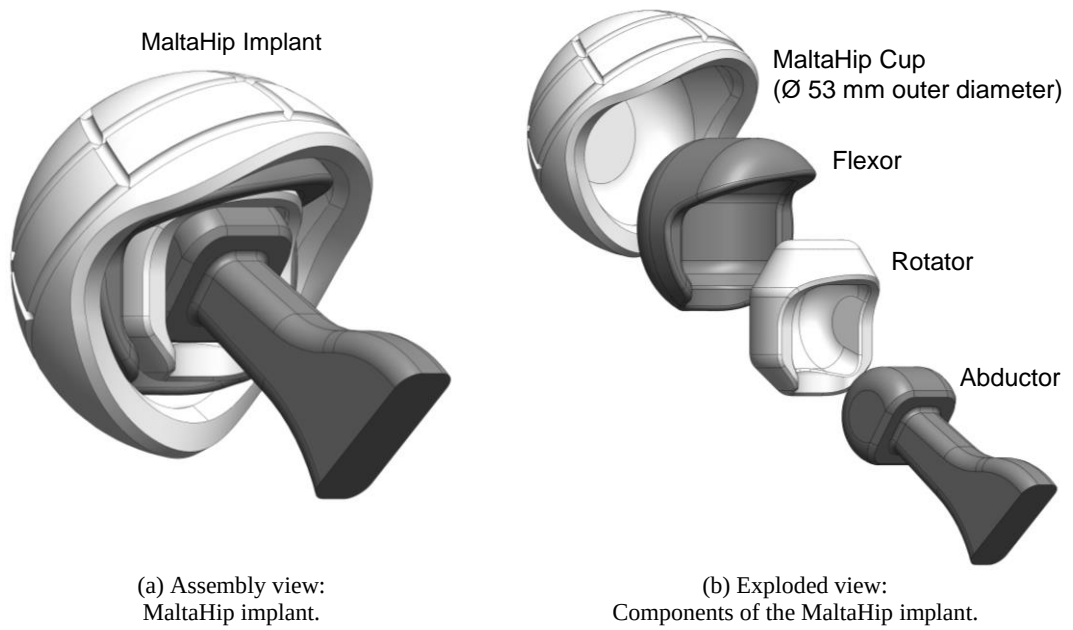


Fig. 3.13: Designations for the finalised design of the MaltaHip implant used throughout this work.

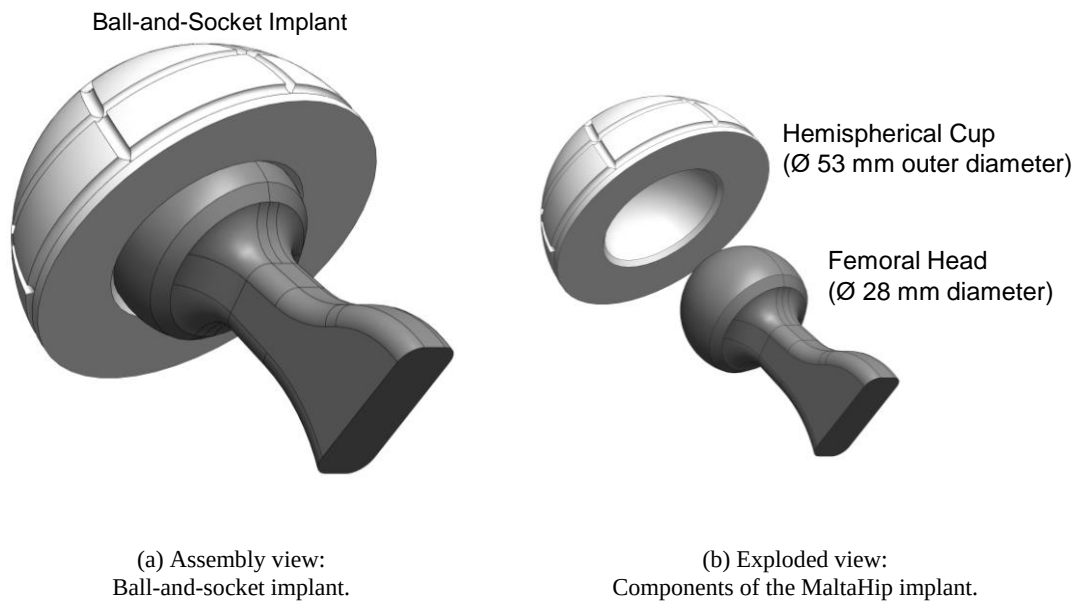


Fig. 3.14: Designations for the ball-and-socket implant used throughout this work.

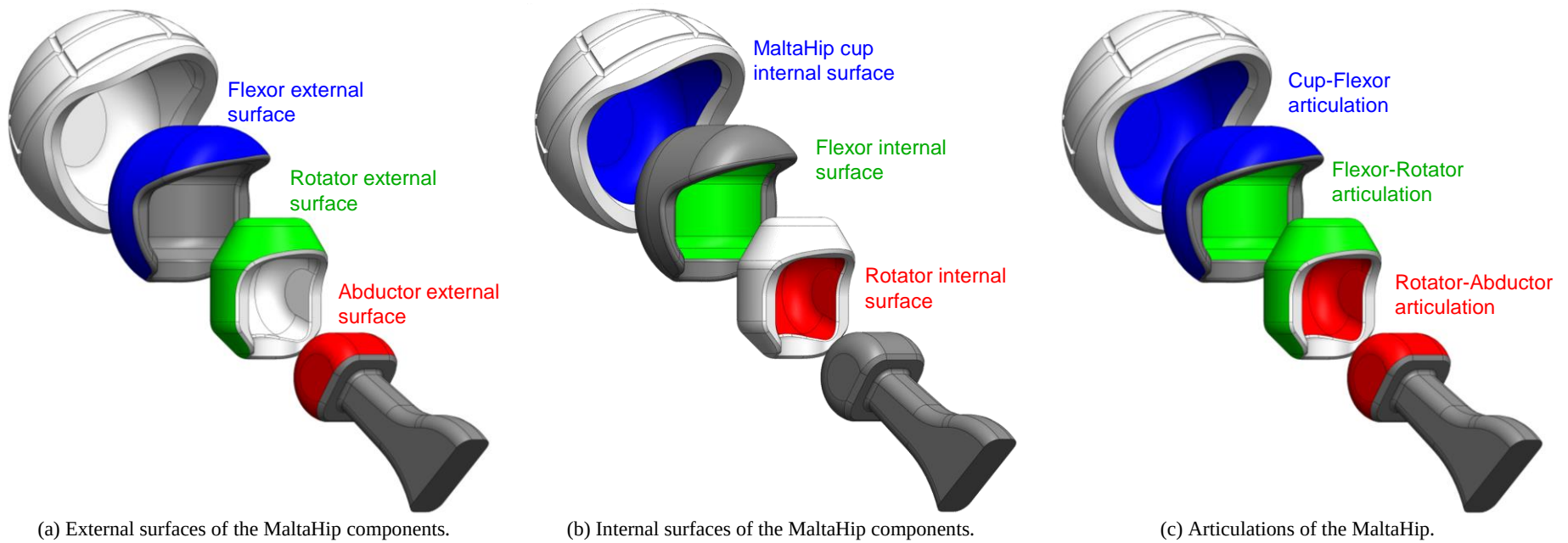


Fig. 3.15: Designations used throughout this work for the final version of the MaltaHip.

The second study involved transient structural simulations on the finalised hip implant design based on the gait cycle outlined in Section 3.1.3 (p. 66). The 53 mm MaltaHip cup outer diameter was chosen as the prosthesis size which falls within the median size range of hip prostheses. The UHMWPE and VEHXPE components used in the finite element simulations were based on Three Network model (calibrated using experimental data). The high-nitrogen austenitic stainless steel, used for the hard bearing components, was assigned an elastic modulus of 200 GPa [319]. The following boundary conditions were applied to the finalised design of MaltaHip (see Fig. 3.16):

- The loading on the hip is applied as a variable force (as specified in Table 3.2, p. 68) which acts on the MaltaHip cup along the y -axis. This is intended to mimic the mechanical loads which occurs on the hip during gait.
- The MaltaHip cup is constrained in such a way that it can only perform translational motion along the y -axis only, thereby transferring the load onto the components. This constrain reproduces the loading mechanism of the hip joint simulator.
- Frictional contacts have been implemented for all articulations (as specified in Fig. 3.14, p. 77). A coefficient of friction of 0.1 was used at the metal-on-polyethylene articulations, which is representative of mixed lubrication conditions which is exhibited for similar ball-and-socket implants [318].
- The abductor is set as a joint, with a ‘body-to-ground’ connection, which enables the component to perform the required motion. The three displacement profiles (FE/IE/AA) are applied to the abductor, as specified in Table 3.1 (p. 67). Since the components are in perfect alignment in the FE model, all translational motions of the abductor are fixed.
- No constraints are applied to the flexor and rotator components. Therefore, the motion of the abductor head will cause the flexor and rotator components to articulate in their respective directions. The absence of any constraints on these components enables the components to self-align accordingly during motion.

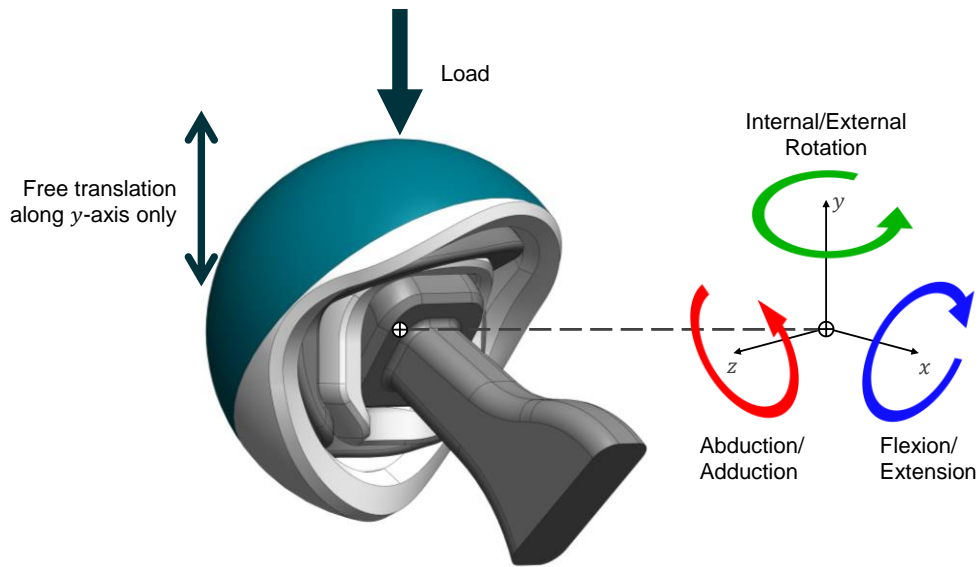


Fig. 3.16: Boundary conditions applied to finalised design of the MaltaHip.

A total of 21 timesteps were used, each consisting between 20 and 200 substeps. The high number of substeps was necessary to solve the non-linearities of the analysis (contact, material and geometric non-linearities). The von Mises, strain, contact stress and contact status were monitored. As outlined earlier, finite element simulations on a ball-and-socket implant were also conducted, which were intended to perform a comparative analysis between the stress values produced in the MaltaHip and the ball-and-socket implant.

3.5. Wear Modelling

3.5.1. Overview

Volumetric wear predictions in this work were computed for the ball-and-socket and MaltaHip implants, based on the wear models proposed by Saikko *et al.* [18], Liu *et al.* [267], Kang *et al.* [303], and Petrella *et al.* [298], as reviewed in Section 3.5.3 (p. 82). Furthermore, the produced wear predictions of the ball-and-socket implant were compared to the wear rate values reported in literature. The flowchart shown in Fig. 3.17 provides the general process required to compute the wear rate of the implant being considered. The wear rate computation required the contact stress values of the polyethylene components (computed by the finite element model), and various slide track characteristics, as produced by the implant under consideration. The main slide track characteristics required for the wear computation include the sliding distance, cross-shear ratio, and slide track memory, depending on the wear model being used. These slide track characteristics were computed for each contact node in the finite element model for both the MaltaHip and ball-and-socket implants.

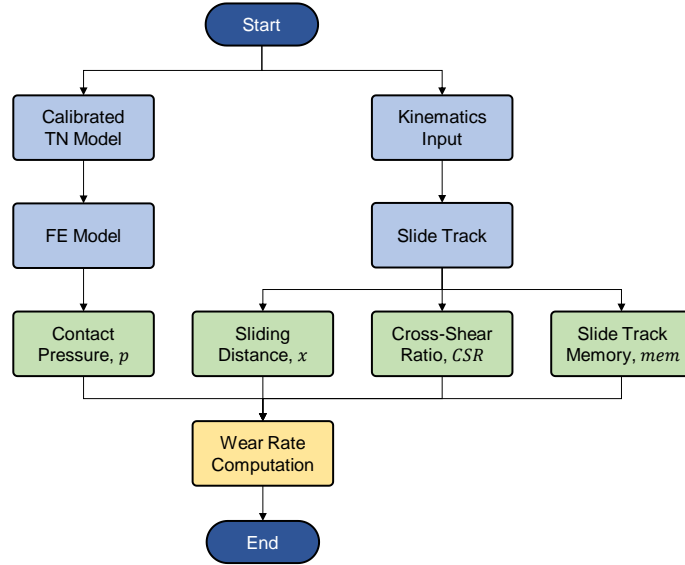


Fig. 3.17: General flowchart of the wear rate computation using finite element (FE) and slide track data.

3.5.2. Slide Track Modelling

The slide track of every contacting node in the finite element model was computed using MATLAB. Therefore, the X , Y and Z coordinates of every contact node from the finite element model were loaded into the MATLAB program. To compute the slide track of an arbitrary node at the articulating surface, the initial coordinates were multiplied by a rotational matrix that corresponds to the rotations specified at the time t of interest. A timestep of 0.01 s was used, which produced a high-resolution slide track. Therefore, a total of 100 different rotational matrices (each corresponding to each timestep) were generated for each contact node. The principal equation that was used to compute the slide tracks is as follows,

$$\vec{p}_t = \mathbf{R}_t \cdot \vec{p}_o \quad \text{Eq. 3.5}$$

where, \vec{p}_o represents initial position, in terms of X , Y and Z coordinates, of the node under consideration (node positions are identified from the mesh of the finite element model), \mathbf{R}_t represents the rotational matrix at timestep t , and \vec{p}_t represents the computed position of the node at timestep t . The rotational matrices were derived by using the equations of motions indicated in Section 3.1.3 (p. 66). Rotational transformations were used to produce the corresponding rotational matrix, according to the kinematic sequence of the prosthesis.

The sliding distance was then calculated by measuring the distance between the node positions at the different timesteps. The cross-shear ratio was computed by considering the frictional work at every segment of the slide track that was produced at every timestep, using Eq. 2.21 (p. 55). Similarly, the slide track memory was computed by considering the relative orientation angle of the slide track segments, using Eq. 2.27 (p. 57).

3.5.3. Wear Computation

The volumetric wear rate was computed in MATLAB according to the four wear models reviewed in this work. Table 3.4 provides a brief summary of the variables required to compute the parameters of each wear model. For example, the contact pressure p , is computed as a function of time t during the gait cycle, as produced by the finite element model results, for all wear models. The sliding distance x , is also computed as a function of time t , based on the distances covered by the articulations during the gait cycle, as determined by Eq. 3.5.

The mathematical function for the wear factor computation differs from one wear model to another. In case of the Saikko [18] and Petrella [298] models, the wear factor is assumed to be a constant. The wear factor in the Liu model [267] is computed as a function of the cross-shear ratio CSR . Lastly, the wear factor in the Kang model [303] is computed as a function of both the cross-shear ratio CSR and contact pressure p .

The computations are carried out on each node of the finite element model. Therefore, by dividing the volumetric wear rate of each node by the corresponding node contact area, the linear wear rate can be deduced. Therefore, this was used to identify maximum linear depth penetration at the articulation. Comparisons were made between the theoretical wear rates obtained for the ball-and-socket and MaltaHip implants. Furthermore, the wear rates obtained for the ball-and-socket implant were compared to values reported in literature by the authors of the wear models, and the experimental wear results produced in this work (as outlined in Section 3.8.1, p. 92).

Table 3.4: Summary of the variables required to computed the parameters of each wear model.

Parameters to be Computed	Variables			
	Saikko Model [18]	Liu Model [267]	Kang Model [303]	Petrella Model [298]
Contact pressure, p	time, t	time, t	time, t	time, t
Sliding distance, x	time, t	time, t	time, t	time, t
Cross-shear ratio, CSR	/	time, t	time, t	time, t
Slide-track memory, mem	/	/	/	cross-shear ratio, CSR
Wear factor, k	Constant	cross-shear ratio CSR	cross-shear ratio, CSR contact pressure, p	Constant

3.6. Fabrication of the MaltaHip Implant

3.6.1. Machining

The physical MaltaHip prototypes were machined at Empav Engineering Ltd using a CNC lathe (DMG Mori, CTX Beta 800, Japan), and a CNC 5-axis milling machine (DMG Mori, DMU 80 monoBLOCK®, Japan). Design efforts on the MaltaHip implant were focussed on minimizing the machining complexity required for producing its parts. To this end, the bulk of the geometrical features were designed to be produced by a CNC lathe, rather than by a CNC milling machine. The main benefits of using a CNC lathe for such design include: (1) ease of machining the axi-symmetrical features of the articulating components, (2) high-speed machining, and (3) high surface finish.

The high surface finish produced by the CNC lathe is attributed to the continuous motion of the tool which acts against the part, thus facilitating the post-polishing processes required to achieve the final surface finish. Milling processes were reduced as much as possible, since this kind of machining operation performs a series of discontinuous machining cuts, resulting in surfaces with a stepped topography and increased machining times (compared to lathe operations). For these reasons, milling operations were only used to machine minor geometrical features, such as the outer profile edge of the components and the grooves for cement fixation, as shown in Fig. 3.18.

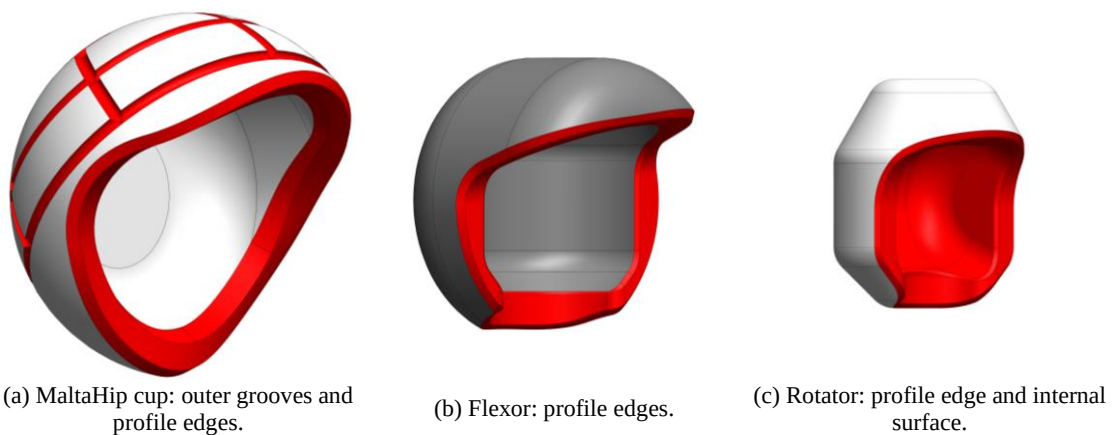


Fig. 3.18: Features produced by 5-Axis CNC Machine are marked in red. Remaining features were produced using a CNC Lathe.

3.6.2. Surface Finish

The components were finished according to the surface roughness (R_a) values stipulated in ISO 7206-2/AMD 1:2016³⁷. The standard stipulates that metallic components require a mirror finish with maximum R_a value of 50 nm, whereas the polymeric components should be provided in their as-machined condition (to prevent any third-body particles to become embedded into the component from the polishing processes), with a maximum R_a value of 2000 nm.

The polishing process of the metallic components is briefly described. Following the machining process, the parts are initially polished using a series of Emery cloths with 400, 2000 and 4000 grit sizes. Different polishing procedures were implemented for the external and internal surfaces of the metallic components. Once the polishing procedure was completed, the surface roughness of the metallic components was measured and verified using a 3D optical profilometer (S Neox, Sensorfar, Spain). The external surface of the flexor and abductor components were polished using a three-stage procedure consisting of different buffing wheels mounted on a bench buffer, and polishing compounds (Fig. 3.19), as described below:

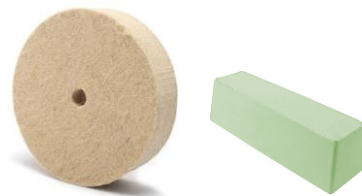
1. **Roughing:** 6-inch round denim buffing polishing wheel, used with a white cutting compound (buffing soap).
2. **Medium finishing:** 4-inch round felt wool buffing polishing wheel, used with a green cutting compound (buffing soap).
3. **Finishing:** 4-inch round felt wool buffing polishing wheel, used with metal polishing paste (AutoSol Metal Polish, AutoSol LLC, USA).



(a) Bench buffer. Source: [320].



(b) First stage (roughing) polishing procedure. Source: [321].



(c) Second stage (roughing) polishing procedure. Source: [321].

Fig. 3.19: Equipment and consumables used during polishing of external surfaces of the metallic components.

³⁷ ISO 7206-2:2011/AMD 1:2016: Implants for surgery — Partial and total hip joint prostheses — Part 2: Articulating surfaces made of metallic, ceramic and plastics materials — Amendment 1.



(a) Handheld pencil grinder (ATA Tools ST100, US) Tool. Source: [322].



(b) Felt bob with cone-pointed tip. Source: [323].



(c) Felt bob with ball tip. Source: [323].

Fig. 3.20: Equipment and consumables used during polishing of internal surface of the flexor component.

The internal surface of the flexor could not be polished using the buffing wheels. Therefore, a handheld pencil grinder (ATA Tools ST100, US) with polishing bits of different shapes and sizes were used to access the internal surface of the flexor (Fig. 3.20), based on a two-stage polishing procedure.

1. **Roughing:** felt bob with cone pointed tip (V76702/G3/8x17, Meusburger Georg GmbH & Co KG, Austria), used with diamond compound (Grade W/O14-STR, Lam Plan, France), which was mainly used to remove high-spots.
2. **Finishing:** ball tip felt bob (V76702/J1/8, Meusburger Georg GmbH & Co KG, Austria), used with metal polishing paste (AutoSol Metal Polish, AutoSol LLC, USA).

3.7. Hip Joint Simulation Testing

3.7.1. Overview

The performance of the fabricated implants was tested using experimental hip joint simulation. The testing regime of hip joint simulation was conducted in two phases.

1. In the first phase, the MaltaHip implant was tested using a single-station hip joint simulator that was built throughout this work (outlined in Section 3.7.2, p. 86). Since the concept of three cylindrical articulations for a prosthetic hip was not investigated prior to this work, the main purpose of the in-house testing was to validate the functionality of the new articulation concept, test its range of motion and to ensure that the prosthesis was able to maintain its stability over prolonged periods of testing. The implant was tested for a limited number of cycles (500k cycles), which also served to provide indications regarding the tribological performance of the MaltaHip prosthesis.

2. The second phase involved comprehensive wear testing of the MaltaHip implants according to ISO 14242-1:2014/Amd 1:2018, which was commissioned at Endolab® Mechanical Engineering GmbH (accredited implant testing facility). Details regarding this wear testing procedure are outlined in Section 3.7.3 (p. 89). Gravimetric wear measurements were recorded throughout the testing procedure in order to calculate the resultant wear rates of the MaltaHip implants.

The specifications on each hip joint simulator, as well as the type of implants, method of fixation, composition of the lubricant and testing regime used in each test are discussed in the following sections.

3.7.2. Implant Testing (In-house)

3.7.2.1. Hip Joint Simulator

A single-station hip joint simulator was developed in this work, as shown in Fig. 3.21. Details regarding the fabricated hip joint simulator are provided in Section 3.10 (p. 97). In brief, the hip joint simulator consists of a three DOF mechanism, which produces the required gait motion (Table 3.1, p. 67) using independently controlled brushless servo DC motors (Maxon Motor, Switzerland). The load profile (Table 3.2, p. 68) is reproduced using a pneumatic cylinder (Festo, Germany), which is controlled via an electronic pressure regulator (Enfield, US). The pneumatic cylinder compresses a pair of springs (Gutekunst Federn, Germany) to impart the load on the acetabular cup being tested. A flexible enclosure is used to contain the implant inside the fluid during testing procedures (note that the flexible enclosure is not shown in Fig. 3.21).

3.7.2.2. Test Implants

A prosthetic MaltaHip implant was prepared for the in-house testing procedure, consisting of UHMWPE (ram extruded GUR 1050, ASTM F648-14) and high-N stainless steel (ASTM 1586-13e1) for its soft and hard bearing components, respectively. Since discrepancies are produced in the wear rate results between different simulators when testing the same prosthesis [324], a ball-and-socket implant was also tested inside the in-house hip joint simulator, to negate the machine factors which may influence the performance of the prostheses. Therefore, a fair comparison could be made between the wear results produced from the two implants. The tested ball-and-socket implant consisted of an Enduron™ (Depuy Synthes, US) hemispherical cup with 53 mm outer cup diameter, and an Elite™ (Depuy Synthes, US) femoral head with 28 mm femoral head diameter. The Enduron™ cup is made from uncrosslinked UHMWPE GUR 1050 ram extruded bar, whereas the femoral head was made from Orton 90™ high-N austenitic stainless steel (Depuy Synthes, US).



Fig. 3.21: In-house developed hip joint simulator. Flexible enclosure which contains the fluid during testing is not shown in the photo.

3.7.2.3. Implant Fixation

The implants were mounted in the anatomically correct position, as shown in Fig. 3.22. In case of the MaltaHip implant, the cup, flexor and rotator were pre-assembled and fitted inside a PTFE (polytetrafluoroethylene) cup holder. A ring flange secures the 3D-printed insert, which conforms to the exact shape of the acetabular cup and was fixed to the upper implant holder. The abductor head was fitted onto a modular neck, which was then secured inside the stem. The stem is fixed to the lower implant holder. The axial load acts at a fixed angle to the acetabular cup, whereas the three DOF mechanism actuates the stem, effectively causing the articulations to slide against each other in the MaltaHip. The DOF mechanism of the hip joint simulator was designed with a wide range of motion, to validate the functionality of the new prosthesis design and test its range of motion.

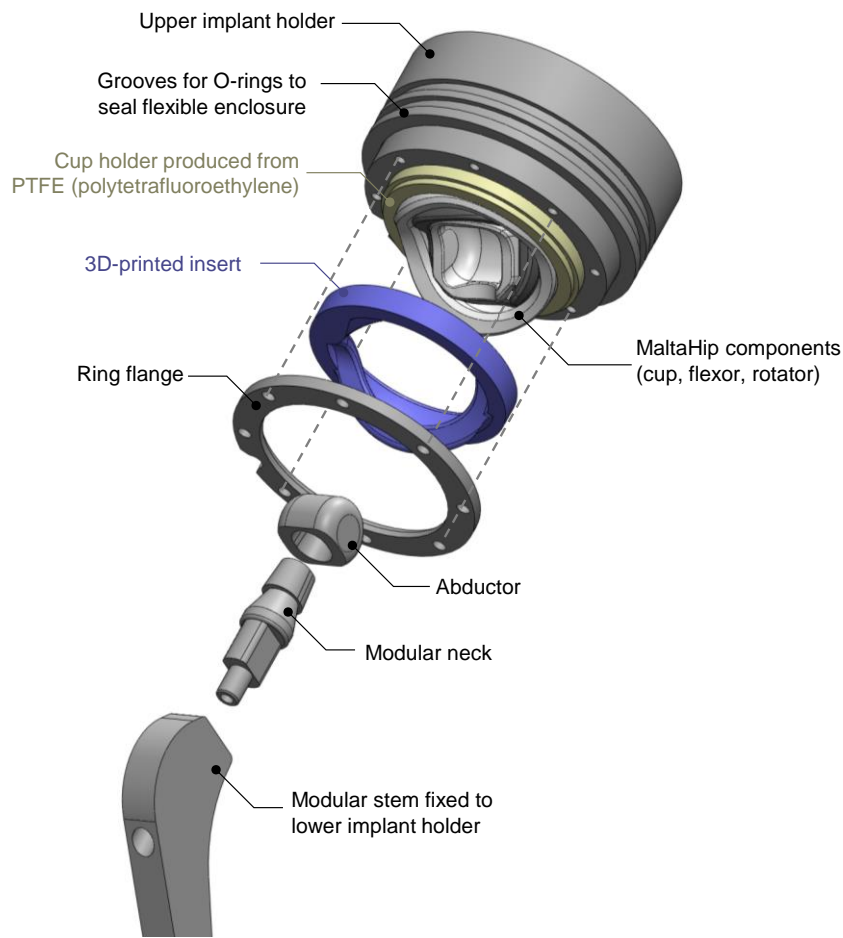


Fig. 3.22: Fixation of the prosthesis in the hip joint simulator.

3.7.2.4. Lubricant

The lubricant for the in-house tests was prepared according to ASTM F732-17³⁸, which is specifically intended for implants with polymeric components. The ISO 14242-1:2014/Amd 1:2018 specifies the composition of the fluid lubricant irrespective of the materials used for the prosthesis. To the best of the author's knowledge, there is no known ISO equivalent to the ASTM F732-17. Due to the specialisation in testing conditions associated with implants consisting polymeric materials, the ASTM F732-17 was used in this work. In fact, minor discrepancies exist in the fluid lubricant composition, particularly in the protein mass concentration.

The standard specifies that the tested implant should be lubricated using bovine serum albumin diluted with deionized water. A volume fraction of 25% filter-sterilized adult bovine serum (Lot no: 16N203, Product code: B9433-6X500ML, Sigma-Aldrich, US) was used to

³⁸ ASTM F732-17 – Standard Test Method for Wear Testing of Polymeric Materials Used in Total Joint Prostheses

simulate the lubrication of the synovial joint, resulting in a solution with a protein mass concentration of 19.5 g/L. A mass fraction of 0.3% sodium azide was added to the solution to retard bacterial growth. Ethylene-diaminetetraacetic (EDTA) salt was added at a concentration of 7.45 g/L, in order to reduce precipitation of calcium phosphate onto the articulating surfaces, which has been shown to have a great influence on the wear properties [325].

Every effort was made to maintain the sterility of the solution, to prevent any bacterial growth. The deionized water, sodium azide and EDTA were initially mixed and sterilized inside an autoclave prior to being added to the bovine serum. The sterilized solution and the filter-sterilized bovine serum albumin were mixed inside a laminar flow hood, to maintain the sterility of the lubricant. The lubricant solution was then stored in a freezer prior to being used inside the hip joint simulator. The simulator requires a minimum of 0.8 L for each test (to fill the flexible enclosure and the heated reservoir).

3.7.2.5. Testing Regime

The primary aim of the in-house testing was to verify the functionality of the prosthesis design and to provide initial indications regarding its tribological behaviour. The in-house hip joint simulator was not intended to provide numerical gravimetric wear data of the MaltaHip prosthesis. For this reason, repeats were not conducted during this testing regime. The MaltaHip and the ball-and-socket implant were each tested to 500k cycles. Prior to the wear test, the polymeric components of the implants were presoaked in the fluid lubricant at room temperature for 14 days (unloaded), to take into account the high level of fluid absorption which occurs during the initial phase of immersion.

3.7.3. Implant Testing (Endolab)

3.7.3.1. Hip Joint Simulator

The Endolab® hip joint simulator, shown in Fig. 3.23, was used for wear testing the MaltaHip implants according to ISO 14242-1:2014/Amd 1:2018. The hip joint simulator consists of six wear testing stations, and two loaded soak control stations. The required load profile (specified in Table 3.2, p. 68) is applied at a constant direction to the cup, using servo hydraulic cylinders. All the articular components of the MaltaHip move relative to the fixed cup through the three rotational degrees-of-freedom motion of the lower implant holder, which replicates the gait cycle (specified in Table 3.1, p. 67), using electric motors.



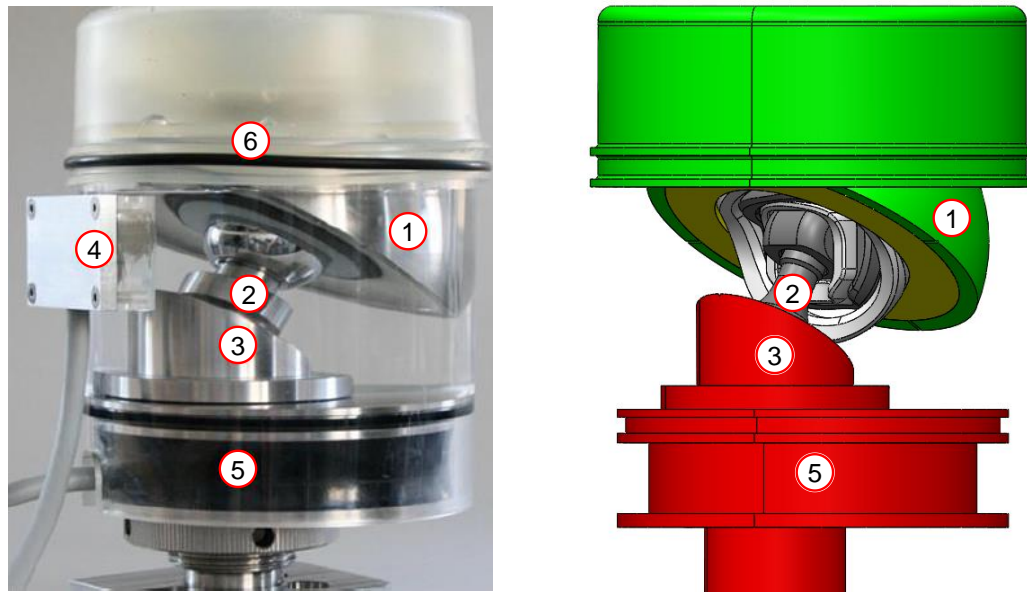
Fig. 3.23: Endolab® Mechanical Engineering GmbH six-station hip joint simulator according to ISO 14242-1:2014/Amd 1:2018. Source: Endolab® report (unpublished).

3.7.3.2. Test Implants

Two sets of four MaltaHip implants each were supplied for the testing procedure. The soft bearing components of the first set were produced from UHMWPE, whereas the soft bearing components of the second set were produced from VEHXPE. All the hard bearing components were produced from high-N austenitic stainless steel. Three implants from each set were subjected to wear testing (serving as repeats), whilst the fourth implant was used as the loaded soak control (to measure the extent of fluid-uptake during wear testing).

3.7.3.3. Implant Fixation

Each test station consists of an upper and a lower implant holder, as shown in Fig. 3.24. The specimens were oriented in the anatomically correct position, therefore the MaltaHip cup was secured to the upper implant holder, whereas the cone adapter (representing the stem of the prosthesis), was secured to the lower implant holder. The MaltaHip cup was designed as a monobloc component, and thus contained longitudinal and lateral grooves on its external surface (which clinically represent the anchoring points for cementation). These grooved features were used to engage to a polyurethane cast resin which was fixed to the upper implant holder (as indicated by label in Fig. 3.24b). Diametral and longitudinal markers were machined on the implant to indicate the correct orientation of the MaltaHip cup with respect to the degrees of motion of the simulator.



(a) A physical single test station (note that an exemplary ball-and-socket hip implant is shown). (b) Arrangement of the MaltaHip inside the Endolab® hip joint simulator.

Fig. 3.24: Single test station of the Endolab® hip joint simulator (1: Upper implant holder containing the polyurethane resin cast holding the acetabular cup, 2: Cone adapter, 3: Lower implant holder, 4: Temperature and fluid level sensor, 5: Heating, and 6: Arrangement to exclude contaminating particles to prevent interference with the wear test). Source: Endolab® report (unpublished).

A cone adapter was fabricated to act as the neck of the femoral stem. The cone adapter was secured by its round taper section to the lower implant holder. Due to the orientation dependence of the implant, a marker was machined on the round tapered section to indicate its orientation, relative to the lower implant holder. The neck of cone adapter consisted of one flat side, which was intended to act as a key for aligning the abductor component. Once the abductor component was engaged to the cone adapter, the upper and lower implant holders are brought close to each other, to complete the assembly of the prosthesis.

3.7.3.4. Lubricant

The arrangement of the implant fixation setup also consisted of a cylindrical chamber to prevent the intrusion of any foreign particles. The test chamber setup could contain 350 ml of test fluid. The implant assembly and the introduction of the fluid was conducted within a laminar flow unit (Clear Air, Netherlands). The lubricant was prepared according to ISO 14242-1/Amd 1:2018. The test fluid consisted of calf serum (Lot no: P141015, PAN Biotech GmbH, Germany) diluted with deionized water, resulting in a protein content of 30 g/l. EDTA was added to the calf serum to bind the calcium phosphate. Amphotericin (250 µg/ml) and gentamicin (10 mg/ml) were added to prevent bacterial and fungal induced degradation. The test fluid was replaced every 0.5 million cycles and stored frozen for later analysis.

3.7.3.5. Testing Regime

The implants were presoaked in the fluid lubricant at 37°C for 26 days, to negate the effect of fluid absorption during gravimetric measurements. Furthermore, an implant from each set acted as the loaded soak control, so that the gravimetric measurements could be corrected due to any further fluid uptake due to loading effects which occur during the testing regime. Details regarding the gravimetric measurements that were conducted during the test are described in Section 3.8.1 (p. 92).

The implants were tested to a total of 5.0 million cycles, thus representing 5 years of use. The implant prototypes were periodically switched to a different testing station to minimize errors generated due to variations in each station. The contact areas of the articular surfaces was inspected at 1.0 and 5.0 million cycles, as outlined in Section 3.8.2 (p. 94). Following completion of the test, the bearing surfaces of the components were inspected using a digital light microscope.

3.8. Wear Test Measurements

3.8.1. Gravimetric Measurements

Wear of the polymeric components tested at Endolab® Mechanical Engineering GmbH was measured gravimetrically method according to ISO 14242-2:2016³⁹. As mentioned in Section 3.7.3.5 (p. 92), the polymeric components were soaked in the fluid lubricant for 26 days, to ensure that the polymer parts become saturated. The components are then removed from the lubricant and are subjected to a cleaning procedure. The components are initially placed in an ultrasonic cleaner containing deionized water for 10 minutes, and then rinsed with deionized water. The procedure is repeated for three times, however during the second time, an ultrasonic cleaning detergent is used in the deionized water. Following the three repetitions, the ultrasonic cleaner is once again used to clean the parts for 3 minutes, and then rinsed with deionised water. The components are dried in a vacuum drying chamber. Once the above procedure is completed, the polymeric components are dried using filtered inert gas. The polymeric components are then soaked in isopropyl alcohol for around 5 minutes. The test specimens are once again dried using a jet of filtered inert gas, and then dried even further inside a vacuum chamber (at least at 13.3 Pa) for around 30 minutes.

³⁹ ISO 14242-2:2016 Implants for surgery – Wear of total hip-joint prostheses – Part 2: Methods of measurement

The polyethylene components are weighed using an analytical balance (Sartorius, BP221D), to the nearest 0.1 mg. The polymeric components are measured on the balance twice within 90 minutes of removal from the vacuum. If the two readings are identical, the components are weighed again after 24 hours. If the difference in the mass values is less than 10%, then the parts are ready for use (as specified in ISO 14242-2:2016). The parts are stored inside a sealed dust-free container.

Mass measurements of the polymeric components of the MaltaHip (cup and rotator) were conducted prior testing and during testing. Gravimetric measurements using the Endolab® hip joint simulator were recorded at the first 0.5 million cycles, and at every interval of 1.0 million cycles throughout the testing period. It should be noted that the cleaning procedure was applied to the components prior to each gravimetric measurement. Mass measurements of the metallic components (flexor and abductor) were conducted prior to testing, and at 3.0 million and 5.0 million cycles. The gravimetric wear of a polymeric component is calculated as,

$$W_n = W_{an} + S_n \quad \text{Eq. 3.6}$$

where, W_n is the net mass loss after n cycles of loading, W_{an} is the average uncorrected mass loss, and S_n is the average increase in mass of the control implant due to fluid absorption.

The gravimetric wear rate for a specific prosthesis $W_{G,i}$ (where i represents the implant under consideration) based on the results obtained between 0.0 and 5.0 million cycles is calculated by using the least squares linear fit relationship (i.e. linear regression) based on the measurements that are plotted using Eq. 3.6. Therefore, the net mass loss after n cycles (W_n) and the gravimetric wear rate for a specific prosthesis ($W_{G,i}$) are related as follows,

$$W_n = W_G \times n + b \Rightarrow W_G = \frac{W_n - b}{n} \quad \text{Eq. 3.7}$$

where, b is a constant that is introduced to prevent the linear regression to intercept the origin. The mean gravimetric wear rate of the prostheses of the same type and material \overline{W}_G is calculated as follows,

$$\overline{W}_G = \frac{1}{N} \sum_{i=1}^N W_{G,i} \quad \text{Eq. 3.8}$$

where, N represents the total number of prostheses under consideration. Gravimetric wear rates were computed during running-in (0.0 – 1.0 million cycles) and steady-state (1.0 – 5.0 million cycles) conditions. The standard error (SE) of the mean gravimetric wear rate during both running-in and steady-state wear was calculated, in order to provide an estimation of how far the

obtained result is likely from the population mean, according to the central limit theorem. The SE was computed by dividing the standard deviation SD by \sqrt{N} , as follows,

$$SE = \frac{SD}{\sqrt{N}} = \frac{1}{\sqrt{N}} \times \sqrt{\frac{\sum_{i=1}^N (W_{G,i} - \bar{W}_G)^2}{N - 1}} \quad \text{Eq. 3.9}$$

3.8.2. Contact Area Inspection

At 1.0 million and 5.0 million cycles, the contacting areas of the polymeric components were macroscopically inspected with the naked eye (Fig. 3.25a). The boundary between the contacting (worn) and non-contacting (unworn) regions was identified and traced with blue marker (Fig. 3.25b). Macroscopic photographs were taken of the marked polymeric components. The contacting (worn) regions within the blue boundaries were highlighted in red on the images, using an image editing software (Fig. 3.25c). Once the photos of the components were complete, the blue marker was wiped using an isopropanol-soaked towel and components were rinsed with deionized water. Furthermore, after 5.0 million cycles, optical microscopy images were produced to analyse the topographical surface.

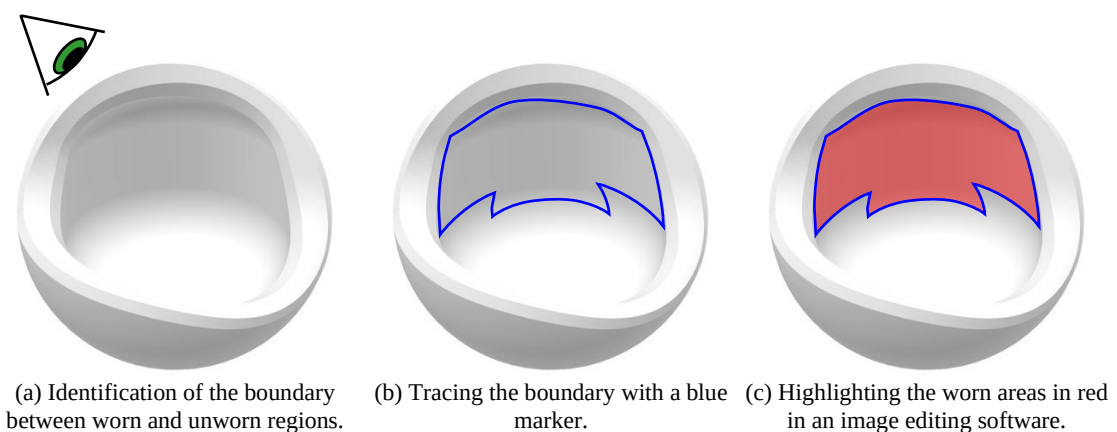


Fig. 3.25: Schematic illustration of the contact area inspection process at 1.0 and 5.0 million cycles.

3.9. Analysis of Wear Particles

3.9.1. Process Description

An analysis of the wear debris was conducted by Endolab® Mechanical Engineering GmbH according to ISO 17853:2011⁴⁰, to obtain information regarding their morphological characteristics. The size of the wear particles provides an indication of the extent of osteolysis that may take place, with smaller wear particles being the most detrimental. Wear particles were extracted from the test fluid that was used during the wear testing procedure of the MaltaHip implants with the Endolab® hip joint simulator. The wear particle analysis was conducted on the defrosted test fluid that was used between 4.5 – 5.0 million cycles, for both the UHMWPE and VEHXPE versions of the MaltaHip implant.

The wear particles produced from 4.5 to 5.0 million cycles are the most representative set of the steady-state wear from all other possible sets which were available. Similar wear particles are likely to be produced over the lifespan of the prosthesis. The wear particles produced from 0 to 0.5 million cycles are representative of the running-in process, and therefore do not represent the majority of wear particles which are likely to be produced over the lifespan of the prosthesis.

The test fluid was initially stirred for approximately 2 minutes, followed by an extraction of 2 ml from the sample. Biological particles (such as native proteins and partially denatured proteins) in the sample were dissolved by adding 8 ml of 37% HCl, as described by the method proposed by Scott *et al.* [326]. The solution was then subjected to an elevated temperature of 50 °C for 1 hour, whilst being continuously stirred. After the organic matter is digested, 1 ml of fluid was diluted with 100 ml of methanol. Volumes of 5 ml from the UHMWPE sample, and 15 ml from the VEHXPE sample were extracted from the different samples. The specific volumes were extracted according to the wear rate values that were generated by the hip joint simulator. The extracted samples were filtered through 0.1 µm polycarbonate filter using a vacuum pump, as shown in Fig. 3.26. The filters were then sputter coated with silver for observation using a field emission scanning electron microscope (FE-SEM) (Hitachi GmbH, SU8230). The secondary electrons emitted by the electron beam were detected using the secondary electron detector. A magnification of 5000x and an acceleration voltage of 5.0kV was used.

⁴⁰ ISO 17853:2011 – Wear of implant materials – Polymer and metal wear particles – Isolation and characterization



Fig. 3.26: Filtration system used for the particle analysis preparation according to ISO 17853:2011. Source: Endolab® report (unpublished).

The morphological features that were measured from the FE-SEM images include the equivalent circle diameter (*ECD*), form factor (*FF*), maximum Feret diameter, minimum Feret diameter, area, perimeter and aspect ratio (*AR*). Such data enables comparison to other wear debris morphological data found in literature. The shape of the wear particles was measured according to the procedure described by Wirth *et al.* [327] using analySIS Pro software tool (Soft Imaging System GmbH, Germany) as the image analysis software.

3.9.2. Definitions of Morphological Characteristics

The morphological characteristics which describe the wear particles are defined in this section. The equivalent circle diameter *ECD* defines the diameter of a fictitious circular object with the same area as the current particle being inspected, which is mathematically defined,

$$ECD = \sqrt{\frac{4A}{\pi}} \quad \text{Eq. 3.10}$$

where, *A* is the area of the wear particle under consideration. The form factor *FF* describes the circularity of an object, based on the perimeter of the outline of the particle. This is calculated as,

$$FF = \frac{4\pi A}{P^2} \quad \text{Eq. 3.11}$$

where, *A* and *P* represent the area and perimeter, respectively, of the wear particle under considering. The maximum Feret diameter⁴¹ defines the largest distance between two imaginary parallel lines, which restrict object movement in the perpendicular direction (Fig. 3.27). Similarly, the minimum Feret diameter defines the smallest distance between two imaginary parallel lines of the same particle being inspected.

⁴¹ This is often referred to as the caliper diameter, as it reproduces the same dimensions when measured by a Vernier caliper when measuring large items.

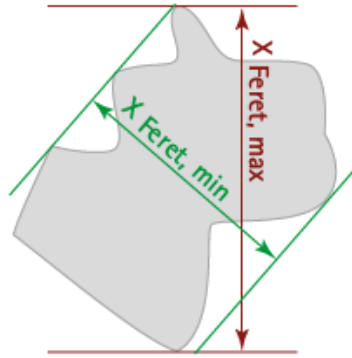


Fig. 3.27: Particle measurements indicating the maximum and minimum Feret diameters. Source: [328]

The aspect ratio AR defines the ratio of the longest distance between any two points on the outline of the particle (d_{max}), to the distance of the line located perpendicular to it (d_{min}), and can be mathematically represented as,

$$AR = \frac{d_{max}}{d_{min}} \quad \text{Eq. 3.12}$$

3.10. Mock Surgery on Cadaver

A mock surgery was conducted using the MaltaHip on a Thiel (soft) embalmed cadaver, with the main purpose being to assess the following factors: ease of achieving the correct MaltaHip cup orientation during implantation, ease of hip reduction, stability of the implant (in terms of minimising the risk for dislocation), and identification of any possible sites of impingement. It should be noted that a standard surgical procedure was followed by the surgeons during the hip joint replacement using the MaltaHip, with only one additional custom tool (pusher) required to fit the new design of the prosthesis. The MaltaHip cup, flexor and rotator are pre-assembled and fixed to the acetabulum. The implantation of the stem and MaltaHip cup are mostly based on standard surgical techniques. The feedback received from the orthopaedic surgeons following the mock surgery is used to improve the future versions of the MaltaHip implant.

4. Experimental Setup

4.1. Overview

A hip joint simulator was developed and constructed based on the design requirements specified in ISO 14242-1:2014/Amd 1:2018. Various hip joint simulator designs with different constructions are available in literature [8, 263, 329–335]. The hip joint simulator developed in this work is based on the same principles but possesses a different constructional design as it was intended to serve as an experimental testbed to validate the functionality of the new articulation concept, test the range of motion of the prosthesis, and assess the stability of the newly developed implant. Furthermore, the hip joint simulator served to provide indications regarding the tribological behaviour of the MaltaHip, based on limited number of cycles (500k cycles). The main systems of the hip joint simulator are the motion mechanism, loading mechanism, and the lubrication system, as shown in Fig. 4.1, which are necessary for reproducing the required testing conditions for the hip implant. The motion and loading mechanisms are mounted to a fixed frame structure, fabricated out of 4 mm square structural hollow sections (ISO 630-2:2011⁴²).

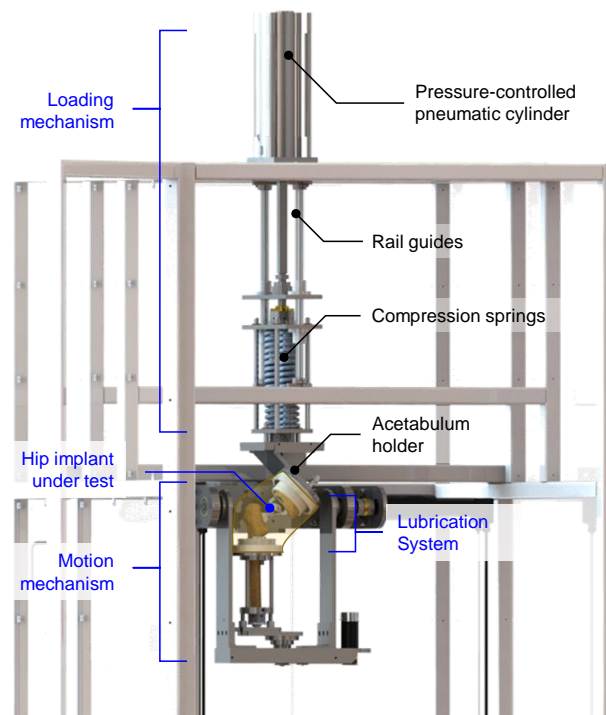


Fig. 4.1: Overview of the hip joint simulator

⁴² ISO 630-2:2011 Structural steels – Part 2: Technical delivery conditions for structural steels for general purposes.

4.2. Motion Mechanism

The motion mechanism, shown in Fig. 4.2, consists of a three stainless steel frame, which are mounted orthogonally to each other, resembling a gimbal system, to reproduce the three anatomical degrees of freedom of the human hip. The cup is mounted onto the upper implant holder which has all of its degrees of freedom constrained. The stem of the hip is mounted on the lower implant, which provides the rotation motion of the prosthesis. The kinematic sequence of the frames is as follows: abduction/adduction, followed by flexion/extension, followed by internal/external rotation, and each of which can be independently-actuated, and thus can achieve any orientation that can be produced by the human hip. It should be noted that the mechanism enables the translational position of the lower implant holder to be manually adjusted for aligning the components of the implant. The mechanism does not allow for any further translational adjustments once the wear testing procedure is initiated.

DC brushless motors were selected for actuating the motion mechanism, due to their high accuracy as compared to pneumatic systems, and low cost as compared to hydraulic actuators. The required power specifications of the individual electric motors were calculated by differentiation of the displacement curves to obtain the velocity and acceleration profiles. The required torque specifications were computed by taking into consideration the moment of inertia of the corresponding rotational frames and the maximum acceleration requirements. The minimum requirements for the motors to reproduce the gait cycle have been computed in Figs. 4.4 to 4.6. Three Maxon motors (Switzerland) were chosen for the actuation of the gait mechanism. The specifications of the selected motors are shown in Table 4.1. The selected motors are sized above the minimum theoretical requirements, in order to compensate for current peaks and to minimize overheating with prolonged use. Gear reduction was necessary to meet the low speed and high torque requirements.

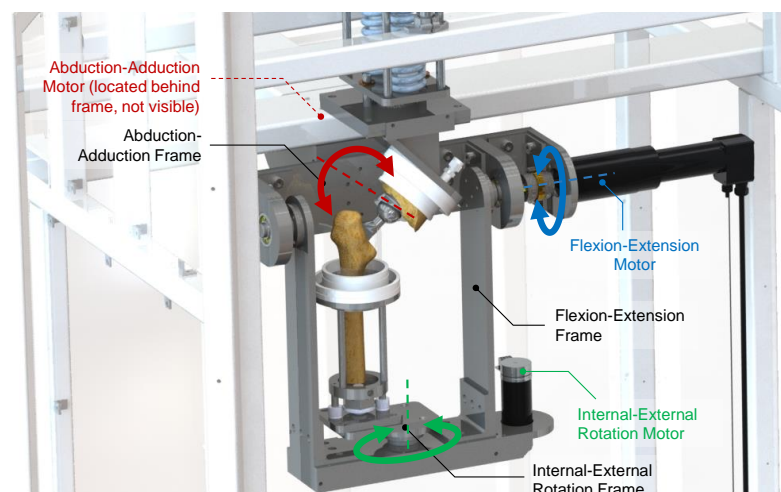


Fig. 4.2: Schematic illustration of the motion mechanism, showing the rotation frames and their corresponding actuators. Note: The pelvic and femoral bone are not used in the actual test setup.

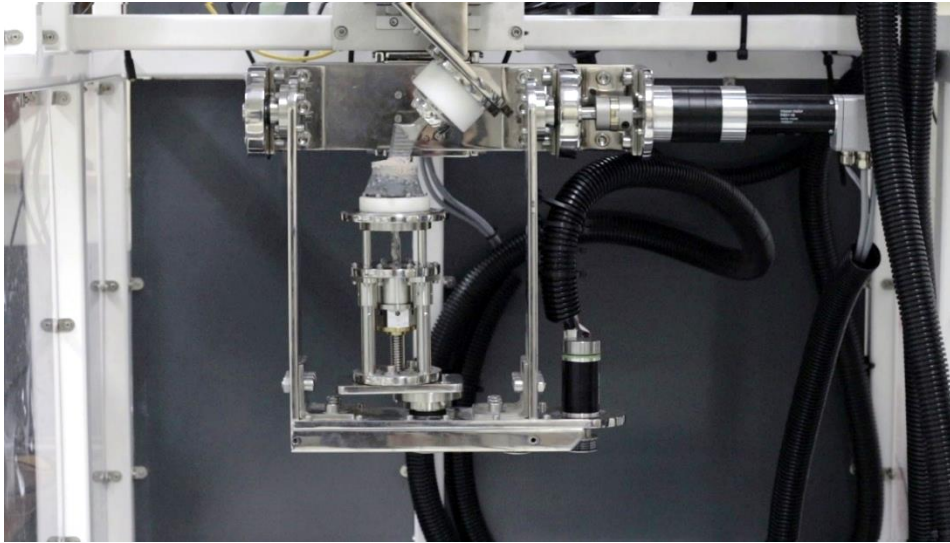


Fig. 4.3: Motion mechanism of the hip joint simulator.

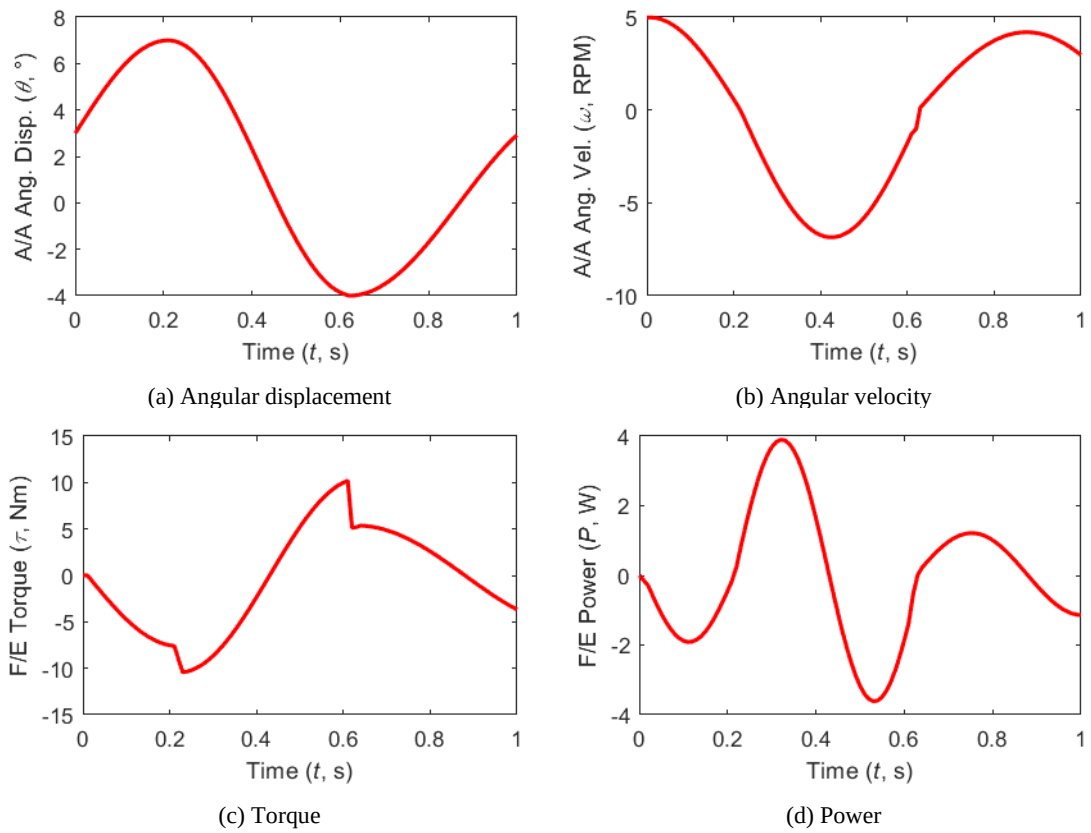


Fig. 4.4: Abduction/Adduction motion theoretical requirements.

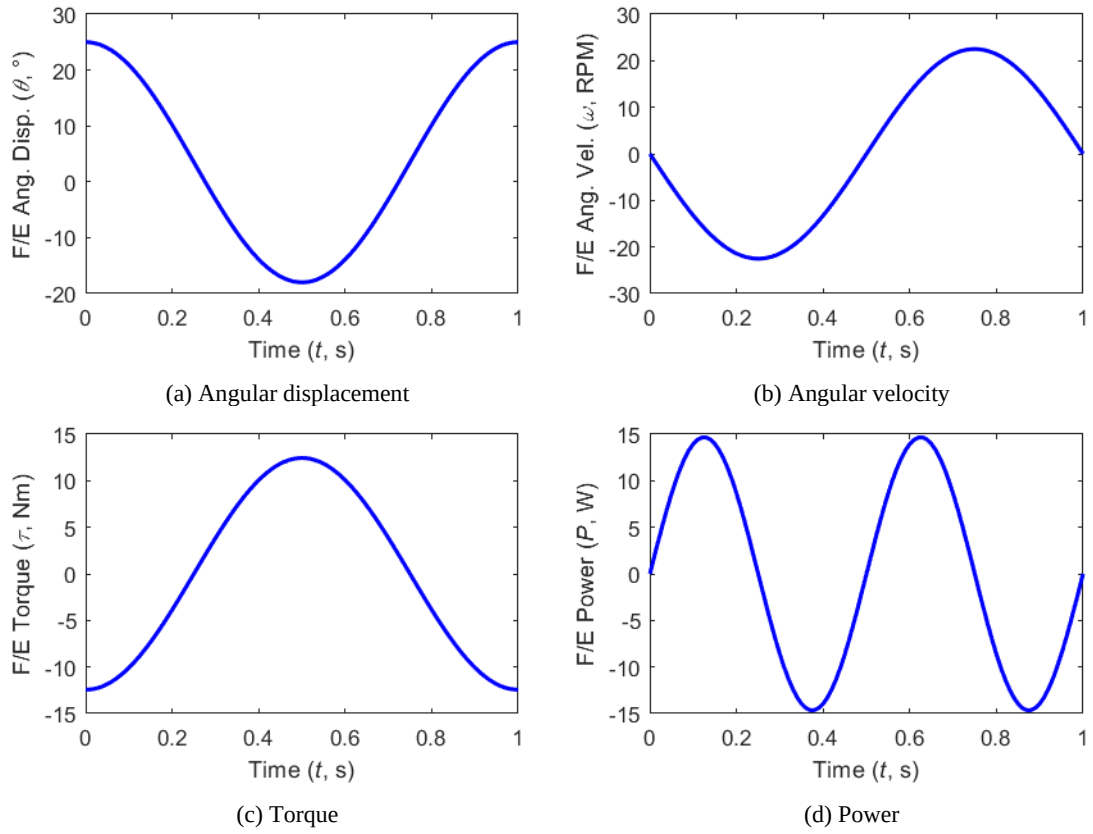


Fig. 4.5: Flexion/Extension motion theoretical requirements.

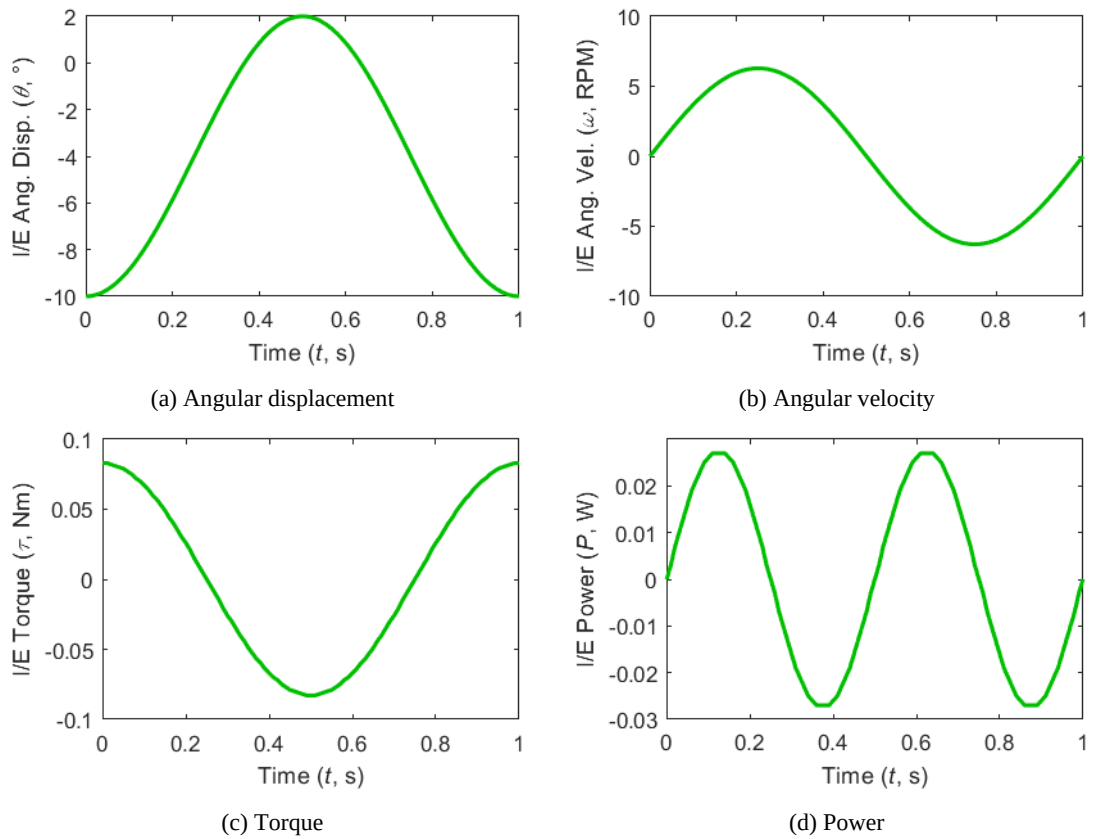


Fig. 4.6: Internal/External motion theoretical requirements.

Table 4.1: Specifications of the selected motors for the motion mechanism.

	Abduction/ Adduction	Flexion/ Extension	Internal/External Rotation
Motor Power (W)	250	250	50
Gearbox ratio	181:1	139:1	81:1
Gearbox efficiency (%)	70	72	86
Nominal torque output (Nm)	44.0	34.7	4.84
Nominal speed output (rpm)	30.3	39.5	40.5
Encoder Resolution (counts per turn, CPT)	500	500	2048
Brake holding torque (Nm)	0.4	0.4	N/A
Maxon Motor Part Numbers			
Motor	136209	136209	339286
Gearbox	110507	110506	203124
Encoder	137959	137959	462005
Brake	228390	228390	N/A
Position Controller	EPOS2 70/10 375711	EPOS2 70/10 375711	EPOS2 24/2 390003

Relative encoders were also purchased in order to replicate the required specific profile motion. This required the electric motors to undergo a homing sequence (i.e. moving the motors to a pre-defined position), every time the electric motors are switched on. To prevent repeating this procedure, a braking system was integrated which would halt the system to a known position. This also prevents the frames from rotating freely due to gravity in case the power supply is cut off. Digital position controllers were used to recreate the desired profile motion. Position controllers EPOS2 70/10 were used for the abduction/adduction, and flexion/extension motion, whereas EPOS2 24/2 were used for internal/external rotation. The motors were linked and synchronized through a CANbus network that received commands from a soft PLC system.

4.3. Loading Mechanism

The wear testing standard (ISO 14242-1) specifies that a uniaxial load should act on the acetabular cup at a constant direction to reproduce the biomechanical loads acting on the prosthetic hip. A 100 mm bore pneumatic cylinder⁴³ is used to compress a pair of springs⁴⁴ (spring constant = 103 N/mm) to impart the uniaxial load on the prosthesis, as shown in Fig. 4.1. Linear rails are used to guide plates which support the springs and are also connected to the cup holder. Therefore, the direction of the load remains vertical, regardless of the orientation of the frames.

⁴³ DDPC-Q-100-200-PA-20E, Festo, Germany.

⁴⁴ D-447, Gudekunst Federn, Germany.

The characteristic variable-load profile is recreated using an electronic pressure regulator⁴⁵. The complete pneumatic circuit, which is used for the loading mechanism in the hip joint simulator, is shown in Fig. 4.7. Unlike conventional solenoid valves, which only allow the piston rod of the pneumatic cylinder in its fully extended or fully retracted positions, the electronic pressure regulator enables a precise proportional control over the pressure output, thus compressing the spring to the required load profile. The electronic pressure regulators are controlled via a 0 – 12 V analogue signal.

A separate load cell is integrated to read the load values that were produced. The load cell was intended to be used for correcting the error in the spring compression. However, since the electronic pressure-regulator that was used consisted of a proportional control over the pressure output, the load cell was not integrated for providing feedback control. The pneumatic cylinder used in the test rig was directly acting on the springs which was continuously corrected via the proportional control of the pressure regulator. Hence, the load cell was only used for providing real-time data of the actual loads being produced. The pneumatic circuit directs the compressed air through the electronic pressure regulator during the wear testing regime. Upon completion of the test, the pneumatic valves are switched, so that the piston rod of the pneumatic cylinder is retracted, which would enable the the prosthesis to be removed from the setup.

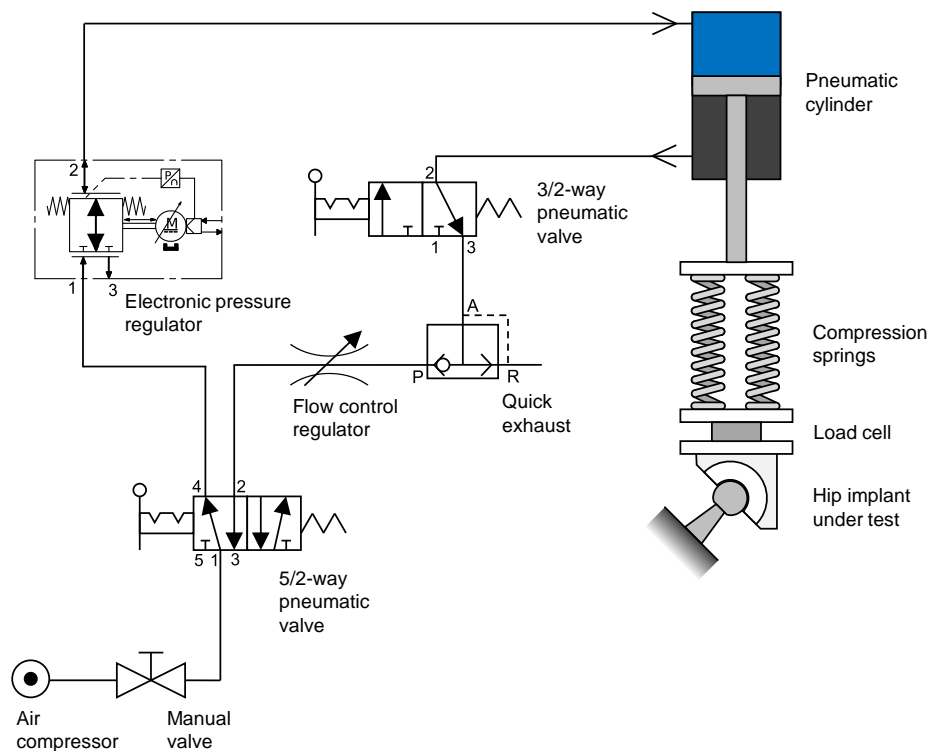


Fig. 4.7: Pneumatic circuit for the loading mechanism of the hip joint simulator.

⁴⁵ TR-025-G10-S, Enfield, US.

4.4. Lubrication System

The implant is surrounded by a flexible enclosure, produced out of a moulded nitrile-butadiene rubber (NBR) bellow⁴⁶, to contain the fluid and lubricate the prosthesis (Fig. 4.8). A peristaltic pump circulated the diluted bovine serum fluid at 520 ml/min to a remote reservoir containing which was immersed in a heated bath containing water. A heating element was used to elevate the temperature of the water-containing bath. A thermocouple was located inside the lubricant reservoir which was used to ensure that the required temperature ($37 \pm 1 \text{ }^\circ\text{C}$) of the lubricant was maintained throughout the testing procedure. The lubrication system was sealed to minimize evaporation, and circulated to maintain the required temperature. The system requires a total of 0.8 L of lubricant, and acts as a heat exchanger since it facilitates heat dissipation which is generated at the articulation. The ends of the bellows are clamped to two tubular sections located above and below the hip implant to be tested. The bellow is clamped using jubilee clips to tubular sections mounted on the machine, which consist of a pair of O-rings to seal the enclosure (Fig. 3.22, p. 88).

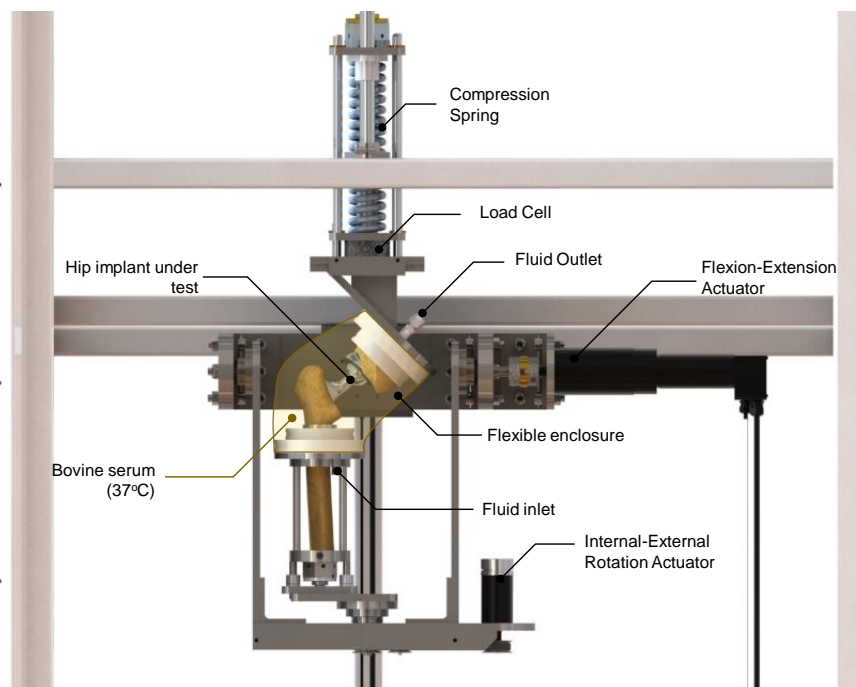


Fig. 4.8: Lubrication system of the hip joint simulator. Note: The pelvic and femoral bone are not used in the actual test setup.

⁴⁶ F-1217-NBR, Steinbock GmbH, Germany.

5. Results

5.1. Introduction

This chapter presents the key findings which lead to the final design solution of the MaltaHip, as well as various results pertaining to the tribological performance of the fabricated prostheses. A preliminary investigation regarding the potential osteolysis effects that may be induced by the generated wear debris was also conducted. Furthermore, the practicality of implanting the new prosthesis was also assessed in this work.

Throughout the design optimisation process, the Three Network model was used to predict the mechanical response of the UHMPWE and VEHXPE polymers that were used as the soft bearing components in the new prosthesis. The material model parameters were calibrated using data retrieved from experimental compression tests (Section 5.2, p. 106).

Finite element analysis was then conducted on various design iterations of the MaltaHip to optimise its structural integrity (Section 5.3, p. 111). The slide track characteristics of the conventional and new prostheses designs were computed (Section 5.4, p. 150), which were then used to predict the theoretical volumetric wear rates using different wear models (Section 5.5, p. 157).

The tribological performance of the prosthesis is highly influenced by the fabrication processes, and therefore the type of machining procedures that were used to manufacture the MaltaHip implants are described in this chapter (Section 5.6, p. 161). A few prototypes were initially tested, using a hip joint simulator that was built in-house, to validate the functionality of the new articulation mechanism of the MaltaHip. The finalised prototypes were subjected to a comprehensive wear testing regime at Endolab® Mechanical Engineering GmbH. A particle analysis on the wear debris produced from the wear testing procedure was also conducted (Section 5.7, p. 187). Furthermore, a mock surgery was conducted on a cadaver using the MaltaHip to assess its practicality and risk of dislocation (Section 5.8, p. 249).

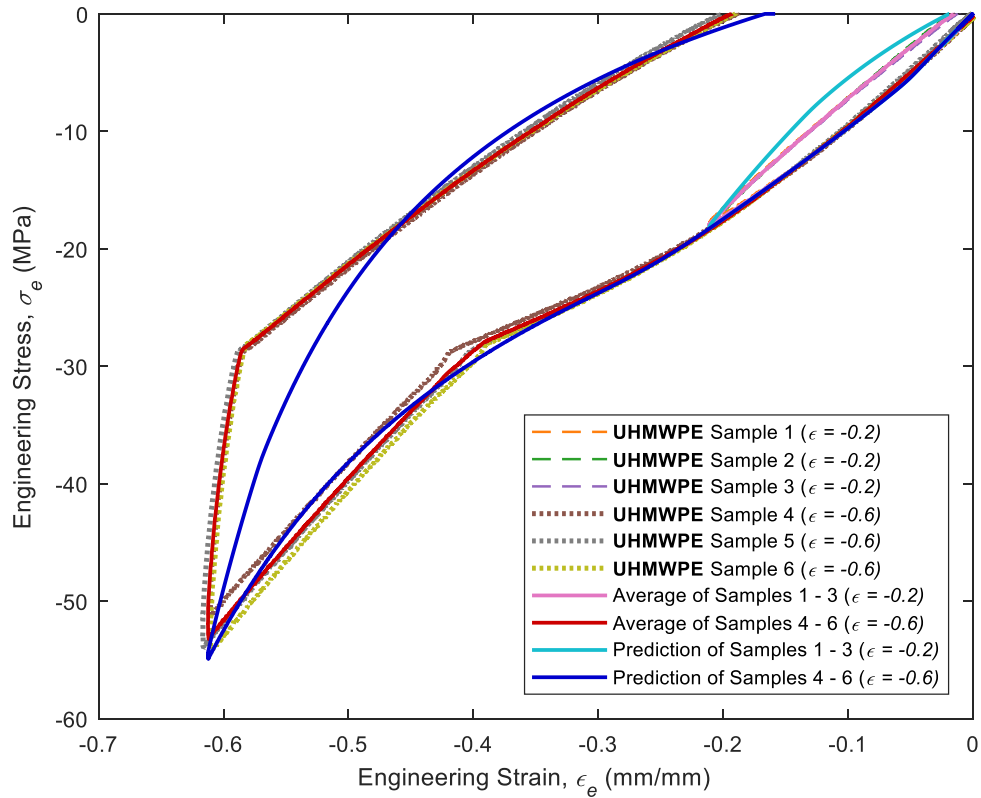
5.2. Material Model Results

5.2.1. Material Model Calibration

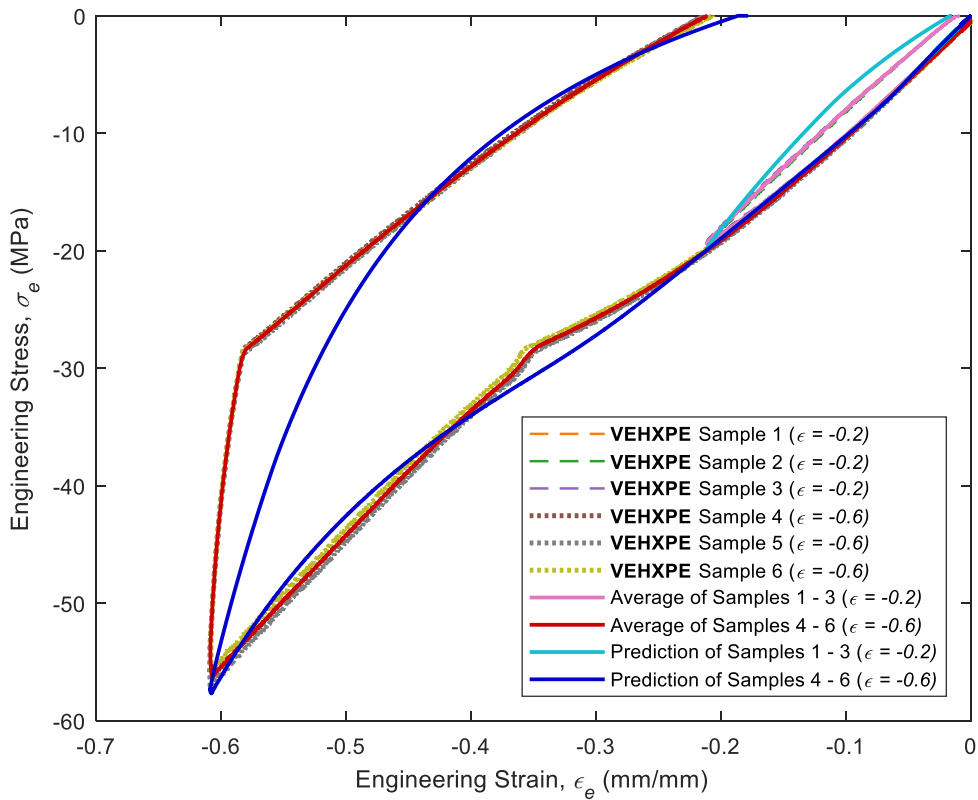
Calibration of the material model parameters involved UHMWPE and VEHXPE samples being subjected to a series of experimental compression tests (schematically represented in Fig. 3.6, p. 69). The samples possessed a cylindrical geometry (10 mm in diameter and 5 mm in height) and were tested using a strain-controlled compression rate of 0.03 s^{-1} . Different batch samples were compressed to maximum engineering strain values of 0.2 and 0.6 and the corresponding engineering stress-strain (σ_e, ϵ_e) values were plotted, as shown in Fig. 5.1. Direct measurements were not conducted to verify whether barrelling occurred. However, on visual inspection, no significant signs of barrelling were observed. The calibrated stress-strain predictions by the Three Network model are superimposed on the same plot. Calibration of the material parameters was conducted using the MCalibration software, and the corresponding results for UHMWPE and VEHXPE are listed in Table 5.1. Both calibrated curves resulted in a coefficient of determination (R^2) value of 0.98 when compared against the experimental data.

The following model parameters were set according to the specifications provided by the authors [31] of the material model. As temperature variations were not considered in the finite element model, temperature-dependency effects of the material model were disregarded by setting $\hat{\theta}$, n and α equal to 0. Due to the uniaxial nature of the compression tests, the parameters a and q were set to 0. The material model necessitates that the flow resistance $\hat{\tau}_A$ to be less than $\hat{\tau}_B$. The parameters m_A and m_B were set to values below 30 to facilitate the convergence of the finite element solution. The values of all remaining parameters were calibrated based on the experimental stress-strain data using MCalibration. The calibration procedure is automated by the MCalibration software tool. In brief, the automated process performs an initial guess of the material model parameters based on the experimental stress-strain data that was provided. Various optimization algorithms⁴⁷ are then used to optimize the material model parameters, to improve upon the initially guessed values. The optimisation algorithm is reiterated until no further improvements can be attained in the R^2 value. The total run time for optimizing the material model parameters for UHMWPE was 104 hours, whereas the total runtime for VEHXPE was 12 hours. The reason for the reduced computation time for the latter polymer is that its initial guessed parameters were based on the values obtained for UHMWPE material model.

⁴⁷ Optimization algorithms used by MCalibration: Nelder-Mead Simplex Method, Random Search, Genetic Algorithm, Levenberg-Marquardt, Quasi-Newton (L-BFGS), Global Optimum Search, NEWUOA (NEW Unconstrained Optimization Algorithm), and CMA-ES (Covariance Matrix Adaption Evolution Strategy).



(a) UHMWPE (GUR 1050) stress-strain relationship.



(b) VEHXPE (GUR1020-e) stress-strain relationship.

Fig. 5.1: Experimental and theoretical engineering stress-strain curves of UHMWPE and VEHXPE. Experimental results are based on compression tests. Theoretical results are based on the Three Network model (calibrated from the same experimental data). A strain rate of 0.03 s^{-1} was used in all tests.

Table 5.1: Calibrated material model parameters of UHMWPE and VEHXPE using MCalibration.

Parameter	Unit	Description	UHMWPE	VEHXPE
μ_A	MPa	Shear modulus of network A	6.36	5.13
$\hat{\theta}$	K	Temperature factor	0	0
λ_L	-	Locking stretch	63.6	71.52
κ	MPa	Bulk modulus	1262.23	2586.06
\hat{t}_A	Pa	Flow resistance of network A	1.00	1.00
a	-	Pressure dependence of flow	0	0
m_A	-	Stress exponential of network A	13.56	13.37
n_t	-	Temperature exponential	0	0
μ_{Bi}	Pa	Initial shear modulus of network B	25.42	27.22
μ_{Bf}	Pa	Final shear modulus of network B	4.62	4.96
β	-	Evolution rate of μ_B	1.98	1.55
\hat{t}_B	Pa	Flow resistance of network B	12.22	16.59
m_B	-	Stress exponential of network B	25.00	20.15
μ_C	Pa	Shear modulus of network C	2.91	1.79
q	-	Relative contribution of I_2 of network C	0	0
α	K ⁻¹	Thermal expansion coefficient	0	0
θ_0	K	Thermal expansion reference temperature	310	310
R^2		Coefficient of determination	0.98	0.98

5.2.2. Material Model Validation

To validate the calibrated parameters values of the Three Network model, the true stress and strain values of the compression-tested samples were compared to the corresponding values produced in a finite element model, using ANSYS, that simulated the same experimental compression testing conditions that was conducted in the previous section (Section 5.2, p. 106, and schematically represented in Fig. 3.6, p. 69). The boundary conditions implemented in finite element model are shown in Fig. 5.2. Frictionless supports were set between the contacting surfaces of the cylindrical coupon, to prevent any barrelling effects on the samples, in order to maintain uniform stress and strain conditions along the cylinder (Fig. 5.2a). A node (point)

located at the centre of the bottom face was fixed, to prevent the sample from slipping away during compression (Fig. 5.2b). When the contact surfaces of the frictionless supports were analysed, it was observed that the contact stress profile was equivalent to the internal normal stress. This implies that during the FE analysis, barrelling was not induced.

To validate the calibrated material parameters of UHMWPE and VEHXPE, three types of plots were produced and compared for each material, as shown in Fig. 5.3. The first plot (red dotted curves) represents the true stress and strain results that were obtained from the compression tests. The second plot (blue curves) represents the true stress and strain curve obtained from the MCalibration software. The third plot (grey curves) represents the normal stress and strain values, along the y -axis, as produced by the finite element model. A slight discrepancy can be observed between the results produced by the MCalibration and ANSYS software tools, which is likely to be attributed to the accumulation of rounding-off errors produced from the numerical solution of the finite element model.

The stress-strain curve obtained from the finite element model resulted in an R^2 value of 0.98, for both UHMWPE and VEHXPE, when compared to the experimental results. This demonstrates that the material model implemented in the finite element simulation provided a reliable solution for predicting the mechanical behaviour of the polymers used in this study.

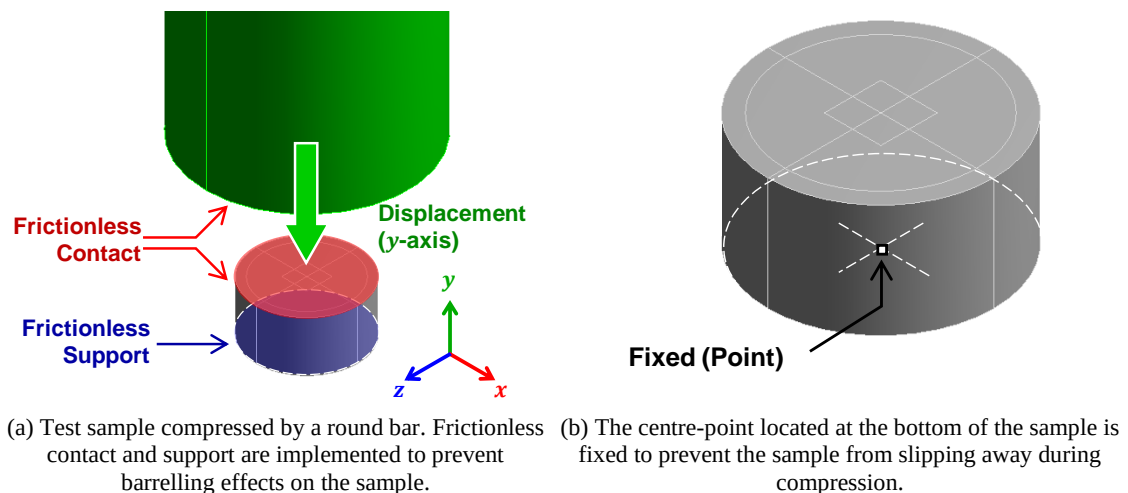
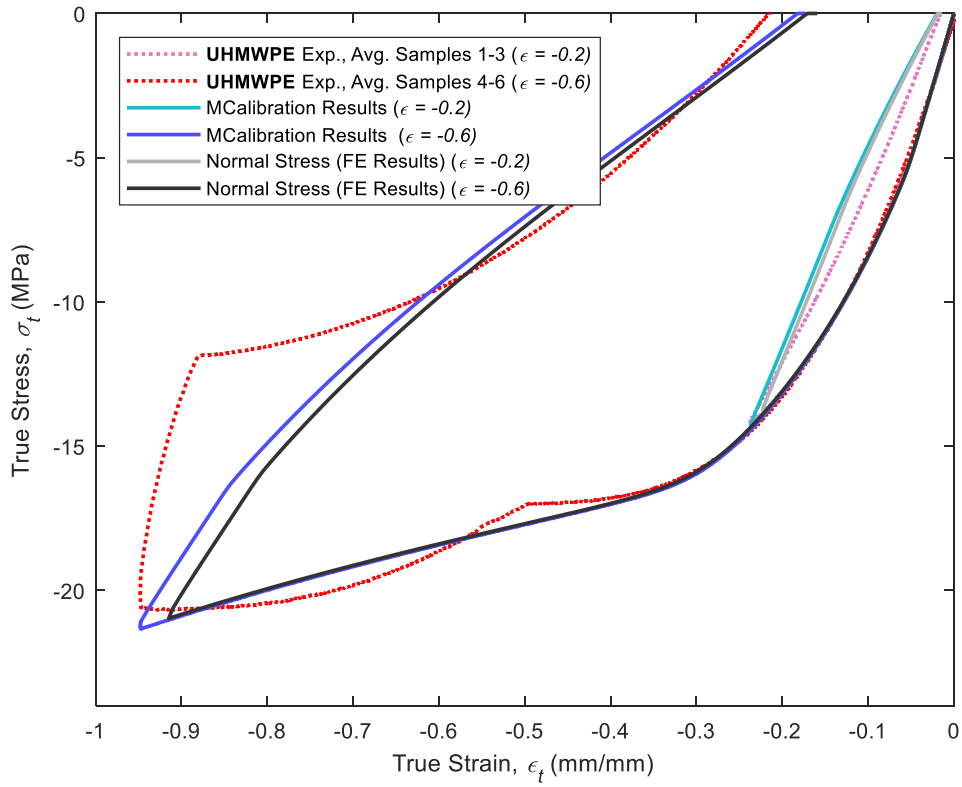
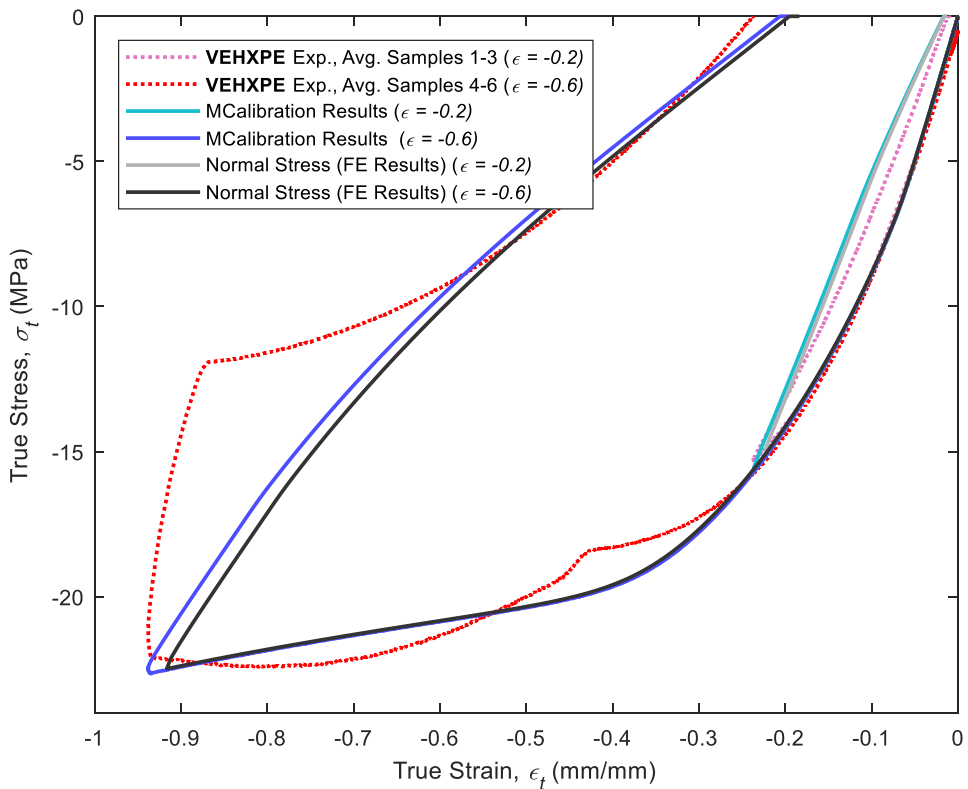


Fig. 5.2: Boundary conditions applied on the cylindrical test samples.



(a) UHMWPE (GUR 1050) stress-strain relationship.



(b) VEHXPE (GUR1020-e) stress-strain relationship.

Fig. 5.3: The true stress-strain relationships of (a) UHMWPE and (b) VEHXPE obtained from the finite element models, being compared to the results obtained from the compressions tests. The average values produced from the experimental results (indicated by 'Exp., Avg. Samples' in legend) for strain values of -0.2 and -0.6 were plotted using samples 1 – 3, and samples 4 – 6, respectively.

5.3. Structural Model and Finite Element Results

5.3.1. Introduction

In this section, the main findings that led to the final geometrical design of the MaltaHip are presented. The design development process consists of four major steps, being: (1) mesh sensitivity analysis, (2) studying the influence of each design parameter on the structural integrity of the prosthesis, (3) development of the interlocking mechanism and (4) comprehensive analysis on the finalised design solution.

5.3.2. Mesh Sensitivity Analysis

A mesh sensitivity analysis was conducted on the MaltaHip model, to attain element-size independency during the finite element computation of the results, as shown in Fig. 5.4. Elements located at the articular surfaces of the components (as highlighted in Fig. 3.15, p. 78) had their size varied for the mesh sensitivity analysis. The analysis was based on a structurally static model of the prosthesis that replicated the conditions at 0.12 s of the standard gait cycle⁴⁸ (see Fig. 3.4, p. 67), during which the applied loads are the greatest (3000 N), and the hip inclination angles are towards those at the extremes of the gait cycle during normal walking. This was intended to generate high contact stress values on the components of the prosthesis, and therefore vulnerabilities in the design were easily detected. In fact, the maximum contact stress values at the three articulations were used as the metrics to determine the feasible element size. Finite element models with element sizes ranging between 0.4 to 1.5 mm, in steps of 0.1 mm, were tested. The maximum contact pressure values of each solution consisting of a different element size were normalised against the largest maximum contact pressure value (for all the components) over the tested range of values. Therefore, the normalised maximum contact pressure values were monitored during the mesh sensitivity analysis to identify the optimum element size. From this analysis, it was observed that an element size of 0.7 mm (located at regions exhibiting high contact stresses) resulted in a solution which attained accurate results with numerical error values being less than 10%. In fact, the maximum error in the maximum contact pressure values resulted to be 7.9%, when compared to the solution using element sizes of 0.4 mm.

⁴⁸ The orientation angles of each individual degree of freedom of the hip (FE, IE and AA) at 0.12 s are greater than those exhibited at 0.5 s

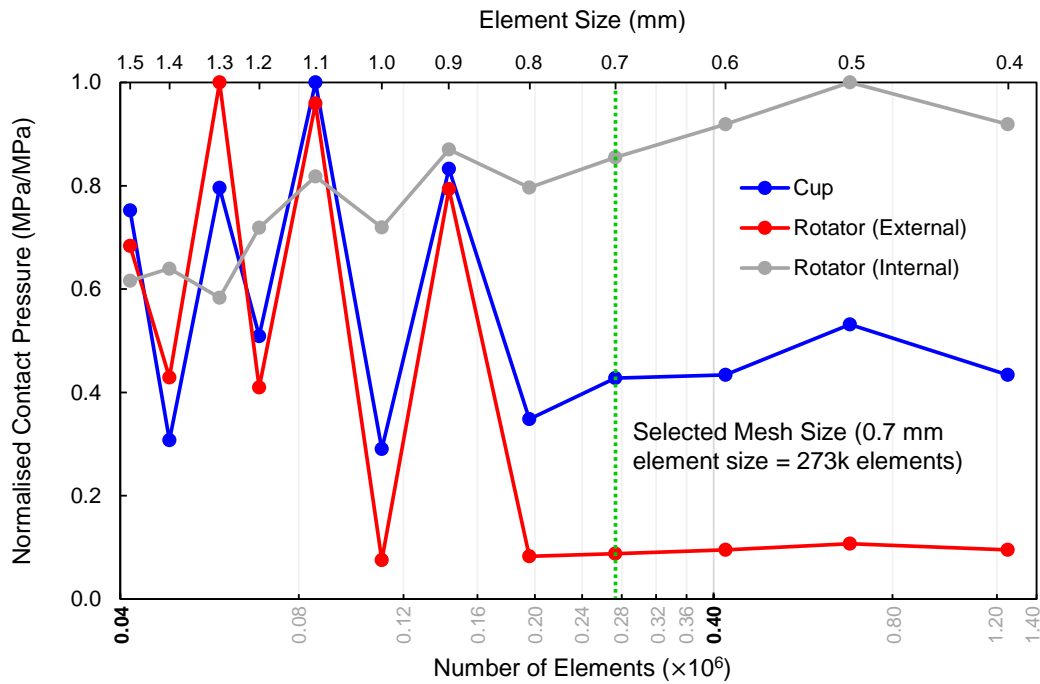


Fig. 5.4: Plot for mesh sensitivity analysis using the normalised maximum contact pressure as the metric for determining the optimised element size.

5.3.3. Influence of Design Parameters on Structural Integrity

5.3.3.1. Introduction

This section is intended to provide insight on the relationships between design parameters, outlined in Figs. 3.8 to 3.12 (p. 72 – 74), and their corresponding effect on the contact stresses (Fig. 5.5) and von Mises stresses (Fig. 5.6) of the MaltaHip components. The study was performed on the smallest MaltaHip cup (48 mm diameter)⁴⁹ which could reasonably fit the prosthesis mechanism. The small MaltaHip cup was selected for the parametric study so that vulnerabilities in design due to the high stresses could be immediately identified. The information retrieved from the 48 mm diameter MaltaHip cup was used as the foundations for scaled prostheses designs with larger diameters.

In fact, a prosthesis with a 53 mm outer diameter MaltaHip cup was developed and used throughout the rest of this work (based on the results retrieved from the previous study using the 48 mm diameter cup). The 53 mm outer diameter MaltaHip cup was used as it classifies under medium-sized prostheses. The larger MaltaHip cup would indeed exhibit reduced stresses under

⁴⁹ Acetabular cup diameters typically range between 44 – 60 mm, however these values may vary, depending on the manufacturer.

the same loading conditions⁵⁰. The relationships that are observed were used to determine whether the design parameters produced any significant effects on the contact and von Mises stresses. The design parameters were maximized or minimized accordingly, whilst ensuring that the complete mechanism fits within the 53 mm outer diameter limit of the MaltaHip cup.

5.3.3.2. Influence on Contact Stresses

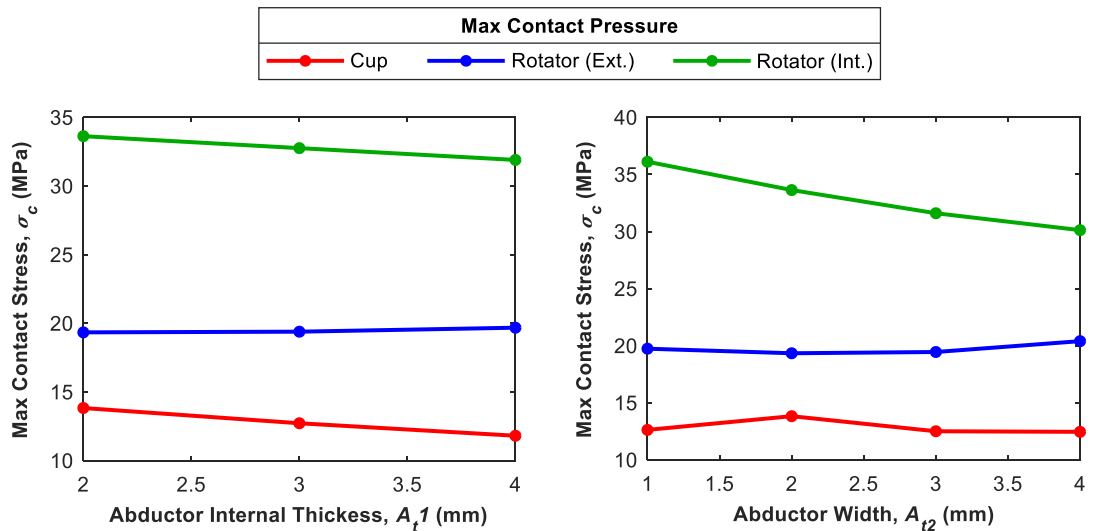
The relationship between the design parameters (Figs. 3.8 to 3.12, p. 72 – 74) and the contact stress are shown in Fig. 5.5. It can be observed that the internal surface of the rotator, which articulates with the abductor, exhibits the highest contact stress for all the range of tested values. This is mainly attributed to the limited area which is available for this articulation. It has been observed that the contact stress at this severely-affected articulation can be greatly reduced by increasing the abductor width (A_{t2} shown in Fig. 5.5b) in order to increase the corresponding contacting area of the rotator. Other design parameter changes that have been observed to reduce the contact stress (to a lower extent), are increasing the internal thickness of the abductor (A_{t1} shown in Fig. 5.5a) and increasing the rotator height (R_{t2} shown in Fig. 5.5e). The former would result in a larger internal diameter of the rotator, thus improving the contact area, and the latter would result in an increase in the overall component thickness. On the other hand, it was noted that increasing the abductor fillet (A_f shown in Fig. 5.5c) did not correspond to any significant reductions in contact stresses at the internal surface of the rotator. This may be attributed to the narrow range of values that could be possibly tested within the limited dimensions of the component.

With regards to the contact stresses at the external surface of the rotator, it can be observed that increasing the rotator diameter (R_d shown in Fig. 5.5f) would result in a reduction in the contact stresses at the flexor and rotator articulation. Once again, varying the size of the edge fillets (R_f shown in Fig. 5.5g) did not produce any appreciable effects. Similar to the previous case, this may be attributed to the narrow range of values which could be practically tested in the current design. Changes in the design parameters of the flexor component (F_{t1} , F_{t2} , F_f) did not produce any significant effects on the contact stresses of the prosthesis system. Variations in the thickness of the polymeric MaltaHip cup (C_t shown in Fig. 5.5k) also did not produce any significant changes to the contact stress results, even when tested over a very wide range of values (2 – 8 mm).

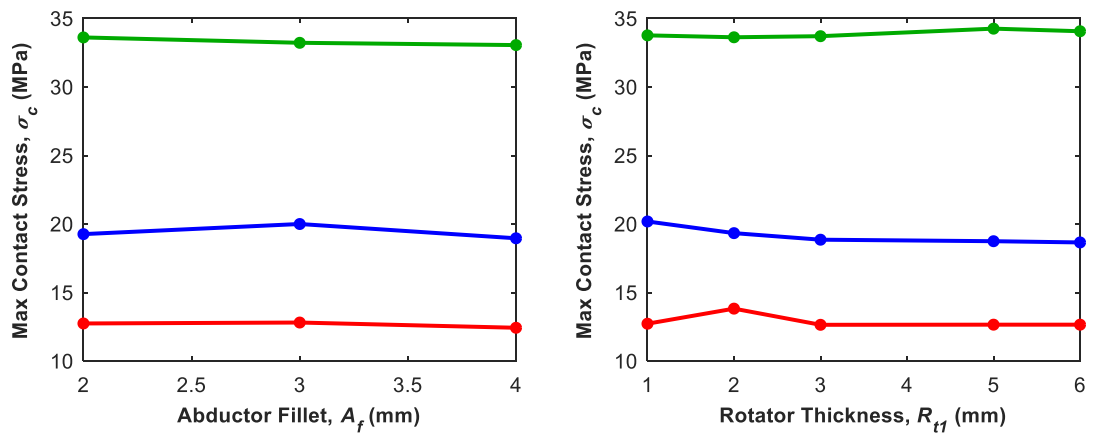
⁵⁰ According to ISO 14242-1:2014/Amd 1:2018, loading conditions are the same for all hip implant sizes.

The influence of the radial clearance values, as specified in ISO 7206-2:2011/Amd 1:2016, on the contact stresses were tested in the finite element model, as shown in Fig. 5.5l. The radial clearances at the different articulations were varied simultaneously (so that the clearances are all scaled equally) and are plotted on the same plot. As outlined in Section 3.3 (p. 69) the ISO standard specifies different radial clearance distances for articulation diameters of different sizes. Increasing the abductor clearance (A_c) and flexor clearance (F_c) caused the contact stress values to escalate. Interestingly, changes in the rotator clearance (R_c) did not seem to reproduce this effect and thus is postulated to be attributed to the different geometries of the articulations. The cup-flexor and rotator-abductor articulations are produced from the curved surface of the cylinder, whereas the flexor-rotator articulation consists of a tapered geometrical design in the form of a truncated cone (Fig. 3.15, p. 78).

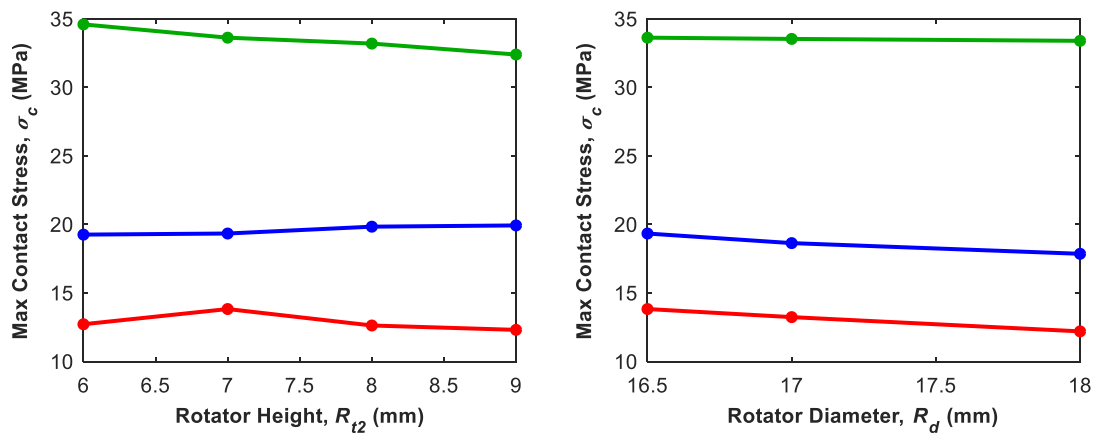
The conformity of the cup-flexor and rotator-abductor articulations is drastically reduced with increasing values of radial clearances (due to its cylindrical design). The flexor-rotator articulation is less sensitive to changes in the clearance values, as a tapered connection maintains contact over a wide range of clearance values. It should be noted that the range of clearance values specified in ISO 7206-2:2011/Amd 1:2016 is fairly wide (0.020 – 0.095 mm, and 0.035 – 0.180 mm, depending articulation diameter), to the extent that it may cause the components to become loose as these approach the upper ends of the ranges; as also noted in other studies [336]. Hence, a practical clearance value is likely to be located towards the lower ends of the ranges. However, it must be ensured that enough clearance is still provided to permit the smooth sliding motion of the components, without inducing extensive frictional effects.



(a) Abductor internal thickness: moderate influence on the cup and the internal surface of the rotator. (b) Abductor width: significant influence on the rotator.



(c) Abductor fillet: negligible influence on the components. (d) Rotator thickness: negligible influence on the components.



(e) Rotator height: moderate influence on the cup and internal surface of the rotator. (f) Rotator diameter: moderate influence on the cup and the external surface of the rotator.

Sub-figures continued on next page \Rightarrow

⇒ Sub-figures continued from previous page.

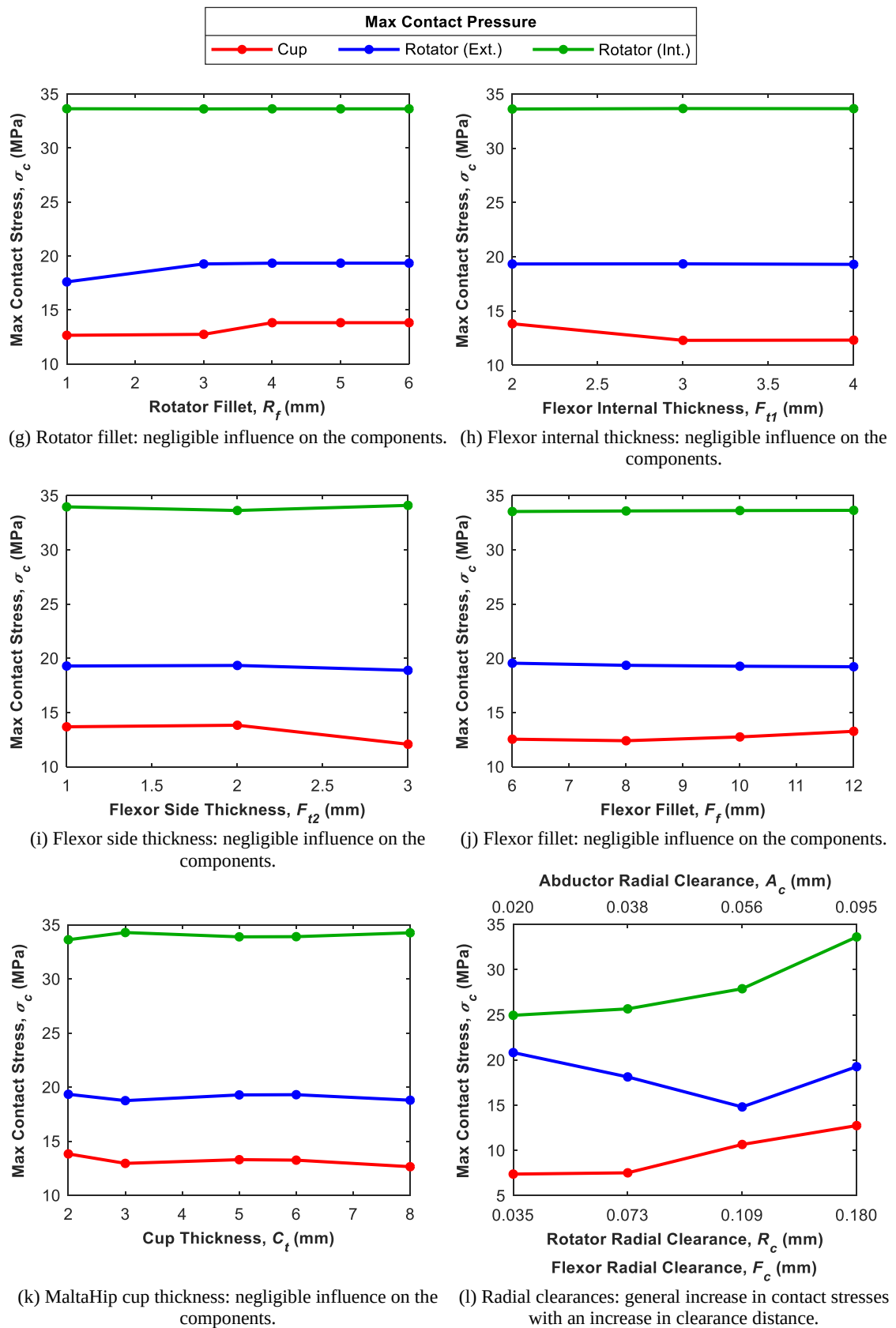


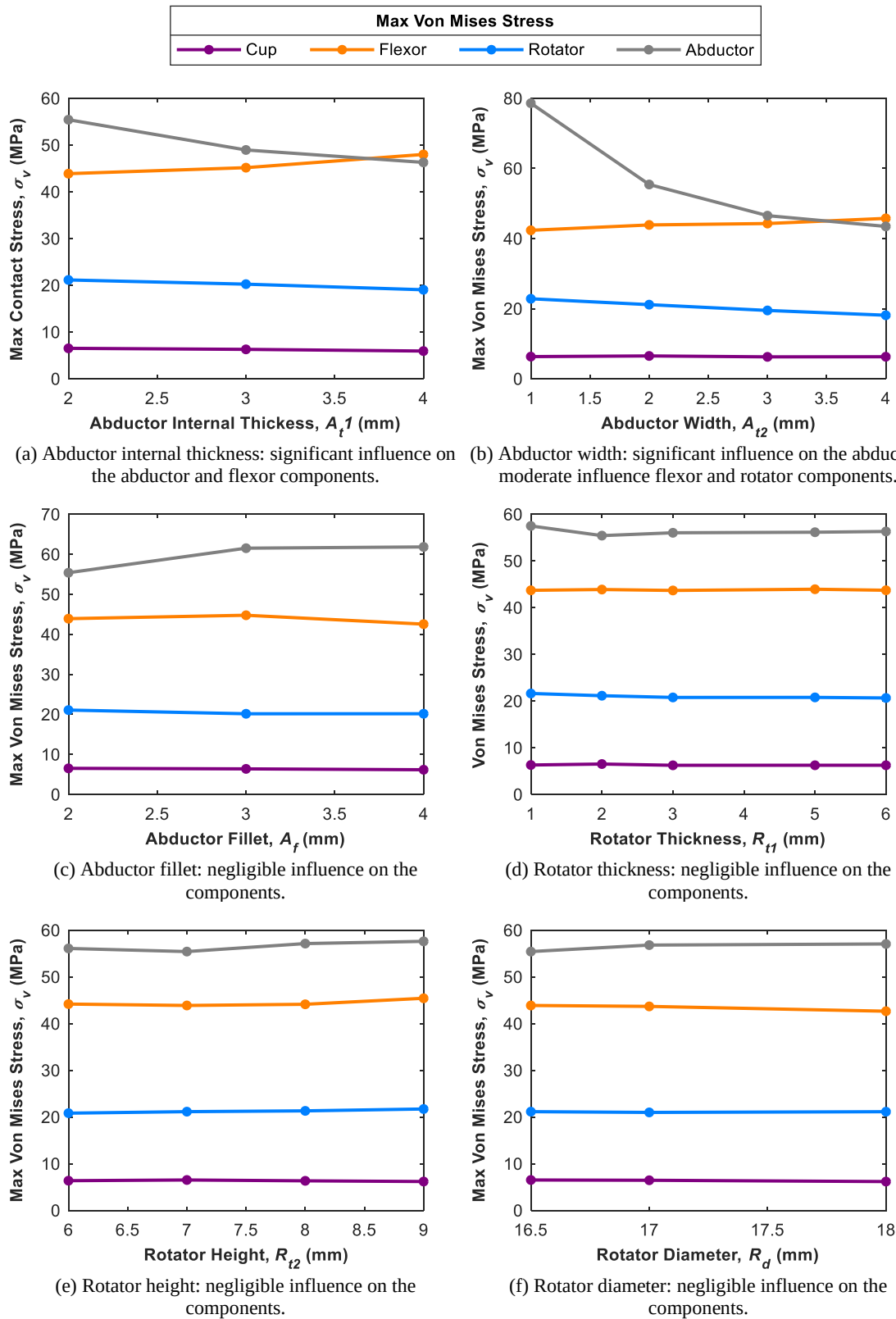
Fig. 5.5: Influence of the MaltaHip design parameters on the maximum contact stresses for each component.

5.3.3.3. Influence on Von Mises Stresses

The relationships between the design parameters (Figs. 3.8 to 3.12, p. 72 – 74) and the von Mises stress values are shown in Fig. 5.6. It can be observed that the rotator exhibits higher stress values than the MaltaHip cup. In fact, the rotator exhibited stress values close to the distributed yield strength of the polymer (21 – 25 MPa). The high-N austenitic stainless steel components inevitably exhibit higher stress values than the polymeric components, due to the material's higher elastic modulus. Nonetheless, all von Mises stress values of the stainless steel components are well below the yield strength (430 MPa) of the material.

The von Mises stresses in the rotator were observed to be mostly improved by maximizing the abductor width (A_{t2} as shown in Fig. 5.6b). Further improvements can be achieved by increasing the abductor internal thickness (A_{t1} as shown in Fig. 5.6a). Decreasing the radial clearances have been observed to significantly improve the von Mises stresses of all the components, except for the flexor (Fig. 5.6l, p. 119). It has been noted that the von Mises stresses of the MaltaHip cup are not significantly influenced by changes in the design parameters, except for the radial clearances (Fig. 5.6l, p. 119). The maximum von Mises stress value of the MaltaHip cup is less than half of the UHMWPE yield strength, which is attributed to its large contacting area which improves the distribution of stresses.

The metallic components have been observed to be highly sensitive to the design parameter changes. Nonetheless, the highest von Mises stress values that were obtained (over the whole range of the tested values), remain significantly lower than the yield strength of the material. Hence, in an effort to improve the overall structural integrity of the MaltaHip prosthesis, the optimization process was focussed on increasing the thickness of the polymeric components, with particular emphasis being put on the rotator component, since it exhibited the highest contact and von Mises stress values, both of which being relatively close to the material's yield strength.



Sub-figures continued on next page ⇒

⇒ Sub-figures continued from previous page.

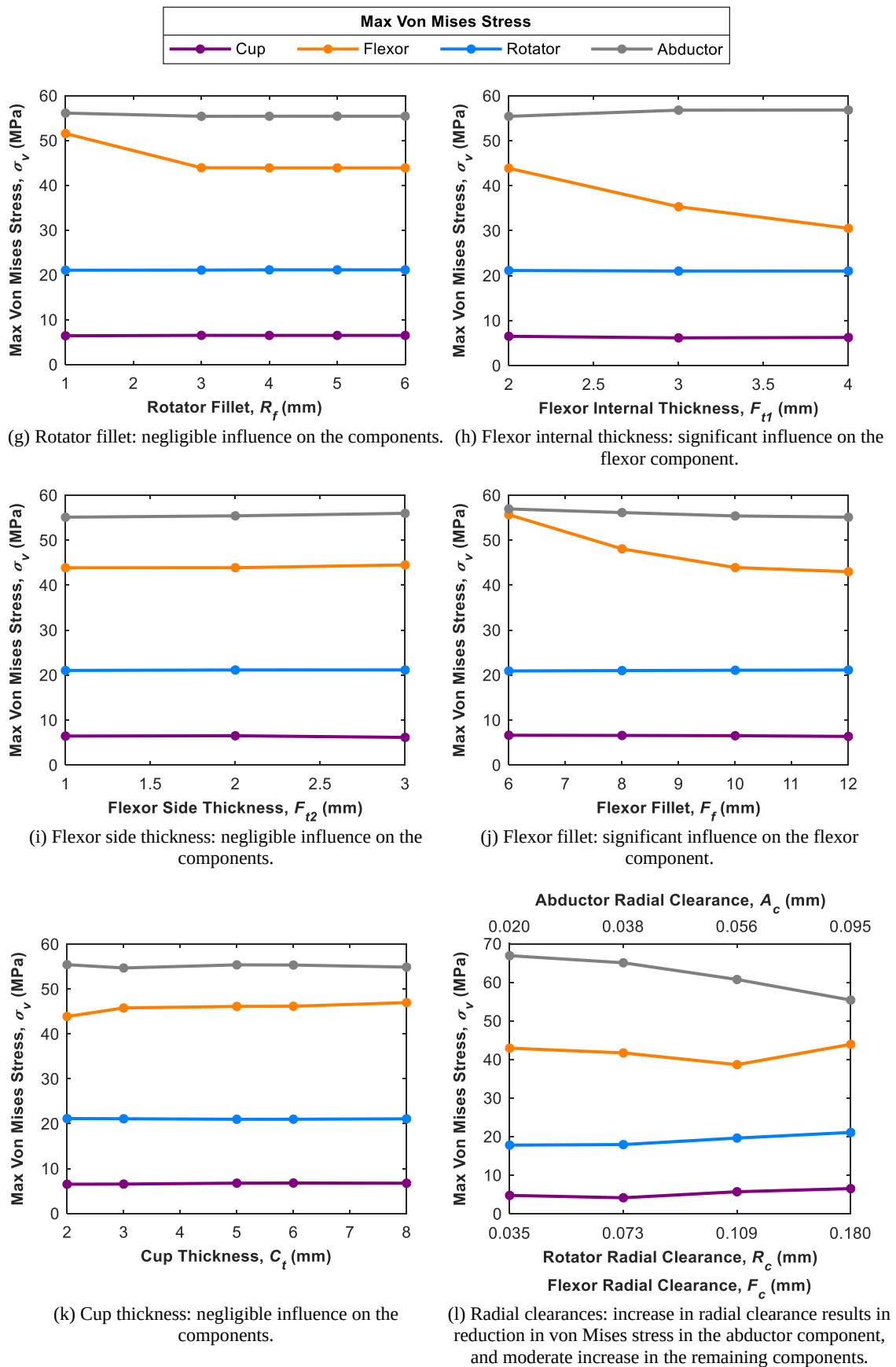


Fig. 5.6: Influence of the MaltaHip design parameters on the von Mises stresses of the components.

5.3.3.4. Finalised Design

By following the relationships between the design parameters and the mechanical response of the MaltaHip (Figs. 5.5 and 5.6, p. 115 - 119), a design for a 53 mm hip implant was developed. Efforts were primarily directed towards minimizing the contact and von Mises stress values on the rotator component, by maximizing the internal thickness (A_{t1}) and width (A_{t2}) as much as possible. Further implementations were adapted by following the observations outlined in the previous section. The finalised principal design parameters of the MaltaHip are shown in Table 5.2.

Table 5.2: Optimised principal design parameters of the MaltaHip.

Component	Design Parameters	Label	Range of Values	Initial Estimate	Final Design
			[mm]	[mm]	[mm]
			48 mm cup	48 mm cup	53 mm cup
Abductor (A)	Min Internal Thickness	A_{t1}	2.0 – 4.0	2.0	3.0
	Min Width Thickness	A_{t2}	1.0 – 4.0	2.0	5.0
	Fillet	A_f	2.0 – 4.0	2.0	5.0
Rotator (R)	Min Thickness	R_{t1}	1.0 – 6.0	2.0	2.0
	Height	R_{t2}	6.0 – 9.0	7.0	7.0
	Diameter	R_d	16.5 – 18.0	16.5	16.0
	Fillet	R_f	1.0 – 6.0	4.0	4.0
Flexor (F)	Min Radial Thickness	F_{t1}	2.0 – 4.0	2.0	0.5
	Min Side Thickness	F_{t2}	1.0 – 3.0	2.0	1.5
	Fillet	F_f	6.0 – 12.0	10.0	9.0
Cup (C)	Min Thickness	C_t	2.0 – 8.0	2.0	5.3
Radial Clearances	Abductor Clearance	A_c	0.020 – 0.095	0.020	0.040
	Rotator Clearance	R_c	0.035 – 0.180	0.035	0.070
	Flexor Clearance	F_c	0.035 – 0.180	0.035	0.070

5.3.4. Interlocking Mechanism

The design of the MaltaHip used for the parametric study did not possess all the detailed (non-structural) features for other functions (primarily for the avoidance of dislocation), as the model was intended to be minimal to reduce the computational expense, whilst providing the ability to analyse the critical contact surfaces. However, such design was noted to be prone to dislocations, due to the short ‘jump’ distances that existed between the components (see example in Fig. 5.7). Following discussions with orthopaedic surgeons, it was deemed necessary to introduce a mechanism to engage and secure the components. Having the finalised dimensions of the contact surfaces at hand (shown in Table 5.2), an interlocking mechanism was introduced to the MaltaHip prosthesis design.

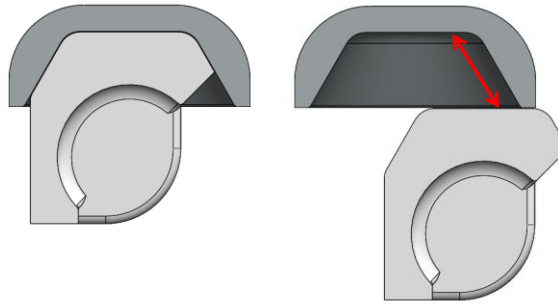


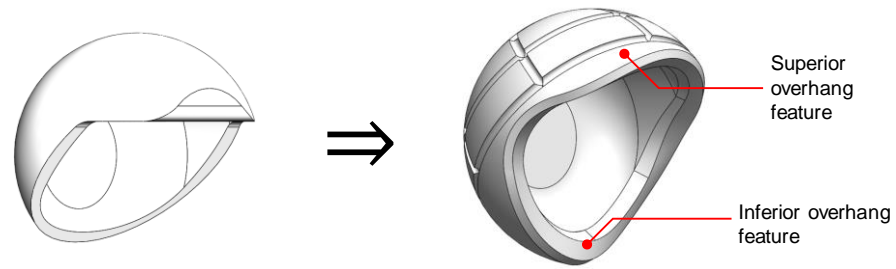
Fig. 5.7: Short ‘jump’ distance with the early version of the MaltaHip as no geometrical features are available to prevent dislocation.

Conventional ball-and-socket implants rely on a variety of mechanisms to minimize hip dislocation. One mechanism that ball-and-socket hip prostheses usually rely on is a partial lip that protrudes from the rim of the hemispherical cup, located posteriorly (i.e. the location at which most hip dislocation occurs). Another mechanism involves a captive hemispherical cup that engages the femoral head using the press-fit technique. Other prosthesis designs make use of additional components (e.g. pins, rings) which are secured onto the hemispherical cup during surgery following the hip reduction⁵¹ process.

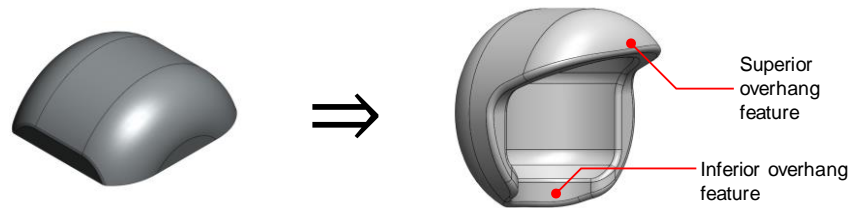
The components of the MaltaHip implant with the finalised dimensions and interlocking mechanism are shown in Fig. 5.8. The interlocking mechanism consists of overhang features (located superiorly and inferiorly) that geometrically constrains all the translation or rotational motions of the components, except for the rotational degree of freedom that corresponds to the articulation motion. Therefore, the components are prevented from ‘jumping’ out from their assigned positions during in service, whilst still being able to perform the desired rotational motion for articulation. In order to bring the components into this specific configuration, the components can only be assembled/disassembled at a specific orientation that is outside the natural range of motion of the hip. This implies that the components cannot be disassembled (i.e. dislocated) at hip orientations which are within the natural range of motion required by the user for activities of daily living.

The superior and overhang features that prevent dislocation can be found in the MaltaHip cup (Fig. 5.8a) and the flexor (Fig. 5.8b) components. Therefore, dislocation of the flexor component is prevented by the overhang features of the MaltaHip cup. Similarly, dislocation of the rotator is prevented by the overhang features of the rotator component. The rotator (Fig. 5.8c) does not consist of any overhang features as it must enable the abductor component to be assembled as easily as possible during the hip reduction process.

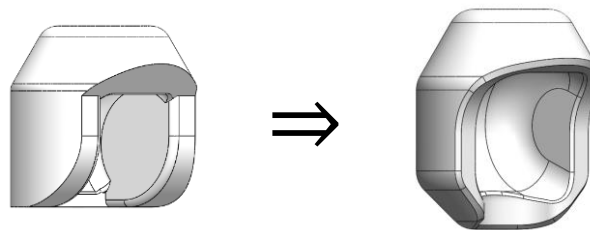
⁵¹ Hip reduction: Manipulation of the hip joint by the orthopedic surgeons during surgery in order to bring the femoral ball into the hemispherical cup.



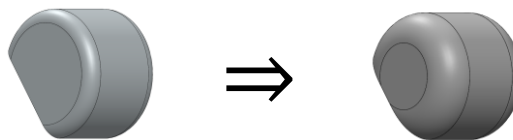
(a) The MaltaHip cup component.



(b) The flexor component.



(c) The rotator component.



(d) The abductor component.

Fig. 5.8: The conversion from the simplified to the finalised MaltaHip. The former (left) illustrates the major bearing surfaces that were used for the parametric study, and the latter (right) illustrates the finalised MaltaHip design which includes the interlocking mechanism.

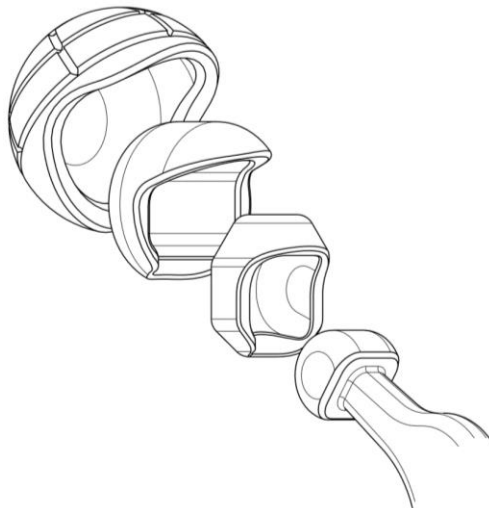
In fact, assembly of the abductor to the rotator is done in the same way the femoral ball is assembled into socket during the hip reduction process. However, the main difference between these two designs is that dislocation of the abductor component can only occur in the lateral direction. On the other hand, dislocation of the femoral ball can occur at any direction. The majority of the dislocations in the ball-and-socket implant occur in the posterior direction. However, due to the cylindrical design of the abductor component, dislocation in the posterior direction is not possible. Furthermore, to minimize the dislocation in the lateral direction of the abductor component, the protruding walls of the rotator (which constrain the relative lateral motion of the abductor) have been extended as much as possible to increase the ‘jump’ distance in the lateral direction.

The complete assembly process of the components using the interlocking mechanism is schematically represented in Fig. 5.9. The exploded view of the Fig. 5.9a shows the components in their normal orientation⁵². The process is initiated by assembling the rotator inside the flexor. This is achieved by rotating the rotator by 180° from its normal orientation about its longitudinal axis (Fig. 5.9b). Insertion of the rotator inside the flexor component is only possible at this specific orientation (Fig. 5.9c). Once the components are engaged, the rotator may be reoriented back to its original orientation inside the flexor component (Fig. 5.9d). The superior and inferior overhang features of the flexor have been specifically designed to form a converging angle between their faces (Fig. 5.9e), to prevent the dislocation of the rotator from the flexor component.

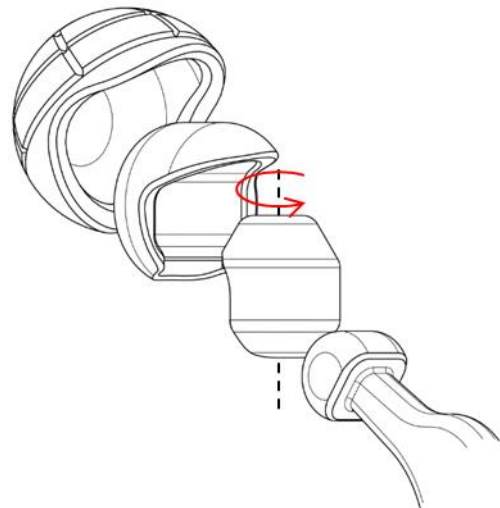
Assembly of the flexor component containing the rotator inside the MaltaHip cup is done similarly to the above approach. Initially, the flexor is rotated by 180° from its normal orientation about its longitudinal axis (Fig. 5.9f). Insertion of the flexor inside the MaltaHip cup is only possible at this specific orientation (Fig. 5.9g). Once the components are engaged, the flexor component can be once again reoriented back to its original orientation (Fig. 5.9h). A similar converging angle between the faces of overhang features of the MaltaHip cup have been designed to prevent the dislocation of the flexor from the MaltaHip cup (Fig. 5.9i).

It should be noted that up to this point, the assembly sequence can be altered such that the flexor-cup assembly is done prior to the rotator-flexor assembly. The prosthesis is completely assembled when the abductor head is brought inside the rotator component (Fig. 5.9j), which is usually done during the surgical hip reduction process, which offers limited range of motion for the surgeons to manipulate the leg. Therefore, to facilitate this procedure, the abductor is designed to be absent from any overhang features, and thus can be assembled inside the rotator in its normal orientation without involving any drastic reorientations of the abductor component. This final assembly step mimics the procedure which is conducted during the hip reduction process of the ball-and-socket implant, as no drastic reorientations of the components are involved in the process.

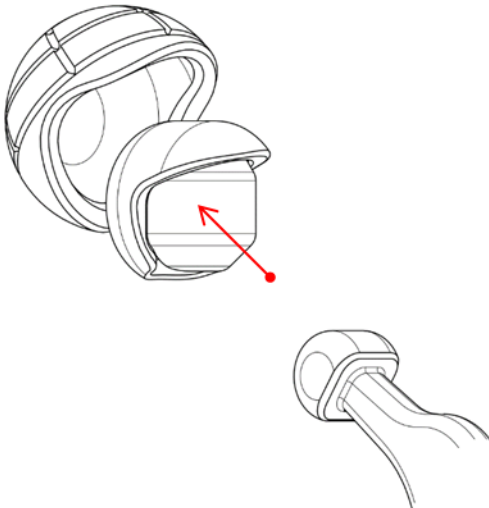
⁵² The term ‘normal orientation’ refers to the orientation that the components assume while the user is in the upright position, standing on two legs.



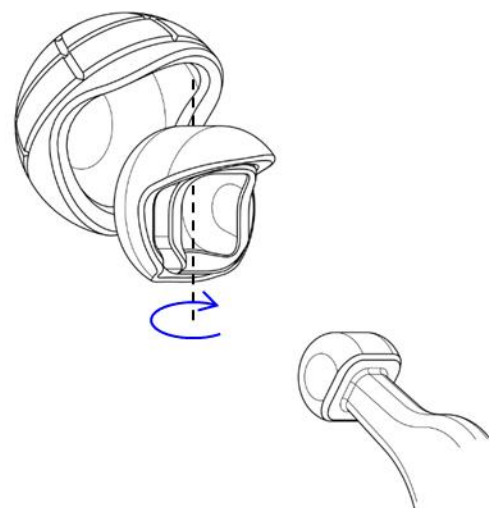
(a) Components of the MaltaHip in their normal orientation.



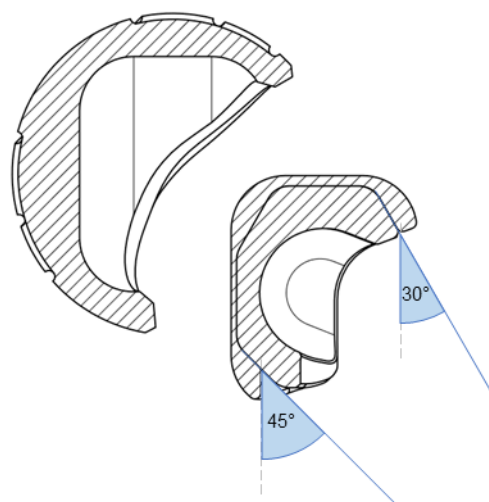
(b) Rotation of the rotator by 180° from its normal orientation.



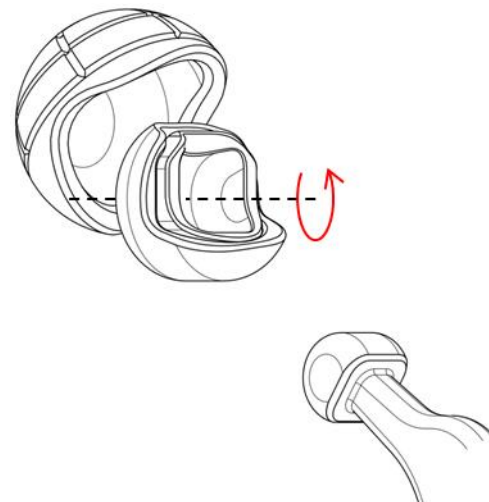
(c) Insertion of rotator inside the flexor.



(d) Reorientation of the rotator to its normal orientation.



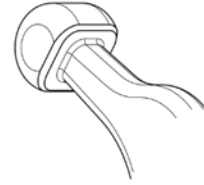
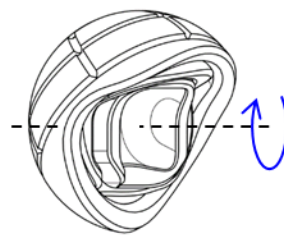
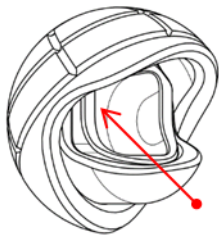
(e) The converging angle of the flexor overhang features prevents the rotator from disengaging.



(f) Rotation of the flexor containing the rotator by 180° from its normal orientation.

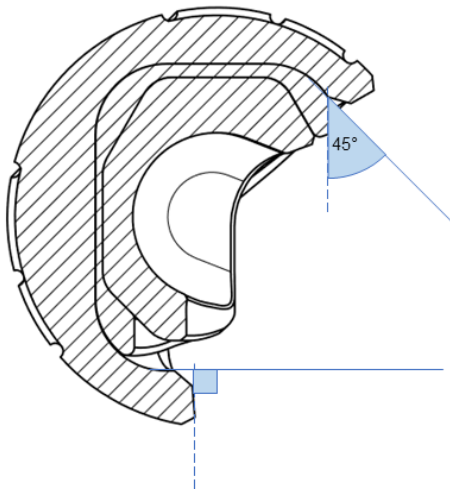
Sub-figures continued on next page ⇒

⇒ Sub-figures continued from previous page

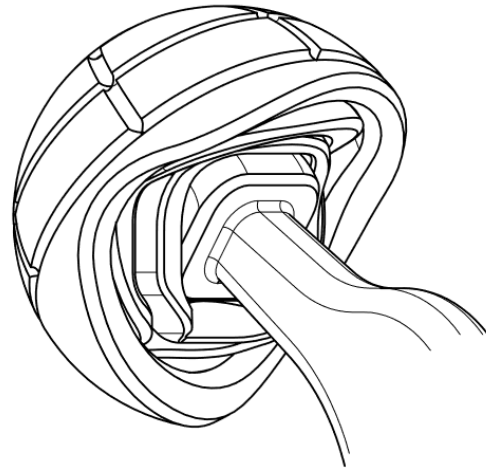


(g) Insertion of the flexor inside the MaltaHip cup.

(h) Reorientation of the flexor to its normal orientation. The prosthesis is ready to be assembled.



(i) The converging angle of the cup overhang features prevents the flexor from disengaging.



(j) Complete assembly of the prosthesis.

Fig. 5.9: Assembly steps involved to interlock the components of the MaltaHip prosthesis.

5.3.5. Structural Analysis of Finalised Design Solution

5.3.5.1. Introduction

Transient mechanical simulations of the ball-and-socket (Section 5.3.5.2) and the MaltaHip (Section 5.3.5.3) implants based on the standard gait cycle (Fig. 3.4, p. 67) were developed and analysed in this work using commercial finite element ANSYS 19.2. Both the UHMWPE and VEHXPE have been tested as the soft bearing materials of the prosthesis. The viscoelastic-viscoplastic behaviours of the polymers were based on the Three Network model (Section 5.2, p. 106). Both the hemispherical and MaltaHip cups possessed a 53 mm outer diameter and were also inclined at 45° (implantation angle [109], as shown in Fig. 2.8a, p. 13). The load profile (specified in Table 3.2, p. 68) was applied to the prosthesis model, which reaches a peak load value of 3000 N. A timestep of 0.05s was used throughout the gait cycle, with each timestep consisting of 20 to 200 substeps, to reach convergence of the numerical computations. The von Mises, strain, contact pressure and contact status⁵³ results produced during the gait cycle are presented in the following sections. Furthermore, the maximum and average stress values at 0.5 s (representing the peak load) were noted for each case.

The finite element results of UHMWPE and VEHXPE were noted to be alike, due to their similar bulk mechanical properties. Therefore, only the results for the UHMWPE are presented in this work., which are primarily intended to outline the polymer behaviour in the new hip implant configuration using the Three Network model.

⁵³ The contact status indicates whether the surfaces under consideration are exhibiting any of these conditions: sticking, sliding, near, far and over constrained.

5.3.5.2. Ball-and-socket Implant

The finite element results of the hemispherical cup of the ball-and-socket implant are presented in Figures 5.10 to 5.13. It can be noted that the maximum von Mises stress of the hemispherical cup is equal to 6.62 MPa, as shown in Fig. 5.10. Furthermore, the average von Mises stress value (at 0.5 s) was noted to be equal to 2.35 MPa. The average and maximum strain values were equal to 0.023 and 0.060, respectively (Fig. 5.11). The peak von Mises and strain values are located at the superior rim of the hemispherical cup; a region that is susceptible to impingement in case the orientation of the implanted hemispherical cup is slightly misaligned.

The contact stresses exhibited at the articular surface of the ball-and-socket are illustrated in Fig. 5.12. The average and peak contact stresses of the hemispherical cup are equal to 4.37 and 11.90 MPa. The contact stresses are mainly located at the superior region of the cup, due to the spherical geometry of the femoral head. The peak contact stresses are concentrated at the edge, as shown in Fig. 5.14. This is a common occurrence with hemispherical cups, usually referred to as edge loading, which can act as a source of wear debris generation since the region is susceptible to impingement if the hemispherical cup is slightly malpositioned during surgery [337, 338]. It is observed that the maximum contact stress value does not exceed the distributed yield strength of UHMWPE (21 – 25 MPa). The contact status results, shown in Fig. 5.13, illustrate that the contact patch is mainly characterised by sliding motion. The detrimental effects of edge loading may be reduced by introducing a rounded edge. Nonetheless, this would increase the risk of hip implant dislocation. This can be counteracted by producing a lip to increase the contacting area and prevent the formation of a sudden increase in contact stress. However, this lip would be prone to impingement.

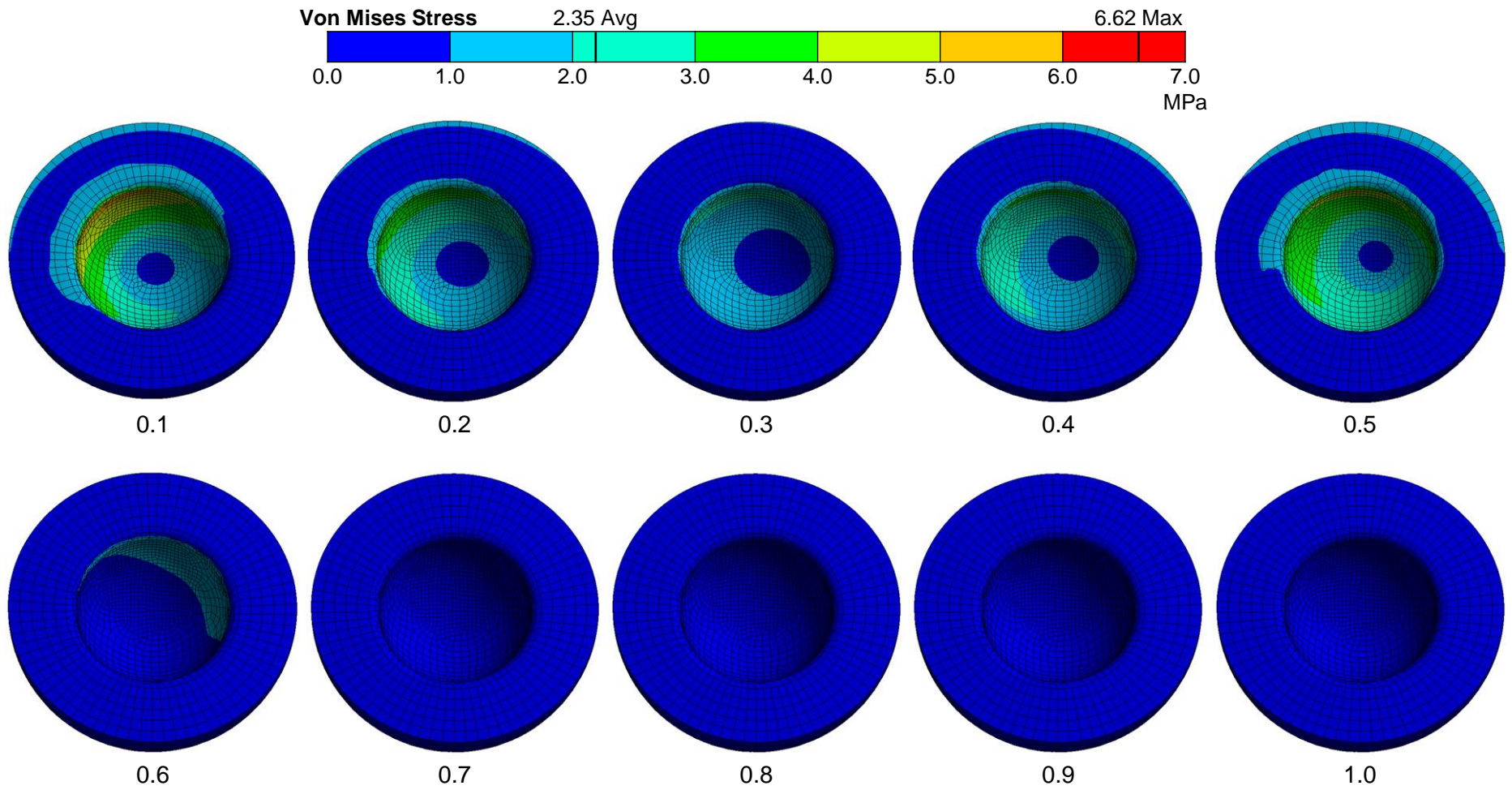


Fig. 5.10: Von Mises stresses on the hemispherical cup during gait cycle, at 0.1 s time intervals.

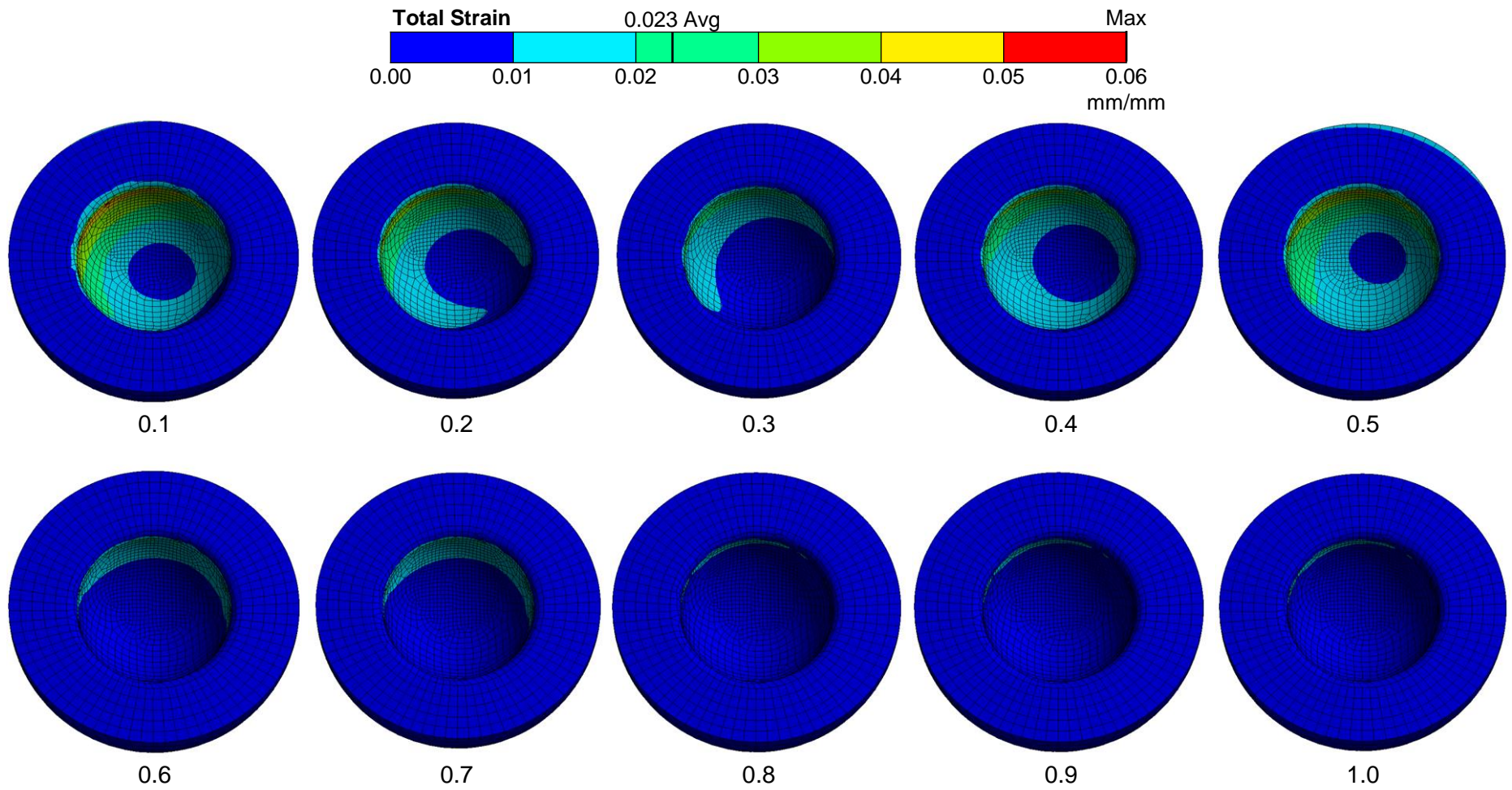


Fig. 5.11: Total strain on the hemispherical cup during gait cycle at 0.1 s time intervals.

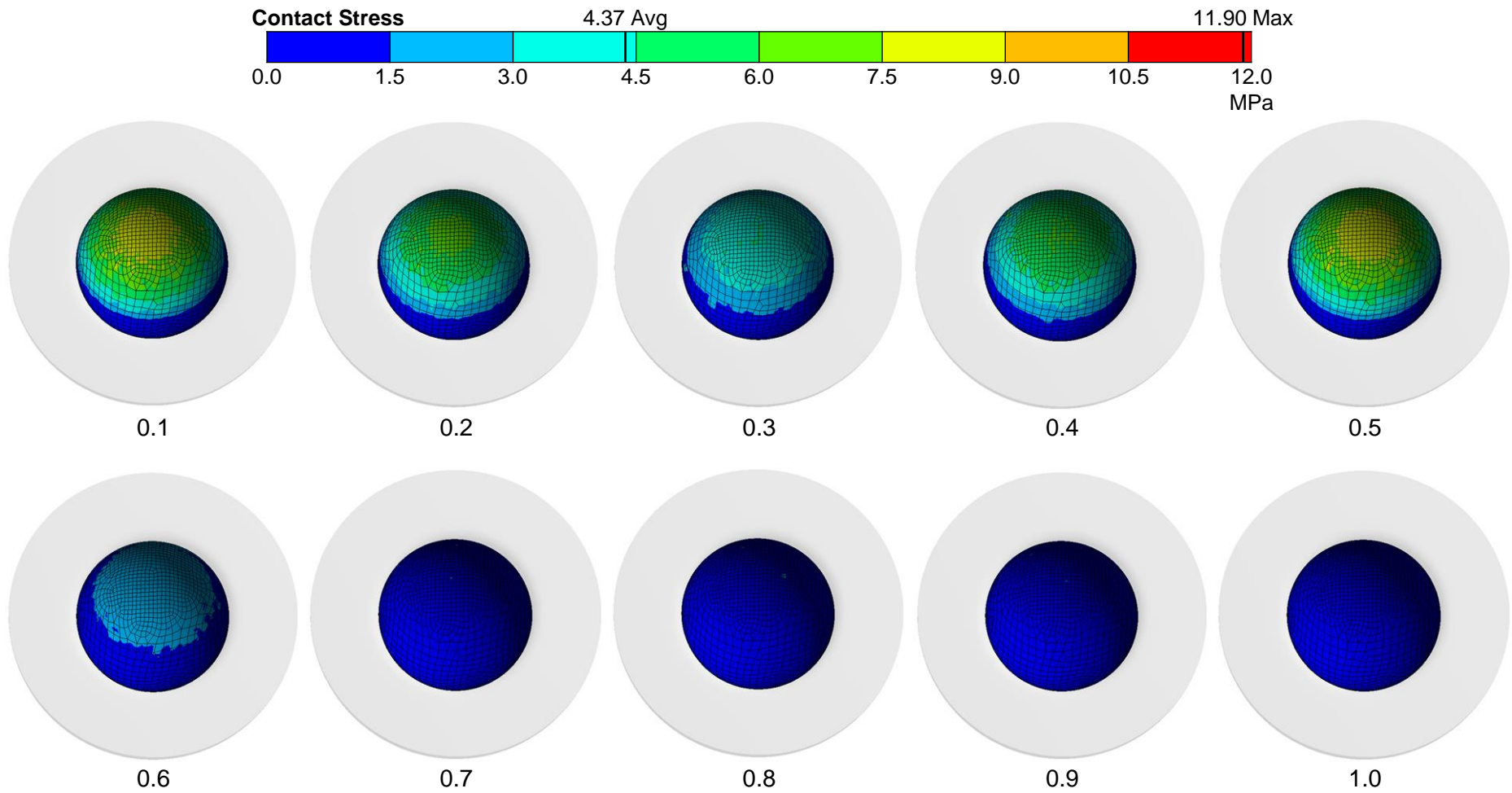


Fig. 5.12: The contact stress values of hemispherical cup during gait cycle at 0.1 s time intervals.

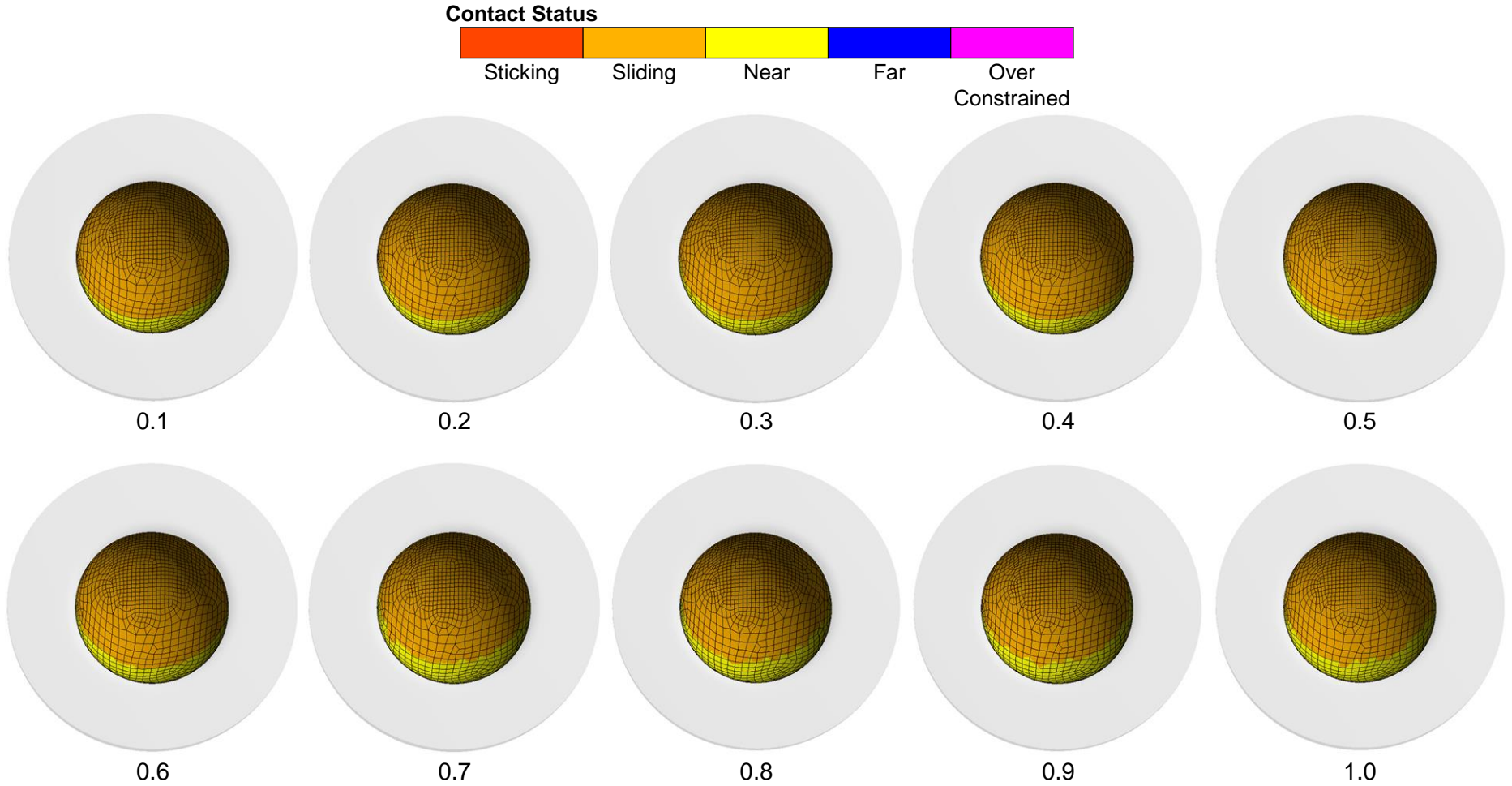


Fig. 5.13: Contact status of the hemispherical cup during gait cycle at 0.1 s time intervals.

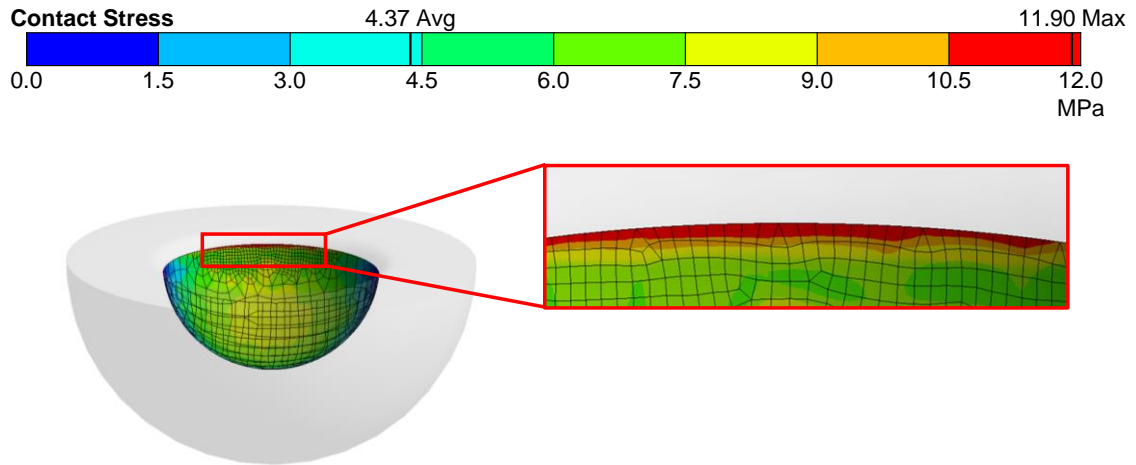


Fig. 5.14: Edge-loading exhibited in the hemispherical cup.

5.3.5.3. MaltaHip Implant

The finite element results (von Mises, total strain, contact stress and contact status) for the MaltaHip cup and rotator are shown in Figs. 5.15 to 5.26. Furthermore, a summary of the stress results in comparison to the ball-and-socket implant is provided in Table 5.3.

Table 5.3: Comparison in stress values between the ball-and-socket and MaltaHip implants.

Type of Stress	Ball-and-socket Implant		MaltaHip Implant		Comparison*
	Component	[MPa]	Component	[MPa]	
Max. von Mises Stress	Hemispherical cup	6.62	Cup	8.94	+35%
	Hemispherical cup	6.62	Rotator	13.46	+103%
Average von Mises Stress	Hemispherical cup	2.35	Cup	2.77	+18%
	Hemispherical cup	2.35	Rotator	4.09	+74%
Max. Contact Stress	Hemispherical cup	11.90	Cup-Flexor	12.00	+1%
	Hemispherical cup	11.90	Flexor-Rotator	22.68	+91%
	Hemispherical cup	11.90	Rotator-Abductor	26.42	+122%
Average Contact stress	Hemispherical cup	4.37	Cup-Flexor	1.64	-62%
	Hemispherical cup	4.37	Flexor-Rotator	3.12	-29%
	Hemispherical cup	4.37	Rotator-Abductor	3.84	-12%

* A positive (+ve) percentage value indicates an increase in the stresses of the MaltaHip implant, compared to the ball-and-socket implant. A negative (-ve) percentage value indicates a reduction in the stresses of the MaltaHip, compared to the ball-and-socket implant.

The maximum von Mises stress value of the MaltaHip cup is 8.94 MPa and is located at the superomedial direction of the component, that corresponds to the thinnest region of the cup (controlled by design parameter C_t), as shown in Fig. 5.15. Despite larger values of C_t were tested, no significant stress reductions were observed. The average von Mises stress of the MaltaHip cup is 2.77 MPa, being 18% greater than that produced by the hemispherical cup.

The maximum von Mises stress of the rotator is equal to 13.46 MPa, as shown in Fig. 5.16 and Fig. 5.17. The peak von Mises stress is located at the internal surface of the rotator which articulates against the abductor. The increase in stress is attributed to the specific orientation of the component that is achieved during 0.12 and 0.50 s of the standard gait cycle (see Fig. 3.4, p. 67), representing the instances when the loads are the greatest, causing the majority of the load to be momentarily supported on the small area offered by the edge fillet of the abductor, leading to a concentration of stress. Despite the peak von Mises stress is twice the stress that is exhibited by the hemispherical cup (6.62 MPa), it is noted to be well below the distributed yield strength of the UHMWPE material (21 – 25 MPa). Furthermore, the average von Mises stress of the rotator has resulted to be 4.09 MPa (Fig. 5.16 and Fig. 5.17). This indicates an increase of 74% in the average von Mises stress, when compared to the hemispherical cup. Despite the apparent significant increase, the absolute values of the average von Mises stress is still considerably low when compared to the distributed yield strength of the polymer (21 – 25 MPa).

The greater von Mises stress values in the MaltaHip components are likely to be attributed to the thinner polymeric components which were required to accommodate the two metallic components of the prosthesis. The thickness profile of the MaltaHip cup and the rotator at the superior region both varied between 5.3 and 7.1 mm. This is nearly half the thickness of the hemispherical cup design, which is 12.5 mm thick. Despite the higher maximum von Mises stress values, all values are lower than the yield strength of the UHMWPE.

The total strain values of the polymeric components are shown in Figs. 5.18 to 5.20. The maximum strain values for the MaltaHip cup and the rotator are 0.10 and 0.19, respectively. The strain values of the MaltaHip demonstrated to be higher than the 0.06 strain value produced by the hemispherical cup. Nonetheless, it should be noted that these maxima are exhibited at highly localised regions.

The maximum contact stress of the MaltaHip cup is equal to 12.0 MPa (Fig. 5.21), which is similar to that obtained for the hemispherical cup (11.90 MPa). The peak contact stress is highly localised, and in fact most of the contact surface exhibits significantly lower contact stress values, producing an average contact stress of 1.64 MPa. It is interesting to note that the average contact stress of the MaltaHip cup is 62.5% lower than that obtained for the hemispherical cup.

This is highly beneficial in reducing the amount of wear that is liberated from the MaltaHip implant, since the MaltaHip cup undergoes long sliding distances since it is aligned along the flexion/extension degree of freedom.

The peak contact stress of the external and internal articulating surfaces of the rotator resulted to be 22.68 and 26.42 MPa, respectively (shown in Fig. 5.22 and Fig. 5.23). These stresses have been observed to be greater than the peak contact stresses produced from the hemispherical cup (11.90 MPa). However, it has been noted that these peak contact stresses are highly localised. The high maximum contact stress of internal articulating surface of the rotator (26.42 MPa), exceeds the distributed yield strength (21 – 25 MPa) of the polyethylene, and therefore may suggest that highly localised plasticity may occur. Nonetheless, the majority of the surface is postulated to undergo elastic deformations at its surface as the average contact stress resulted to be equal 3.84 MPa. A fatigue analysis would be further required in order to determine the absolute acceptance criteria for the rotator component.

The average contact stress values of the external surface (Fig. 5.22) and internal surface (Fig. 5.23) of the rotator components are 3.12 and 3.84 MPa, respectively. The contact stresses of the rotator are notably higher, which is attributed to their smaller contact area. However, despite the higher contact stresses, it should be noted that the two articulations of the rotator will require less than half of the sliding distance that is required by the hemispherical cup, due to the narrow range of motion that is required during the gait cycle by the internal/external rotation and abduction/adduction motions. Hence, the amount of wear debris that is generated by the rotator is postulated to be minimal. Furthermore, it is worth noting that the external and internal surfaces of the rotator exhibit 29% and 12% lower contact stress, when compared to the hemispherical cup.

Results for the contact status have been produced for the two polymeric components investigated in this work. The type of contact status is defined according to the position and motion of the contact element under consideration with respect to the associated target surface. A contact element is considered to be in the near-field contact when the nodal points are within a calculated distance that corresponds to the target surface. The contact statuses of load bearing surfaces of the MaltaHip cup (Fig. 5.24) and the rotator (Fig. 5.25 and Fig. 5.26) are mostly characterized as sliding throughout the complete gait cycle. The contact status of the rotator external bearing surface has been noted to undergo some brief instances of sticking, which implies that for brief instances no tangential motion occurs between the contacting nodes.

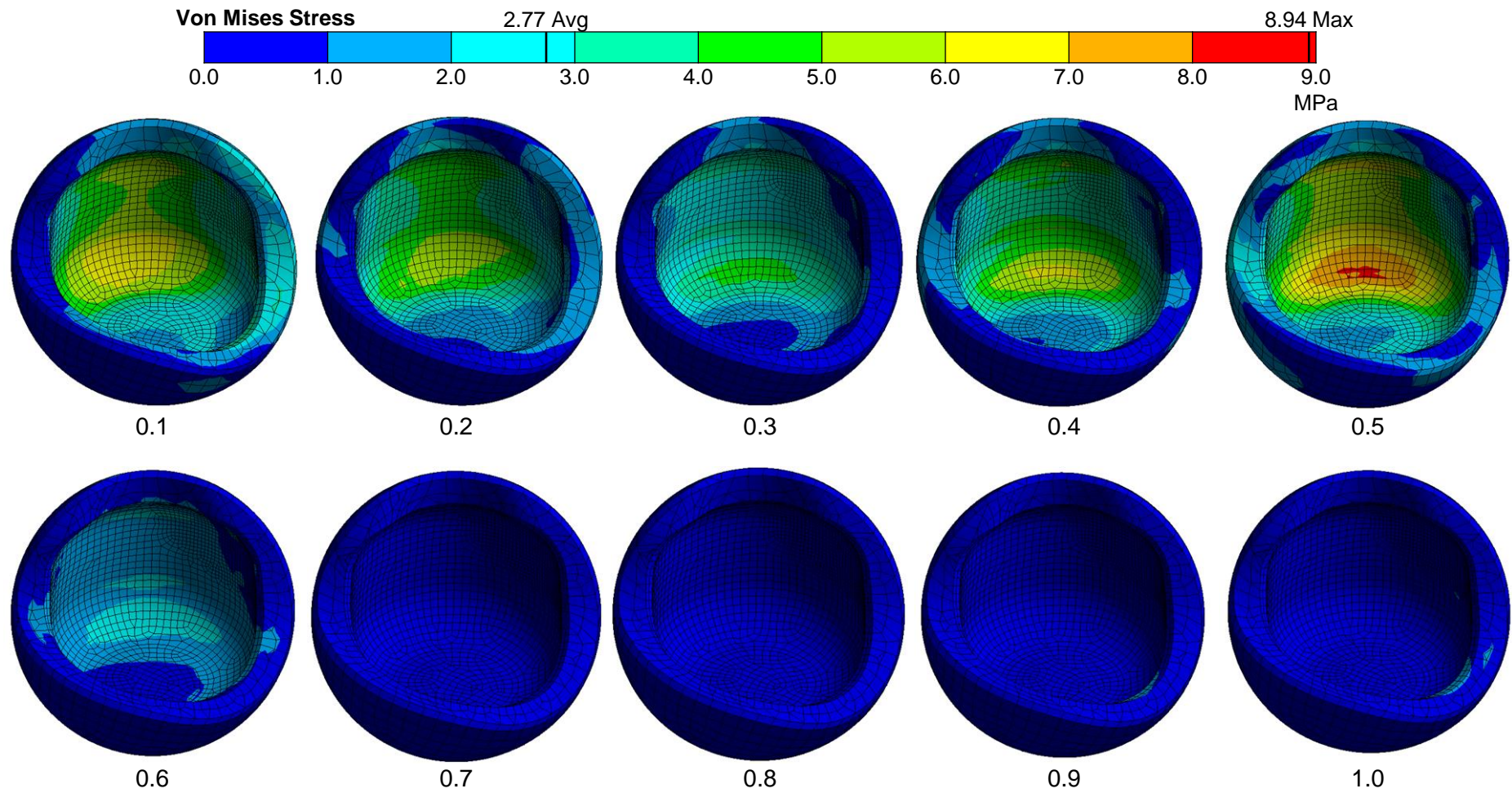


Fig. 5.15: Von Mises stresses on the MaltaHip cup (interior view) during gait cycle at 0.1 s time intervals.

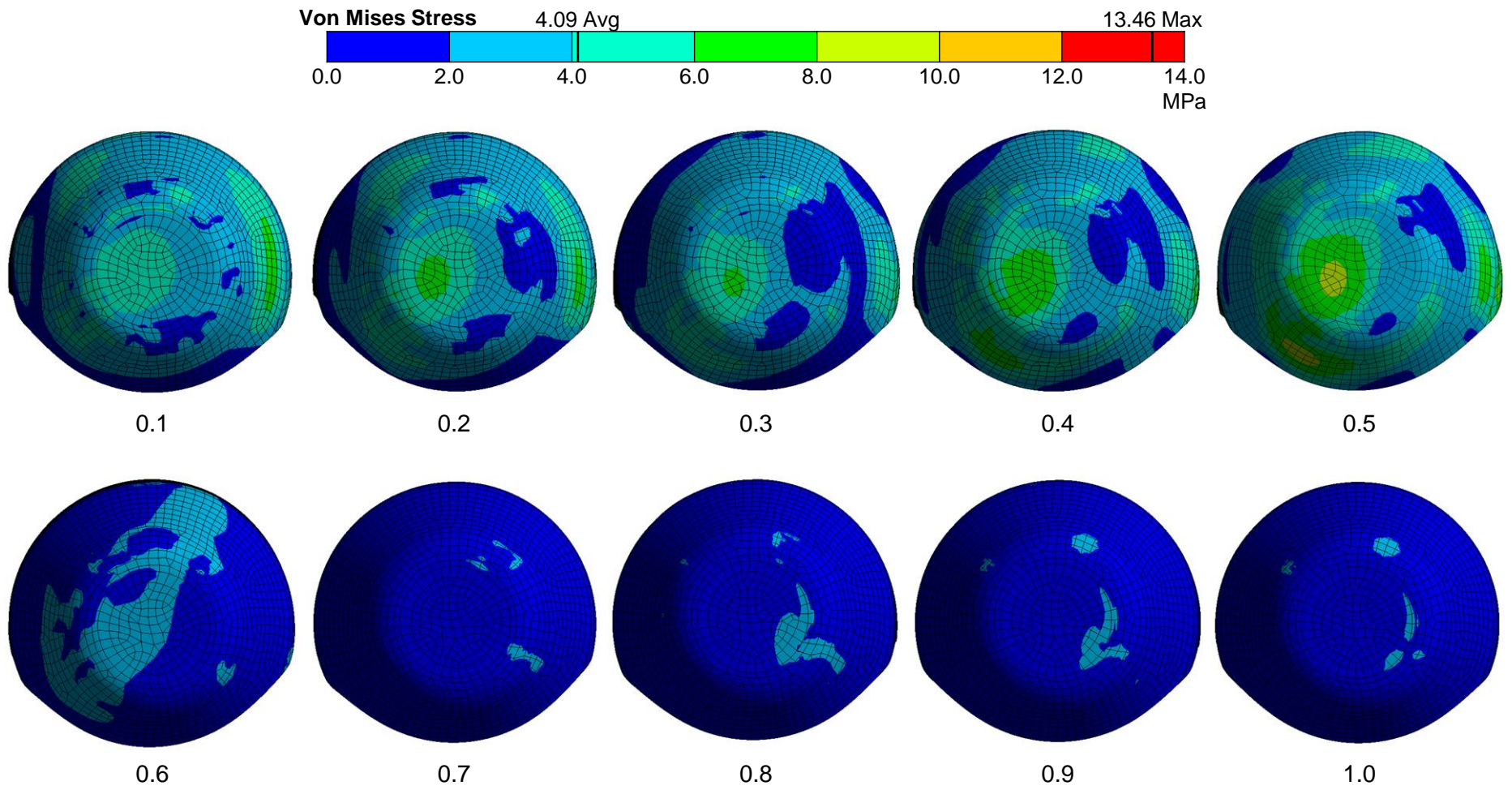


Fig. 5.16: Von Mises stresses on the MaltaHip rotator (superior view) during gait cycle at 0.1 s time intervals.

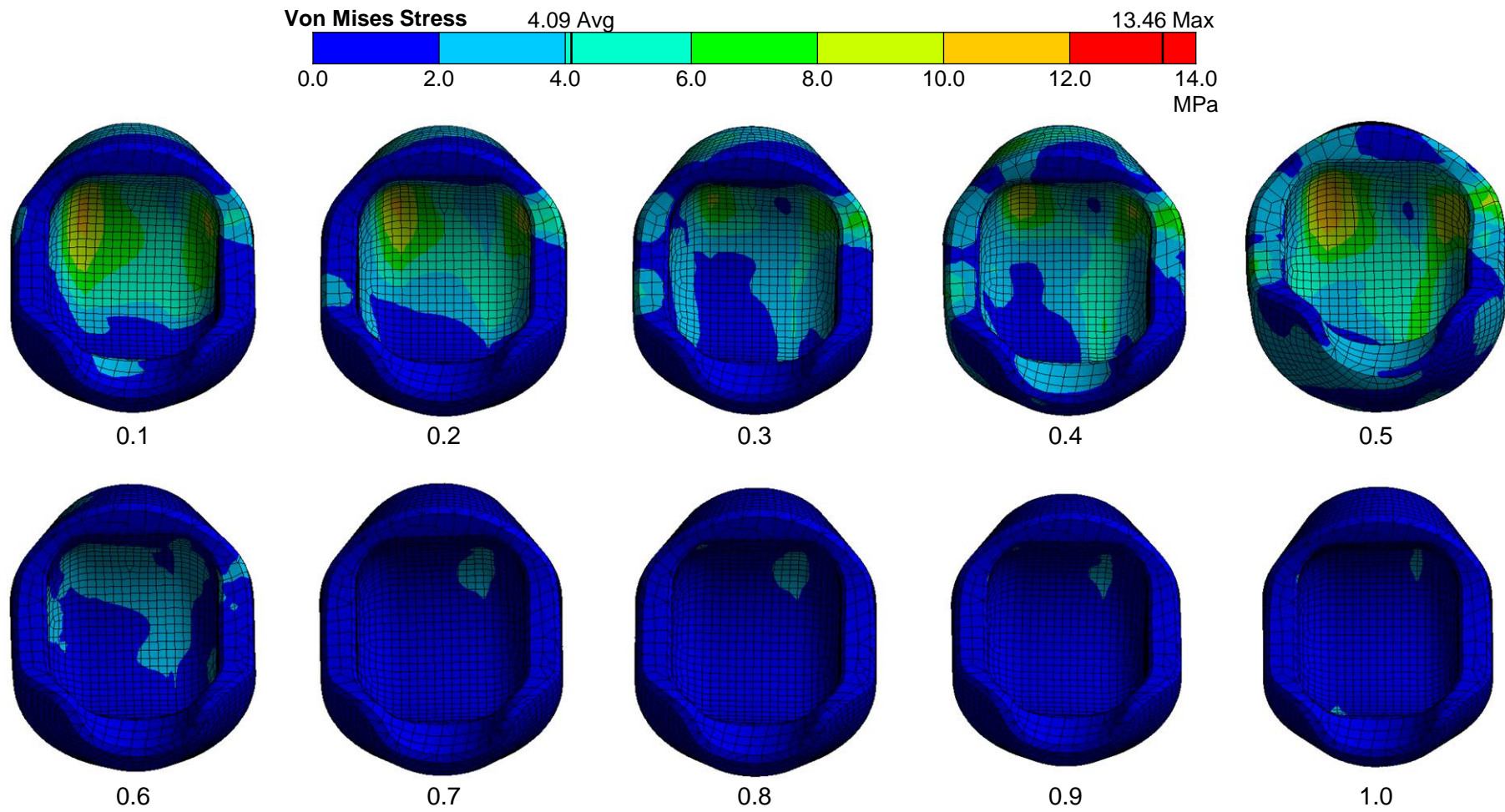


Fig. 5.17: Von Mises stresses on the MaltaHip rotator (medial view) during gait cycle at 0.1 s time intervals.

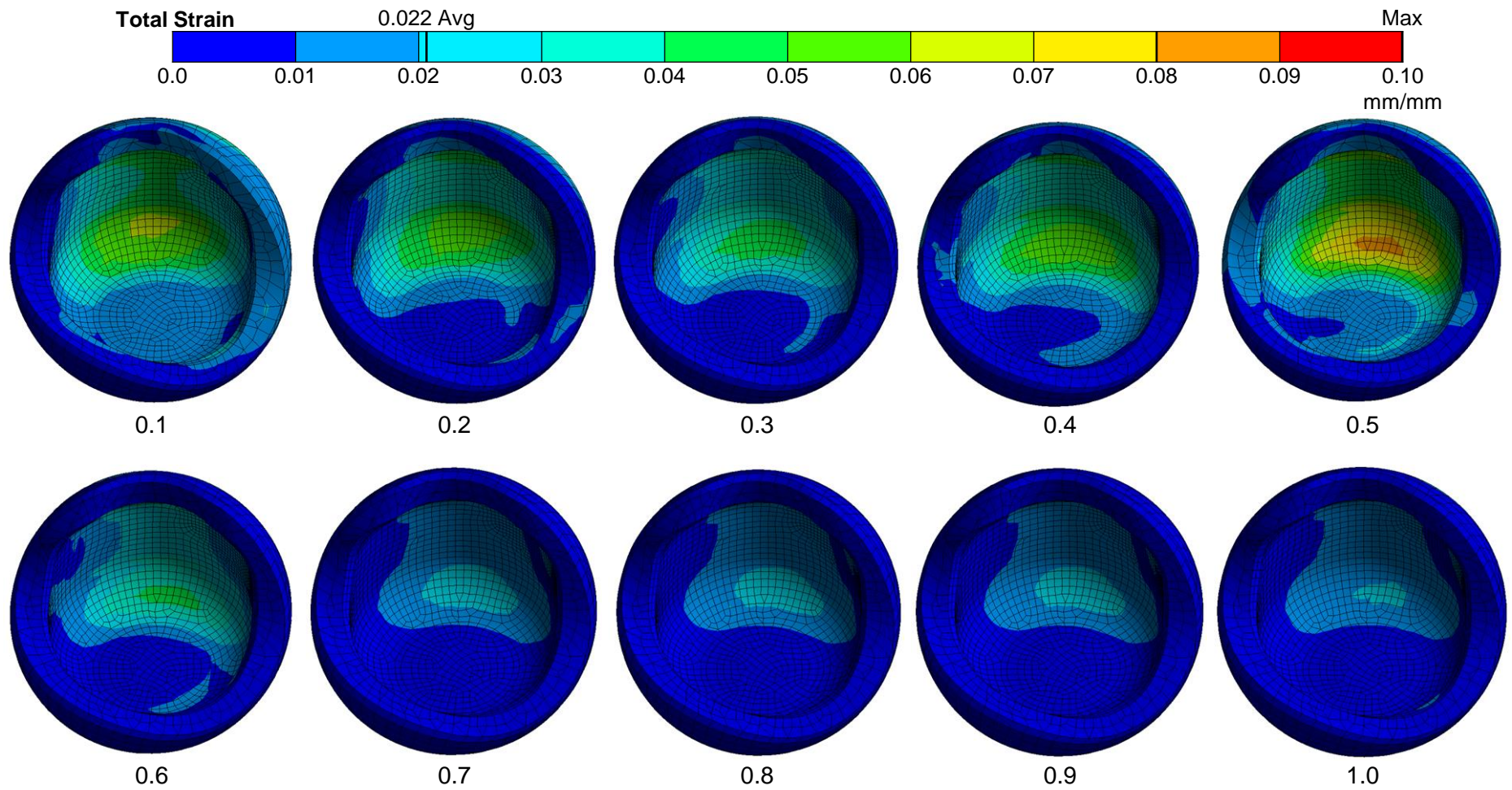


Fig. 5.18: Total strain on the MaltaHip cup during gait cycle at 0.1 s time intervals.

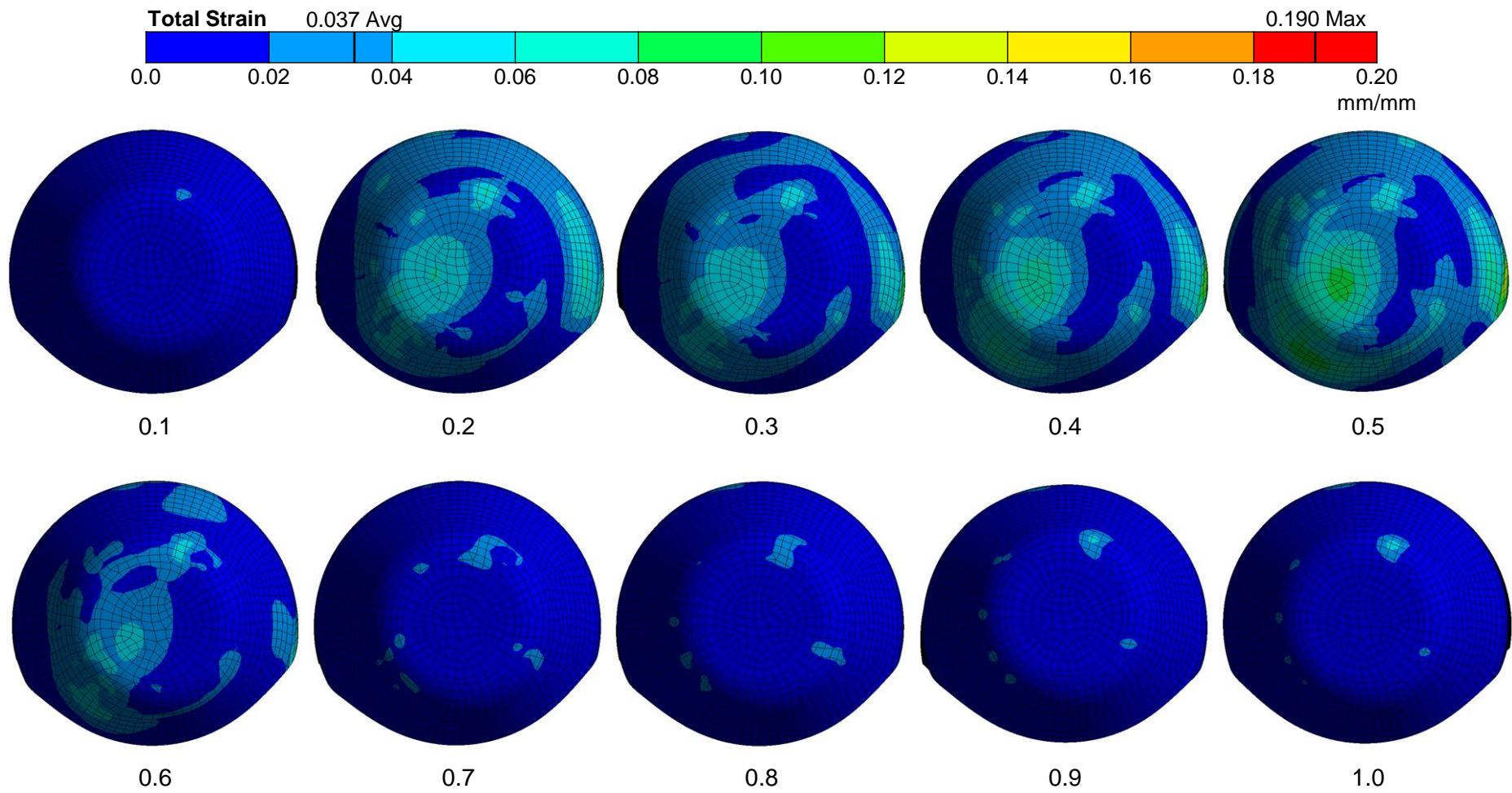


Fig. 5.19: Total strain on the MaltaHip rotator (superior view) during gait cycle at 0.1 s time intervals.

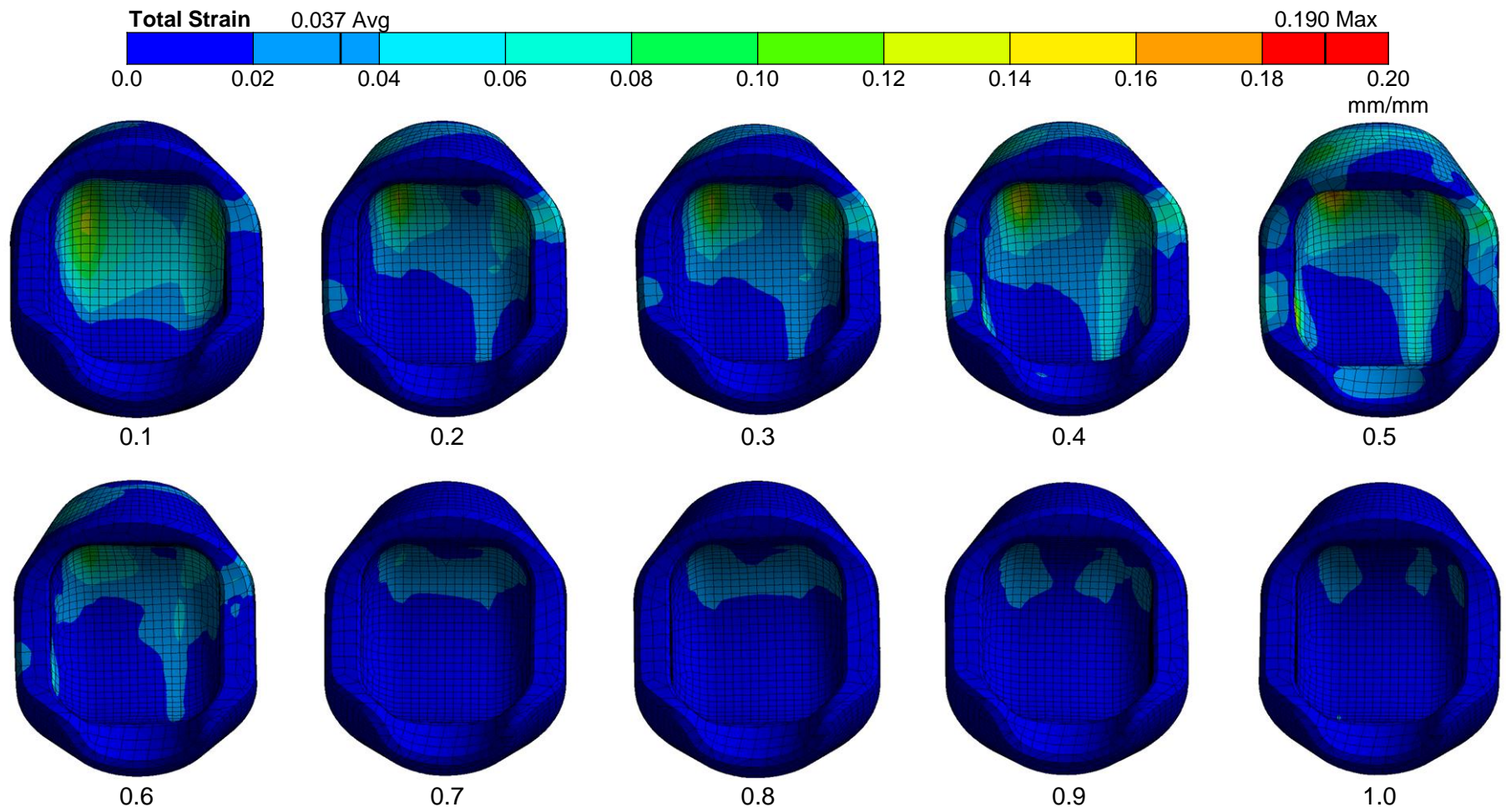


Fig. 5.20: Total strain on the MaltaHip rotator (medial view) during gait cycle at 0.1 s time intervals.

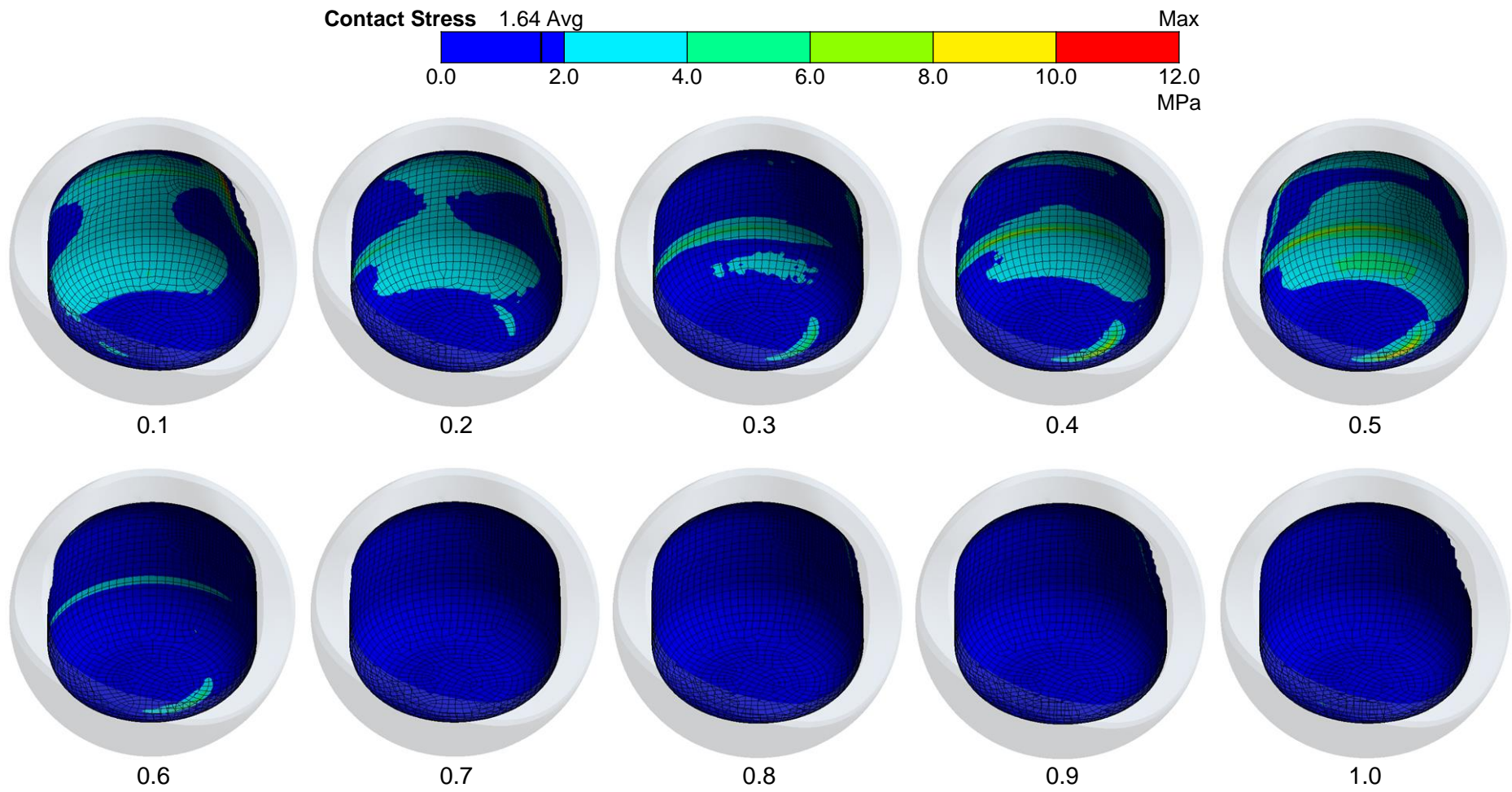


Fig. 5.21: Contact stress on the MaltaHip cup during gait cycle at 0.1 s time intervals.

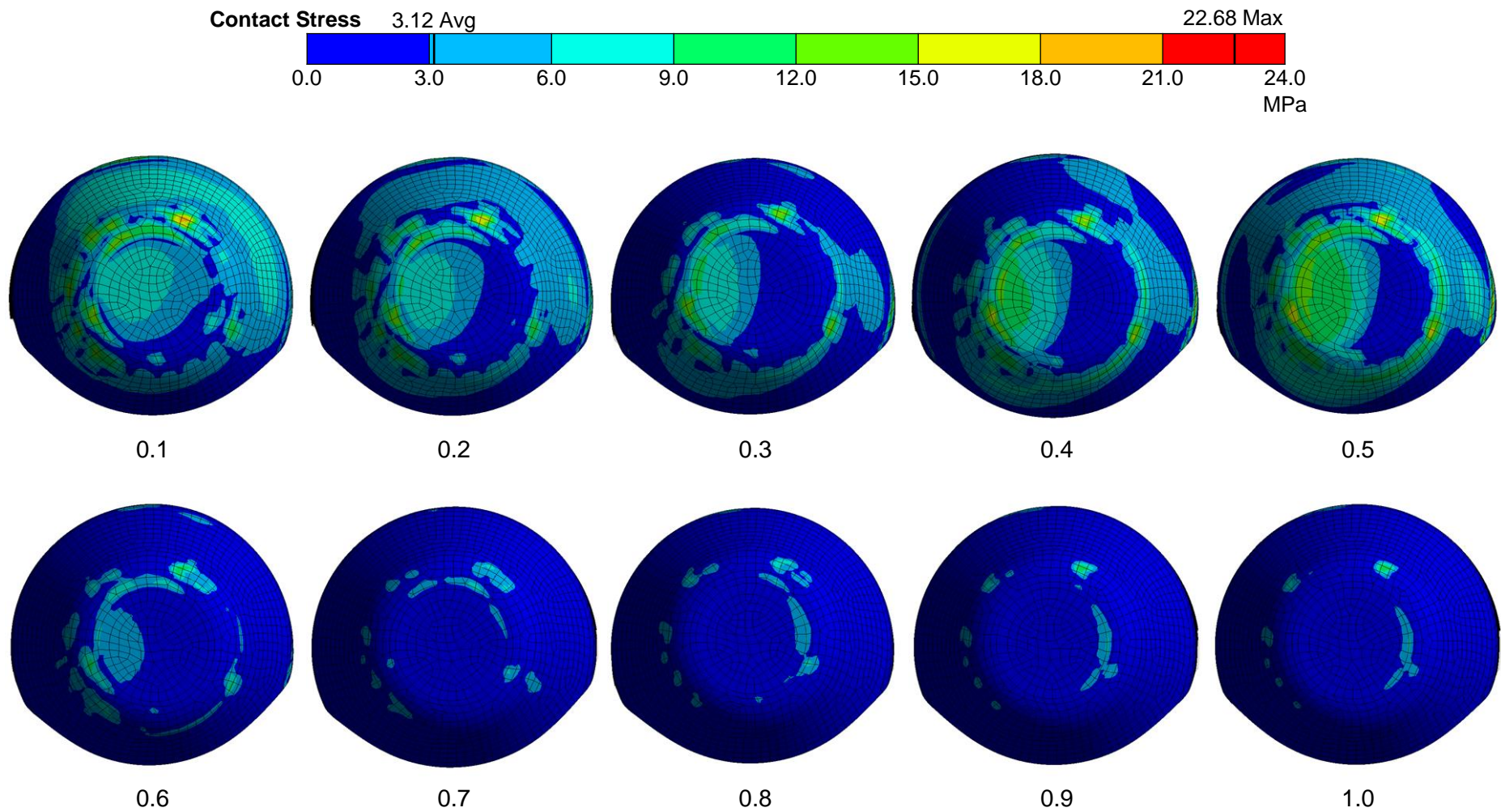


Fig. 5.22: Contact stress on the MaltaHip rotator (superior view) during gait cycle at 0.1 s time intervals.

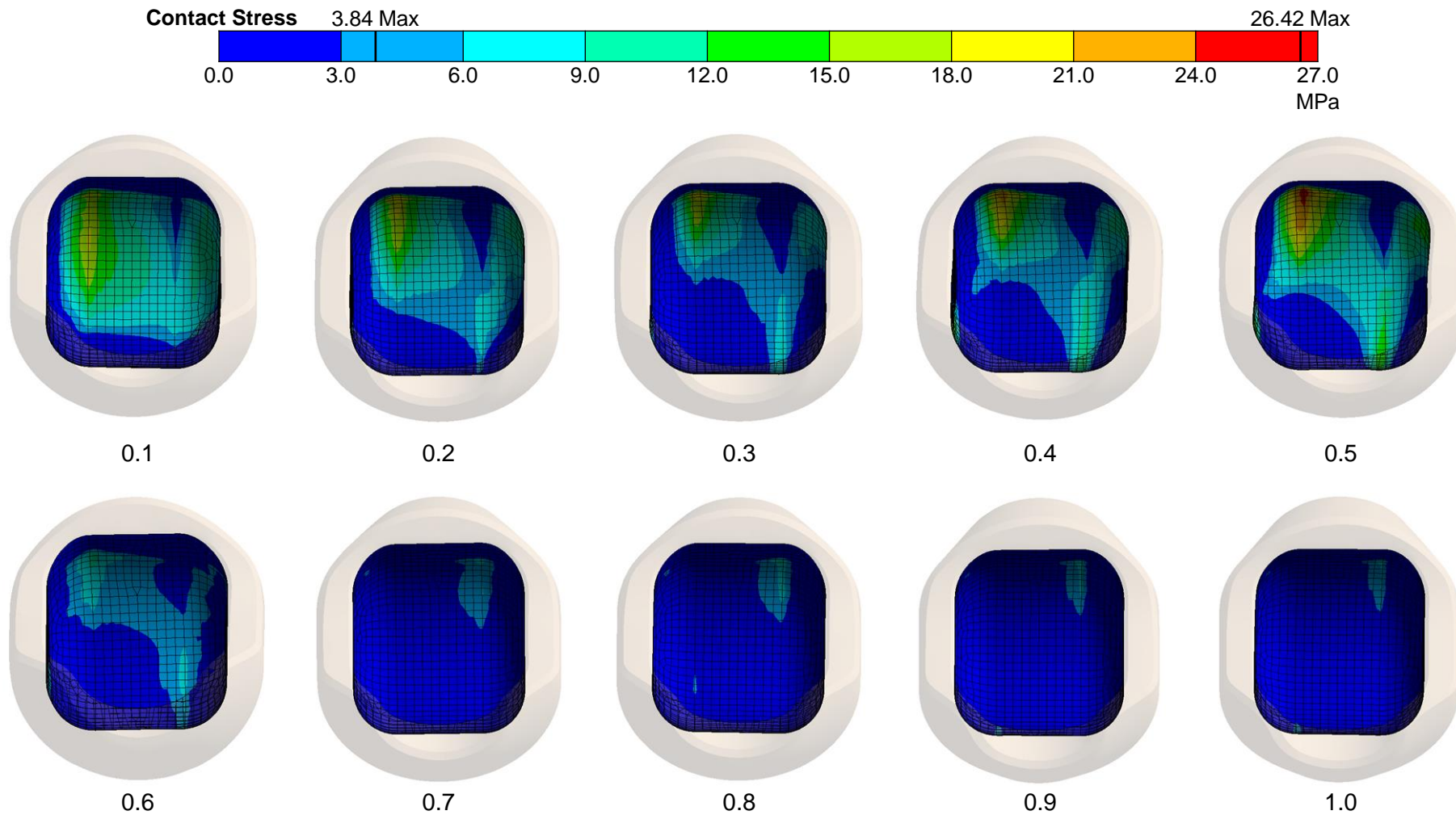


Fig. 5.23: Contact stress on the MaltaHip rotator (medial view) during gait cycle at 0.1 s time intervals.

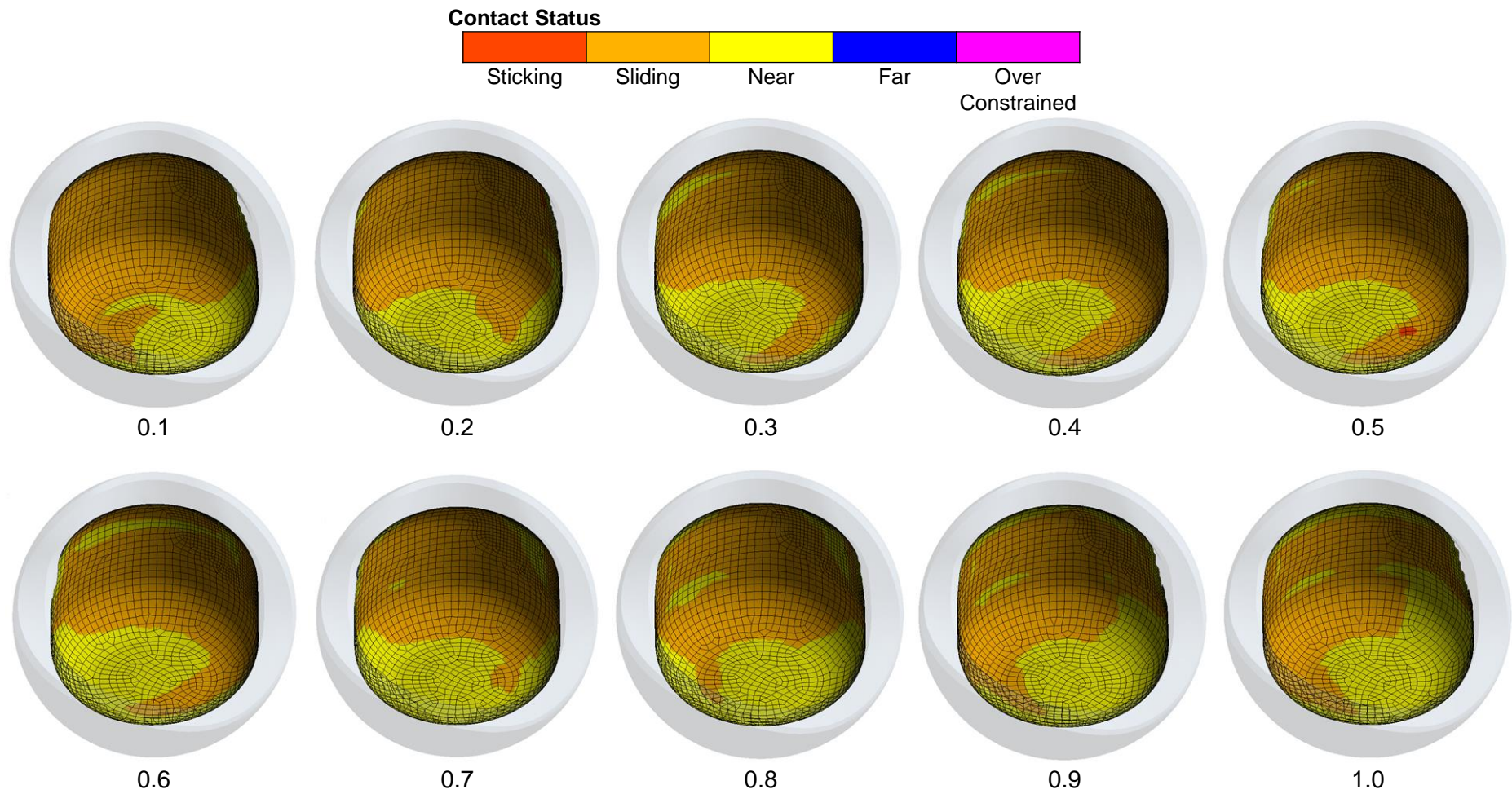


Fig. 5.24: Contact status of the MaltaHip cup (interior view) during gait cycle at 0.1 s time intervals.

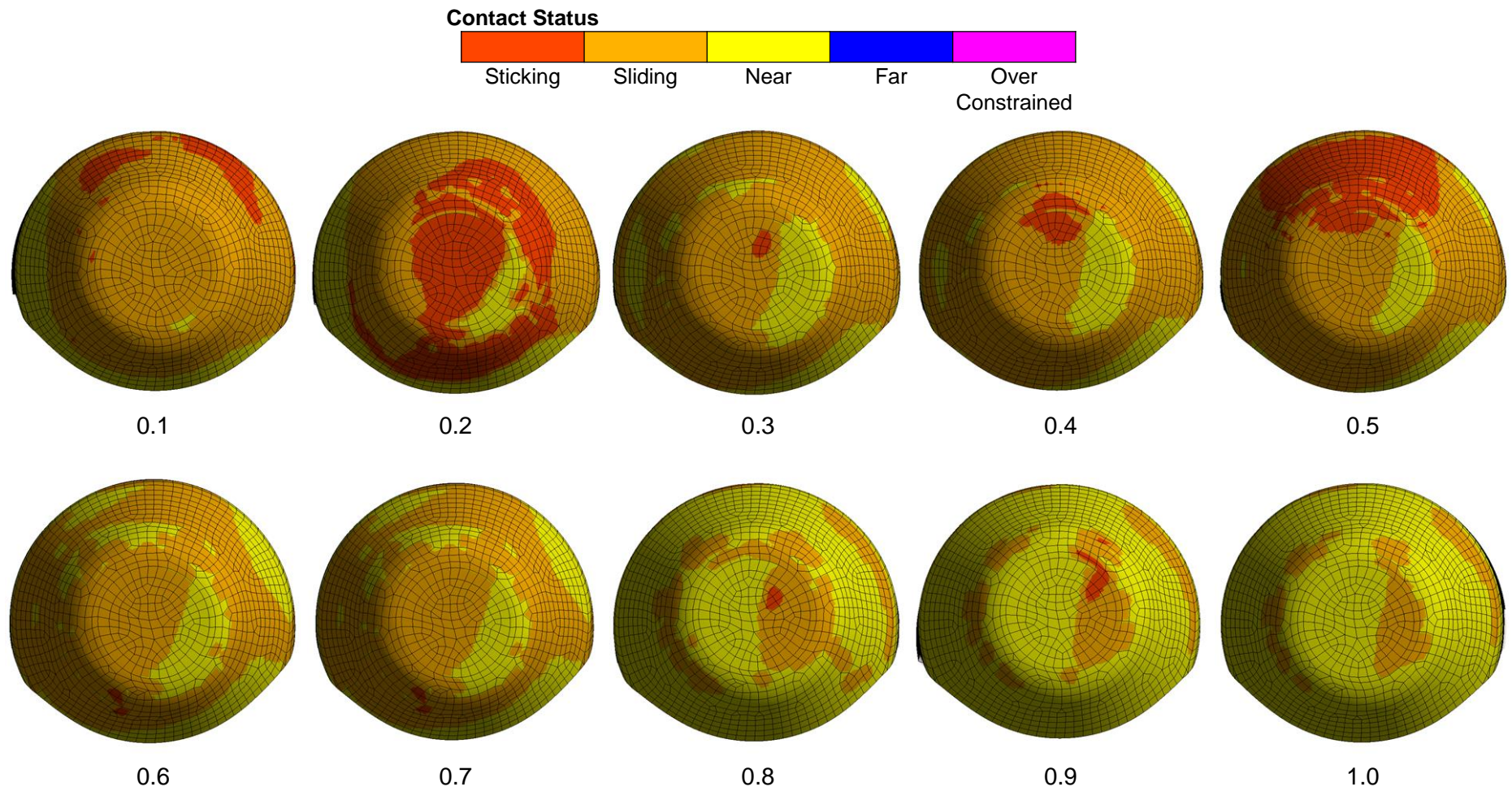


Fig. 5.25: Contact status of the MaltaHip rotator (interior view) during gait cycle at 0.1 s time intervals.

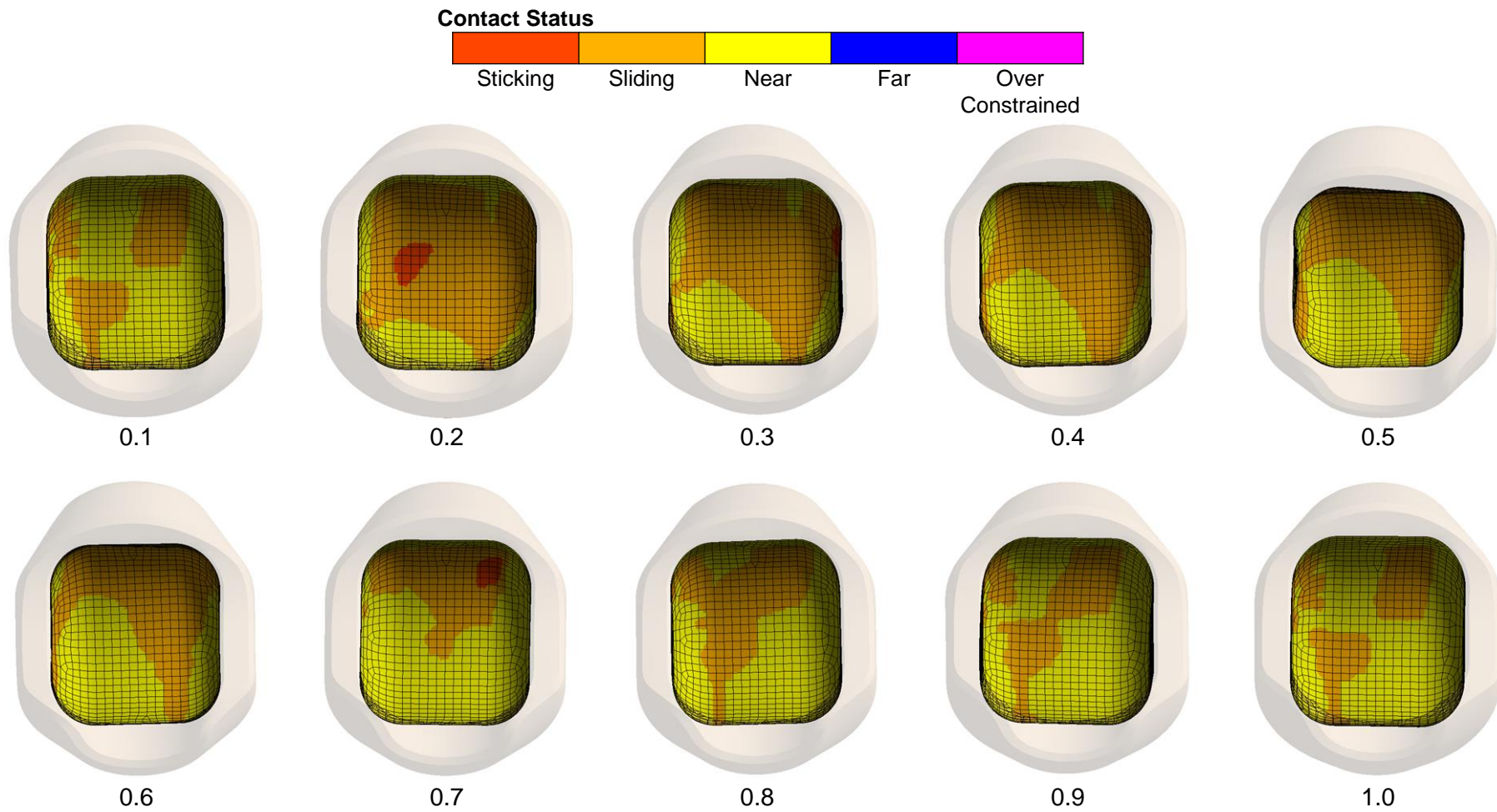


Fig. 5.26: Contact status of the MaltaHip rotator (interior view) during gait cycle at 0.1 s time intervals.

The von Mises stress values of the metallic flexor have been computed, with views of the external and internal surfaces being shown in Fig. 5.27 and 5.28. The maximum von Mises stress value of 121.3 MPa is highly localised and is exhibited at the superior surface which articulates against the MaltaHip cup. It can be observed that the remainder of the stresses are well distributed on both surfaces. The strain values of the flexor component are not presented in this work due to the drastically low range of values that were attained (in fact, the maximum strain that was produced during the gait cycle was 0.7×10^{-3}). These results demonstrate the suitability of utilizing relatively thin design features in the high-N austenitic stainless steel components (some sections being 0.5 mm thin) for the MaltaHip implant. The finite element results of the metallic abductor have not been presented in this work due to low range of stress values that were exhibited (maximum von Mises stress value was equal to 12.94 MPa).

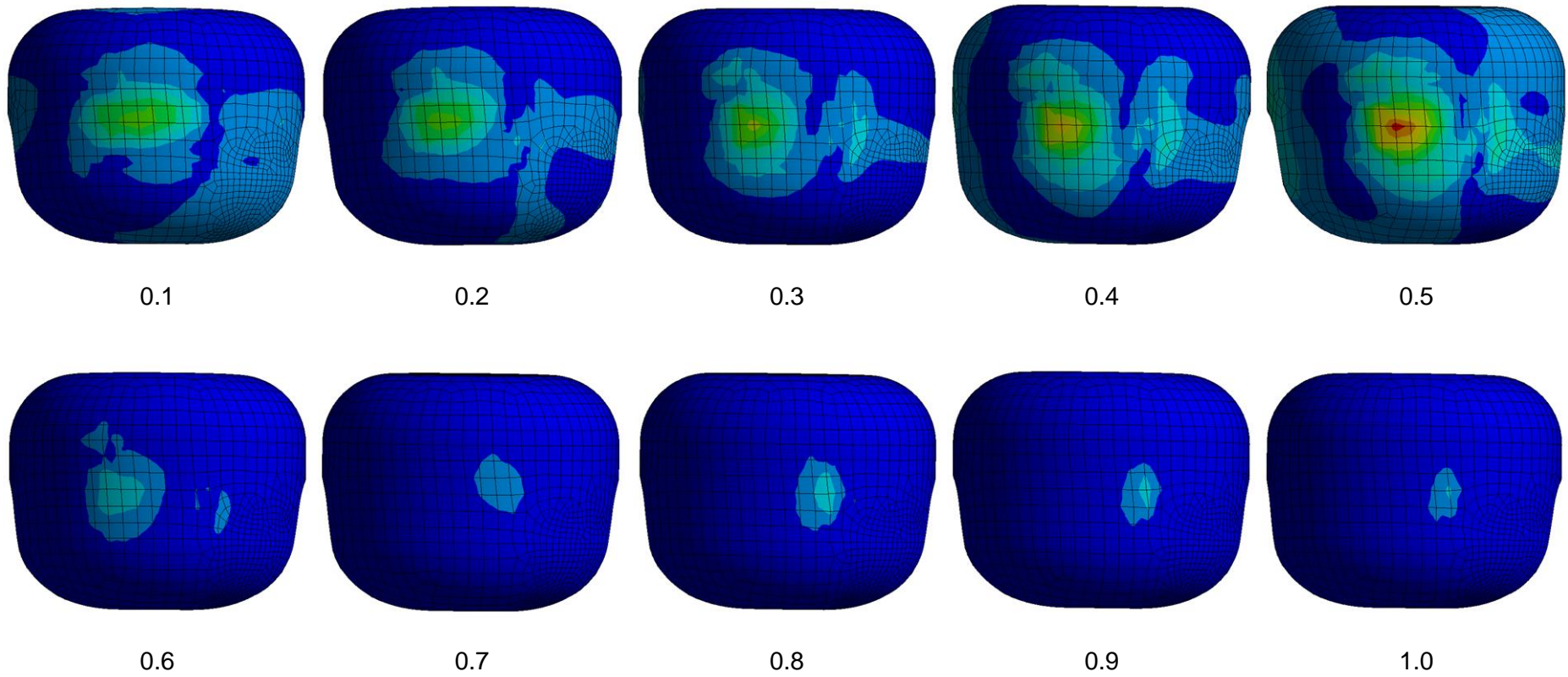
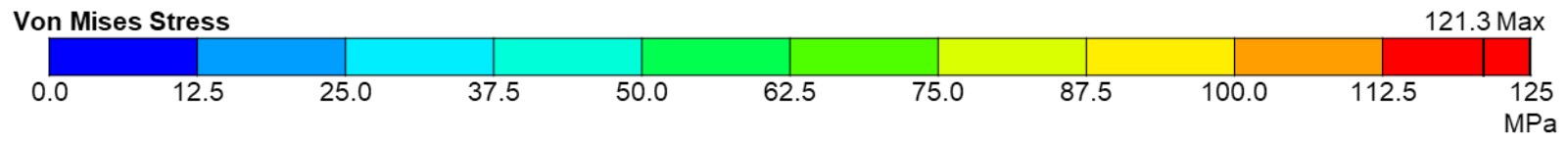


Fig. 5.27: Von Mises stresses on the MaltaHip flexor (superior view) during gait cycle at 0.1 s time intervals.

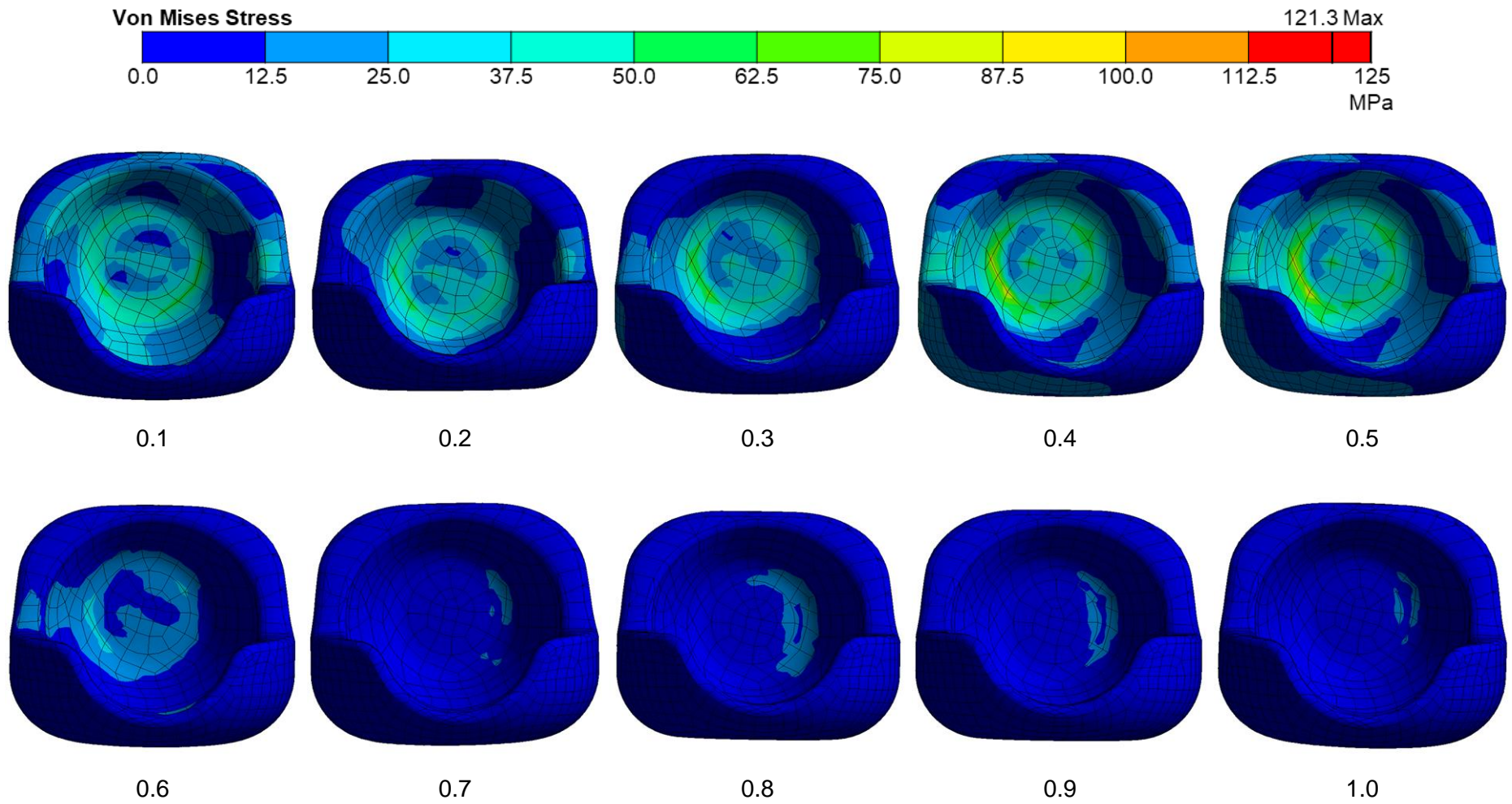


Fig. 5.28: Von Mises stresses on the MaltaHip flexor (inferior view) during gait cycle at 0.1 s time intervals.

5.4. Sliding Track Properties

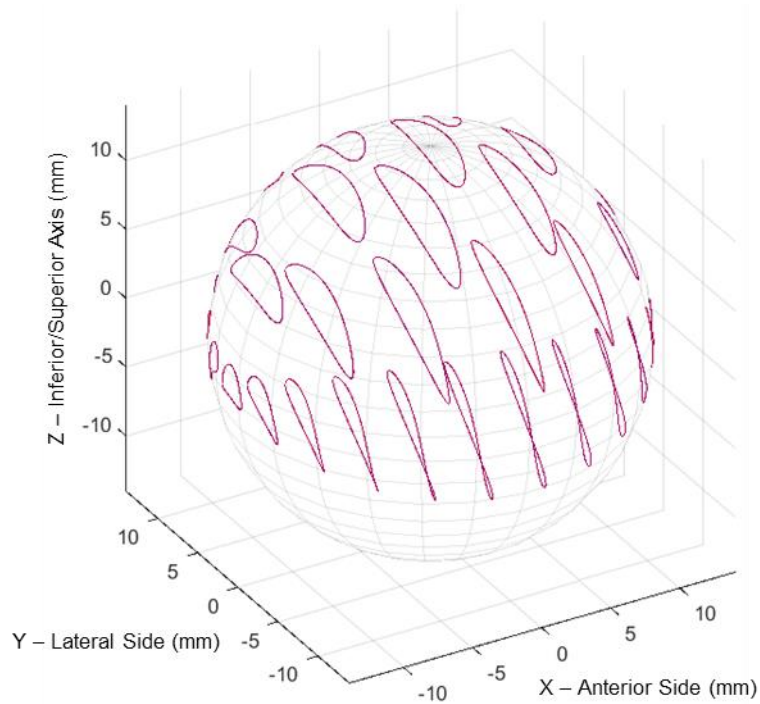
5.4.1. Cross-shear Ratio (CSR)

In order to predict the wear volume produced by the different implant designs (ball-and-socket and MaltaHip), it was necessary to first generate the slide tracks produced by each articulation, and compute their extent of misalignment relative to the principal molecular orientation. The misalignment of the slide tracks is quantitatively represented by the cross-shear ratio (CSR) parameter. All computations of the slide tracks that are presented in this work are based on the standardized gait cycle specified in ISO 14242-1:2014/Amd 1:2018.

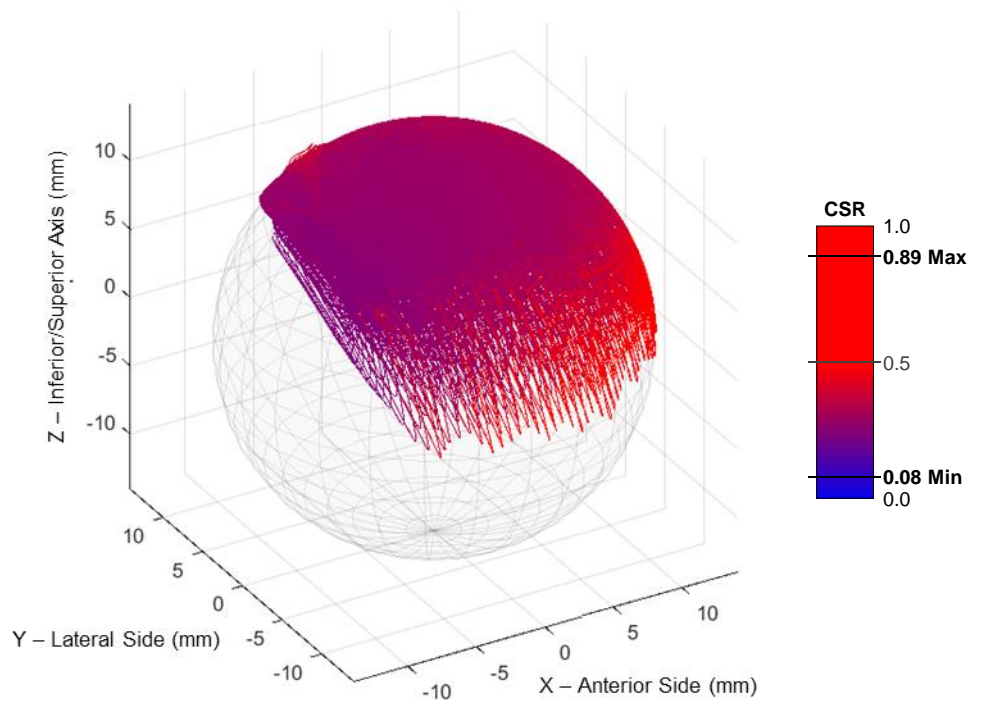
The slide track of the conventional ball-and-socket implant based on a single gait cycle are shown in Fig. 5.29 (anterolateral view) and in Fig. 5.30 (anteromedial view). Slide tracks of equally-spaced nodes are shown in Fig. 5.29a and Fig. 5.30a, which are intended to clearly illustrate the different trajectories that are generated on the articular surface. The slide tracks of all the contacting nodes from the finite element model (3441 in total), are shown in Fig. 5.29b and Fig. 5.30b.

Most of the slide track patterns resemble a teardrop shape, with their aspect ratio being increased as they approach the equator of the femoral head. A small number of slide track patterns with high aspect ratios resemble a figure-of-eight. The slide tracks have been colour-coded according to their CSR value. In general, the CSR of the slide tracks have been observed to vary between 0.08 and 0.89, although only a few slide tracks produced CSR values higher than 0.60. The mean CSR value of all slide tracks is equal to 0.29. It can be observed that the slide track patterns with the low CSR values are located towards the pole of the cup, whereas those with higher CSR values are located towards the equator, as indicated by their red appearance.

The variation of the average CSR value of the whole prosthesis during the gait cycle is shown in Fig. 5.31b. It can be observed that the highest CSR values are achieved at the start, end, and halfway through gait cycle. The lowest CSR value (0.08) is obtained only momentarily at 22% of the gait cycle. During the stance phase (between 0 – 60%), which exhibits the highest loads, the average CSR value is 0.33, and is likely to contribute to the high wear rates of the ball-and-socket implant. Although low CSR values are obtained during the majority of the swing phase (between 60 – 90%) this is hardly effective in minimizing the wear rate since the loads are very low (300 N) at this phase.

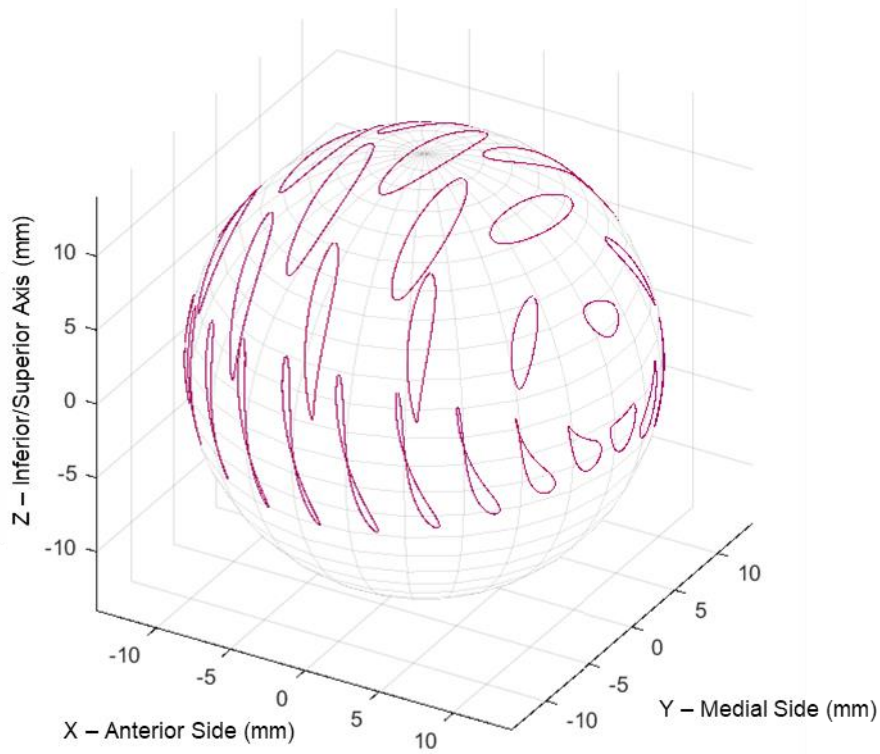


(a) Slide tracks of selected nodes, shown from an anterolateral view, intended to illustrate the changing trajectory patterns over the surface area of the hemispherical cup.

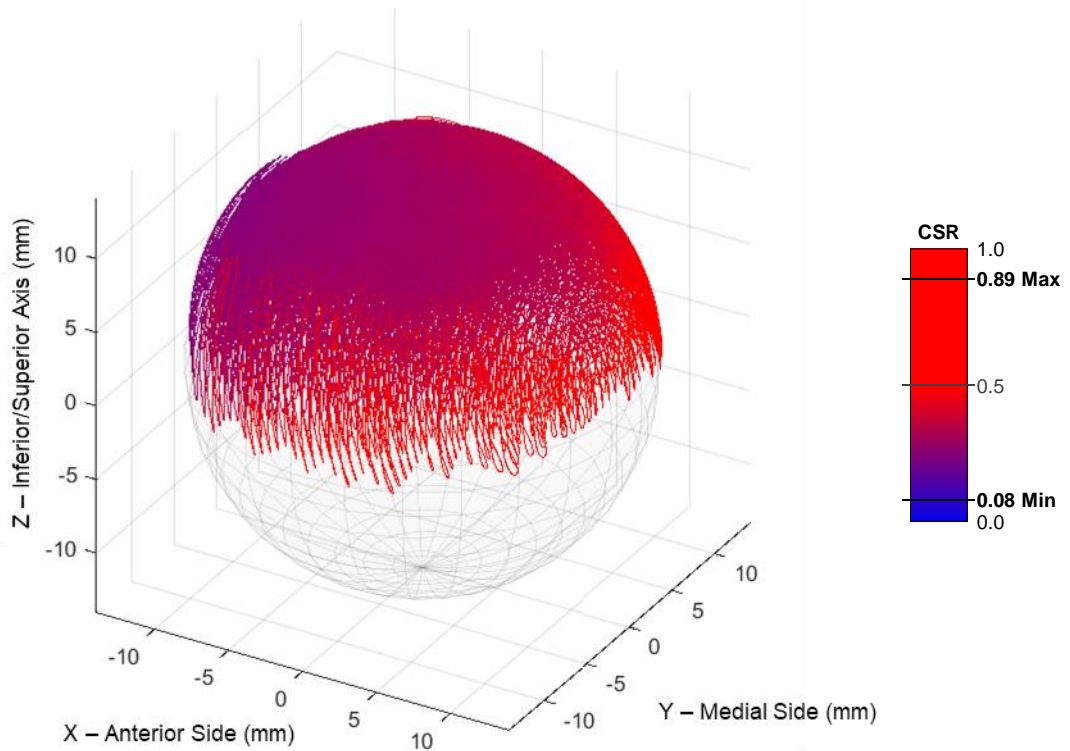


(b) Slide tracks of all contacting nodes, shown from an anterolateral view (the shaded region is due to the high number of superimposing slide-tracks). A colour-map is used to illustrate the cross-shear values of the individual slide tracks.

Fig. 5.29: Anterolateral view: Typical slide tracks of a ball-and-socket implant resulting in cross-shear ratio values ranging between 0.08 and 0.89.



(a) Slide tracks of selected nodes, shown from an anteromedial view, intended to illustrate the changing trajectory patterns over the surface area of the hemispherical cup.



(b) Slide tracks of all contacting nodes, shown from an anteromedial view (the shaded region is due to the high number of superimposing slide-tracks). A colour-map is used to illustrate the cross-shear values of the individual slide tracks.

Fig. 5.30: Anteromedial view: Typical slide tracks of a ball-and-socket implant resulting in cross-shear ratio values ranging between 0.08 and 0.89.

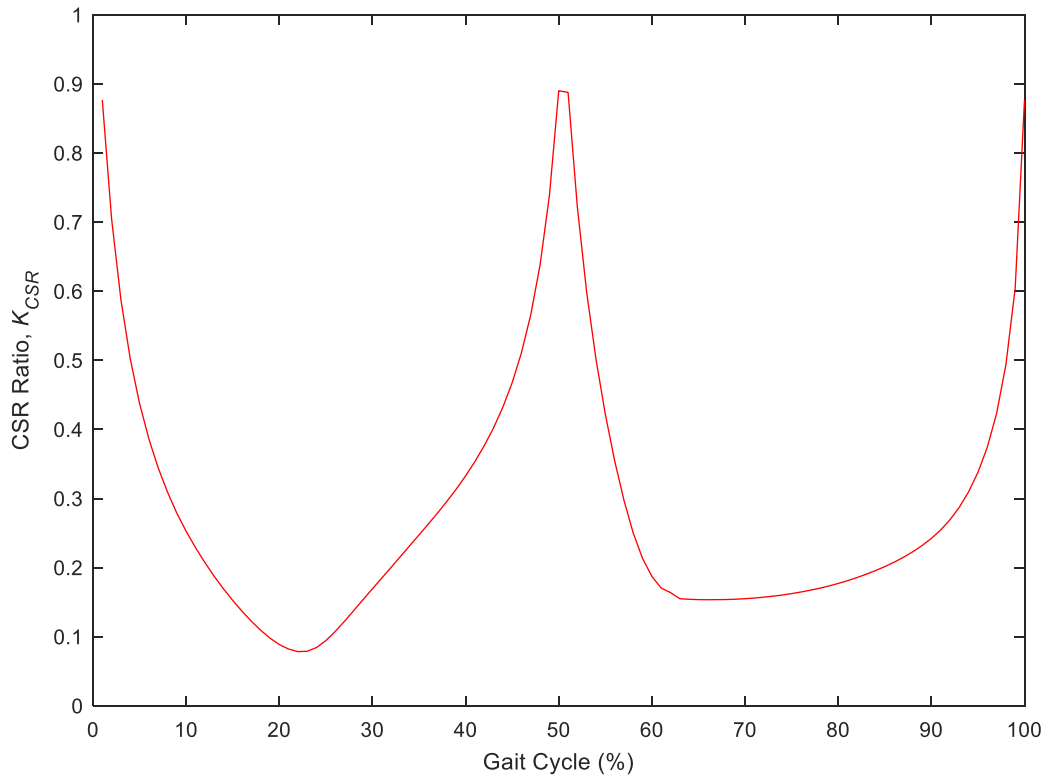


Fig. 5.31: Variation of the CSR values of slide tracks during the gait cycle.

The slide tracks of the contacting nodes of the MaltaHip components that would be projected on the polymeric components are shown in Fig. 5.32. Each articulation of the MaltaHip exhibits a CSR value of 0, due to its design which inherently constrains all rotational motions to occur about the longitudinal axis of the respective components. The articulation effectively maximizes the orientation hardening of the surface polymer chains. The trajectory of the produced slide tracks can be described by a planar (2D) curvilinear (circular) shape whose centre of rotation coincides with the axis of rotation of the components.

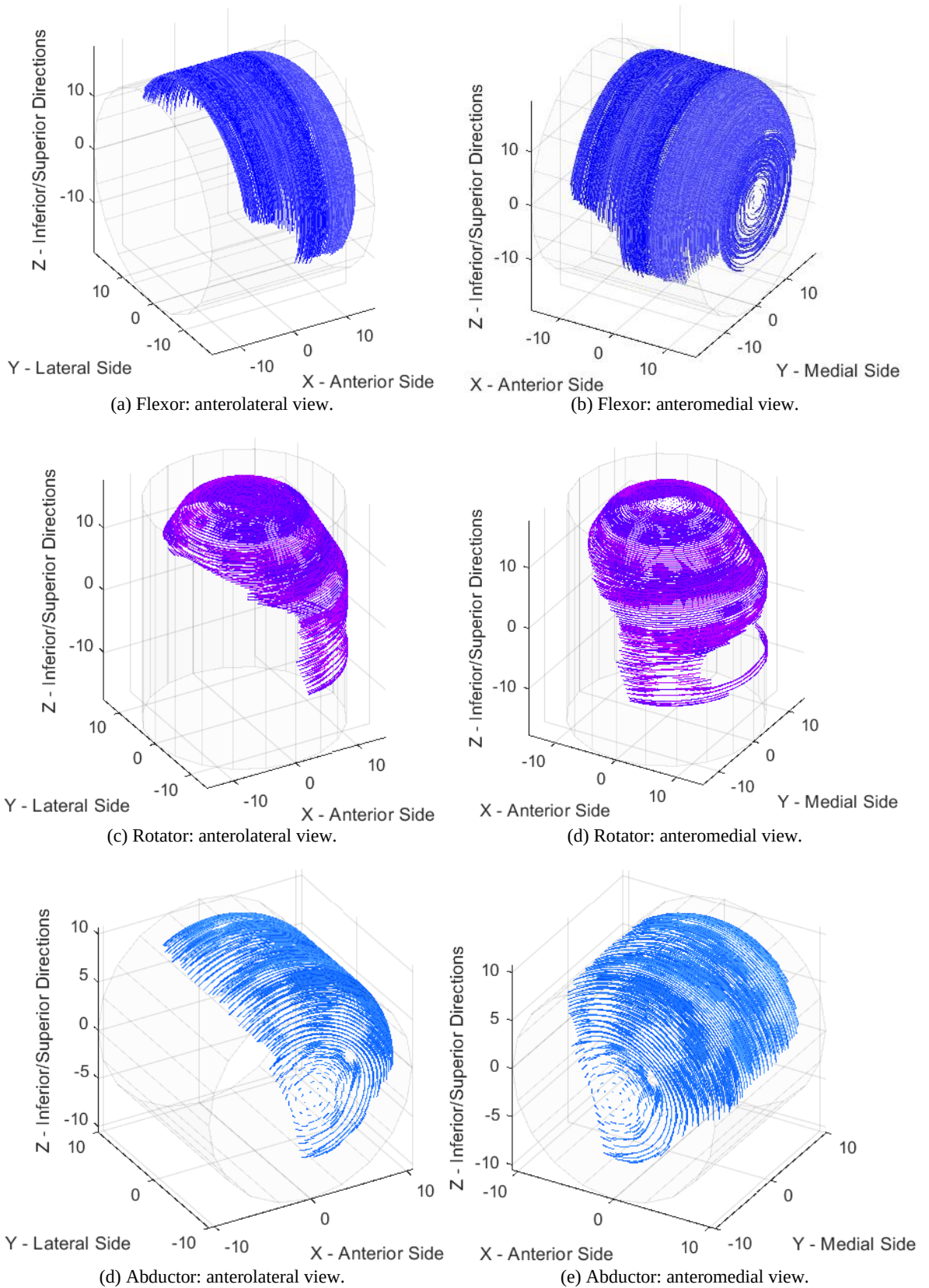


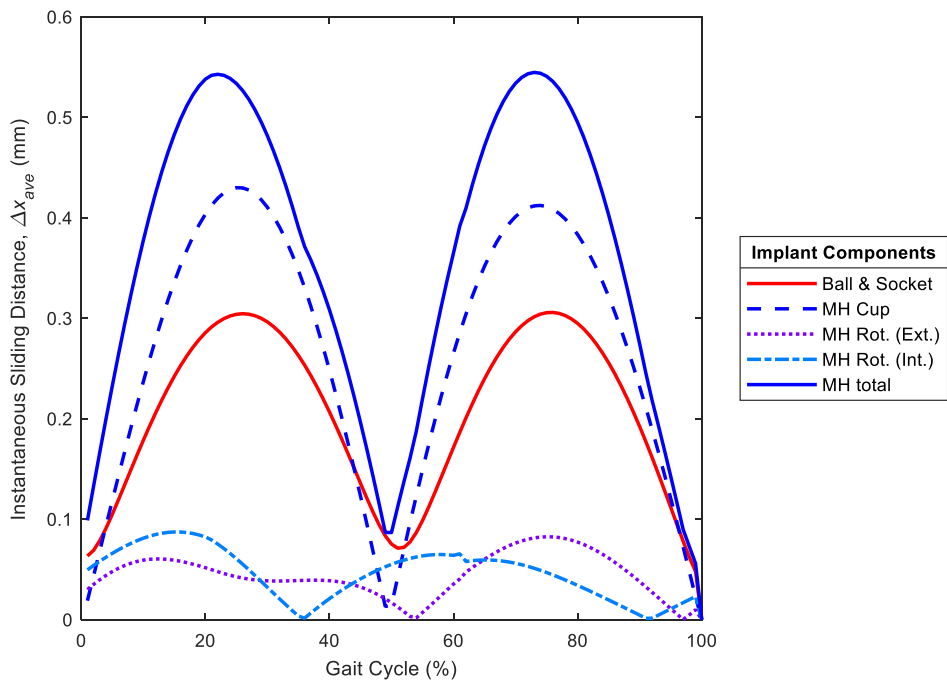
Fig. 5.32: Slide tracks of the MaltaHip components. All components possess a cross-shear ratio of 0. The different colouring schemes are only used to distinguish between the different components of the MaltaHip. Note that all axes are in mm.

5.4.2. Sliding Distance

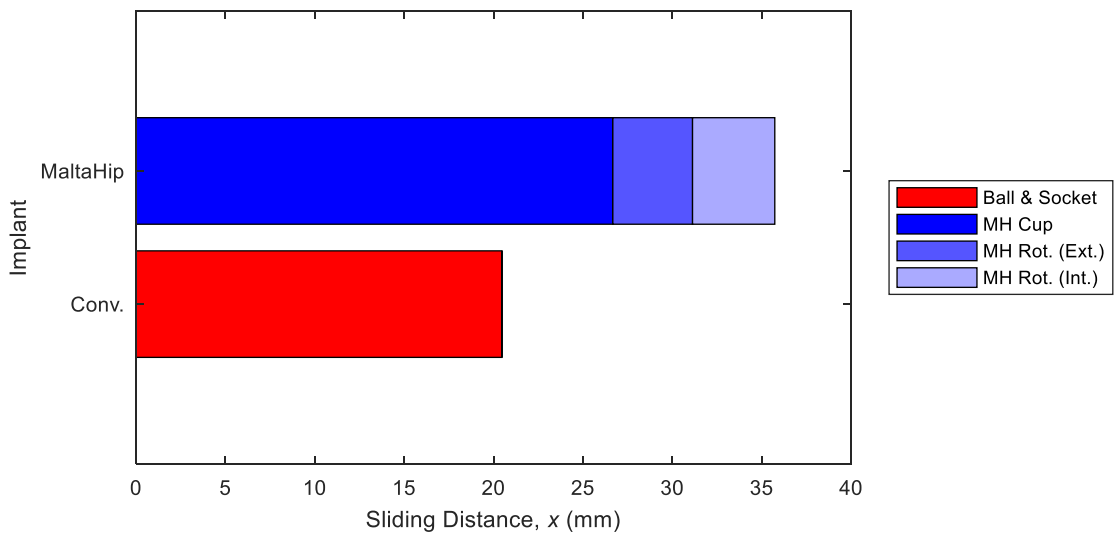
The sliding distance⁵⁴ that is generated during the gait cycle has been calculated for both the ball-and-socket and the MaltaHip implants. More specifically, the mean distance produced by all the nodes at every time step of 0.01 s has been calculated, which is referred to as the instantaneous sliding distance (i.e. sliding distance covered at 0.01 s), as shown in Fig. 5.33a. It can be observed that the MaltaHip produces nearly twice the distance that is produced by the ball-and-socket implant at every time step. It is interesting to note that the profiles of the instantaneous sliding distance possess similar shapes (i.e. two valleys and two peaks), despite the implants having completely different kinematic structures. The similarity between the two profiles is attributed to the cup-flexor articulation being intentionally designed to be aligned to the anatomical flexion/extension axis. As a result, the rotator and abductor components require very short sliding distances to reproduce the multi-directional motion of the gait cycle, as evident by their low distance profiles, as shown in Fig. 5.33a.

The total sliding distances of the ball-and-socket and MaltaHip implants produced in a gait cycle are shown in Fig. 5.33b. The total sliding distance of each implant was calculated by considering the mean sliding distance of all the contacting nodes. These values are equivalent to the areas under the plots shown in Fig. 5.33a. The average sliding distance of the ball-and-socket articulation over a complete gait cycle resulted to be 20.5 mm. In comparison, the average distances of the cup-flexor, flexor-rotator, and rotator-abductor articulations are 26.7, 4.5, and 4.6 mm, respectively, resulting in a combined sliding distance of 35.8 mm, which is 75% greater than that of the conventional ball-and-socket design. In fact, the cup-flexor articulation of the MaltaHip, was designed with a large contacting area to reduce the contact stresses of the articulation to minimize the amount of wear debris it generates due to its long sliding distance. On the other hand, the flexor-rotator and rotator-abductor, which possesses smaller contacting areas were aligned in such a way to produce short sliding distances to minimize the wear debris generation.

⁵⁴ The sliding distance represents the relative distance that is travelled between the two articulating surfaces (i.e. polymer and metallic surface). Therefore, the distance shown for the polymer also represents the distance for the metallic component, but in opposite direction.



(a) Comparison of the instantaneous sliding distance of the different articulations, calculated by considering the mean sliding distance of all contacting nodes at every time step.



(b) Total sliding distance of the ball-and-socket and MaltaHip implants produced per gait cycle.

Fig. 5.33: Comparison of the sliding distances of the ball-and-socket and MaltaHip implants.

5.4.3. Contact Area

The resultant contact areas of the ball-and-socket and the MaltaHip components as computed from the finite element model are shown in Fig. 5.34. The contact area of the hemispherical cup (28 mm femoral head diameter) resulted to be 505.3 mm². In comparison, the internal cylindrical geometry of the MaltaHip cup resulted in a contact area of 1060.4 mm², being practically twice the size of the contact area of the hemispherical cup. The external and internal contacting areas of the rotator are equal to 815.8 and 377.8 mm², respectively. The relatively large contacting area of the external surface of the rotator is mainly attributed to the flat surface (located normal to the longitudinal axis of rotation), and the tapered section. The contacting area of the rotator internal surface resulted to be smaller than that produced by the ball-and-socket design. Nonetheless, considering the small diameter size of the cylinder (21 mm), compared to the diameter of the femoral head (28 mm), the internal surface of the rotator is still able to provide a modest contact patch with a highly conformal design.

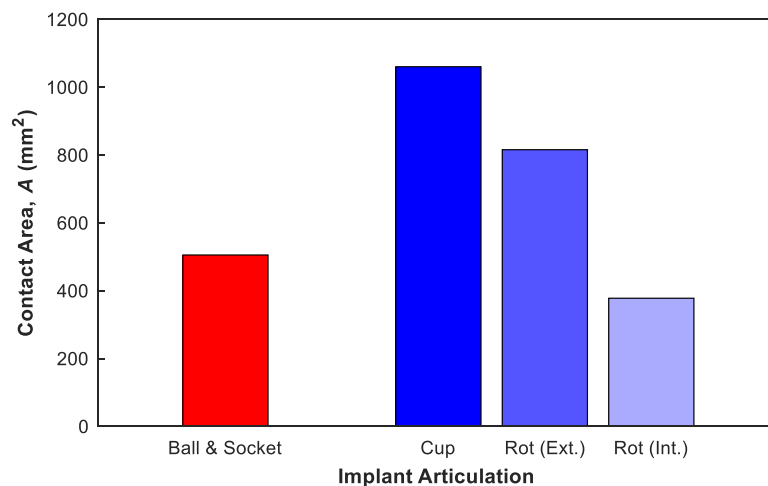


Fig. 5.34: Contacting areas of the articulations of the ball-and-socket and MaltaHip implant designs.

5.5. Wear Model Results

5.5.1. Introduction

The cumulative volumetric wear occurring during one gait cycle, according to the four theoretical wear models (Saikko, Liu, Kang and Petrella) outlined in the literature review (Section 2.6, p. 53), have been computed for the ball-and-socket and MaltaHip implants. The volumetric wear predictions are computed for UHMWPE only, since empirical coefficients (wear factors) were only available for this grade of polymer only. It should be noted that the wear models do not take into account the changing lubricity, temperature effects, uptake of the fluid lubricant and imperfections of the physical components. As physical imperfections are not taken into account

by the FE and wear models, it would not be possible to produce wear rates that correspond to the running-in and steady-state regimes. Furthermore, due to the high computational expense that was involved in simulating the mechanical response of the implants, it was not possible to compute the results for million cycles to simulate years of use. Therefore, for the sake of simplicity, the wear rate over one million cycle was extrapolated from the wear that was generated over the first cycle. The extrapolation of the wear rate over one million cycles is unlikely to be accurate, but rather can be used to provide an indication of the order of magnitude of the wear rate according to the wear model under consideration.

5.5.2. Saikko Model

The wear results over one gait cycle for the two implant designs being investigated in this work according to the Saikko model [18] are shown in Fig. 5.35. Since cross-shear effects are not taken into consideration by the wear model, the wear of the MaltaHip resulted to be double of that produced by the ball-and-socket design. The model is based on the premise that the volumetric wear is proportional to the contact pressure and the sliding distance. The gradient of the curves provides an indication of the rate of wear taking place during a single gait cycle. No sudden peaks in wear were observed from the Saikko model, since the sliding distances at 12% and 50% of the gait cycles (which correspond to the highest loads), produce nearly the shortest sliding distances. According to the Saikko model, wear being produced either due to long sliding distance or high contact pressures at any instant (but not both at the same time). However, it should be noted that slightly higher wear rates were produced during the initial phase of the gait cycle, due to the greater loads being exhibited in the stance phase (0 – 60 % of the gait cycle). By extrapolation, the total volumetric wear rates of the ball-and-socket and the MaltaHip implants over one million cycles are equivalent to 20.1 mm³ and 40.3 mm³, respectively.

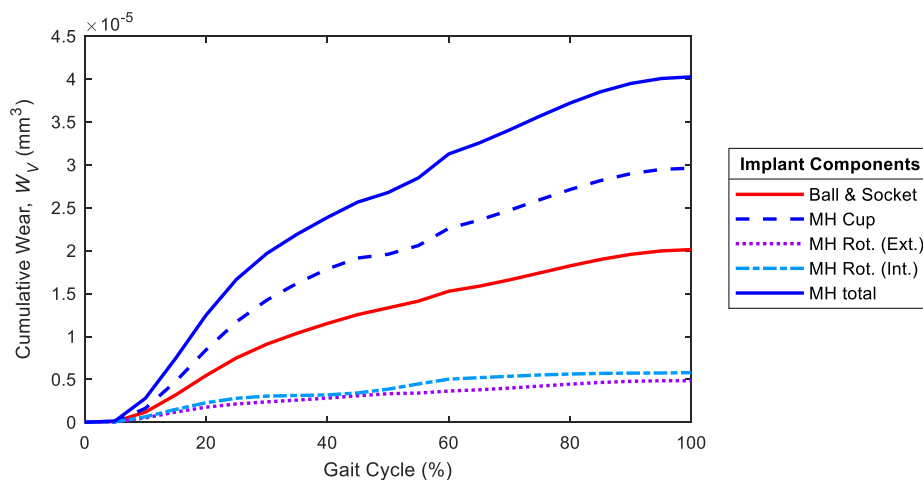


Fig. 5.35: Predicted cumulative wear during a gait cycle for UHMWPE ball-and-socket and MaltaHip implants using the Saikko wear model [18].

5.5.3. Liu Model

The predicted cumulative volumetric wear of the ball-and-socket and the MaltaHip implants according to the Liu model [267] are presented in Fig. 5.36. Since the model considers the cross-shear effects, it can be observed that the volumetric wear of the MaltaHip resulted to be half of that produced by the conventional ball-and-socket design. According to the model, the majority of the wear is attributed the MaltaHip cup, due to its longer sliding distances. On the other hand, the model predicts that wear on the articular surfaces of the rotator is minimal, as can be observed in the plot. The total volumetric wear rates over a million cycles of the ball-and-socket and the MaltaHip implants are 19.7 mm^3 and 10.0 mm^3 , respectively.

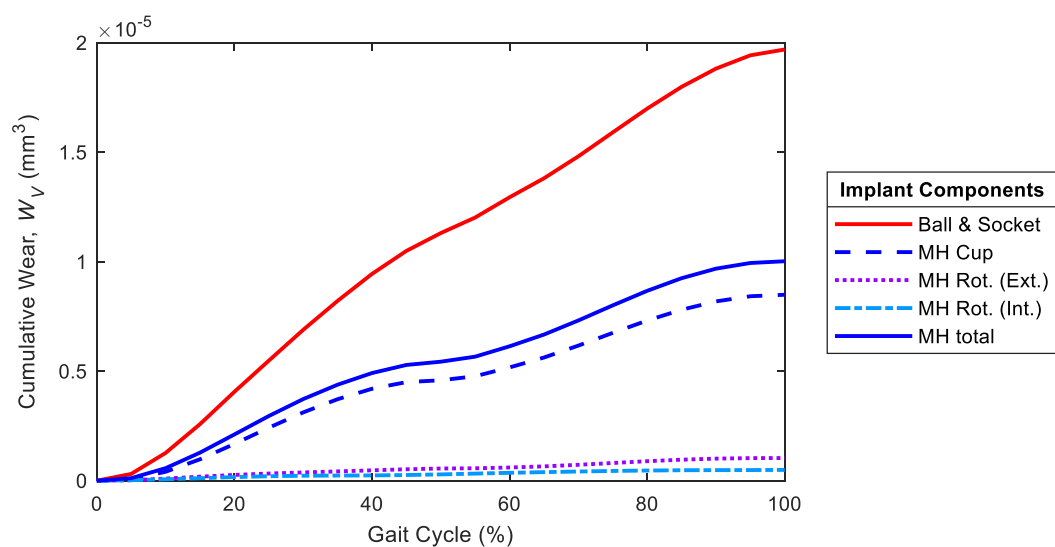


Fig. 5.36: Predicted cumulative wear during a gait cycle for UHMWPE ball-and-socket and MaltaHip implants using the Liu wear model [267].

5.5.4. Kang Model

Similar to the previous cases, the cumulative volumetric wear results during the gait cycle of both implants was calculated based on the wear model proposed by Kang *et al.* [303], as shown in Fig. 5.37. The wear factor utilized in this model was computed as a function of the contact pressure and the cross-shear ratio. The total volumetric wear rates over one million cycles of the ball-and-socket and the MaltaHip design are 21.6 mm^3 and 24.3 mm^3 , respectively. Even though the model accounts for the cross-shear effects, it can be observed that the model predicts that the MaltaHip design would produce slightly higher wear, even though the cross-shear effects are absent in such design. It has been observed that the model overestimates the wear factor for very low values of CSR, as can be observed in Fig. 5.38.

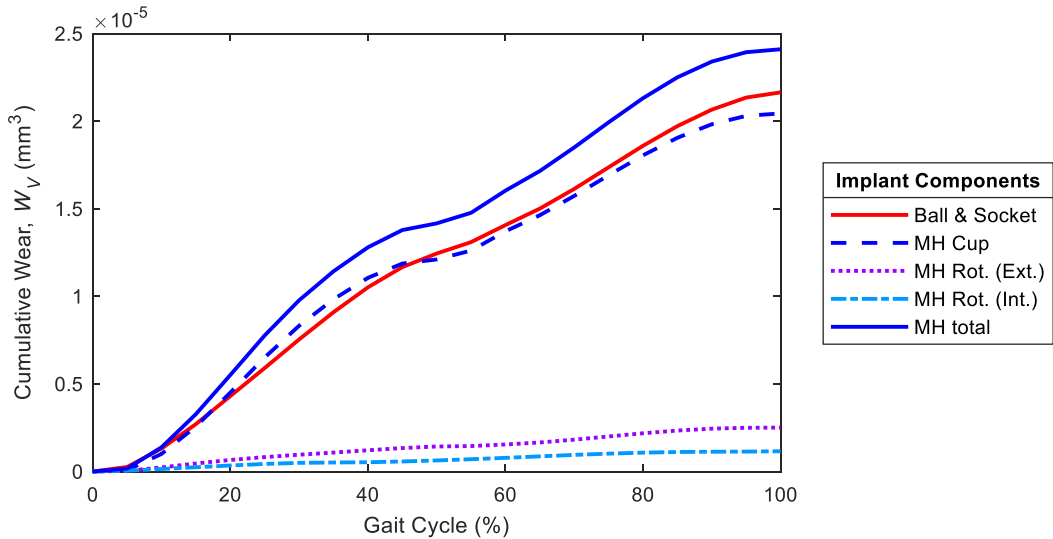


Fig. 5.37: Predicted cumulative wear during a gait cycle for UHMWPE ball-and-socket and MaltaHip implants using the wear model proposed by Kang *et al.* [303].

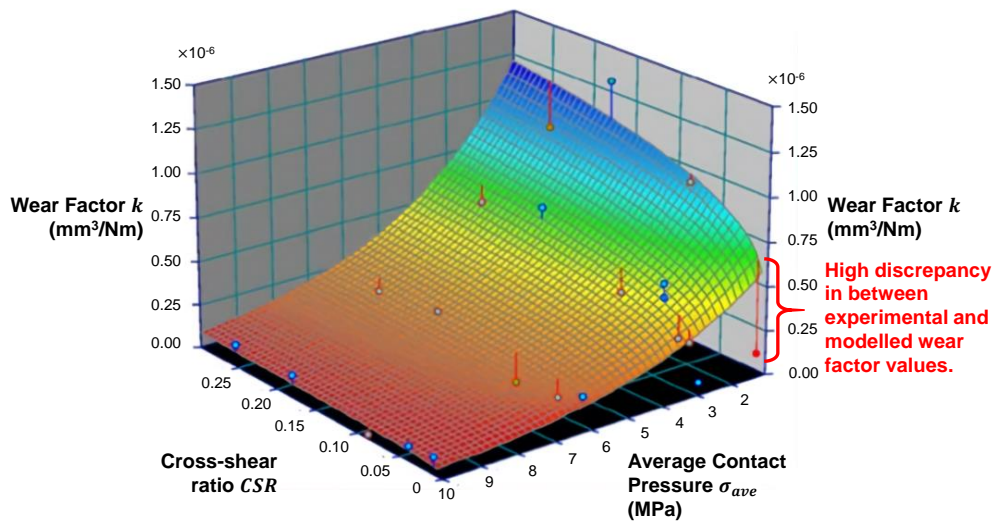


Fig. 5.38: Overestimation of the wear factor values for UHMWPE at low values of cross-shear ratio, due to the high discrepancy between the experimental and modelled values. Adapted from: [303].

5.5.5. Petrella Model

The cumulative volumetric wear of the ball-and-socket and the MaltaHip according to the Petrella wear model [298] can be observed in Fig. 5.39. The model predicts that the MaltaHip design will exhibit less than half of the wear that is produced by the conventional ball-and-socket implant. It should be noted that this model does not directly take into account the cross-shear effects, but instead, considers the instantaneous molecular orientation, which has been referred to as the material memory feature by the authors [298] of the proposed wear model, as reviewed in Section 2.6.6 (p. 57). Since the ball-and-socket implant exhibits slide tracks with convoluted trajectories, the surface polymer chains are continuously being subjected to cyclic rearrangement.

The Petrella wear model acts as a penalty function by increasing the amount of wear according to the deviations done in the slide track from the previous step. This is achieved by dividing the slide track into a number of segments and comparing their orientation. The accuracy of the result can be improved by increasing the number of segments (i.e. which increases the resolution of the computation). The plot shows that the ball-and-socket design exhibits a steep curve during the initial phase of the gait, implying a high volume of wear being produced due to extensive molecular rearrangement being done. The inclination of the curve becomes gentler during the swing phase, implying that minimal path deviations are done as the joint returns back to its original position. The total volumetric wear rates over a million cycles of the ball-and-socket and the MaltaHip design are 16.5 mm^3 and 7.8 mm^3 , respectively.

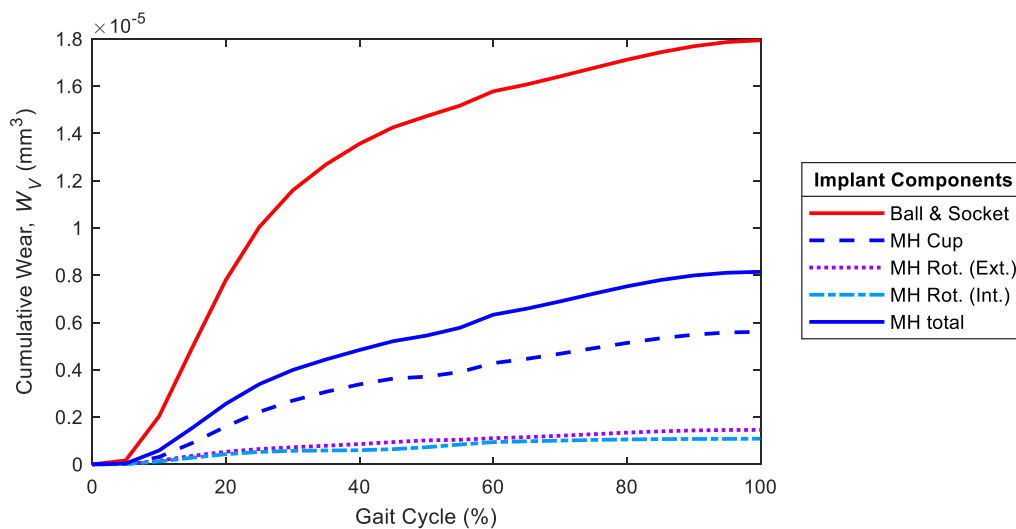


Fig. 5.39: Predicted cumulative wear during a gait cycle for UHMWPE ball-and-socket and MaltaHip implants using the wear model proposed by Petrella *et al.* [303].

5.6. The Fabricated Implant

5.6.1. Machining Processes

The orientation of the molecular chains of the articulating surfaces is highly dependent on the type of machining processes that were applied to the components of the MaltaHip. Therefore, the wear produced by the polymeric components must be interpreted in relation to the machining processes which were used for the different surfaces of the components. In light of this, the purpose of this section is to provide details regarding the resultant machining principles that were implemented for the fabrication of the MaltaHip.

The unique geometrical design of the MaltaHip required the development of a new machining procedure to meet the required geometry, surface finish, and polymer chain orientation. Machining of the MaltaHip components was not trivial as some of the components consisted of overhang features which are inherently difficult to access by conventional machining techniques. Furthermore, some components also consisted of two cylindrical faces that are oriented perpendicular to each other, requiring reorientation of the part between different machining operations.

Efforts were focussed on simplifying the machining processes required for the prosthesis. The use of cylindrical features, being axisymmetric in nature, enabled the majority of each part to be machined using turning operations. The use of turning operations over milling operations is highly beneficial as components are manufactured at faster rates (due to the higher machining speeds of the lathe), whilst also providing an exceptional surface finish. On the other hand, milling processes are slower since machining speeds between the tool and the cutter are relatively lower (compared to the machining speeds which are achieved by a lathe machine). Furthermore, limited material volumes are removed within each machining step of the milling process. Nonetheless, the main benefit of the milling technique is that it allows for highly complicated geometrical features (without any symmetrical features) to be produced with relative ease.

Although the components possess different geometrical designs, the general machining procedure that was applied to the components mainly involved a series of turning operations, followed by minor milling operations. The resultant machining techniques adopted for each component are briefly described. For the MaltaHip cup, slightly different machining techniques were adopted for the ram extruded UHMWPE and compression moulded VEHXPE materials, due to the different ways the materials were produced.

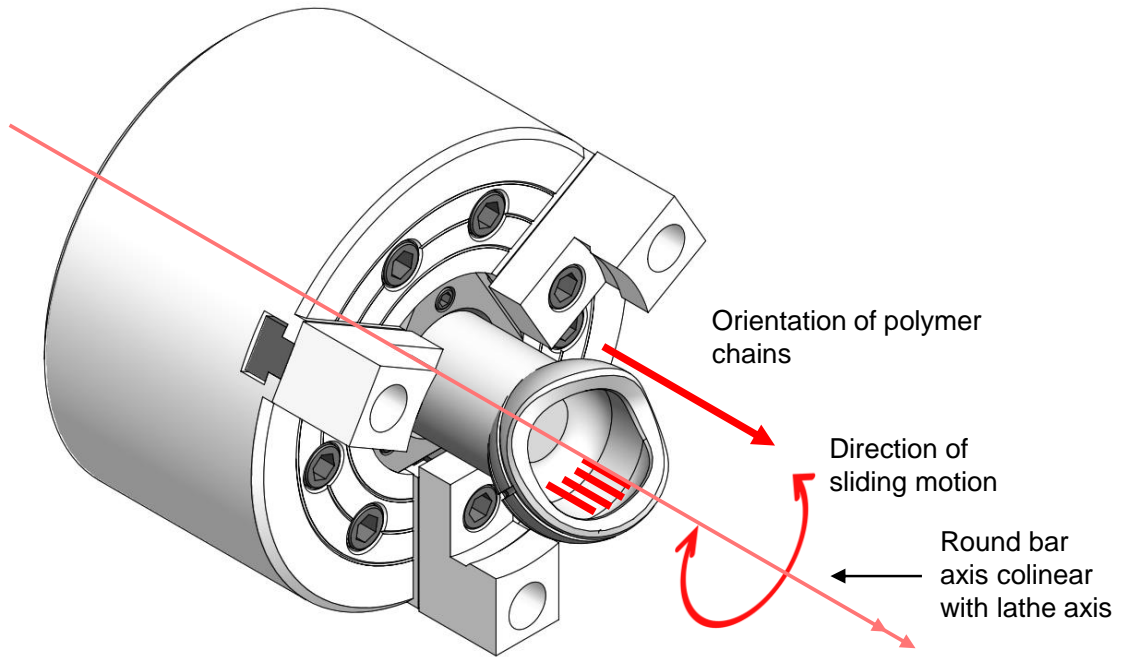
The supplied ram extruded UHMWPE round bar was annealed below its melt temperature and therefore the material exhibited increased crystallinity. However, during annealing, UHMWPE exhibits non-uniform crystallisation due to its low thermal conductivity and hence some degree of anisotropy along the direction of extrusion is retained [149, 339]. If the UHMWPE ram extruded bar is mounted on the lathe machine in the conventional manner (i.e. longitudinal axis of the bar being parallel to that of the lathe, as shown in Fig. 5.40a), this would result in the machined component with polymer chains being perpendicular to the sliding motion of the flexor. In order to leverage the fact that wear resistance is highest when sliding is aligned with the molecular chains, the UHMWPE round bar was oriented with its longitudinal axis being perpendicular to the mounting axis of the lathe, as shown in Fig. 5.40b. As a result,

the molecular chains on the internal load-bearing surface of the MaltaHip cup become oriented parallel to the uni-directional sliding motion of the flexor, effectively forcing the articulation to slide on the most wear resistant molecular structure of the polyethylene.

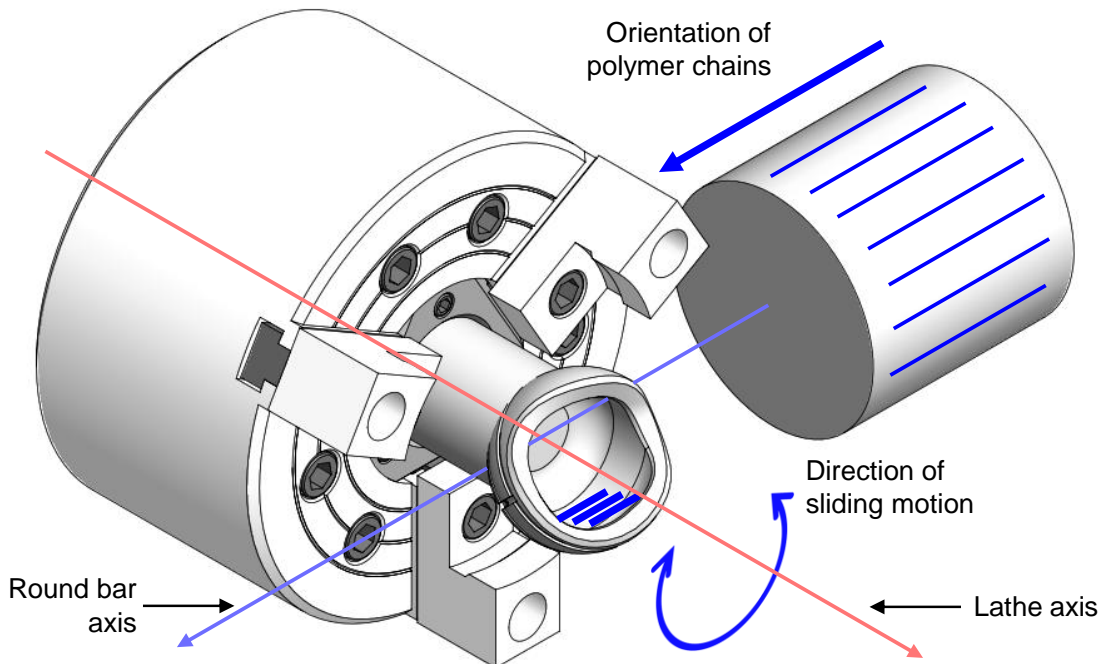
Due to the unconventional mounting orientation of the ram extruded UHMWPE rod, 53 mm diameter rods were initially machined laterally from an 80 mm diameter round bar, as schematically illustrated in Fig. 5.41a. In case of the VEHXPE material, which is fabricated through compression moulding, the round bar was mounted with its axis parallel to that of the lathe (as shown in Fig. 5.40a), due to the lower level of anisotropy and crosslinked structure in the material.

The MaltaHip cup is one of two components of the prosthesis that consists of an overhang feature, which is required for the interlocking mechanism. The overhang feature is inherently one of the most difficult geometrical attributes to be machined due to the limited access that is available for the machine tooling. The use of turning operations to machine the overhang feature of the MaltaHip drastically reduces the required machining time, despite its inherent complicated design. A sectioned view of the MaltaHip cup is shown in Fig. 5.41a that illustrates the overhang feature, comprising of an internal surface which resembles a partial cylinder with a large diameter (denoted as $\emptyset D$), leading to a small diameter opening (denoted $\emptyset d$). The lathe tooling is sized and programmed to access the internal surface from the small-diameter opening and perform machining operations on the large-diameter surface without colliding with the surrounding material. Fig. 5.41b shows a turning operation being conducted on the internal surface. Intermediate observations and checks on the machined internal surface are limited during this stage due to the restricted access imposed by the overhang feature. Once machining of this feature is completed, the external spherical surface of the MaltaHip cup is machined, as shown in Fig. 5.41c.

Following completion of all the turning operations, the external curved profile of the MaltaHip cup is machined using a 5-axis CNC milling machine. The specific geometry of the external curved profile contributes to the functionality of the interlocking mechanism, whilst at the same time minimizes the extent of prosthesis impingement. The external profile is machined using the swarf milling technique (Fig. 5.42), whereby the final cut is done with the side of the tool, rather than by the tip of the tool as usually done in conventional milling operations. The motion of the 5-axis CNC machine enables the exact shape of the curvature to be produced with relative ease whilst enabling the cup to achieve its intended functionality.

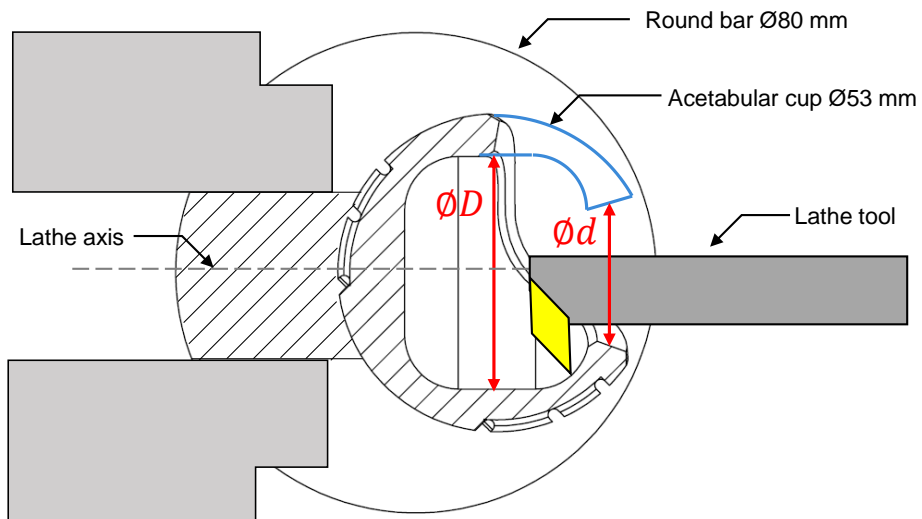


(a) Conventional machining: Round bar axis is aligned parallel and coinciding to the lathe axis. Cross-shear effects would be maximised when machining new surfaces from the ram extruded bar. However, this approach was used to machine components produced from the compression moulded round bar.

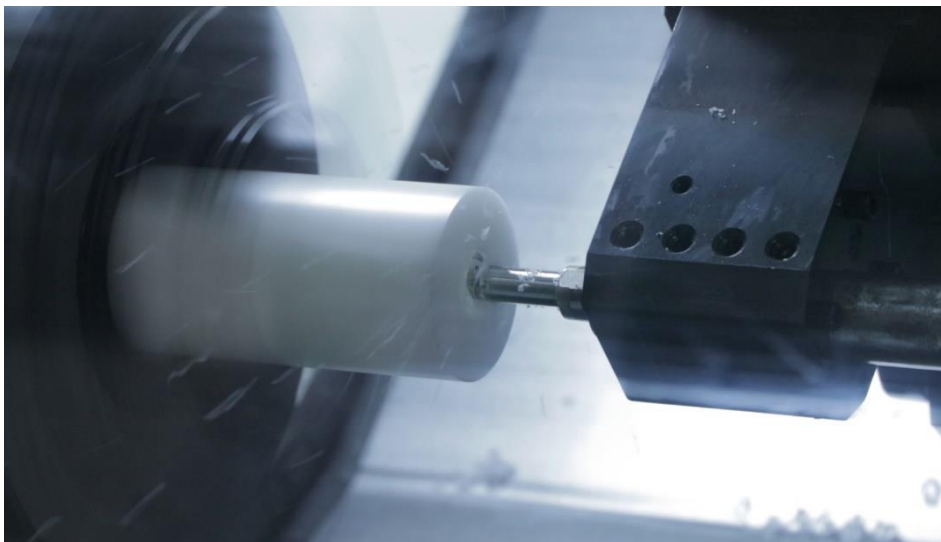


(b) Unconventional machining: Round bar axis is aligned perpendicular to the lathe axis. Cross-shear effects are minimal throughout the whole depth profile when machining a ram extruded round bar.

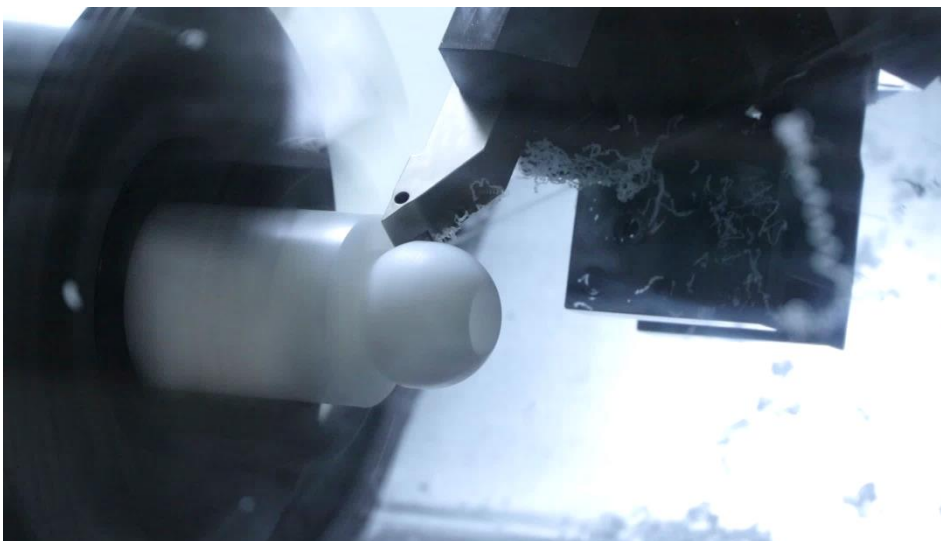
Fig. 5.40: The direction of the polymer chains on the surface of the MaltaHip cup is dependent on the mounting orientation of the ram extruded bar.



(a) Schematic diagram of internal surface machining. The diameter at the opening $\varnothing d$ is smaller than the diameter of the internal surface $\varnothing D$ that needs to be machined

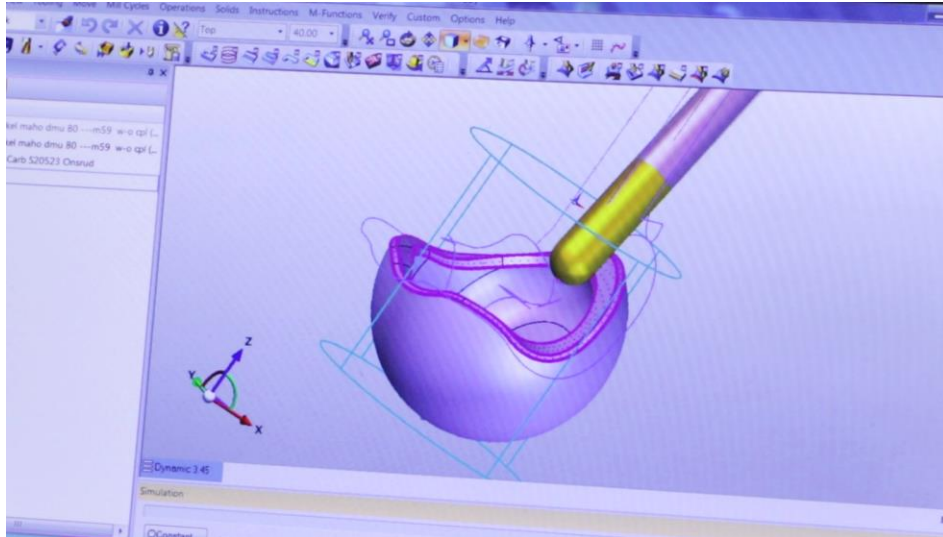


(b) Internal surface machining of the overhang feature.



(c) External surface machining.

Fig. 5.41: Turning processes on the MaltaHip cup using a CNC lathe.



(a) Generation of tool paths to machine the outer edge profile of the MaltaHip cup.



(b) Machining of the MaltaHip cup using the swarf milling technique.



(c) Close-up of the outer edge profile being machined.

Fig. 5.42: The unique geometry of the outer profile of the MaltaHip components was machined using a 5-Axis CNC milling using the swarf milling technique (as opposed to surface milling) to obtain a smooth and continuous surface.

The flexor component, produced out of high-N austenitic stainless steel, was machined in a similar manner to the MaltaHip cup. A summary of the procedure is illustrated in Fig. 5.43, which mainly involves: (a) turning of the external surface, (b) re-orientation of the part, followed by turning of the internal surface, (c) swarf milling of the external profile, and (d) parting of the flexor component. During the first step (Fig. 5.43a), machining of the external surface is done by having the longitudinal axis of the round bar mounted parallel to that of the lathe. Due to the perpendicular orientation of the internal cylinder, enough material is retained at the ends of the cylindrical bar in preparation for the second machining process, such that the component can be mounted perpendicularly to the lathe axis (Fig. 5.43b). In this configuration, the longitudinal axis of the internal cylinder matches that of the lathe, which facilitates the machining procedure of the internal articular surface. Similar to the MaltaHip cup, the internal surface possesses an overhang feature, and thus a highly specific tool path was generated to achieve the required geometrical profile, whilst avoiding any collisions with the surrounding material. The external curved profile of the flexor was machined using once again the swarf milling technique, as shown in Fig. 5.43c. The machining procedure is completed by parting off the flexor component from the cylindrical rod (Fig. 5.43d).

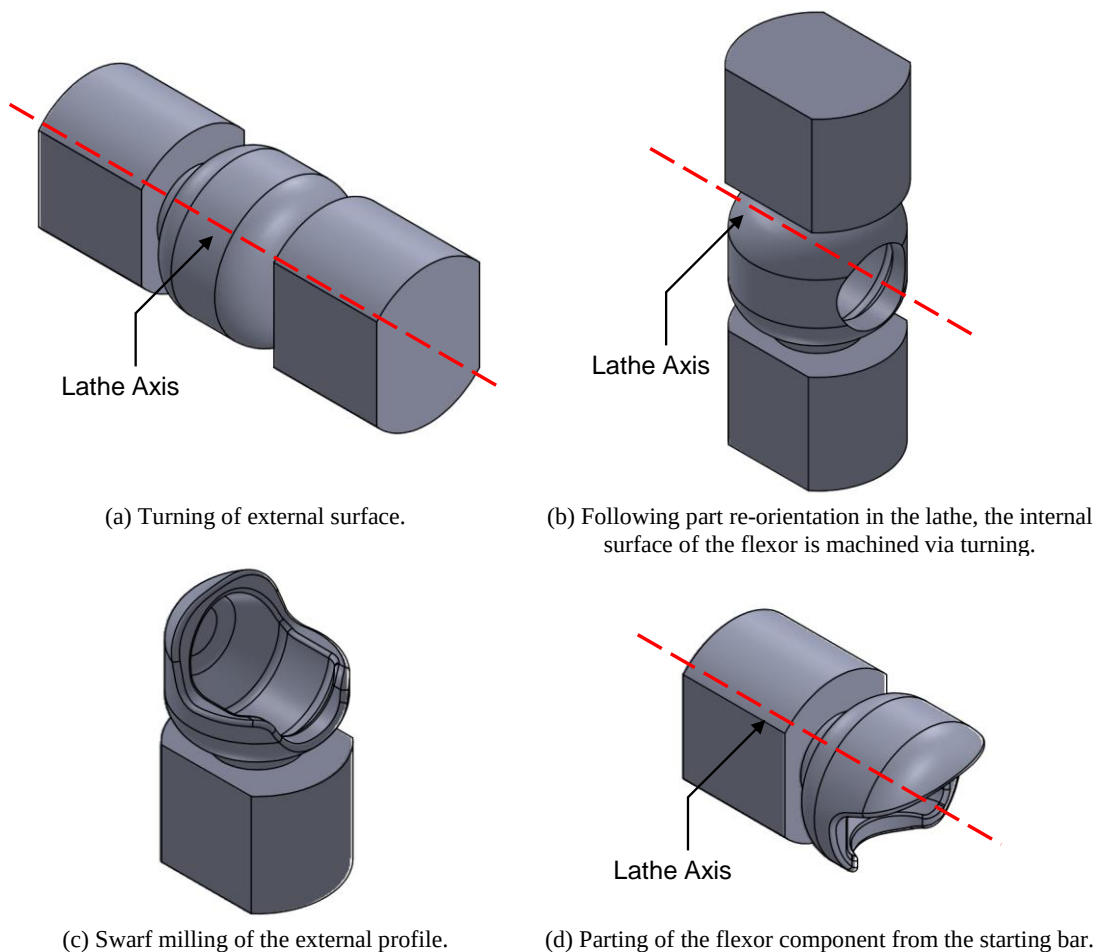


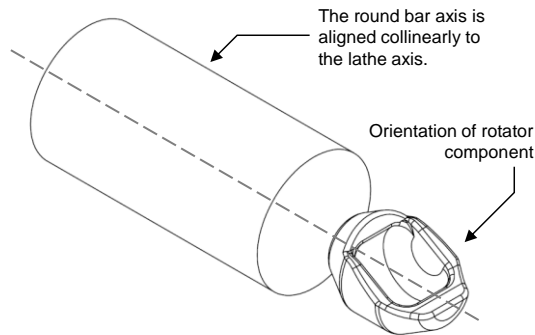
Fig. 5.43: Machining procedure used for the fabrication of the flexor component.

Machining of the rotator component required less complicated machining procedures, compared to the cup and flexor components, due to the absence of the overhang feature. Machining of the rotator mainly involved a turning (Fig. 5.44a) and a milling procedure (Fig. 5.44b). Despite the anisotropy of the UHMWPE ram extruded bar, machining of the rotator was done by mounting the round bar in the conventional orientation, as shown in Fig. 5.44a, due to reasons outlined below.

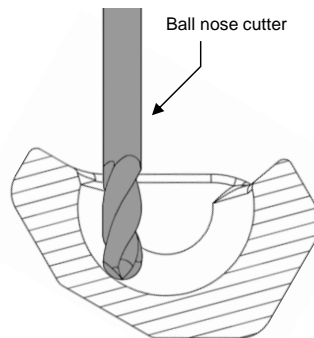
Firstly, the rotator consists of two articulating surfaces: the external surface that articulates against the flexor, and the internal surface that articulates against the abductor. As a result, the two articulations perform sliding motions that are perpendicular to each other. Therefore, it was not possible to orient the round bar in the lathe machine in such a way that the machining operations would satisfy the different orientations of the two articulations.

Secondly, the combined sliding distance of the two articulating surfaces of the rotator is less than half of sliding distance of the MaltaHip cup, and hence it was postulated that the amount of wear generated would be minimal, as predicted by the theoretical wear results.

Thirdly, machining of the rotator internal surface using turning processes was not possible, due to the absence of a geometrical opening that would need to be located normal to the longitudinal axis of the internal surface. Such geometrical opening would need to enable access to the lathe tools to machine the internal surface of the rotator. However, such opening was not included in the design of the rotator, as it would have compromised the structural integrity of the component and the overall stability of the prosthesis. Hence, the internal surface of the rotator was machined by means of a milling process using a ball-nose cutter, as indicated in Fig. 5.44b. The use of a ball nose cutter inevitably caused the surface polymer chains to exhibit highly localised orientation softening effects at the surface due to the milling action of the cutter. Notwithstanding this, a specialised cutter was used to minimize the orientation softening effects and to also produce a high-quality surface finish. It should be noted that polishing of the polymeric components following machining is prohibited by ISO 7206-2:2011/Amd 1:2016, and thus polymeric orthopaedic components should be supplied and tested in their as-machined condition.



(a) Turning operations: orientation of the rotator component is shown as produced from the round bar being mounted in the conventional manner (i.e. round bar axis aligned collinearly to the lathe axis)



(b) Milling operations: the internal surface is machined using a ball nose cutter.

Fig. 5.44: Machining processes involved in the rotator component.

Machining of the abductor component was relatively straightforward, due to its simple geometrical design that consisted of a partial cylinder with a tapered hole. The latter was used as a means of securing the abductor to the cone adapter which was intended to mimic the stem during testing inside the hip joint simulator. Unlike the conical tapered design of the stem trunnion, a flat surface was integrated to the taper design, which served as a key for orienting the abductor component in the required orientation (Fig. 5.45). Correct orientation of the abductor component is necessary to achieve the required articulation of the MaltaHip components.

The fabricated MaltaHip implants consisting of high-N austenitic stainless steel components, combined with UHMWPE and VEHXPE components are shown in Fig. 5.46 and Fig. 5.47. The individual components constituting the MaltaHip are shown in Fig. 5.48a. The eight MaltaHip implants that were sent to Endolab® Mechanical Engineering GmbH for wear testing are shown in Fig. 5.48b.

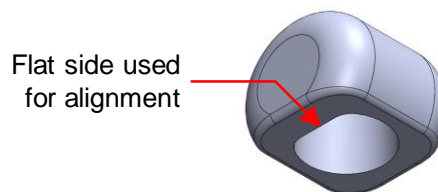


Fig. 5.45: Flat side machined in the taper of the abductor used for alignment.

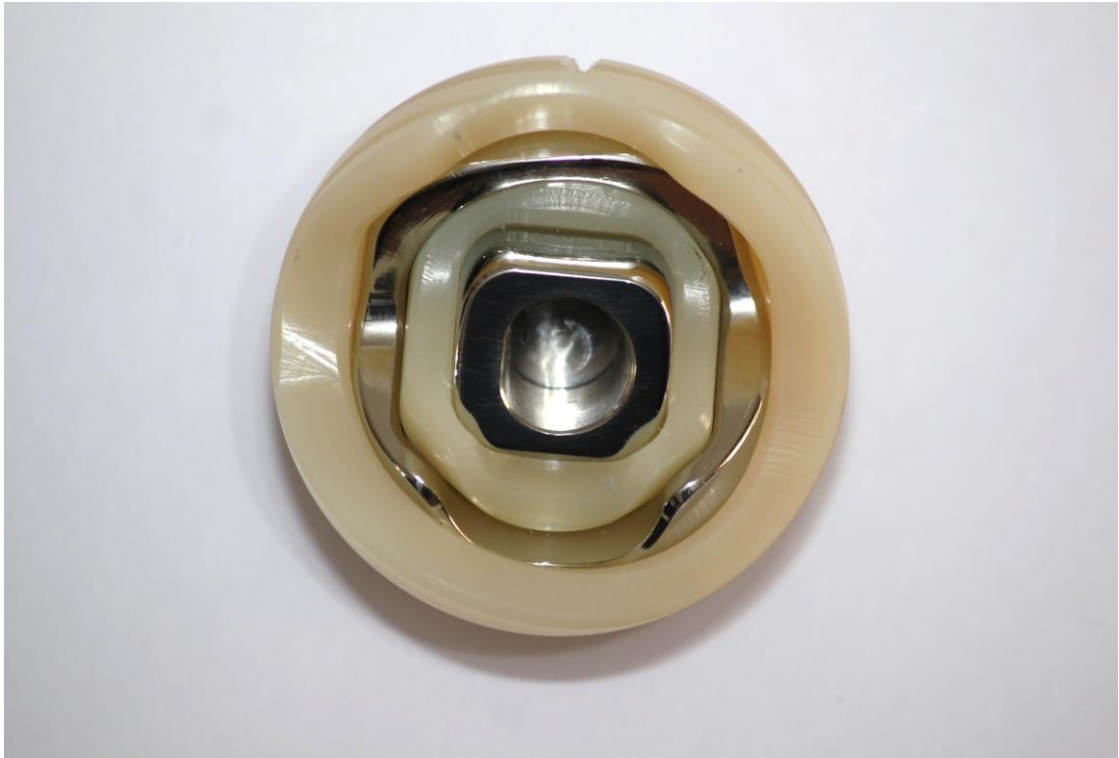


(a) The components of the MaltaHip produced out of high-N austenitic stainless steel and UHMWPE components.



(b) The MaltaHip implant assembled to a commercial stem.

Fig. 5.46: The MaltaHip implant with UHMWPE polymeric components.



(a) The components of the MaltaHip produced out of high-N austenitic stainless steel and VEHXPE components.



(b) The MaltaHip implant assembled to a commercial stem.

Fig. 5.47: The MaltaHip implant with VEHXPE polymeric components.



(a) The components of the MaltaHip with two different polymeric materials: UHMWPE (top) and VEHXPE (bottom).



(b) The eight implants that were tested at Endolab: UHMWPE (top) and VEHXPE (bottom).

Fig. 5.48: The MaltaHip implants that were fabricated and wear tested in the Endolab® hip joint simulator.

5.6.2. The Resultant Interlocking Mechanism

The interlocking mechanism of the MaltaHip was necessary to secure the various components during implantation and to minimize the risk of dislocation. The absence of the interlocking mechanism in earlier prototypes was highlighted by the orthopaedic surgeons, since it made the new prosthesis difficult to be implanted, as illustrated in Fig. 5.49. The proposed interlocking mechanism successfully achieved its functionality as predicted during the design phase in Section 5.3.4 (p. 120). Step-by-step illustrations of the interlocking mechanism in action are shown in Fig. 5.50. The assembly of the physical implant resulted in the parts engaging to each other with relative ease. The assembly procedure basically involves orientating and sliding the parts in their corresponding locations. This provides a major benefit over ball-and-socket hip implants that make use of hemispherical cups with a captive design, which usually require a specialised vice to force the femoral head inside the cup. Furthermore, the interlocking mechanism of the MaltaHip demonstrated that the hip implant can achieve a wide range of flexion/extension motion without a reduced risk of dislocation.



Fig. 5.49: Assembly of initial version of the MaltaHip implant design which did not include the interlocking mechanism.



(a) Step 1: The individual components of the MaltaHip are laid out in preparation for the assembly procedure.



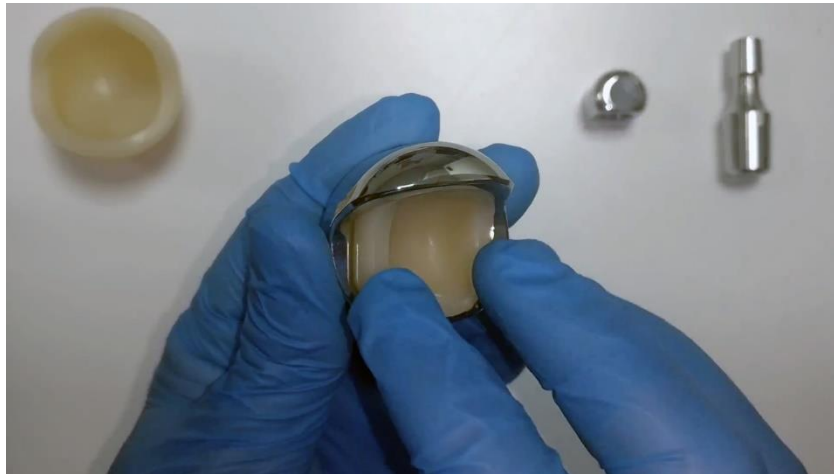
(b) Step 2: The process starts off with the assembly of the rotator inside the flexor component.



(c) Step 3: The rotator is rotated from its normal orientation by 180° about its axis.



(d) Step 4: The rotator is inserted inside the flexor component.



(e) Step 5: Once inserted inside the flexor, the rotator becomes engaged and can be rotated back to its normal orientation.



(f) Step 6: The next step is to engage the flexor-rotator subassembly inside the MaltaHip cup.



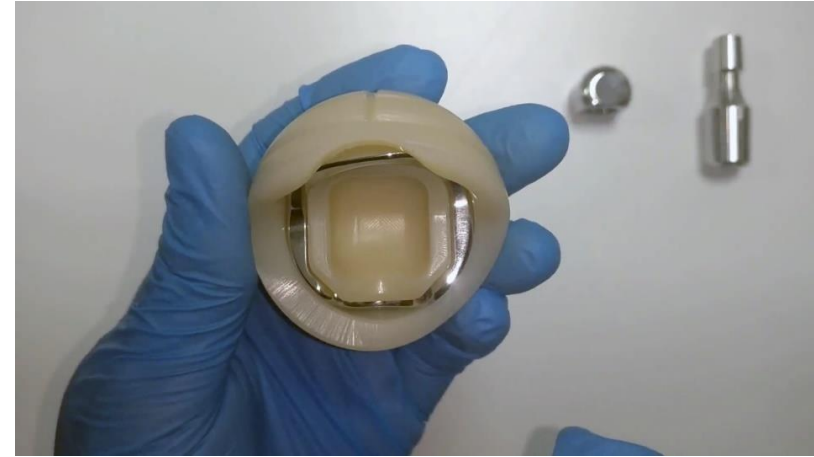
(g) Step 7: The flexor-rotator subassembly is rotated by 180° about the flexor axis.



(h) Step 8: The flexor-rotator subassembly is inserted inside the MaltaHip cup.



(i) Step 9: Once inserted inside the MaltaHip cup, the subassembly becomes engaged and can be rotated back to its normal orientation.



(j) Step 10: The complete MaltaHip cup assembly can be directly implanted inside the acetabulum. At this point, the assembled cup is ready to receive the abductor head.



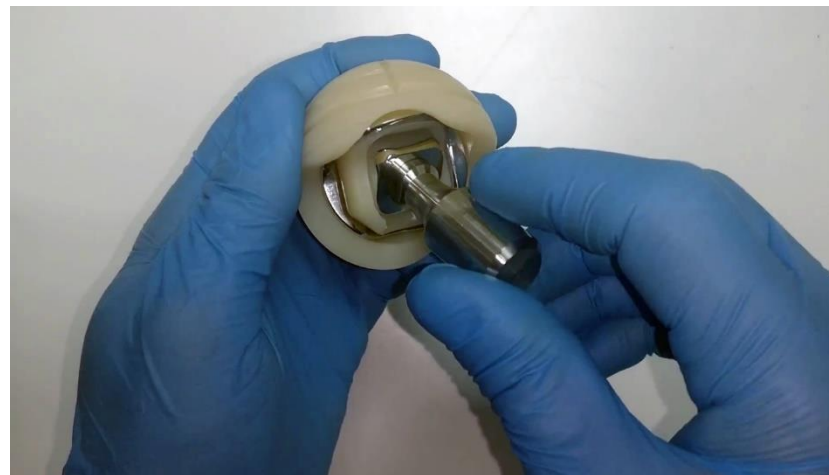
(k) Step 11: Due to the orientation-dependency of the design, a flat surface has been incorporated which act as a key for aligning the components.



(l) Step 12: The abductor head is aligned when fitted inside the tapered neck of the femoral head.



(m) Step 13: The assembly of the abductor head inside the MaltaHip cup, mimics that of the ball-and-socket implant. The assembly can be done at a wide range of different orientations, which is an important characteristic in order to facilitate the hip reduction during surgery.



(n) Step 14: Assembly of the MaltaHip is completed and thus the abductor head can be manipulated in any direction to replicate the three DOFs of the natural hip joint.

Fig. 5.50: Assembly of the MaltaHip components.

5.6.3. Surface Roughness

The surface roughness of hard articulating components influences the extent of polymeric wear debris generation, both in terms of wear volume and particle morphology [340]. The ISO 7206-2:2011/Amd 1:2016 specifies the required surface roughness of the prosthetic components in terms of the R_a value only. The ISO standard specifies that the surface roughness of the polymeric and metallic components should not exceed R_a values of 2000 and 50 nm, respectively. A 3D optical profilometer (S Neox, Sensofar, Spain) coupled with the acquisition and analysis software (S Neox, SensoSCAN) were used to measure the surface roughness of a sample batch of the MaltaHip (Table 5.4) and ball-and-socket (Table 5.5) implants. The size of the scanning areas varied between $877 \times 660 \mu\text{m}$ (smallest) to $2455 \times 1848 \mu\text{m}$ (largest), depending on the geometry of the area being inspected. The form and curvature of the region being inspected was automatically negated by the acquisition and analysis software according to ISO 25178-1⁵⁵. It was not always possible to access all surfaces with the profilometer, due to the component either being too large to fit in the inspection area or having geometrical features which obstructed access to the profilometer lens. As a result, the internal surfaces of the rotator and the flexor could not be inspected.

The surface roughness results for the MaltaHip implant are summarised in Table 5.4. The corresponding surface topography of each inspected sample are illustrated in Figs. 5.51 to 5.59. A series of highly aligned peaks and valleys can be observed for the polymeric components (Figs. 5.51 to 5.55), which correspond to the machining marks produced by turning operations using the lathe machine. Furthermore, these aligned peaks and valleys match the direction of sliding motion. Polishing marks in various directions can be observed for the flexor components, as shown in Fig. 5.57. The surface topography of the abductor component can be observed in Fig. 5.59. The polishing marks are not visible in the optical profilometry images of the abductor since the curvature of the scanned section of the abductor component is significantly larger than the polishing marks. Nonetheless, the flexor and abductor components resulted in similar average $\overline{R_a}$ values, being equivalent to 2.4 and 3.6 nm, respectively.

Surface roughness measurements were also recorded for ball-and-socket implants consisting of an Enduron™ (Depuy Synthes, US) hemispherical cup with 53 mm outer cup diameter, and an Elite™ (Depuy Synthes, US) femoral head with 28 mm diameter. The surface roughness results of the ball-and-socket implant are summarised Table 5.5, and the detailed results of each inspected sample are illustrated in Figs. 5.61 to 5.64. The concentric valleys and peaks represent the machining marks in the polar region of the hemispherical cup (Fig. 5.61). On

⁵⁵ ISO 25178: Geometrical product specifications (GPS) — Surface texture: Areal

the other hand, the femoral head (Fig. 5.63) can be observed to possess a smooth surface. Nonetheless, it can be noted that a high number of pits (as indicated by the dark dots) are shown scattered around the surface. Although the exact reason is not known for the formation of these pits on the commercial femoral head, this is likely to be attributed to the machining and polishing techniques which were used during fabrication. It should be noted that the inspected femoral head was brand new (opened from package) and was never subjected to any kind of wear testing.

Table 5.4: Summary of surface roughness values (R_a) of the MaltaHip implant.

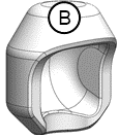
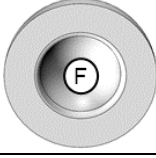
Area Label	Component, Area Description	Sample	R_a , [nm]	$\overline{R_a}$, [nm]
	MaltaHip cup, Internal superior surface (curved)	A1	105.9	104.1
		A2	218.0	
		A3	56.3	
		A4	36.0	
	Rotator, External superior surface (flat)	B1	45.9	35.4
		B2	21.5	
		B3	38.7	
	Rotator, External superior surface (taper)	C1	190.3	138.1
		C2	110.7	
		C3	113.2	
	Flexor, External medial surface (flat)	D1	3.9	2.4
		D2	2.2	
		D3	1.2	
	Abductor, External superior surface (curved)	E1	5.6	3.6
		E2	2.7	
		E3	2.4	

Table 5.5: Summary of surface roughness values (R_a) of the ball-and-socket implant.

Area Label	Component, Area Description	Sample	R_a , [nm]	$\overline{R_a}$, [nm]
	Depuy Enduron™ Hemispherical cup, Internal superior pole	F1	25.8	216.9
		F2	407.9	
	Depuy Elite™ Femoral Head, External superior pole	G1	1.3	3.7
		G2	6.0	

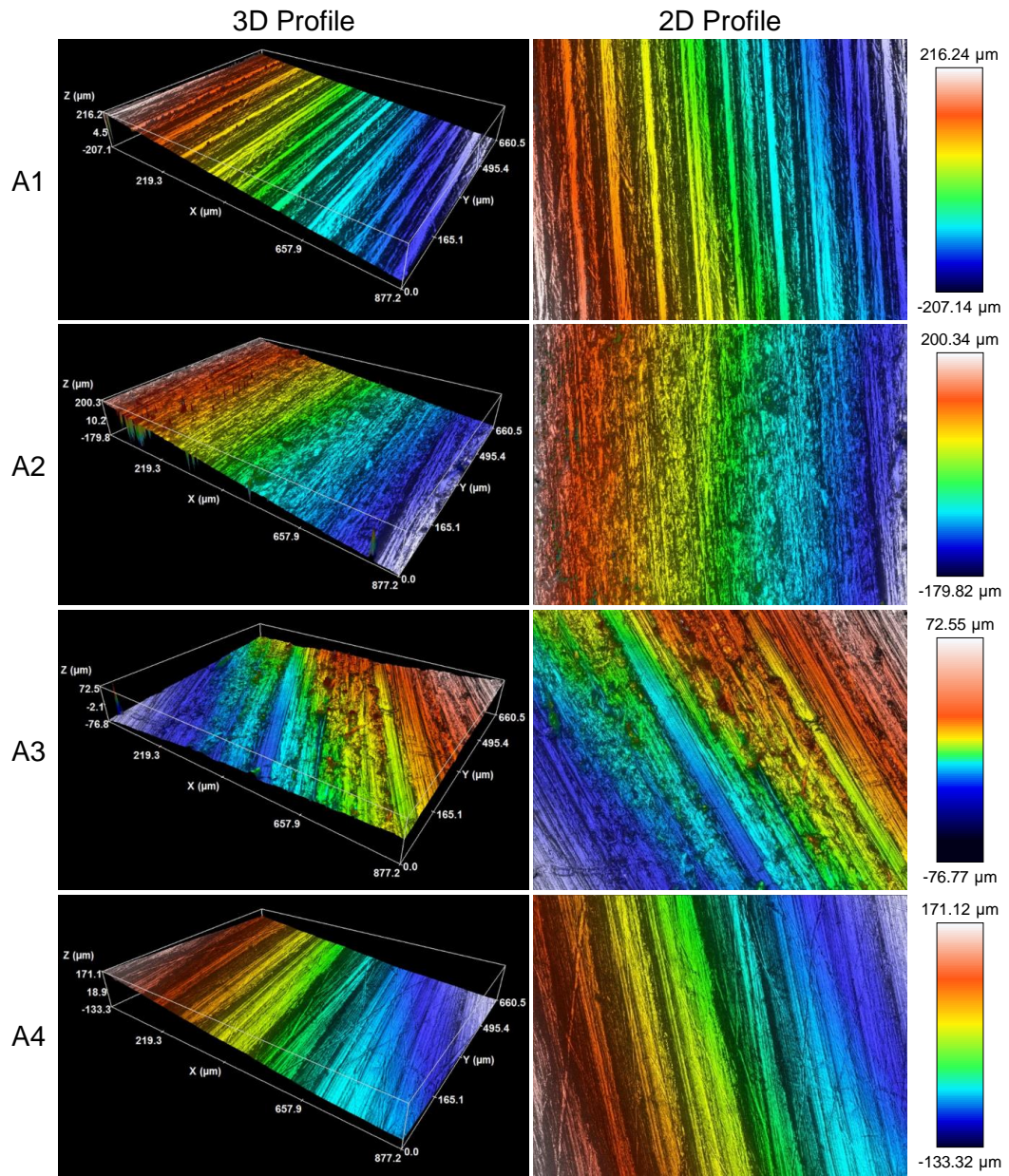


Fig. 5.51: MaltaHip cup, internal superior surface (curved).

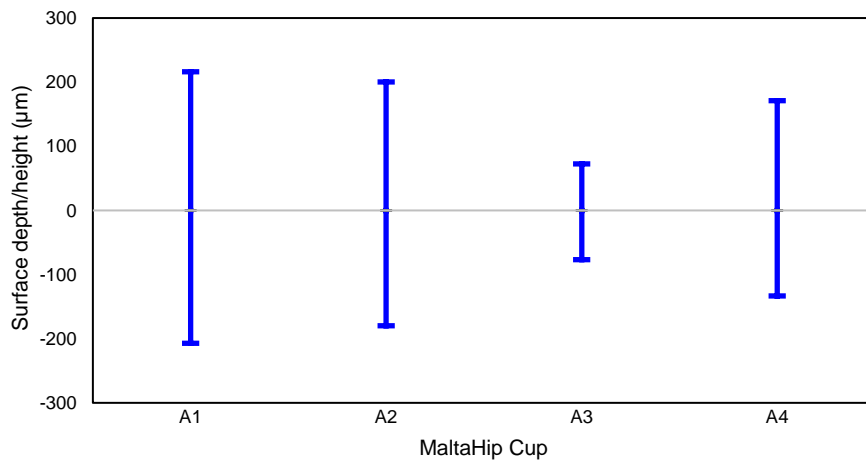


Fig. 5.52: Range of surface roughness values produced by the MaltaHip cups.

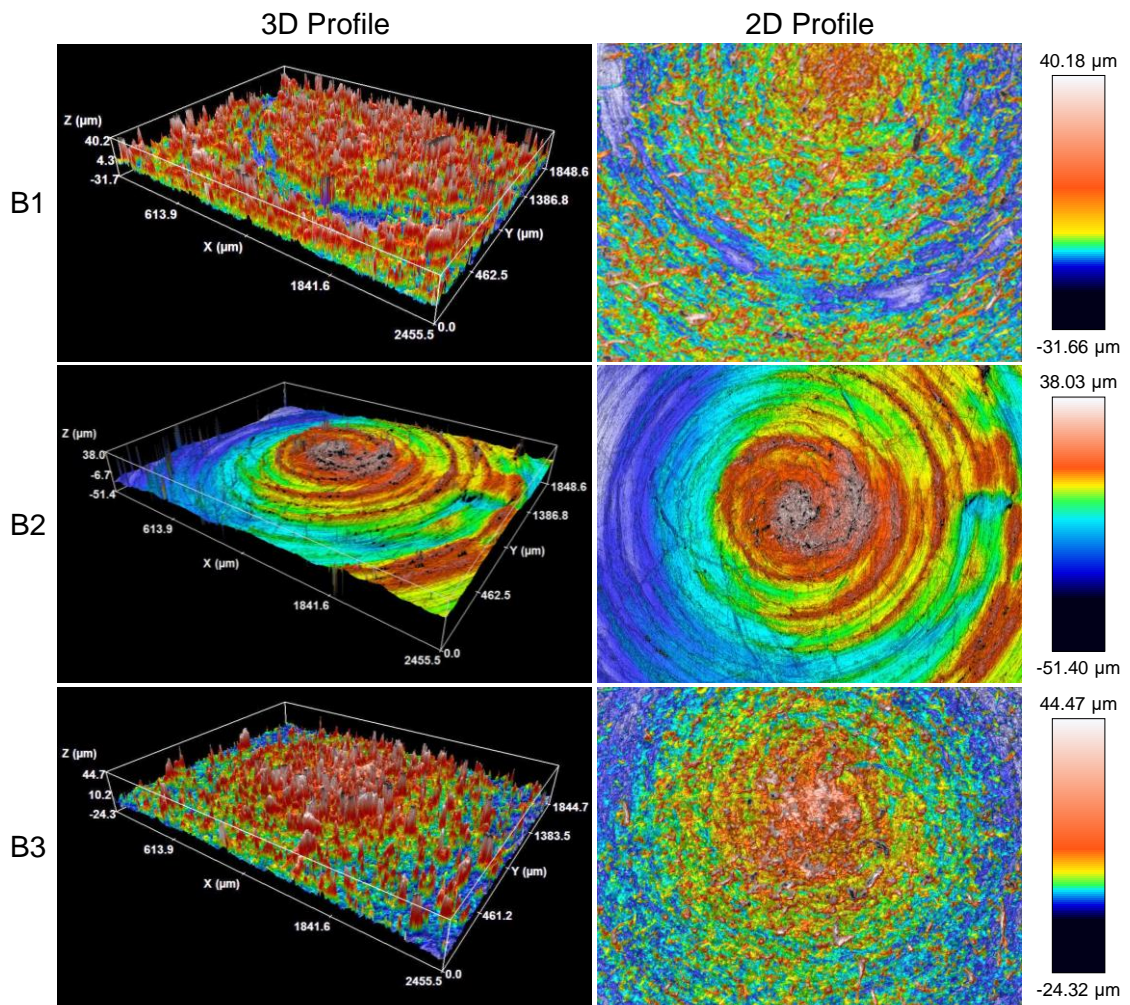


Fig. 5.53: MaltaHip rotator, external superior surface (flat).

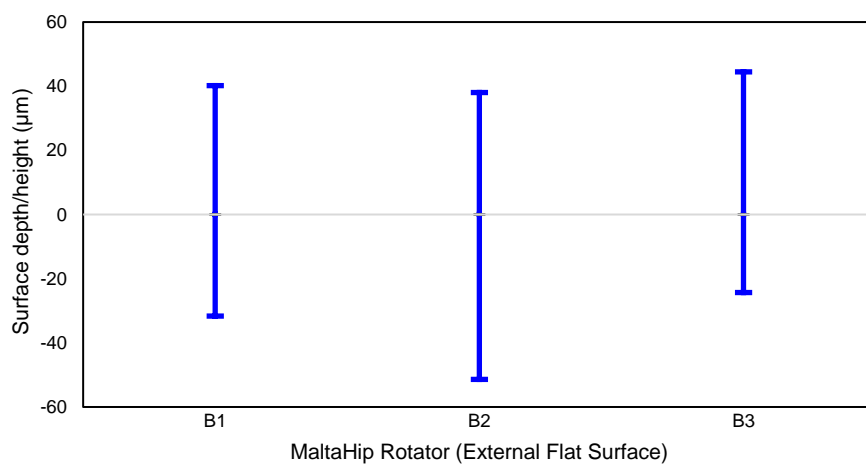


Fig. 5.54: Range of surface roughness values produced by the MaltaHip rotators external flat surfaces.

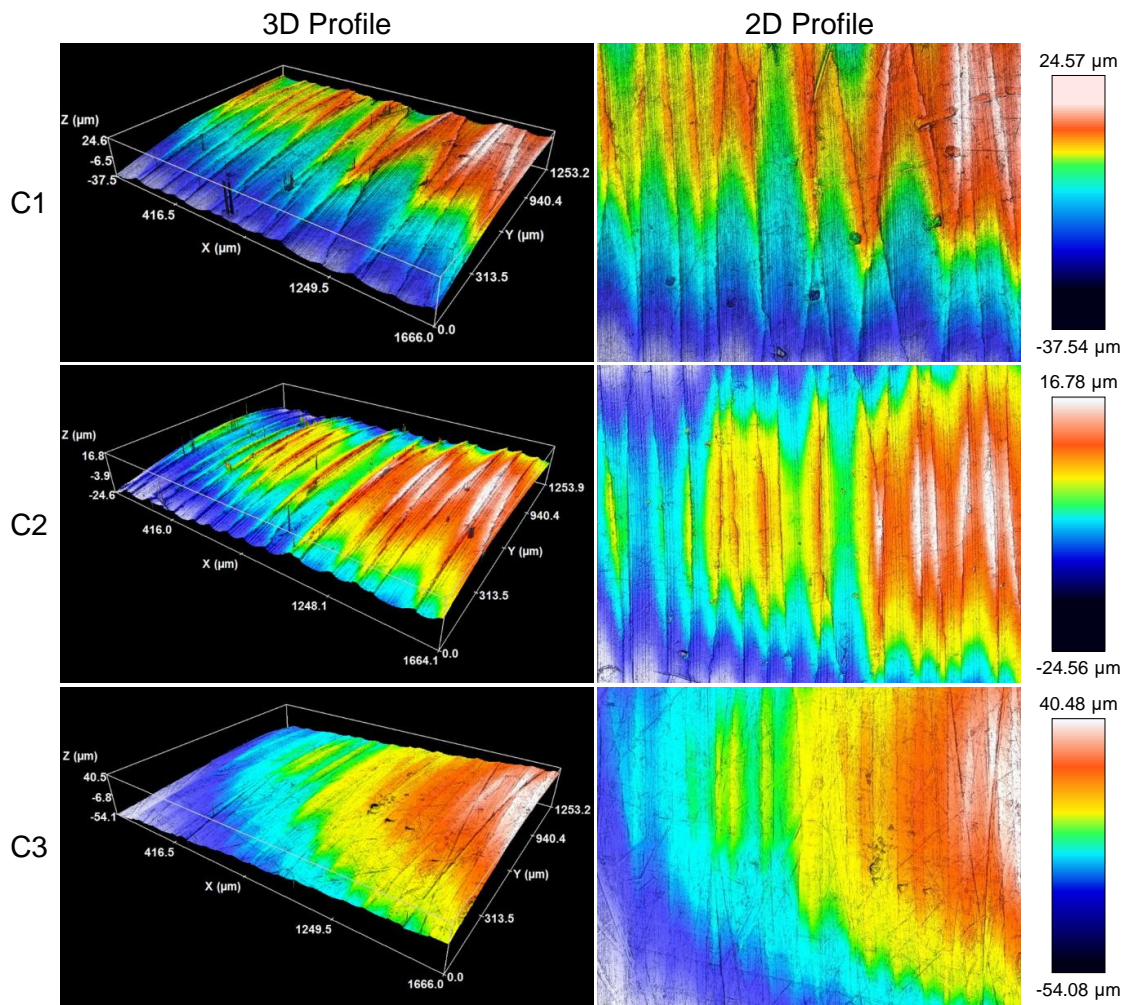


Fig. 5.55: MaltaHip rotator, external superior surface (taper).

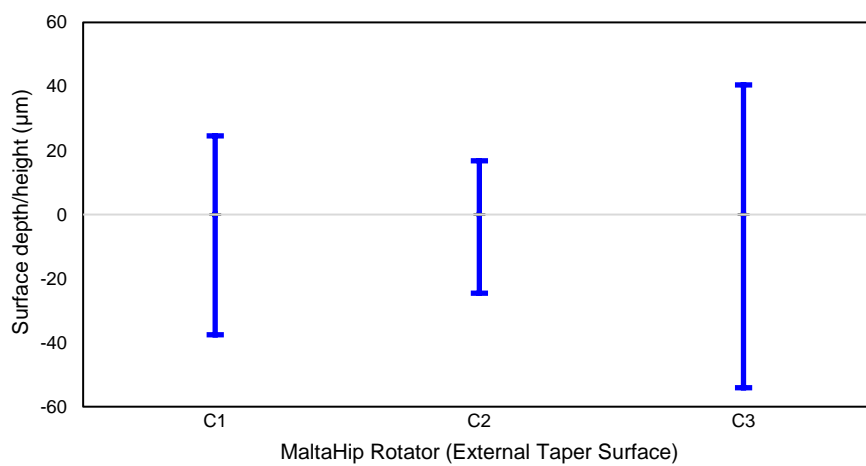


Fig. 5.56: Range of surface roughness values produced by the MaltaHip rotators external taper surfaces.

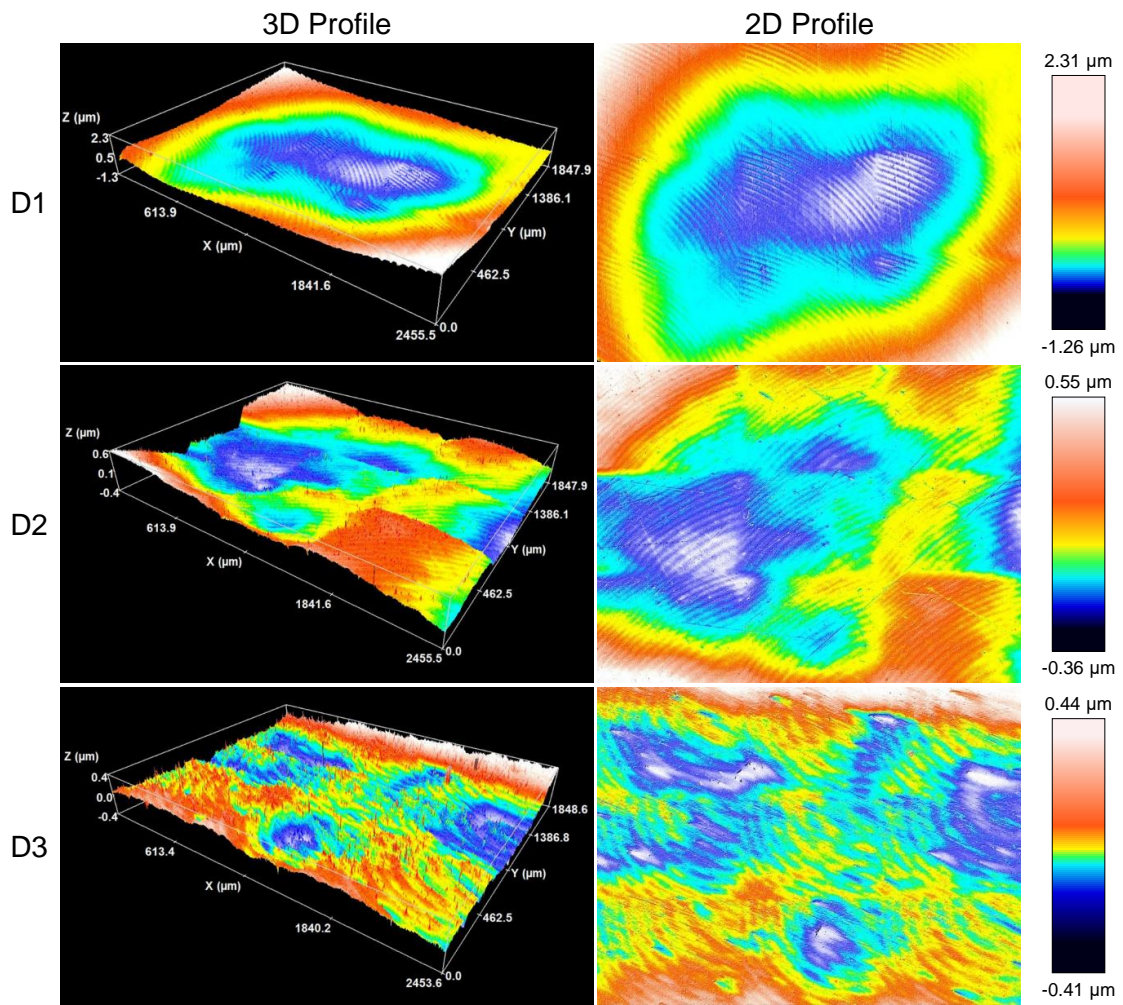


Fig. 5.57: MaltaHip flexor, external medial surface (flat).

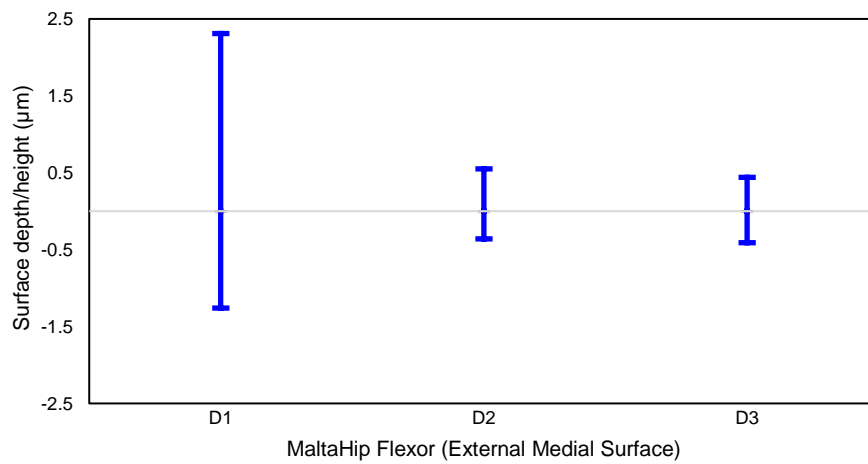


Fig. 5.58: Range of surface roughness values produced by the MaltaHip flexors (external taper surfaces).

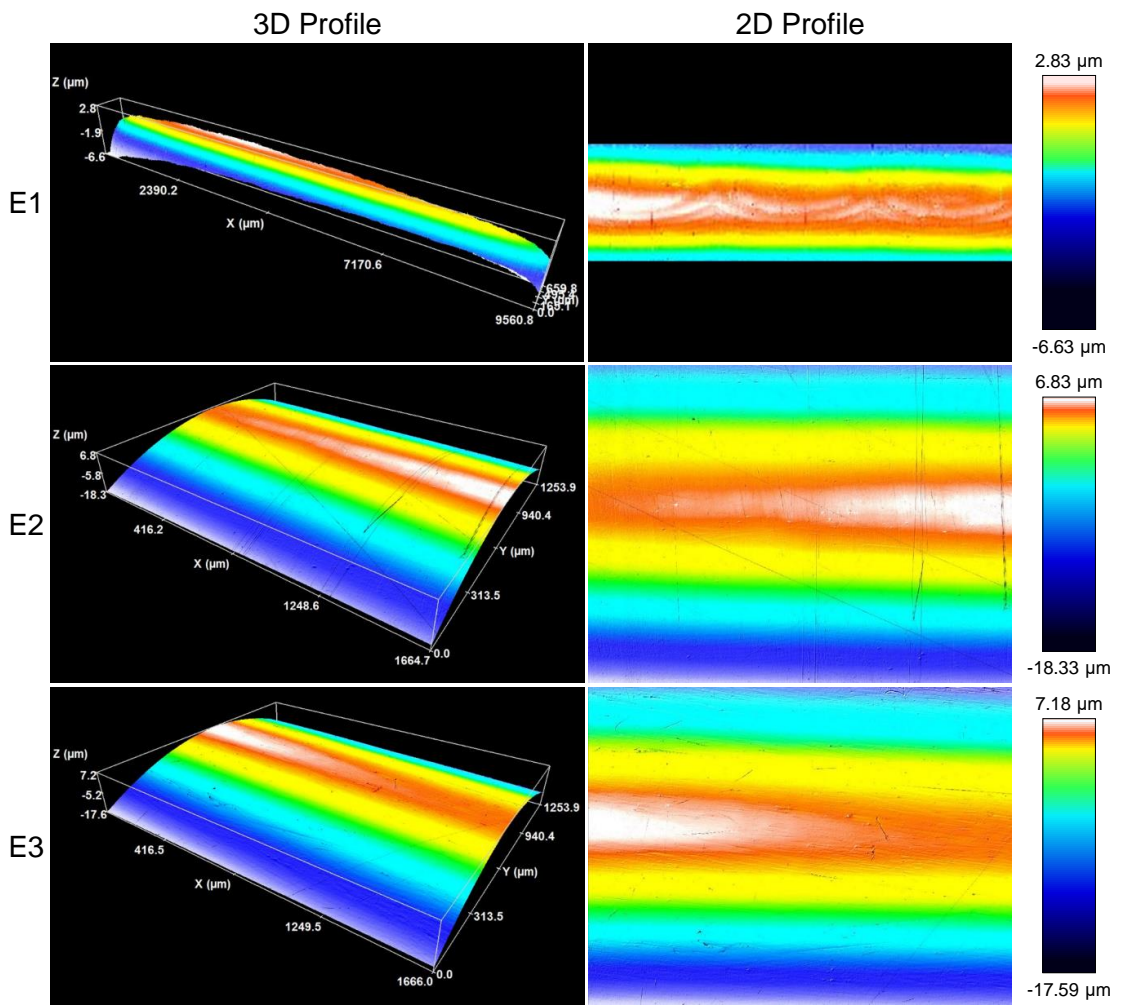


Fig. 5.59: MaltaHip abductor, external superior surface (curved).

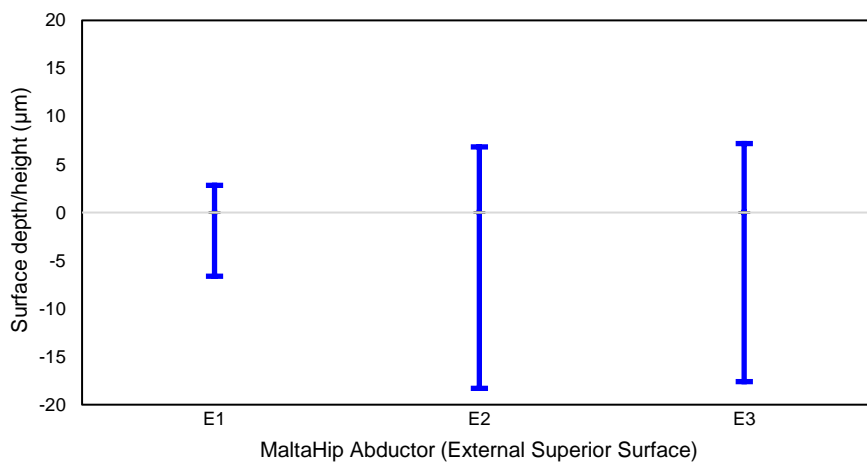


Fig. 5.60: Range of surface roughness values produced by the MaltaHip abductors (external superior surface).

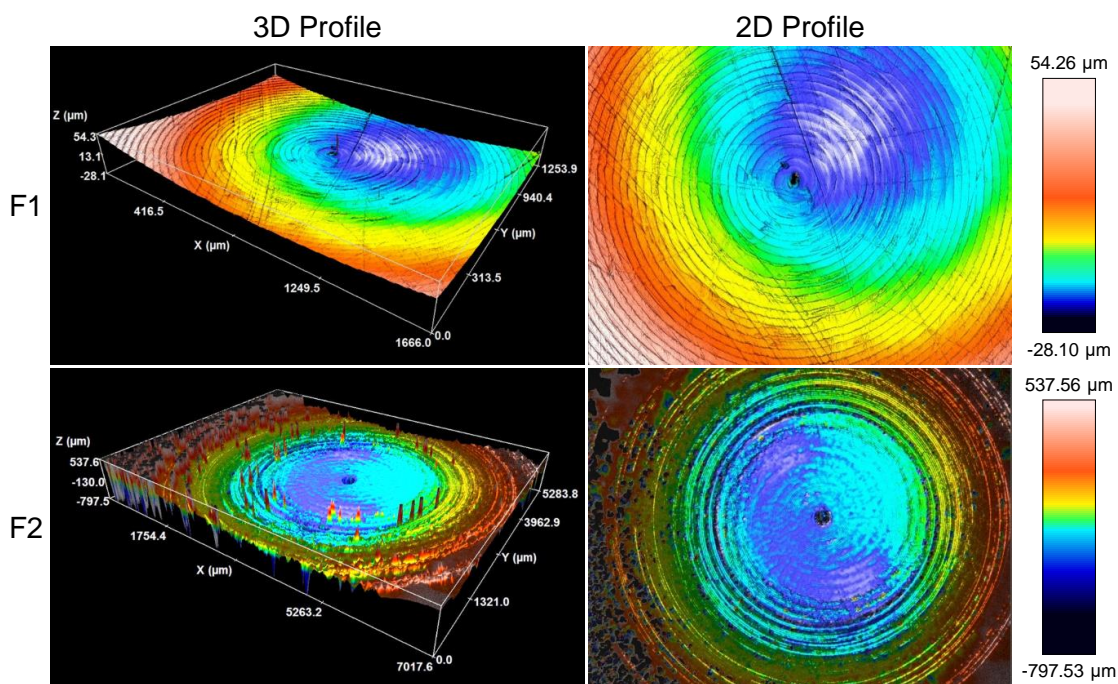


Fig. 5.61: Ball-and-socket hemispherical cup, internal superior pole.

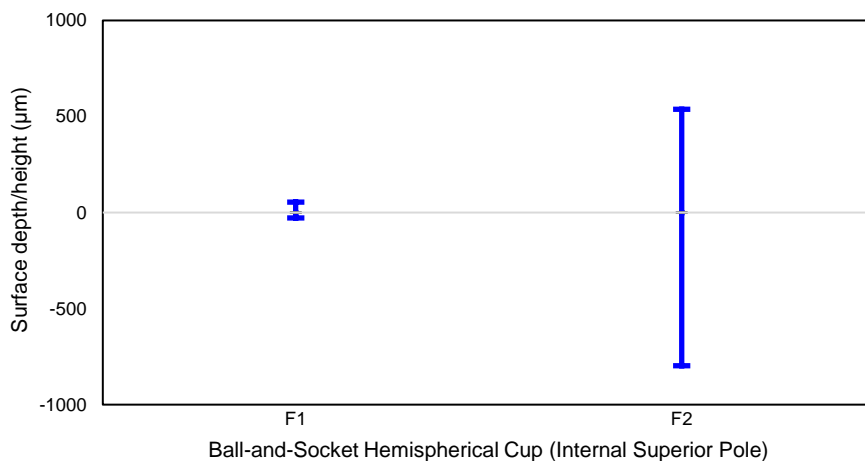


Fig. 5.62: Range of surface roughness values produced by the ball-and-socket hemispherical cups (internal superior pole). The surface roughness of the hemispherical cup F2 is still below the 2000 μm threshold as stipulated by the ISO 7206-2. The high discrepancy is likely to be attributed due to different machining techniques that might have been employed as both components were produced from different batches.

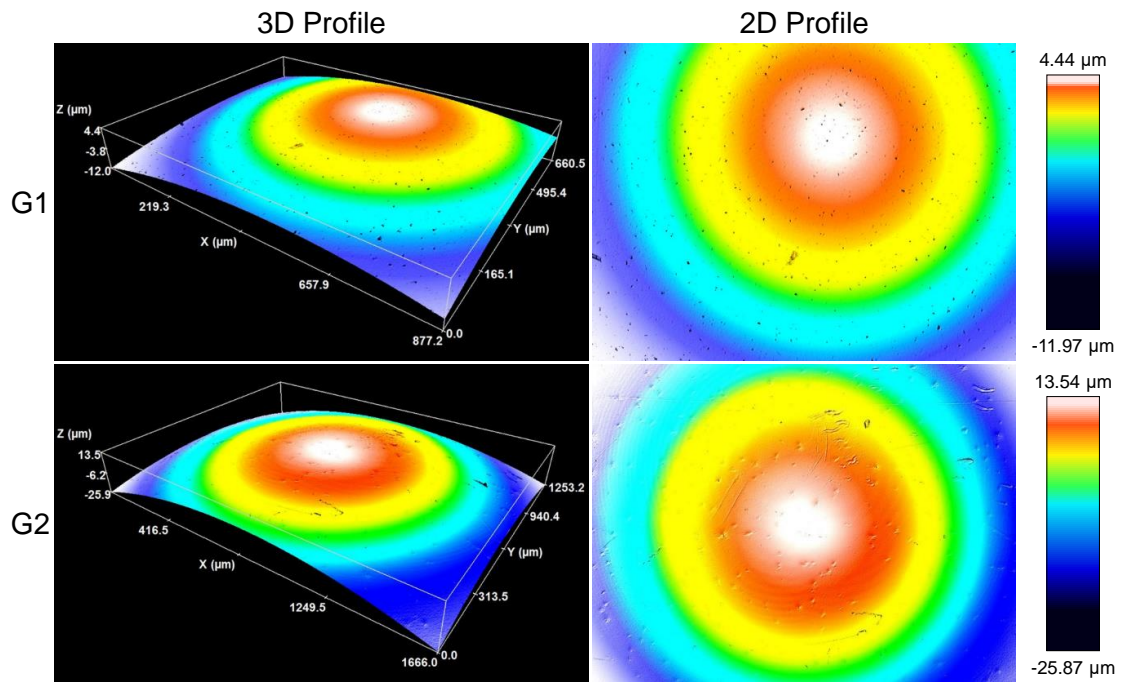


Fig. 5.63: Ball-and-socket femoral head, external superior pole.

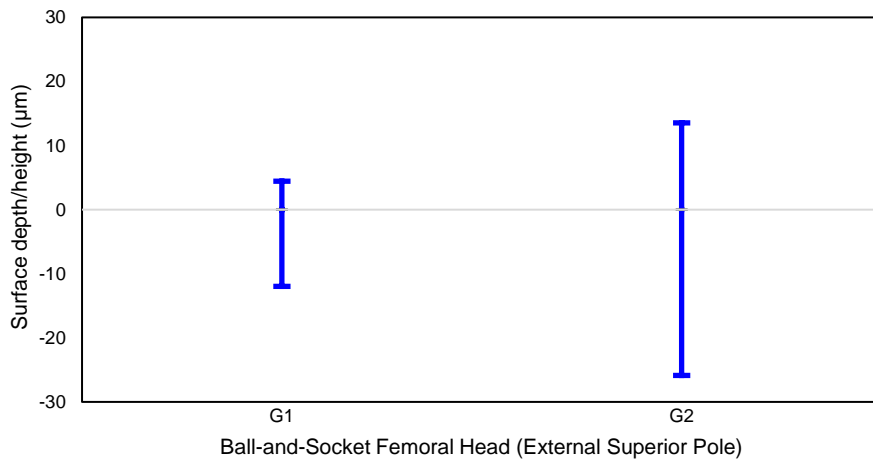


Fig. 5.64: Range of surface roughness values produced by the ball-and-socket femoral heads (external superior pole).

5.7. Experimental Wear Testing Results

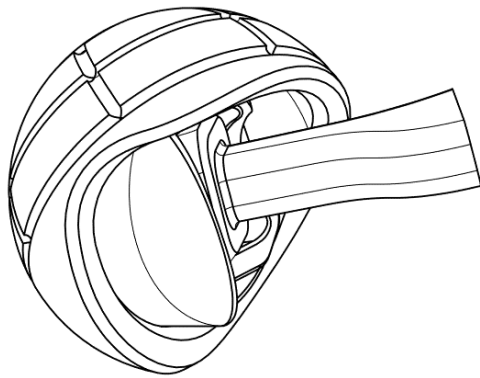
5.7.1. Implant Functionality (In-House Testing)

The primary purpose of this hip joint simulator was to act as a testbed to validate the functionality of the MaltaHip prosthesis. Therefore, the prosthesis was initially tested for its ability to reproduce the gait motion whilst maintaining its stability, by moving the individual degrees of freedom of the hip joint simulator. The physical test verified that the new articulating mechanism could reproduce the same flexible motion as the ball-and-socket implant. Furthermore, the range of motions (ROM) of the hip implant were tested as specified in ISO 21535:2007/Amd 1:2016⁵⁶ using both the CAD software and the hip joint simulator. The range of motion results produced by the MaltaHip are presented in Table 5.6, and Figs. 5.65 to 5.67. The MaltaHip implant demonstrated that the new design was able to attain the minimum range of motion requirements along the three anatomical degrees of freedom.

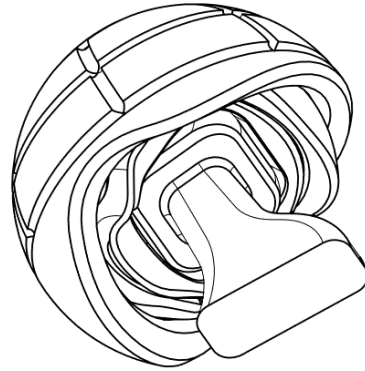
Table 5.6: The minimum range of motion (ROM) required by ISO 21535:2007/Amd 1:2016, and the results produced by the MaltaHip.

	Minimum ROM Requirements	MaltaHip ROM Results	Reference
Flexion/Extension	100°	235° (130° + 105°)	Fig. 5.65
Internal/External Rotation	90°	145° (75° + 70°)	Fig. 5.66
Abduction/Adduction	60°	90° (50° + 40°)	Fig. 5.67

⁵⁶ ISO 21535:2007/Amd 1:2016 – Non-active surgical implants – Joint replacement implants – Specific requirements for hip-joint replacement implants – Amendment 1

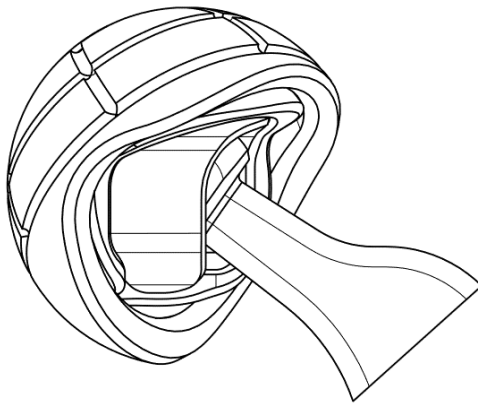


(a) MalteseHip flexion ROM: 130°.

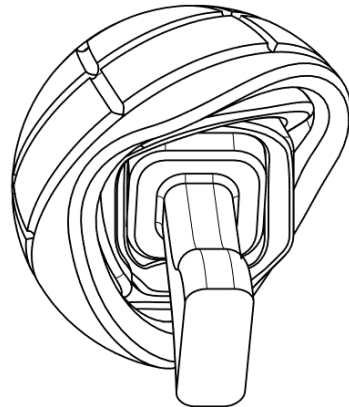


(b) MalteseHip extension ROM: 105°.

Fig. 5.65: Flexion/Extension (FE). Minimum FE ROM requirement: 100°.
MalteseHip FE ROM result: 235° (130° + 105°).

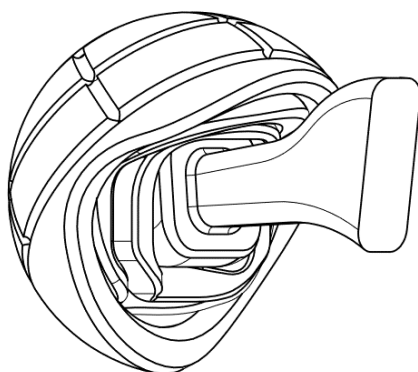


(a) MalteseHip internal rotation ROM: 75°.

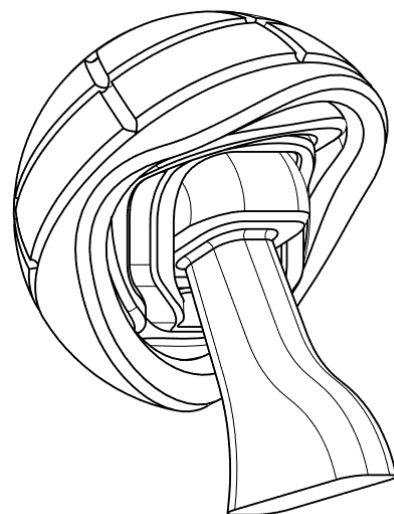


(b) MalteseHip external rotation ROM: 70°.

Fig. 5.66: Internal/External (IE) rotation. Minimum IE ROM requirement: 90°.
MalteseHip IE ROM result: 145° (75° + 70°).



(a) MalteseHip abduction ROM: 50°.



(b) MalteseHip adduction ROM: 40°.

Fig. 5.67: Abduction/Adduction (AA). Minimum AA ROM requirement: 60°.
MalteseHip AA ROM result: 90° (50° + 40°).

5.7.2. Wear Performance (In-House Testing)

Prior to the full wear testing campaign of the MaltaHip implants at Endolab®, in-house preliminary wear testing was conducted using the single-station hip joint simulator that was developed in this work. Testing using the hip joint simulator was limited to 500k cycles. Only two UHMWPE prostheses were made available for the testing phase. Unfortunately, one of the wear test results was invalidated due to an error in the equipment which occurred during the testing phase. It should be noted that this study was only used as a preliminary test to provide a general indication of the performance of the prosthesis, prior to the actual wear testing regime.

The wear test results of the MaltaHip were also compared to a ball-and-socket prosthesis, as shown in Fig. 5.68. The bar chart illustrates two important characteristics of each prosthesis. The first bar of each group represents the amount of fluid uptake during the initial soaking phase, which lasted 14 days. The second bar of each group represents the gravimetric measurement, following 500k cycles of wear testing. Interestingly, both prostheses resulted in increased mass after 500k cycles due to extensive fluid absorption. This implies that the rate of fluid uptake was greater than the rate of wear in all cases. It should be noted that the results were not corrected for fluid absorption, due to the absence of a loaded soak control station. Hence, the gravimetric measurements shown in the bar chart represent the absolute gains in mass by the components.

From the gathered results, the following deductions were made. Comparing the first bar of each set, it can be observed that the hemispherical cup absorbed a greater mass of fluid during the initial soaking phase, as compared to the MaltaHip components. This is very likely to be attributed to the greater volume of the hemispherical component.

It is interesting to note that the MaltaHip components absorbed nearly 3 – 4 times the amount of fluid during wear as compared to the soaking phase, whereas the hemispherical cup absorbed just 1.2 times. Furthermore, the similar proportions of fluid absorption during the different phases obtained for the MaltaHip cup and rotator indicate that these components are very likely to have exhibited similar wear mechanisms as a result of the uni-directional motion of the articulations. Thus, this may suggest that the rate of wear of the MaltaHip was much lower than the rate of fluid absorption. On the other hand, even though the ball-and-socket component resulted in an increased gravimetric value, this increase was not as significant, due to the amount of material removed as a consequence of its higher wear rate. It should be noted that since no repeats could be done at this stage during this study, it would have not been possible to determine whether these results would be reproduced.

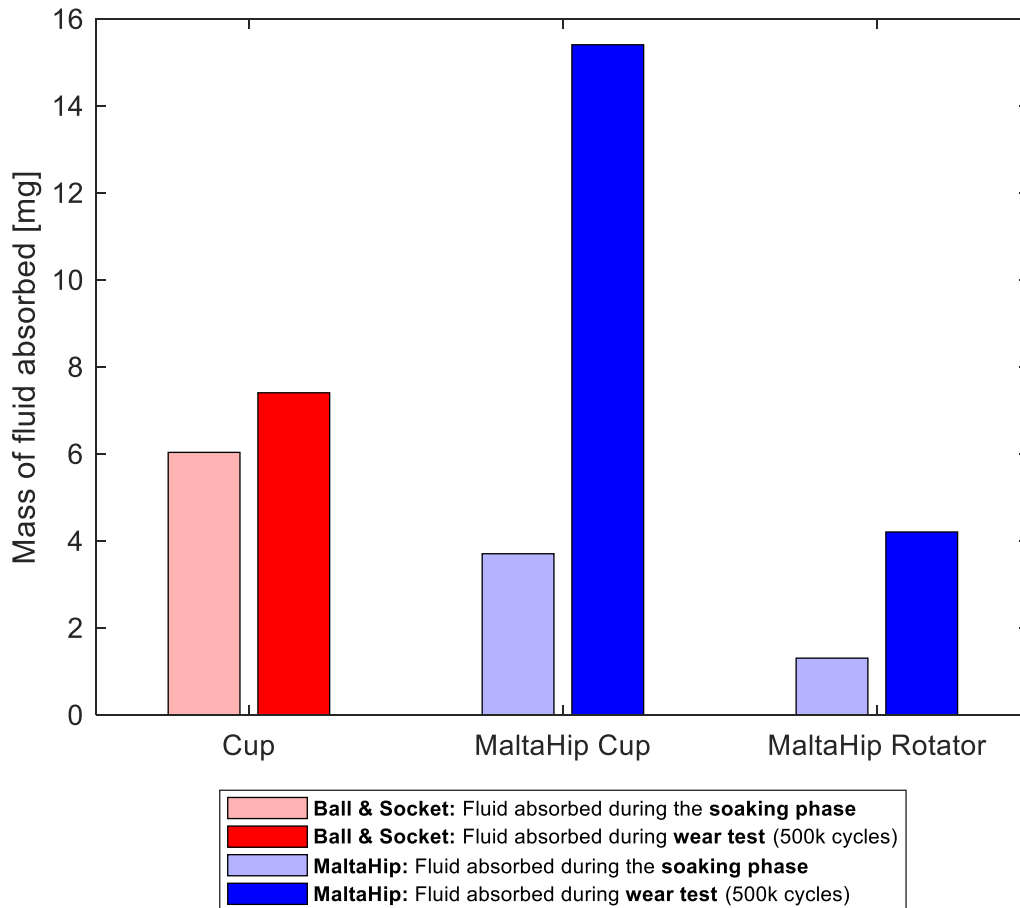


Fig. 5.68: Fluid uptake during the initial soaking and wear testing (500k cycles) of the ball-and-socket and MaltaHip, as produced from the in-house built hip joint simulator.

A visual inspection of the MaltaHip articular surfaces following the 500k cycles was conducted, and no signs of scratches were observed on the surfaces. The rotator was visibly noted to exhibit some regions that were highly polished. Nonetheless, the gains in the gravimetric measurement demonstrated that the MaltaHip design could potentially result in low wear rates. It should be noted that the above statements were only indicative and do not provide any conclusive results regarding the absolute wear rates of the MaltaHip components, due to the limited number of test samples and test cycles that were performed. Nonetheless, the positive indications validated the basic functionality of the new prosthesis design, and thus the next definite step was to subject the MaltaHip implants to the comprehensive wear testing regime according to ISO 14242-1:2014/Amd 1:2018 at Endolab® Mechanical Engineering GmbH.

5.7.3. Wear Rate Results

5.7.3.1. Summary of Results and Hypothesis Testing

The resultant wear rates of the MaltaHip implants produced from wear testing according to ISO 14242-1:2014/Amd 1:2018 which were conducted at Endolab® Mechanical Engineering GmbH are summarised in Tables 5.70 and 5.8, and Fig. 5.69. It was observed that different wear rate results were produced during the running-in and steady-state periods. Therefore, the presented results are based on the steady-state wear rates, and were compared to ball-and-socket implants (consisting of 28 mm femoral head diameter) using the same materials that were tested under the exact conditions (data was provided by Endolab®). The steady-state wear rate results presented in this section are based on the mean gravimetric wear rates as obtained from the linear regression results (\overline{W}_G) (calculated using Eq. 3.8, p. 93) between 1.0 and 5.0 million cycles, followed by their corresponding standard error (SE) values (calculated using Eq. 3.9, p. 94). The detailed results for the gravimetric wear throughout the wear testing regime of the individual components of the MaltaHip are presented in Sections 5.7.3.2 and 5.7.3.3.

The UHMWPE MaltaHip cup and rotator components resulted in steady-state gravimetric wear rates \overline{W}_G equivalent to -2.17 ± 0.24 and 8.59 ± 0.04 mg/mc, respectively, as shown in Table 5.8 and Fig. 5.69a. The negative wear rate of the MaltaHip cup indicates that the rate of fluid absorption was greater than the rate of wear, even though the value has been corrected for fluid uptake using the data retrieved from the loaded soak control. This indicates that further fluid absorption occurred during the sliding motion of the components. The combined mean gravimetric wear rate of the UHMWPE polymeric components in the MaltaHip implants resulted to be equal to 6.44 ± 0.33 mg/mc. The wear rate of the UHMWPE hemispherical cups of the ball-and-socket implants resulted in a wear rate of 29.1 ± 3.0 mg/mc when tested under the same loading conditions.

The VEHXPE cup and rotator of the MaltaHip resulted in wear rates equivalent to -0.99 ± 0.51 and -0.00 ± 0.20 mg/mc, respectively, as shown in Table 5.10 and Fig. 5.69b. Similar to the previous case, the negative wear rate values represent that the rate of fluid absorption was higher than the actual material removal rate, even after the data has been corrected to compensate for any fluid uptake which occurred from the loaded soak controls. The combined mean gravimetric wear rate of the VEHXPE polymeric components in the MaltaHip implants resulted to be equal to -1.00 ± 0.55 mg/mc. The mean gravimetric wear rate of VEHXPE hemispherical cups of the ball-and-socket design resulted in a wear rate of 4.5 ± 2.3 mg/mc when tested under the same loading conditions.

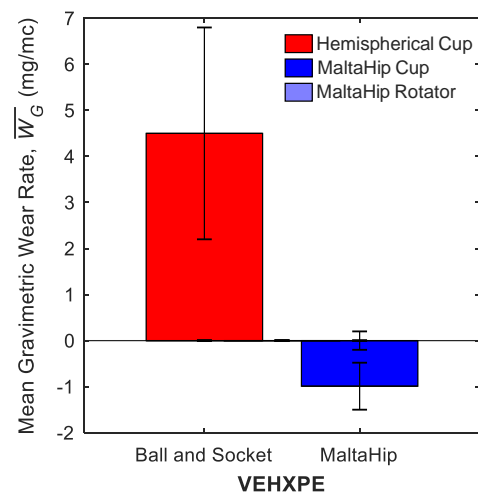
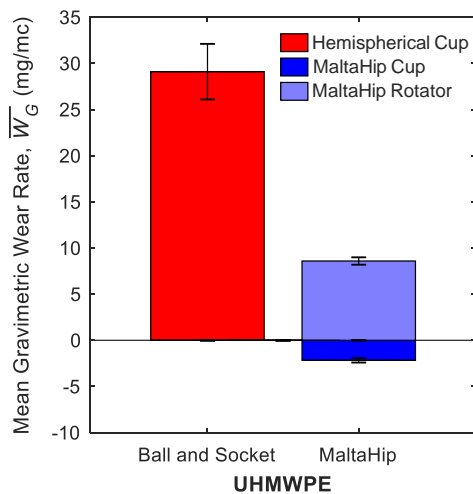
It can be observed that lower gravimetric wear rates were obtained with the MaltaHip design, as compared to the ball-and-socket design. The VEHXPE version of the MaltaHip resulted in the lowest wear. All components of the MaltaHip resulted in negative wear rate values, except for the UHMWPE rotator. This may be attributed to the small contact area of the component.

Table 5.7: Summary of steady-state gravimetric wear rates using UHMWPE bearing components. The steady-state gravimetric wear rate results of the individual polymeric components of the MaltaHip, as well as their combined effect (considered as a whole implant) are presented. All values have been corrected by the fluid absorption data obtained from the loaded soak control.

UHMWPE Gravimetric Wear Rates			
$\overline{W}_G \pm SE$ (Mean \pm Standard Error) [mg/mc]			
	MaltaHip Individual Components (n = 3)	MaltaHip Implants (n = 3)	Ball-and-Socket Implants (n = 33)
Cup	-2.17 \pm 0.24		
Rotator	8.59 \pm 0.40	6.44 \pm 0.33	29.1 \pm 3.0

Table 5.8: Summary of steady-state gravimetric wear rates using VEHXPE bearing components. The steady-state gravimetric wear rate results of the individual polymeric components of the MaltaHip, as well as their combined effect (considered as a whole implant) are presented. All values have been corrected by the fluid absorption data obtained from the loaded soak control.

VEHXPE Gravimetric Wear Rates			
$\overline{W}_G \pm SE$ (Mean \pm Standard Error) [mg/mc]			
	MaltaHip Individual Components (n = 3)	MaltaHip Implant (n = 3)	Ball-and-Socket Implant (n = 4)
Cup	-0.99 \pm 0.51		
Rotator	-0.00 \pm 0.20	-1.00 \pm 0.55	4.5 \pm 2.3



(a) Implants with UHMWPE soft-bearing components. (b) Implants with VEHXPE soft-bearing components.

Fig. 5.69: Mean gravimetric wear rates \overline{W}_G of the ball-and-socket, and MaltaHip implants that were wear tested at Endolab® Mechanical Engineering GmbH. Standard error (SE) values are also shown in the bar charts.

Hypothesis testing was conducted to determine whether the reduction in wear is statistically significant at a confidence interval (CI) of 99%. Due to the small sample size ($n=3$), the test statistic T_{st} was evaluated based on the t -distribution using a left-tailed test (shown in Fig. 5.70), and calculated as follows,

$$T_{st} = \frac{\mu - \mu_0}{SD/\sqrt{n}} = \frac{\mu - \mu_0}{SE} \quad \text{Eq. 5.1}$$

where, μ is the sample mean that is equivalent to the mean gravimetric wear rate $\overline{W_G}$, μ_0 is the population mean that is based on the mean gravimetric wear rate obtained from the ball-and-socket results, SD is the standard deviation of sample, and n is sample size and SE is the standard error of the mean. The test statistic T_{st} for UHMWPE and VEHXPE are computed as shown in Table 5.9. The significance level α is computed using $1-CI$, which equates to 0.01, whereas the statistical degrees of freedom are computed using $df = n - 1 = 2$. Therefore, the critical value $-t_\alpha = -t_{0.01} [df=2]$ is equal to -6.965 (using the standard statistical critical value of t table). Therefore, the rejection region for the hypothesis H_0 in Fig. 5.70 is located between $(-\infty, -6.965)$.

Table 5.9: Summary of the statistical data used to compute the test statistic T_{st} .

Statistical Parameters	Symbol	UHMWPE	VEHXPE
Sample size	n	3	3
Sample mean	μ	6.44	-1.00
Population mean	μ_0	29.10	4.50
Standard error mean	SE	0.33	0.66
Test statistic	T_{st}	-69.26	-8.30

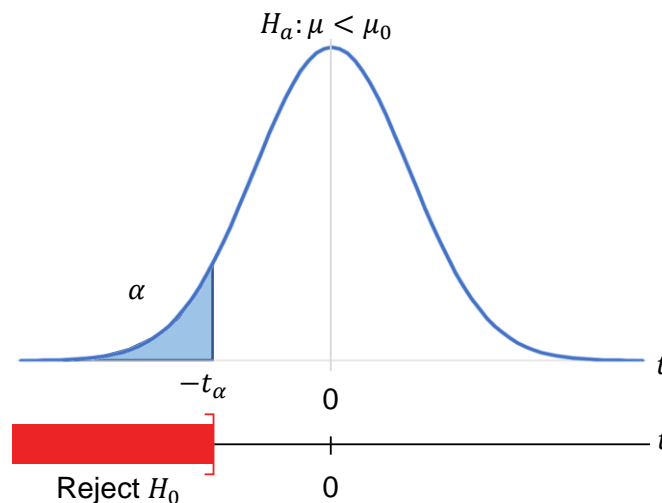


Fig. 5.70: The t -distribution (left-tailed test) used for the small sample size to determine whether H_0 should be rejected or not, for the case investigating $H_a: \mu < \mu_0$.

The test statistic T_{st} for UHMWPE and VEHXPE resulted to be equal to -69.260 and -8.30 , both of which are located in the H_0 rejection region. Therefore, in this context, at 99% confidence interval, the reduction in the mean gravimetric wear rate obtained for the MaltaHip is statistically significant when compared to the mean gravimetric wear rate for the ball-and-socket implants.

On further inspection, it was observed that the wear rate of the UHMWPE cup resulted to be lower than that of the VEHXPE cup. Nonetheless, it should be pointed out that the difference between the two components was not statistically significant at a confidence interval of 95% using the t -test.

5.7.3.2. Wear Results of the MaltaHip with UHMWPE Components

The gravimetric wear W_n of the MaltaHip UHMWPE cup and rotator at the first 0.5 million cycles, and at every 1.0 million cycles, are shown in Figs. 5.71 and 5.72, respectively. Furthermore, the gravimetric wear rates W_G according to the linear regression, and the mean gravimetric wear rate $\overline{W_G}$ during running-in and steady-state conditions (calculated using Eq. 3.8, p. 93) for the cup and rotator are provided in Tables 5.10 and 5.11, respectively. All results also include the gains in mass by the loaded soak control components, which were used to correct all the data for any fluid uptake using Eq. 3.6 (p. 93). The combined gravimetric wear and gravimetric wear rates for each MaltaHip UHMWPE implant (consisting of the cup and rotator) are presented in Fig. 5.73 and Table 5.12.

The gravimetric wear W_n for the flexor and abductor components used in the MaltaHip UHMWPE implant at 3.0 and 5.0 million cycles are shown in Figs. 5.74 and 5.75, respectively. The corresponding gravimetric wear rates W_G , and the mean gravimetric wear rate $\overline{W_G}$ for the flexor and abductor components (used in the MaltaHip UHMWPE implant) are presented in Tables 5.13 and 5.14. Stainless steel components possess a longer running-in phase, due to their higher wear resistance. Due to the limited data that was available, no clear distinction could have been made between running-in and steady-state wear. Therefore, the tribological behaviour of the stainless steel components is collectively represented using linear regression.

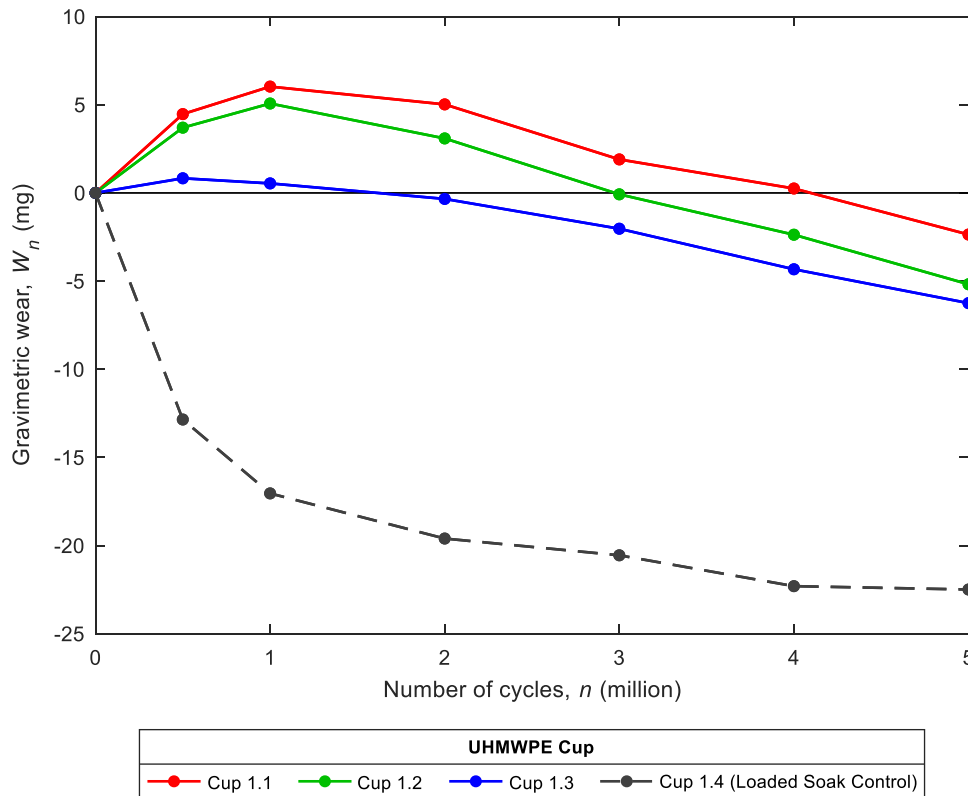


Fig. 5.71: Wear vs. number of cycles of the MaltaHip UHMWPE cup components. Results produced by Endolab®.

Table 5.10: The mean gravimetric wear rate (mg/million cycles) is computed during the running-in and steady-state periods, and the overall duration, based on linear regression results of MaltaHip UHMWPE cups 1.1 – 1.3. The rate of fluid absorption (mg/million cycles) is also presented based on the loaded soak control MaltaHip UHMWPE cup 1.4. Note that R^2 represents the regression coefficient, whereas SE represents the standard error.

Data Analysed	Data Format	Component	Gravimetric Wear Rate [mg/million cycles]		
			Running-In 0 – 1 million cycles	Steady-State 1 – 5 million cycles	Overall 0 – 5 million cycles
Gravimetric Wear Rate	$W_n (R^2)$	MaltaHip UHMWPE Cup 1.1	6.03 (0.93)	-2.16 (0.98)	-0.99 (0.36)
		1.2	5.07 (0.93)	-2.60 (1.00)	-1.52 (0.62)
		1.3	0.54 (0.41)	-1.76 (0.98)	-1.37 (0.90)
Mean Wear Rate	$W_G \pm SE$	1.1, 1.2, 1.3	3.88 ± 1.69	- 2.17 ± 0.24	-1.30 ± 0.16
Fluid Absorption	$S_n (R^2)$	Loaded soak control 1.4	-17.04 (0.92)	-1.36 (0.93)	-3.43 (0.64)

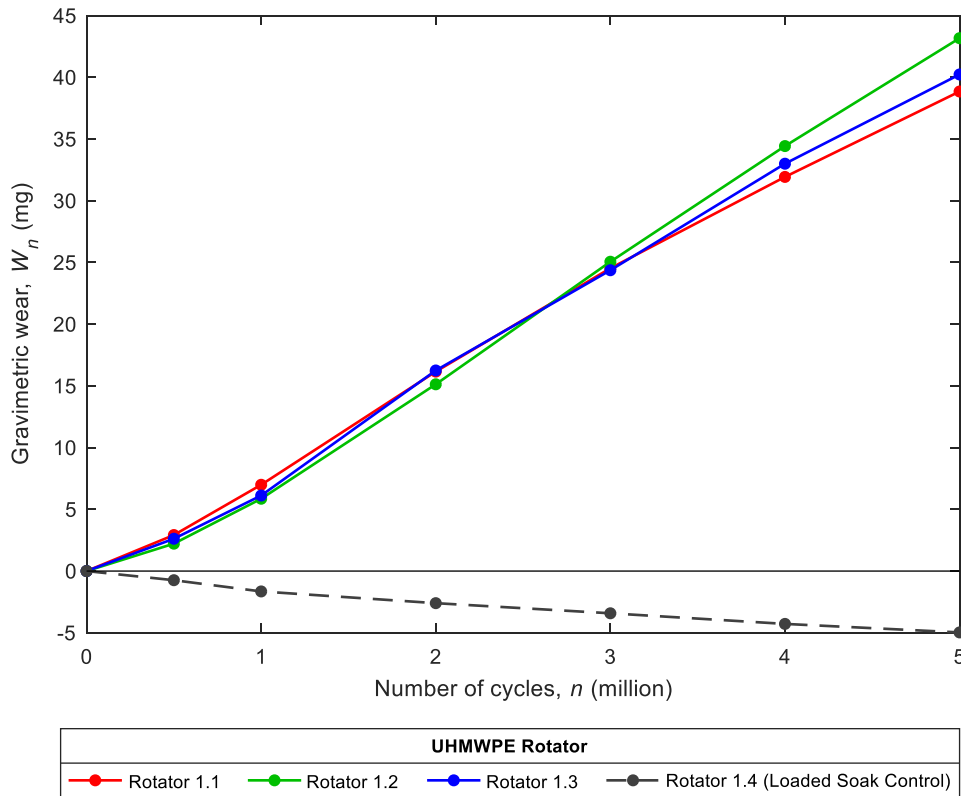


Fig. 5.72: Wear vs. number of cycles of the MaltaHip UHMWPE rotator components. Results produced by Endolab®.

Table 5.11: The mean gravimetric wear rate (mg/million cycles) is computed during the running-in and steady-state periods, and the overall duration, based on linear regression results of MaltaHip UHMWPE rotators 1.1 – 1.3. The rate of fluid absorption (mg/million cycles) is also presented based on the loaded soak control MaltaHip UHMWPE rotator 1.4. Note that R^2 represents the regression coefficient, whereas SE represents the standard error.

Data Analysed	Data Format	Component	Gravimetric Wear Rate [mg/million cycles]		
			Running-In 0 – 1 million cycles	Steady-State 1 – 5 million cycles	Overall 0 – 5 million cycles
Gravimetric Wear Rate	$W_n (R^2)$	1.1	6.99 (0.99)	7.95 (1.00)	8.01 (1.00)
		1.2	5.86 (0.98)	9.32 (1.00)	8.95 (1.00)
		1.3	6.12 (0.99)	8.50 (1.00)	8.35 (1.00)
Mean Wear Rate	$W_G \pm SE$	1.1, 1.2, 1.3	6.32 ± 0.34	8.59 ± 0.40	8.43 ± 0.27
Fluid Absorption	$S_n (R^2)$	Loaded soak control 1.4	-1.65 (1.00)	-0.83 (1.00)	-0.97 (0.98)

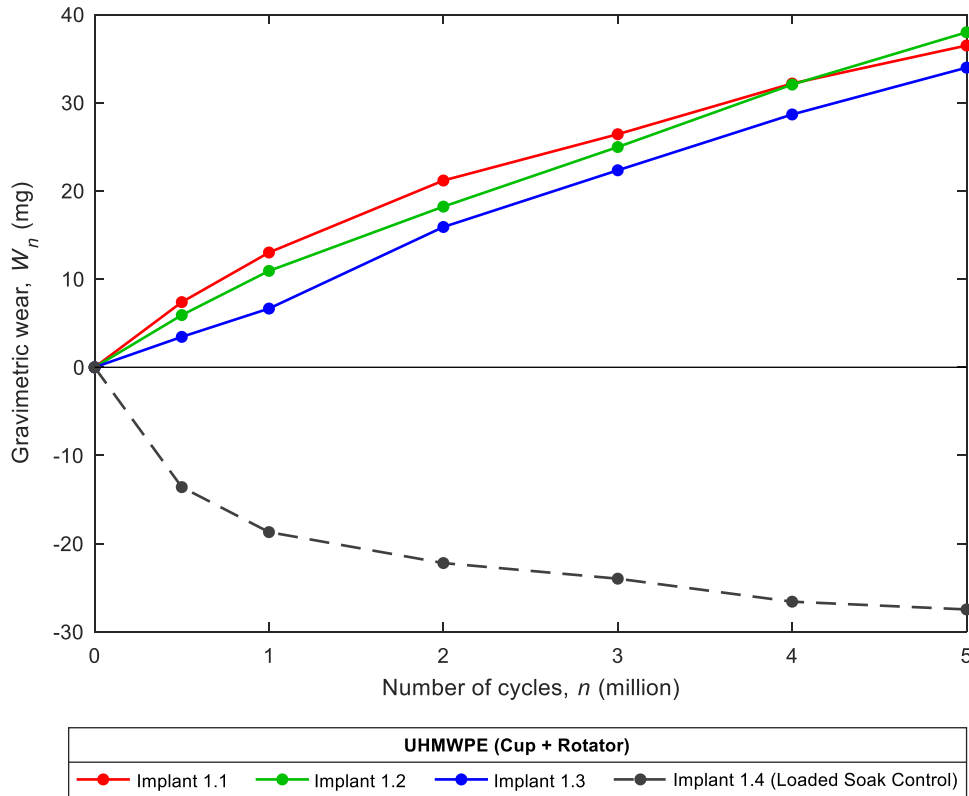


Fig. 5.73 Wear vs. number of cycles of the MaltaHip UHMWPE cup and rotator components. Results produced by Endolab®.

Table 5.12: The mean gravimetric wear rate (mg/million cycles) is computed during the running-in and steady-state periods, and the overall duration, based on linear regression results of MaltaHip UHMWPE cups and rotators 1.1 – 1.3. The rate of fluid absorption (mg/million cycles) is also presented based on the loaded soak control MaltaHip UHMWPE cup and rotator 1.4. Note that R^2 represents the regression coefficient, whereas SE represents the standard error.

Data Analysed	Data Format	Component	Gravimetric Wear Rate [mg/million cycles]		
			Running-In 0 – 1 million cycles	Steady-State 1 – 5 million cycles	Overall 0 – 5 million cycles
Gravimetric Wear Rate	$W_n (R^2)$	1.1	13.02 (0.99)	5.79 (0.99)	7.02 (0.96)
		1.2	10.93 (1.00)	6.80 (0.99)	7.42 (0.99)
		1.3	6.66 (1.00)	6.74 (0.99)	6.98 (0.99)
Mean Wear Rate	$W_G \pm SE$	1.1, 1.2, 1.3	10.20 ± 1.87	6.44 ± 0.33	7.14 ± 0.14
Fluid Absorption	$S_n (R^2)$	Loaded soak control 1.4	-18.69 (0.94)	-2.19 (0.96)	-4.40 (0.73)

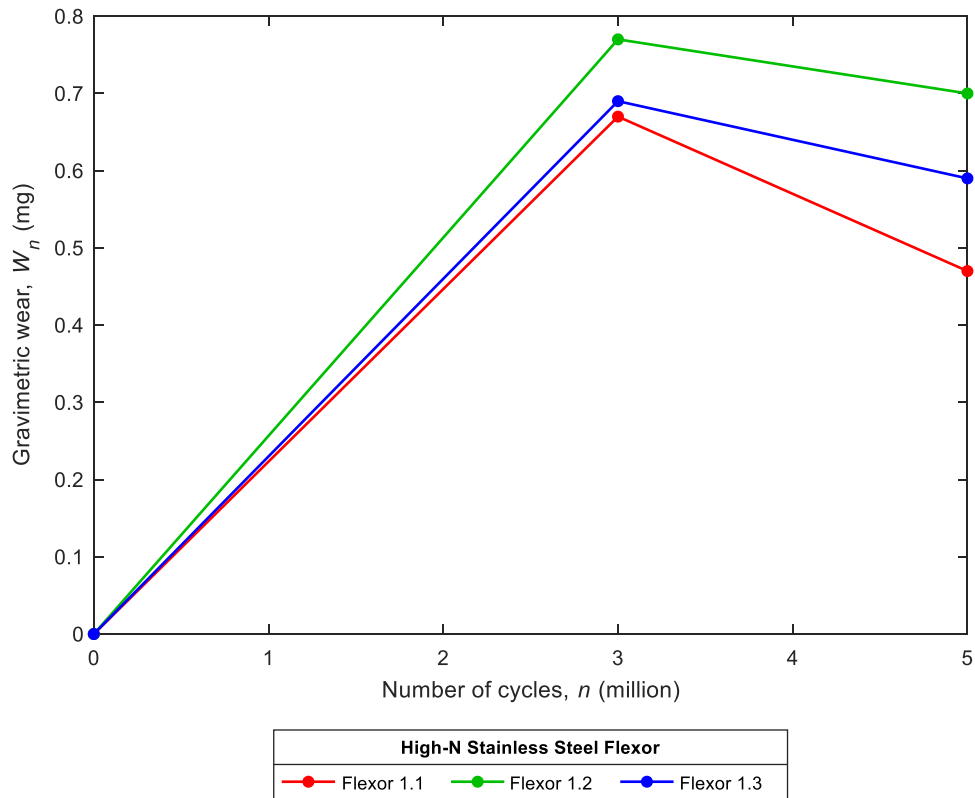


Fig. 5.74: Wear vs. number of cycles of the MaltaHip high-N austenitic stainless steel flexor components. Results produced by Endolab®.

Table 5.13: The mean gravimetric wear rate (mg/million cycles) is computed based on linear regression results of MaltaHip High-N stainless steel flexors 1.1 – 1.3.

Component	0.0 – 5.0 million cycles	
	Gravimetric Wear Rate Linear regression (Regression Coefficient) $W_G (R^2)$ [mg/million cycles]	Mean Wear Rate Mean \pm Standard Error $\bar{W}_G \pm SE$ [mg/million cycles]
MaltaHip High-N Stainless Steel Flexor [Implant No.]		
1.1	0.10 (0.58)	0.13 \pm 0.01
1.2	0.15 (0.78)	
1.3	0.13 (0.73)	

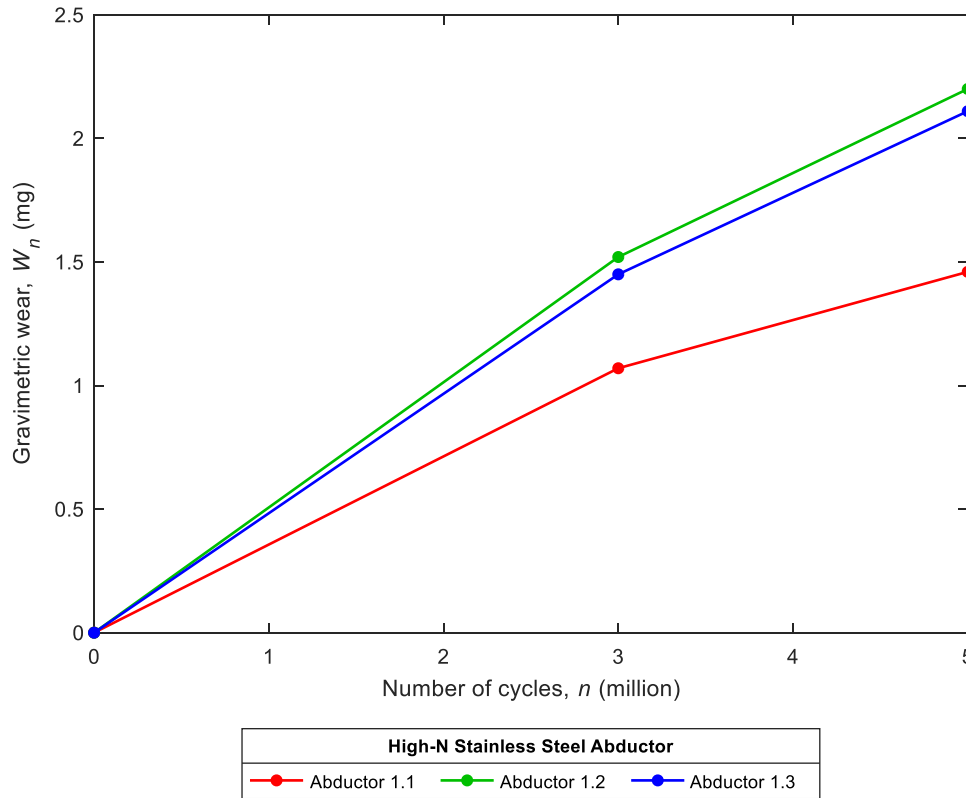


Fig. 5.75: Wear vs. number of cycles of the MaltaHip high-N austenitic stainless steel abductor components. Results produced by Endolab®.

Table 5.14: The mean gravimetric wear rate (mg/million cycles) is computed based on linear regression results of MaltaHip high-N stainless steel abductors 1.1 – 1.3.

Component MaltaHip High-N Stainless Steel Abductor [Implant No.]	0.0 – 5.0 million cycles	
	Gravimetric Wear Rate Linear regression (Regression Coefficient) $W_G (R^2)$ [mg/million cycles]	Mean Wear Rate Mean \pm Standard Error $\overline{W}_G \pm SE$ [mg/million cycles]
1.1	0.30 (0.98)	0.39 \pm 0.05
1.2	0.45 (0.99)	
1.3	0.43 (0.99)	

5.7.3.3. Wear Results of the MaltaHip with VEHXPE Components

The gravimetric wear W_n of the MaltaHip VEHXPE cup and rotator at the first 0.5 million cycles, and at every 1.0 million cycles are shown in Figs. 5.76 and 5.77, respectively. Furthermore, the gravimetric wear rates W_G according to the linear regression, and the mean gravimetric wear rate $\overline{W_G}$ during running-in and steady-state conditions (calculated using Eq. 3.8, p. 93) for the cup and rotator are provided in Tables 5.16 and 5.17, respectively. All results also include the gains in mass by the loaded soak control components, which were used to correct all the data for any fluid uptake using Eq. 3.6 (p. 93). The combined gravimetric wear and gravimetric wear rates for each MaltaHip VEHXPE implant (consisting of the cup and rotator) are presented in Fig. 5.78 and Table 5.17, respectively.

The gravimetric wear W_n for the flexor and abductor components used in the MaltaHip VEHXPE implant at 3.0 and 5.0 million cycles are shown in Figs. 5.79 and 5.80, respectively. The corresponding gravimetric wear rates W_G , and the mean gravimetric wear rate $\overline{W_G}$ for the flexor and abductor components (used in the MaltaHip VEHXPE implant) are presented in Tables 5.18 and 5.19. Stainless steel components possess a longer running-in phase, due to their higher wear resistance. Due to the limited data that was available, no clear distinction could have been made between running-in and steady-state wear. Therefore, the tribological behaviour of the stainless steel components is collectively represented using linear regression.

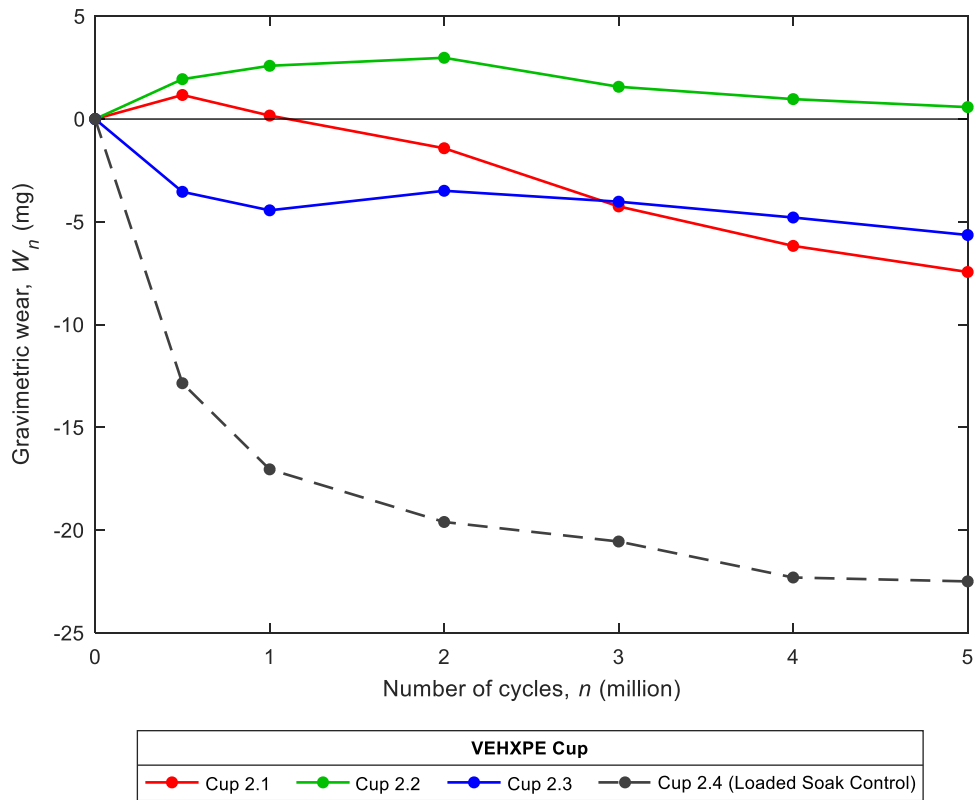


Fig. 5.76: Wear vs. number of cycles of the MaltaHip VEHXPE cup components. Results produced by Endolab®.

Table 5.15: The mean gravimetric wear rate (mg/million cycles) is computed during the running-in and steady-state periods, and the overall duration, based on linear regression results of MaltaHip VEHXPE cups 2.1 – 2.3. The rate of fluid absorption (mg/million cycles) is also presented based on the loaded soak control MaltaHip VEHXPE cup 2.4.

Note that R^2 represents the regression coefficient, whereas SE represents the standard error.

Data Analysed	Data Format	Component	Gravimetric Wear Rate [mg/million cycles]		
			Running-In 0 – 1 million cycles	Steady-State 1 – 5 million cycles	Overall 0 – 5 million cycles
Gravimetric Wear Rate	$W_n (R^2)$	2.1	0.17 (0.02)	-2.00 (0.98)	-1.77 (0.95)
		2.2	2.59 (0.92)	-0.60 (0.86)	-0.12 (0.04)
		2.3	-4.44 (0.89)	-0.37 (0.52)	-0.73 (0.57)
Mean Wear Rate	$W_G \pm SE$	2.1, 2.2, 2.3	-0.56 ± 2.06	-0.99 ± 0.51	-0.87 ± 0.48
Fluid Absorption	$S_n (R^2)$	Loaded soak control 2.4	-15.75 (0.90)	-1.87 (0.97)	-3.65 (0.72)

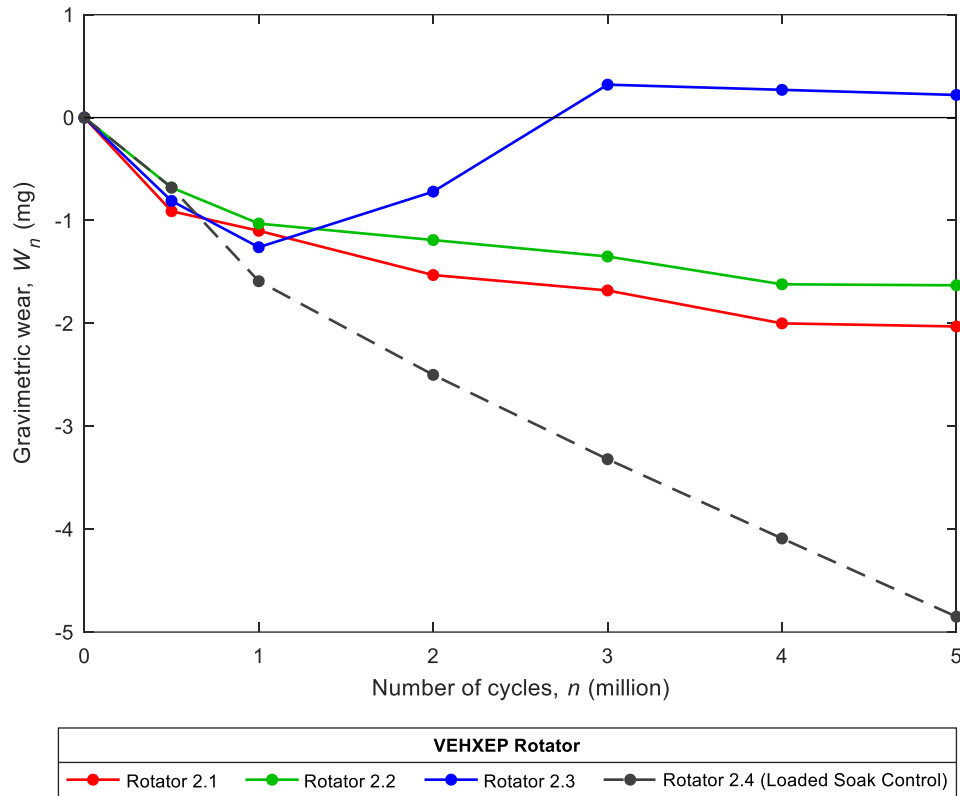


Fig. 5.77: Wear vs. number of cycles of the MaltaHip VEHXPE rotator components. Results produced by Endolab®.

Table 5.16: The mean gravimetric wear rate (mg/million cycles) is computed during the running-in and steady-state periods, and the overall duration, based on linear regression results of MaltaHip VEHXPE rotators 2.1 – 2.3. The rate of fluid absorption (mg/million cycles) is also presented based on the loaded soak control MaltaHip VEHXPE rotator 2.4. Note that R^2 represents the regression coefficient, whereas SE represents the standard error.

Data Analysed	Data Format	Component	Gravimetric Wear Rate [mg/million cycles]		
			Running-In 0 – 1 million cycles	Steady-State 1 – 5 million cycles	Overall 0 – 5 million cycles
Gravimetric Wear Rate	$W_n (R^2)$	2.1	-1.10 (0.88)	-0.23 (0.93)	-0.35 (0.83)
		2.2	-1.03 (0.97)	-0.16 (0.95)	-0.28 (0.81)
		2.3	-1.26 (0.97)	0.40 (0.76)	0.21 (0.38)
Mean Wear Rate	$W_G \pm SE$	2.1, 2.2, 2.3	-1.13 ± 0.07	0.00 ± 0.20	-0.14 ± 0.18
Fluid Absorption	$S_n (R^2)$	Loaded soak control 2.4	-1.59 (0.99)	-0.81 (0.99)	-0.95 (0.98)

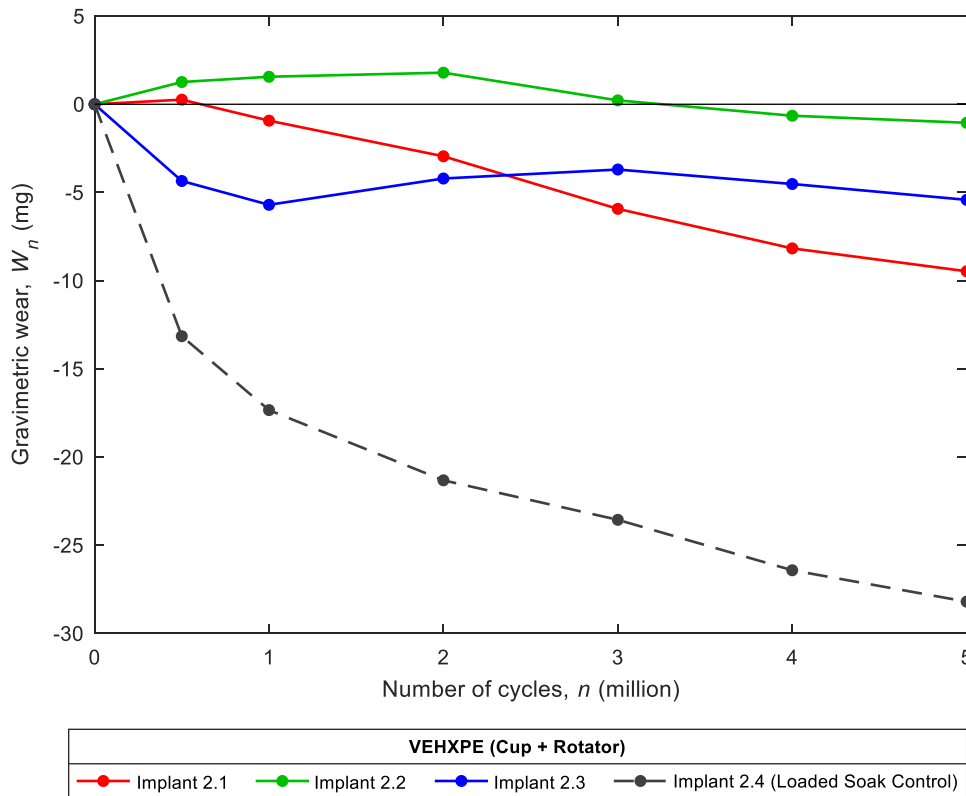


Fig. 5.78: Wear vs. number of cycles of the MaltaHip VEHXPE cup and rotator components. Results produced by Endolab®.

Table 5.17: The mean gravimetric wear rate (mg/million cycles) is computed during the running-in and steady-state periods, and the overall duration, based on linear regression results of MaltaHip VEHXPE cups and rotators 2.1 – 2.3. The rate of fluid absorption (mg/million cycles) is also presented based on the loaded soak control MaltaHip VEHXPE cup and rotator 2.4. Note that R^2 represents the regression coefficient, whereas SE represents the standard error.

Data Analysed	Data Format	Component	Gravimetric Wear Rate [mg/million cycles]		
			Running-In 0 – 1 million cycles	Steady-State 1 – 5 million cycles	Overall 0 – 5 million cycles
Gravimetric Wear Rate	$W_n (R^2)$	2.1	-0.93 (0.55)	-2.23 (0.99)	-2.12 (0.98)
		2.2	1.56 (0.89)	-0.77 (0.90)	-0.40 (0.45)
		2.3	-5.7 (0.92)	0.03 (0.00)	-0.52 (0.26)
Mean Wear Rate	$W_G \pm SE$	2.1, 2.2, 2.3	-2.73 ± 1.50	-1.00 ± 0.55	-1.01 ± 0.55
Fluid Absorption	$S_n (R^2)$	Loaded soak control 2.4	-17.34 (0.91)	-2.68 (0.98)	-4.59 (0.78)

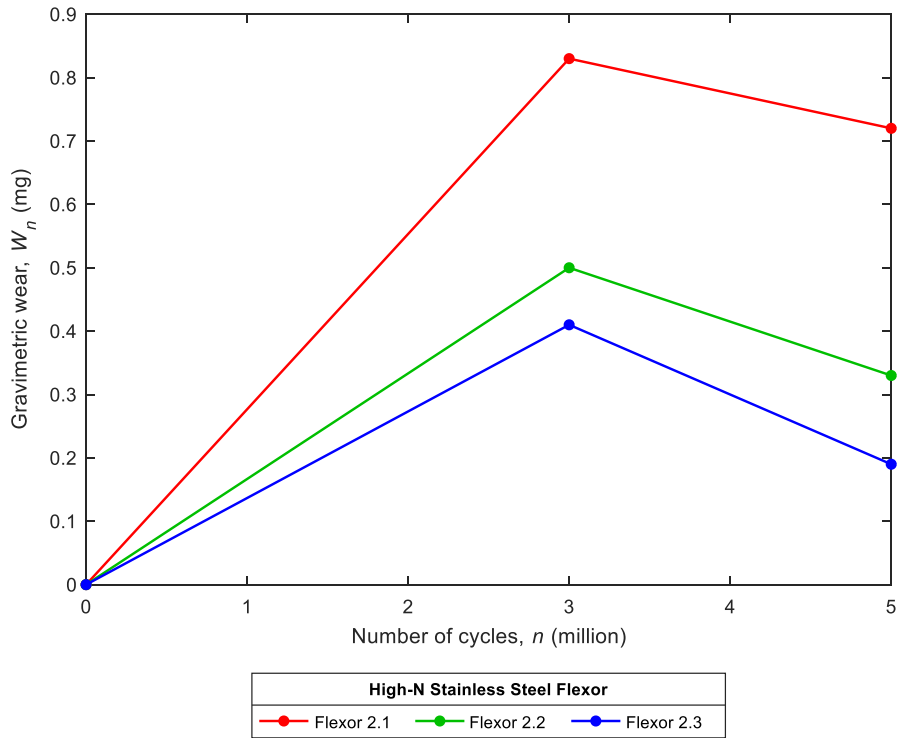


Fig. 5.79: Wear vs. number of cycles of the MaltaHip high-N stainless steel flexor components. Results produced by Endolab®.

Table 5.18: The mean gravimetric wear rate (mg/million cycles) is computed based on linear regression results of MaltaHip High-N Stainless Steel Flexors 2.1 – 2.3.

Component	0.0 – 5.0 million cycles	
	Gravimetric Wear Rate Linear regression (Regression Coefficient) $W_G (R^2)$ [mg/million cycles]	Mean Wear Rate Mean \pm Standard Error $\overline{W_G} \pm SE$ [mg/million cycles]
MaltaHip High-N Stainless Steel Flexor [Implant No.]		
2.1	0.15 (0.74)	0.09 \pm 0.03
2.2	0.07 (0.54)	
2.3	0.05 (0.32)	

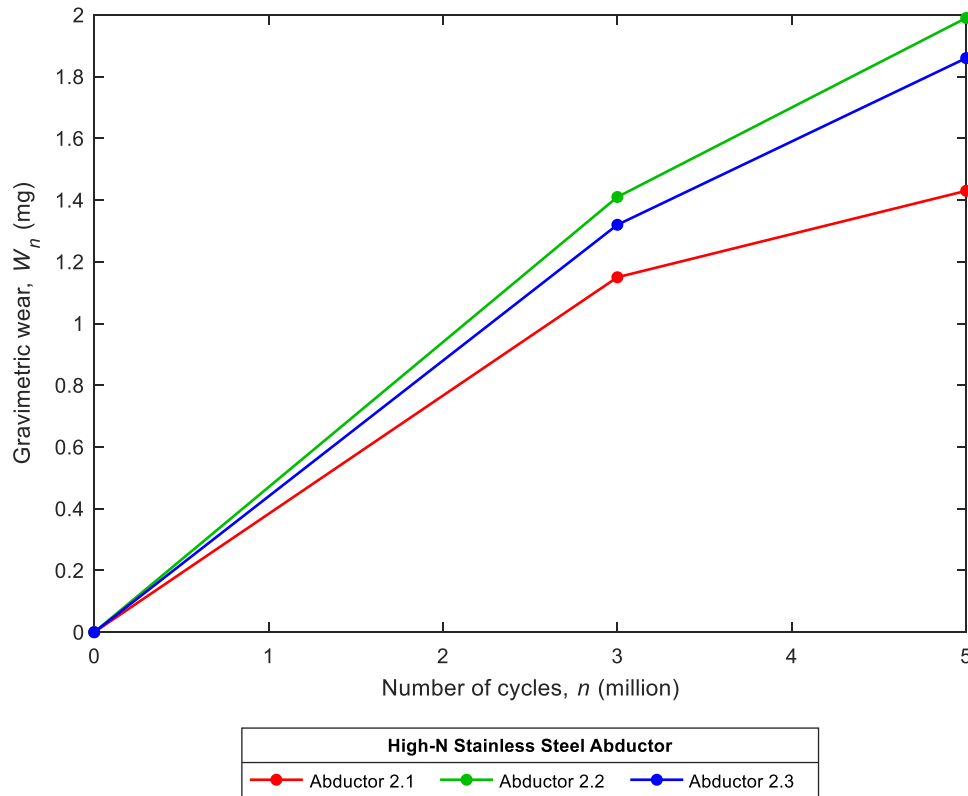


Fig. 5.80: Wear vs. number of cycles of the MaltaHip high-N stainless steel abductor components. Results produced by Endolab®.

Table 5.19: The mean gravimetric wear rate (mg/million cycles) is computed based on linear regression results of MaltaHip high-N stainless steel abductors 2.1 – 2.3.

Component	0.0 – 5.0 million cycles	
MaltaHip High-N Stainless Steel Abductor [Implant No.]	Gravimetric Wear Rate Linear regression (Regression Coefficient) $W_G (R^2)$ [mg/million cycles]	Mean Wear Rate Mean \pm Standard Error $\overline{W}_G \pm SE$ [mg/million cycles]
2.1	0.29 (0.95)	0.36 \pm 0.03
2.2	0.40 (0.99)	
2.3	0.38 (0.99)	

5.7.4. Contact Areas

5.7.4.1. Introduction

The contact areas of the MaltaHip for the UHMWPE and VEHXPE components are marked in light red in Figs. 5.81 to 5.10. The contact areas were inspected and marked at 1.0 and 5.0 million cycles. As the contact area is highly dependent on the geometrical design, similar contact areas have been achieved between the UHMWPE and VEHXPE components. Hence, the results for both materials are presented in the same section. Furthermore, it can be noted that, highly reproduceable results were achieved across the three repeat samples. The increased contact area over the number of cycles demonstrates that the conformity of the components was improved with the increasing number of cycles. The increased conformity is likely to be attributed to wear processes coupled with minor creep effects. High wear rates occurred during the running-in process of the prosthesis (up to approximately 1 million cycles), whereas reduced wear rates occurred at later stages which may be attributed to the increased conformity of the components, representing the steady-state wear.

5.7.4.2. Acetabular Cups

Considering the load bearing surface of the MaltaHip cups (Figs. 5.81 and 5.82), it can be observed that adequate contact with the flexor component has been achieved, even during the running-in process. It can be observed that MaltaHip cup 1.3 exhibited a slightly smaller contact area during the first 1.0 million cycles, compared to MaltaHip cups 1.1 and 1.2, which may be attributed to minor deviations caused during machining⁵⁷. In fact, this cup resulted in the lowest overall wear, even during the initial stages of the wear test, when compared to the other UHMWPE cups. However, by 5.0 million cycles, the contact area of cup 1.3 achieves a similar shape to those exhibited by the other cups.

It can be observed that contact is primarily made at the curved surface of the partial cylinder (label A), whereas a sudden reduction in contact is observed at the region with the filleted edge section (label B). The non-load bearing surface of the MaltaHip cup (Figs. 5.83 and 5.84) exhibits minimal contact at label C, which is a highly desirable characteristic at this region to minimize wear, as this surface is only intended to constrain the flexor motion.

⁵⁷ UHMWPE and polymers alike are inherently more difficult to machine than metals due to their viscoelastic-viscoplastic behavior and high sensitivity to temperature changes.

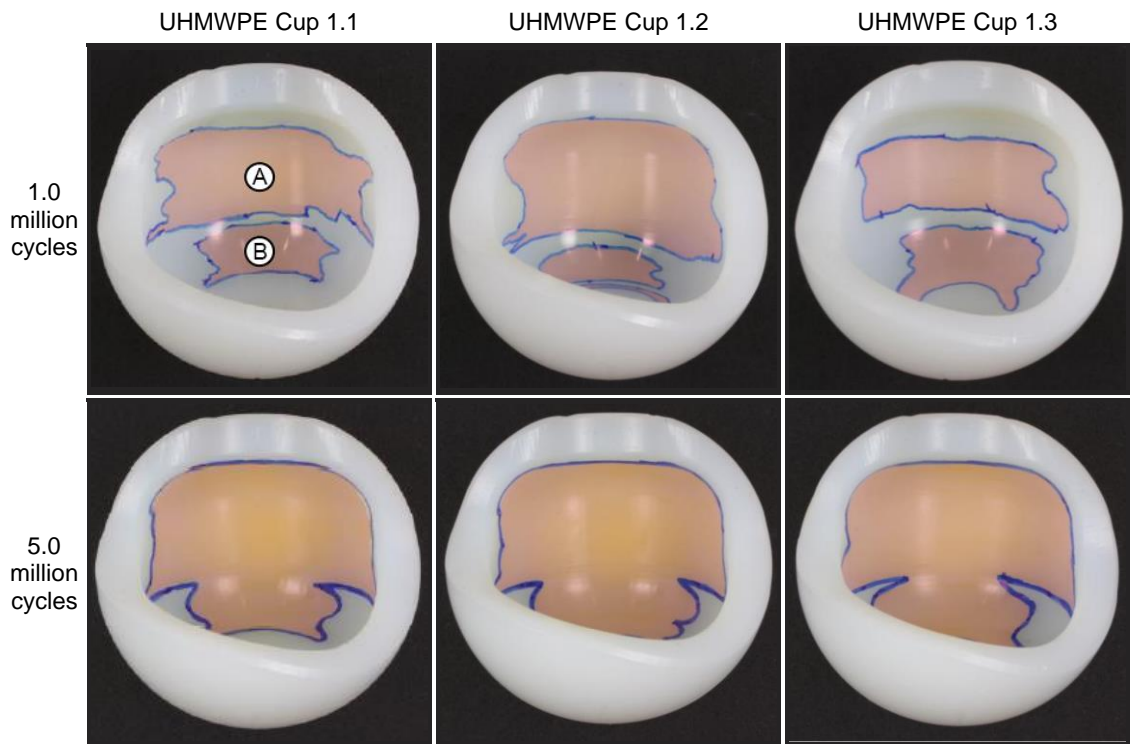


Fig. 5.81: Load bearing surface of the UHMWPE MaltaHip cups showing extensive contact (inferior view). Results produced by Endolab®.

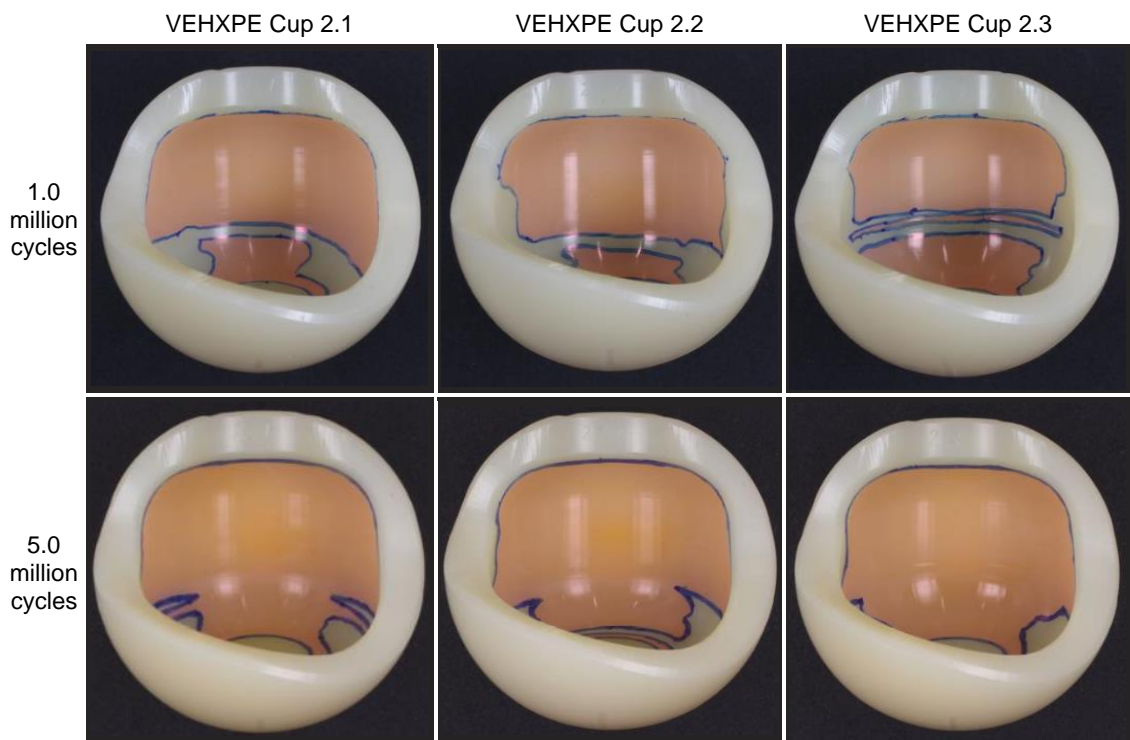


Fig. 5.82: Load bearing surface of the VEHXPE MaltaHip cups showing extensive contact (inferior view). Results produced by Endolab®.

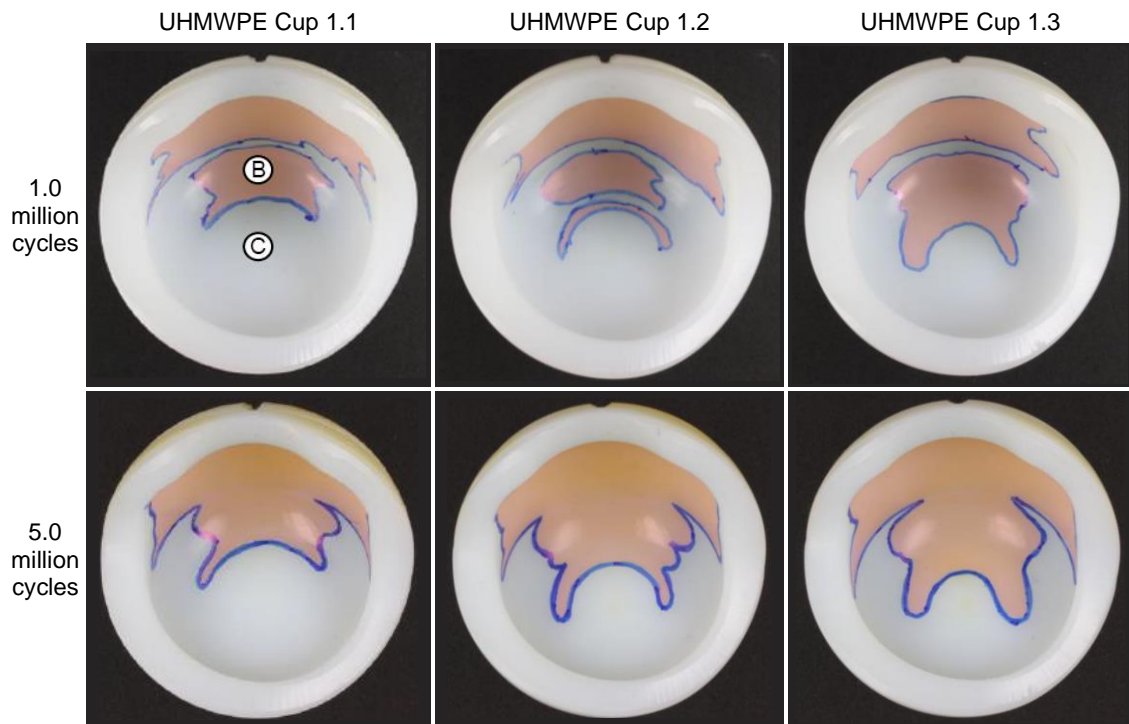


Fig. 5.83: Non-load bearing surface of the UHMWPE MaltaHip cups showing minimal contact (lateral view). Results produced by Endolab®.

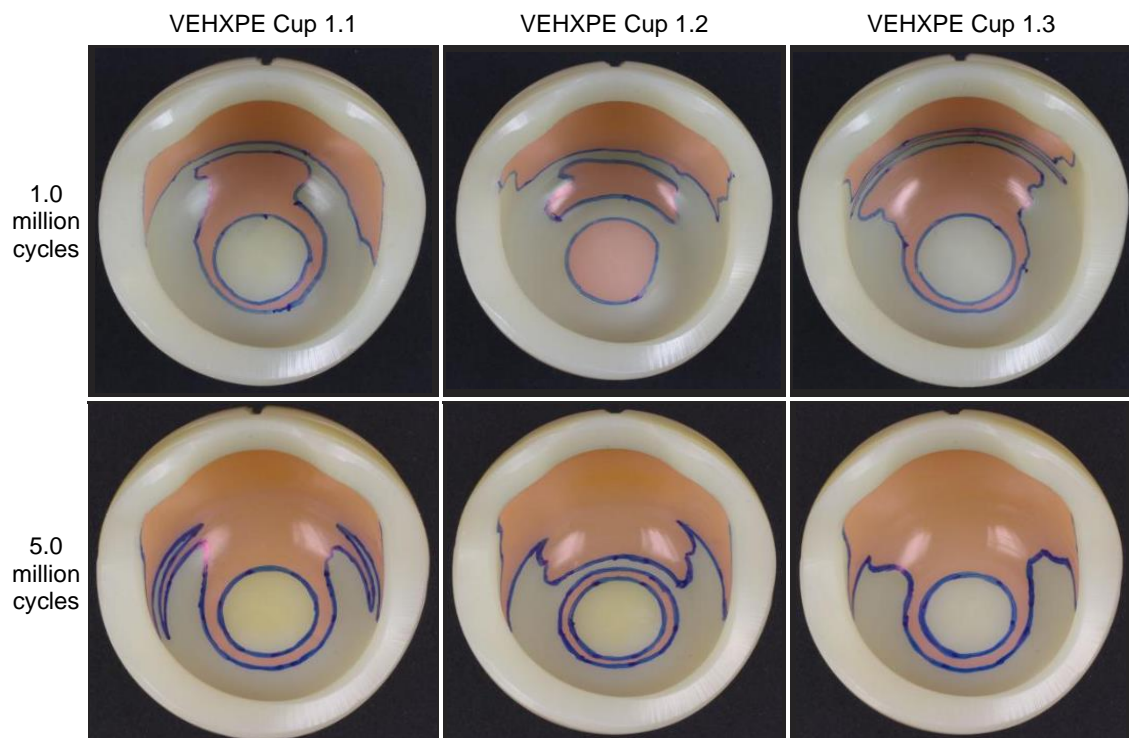


Fig. 5.84: Non-load bearing surface of the VEHXPE MaltaHip cups showing minimal contact (lateral view). Results produced by Endolab®.

5.7.4.3. Rotator External Surface

The contact areas at the second articulation of the MaltaHip on the external surface of the rotator are shown in Figs. 5.85 to 5.93. The superior views of the rotators shown in Figs. 5.85 and 5.75, indicate that the majority of the load transfer occurred at the tapered section (label E), rather than the flat surface (label D) as contact is not thorough at the latter region (with the exception of rotator 2.2). In fact, only minor increments in the contact area at label D at 5.0 million cycles can be observed.

Figs. 5.87 and 5.88 provide the medial view of the rotator. This tapered region is also labelled E in the illustrations, as it represents the same tapered surface that was mentioned earlier in Fig. 5.85. It can be observed that no contact is made at the lower end of the taper in the region labelled E (Figs. 5.87 and 5.88). The absence of contact at label D (Fig. 5.85), E (Fig. 5.87) and F (Fig. 5.87) at the medial region may suggest that the component may become slightly abducted from its original position during wear testing, as indicated in Fig. 5.89. Only minor increments are observed in the contacting area in the medial area after 5.0 million cycles.

Figs. 5.90 and 5.91 represent the anterior region, whereas Figs. 5.92 and 5.93 represent the posterior region of the rotator. The curved surface of the partial cylinder of the anterior and posterior regions are labelled G and H, respectively. A thin band of contact area can be observed on both cases, which is undesirable as it does not provide any significant load bearing capabilities. Although the exact reason for the generation of this contact area is not known, two theories are proposed. In the first theory, it is postulated that the rotator may become slightly widened during milling of the internal surface (on the order of 0.01 mm), as shown in Fig. 5.44b (p. 169). In the second theory, it is postulated that the small flats at the inner rotator surface generate high radial torsion when transferring torsion. Due to high stiction effects which are generated during the twin-peak loads at each gait cycle, high torsional moments cause the outer surfaces of the rotator to become widened. Again, the contacting area increases only marginally after being inspected at 5.0 million cycles, and therefore wear is postulated to be minimal from this region.

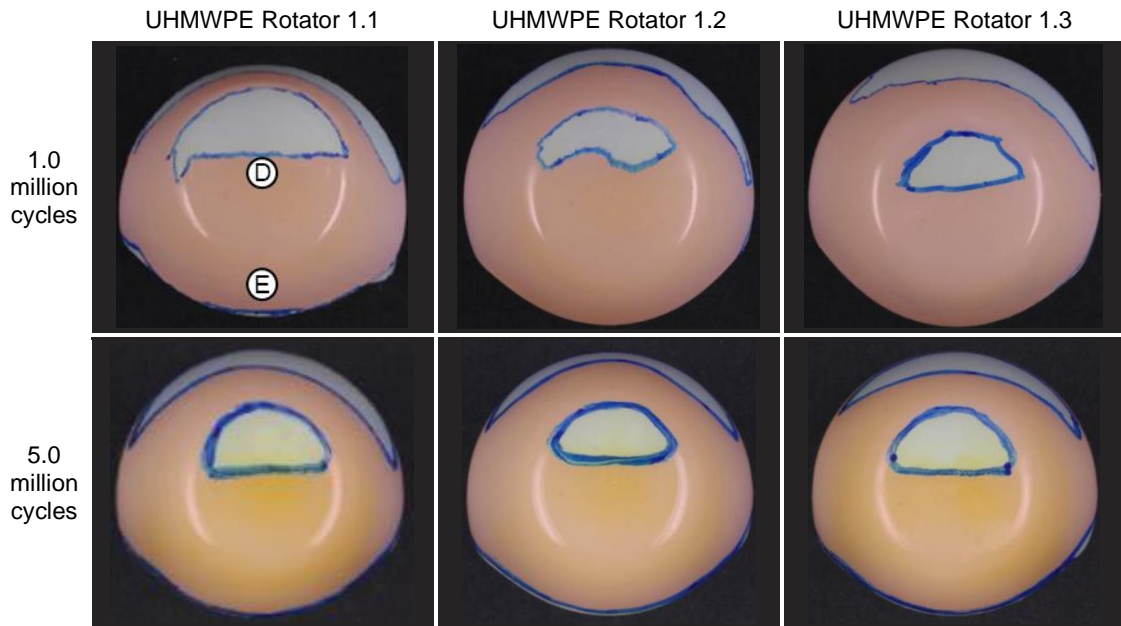


Fig. 5.85: Load bearing surface of the UHMWPE rotator illustrate extensive contact with the internal surface of the flexor (superior view). Results produced by Endolab®.

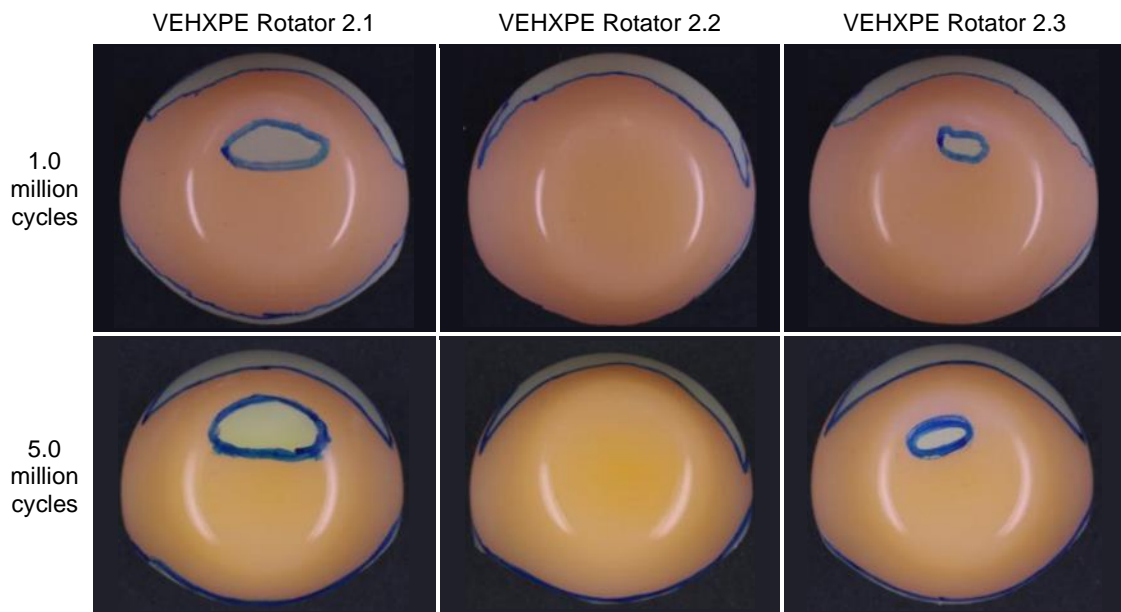


Fig. 5.86: Load bearing surface of the VEHXPE rotator illustrate nearly complete contact with the internal surface of the flexor (superior view). Results produced by Endolab®.

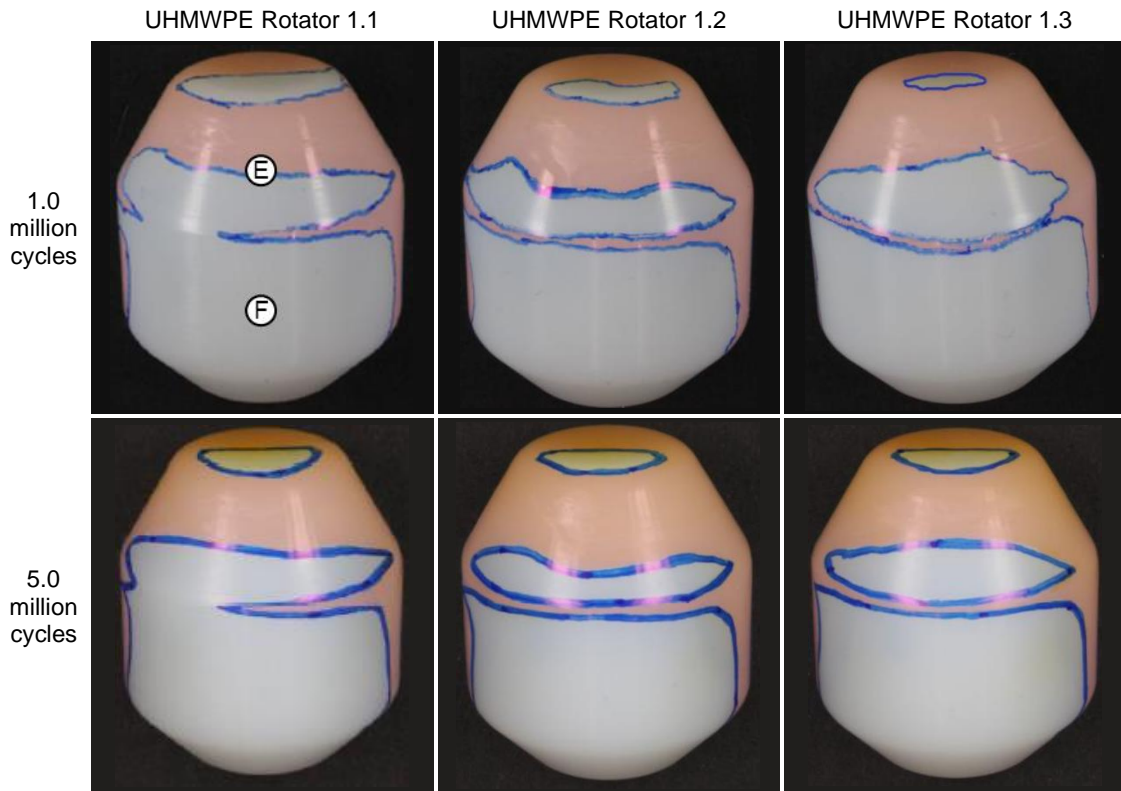


Fig. 5.87: Medial view of the UHMWPE rotator illustrating extensive contact at the tapered section (load bearing surface) with the internal surface of the flexor, and minimal contact at the cylindrical section (non-load bearing surface) with the internal surface of the flexor. Results produced by Endolab®.

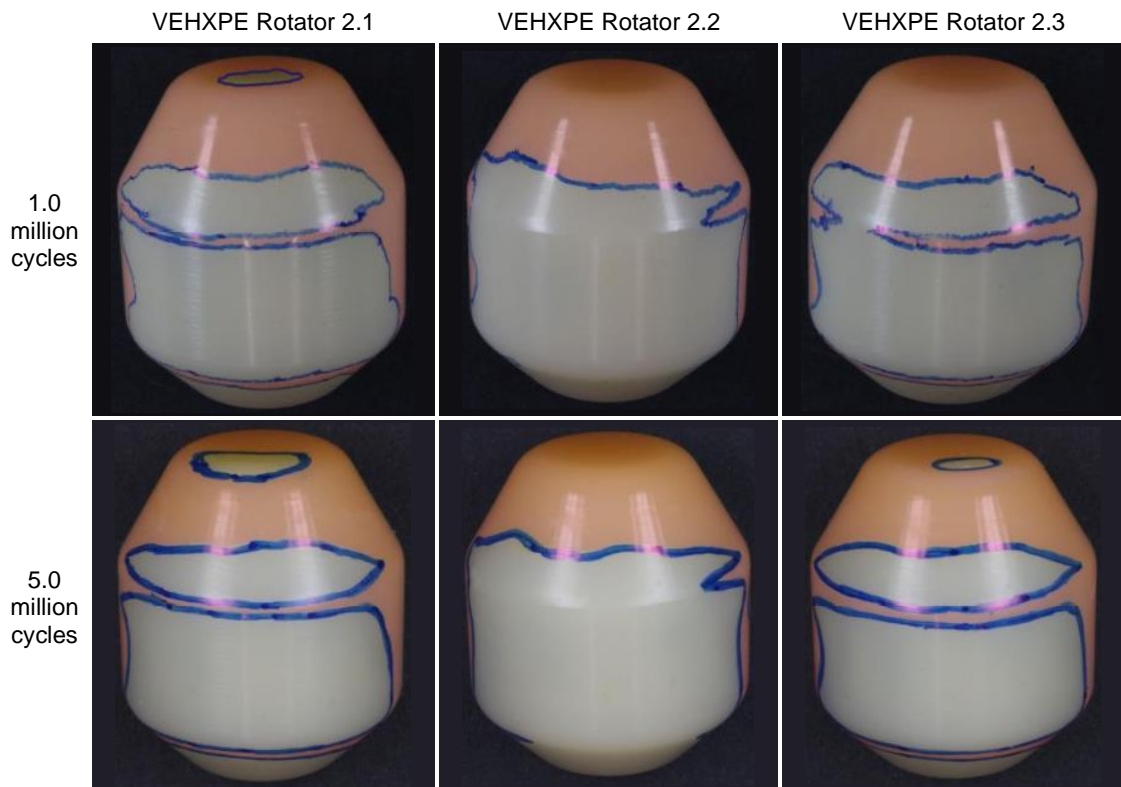


Fig. 5.88: Medial view of the VEHXPE rotator illustrating extensive contact at the tapered section (load bearing surface) with the internal surface of the flexor, and minimal contact at the cylindrical section (non-load bearing surface) with the internal surface of the flexor. Results produced by Endolab®.

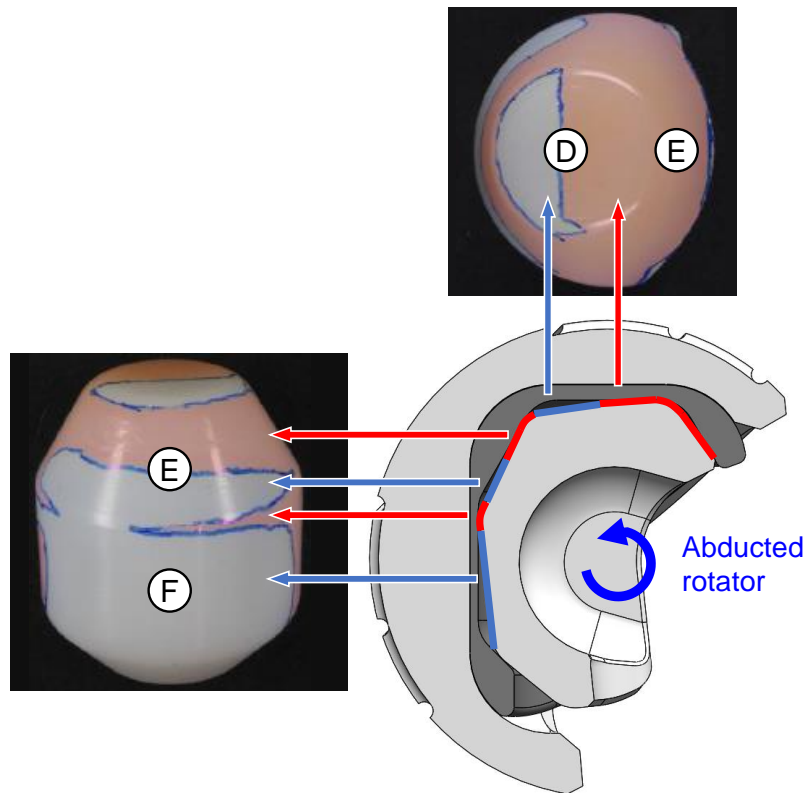


Fig. 5.89: Possible abduction rotation, causing contacting and non-contacting regions (Scale of abduction rotation effect is exaggerated for ease of visualisation).

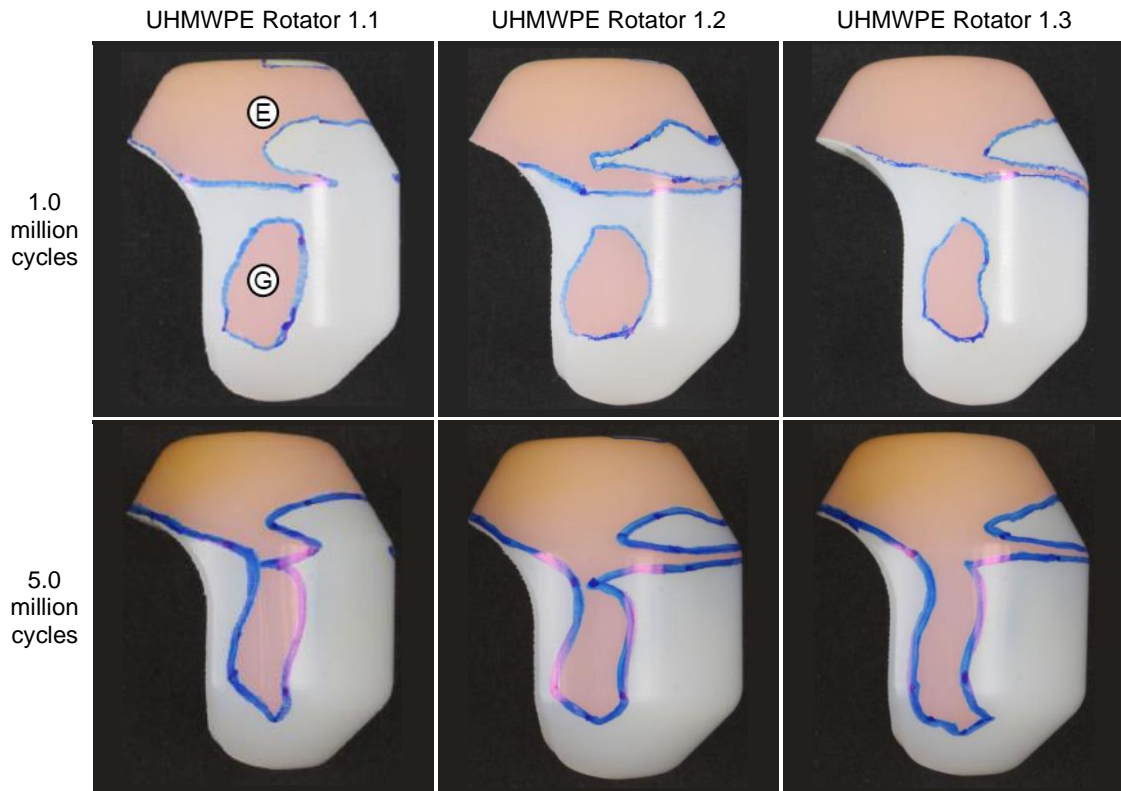


Fig. 5.90: Anterior view of the UHMWPE rotator component illustrating extensive contact at the taper section (load bearing surface) and minimal contact at the cylindrical section (non-load bearing surface) with the internal surface of the flexor. Results produced by Endolab®.

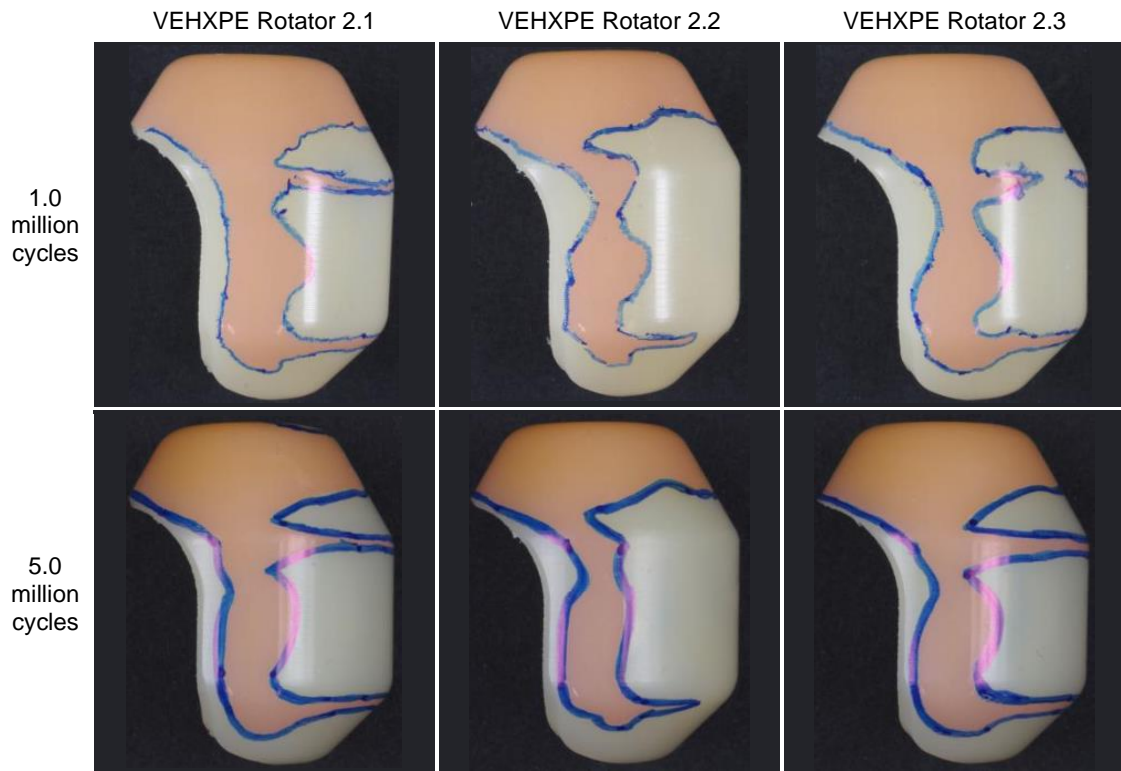


Fig. 5.91: Anterior view of the VEHXPE rotator component illustrating extensive contact at the tapered section (load bearing surface) and minimal contact at the cylindrical section (non-load bearing surface) with the internal surface of the flexor. Results produced by Endolab®.

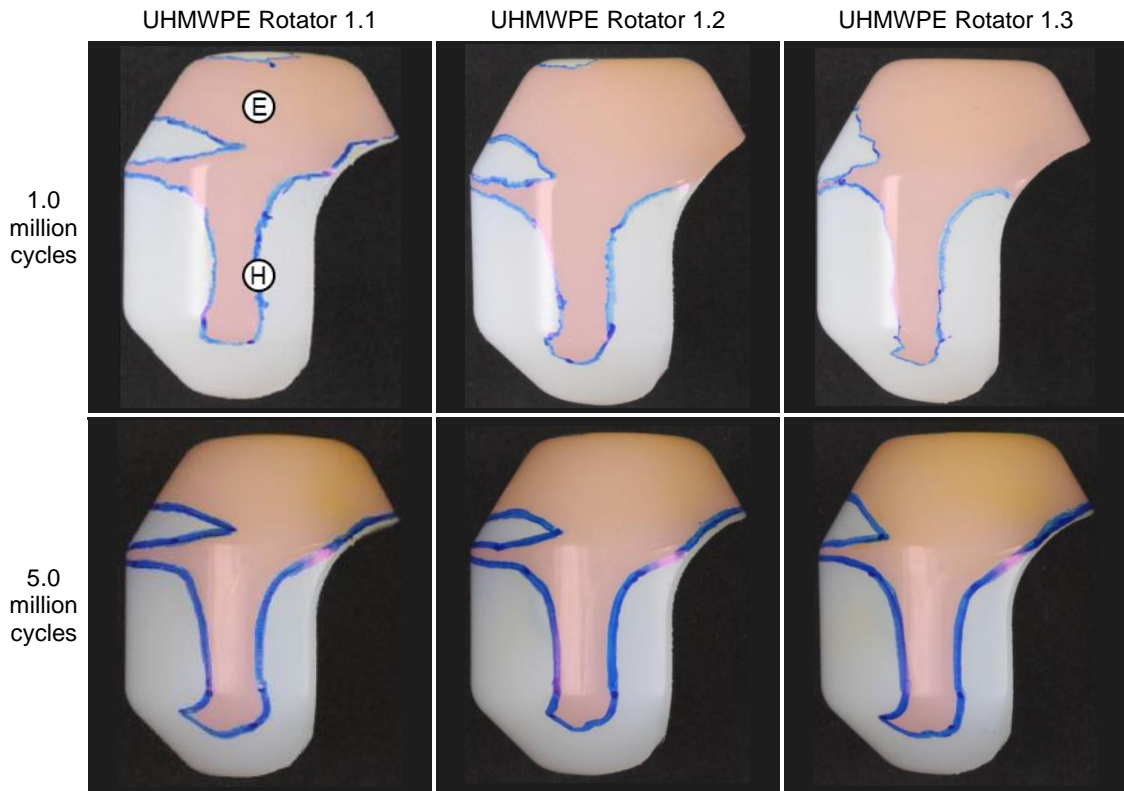


Fig. 5.92: Posterior view of the UHMWPE rotator component illustrating extensive contact at the taper (load bearing surface) and moderate contact at the cylindrical section (non-load bearing surface) with the internal surface of the flexor. Results produced by Endolab®.

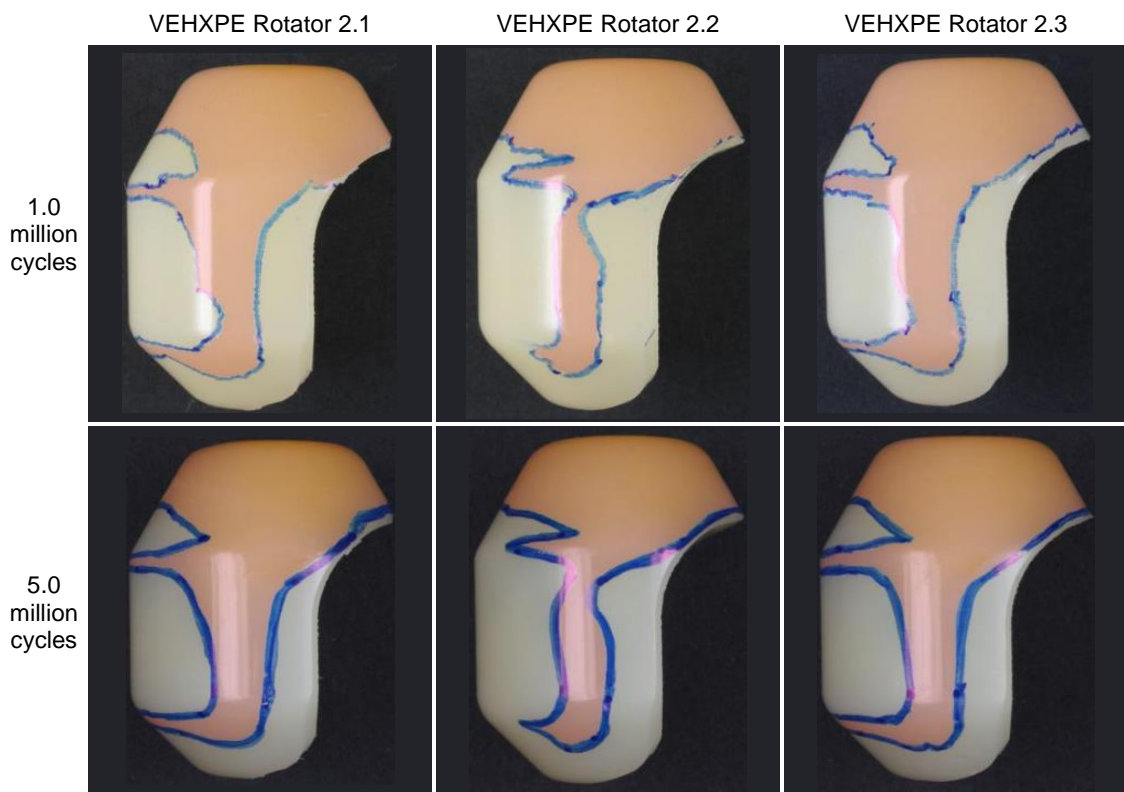


Fig. 5.93: Posterior view of the VEHXPE rotator component illustrating extensive contact at the taper (load bearing surface) and moderate contact at the cylindrical section (non-load bearing surface) with the internal surface of the flexor. Results produced by Endolab®.

5.7.4.4. Rotator Internal Surface

The contact areas of the rotator internal surface are shown in Figs. 5.94 to 5.97. Extensive contact is achieved at the superior region of the load bearing surface (label I), even at 1.0 million cycles. No drastic growth can be observed in the contacting area after 5.0 million cycles, since the majority of the surface area is already in contact during the early stages of the test. The generation of the large contact patch being made at this region is likely to be attributed to the higher deformations which are exhibited by the component. Minimal contact is made at the inferior region of the internal surface of the rotator, as indicated by label J, with no significant increments being made at 5.0 million cycles.

The anterior and posterior sides of the rotator internal surface are shown in Figs. 5.98 to 5.101, labelled K and L, respectively. Such surfaces are primarily intended to constrain the motion of the abductor component. At 5.0 million cycle, it can be observed that moderate contact is generated at these walls of the rotator. This type of contact is postulated to be generated during high joint angles, causing the rotator to become highly inclined which effectively forces its internal side surfaces to momentarily act as load bearing surfaces.

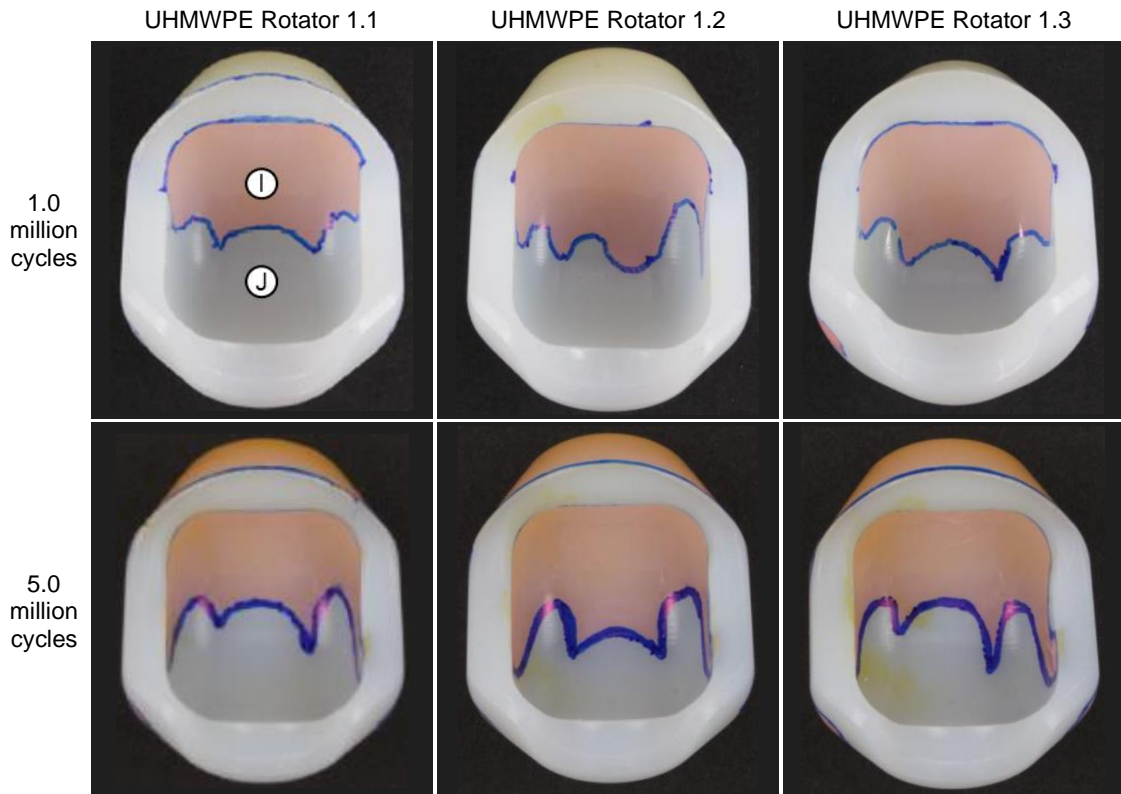


Fig. 5.94: Internal surface of the UHMWPE rotator illustrating extensive contact with the abductor component (inferolateral view). Results produced by Endolab®.

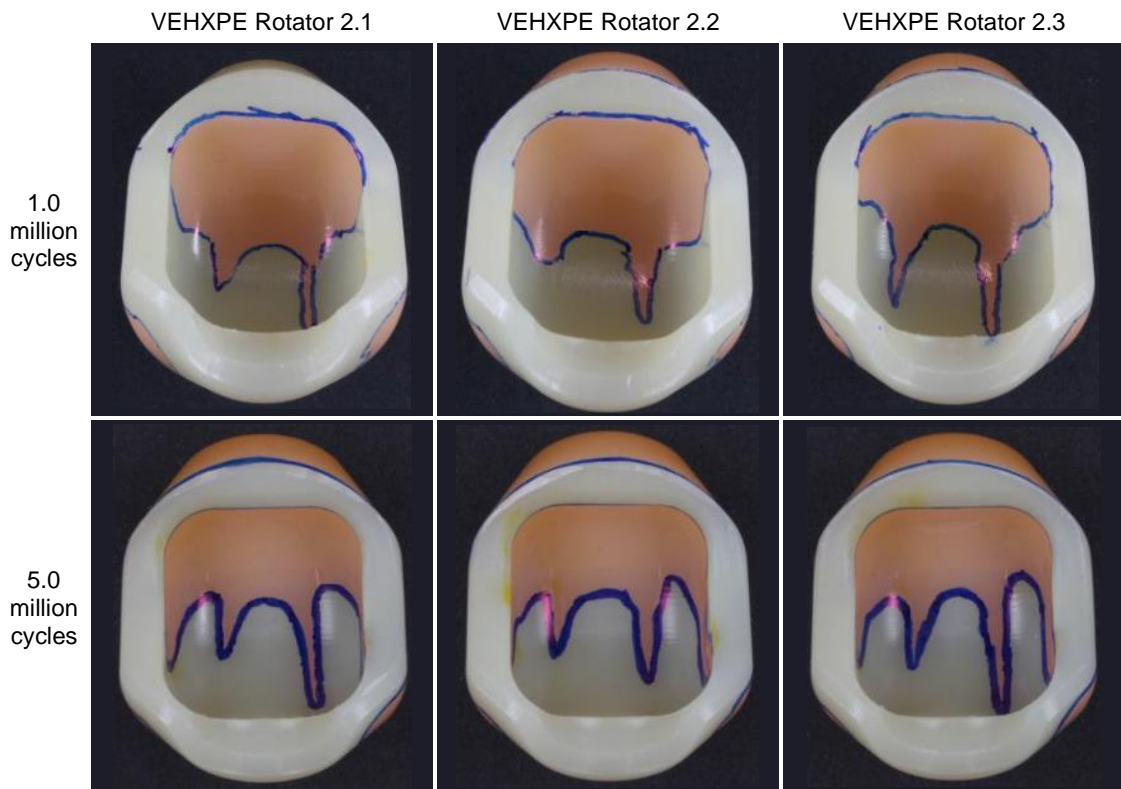


Fig. 5.95: Internal surface of the VEHXPE rotator illustrating extensive contact with the abductor component (inferolateral view). Results produced by Endolab®.

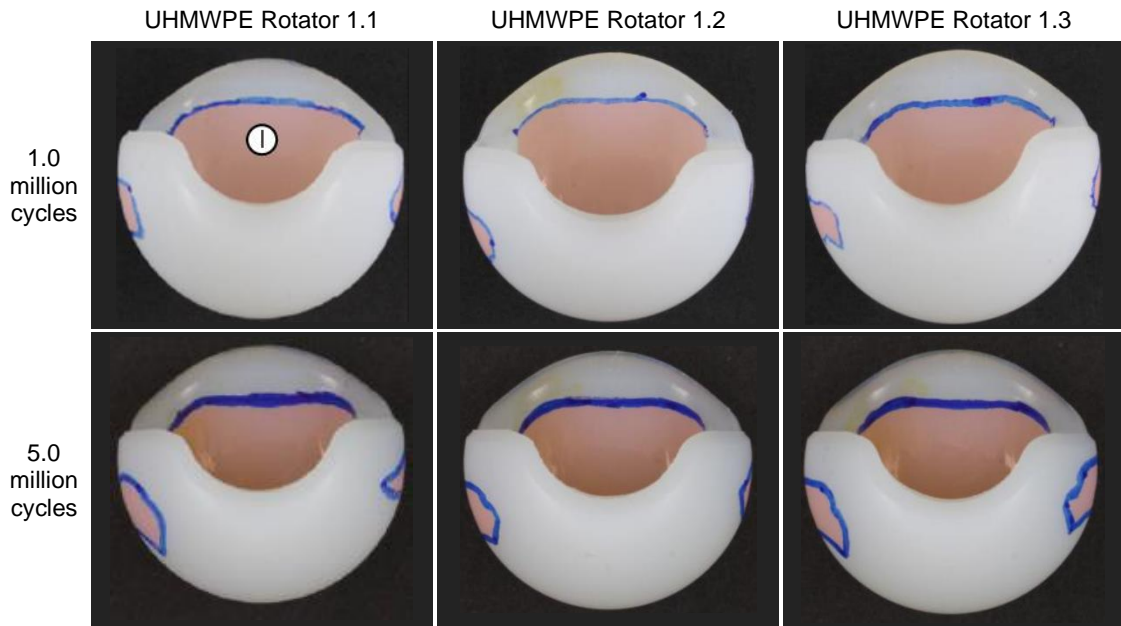


Fig. 5.96: Internal load bearing surface of the UHMWPE rotator illustrating full contact with the abductor component (inferior view). Results produced by Endolab®.

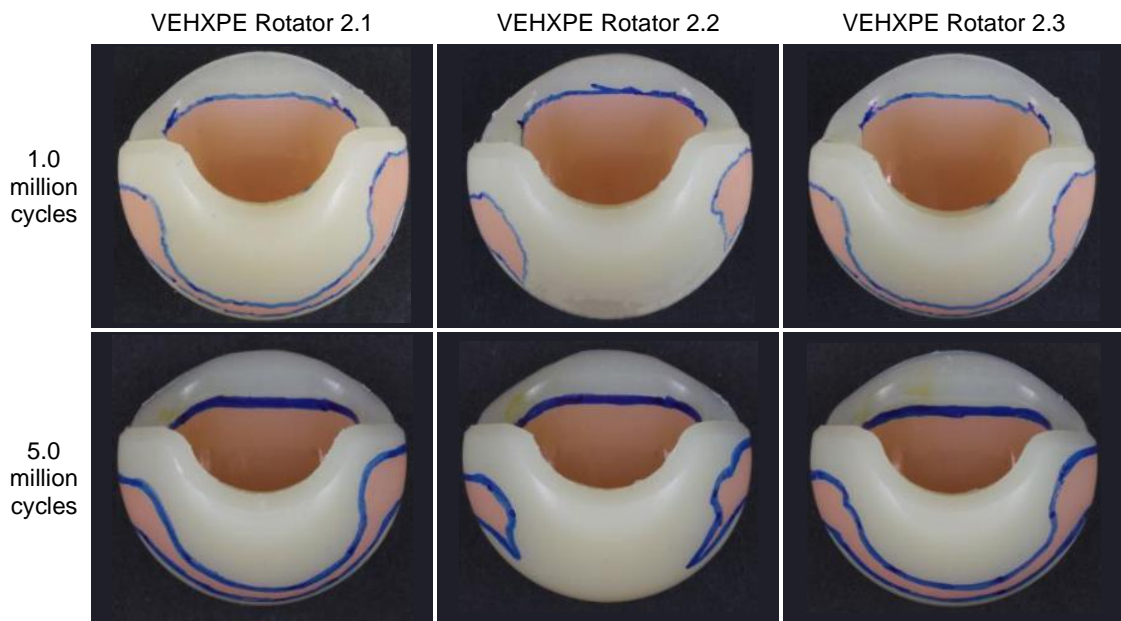


Fig. 5.97: Internal load bearing surface of the VEHXPE rotator illustrating full contact with the abductor component (inferior view). Results produced by Endolab®.

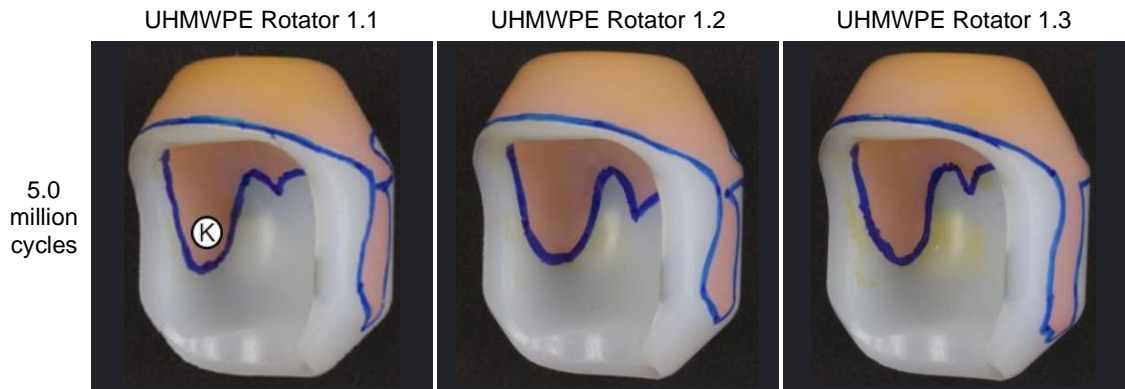


Fig. 5.98: Anterolateral view of the UHMWPE rotator component illustrating extensive contact at the tapered section (load bearing surface) with the internal surface of the flexor, and moderate contact at its internal section (non-load bearing surface) with the abductor component. Contact area for 1.0 million cycles is not available. Results produced by Endolab®.

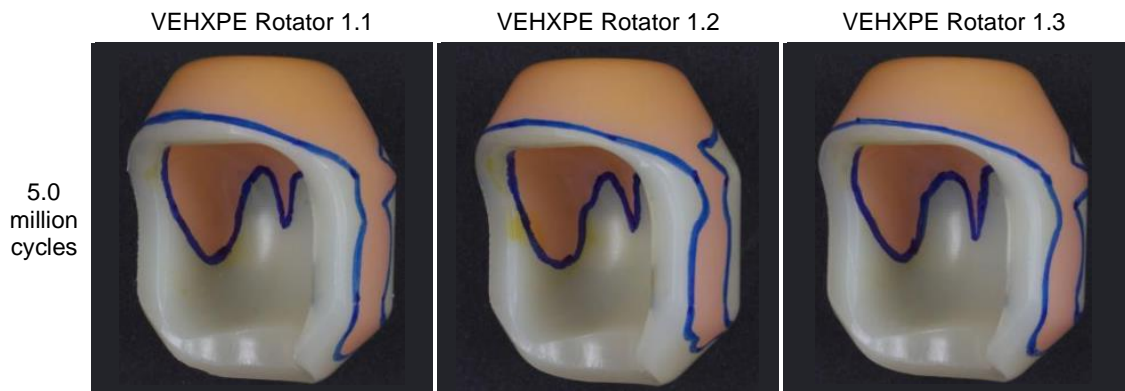


Fig. 5.99: Anterolateral view of the VEHXPE rotator component illustrating extensive contact at the tapered section (load bearing surface) with the internal surface of the flexor, and moderate contact at its internal section (non-load bearing surface) with the abductor component. Contact area for 1.0 million cycles is not available. Results produced by Endolab®.

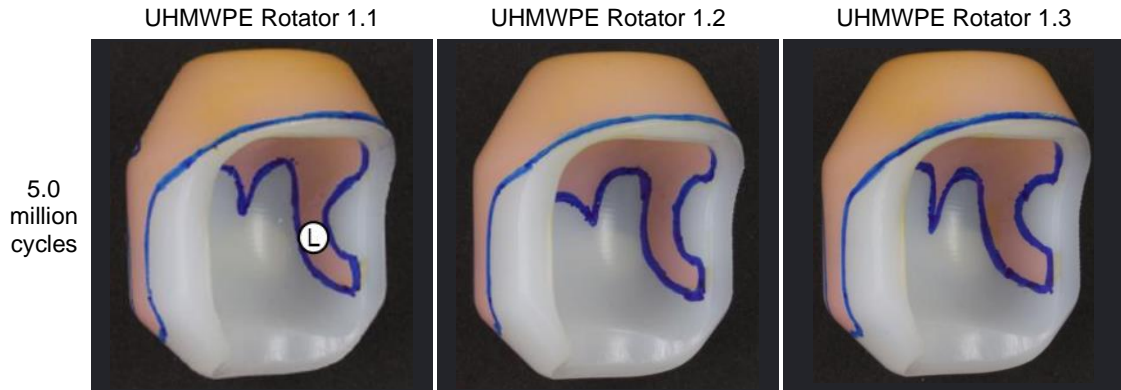


Fig. 5.100: Posterolateral view of the UHMWPE rotator component illustrating extensive contact at the tapered section (load bearing surface) with the internal surface of the flexor, and moderate contact at its internal section (non-load bearing surface) with the abductor component. Contact area for 1.0 million cycles is not available. Results produced by Endolab®.

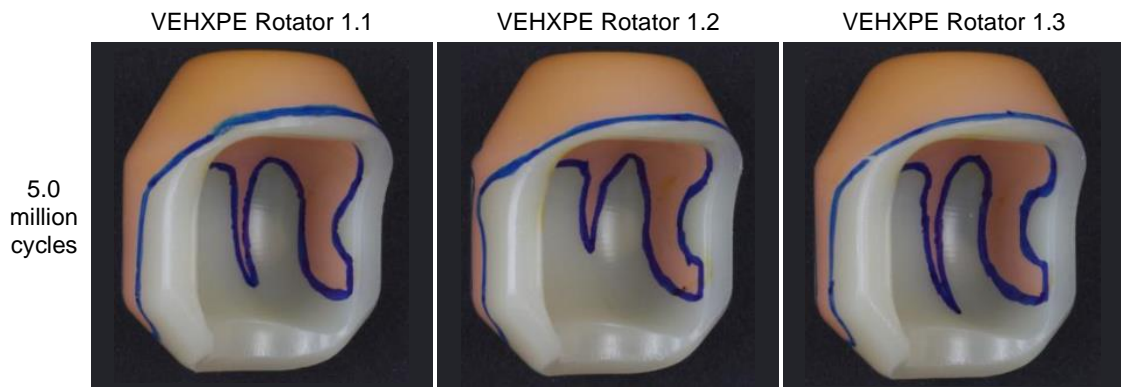


Fig. 5.101: Posterolateral view of the VEHXPE rotator component illustrating extensive contact at the tapered section (load bearing surface) with the internal surface of the flexor, and moderate contact at its internal section (non-load bearing surface) with the abductor component. Contact area for 1.0 million cycles is not available. Results produced by Endolab®.

5.7.5. Optical Microscopy Images

5.7.5.1. Introduction

Optical microscopy images of UHMWPE and VEHXPE components were captured following the wear testing regime of 5.0 million cycles. The results for UHMWPE are presented in Section 5.7.5.2, whereas results for the VEHXPE are presented in Section 5.7.5.3. Furthermore, the optical microscopy images of the high-N austenitic stainless steel components are shown in Section 5.7.5.4. For ease of reference, the labels used in this section correspond to the same labelling scheme which was used in the previous section containing the contact area results (Section 5.7.4, p. 206).

5.7.5.2. UHMWPE Components

Optical microscopy images of the UHMWPE MaltaHip cups (Figs. 5.102 and 5.103) illustrate the minimal levels of wear exhibited by these components, as evident by the presence of the machining marks following 5.0 million cycles. The drastic reduction in wear is primarily owed to the uni-directional motion of the articulation which coincides with the principal molecular orientation of the surface polymer chains following machining of the surface. No signs of polished or glossy regions can be observed, which is usually a characteristic associated with worn UHMWPE hemispherical cups.

A comparison between a pristine (non-contact) and a worn (contact) area can be seen in the same optical microscopy image in Fig. 5.103 (label B). It is interesting to note that the machining marks on the worn surface possess similar characteristics to those observed in the pristine region, thus highlighting the low levels of wear. A number of scratches can be observed in the interior medial area of the MaltaHip cup, as shown in Fig. 5.103 (label C). Nonetheless, it should be pointed out that these scratches were already present prior to the wear testing regime. In fact, these scratches are located well outside the contact area, and thus could not have been generated during wear testing procedure. Furthermore, the orientations of these scratches do not coincide with the sliding motion direction of the flexor component. These scratches were in fact generated due to a manual process which was used during the fabrication of the implants. When the surface was subjected to turning processes, a small protrusion was generated at the centre of the face, which was then manually removed, causing the generation of these scratches during the process.

Optical microscopy images of the external load bearing surface of UHMWPE rotator are shown in Figs. 5.10 to 5.11. The worn areas are clearly distinguished from the non-contact regions, due to their glossy and polished appearance and lack of machining marks. In fact, the non-contacting areas still clearly retain the original machining marks. The glossy appearance at the worn regions can be observed both at the flat (label D) and tapered (label E) regions of the load bearing surface in Fig. 5.104. Wear at this articulation is likely to be attributed to the smaller contacting area (compared to the MaltaHip cup), and thus resulting in the generation of higher contact stresses.

The external non-load bearing surfaces of the rotator are illustrated in Fig. 5.105. It can be seen that the anterior region (label G) exhibited some degree of wear due to the glossy appearance of the surface. However, signs of the original machining marks are still partially visible. On the other hand, the machining marks on the posterior region (label H) are more prominent than the previous case, which indicates that this region exhibited lower levels of wear.

Optical microscopy images of the internal load bearing surface of the rotator are shown in Fig. 5.106. As discussed previously, the surface at this articulation possesses the smallest contact area and was fabricated using a milling process rather than a turning process, as illustrated in Fig. 5.44 (p. 169). It can be clearly observed that the high levels of wear occurred at this articulation (Fig. 5.106, label I) due to the glossy appearance of the surface that evidently lacks the machining marks. The orientation softened polymer chains (as a consequence of the milling process), coupled with high levels of contact stress and the uni-directional sliding motion at this articulation, all contributed to significant wear that occurred at this articulation. The walls of the rotator (Fig. 5.106, labels K and L) can be seen to be partially worn as evident from the glossy appearance of the surface. Machining marks can be clearly observed surrounding the worn area, which represent the non-contacting regions of the articulation.

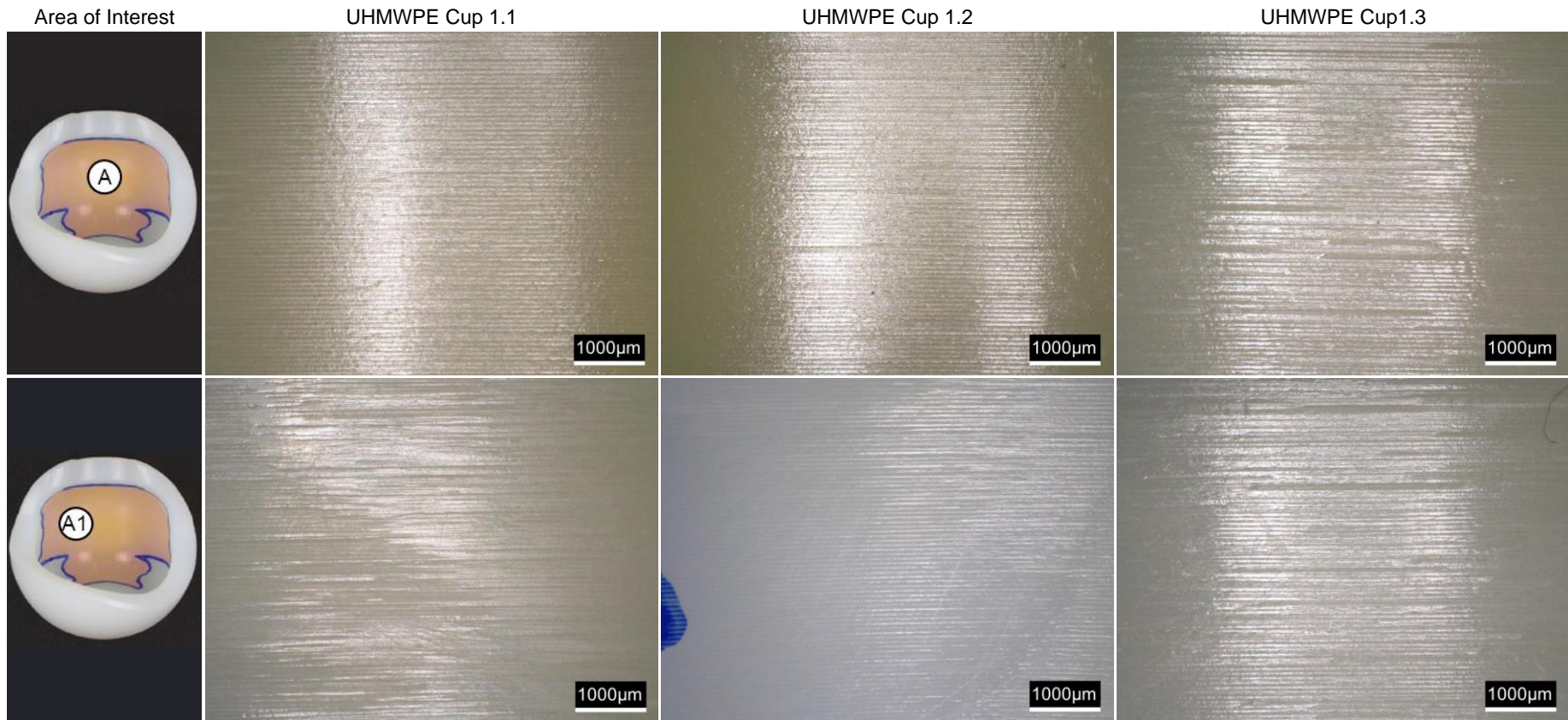


Fig. 5.102: Microscopic images of the MaltaHip UHMWPE cup at the internal superior surface. Results produced by Endolab®.

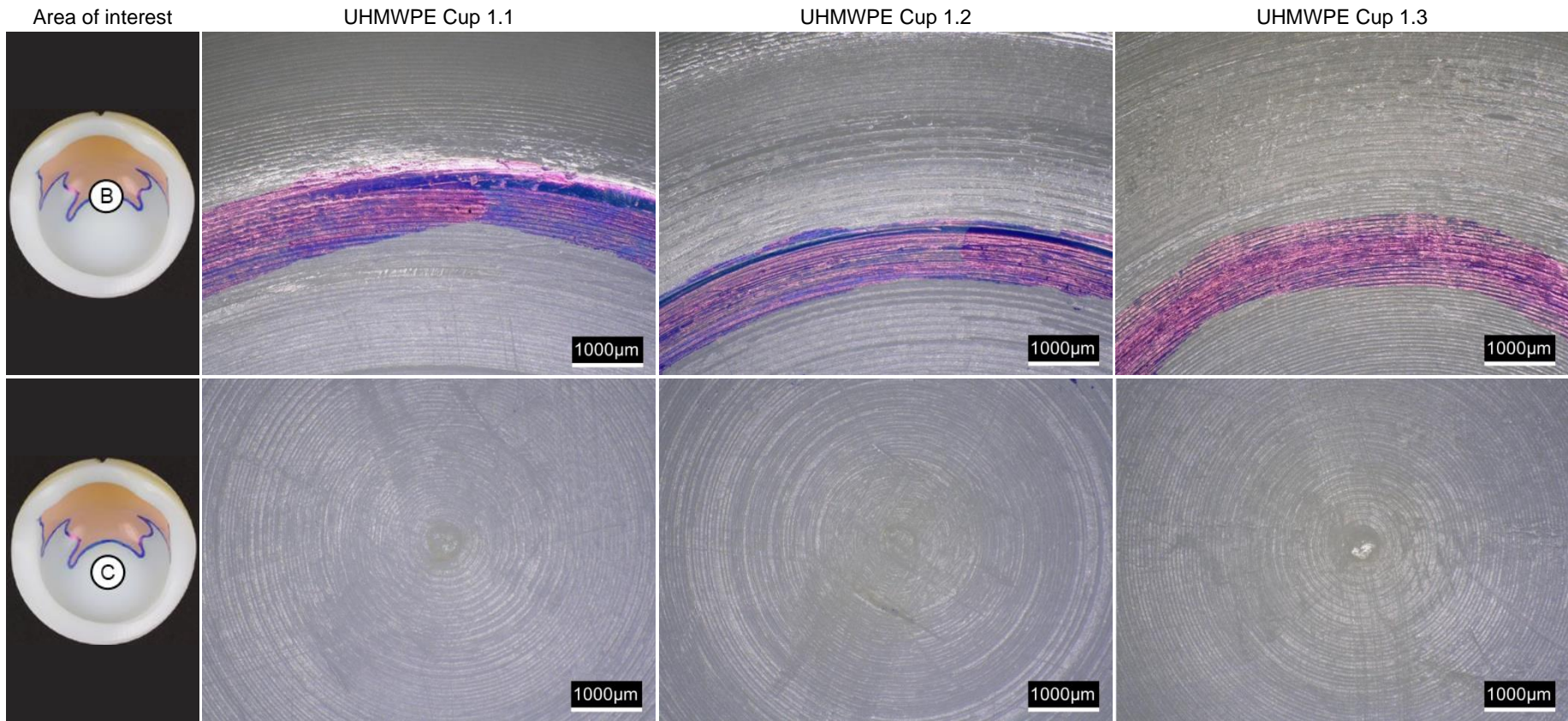


Fig. 5.103: Microscopic images of the MaltaHip UHMWPE cup at the internal medial surface. Results produced by Endolab®.

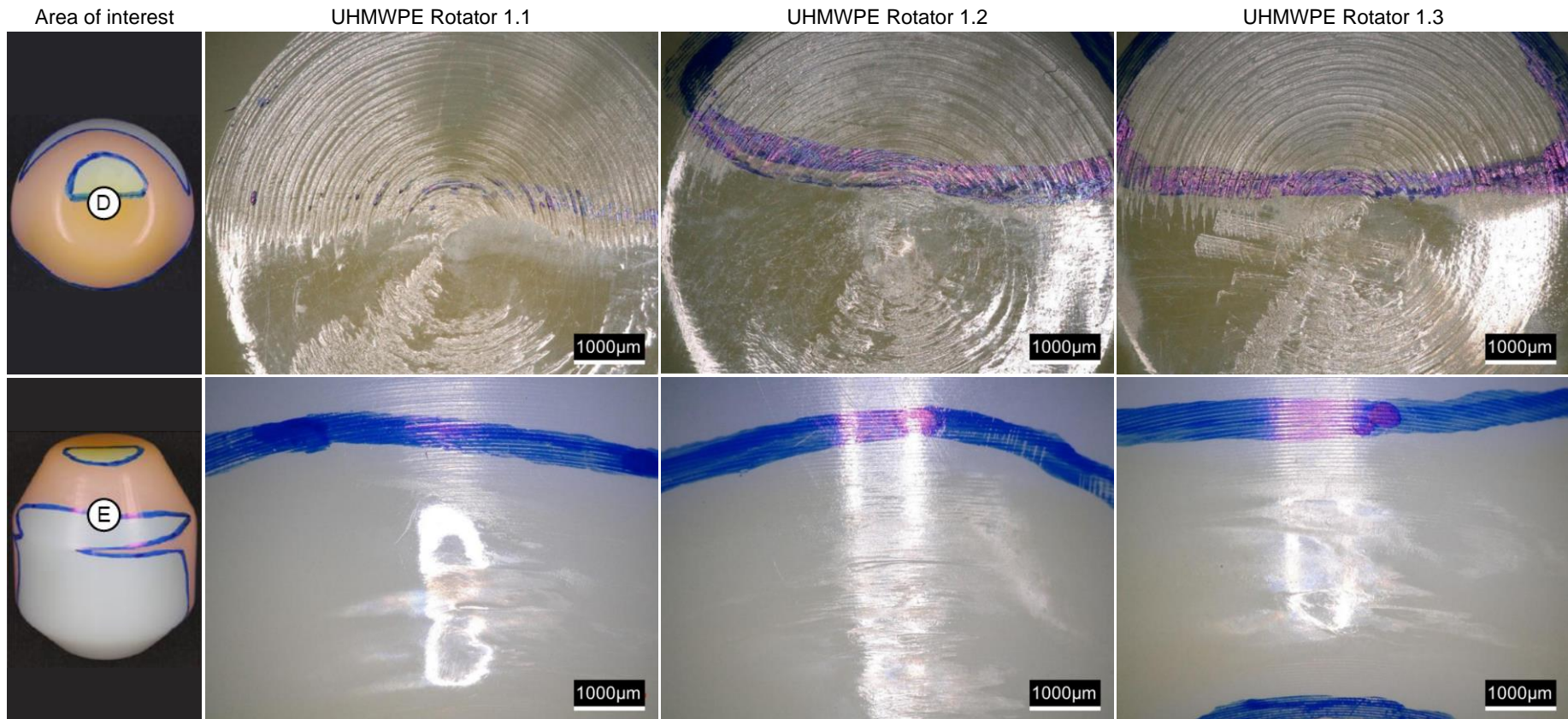


Fig. 5.104: Microscopic images of the MaltaHip UHMWPE rotator at the external superior surface. Results produced by Endolab®.

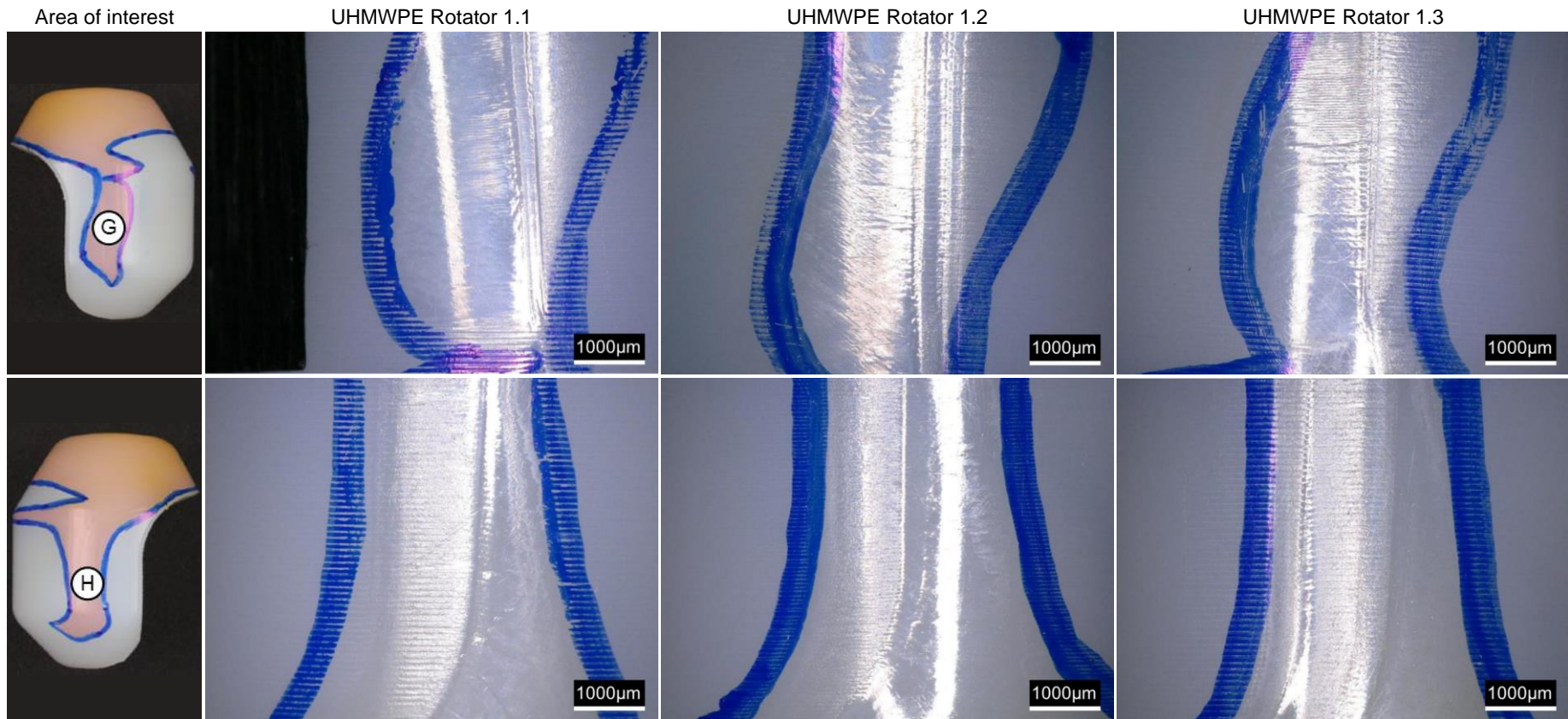


Fig. 5.105: Microscopic images of the MaltaHip UHMWPE rotator at the external anterior and posterior non-load bearing surfaces. Results produced by Endolab®.

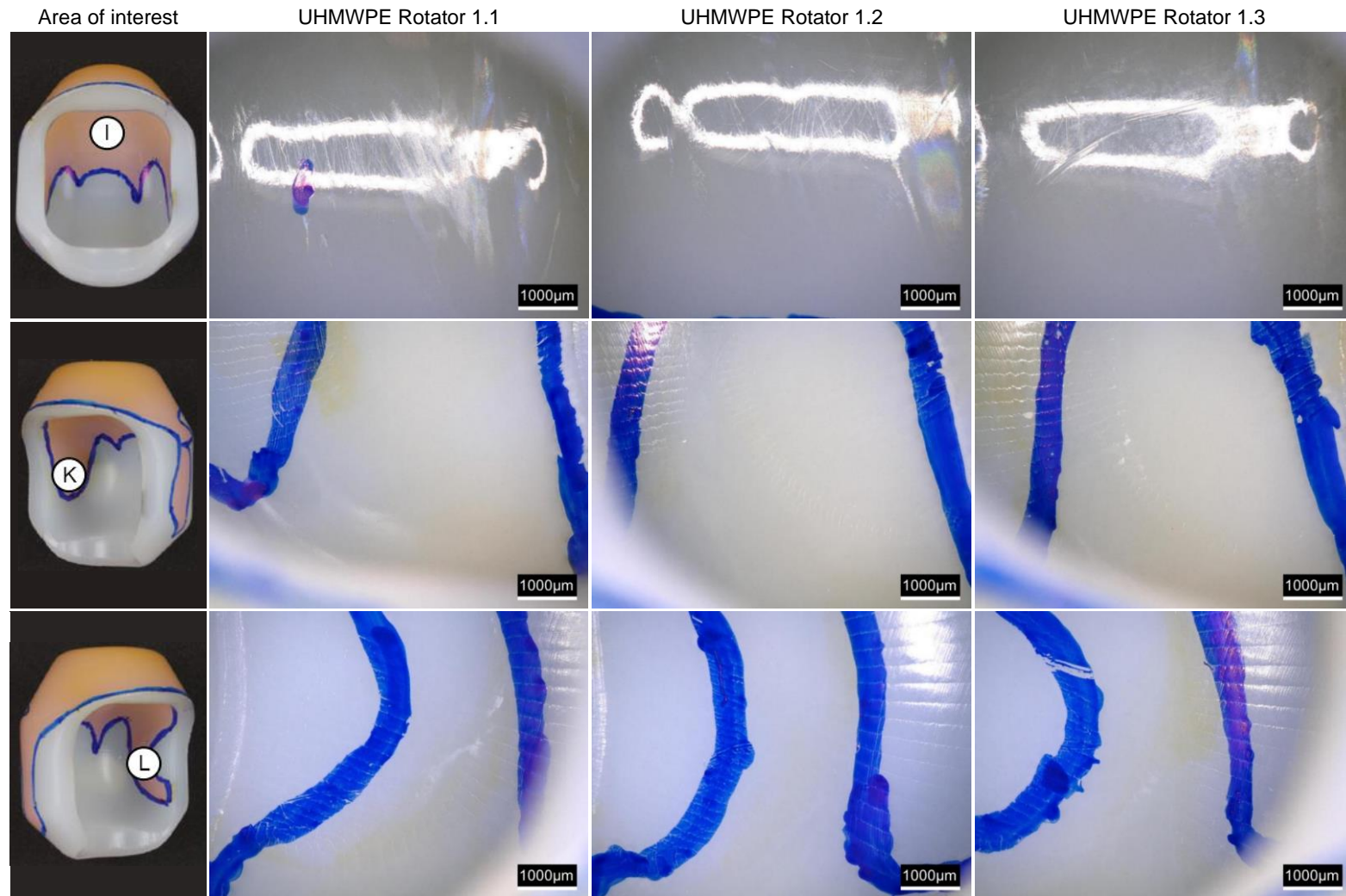


Fig. 5.106: Microscopic images of the MaltaHip UHMWPE rotator at the internal surface. Results produced by Endolab®.

5.7.5.3. VEHXPE Components

The optical microscopy images of the internal surface of VEHXPE MaltaHip cup can be observed in Figs. 5.107 and 5.108. As indicated by the wear measurement results, the surface of the MaltaHip cup exhibited minimal wear, as evident from the presence of the machining marks. As discussed in the literature review (Section 2.5.6, p. 50), the surface of a worn crosslinked hemispherical cup is characterised by a series of multi-directional scratches overlaying the machining marks (Fig. 2.37, p. 53). In case of the VEHXPE cup of the MaltaHip, no signs of scratches can be observed. In fact, the machining marks in the worn region retain the same geometrical features to those which are present in the pristine region, thus corresponding to the low levels of wear.

The load bearing surfaces of the VEHXPE rotator components are shown in Fig. 5.109. Considering the flat surface of the articulation (Fig. 5.109, label D), signs of wear can be noted due to the machining marks in the worn area having a different pattern than that observed in the pristine region. The texture of the machining marks in the worn region are less fine, and in some cases seem to be overlapped by a few ripples. Similarly, indications of wear can also be noted on the tapered section (Fig. 5.109, label E) due to the different textures of the machining marks. Fig. 5.110 shows the external non-load bearing surface of the rotator. Only minor signs of wear can be observed on these surfaces (Fig. 5.110, labels G and H), as the majority of the machining marks were retained.

Optical microscopy images of the internal load bearing surface of the VEHXPE rotator are shown in Fig. 5.111. The surface can be observed to be highly polished without any machining marks, suggesting that significant wear occurred at the articulation. As discussed previously (Section 5.6.1, p. 161), the internal surface of the rotator is machined using the ball-nose milling cutter (Fig. 5.44, p. 169) and thus a considerable degree of orientation softening is likely to have occurred, inducing relatively high levels of wear. Furthermore, the surface exhibits high levels of contact stress, which exacerbates the amount of wear that is generated. Similar to the UHMWPE rotator, machining marks are retained on the walls of the rotator (Fig. 5.111, label K and L), as only partial contact is made at this region.

It was observed that the surface of VEHXPE to be highly polished, exhibiting no machining marks indicating significant wear, while the gravimetric wear (Fig. 5.77, p. 202) was minimal compared to that of the UHMWPE. It should be noted that the rotator undergoes significantly higher stresses than the cup, due to its smaller contacting area. The glossy and polished surface implies that sufficient contact stress has been induced in both rotators to cause the machined layer to be worn off. However, the glossy and polished surface does not indicate the extent and volume of wear which occurred, but rather only suggests that sufficient wear has

occurred to remove the surface layer. Therefore, it is very likely that the wear scar produced in the UHMPWE to be deeper than that produced in the VEHXPE rotator. The reason for the lower wear generated in VEHXPE is attributed to its crosslinked structure, which according to the wear results produced in this work, is more resistant to wear at higher contact stresses which hinders the liberation of wear particles.



Fig. 5.107: Microscopic images of the MaltaHip VEHXPE cup at the internal superior surface. Results produced by Endolab®.

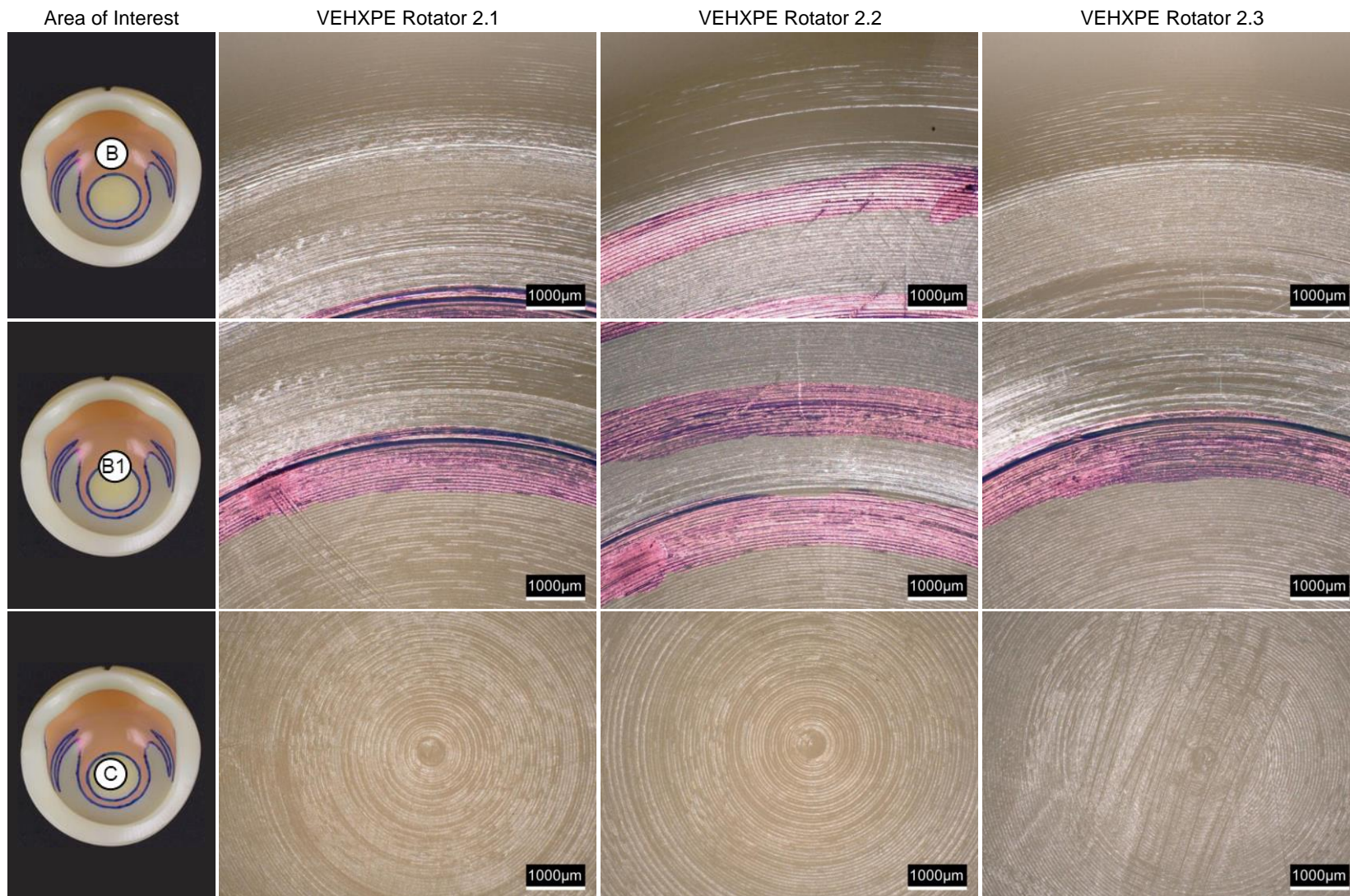


Fig. 5.108: Microscopic images of the MaltaHip VEHXPE cup at the internal medial surface. Results produced by Endolab®.

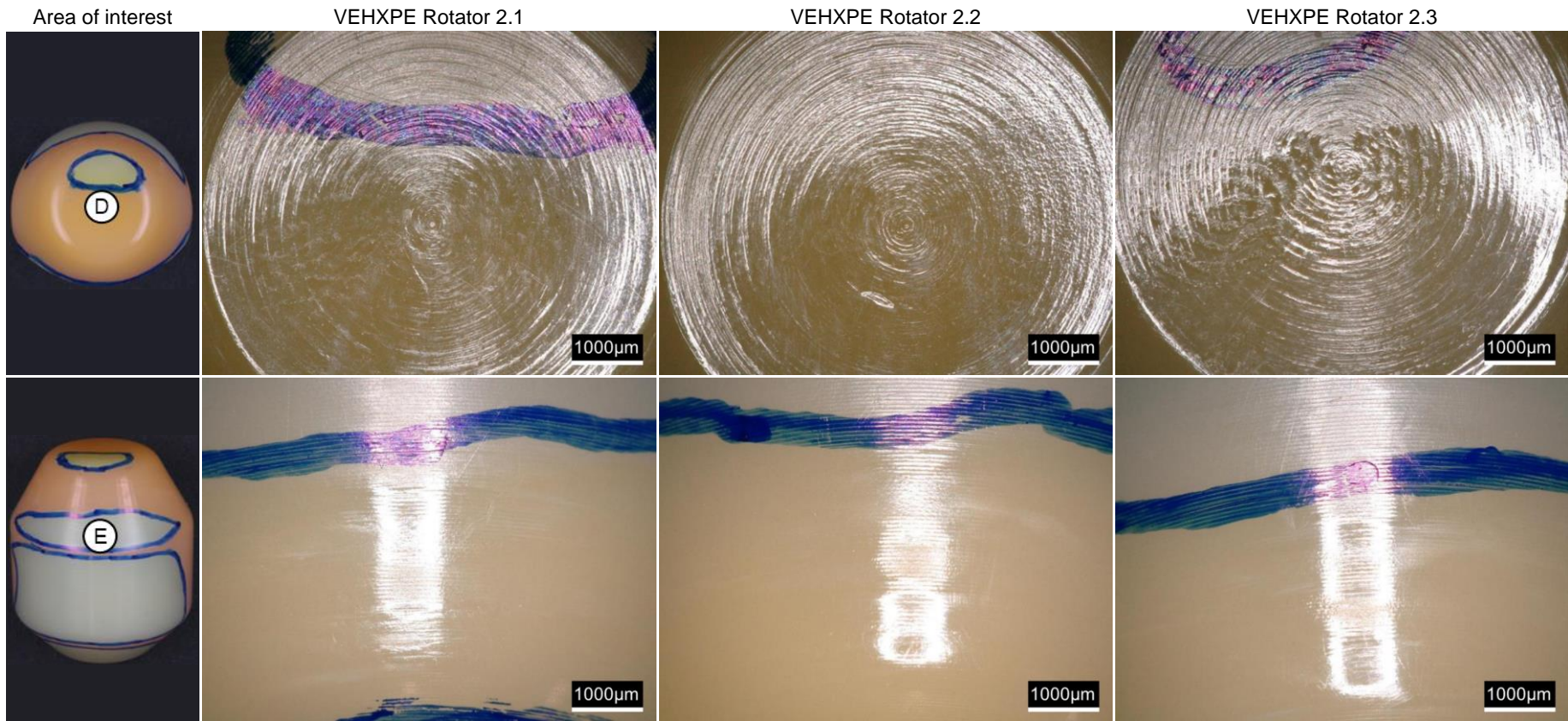


Fig. 5.109: Microscopic images of the MaltaHip VEHXPE rotator at the external superior surface. Results produced by Endolab®.

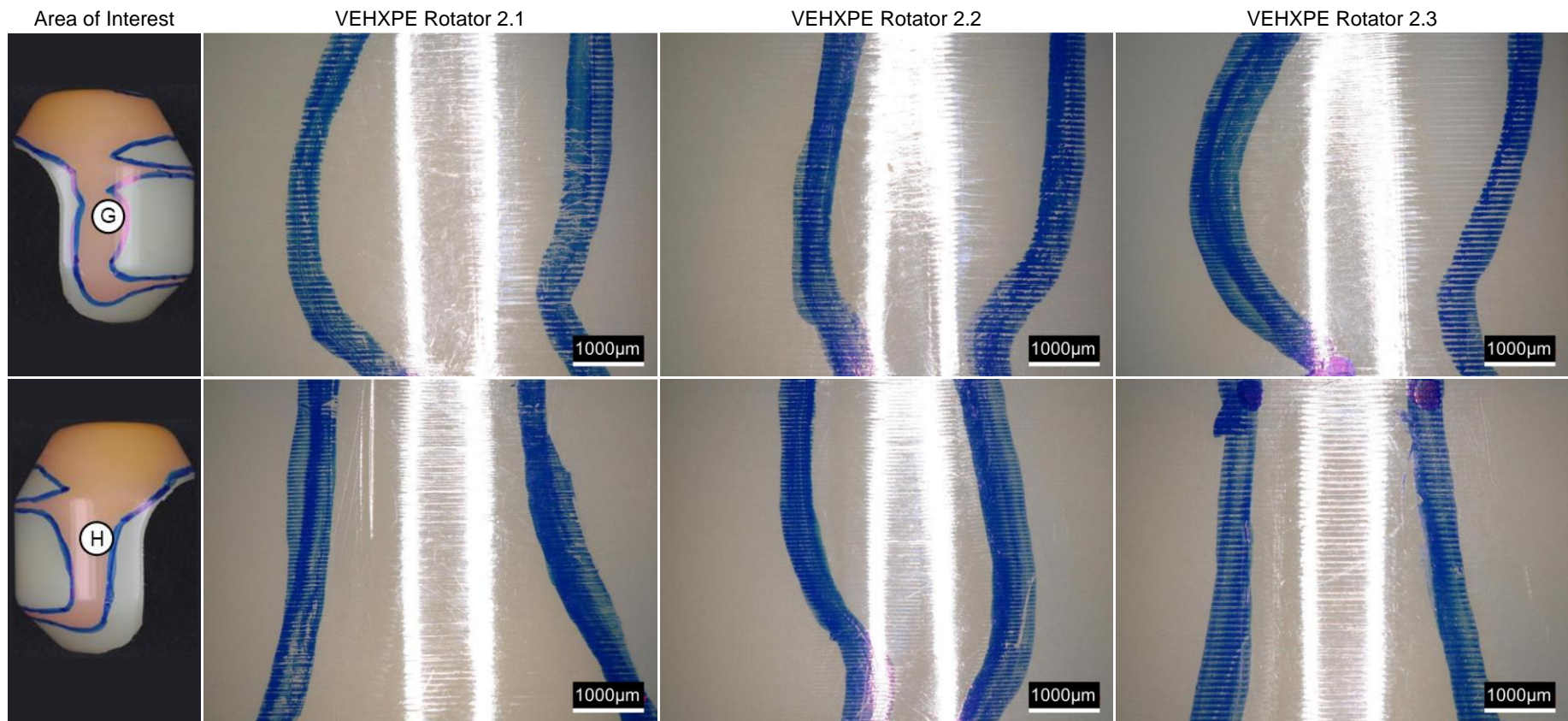


Fig. 5.110: Microscopic images of the MaltaHip VEHXPE rotator at the external anterior and posterior surfaces. Results produced by Endolab®.

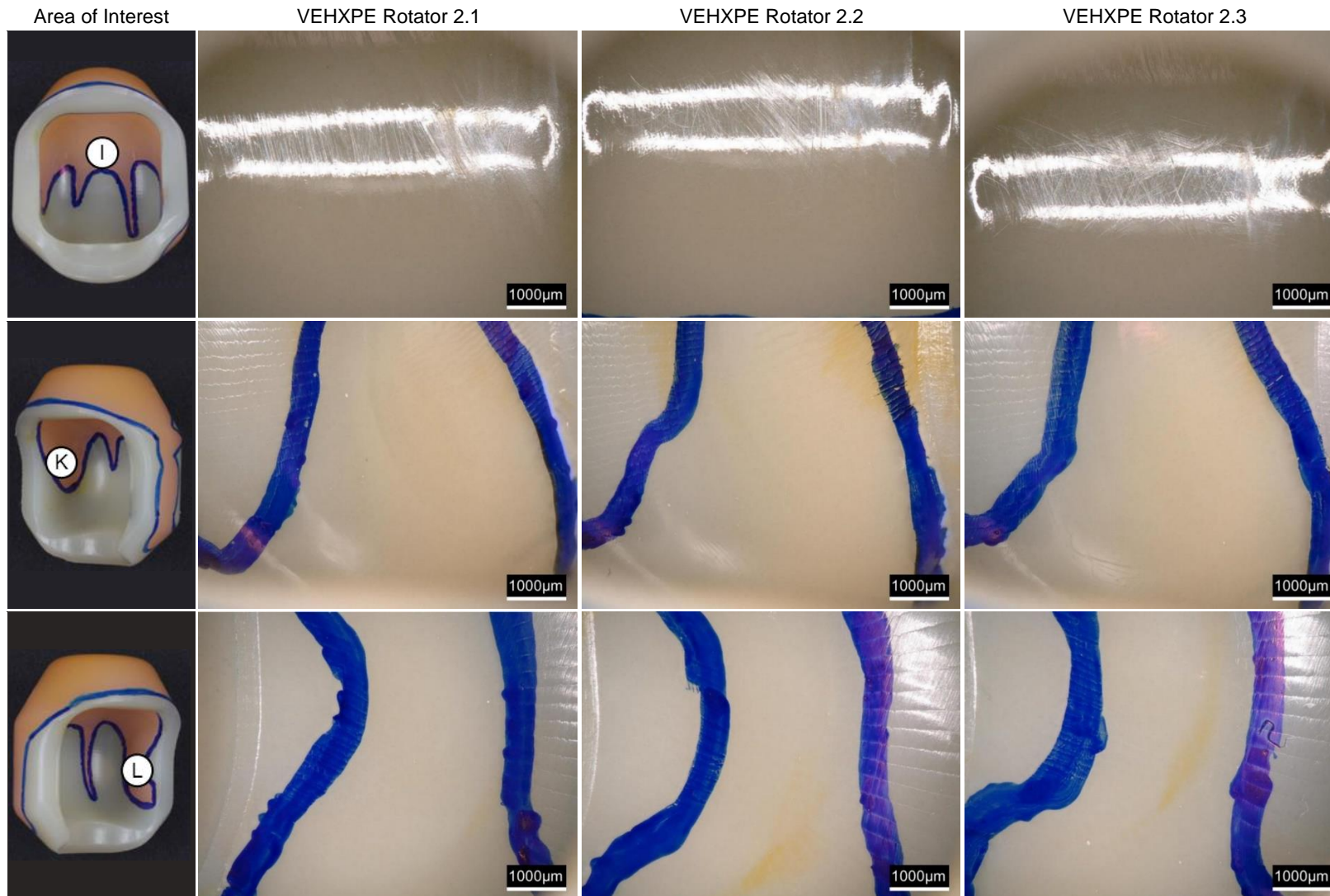


Fig. 5.111: Microscopic images of the MaltaHip VEHXPE rotator at the internal surface. Results produced by Endolab®.

5.7.5.4. High-N Austenitic Stainless Steel Components

The optical microscopy images of the MaltaHip flexor and abductor components following the wear tests are shown in Figs. 5.112 to 5.119. In general, it can be noted that the topographies of both the flexor and abductor components remained relatively intact following the wear testing procedure, as evident from their pristine condition. Abrasive wear due to three-body wear was absent as the prostheses were tested inside a sealed chamber which prevented the ingress of any external particles.

Polishing marks with varying densities can be seen across the optical microscopy images of the components. Dominant evidence of polishing marks can be observed in the external surface of the flexor in all components in the region labelled A (Fig. 5.112), flexor 1.1 in the region labelled D (Fig. 5.113), and abductor 1.1 in the region labelled E (Fig. 5.117). Most of the polishing marks are located in the region labelled A (Fig. 5.112), and are aligned to the direction of sliding motion. Only a few polishing marks are aligned perpendicular to the direction of sliding motion, which were intentionally produced to eliminate high spots in every direction. The polishing marks of flexor 1.1 in the region labelled D (Fig. 5.113) and abductor 1.1 in the region labelled E (Fig. 5.117) are noted to not coincide with the direction of sliding motion. However, such surfaces do not act as load bearing surfaces and hence it is very unlikely that these polishing marks may have contributed to the generation of wear debris on the polymeric components. The variation in the polishing marks densities is attributed to the different techniques which were used to polish the different surfaces of the component.

Furthermore, it has been observed that the majority of the remaining regions of the other components are absent from any obvious signs of polishing marks, which indicates the high level of surface finish that these components possess. Examples of these highly-polished regions include: labels B and C (Fig. 5.112), label D (flexor 1.2 and 1.3 in Fig. 5.113), label G (Fig. 5.114), label H (Fig. 5.115), label D (Fig. 5.117), and labels D and E (Fig. 5.119).

Some regions are characterised by dark lines, which may indicate signs of scratches or grooves. Examples of such scratches can be observed in label B and C (flexor 1.3 in Fig. 5.112), label E (flexor 1.3 in Fig. 5.113), label E (flexor 1.3 in Fig. 5.115) and label A (abductor 1.2 in Fig. 5.116). Since these scratches are located in highly localised regions (and not spread out through the entire area), it is likely that these grooves may have been generated manually during the polishing procedure. It is postulated that minor quantities of metallic debris, which are released during the polishing process, may have become entrapped during the final stages of the polishing procedure, causing scratches to be easily formed on the highly polished surfaces. Since pressure is applied during the polishing process to smoothen the surface, the entrapped fine debris produce highly localised contact stress. It can be noted that the grooves are not deep, which

indicate that these were generated by very fine particles. Due to the high surface finish that was produced on the metallic components, the polished surfaces are prone to scratches and grooves.

A series of pits can be observed in one of the optical microscopy images, being in the flexor component in Fig. 5.114 (label F). These pits are characterized by comet tails which protrude along the polishing direction. Similar pits have been noticed in a brand new Elite™ femoral heads, as shown in (Fig. 5.63, p. 186). Their nature of origin of these pits is not known, both for the flexor and the femoral head. However, since these pits are spread out all over the surface, it is postulated that such pits are generated during machining processes, due to for example a worn machining tool. Therefore, the pits shown in the flexor component Fig. 5.114 (label F) are very unlikely to have occurred during the wear testing procedure. Both the wear testing standards used in this work (ASTM F732-17 and ISO 14242-1:2014/Amd 1:2018) require that the solution is diluted with deionized water, rather than Ringer's solution or phosphate-buffered saline (PBS), hence being absent from chloride content. In fact, it was observed that that the flexor component did not exhibit any signs of pitting corrosion. Considering that only one of the flexor components possessed these pits, it is likely that their formation can be avoided in future versions of the MaltaHip prosthesis.

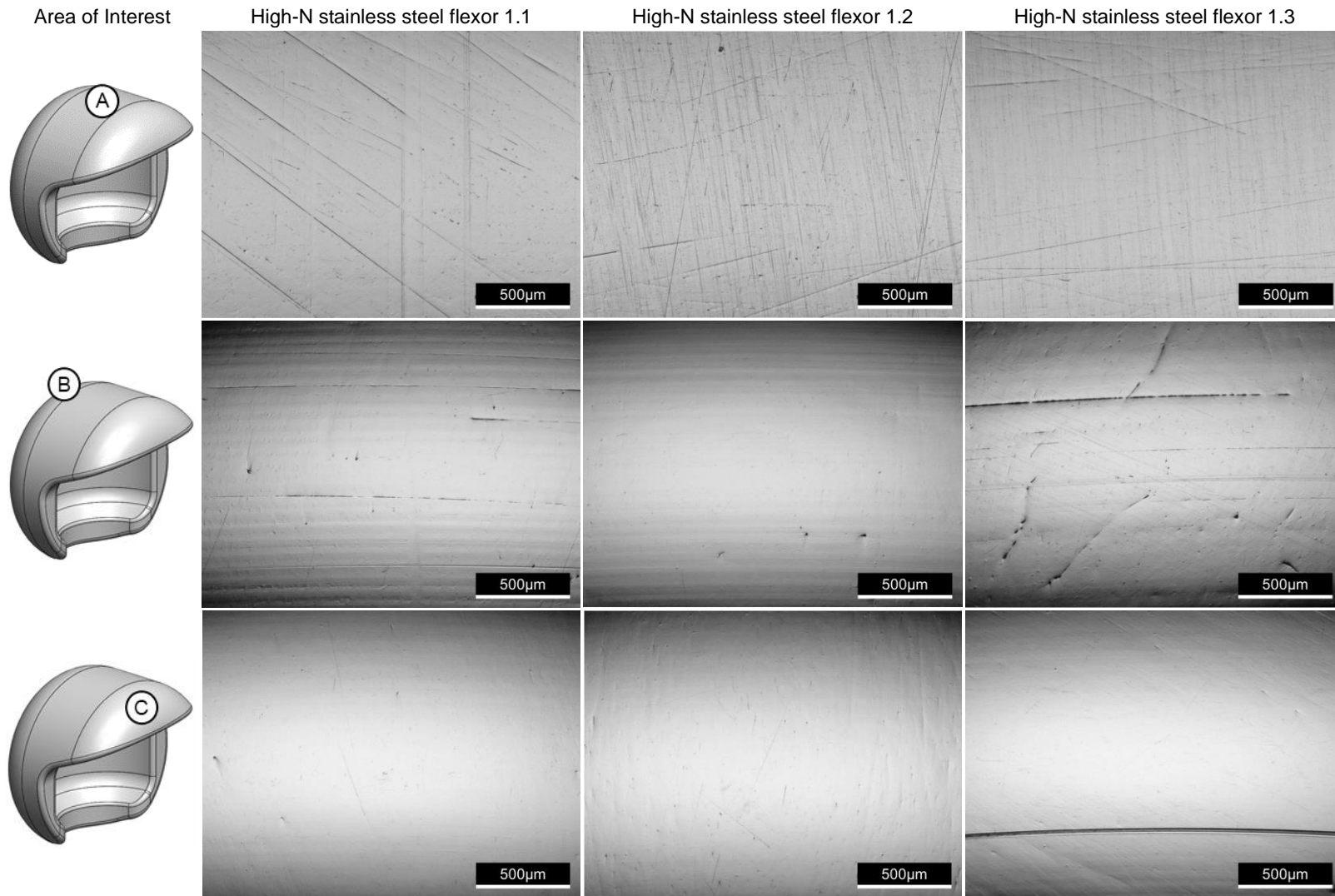


Fig. 5.112: External superior load bearing surface of the flexor. Results produced by Endolab®.

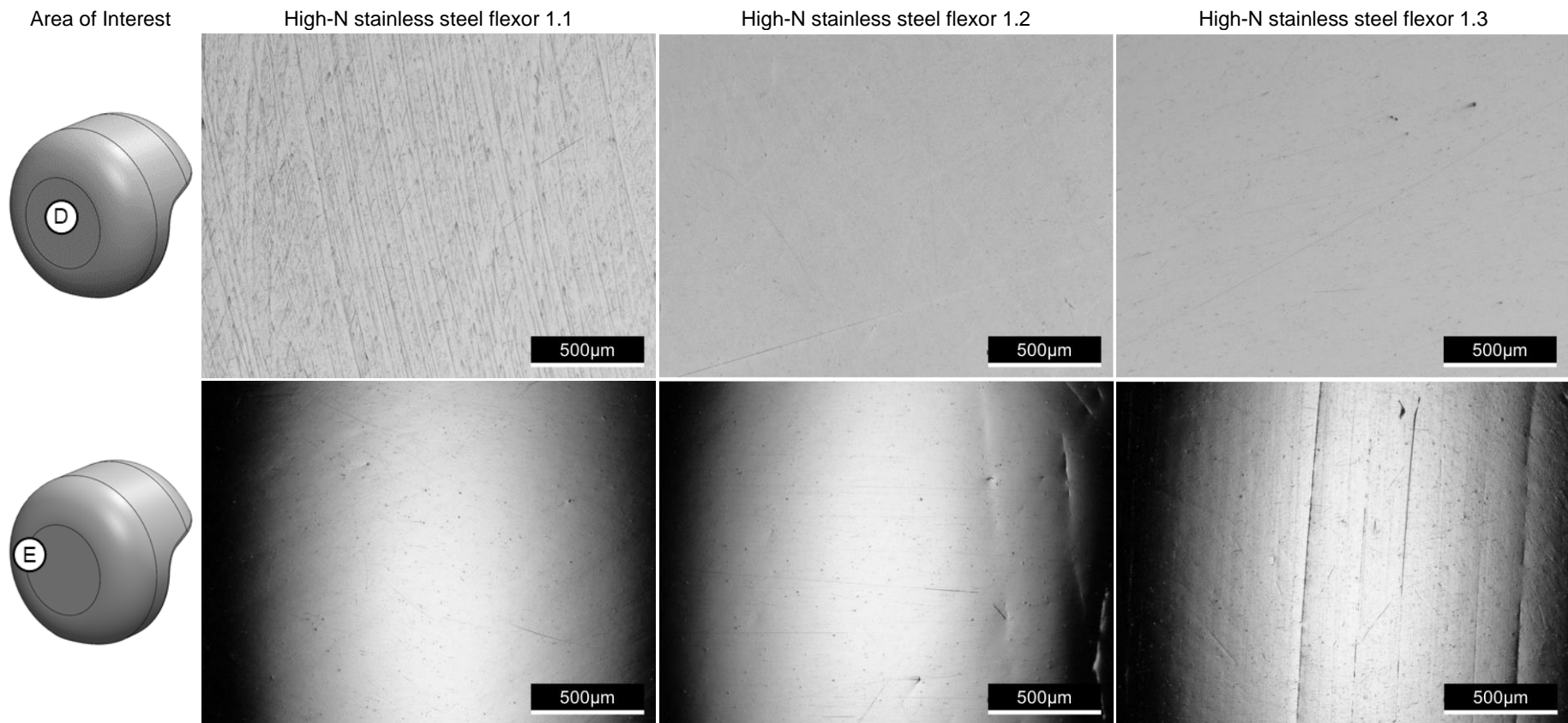


Fig. 5.113: External load bearing surfaces of the flexor (regions D and E). Results produced by Endolab®.

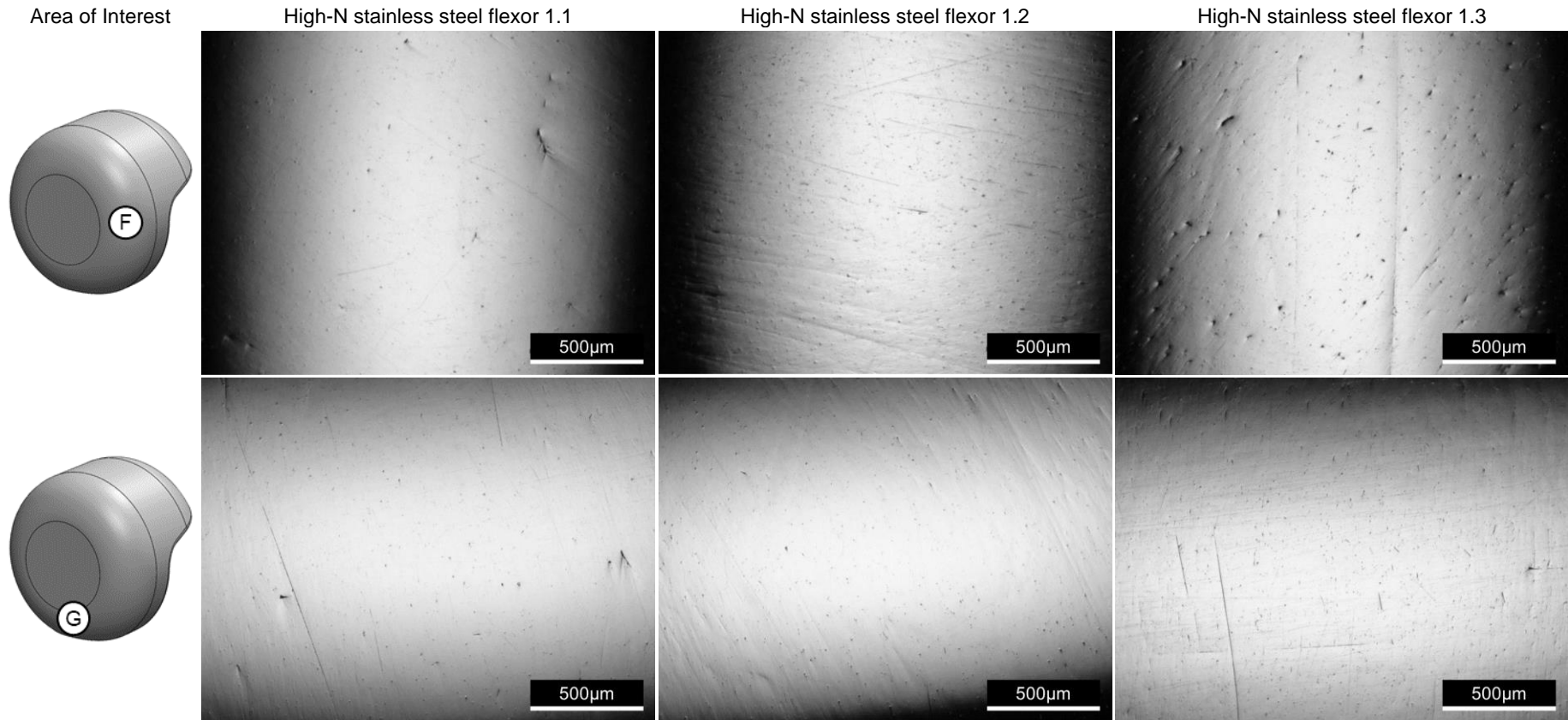


Fig. 5.114: External load bearing surfaces of the flexor (regions F and G). Results produced by Endolab®.

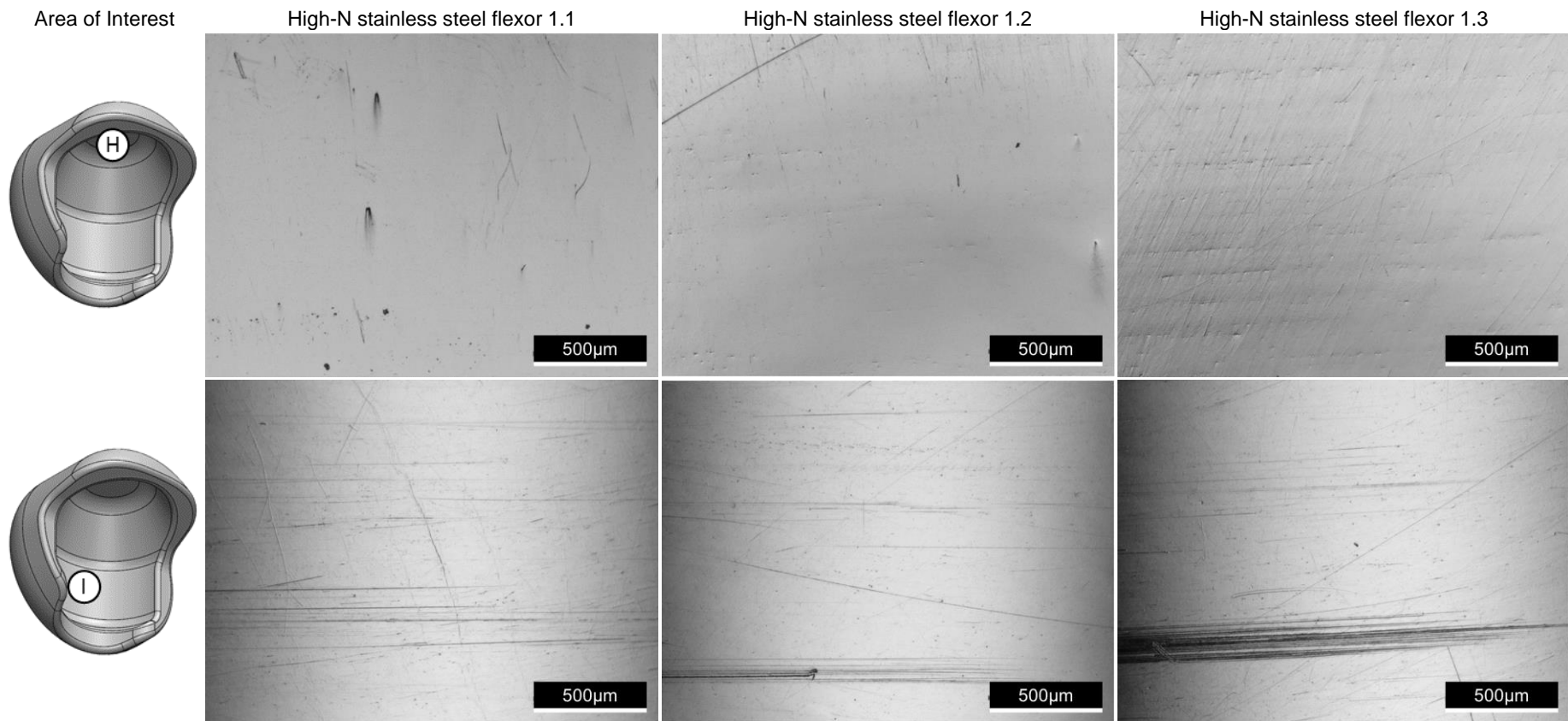


Fig. 5.115: Internal surfaces of the flexor (regions H and I). Results produced by Endolab®.

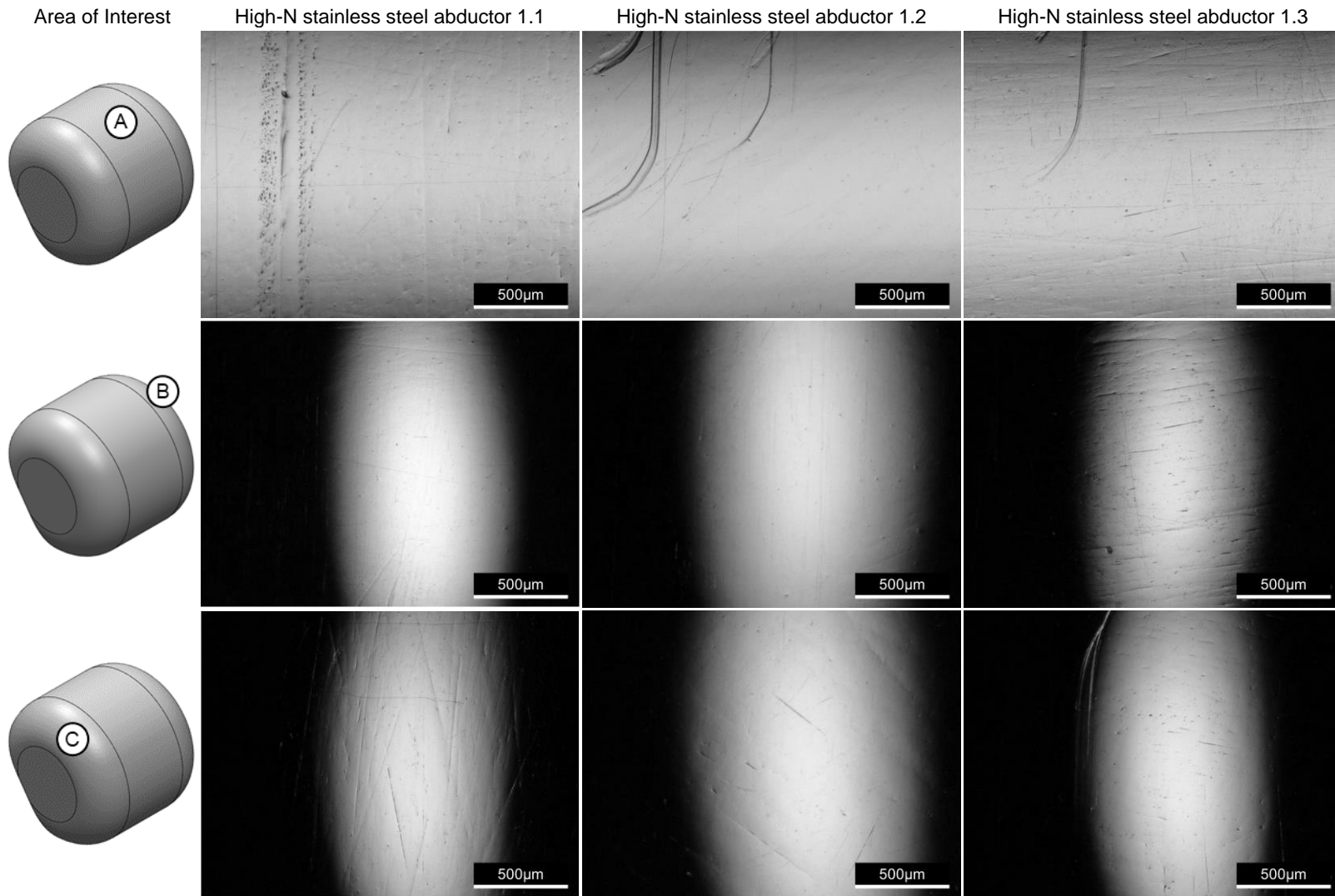


Fig. 5.116: Load bearing surface of the abductor. Results produced by Endolab®.

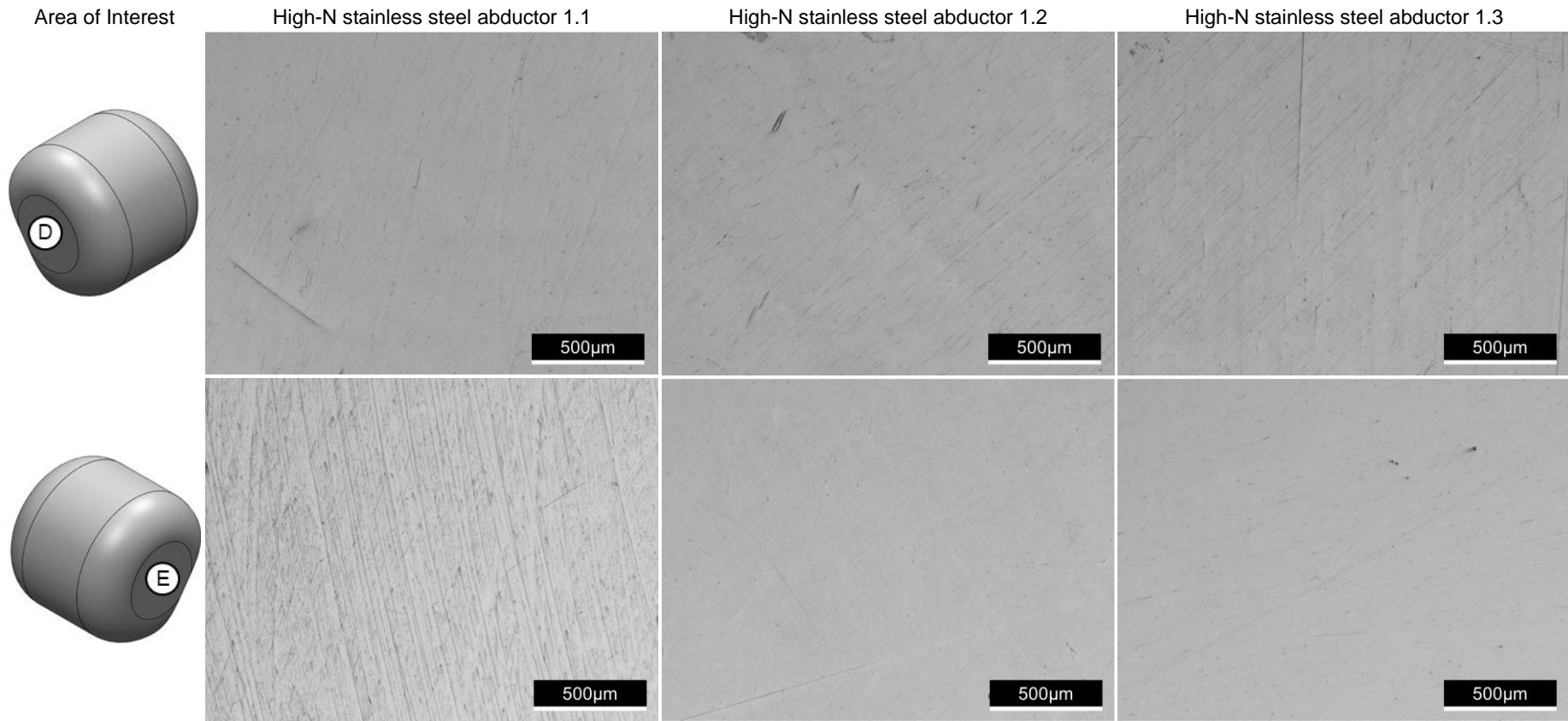


Fig. 5.117: External surface of the abductor. Results produced by Endolab®.

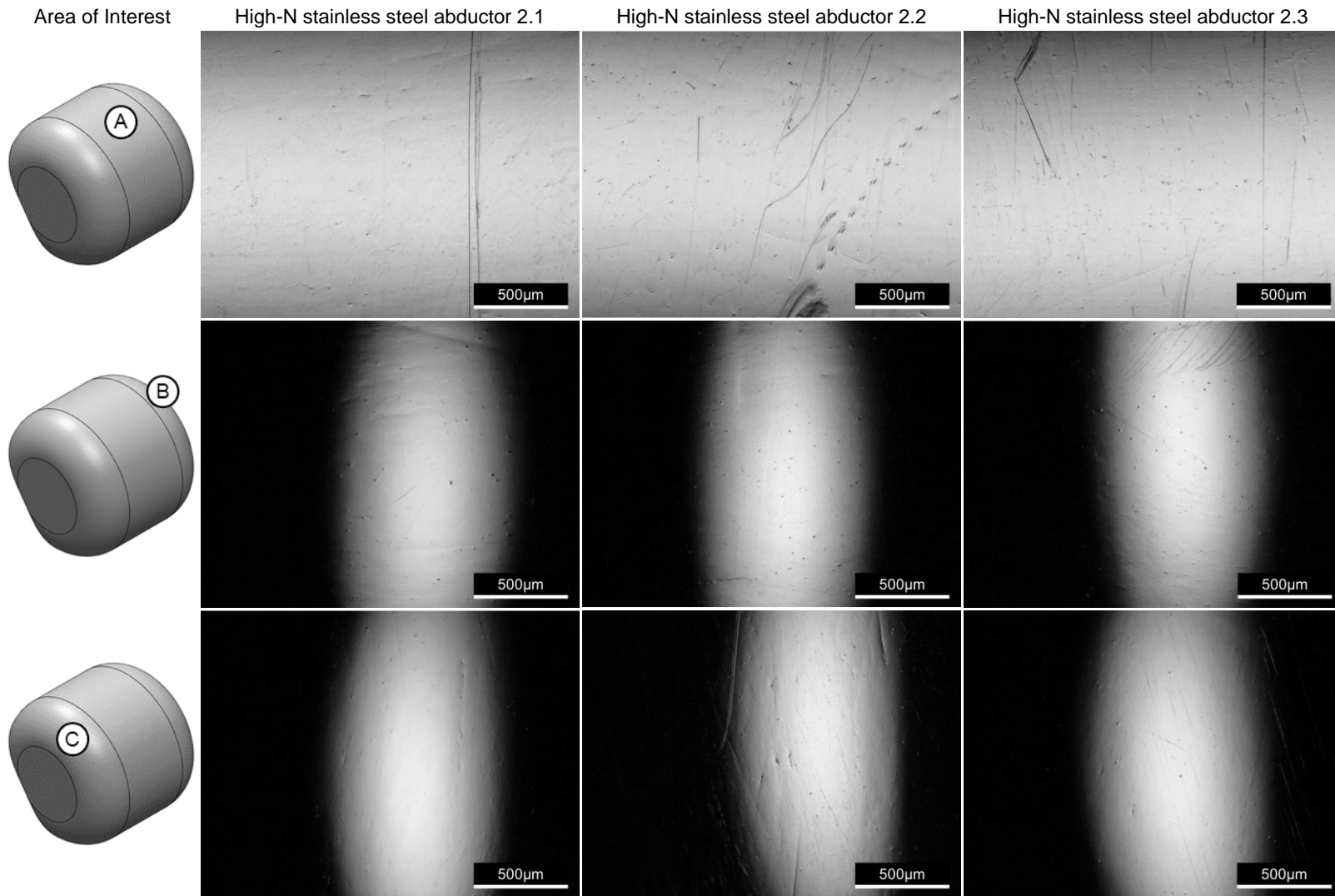


Fig. 5.118: Load bearing surface of the abductor. Results produced by Endolab®.

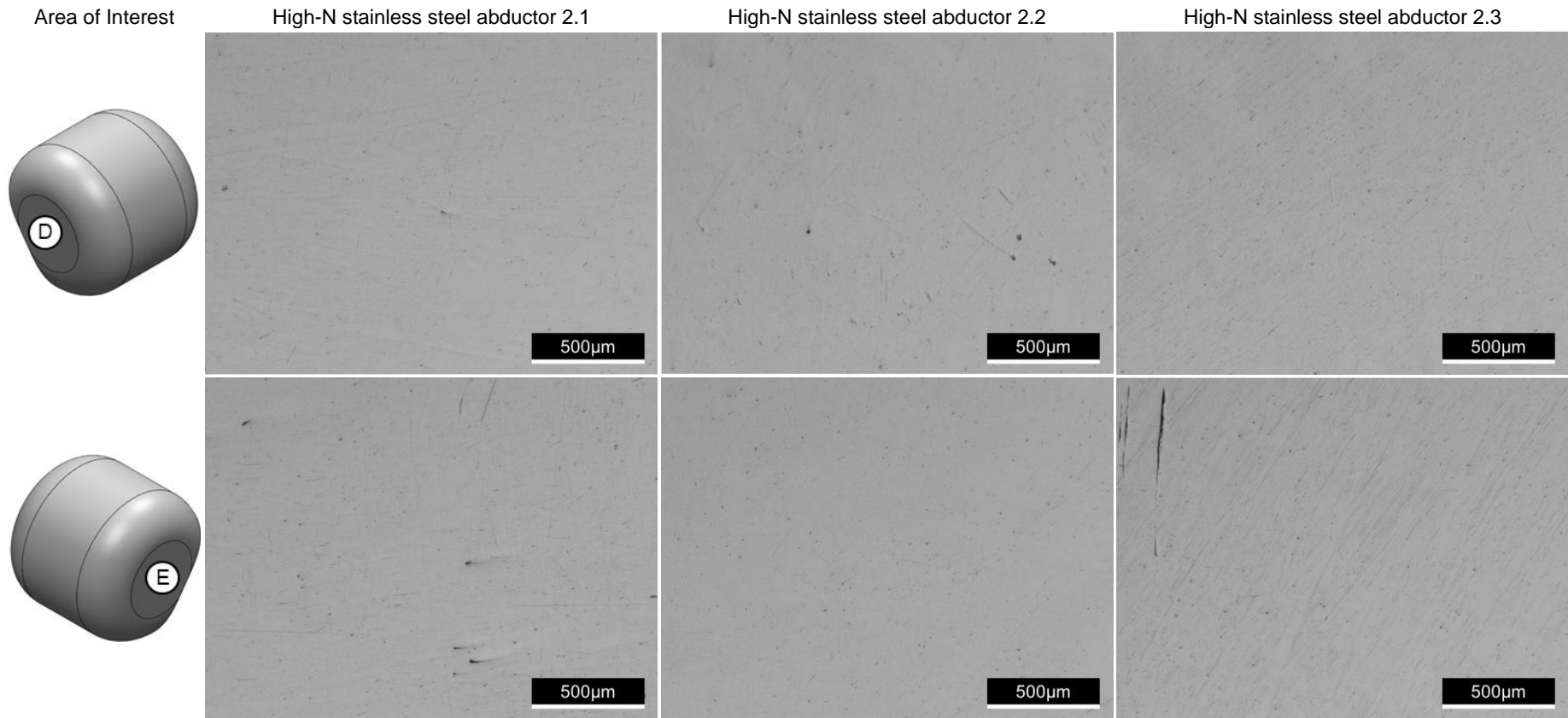


Fig. 5.119: External surface of the abductor. Results produced by Endolab®.

5.7.6. Wear Particles

A wear particle analysis according to ISO 17853:2011 was conducted by Endolab® Mechanical Engineering GmbH following wear testing of the MaltaHip implants consisting of the UHMWPE and VEHXPE soft bearing materials. The analysed wear particles were isolated from the fluid lubricant of the hip joint simulator that were used between 4.5 and 5.0 million cycles. Agglomerates made out of numerous particles were excluded from the analysis during the filtration process.

The wear particle analysis is intended to capture the morphology (shape and size) of the particles during steady-state wear. The equations behind the defined geometric factors are outlined in the Section 3.8.2 (p. 94). A summary of the morphological characteristics of the UHMWPE and VEHXPE particles are shown in Tables 5.20 and 5.21, respectively. The magnitude of the equivalent circle diameter (ECD) clearly demonstrate that the generated wear particles are located within the smallest size range, as indicated in Fig. 2.42 (p. 62). Box plots (explained in Fig. 5.120) illustrating the statistical data of the ECD are shown in Fig. 5.121. The frequency plots for the ECD for UHMWPE and VEHXPE materials are shown in Fig. 5.122 and Fig. 5.123, respectively.

It should be noted that the aim of the particle analysis is to determine the size and shape of the produced particles, and thus does not provide details regarding the quantity of wear particles produced and/or the wear rate (the wear rate is directly determined from the wear test results). The resultant FE-SEM images of UHMWPE and VEHXPE wear particle are shown in Fig. 5.123.

Flaked particles have been observed from the SEM images of the VEHXPE particles, as shown by the red markers in Fig. 5.123b. Flaked particles tend to be associated with wear of XPE implants [91]. Such particles are incorrectly recognized by the software and hence are excluded during the evaluation.

Table 5.20: Morphological characterisation of the UHMWPE analysed particles generated between 4.5 and 5.0 million cycles. Results produced by Endolab®.

MaltaHip Implant 1.1 (UHMWPE)	Mean (n = 462)	Standard Deviation	Max.	Min.
Equivalent Circle Diameter (ECD) [µm]	0.21	0.12	0.72	0.05
Form Factor	0.70	0.19	1.00	0.06
Max. Feret Diameter [µm]	0.31	0.23	2.93	0.08
Min. Feret Diameter [µm]	0.20	0.13	1.34	0.02
Area [µm²]	0.05	0.06	0.41	<0.01
Perimeter [µm]	0.87	0.72	9.12	0.18
Aspect Ratio	1.55	0.40	5.00	1.06

Table 5.21: Morphological characterisation of the VEHXPE analysed particles generated between 4.5 and 5.0 million cycles. Results produced by Endolab®.

MaltaHip Implant 1.1 (UHMWPE)	Mean (n = 774)	Standard Deviation	Max.	Min.
Equivalent Circle Diameter (ECD) [µm]	0.22	0.12	0.96	0.05
Form Factor	0.58	0.20	1.00	0.08
Max. Feret Diameter [µm]	0.36	0.23	2.16	0.07
Min. Feret Diameter [µm]	0.22	0.22	0.13	0.04
Area [µm²]	0.05	0.06	0.72	<0.01
Perimeter [µm]	1.07	0.89	10.68	0.15
Aspect Ratio	1.60	0.39	3.36	1.00

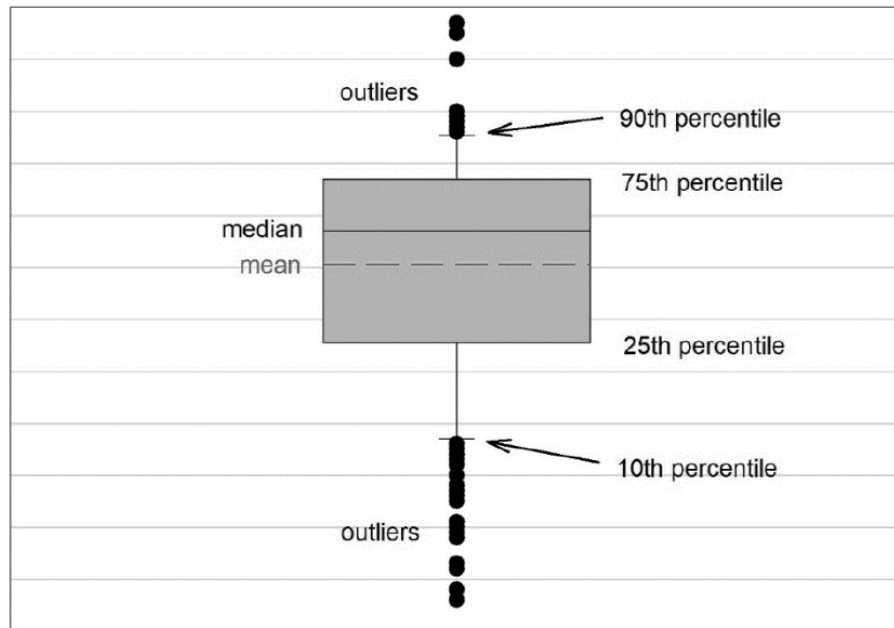


Fig. 5.120: Representative boxplot, illustrating the statistical mean, median and the different zones of the percentiles used in this work. Source: Endolab® report (unpublished).

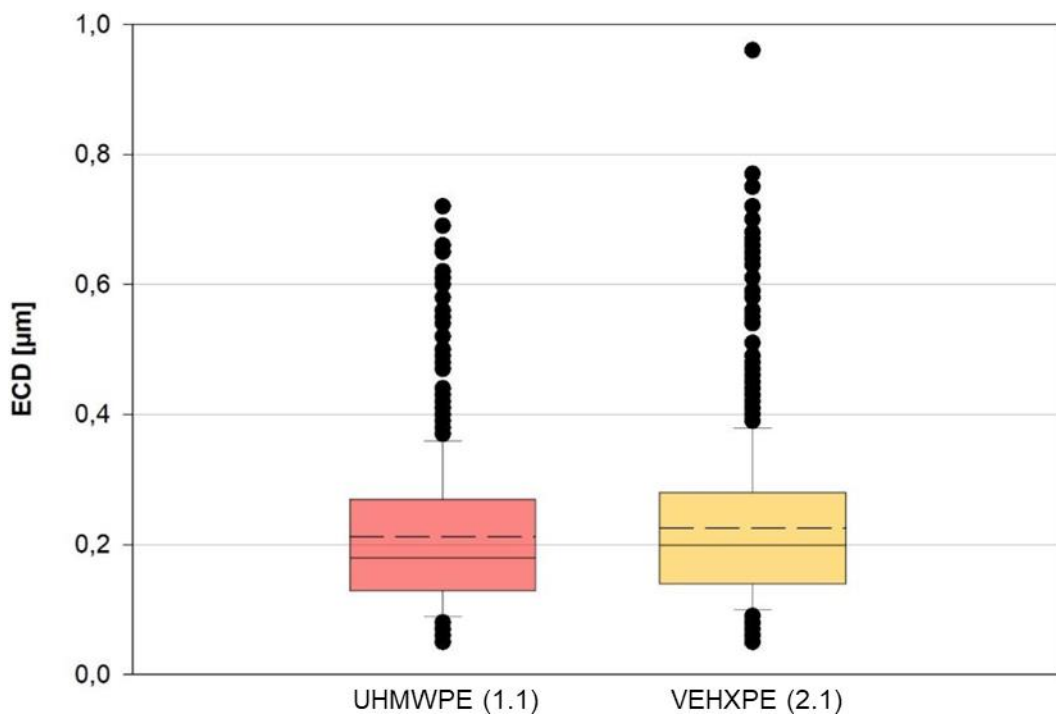
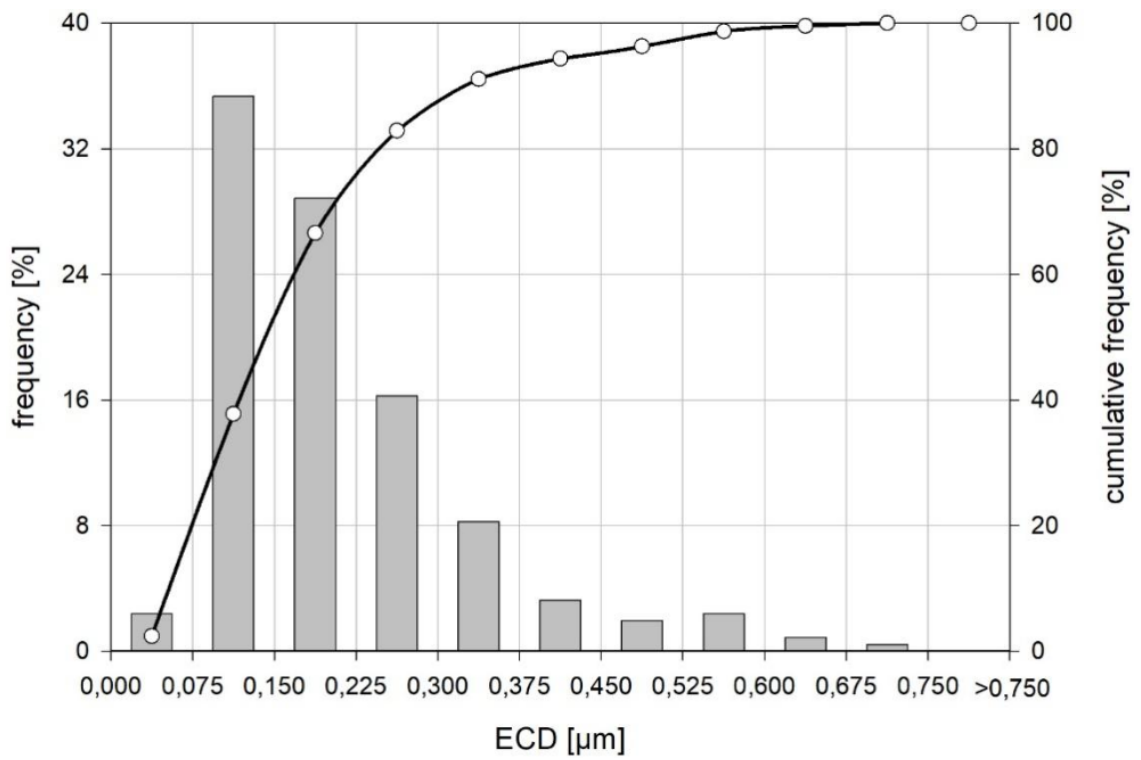
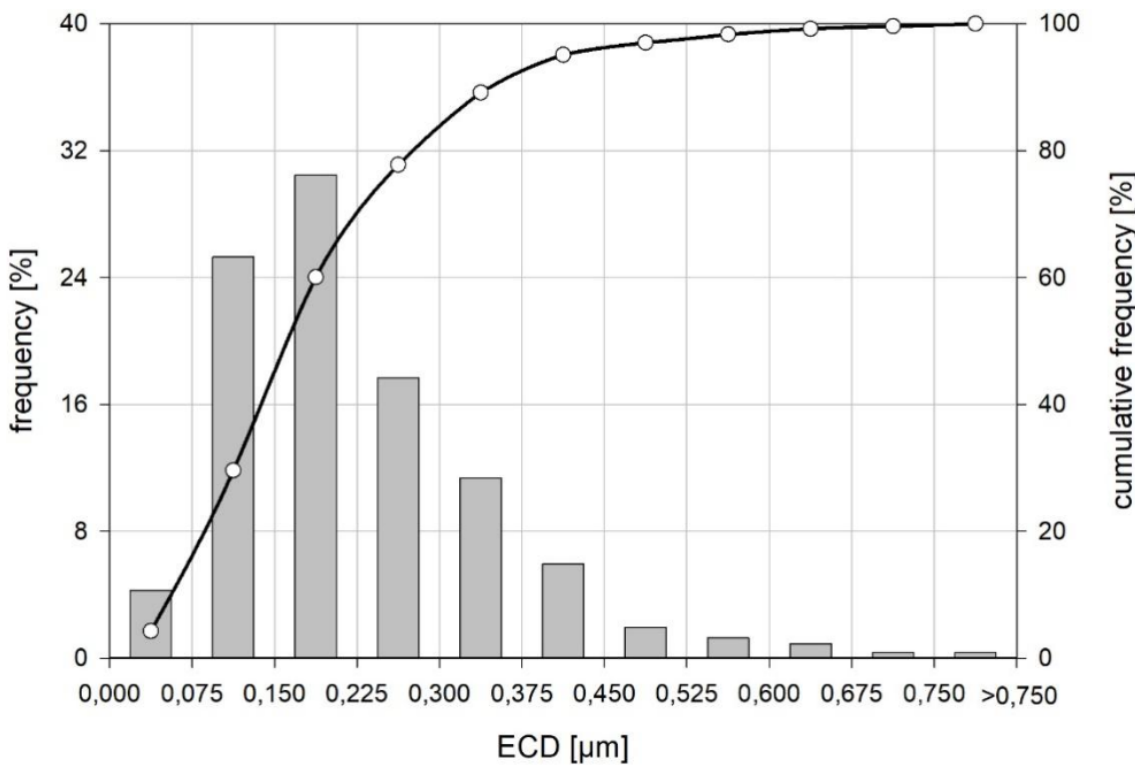


Fig. 5.121: Box plot illustrating the equivalent circle diameter (ECD) of the UHMWPE (1.1) and VEHXPE (2.1) wear particles. Results produced by Endolab®.

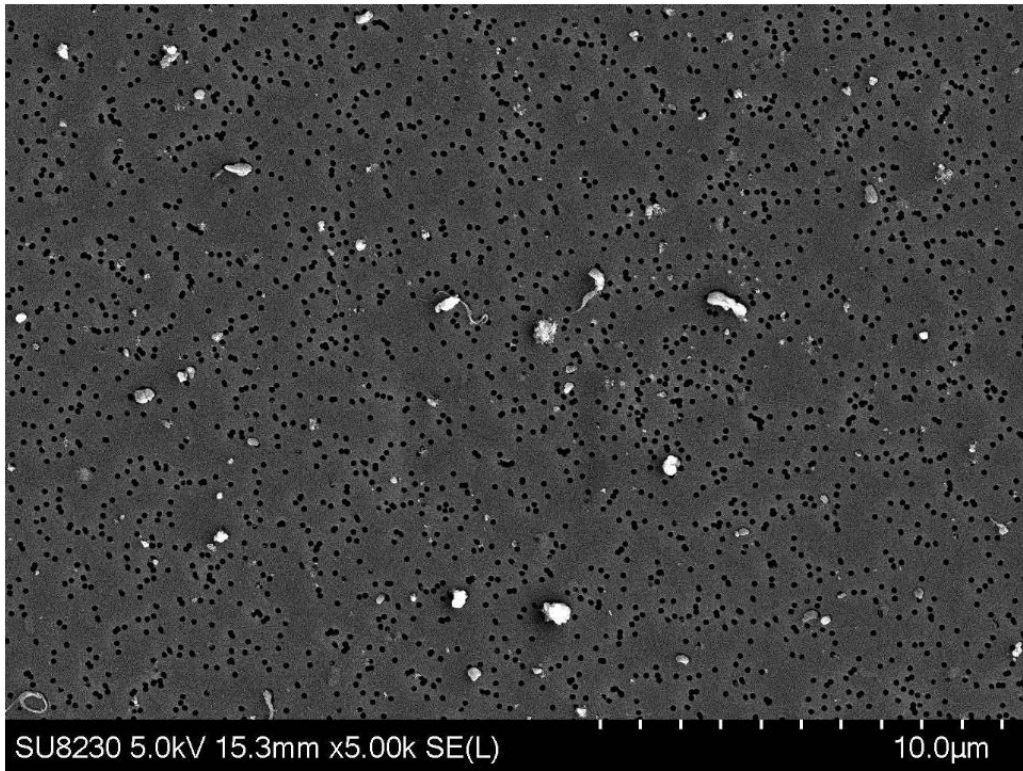


(a) Equivalent circle diameter (ECD) of UHMWPE wear particles.

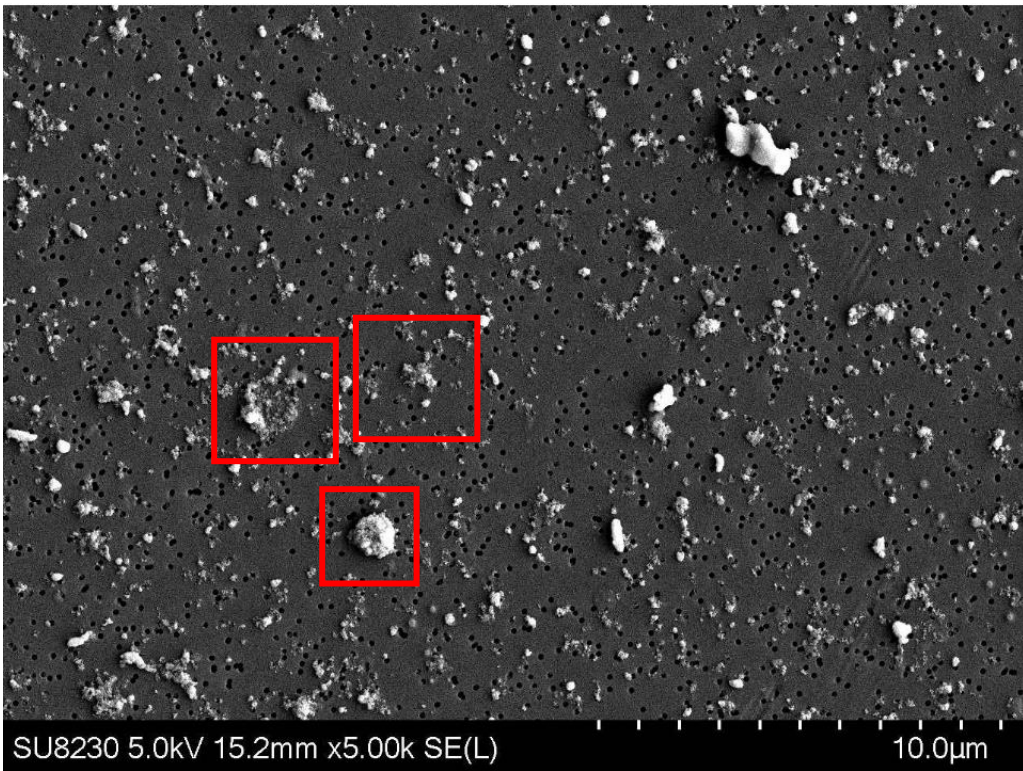


(b) Equivalent circle diameter (ECD) of VEHXPE wear particles.

Fig. 5.122: Frequency and cumulative frequency of the equivalent circle diameter (ECD) for the two main type of polymers being investigated in this work. Results produced by Endolab®.



(a) UHMWPE wear particles.



(b) VEHXPE wear particles.

Fig. 5.123: FE-SEM images of (a) UHMWPE and (b) VEHXPE wear particles generated by the MaltaHip implants between 4.5 and 5.0 million cycles. Results produced by Endolab@.

5.8. Mock Surgery on Cadaver

A mock surgery was conducted using the MaltaHip on a Thiel embalmed cadaver on the 11th June 2019 at the Department of Anatomy (Faculty of Medicine & Surgery, University of Malta). The cadaveric exercise was intended to gain insight by the orthopaedic surgeons on the practicality of implanting a radically different prosthesis. Orthopaedic surgeons, Mr Ray Gatt MD FRCS MA and Mr Ryan Giordimaina MD FRCS, were assisted by theatre nurse Mr Herbert Doublet to conduct the total hip replacement surgery using the MaltaHip prototype (Fig. 5.124). The lateral approach was used on the cadaver, based on the surgeons' preference. The implantation of the stem and MaltaHip cup were mostly based on standard surgical techniques, and are schematically represented in Figs. 5.125 and 5.126, respectively.

A MaltaHip cup with a 53 mm diameter was used to match an existing off-the-shelf surgical cup reamer (Fig. 5.126b). An Exeter stem (size no. 3) with a V40 round taper ($\text{Ø}11.3 \text{ mm}$, $5^\circ 4'$ taper angle) was also used in conjunction with the MaltaHip components. A V40 female round taper was machined in the abductor to match the neck geometry of the Exeter stem. It should be noted that if the abductor is not carefully aligned, the round taper could cause the abductor to assume any orientation when being fitted onto the stem, due to the absence of any mechanical key to constrain its orientation (Fig. 5.45, p. 169). Hence caution was exerted during the assembly of the two components to ensure that the required orientation is achieved. The round taper was used as a temporary means of integrating the available commercial stem to the abductor.



Fig. 5.124: Total hip replacement using the MaltaHip implant.

The correct functionality of the MaltaHip relies on achieving the specified orientation of the cup inside the acetabulum. This detail provides a less straightforward solution than the typical hemispherical cup, which gives a greater leeway during implantation due to its axisymmetric design. The surgeons suggested to introduce simple markers on the MaltaHip cup to indicate its superior and inferior directions to facilitate the orientation process during implantation.

To facilitate the surgical procedure, cementation of the MaltaHip cup should be conducted with the flexor and rotator being already pre-assembled inside the cup. Only a single additional surgical instrument was required to accommodate the MaltaHip design, being a pusher tool which is shaped to match the inside of the rotator component (Fig. 5.126c) where the abductor component would later fit. This tool is required to press the implant assembly (MaltaHip cup, flexor and rotator) into the cement until it cures. The pusher tool is intended to be pressed against the rotator component to transfer the applied load to the MaltaHip cup, which effectively applies pressure onto the cement.

Following the cement curing process, the surgeons proceeded to conduct the hip reduction procedure. The surgeons pointed out that the final hip reduction was done with relative ease, and with no drastic changes required from the conventional approach. The surgeons then proceeded to check the range of motion of the implanted hip (Fig. 5.126f). The implant demonstrated excellent flexion/extension (easily achieving over 90° of flexion), abduction/adduction and medial/lateral rotation, with no signs of dislocation or impingement, as shown in detail in Fig. 5.67 (p. 188). The surgeons pointed out that such movements were achieved with a high degree of implant stability.

The mobility-check of the new prosthesis was then taken a step further as an attempt was made to identify the possibility of performing a ‘figure of four squat’ position with the new prosthesis, which involves high flexion and abduction angles, coupled with external rotation. It was observed that the squat position could be achieved without incurring any signs of dislocation, which may suggest that the new design may provide a possible improvement in the range of motion of the hip when compared to the conventional ball-and-socket prosthesis.

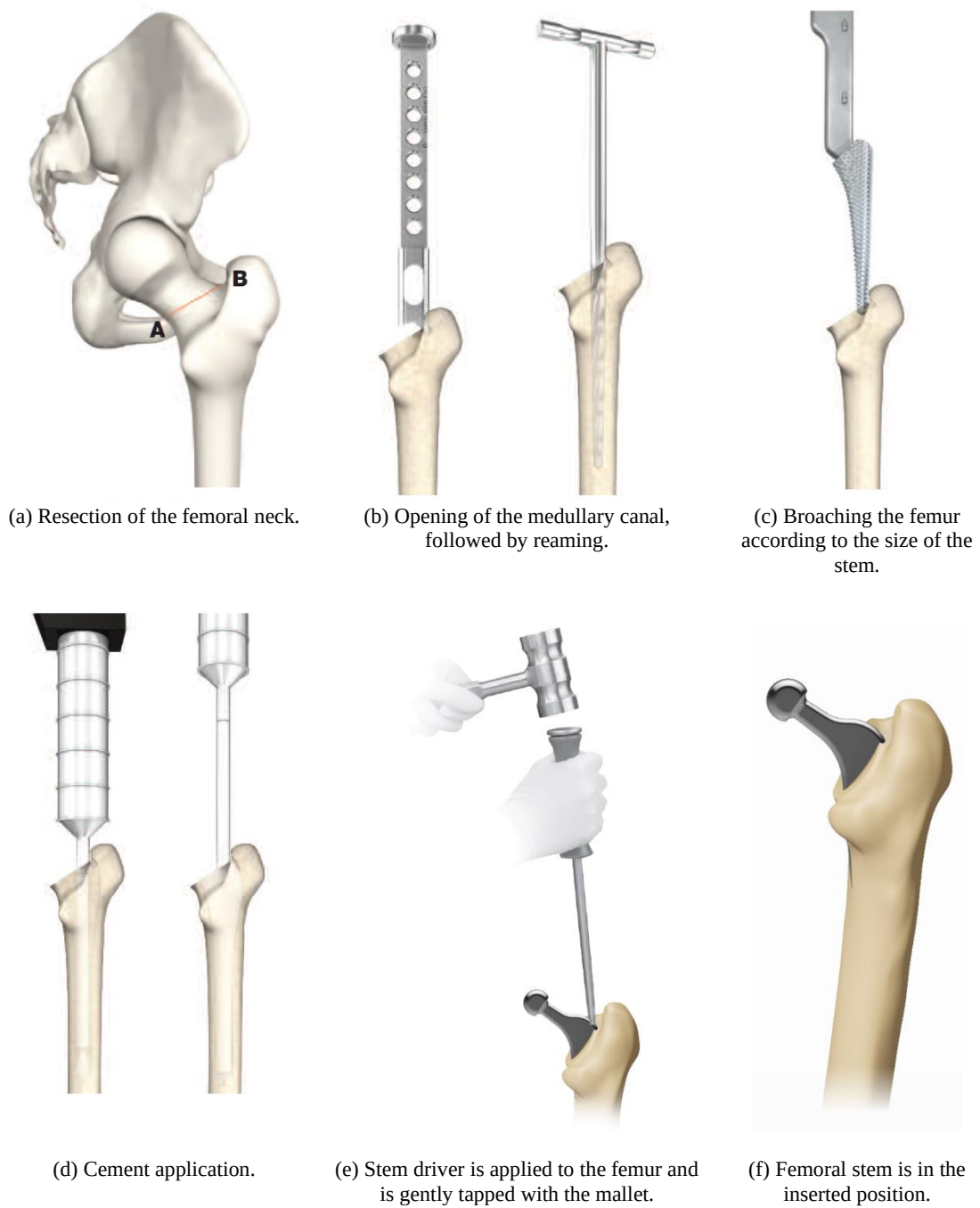
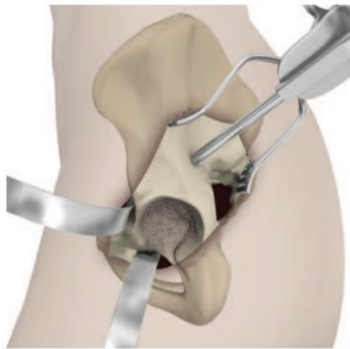
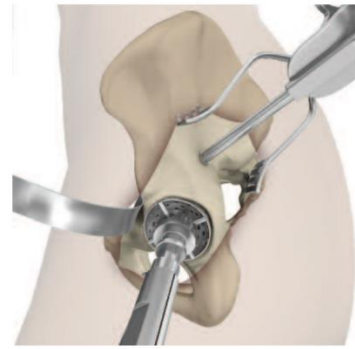


Fig. 5.125: Preparation of the femur bone and insertion of the femoral implant.



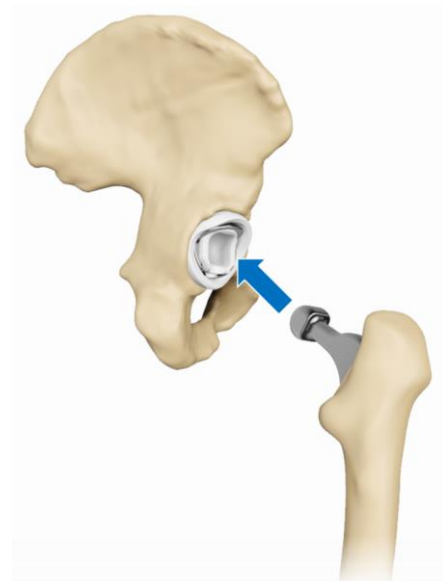
(a) Preparation of the bony socket for implant insertion.



(b) Reaming of the acetabulum.



(c) Cup insertion. Cement pressurization applied using the new pusher tool which fits into the rotator.



(d) Following cement curing, the abductor is reduced into the rotator component.



(e) Final implant is in the inserted position.



(f) Testing intra-operative range of motion.

Fig. 5.126: Implantation of the MaltaHip cup and reduction of the hip.

5.9. Summary of Results

In this work, a parametric CAD model of the MaltaHip was developed, which was used for optimising the design of the prosthesis through systematic variations of the model dimensions. Finite element simulations were conducted on each design iteration, to identify the influence of each design parameter on the von Mises and contact stresses generated on the implant. The Three Network model was implemented to model the viscoelastic-viscoplastic behaviour of the two polyethylene materials (UHMWPE and VEHXPE) that were used in this work.

The finite element simulations on the finalised design solution demonstrated that the bulk of the components undergo elastic deformation during use. Furthermore, it was observed that deformations due to contact stress were mainly elastic, except for the rotator-abductor articulation, which exhibited a highly localised region that underwent plastic deformation. Theoretical wear models were used to predict volumetric wear produced by the MaltaHip implant. Even though the wear models were highly indicative of the wear volume produced by the ball-and-socket implants, it was observed that they were not suitable to model the wear volume produced by the cylindrical articulations of the MaltaHip, even though the cross-shear effects are taken into account by the Liu and Petrella models, since these resulted in overestimating the wear rate of the MaltaHip cup.

Physical prototypes of the MaltaHip were produced using high-nitrogen austenitic stainless steel for the hard bearing components, and UHMWPE and VEHXPE were used for the soft bearing components, creating two versions of the MaltaHip. The axi-symmetrical geometry of the articulations enabled the majority of the components to be fabricated using a CNC lathe, which in general performs faster machining processes than CNC milling machine.

The physical prototypes were wear tested according to ISO 14242-1:2014/Amd 1:2018 at Endolab® Mechanical Engineering GmbH to 5.0 million cycles. The wear test results have demonstrated that the UHMWPE version of the MaltaHip resulted in a wear rate of 7.9 ± 0.3 mg/mc, whereas the ball-and-socket implants produced out of UHMWPE hemispherical cups resulted in a wear rate of 29.1 ± 3.0 mg/mc. Furthermore, the VEHXPE version of the MaltaHip resulted in a wear rate of -1.1 ± 1.0 mg/mc, whereas the ball-and-socket implants produced out of VEHXPE hemispherical cups resulted in a wear rate of 4.5 ± 2.3 mg/mc. Hypothesis testing indicated that the reductions attained with the MaltaHip implant were statistically significant, at 99% confidence interval.

Optical microscopy images of the articulating surfaces have been captured following the wear testing regime. It was noticed that different topographical surfaces were produced in the MaltaHip implants, compared to those which are typically observed in ball-and-socket implants.

Both the UHMWPE and VEHXPE MaltaHip cups retained the original machining marks after the wear test. On the other hand, signs of wear were visibly noted on the rotator components. The wear particles produced during the wear testing regime possessed the smallest sizes, which are associated with highly inflammatory reactions. Nonetheless, low volumes of wear particles were produced by the implants, and hence it is postulated that their overall biological reactions could be minimal.

A mock surgery was conducted on the cadaver to assess the feasibility of implanting the new prosthesis design. The orthopaedic surgeons pointed out that the MaltaHip could be implanted using the standard surgical technique. Intra-operative testing conducted by the surgeons demonstrated that the implant could produce wide ranges of motion that were achieved with a high level of stability.

6. Discussion

6.1. Introduction

In this work, a provisional design for a novel low-wearing hip implant is investigated and developed. Throughout the design optimisation process, finite element models were developed which simulated the loading conditions during the gait cycle. The polyethylene components were based on the Three Network model to model their viscoelastic-viscoplastic behaviours.

The finite element results enabled the identification of the key design features which minimized the stress concentrations in the MaltaHip components. Furthermore, the differences between the various stress levels which are exhibited by the MaltaHip and ball-and-socket implants are discussed. The generated finite element results, together with slide track data, were then used to compute the theoretical wear rates of the MaltaHip and ball-and-socket implants using the different wear models that were reviewed in literature.

The theoretical wear rates were compared to those that were generated by experimental wear tests. A number of key differences were observed between the predicted and actual wear results. Therefore, the factors which may have led to these discrepancies are discussed. The optical microscopy images enabled the physical worn surfaces to be analysed in detail. Possible wear mechanisms that are likely to have contributed to the worn topography of these surfaces are discussed.

Following the particle analysis results, an attempt is made to provide a quantitative index of the extent of osteolysis that might occur as a consequence of the specific wear debris that is generated by the MaltaHip implants. Lastly, the potential benefits attained by the MaltaHip, as well as improvements that could be implemented to future versions of the MaltaHip are discussed.

6.2. Structural Model

6.2.1. Material Characterisation and Modelling

The finite element modelling conducted in this work served to provide insight on the von Mises and contact stresses generated on the MaltaHip prosthesis, which influence the structural integrity of the bulk and surfaces of the various components. The contact stress values also act as the basis for predicting the wear rates.

Although finite element studies on hemispherical cups found in literature usually investigate both the von Mises and contact stress [219, 338, 341, 342], most studies are mainly concerned with analysing the contact stresses that are generated at the articulation [18, 33, 257, 299, 343, 344]. Contact stress studies in published literature are primarily intended to provide the necessary mechanical response data for predicting the theoretical wear rates of the hemispherical cup.

The main reason for the limited studies on the von Mises stress values of hemispherical cups is attributed to their substantially thick sections that can easily handle the range of stress values that are exhibited during the gait cycle. In fact, polyethylene hemispherical cups exhibit a relatively wide margin of safety since their von Mises stress values are usually located well below the material's yield strength. In fact, fracture failures of hemispherical cups are an infrequent clinical complication [345]. Nonetheless, thinner polyethylene sections had to be used for the MaltaHip components, due to the greater number of articulating components being incorporated in the design, and thus an analysis on the von Mises stress values was required.

It was observed that several finite element models simulating the polyethylene hemispherical cup made use of linear elastic or elastic-plastic (bi-linear or multi-linear kinematic hardening) models. Such models do not take into account the viscoelastic-viscoplastic behaviour of the polyethylene material, and thus neglect the load rate dependency and creep effects that are induced by the material [132, 192, 227, 228, 219–226]. This results in an overestimation of the stresses imposed on the polyethylene component, as outlined by the stress-strain curves in Fig. 2.19 (p. 29). Furthermore, the reported UHMWPE stress-strain curves in literature that are obtained from physical tests (i.e. tensile or compression tests), which are used to characterise the mechanical behaviour of polyethylene for the finite element simulations, often fail to provide the strain rate value which was used during the test [132, 192, 227, 228, 219–226]. Consequently, a great discrepancy exists in the polyethylene stress-strain curves which are usually reported in these types of studies. In this work, it was observed that hemispherical cups could reach strain

values of 6.0% (Fig. 5.11, p. 129), and thus stress overestimations can indeed be produced by these models.

The Three Network model was used to reproduce the complex viscoelastic-viscoplastic mechanical behaviour of UHMWPE, as shown by the modelled stress-strain curves which were calibrated using experimental data Fig. 5.3 (p. 110). It should be noted that the MCalibration software requires a minimum of two different stress-strain curves representing different loading conditions, for each material being calibrated. For this work, two stress-strain curves produced at equal strain rate values but with different maximum strain values were used for the calibration procedure. Discrepancies between the experimental and the calibrated stress-strain curves were observed. The Three Network Model is based on a continuum model and therefore discrepancies are attributed to the inability of the model to consider microstructural changes in the polymer, which become significant at large strains. The model would fit very well for experimental data at low maximum strain values. The accuracy of the calibrated model could be enhanced by incorporating further stress-strain curves, possibly conducted at different strain rates. However, such improvements are achieved at the expense of increased computational expense to calibrate the model.

It was observed that the UHMWPE and VEHXPE materials exhibited similar mechanical behaviours. Due to the different molecular weights of UHMWPE and VEHXPE, the parameters of the material model cannot be directly compared to each other. UHMWPE is produced from GUR 1050 consisting of a molecular weight of 6.0 million g/mol and possesses a linear structure, whereas VEHXPE is produced from GUR 1020 consisting of a molecular weight of 3.5 million g/mol and possesses a crosslinked structure. The higher molecular weight of GUR 1050 would imply a stiffer structure over GUR 1020, provided that the molecular structure would be the same. However, in this case, the lower molecular weight of the VEHXPE structure is sustained by the presence of crosslinks, causing the structure to become stiffer. As a result, on a macro level, similar mechanical behaviour was observed, as evident by the high similarity between the parameters of the material model, as well as the stress-strain curves produced during the compression tests. The main differences between UHMWPE and VEHXPE are clearly observed on a micro-level, due to the different wear rates which were produced. The wear processes are highly influenced by micro-level interactions since the liberation of wear particles is highly influenced by the molecular arrangement.

All parameters of the material model were calibrated at a constant temperature of 37°C, and thus temperature-dependency effects were not taken into account, due to the difficulties involved in generating a temperature map of the articular surface in the finite element model, and the unavailability of empirical data regarding the range of temperatures that are exhibited by the

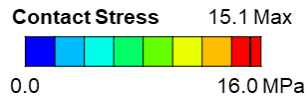
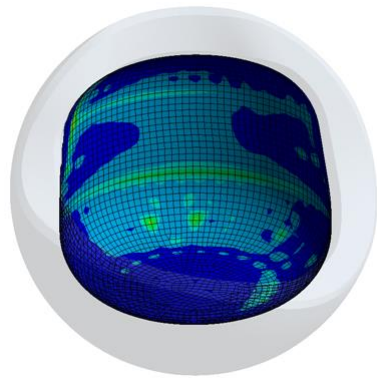
articulations of the MaltaHip. Furthermore, this would have increased the computational expense involved in the FE model, due to the increased complexity of the Three-Network Model.

To the best of the author's knowledge, the use of the Three Network material model to compute the mechanical behaviour of a hip joint prosthesis during a transient gait cycle has not been published in literature. Nonetheless, it was observed that that the Three Network model was used to simulate the behaviour of knee implants (e.g. [346]) and test coupons with simplified geometry (e.g. [347]). Hence, comparisons between the current work and literature results could only be made to ball-and-socket implants which made use of the elastic or elastic-plastic models. Furthermore, the MaltaHip implant was also simulated using the elastic model for polyethylene components, as shown in Fig. 6.1 and Fig. 6.2, to analyse the discrepancies that are generated between the two material models. In fact, the simulation of the MaltaHip implant using the Three Network model resulted in a reduction in the maximum contact stress by 17 – 41 %, compared to the linear elastic model, as shown in Fig. 6.1. Similarly, the maximum von Mises stress values produced by the Three Network model resulted in a reduction in the maximum contact stress by 11 – 21 % compared to the linear elastic model, as shown in Fig. 6.2. This highlights the significance of using the appropriate material model for simulating polyethylene components.

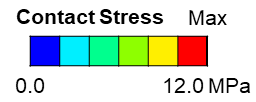
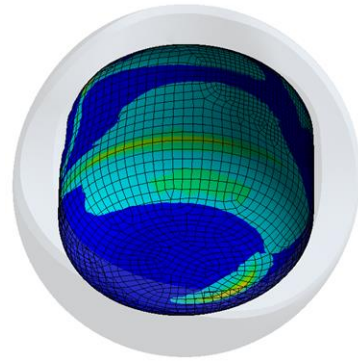
The simulation of the MaltaHip prosthesis undergoing the gait cycle was computationally expensive, as a result of the fine mesh, short time steps, high number of contacting surfaces of the model, and the use of the non-linear material model to simulate the behaviour of the polyethylene material. In fact, simulating one gait cycle (representing 1.0 second of hip motion) using the MaltaHip required 6.4 days of computation, and 1060.5 GB of data to be stored. As a consequence, it was unfeasible to simulate numerous gait cycles to induce further creep deformations. To bring this into context, experimental data have demonstrated that at least 2.5 million cycles are required to produce 0.09 mm creep deformations on a 9.0 mm thick UHMWPE hemispherical cup [200]. Therefore, it was anticipated that a higher number of cycles would be required to induce similar creep deformations on the MaltaHip cup, due to thinner polyethylene sections being used. Hence, this justifies the use of simplified creep laws in published literature (as reviewed in Section 2.4.1, p. 27), which are based on empirical data, to predict the creep deformations [191, 227]. However, due to the absence of empirical data on the new prosthesis design, the creep deformations could not be estimated. Therefore, the finite element analysis in this work was limited to one gait cycle. One way of reducing the computational expense is to use a 2D model. However, this would still not provide an accurate account of the actual creep effects, due to the absence of axi-symmetrical features in the actual 3D model.

It should be also noted that the contact pressure changes attributed to the lubricant and wear mechanisms were not included in the finite element simulation, due to the high level of

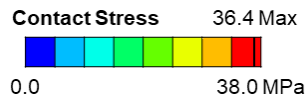
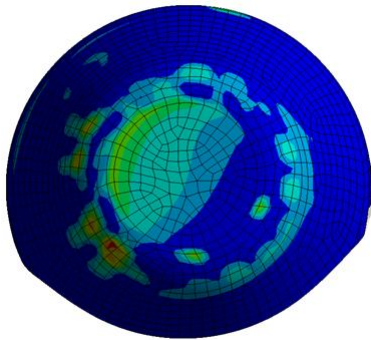
complexity involved in simulating such processes. Furthermore, the contact pressure changes generated from these processes are likely to have been much greater than those produced by the creep deformations [331]. During the cyclic tests, it is likely that the lubricant may not have always been present at the articulation. Therefore, during instances when the lubricant may not have been present in the articulation, it is likely that localised contact stresses may have been generated, due to incomplete contact being made between the articulations on a micro-level. On the other hand, when the lubricant is present at the articulation, the lubricant is able to carry loads and improve the distribution of contact stresses. These contact pressure changes are likely to be more significant than those produced by creep deformation effects. Nonetheless, the analysis presented in this work has already provided an improved representation of the actual stress values exhibited by both the ball-and-socket and MaltaHip implants through the implementation of the Three Network model.



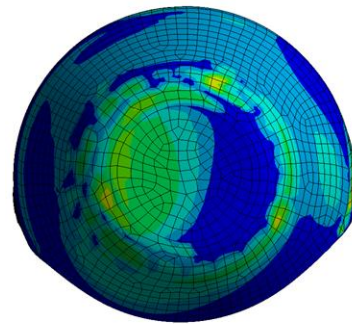
(a) Elastic linear model: MaltaHip Cup



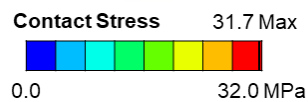
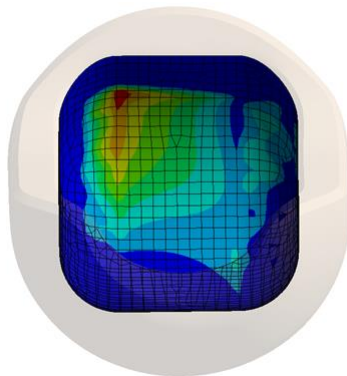
(b) Three Network model: MaltaHip Cup
(21% lower maximum contact stress)



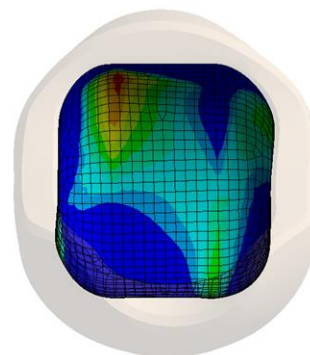
(c) Elastic linear model: Rotator



(d) Three Network model: Rotator
(41% lower maximum contact stress)

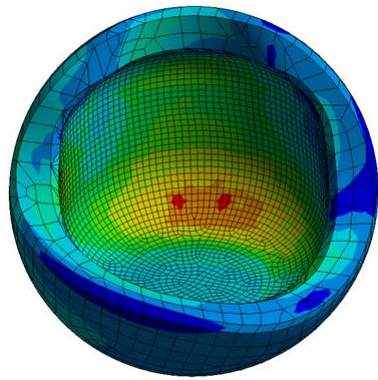


(e) Elastic linear model: Rotator

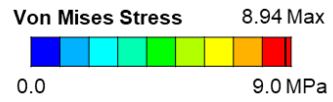
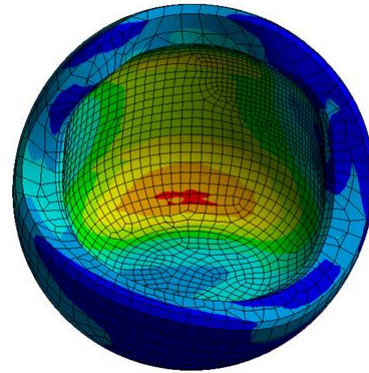


(f) Three Network model: Rotator
(17% lower maximum contact stress)

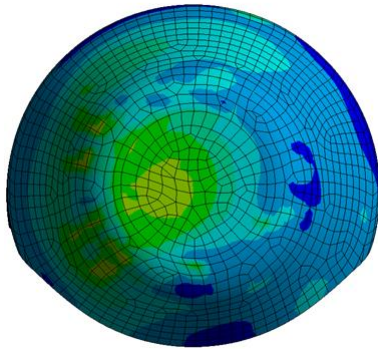
Fig. 6.1: Comparison of contact stress values of the MaltaHip components using elastic linear model and the Three Network model. The elastic linear model overestimates the actual stress values.



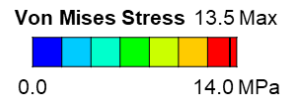
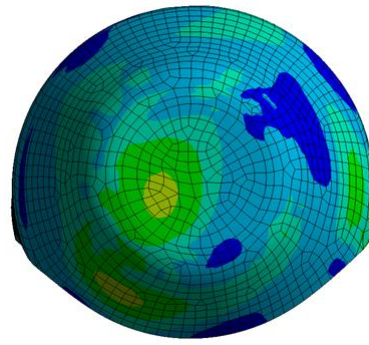
(a) Elastic linear model: MaltaHip Cup



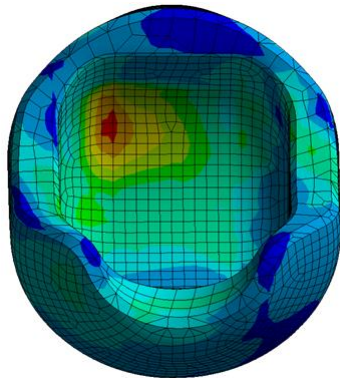
(b) Three Network model: MaltaHip Cup
(11% lower maximum von Mises stress)



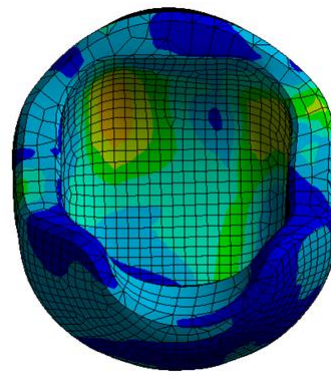
(c) Elastic linear model: Rotator



(d) Three Network model: Rotator
(21% lower maximum von Mises stress)



(e) Elastic linear model: Rotator



(f) Three Network model: Rotator
(21% lower maximum von Mises stress)

Fig. 6.2: Comparison of von Mises stress values of the MaltaHip components using elastic linear model and the Three Network model. The elastic linear model overestimates the actual stress values.

6.2.2. Component Design

The parametric CAD model of the MaltaHip was fundamental to study the effect of each design parameter on the von Mises and contact stresses of the new components. As discussed in Section 3.4.1 (p. 74) and Section 5.3.3.1 (p. 112), the exercise was based on a 48 mm MaltaHip cup (i.e. the smallest cup that could practically fit the MaltaHip mechanism), so that vulnerabilities in design due to high stresses could be immediately identified.

The study outlined that even though the stresses on the metallic bearings of the MaltaHip (i.e. flexor and rotator) were highly sensitive to design changes, these were able to sustain the whole range of von Mises stress values that were generated by all the design parameter variations that were tested. In fact, the greatest von Mises stress value resulted to be 80 MPa, being well below the yield strength of the material. Hence, this allowed a high level of flexibility in the design of the metallic components. Hence, the thicknesses of the metallic components of the MaltaHip were reduced as much as possible, such that these components occupy the least volume in the prosthesis, and make room for the polymeric components with thicker sections. Furthermore, the low von Mises stress values of the high-N austenitic stainless steel components suggest that these can be substituted with other medical-grade metals, such as 316LVM stainless steel or cobalt–chromium–molybdenum (CoCrMo) alloy, depending on the manufacturer's preference. The 316LVM stainless steel is easier to machine [348], and costs less than CoCrMo [66]. On the other hand, CoCrMo offers improved corrosion [349] and abrasion [350] resistance. Nonetheless, their actual benefits in relation to the uni-directional motion of the MaltaHip prosthesis would necessitate further investigations.

On the other hand, the designs of the UHMWPE components (i.e. MaltaHip cup and rotator) offered less flexibility in their design, when compared to the metallic components, as a consequence of their low yield strength. Thus, these components required a highly optimized design solution to sustain the von Mises and contact stress values.

It is interesting to note that decreasing the MaltaHip cup thickness (achieved by varying C_t), produced no changes to the von Mises stress values (Fig. 5.6k, p. 119) and only minimal changes were observed in the contact stress values (Fig. 5.5k, p. 116). The main reason is likely to be associated to its relatively large geometrical design, hence rendering it insensitive to the narrow range of values which could be practically tested. In fact, since the von Mises stress value was noted to remain relatively the same with thinner MaltaHip cup sections, smaller cups may be produced to enable hydroxyapatite-coated metallic shells to be integrated to the prosthesis to enable cementless fixation. Nonetheless, further studies would be required to investigate the fatigue resistance of the thinner MaltaHip cup.

In this work, a minimum thickness of $C_t = 5.3$ mm was maintained at the thinnest region of the MaltaHip cup⁵⁸. Due to the varying thickness profile of the MaltaHip cup, this resulted in a maximum thickness values of 7.1 and 11.1 mm at the load bearing and non-load bearing surfaces, respectively, as shown in Fig. 6.3a.

On the other hand, it was observed that the contact stresses of the rotator were highly sensitive to parameter changes, as shown in Fig. 5.5a and b (p. 115), as a result of its limited size which could only provide a relatively small contacting area for the articulations. The maximum von Mises and contact stress values were highly dependent on the size of the internal articulation. Therefore, designing efforts were focussed on maximising the contacting area of this articulation. Once again, it was observed that both the contact and von Mises stress values were not influenced by different thicknesses (R_{t1} and R_{t2}) of the rotator component, as shown in Fig. 5.5d and e (p. 115), and Fig. 5.6d and e (p. 118). Nonetheless it was ensured the a minimum of 5 mm thickness was maintained at the thinnest section of the load bearing surface of the component (as shown in Fig. 6.3b). The 3.7 mm section is a non-load bearing structure and in fact was subjected to low levels of von Mises stress (less than 6.0 MPa), as can be observed in Fig. 5.17 (p. 137), and thus is unlikely to pose any risk for fatigue failure.

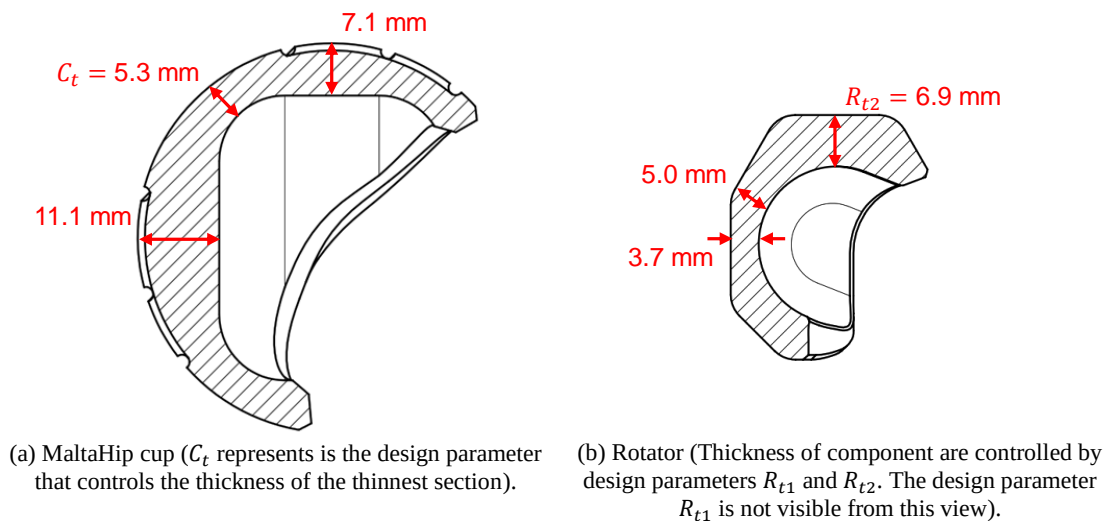


Fig. 6.3: Thickness profile of the MaltaHip polymeric components.

⁵⁸ The recommended minimum thickness value for standard ball-and-socket implants is 5.0 mm, although thinner acetabular cups of 3.0 – 3.8 mm have been reported in literature [374, 375].

6.2.3. Comparison of Finalised MaltaHip and Ball-and-Socket Designs

6.2.3.1. Overview

Since the MaltaHip and the ball-and-socket implants possess distinct designs, the polymeric components exhibit different stress levels. In general, the MaltaHip components can be described to possess greater contacting surface areas, but having thinner sections, as compared to the hemispherical cup. As a result, the MaltaHip components exhibit lower contact stress values, but greater von Mises stress values than the hemispherical cup of the ball-and-socket implant. The details regarding the different contact and von Mises stress values which are exhibited by the MaltaHip and ball-and-socket designs are described below.

6.2.3.2. Contact Stress

The maximum contact pressure value obtained for the 28 mm ball-and-socket implant in this work resulted to be 11.90 MPa, as shown in Fig. 5.12 (p. 130). Other studies which made use of the time-invariant elastic models to simulate hemispherical cup under similar conditions have reported maximum contact stress values ranging between 8.1 – 26.0 MPa [224, 225, 344, 351, 352]. The discrepancies in these results are not only attributed to the use of different material models, but also to different physical material properties (e.g. fabrication and sterilisation processes used), different boundary conditions (e.g. load profile and magnitude) and geometrical models (e.g. clearance values).

As the hemispherical cup and the MaltaHip components are based on different designs, different patterns of contact stress distributions are formed. The ball-and-socket articulation forms concentric stress patterns (Fig. 5.12, p. 130), with stress concentrations being formed on its rim, also known as edge loading, as shown in Fig. 5.14 (p. 132). On the other hand, it can be observed that the contact stresses of the cup-flexor (Fig. 5.21, p. 141) and flexor-rotator (Fig. 5.22, p. 142) articulations are well distributed, with no significant stress concentrations being formed.

A stress concentration is noted to be generated at the rotator-abductor articulation, as a result of its limited size, as shown at the 0.5 s of the gait cycle in Fig. 5.23 (p. 143). This stress concentration is located at the filleted edge of the component and occurs during high flexion angles, which causes the curved surface to momentarily bear the majority of the load. Nonetheless, it was observed that the average contact stress of the rotator-abductor articulation,

3.84 MPa (Fig. 5.23 p. 143), was lower than the average contact stress that was produced by the hemispherical cup, 4.37 MPa (Fig. 5.12, p. 130). This is highly beneficial considering that the rotator articulation occupies a smaller volume (cylinder, Ø 21 mm, H 20 mm) in the prosthesis than the ball-and-socket articulation (sphere, Ø 28 mm). As demonstrated from the wear testing results conducted in this work, no signs of cracks or delamination were observed after 5 million cycles in any of the components. Therefore, under operating conditions, it is unlikely that the premature failure of the prosthesis takes place. A similar application involving UHMWPE components with similar thickness and exhibit similar contact stress levels are the tibial inserts of knee implants [71]. Therefore, these have been observed not to cause fail prematurely when a person experiences a minor fall. Furthermore, despite that the prosthesis possesses an interlocking mechanism, the components are able to freely rotate, enabling subluxation of the prosthesis, thus preventing the generation of high contact stresses. However, complete physical testing would be required in order to produce any conclusions regarding the survivability of the rotator component under impact loading conditions.

The low contact stress values achieved in the MaltaHip implants is of great importance for the long-term survival of the prosthesis. Furthermore, the actual contact stress values are likely to further decrease as the number of gait cycles increases, as a result of the running-in and creep processes which enhance the conformity of the articulations over time. The design of a large articulation has demonstrated to work very well for the cup-flexor articulation, as it resulted in the lowest contact stress value, thus indicating that low volumes of wear debris were generated.

6.2.3.3. Von Mises Stress

The von Mises stress values induced in the MaltaHip components correspond to the bulk structural integrity of the prosthesis. As outlined earlier, when the metallic components (flexor and abductor) were analysed for their mechanical response during the standard gait cycle, it was observed that these exhibited von Mises stress values that are well below the material's yield strength (430 MPa). Furthermore, their resultant strain values were reported to be very low (maximum strain that was exhibited over the gait cycle is 0.7×10^{-3}), as discussed in Section 5.3.5.3. (p. 132). Hence, from a structural point of view, the metallic components effortlessly meet the requirements to sustain the applied loads.

On the other hand, a relatively narrow margin exists between the von Mises stress and yield strength of the polyethylene components of the MaltaHip. As outlined in the results section, the maximum von Mises stress of the MaltaHip UHMWPE cup was found to be 8.94 MPa, as shown in Fig. 5.15 (p. 135), whereas the maximum von Mises stress of the MaltaHip UHMWPE rotator resulted to be 13.46 MPa, as shown in Fig. 5.15 (p. 135) and Fig. 5.16 (136). Nonetheless, such values are still lower than the distributed yield strength values of UHMWPE (21 - 25 MPa

[152, 254]), discussed in Section 2.5.2 (p. 36). This implies that the bulk deformations of the polyethylene components would be elastic in nature.

In comparison, the maximum von Mises stress value for the UHMWPE ball-and-socket implant resulted to be 6.6 MPa, as shown in Fig. 5.10 (p. 128). When compared to other results obtained in literature, slightly higher von Mises stress levels were reported for ball-and-socket implants (8.0 – 16.9 MPa [225, 351, 353]), which are likely to be attributed to the use of the linear elastic or elastic-plastic models. Furthermore, such discrepancies may also be due to different boundary conditions and geometrical designs that are used during the finite element simulations.

The distribution of the von Mises stresses are noted to be different between the ball-and-socket and MaltaHip components. The von Mises stresses generated in the ball-and-socket are observed to form concentric patterns, as illustrated in Fig. 5.10 (p. 128), with the peak stress being located in the superolateral edge; a region which is susceptible to impingement. On the other hand, the von Mises stress values in the MaltaHip components are noted to be well distributed, as shown in Fig. 5.15 (p. 135). The peak stress in the MaltaHip cup is located in the superomedial direction (which is shown at 0.5 s in the gait cycle in Fig. 5.15, p. 135). This corresponds to the thinnest section of the component. Peak stresses are absent in the superolateral direction of the MaltaHip cup, as the superior overhang feature provides a continuous contacting surface which improves the distribution of the stresses. It is noted that the peak von Mises stresses in the rotator component are located at its internal surface (Fig. 5.17, p. 137), which are likely to be generated at high flexion angles of the hip. The absence of peak von Mises stresses at the superolateral directions in the MaltaHip components could reduce the fatigue damage upon impingement, as compared to the ball-and-socket prosthesis.

Even though higher von Mises stress values are exhibited in the MaltaHip implant when compared to the ball-and-socket implant, the finite element results have demonstrated that bulk plastic deformation is unlikely to occur in the polymeric components, since the stresses are located well below the material's yield strength. However, the material may start to yield at lower stress values as the number of cycles increases for the same level of stress due to fatigue, as indicated in Fig. 2.33 (p. 47) [282]. Although no signs of macroscopic fatigue wear were observed in the MaltaHip components, further experimental studies may be required to analyse their resistance to crack propagation under abnormal conditions (e.g. sudden impact to simulate tripping). Furthermore, the suitability of the thin VEHXPE components may need to be investigated in further detail due to its lower fatigue strength [20, 71].

6.3. Wear Model Results

The wear predictions of the ball-and-socket and the MaltaHip implants according to the different wear models are shown in Fig. 6.4. Two types of wear results are presented: the volumetric wear rate (Fig. 6.4a) and maximum linear wear depth (Fig. 6.4b). The latter represents the maximum depth exhibited at the surface of the component arising from the wear processes. The depth is measured as the distance between the original and the newly formed surface. For each plot, three types of data bars are presented:

- Grey bar: the wear on the ball-and-socket as predicted by the original works of the authors of the wear models (results are based on slightly different boundary conditions).
- Red bar: the wear on the ball-and-socket as calculated in this work (the same boundary conditions are used throughout the computations of the different wear rates).
- Blue bar: the wear on the MaltaHip as calculated in this work.

Considering the volumetric wear rates of the ball-and-socket implants as deduced by the different authors of the wear models (grey bars in Fig. 6.4a), discrepancies between the results can be observed. Such discrepancies are primarily owed to the different theoretical principles that are applied to the wear models. Furthermore, the authors of the wear models made use of different boundary conditions (different material properties, slide track patterns, contact conditions and load magnitude). For instance, in the work presented by Saikko [18], the wear prediction was based on a gait cycle composed of two DOFs only (flexion/extension and abduction/adduction). Furthermore, the load profile was noted to be different from the one that is specified in ISO14242-1. The volumetric wear data for the Petrella model [298] was not made available, since the authors focused on the wear that was generated by pin-on-disk setups. Similarly, discrepancies can be observed in the maximum linear wear provided by the authors of the wear models, as shown by the grey bars in Fig. 6.4b. The maximum linear wear depth results by Saikko *et al.* [18] and Petrella *et al.* [298] were not presented in their studies.

Hence, in light of the different boundary conditions that were used by the different authors, the wear on the ball-and-socket implants were recalculated in this work using the same input parameters to obtain comparable results, as shown by the red bars in Fig. 6.4. The volumetric wear rates (Fig. 6.4a) on the ball-and-socket implants computed in this work as predicted by the Saikko, Liu, Kang and Petrella models are 20.1, 19.7, 21.6 and 16.5 mm³, respectively, resulting in a maximum discrepancy of 5.1 mm³. The computed maximum linear wear depth (Fig. 6.4b) in this work according to the Saikko, Liu, Kang and Petrella models are 83, 59, 54 and 68 μm, respectively, resulting in a maximum discrepancy of 29 μm. The Petrella model computes the wear at each node according the trajectory of the slide track which occurred

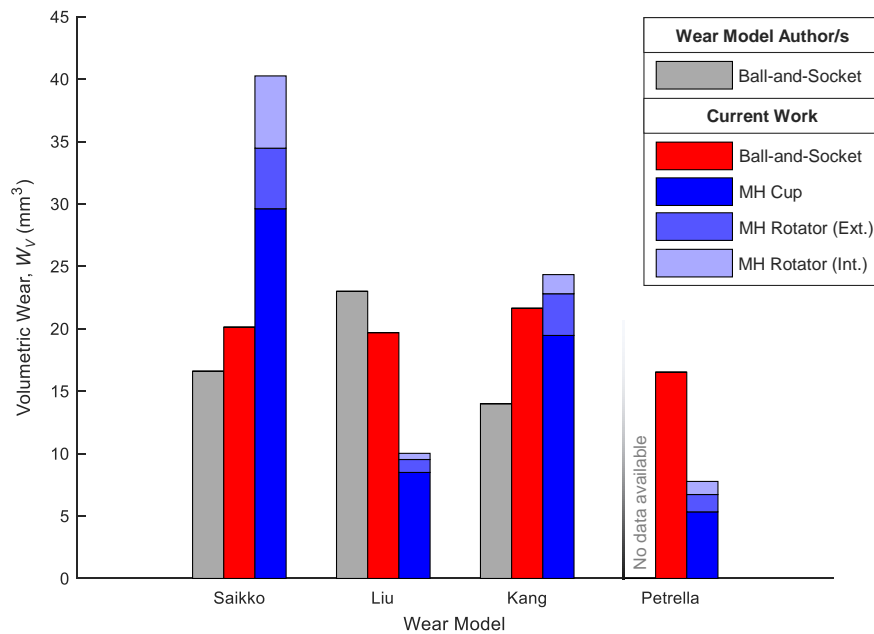
during past time intervals. On the other hand, the other models only compute the wear based on the trajectory shape of one time interval. Therefore, the Petrella model results in an increase the depth of wear for nodes producing highly complex trajectories. The results suggest that such wear models provided general indications of the wear behaviour of ball-and-socket implants, even though the theories behind the different wear models do not represent the complete physical phenomena occurring behind the wear process.

Finally, these wear models were used to predict the wear behaviour of the MaltaHip, as observed by the blue bars in Fig. 6.4. Significant discrepancies can be seen between the predicted wear for the MaltaHip when the different wear models were used. In fact, according to the Saikko, Liu, Kang and Petrella wear models, the volumetric wear values are equivalent to 40.3, 10.0, 24.3 and 7.8 mm³, respectively, resulting in a maximum discrepancy of 32.5 mm³. Similarly, the maximum linear wear values resulted to be equal to 32, 13, 16 and 26 µm, respectively.

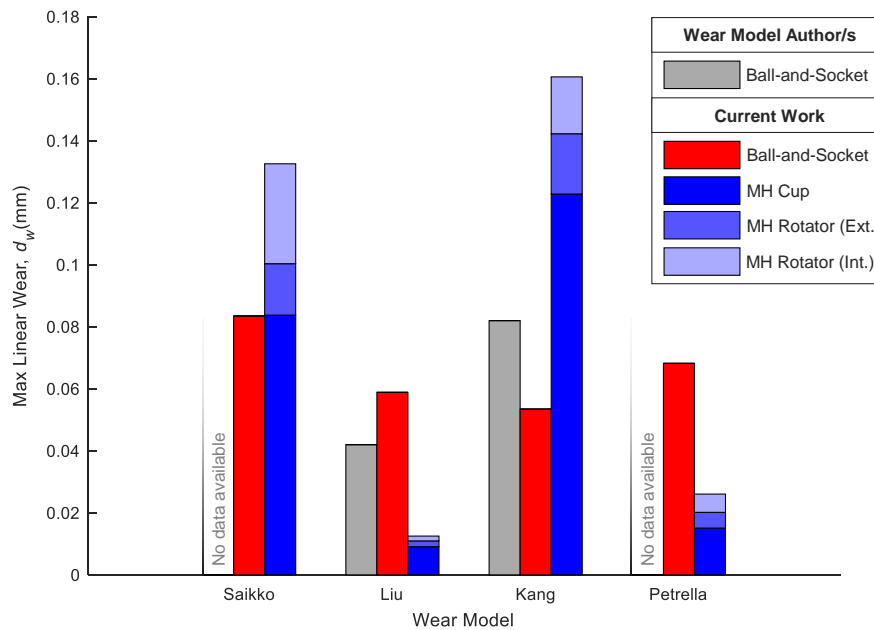
The wear results obtained for the MaltaHip indicate that some of the wear models do not reflect the actual physical mechanisms that occur during the wear process, hence producing unreliable predictions. Consequently, such wear models cannot be used to provide wear predictions of articulating surfaces with geometries other than the ball-and-socket hip implants. Furthermore, in some instances, wear factors and other related coefficients were directly retrieved from empirical wear data produced by hip joint simulators whilst following specific testing conditions (which do not always abide by ISO 14242-1). For this reason, such wear models should not be generalized to predict the wear behaviour of slightly different testing scenarios (e.g. different hip joint simulators), since machine factors greatly influence the tribological performance of the prosthesis.

Some of the shortcoming of the reviewed models are briefly described. The Saikko wear model is omitted for the final comparison between the theoretical and experimental results since the cross-shear effects are not considered in the model. The Saikko wear model would be best suited to model the wear behaviour of metal-on-metal prosthesis (or any other prosthesis which does not use polyethylene), due to the absence of the cross-shear effects in the model, causing the wear to be greater than that produced by the Liu model by a factor of 4. The Liu model does not take into consideration the contact pressure exhibited at the articulation, which could provide inaccurate results, particularly designs involving articulations that exhibit a wide range of contact pressure values. Although the Kang model takes into account the cross-shear effects, it has been observed not to be suitable for very low CSR values, due to the overestimation of the wear factor (Fig. 5.38, p. 160). The Petrella model introduces a novel weight factor to determine the amount of wear that is generated depending on the shape of the slide track. However, limited literature is available on this model and thus further verification would be required. It should be noted that

none of the models are able to take into account the orientation of the machined parts, which further create discrepancies between the predicted and actual volumetric wear rates. In light of this, it was postulated that the models proposed by Liu and Petrella are most likely to provide the most accurate wear predictions for the MaltaHip prosthesis, since these models consider the molecular arrangement of the polymer. The theoretical and experimental results are later compared in the Section 6.4.2 (p.272).



(a) Predicted volumetric wear per million cycles using different theoretical wear models.



(b) Predicted linear wear per million cycles using different theoretical wear models.

Fig. 6.4: Comparison of wear models on conventional ball-and-socket and MaltaHip implants.

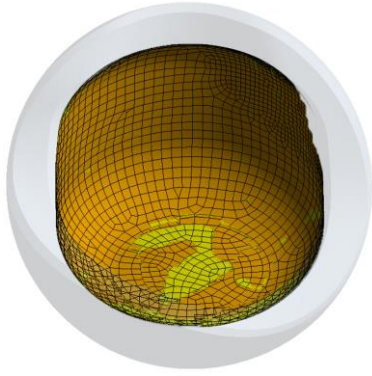
6.4. Theoretical and Experimental Comparisons

6.4.1. Contact Area

A comparison between the theoretical contact (based on finite element analysis) and experimental contact of the polymeric components of the MaltaHip is presented in Fig. 6.5. It should be pointed that the contact results shown for the finite element analysis are based on one complete gait cycle, whereas the experimentally derived contact areas are based on the results obtained after one million gait cycles. Due to the high computational expense that was involved in simulating a single gait cycle, it was deemed unfeasible to run the simulation for one million cycles. The contact produced from the finite element results represents the contact status at different timesteps of the gait cycle being superimposed on each other.

It can be observed that the theoretical contacts have resulted in larger areas than those produced by experimental tests. Considering the MaltaHip cup, it can be observed that the finite element result (Fig. 6.5a) predicated a larger contact area at the non-load bearing surface (located medially), as compared to that obtained from the experimental result (Fig. 6.5b). The external surface of the rotator according to the finite element result (Fig. 6.5c) is practically in full contact, and is characterised by a combination of sliding and sticking contact. In comparison, the contact area produced from the experimental test (Fig. 6.5d) illustrates that the top flat surface was partially out of contact. Similarly, the internal contact surface of the rotator has been predicted to be greater than that obtained from the experimental test, as shown in Fig. 6.5e and f.

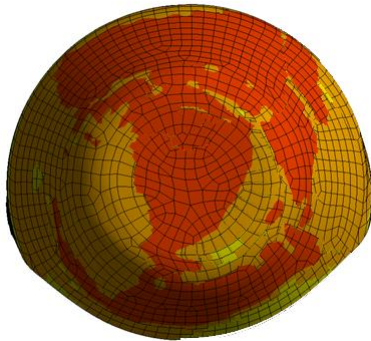
It was observed that the finite element analysis may have overpredicted the contact at non-load bearing areas. It is very difficult to pin-point the exact reason for the discrepancies between the finite element and experimental results. However, it is likely that the lubricant (calf bovine serum) may have produced regions with full fluid-film lubrication. Such conditions might have been aided by the uni-directional motion of the components. The finite element simulations only consider the structural aspect, which assumes dry sliding conditions and consequently does not consider the lubricity due to the fluid. This may suggest that a thin lubricant film did in fact penetrate between surfaces with low contact stresses. Furthermore, it should be noted that the finite element model assumes ideal surface conditions (i.e. a perfectly smooth surface). As observed in the surface roughness results (Table 5.4, p. 179), the surfaces of the polymeric components exhibit some degree of roughness (R_a), which is not taken into account by the finite element model. Although the surface roughness values are relatively low and well within the specifications of ISO 7206-2, these may contribute to slight discrepancies in the contact regions than those produced by the finite element model.



(a) MaltaHip cup: theoretical contact status.



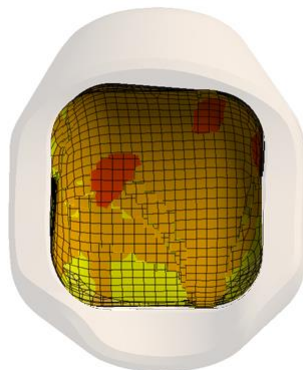
(b) MaltaHip cup: experimental contact status.



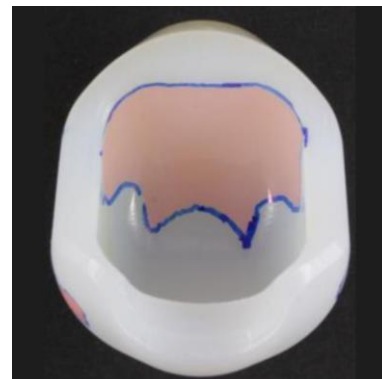
(c) Rotator (external surface): theoretical contact status.



(d) Rotator (external surface): experimental contact status.



(e) Rotator (internal surface): theoretical contact status.



(f) Rotator (internal surface): experimental contact status.

Fig. 6.5: Comparison of the theoretical contact area based on finite element analysis and experimental testing. Note: yellow area indicates that surfaces are near. Light orange area indicates sliding contact. Dark orange area indicates sticking contact.

The largest discrepancies between the contact areas in the FE model and the tested components are exhibited in the MaltaHip cup. Since the contact stress exhibited in the MaltaHip cup are significantly low, it is unlikely that the overprediction of contact stress would cause regions exceeding the yield strength. The discrepancies between the contact areas in the FE model and the tested components are small, since in both cases large contact areas were produced. Therefore, it is unlikely that significantly higher stresses exceeding the yield strength are generated.

6.4.2. Wear Results

A comparison between the volumetric wear rates produced from the theoretical models and the experimental setups of the two implant designs, consisting of UHMWPE components, are illustrated in Fig. 6.6. The results produced by the Saikko model were omitted due to the absent implementation of the cross-shear effects, whereas the results produced by the Kang model were omitted due to the inadequate implementation of the cross-shear effects, as outlined in Fig. 5.38 (p. 160). Hence, only the wear models according to Liu and Petrella are presented in this section. The results for the ball-and-socket design (Fig. 6.6a) indicate that the wear models predicted lower wear rates than those that were actually produced by the experimental setup.

The wear results for the MaltaHip design in Fig. 6.6b indicate that the wear models predicted higher wear rates for the cup, and lower wear rates for the rotator component. Furthermore, all wear models predicted that the MaltaHip cup would wear at a greater rate than the rotator, which is in disagreement with the results that were obtained experimentally. The drastically reduced wear rate of the experimentally tested MaltaHip cup demonstrates the importance of reducing the contact stresses at the articular surface (by increasing the contact area), despite that this may increase the sliding distance. In fact, the MaltaHip cup slides nearly three times as much (26.7 mm) as the rotator component (9.1 mm).

The discrepancy between the theoretical and experimental wear rates of the MaltaHip cup results is primarily owed to the inability of wear models to collectively take into account the influence of cross-shear motion, sliding distance, contact stress and the effects of the lubricant on the tribological behaviour of the prosthesis. An improved wear model would be one which measures the relation between wear and the different attributes that have been outlined. For instance, even though the implementation of a loaded soak control provides the exact amount of fluid that is absorbed during loading, further fluid is absorbed by the sliding action of the polymeric components, which effectively increases the surface temperature [309, 310]. In fact, it was observed that the rate of fluid absorption increases by two-fold during sliding at 37°C, when compared to sliding motion taking place at room temperature [311]. The quantification of the fluid uptake has demonstrated to be a challenging feat in the field of tribology, due to combined effect of fluid absorption and material loss during the wear process.

The higher wear rates of the rotator component obtained from the experimental result are likely to be attributed to the high contact stresses exhibited on its internal surface. Furthermore, it is postulated that the use of the milling processes may have subjected the articular surface to orientation softening on the internal surface, thus contributing to the generation of increased wear.

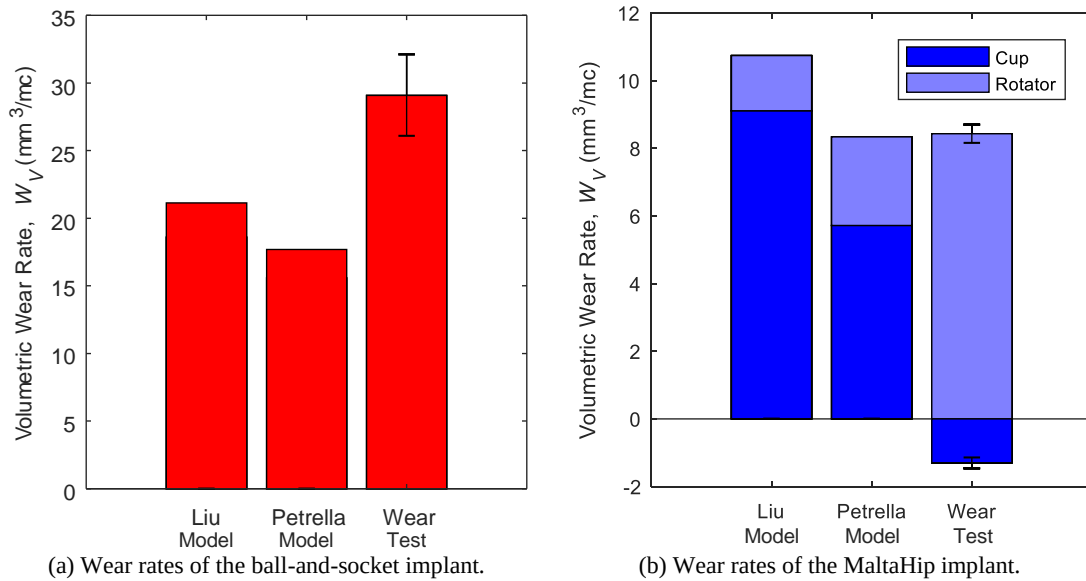


Fig. 6.6: Comparison between the volumetric wear rates obtained in this work using the theoretical wear models (Liu and Petrella), and experimental results (produced by Endolab® hip joint simulator).

6.5. Analysis on Tribological Performance

6.5.1. Physical Performance of Implants

6.5.1.1. Wear Rates

A detailed analysis on the wear mechanisms of UHMWPE and VEHXPE taking place at the different articulating surfaces of the MaltaHip is presented in this section. Comparison is also made to wear mechanisms that are exhibited in ball-and-socket implants. Even though the actual wear mechanisms are controlled by molecular-scale interactions [354], the discussions are based on observations that are made from the wear rate results (Section 5.7.3, p. 191), contact area results (Section 5.7.4, p. 206), optical microscopy images (Section 5.7.5, p. 220) and wear debris analysis (Section 5.7.6, p. 244).

The standard error of mean (SE) values of all tested MaltaHip implants were noted to be relatively low Fig. 5.69 (p. 192), thus demonstrating that the obtained wear rate results are highly reproducible. The gravimetric analysis revealed that the overall mean wear rates of the MaltaHip were lower than the mean wear rate of ball-and-socket implants produced out of the same materials that were tested using the Endolab® hip joint simulator, for both UHMWPE and VEHXPE materials. The hypothesis test demonstrated that the reductions are statistically significant at a confidence interval of 99%.

Direct comparison to other wear rate results produced from other hip joint simulators is not possible, as specific machine factors have been observed to have a great influence on the wear performance of the prosthesis [324]. A simple comparison between the wear rate results obtained using the same prosthesis across different hip joint simulators is shown in Fig. 6.7. Therefore, a valid direct comparison can only be made when the resultant wear rates are produced by the same hip joint simulator equipment.

Wimmer and Laurent [318] reported the wear rates of other several implants that were tested using the Endolab® hip joint simulator, as shown in Fig. 6.8. It should be noted that each dot represents the average wear rate of three prostheses as produced by the same manufacturer. Although a direct comparison cannot be made, due to their variations, it can be observed that the overall wear rates obtained by the MaltaHip UHMWPE and VEHXPE implants shown in the figure are lower than the majority of the wear rates that have been reported in the plot.

Furthermore, Wimmer and Laurent [318] stated that the wear rate of CoP bearings consisting of a 28 mm femoral head diameter (also tested at Endolab®) produced a wear rate of 19.4 ± 3.9 mg/mc. This is higher than the wear rate of the MaltaHip prosthesis which makes use of UHMWPE components (6.44 ± 0.33 mg/mc), as shown in Table 5.7a (p. 192). This indicates that a MaltaHip prosthesis made out of metal and polyethylene bearing surfaces produced a lower wear rate than the CoP ball-and-socket implant tested by Wimmer and Laurent [318].

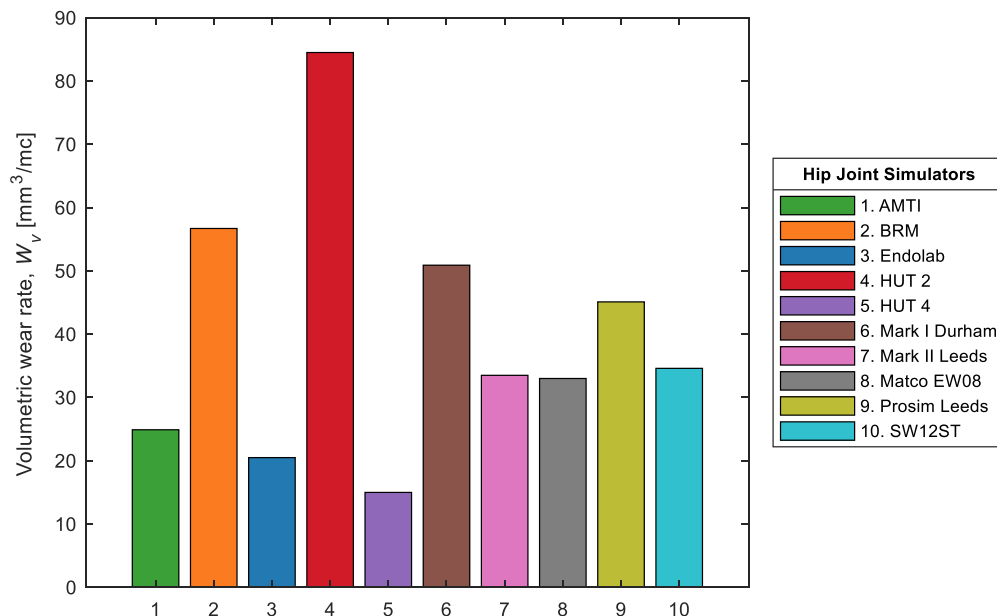


Fig. 6.7: Variation of volumetric wear rates across different hip joint simulators obtained during wear testing with the same metal-on-polyethylene implant design. Adapted from: [324].

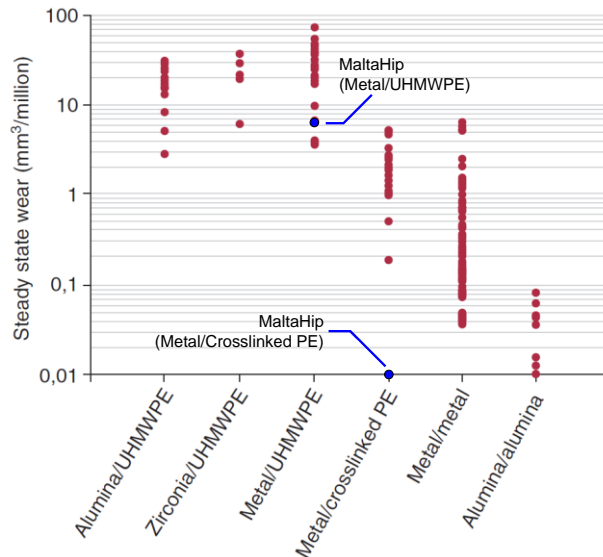


Fig. 6.8: Steady-state wear rates of commonly used material couples in hip implant bearings as tested using the Endolab® hip joint simulator. Each dot represents the average of three bearing couples of the same design. Adapted from: [66].

6.5.1.2. Wear Mechanisms

The worn topographical surfaces observed in the MaltaHip are distinct from those that are observed in the ball-and-socket implant, as the bearing surfaces of the implants are postulated to have exhibited different molecular orientation mechanisms. A further difference is also observed in the worn topographical surfaces between the MaltaHip cup and rotator, due to their different contacting areas, despite both components being subjected to uni-directional sliding conditions.

In fact, the MaltaHip cup exhibited low contact stresses (Fig. 5.21, p. 141) and long sliding distances (Fig. 5.33b, p.156). On the contrary, the MaltaHip rotator exhibited high contact stresses (Fig. 5.22, p. 142 and Fig. 5.23, p. 143) and short sliding distances (Fig. 5.33b, p. 156). The lower wear rate obtained by the MaltaHip cup (-2.17 ± 0.24 mg/mc, as computed in Table 5.10, p. 195), when compared to the rotator (8.59 ± 0.40 mg/mc, as computed in Table 5.11, p. 196), indicates the varying contribution of the contact stress and sliding distance on the wear rate of the components. The low wear rate results (Fig. 5.69, p. 192) produced from the MaltaHip implant imply that a highly aligned molecular structure is attained during uni-directional motion of the cylindrical articulations, based on the molecular reorientation theory proposed by Wang *et al.* [243]. As a result, frictional effects are reduced, thus permitting articulations to possess even larger surface areas

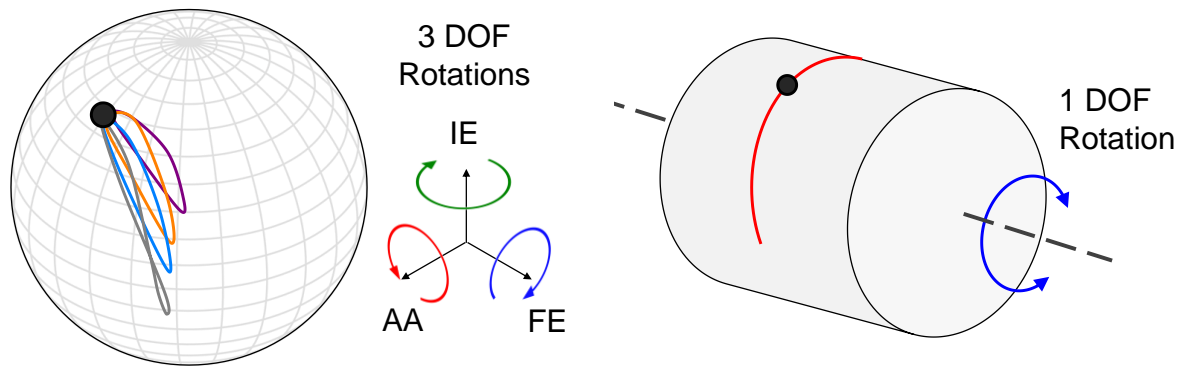
As suggested by the unified theory for wear of UHMWPE, proposed by Wang *et al.* [201], the articulation motion in the hemispherical cup generates a multi-directional stress field, composed of the longitudinal and transverse stress components (illustrated in Fig. 2.27, p. 41), which approximately coincide with the flexion/extension abduction/adduction motions,

respectively. Due to the longitudinal stress being greater than the transverse stress, the surface molecules orient preferentially to the former direction [15, 261]. Consequently, weakening of the molecular structure occurs in the transverse direction (i.e. orientation softening). The overall result is the generation of locally oriented crystalline lamellae which are effectively less wear resistant [15, 201]. The local transverse stress causes the separation (i.e. rupturing) of the oriented molecular chains, as shown by the transverse failure in Fig. 2.28 (p. 41). The surface rupturing processes transfer the transverse stress to the subsurface shear plane of the oriented molecular chains. Under extensive plastic flow, the molecular chains are sheared at the subsurface, causing the formation of pulled-out fibrils and the consequent liberation of wear particles [15, 201].

Abrasive wear is highly dependent on the surface finish condition and the ingress of third-body particles which can cause extensive material ploughing [61, 152, 203, 243]. Abrasive wear is very unlikely to have been exhibited by any of the MaltaHip components at any point in time during the wear testing regime, as no signs of ploughing were evident on any of the surfaces of the polymeric components which are shown in the optical microscopy images (Fig. 5.102 to Fig. 5.111, p. 222 - 233). Furthermore, it was observed that the metallic bearing surfaces of the MaltaHip were free from any indentations or any accumulated material which could have acted as protrusions, as indicated by the surface roughness measurements in Table 5.4 (p. 179) and optical microscopy images (Figs. 5.112 to 5.119, p. 236 to 243).

It is postulated that the extent of abrasion wear damage produced by an embedded hard particle in a uni-directional articulation may be lower than that produced in a multi-directional articulation. In the MaltaHip implant, each articulation produces motion along a specified linear path, and therefore, abrasion wear may only occur along a very confined linear path. On the other hand, the multi-directional motion of the ball-and-socket implant may generate drastically a number of different slide tracks with different activities that are performed by the implant-bearer, thus resulting in new abraded paths being produced with each new slide track that is formed (as shown in Fig. 6.9).

Surface fatigue contributes to the least amount of wear in conventional artificial hip implants (Fig. 2.32, p. 45), which is primarily attributed to the low contact stress levels that are exhibited by the hemispherical cup as a result of its highly conforming design (Fig. 2.26, p. 39). Extensive surface fatigue wear occurs in components that are subjected to high levels of contact stress, causing the accumulation of extensive plastic strain and subsequent failure of the surface asperities [243]. In fact, tibial inserts from knee replacements undergo extensive fatigue damage due to their non-conformal design which generates high levels of contact stress. Surface fatigue damage also manifests itself in gamma irradiated components which undergo accelerated oxidation effects (when not diffused with Vitamin E) [132].



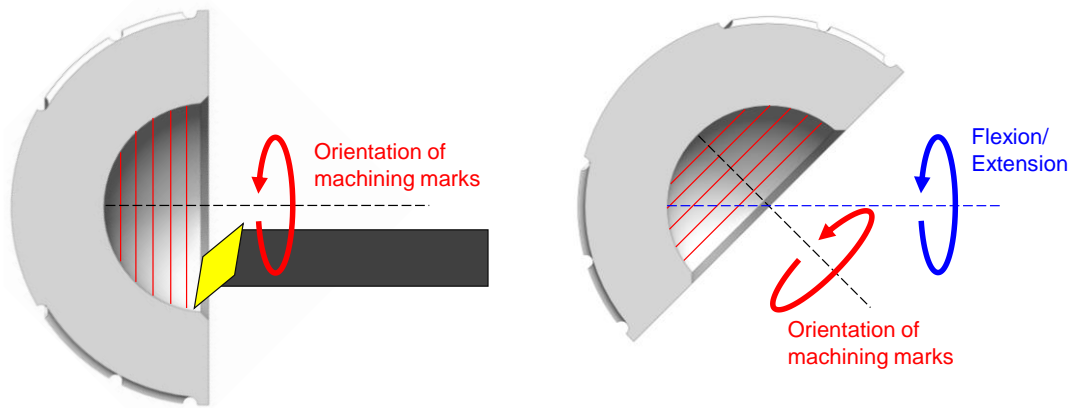
(a) Spherical articulation produces different slide tracks with different user activities, thus increasing the number of abrasion wear. (b) Cylindrical articulation produces the same slide track for any type of activity performed by the user; therefore, abrasion wear is limited to a confined linear path.

Fig. 6.9: Postulated abrasion wear due to different slide tracks being generated as a consequence of an embedded hard particle (represented by the black dot) with different activities performed by the implant-bearer.

The MaltaHip components exploit a highly conformal design to minimize the extent of surface fatigue wear. To further minimize the risk of fatigue damage, the MaltaHip polyethylene components were vacuum-packed and subjected to low levels of gamma irradiation (25kGy), to limit the extent of oxidation taking place. Ideally the MaltaHip components should have been sterilised using ethylene oxide (EtO) or gas plasma processes to further prevent the risk of oxidation taking place (however, when approaching the companies that perform this type of treatments, it was noted that only orders with large quantities of implants are catered for). Nonetheless, the optical microscopy images of the MaltaHip did not show any signs of surface fatigue wear (Figs. 5.10 to 5.111, p. 222 - 233), suggesting that oxidation effects were suppressed.

6.5.2. Analysis of MaltaHip UHMWPE Components

It can be noted that the articular surface of the MaltaHip cup was relatively intact after wear testing at 5 million cycles, as evident by the preservation of the machining marks and absence of any polished and glossy regions, as shown in optical microscopy images in Fig. 5.102 (p. 222) and Fig. 5.103 (p. 223). Due to the motion-dependency behaviour of UHMWPE, the uni-directional motion acting on the cup-flexor articulation maximises the number of covalent bonds that are oriented in the direction of sliding motion, producing extensive molecular orientation hardening. Stresses across the surface polymer chains, are practically absent and therefore fibril rupturing is very unlikely to occur. As all motions occur parallel to the principal fibre direction, higher stress levels are required to liberate wear debris from the surface, due to the increased number of covalent bonds that are aligned to the direction of sliding motion. Hence, this results in a drastic increase in the threshold shear stress value that is required to release wear particles.



(a) Orientation of the surface polymer chains, correspond to the direction of the machining marks. (b) Orientation of flexion/extension motion relative to the orientation of the polymer chains dur to machining processes.

Fig. 6.10: Hemispherical cup is prone to high rates of wear during running-in due to orientation softening as a consequence of the machining process.

The type of machining processes which were implemented have also played a critical role in orienting the surface molecular chains along the direction of sliding motion. In the case of the UHMWPE MaltaHip cup, the annealed ram extruded bar during machining is oriented such that the extruded polymer chains located at its core (as a result of its low thermal conductivity) become aligned to the direction of sliding motion, as shown in Fig. 5.40b (p. 164). Furthermore, the tool cutting action involved during the turning processes also produce extensive plastic deformations on the articulation surfaces. This machining process is highly advantageous for the cup-flexor and flexor-rotator articulations, since the polymer chains on the surfaces are readily aligned to the direction of the sliding motion. This highly contrasts with the way hemispherical cups are machined (Fig. 6.10a), since the turning machining processes produce orientation hardened molecular chains that are aligned at 45° to the flexion/extension motion (Fig. 6.10b) [291]. As a consequence, the hemispherical cups are prone to molecular orientation softening, resulting in high rates of wear during the running-in process.

Furthermore, the large contacting surface area of the MaltaHip cup results in a reduction in the overall contact stress values (Fig. 5.21, p. 141), when compared to the hemispherical cup (Fig. 5.12, p. 130). Thus, the MaltaHip cup behaves as a highly wear-resistant structure which is subjected to low contact stress values, which effectively restricts the liberation of wear particles. The conditions generated at the articular surface of the cup-flexor articulation may suggest that adhesive wear was nearly absent. This contrasts with the high wear rates that are usually associated with adhesive wear of hemispherical cups (Fig. 6.8, p. 275) [54, 152, 276].

The preservation of the machining marks Fig. 5.102 (p. 222) and the low contact stress values (Fig. 5.21, p. 141) that were exhibited by the MaltaHip cup corroborate with the corresponding low wear rate results (Table 5.7, p. 192). In fact, the resultant low wear rate of the

MaltaHip cup is postulated to be owed to micro-fatigue mechanisms since these contribute to low wear volumes, as suggested by Wang *et al.* [152] (see Fig. 2.32, p. 45). However, no evidence of micro-fatigue was found from the optical microscopy images. Scanning electron microscopy imaging would likely be needed to verify whether micro-fatigue mechanisms occurred in the MaltaHip cup. Micro-fatigue causes the contacting microscopic asperities to be sheared off due to the accumulation of plastic strain, which is generated due to cyclic surface stress. However, in contrast to fatigue processes which occur in the ball-and-socket implant, higher plastic strain accumulation is required on the MaltaHip cup surface to release the wear particles, as a result of the highly orientation hardened structure.

The non-load bearing surfaces of the MaltaHip components (intended to constrain the motion of the articulation) have been observed to be mostly not in contact (Fig. 5.83, p. 208, Fig. 5.90, p. 213, and Fig. 5.92, p. 214), and in fact managed to preserve the majority of the machining marks (Fig. 5.103, p. 223 and Fig. 5.105, p. 225). On the other hand, it was noticed that the rotator exhibited regions with glossy and polished appearances (Fig. 5.104 - Fig. 5.106, p. 224 - 226), similar to the typical worn regions that are observed in hemispherical cups, as reviewed in literature (Fig. 2.35a and b, p. 50). As opposed to the MaltaHip cup, wear generated by the rotator component is likely to be attributed to adhesive wear occurring along the fibre direction due to the formation of glossy and polished surfaces, similar to that observed in hemispherical cups (Fig. 2.35a, p. 50) [54, 152, 276]. The relatively high contact stresses generated at the articular surfaces of the rotator (Fig. 5.22, p. 142 and Fig. 5.23, p. 143) are likely to have limited the ingress of the lubricant, thus resulting in boundary lubrication conditions. As a consequence, interfacial forces greater than the material molecular bonds are postulated to have been generated, thus resulting in adhesive wear.

Even though wear of the rotator component is predominantly attributed to adhesive wear, an important distinction exists between the wear generation processes occurring in the rotator component and those occurring in the hemispherical cup. The wear debris liberation process requires higher stress levels in the rotator component than those required for the ball-and-socket hemispherical cup. The main reason being that the rotator still exhibits extensive orientation hardening. On the other hand, the hemispherical cup undergoes extensive orientation softening. As a result, it is more difficult for wear particles to be released from the rotator component than the hemispherical cup. Furthermore, wear produced by the rotator component is also reduced since its articulations have been designed to produce short sliding distances (Fig. 5.33b, p. 156), thus limiting the amount of wear debris that is released.

6.5.3. Analysis of MaltaHip VEHXPE Components

The MaltaHip VEHXPE components exhibited low wear rate values (Table 5.15, p. 201 and Table 5.16, p. 202) and preserved the machining mark on the articular surfaces of the MaltaHip cup (Fig. 5.107, p. 229 and Fig. 5.108, p. 230) and external surface of the rotator component (Fig. 5.109, p. 231 and Fig. 5.110, p. 232). On the other hand, it was observed that the machining marks on the rotator-abductor surface, which possesses the smallest contact surface area, were absent (Fig. 5.111, p. 233).

Despite the VEHXPE components being populated with crosslinks, they are still susceptible to significant molecular reorientations [269]. However, the rate at which the orientation occurs, and the amount of polymer chains which can be reoriented, is lower than that produced by UHMWPE, as can be shown in Fig. 2.30 (p. 44). The ability of the VEHXPE components to undergo molecular reorientation is key in minimizing the amount of wear debris generated by this type of polyethylene when implemented in the MaltaHip prosthesis.

The MaltaHip VEHXPE cup can be observed not to have any surface scratches (Fig. 5.107, p. 229 and Fig. 5.108, p. 230), which are usually associated with wear of XPE hemispherical cups, as reviewed in literature (Fig. 2.37, p. 53). The articulating surface of the MaltaHip cup (Fig. 5.107, p. 229) retained the same topographical features as those that were observed in the non-contacting areas of the same component (Fig. 5.108, p. 230). These non-contacting areas represent the surface condition that was produced just after finishing the machining processes. It is likely that the MaltaHip VEHXPE cup (Fig. 5.107, p. 229) exhibited similar wear mechanisms to those that were exhibited by the MaltaHip UHMWPE cup due to their similar appearances (Fig. 5.102, p. 222). Thus, it is likely that the VEHXPE cup also exhibited hydrodynamic lubrication, coupled with few instances of micro-fatigue wear. However, the hindered mobility of the molecular chains in the VEHXPE cup may have contributed to its slightly higher wear rate (Table 5.15, p. 201), when compared to that produced by the UHMWPE cup (Table 5.10, p. 195). It is likely that some of the molecular chains could not be oriented favourably to the direction of sliding motion due to the presence of crosslinks. Hence, the molecular strength of a small number of isolated sites is likely to have been lower than that exhibited by the highly orientation hardened regions. As a result, the unoriented sites are likely to have possessed lower failure strength values, thus causing their premature fibril rupturing.

A distinction was observed between the external (Fig. 5.109, p. 231) and internal (Fig. 5.111, p. 233) load-bearing surfaces of the VEHXPE rotator. Most of the machining marks on the external surface were retained, whereas those on the internal surface were no longer visible. This discrepancy is likely to be due to the high contact stress levels exhibited on the internal

surface, as a result of its smaller contacting area (similar to the case of UHMWPE shown in Fig. 5.23, p. 143). Furthermore, the internal surface of the rotator was produced using milling processes, which results in a highly convoluted surface molecular structure, therefore being weaker than the external surface of the rotator that was produced using turning processes. Therefore, the majority of wear generated from the rotator component is likely to have originated from its internal surface, which contributes to the abduction/adduction motion of the hip. It can be observed that the external surface of the rotator retained the majority of the machining marks, with only minor regions lacking such marks. Upon closer inspection, it can be seen that the texture of the machining marks on the external contact area became coarser, when compared to the fine machining textures that are present at the intact regions (see Fig. 5.86, p. 210, for contact and non-contact regions). This observation indicates that the VEHXPE external surface of the rotator exhibited moderate plastic flow effects, which greatly contrasts with the minimal plastic strain induced in the VEHXPE cup (Fig. 5.107, p. 229). The increased levels of plastic strain at the external surface of the rotator may have instigated some levels of adhesive wear, as a result of the polished regions (Fig. 5.109, p. 231), coupled with micro-fatigue processes, due to the formation of small diameter wear particles (Fig. 5.122b, p. 247, and Fig. 5.123b, p. 248).

The formation of glossy surfaces in XPE cups has not been reported in literature, as in most cases these have been characterised by deep scratches, as shown in Fig. 2.36 (p. 52). The absence of the machining marks at the internal surface of the rotator component (Fig. 5.111, p. 233) is hence postulated to be partially attributed to adhesive wear processes, due to the formation of the glossy surface (Fig. 2.35a, p. 50). Furthermore, the disappearance of the machining marks may also be caused by the flattening of machining marks, as outlined by Jasty *et al.* [291] as the main mechanism which occurs in XPE, as shown by Fig. 2.36 (p. 52). Due to the decreased contact area (Fig. 5.34, p. 157), the generation of the high contact stresses (similar to the case of UHMWPE shown in Fig. 5.23, p. 143) might have contributed to some degree of adhesive wear. However, its contribution may have been very limited, due to the relatively low wear rate values that were attained (Table 5.16, p. 202). The combination of high contact stresses and the highly conforming abductor head (against the internal surface of the rotator) is likely to have also generated some degree of plastic deformations, thus causing flattening of the machining marks.

6.5.4. Analysis and Comparison of the MaltaHip Components

Wang *et al.* [15] pointed out that the failure strength of a highly anisotropic UHMWPE structure subjected to uniaxial stress applied to the direction of principal orientation is higher than the failure strength of a highly isotropic XPE structure. Congruously, the failure strength of a highly anisotropic UHMWPE structure subjected to uniaxial stress applied to any direction other than that which corresponds to the principal orientation is lower than the failure strength of a highly isotropic XPE structure.

Both UHMWPE and VHEXPE components resulted in negative steady-state wear rates. The true gravimetric wear rate remains unknown since fluid absorption due to sliding motion could not be compensated. Therefore, it will be assumed that the UHMWPE and VHEXPE cup absorbed the same amount of fluid. The VHEXPE cup resulted in a smaller negative steady-state wear rate (-0.99 ± 0.51 mg/mc, Table 5.7, p. 192), as compared to that produced by UHMWPE cup (-2.17 ± 0.24 mg/mc, Table 5.8, p. 192). This indicates that the VHEXPE cup underwent greater wear than the UHMWPE cup. The contact area results indicate that the VHEXPE cup (Fig. 5.82, p. 207) resulted in a larger contacting area, than the UHMWPE cup (Fig. 5.81, p. 207). Therefore, the greater wear produced in the VHEXPE cup is attributed to the increased regions of contact.

Hence, the MaltaHip cup wear rate results indicate that given that the contact area is large enough, such that the contact stress is sufficiently low, lower wear rates may be produced as demonstrated by the lower rates of wear of the cups as compared to the rotators for both type of polymers used in this work. This is attributed to the molecular chains of the polyethylenes which are readily available to mobilise themselves and thus align the covalent bonds along the direction of sliding motion. Therefore, the covalent bonds are immediately used in an efficient manner to sustain the uni-axial stresses which are incurred during uni-directional sliding motion. This minimises the amount of ineffective covalent bonds that act in directions which are not subjected to high stresses.

The benefits of using ram extruded UHMWPE can only be exploited by the MaltaHip cup. Since UHMWPE was produced using a ram extruded process, it is likely that it possesses a greater bulk volume of oriented molecular chains, as compared to the VHEXPE components produced using the compression moulding process. On the other hand, as both UHMWPE and VHEXPE components underwent the same machining processes, the surface molecular chains of both polymers achieved practically the same orientations. Therefore, the different production processes used for the two polymers used in this work are not likely to have influenced the

performance of the prosthesis for wear occurring on the machined surfaces. However, the benefits of the bulk oriented molecular chains are likely to be exploited after the machined layers are worn off (i.e. at very high number of wear test cycles).

It has been observed that the flexor components coupled with UHMWPE and VEHXPE components resulted in loss in weight (between 1 to 3 million cycles), followed by an unusual increase in weight between (between 3 to 5 million cycles), as shown in Fig. 5.74 (p. 198) and Fig. 5.79 (p. 204), respectively. The initial loss in weight in the flexor component is likely attributed to the shearing of microscopic asperities, by the repetitive cyclic sliding action of the articulation. The shearing of these microscopic asperities is likely to have led to the formation of tribo-oxide films at the worn regions. As the cup-flexor articulation is characterised by low contact stress values (Fig. 5.21, p. 141), the tribo-oxide layer is likely to have retained its structural integrity, resulting an increase in weight. In this scenario it is likely that the rate of tribo-oxide layer formation is greater than the rate of material removal, and therefore asperity-to-asperity contact between the polyethylene and the metal are minimized which corroborates with the low wear rates of the MaltaHip cups (Fig. 5.71, p. 195 and Fig. 5.76, p. 201). To the best of the author's knowledge, such behaviour was never reported for ball-and-socket implants, as high contact stresses are likely to be produced by the spherical geometry of the femoral head. Nonetheless, similar results have been observed by Wei *et al.* [355] for pin-and-disk setup involving stainless steel components, as the worn components resulted in increased weight at slightly elevated temperatures (200°C). The reason that the abductor components do not exhibit increased weight (Fig. 5.72, p. 196 and Fig. 5.77, p. 202), but rather higher wear rates than the initial wear rate of the flexor components, is due to the high contact stresses of the articulation (Fig. 5.22, p. 142). The high contact stresses generated at the abductor are likely to cause the breakage of oxide film and subsequent loss of the material.

6.5.5. Creep

The polyethylene components are susceptible to creep deformations during in-service conditions due to their low T_g value [137]. However, creep behaviour in artificial hip implants is not considered to compromise the functionality of the device, since in most cases the resultant deformation results in improving the conformity of the articulation [356]. Such characteristic is highly desirable for minimizing the surface damage of articular joints [192, 227, 357]. Furthermore, polyethylene components exhibit limited creep deformations, since the long and highly entangled molecular chains limit the extent of molecular mobility [36, 191].

Creep studies in the field of arthroplasty are mainly intended to provide insight on femoral head penetrations into the hemispherical cups. In fact, the amount of wear generated by *in vivo* hemispherical cup is calculated by subtracting the amount of femoral head penetration that is incurred by creep deformations [24, 200, 358]. In fact, it was reported in literature that around 90% of the ultimate creep deformations in conventional UHMWPE cups occur within the first 2.0 – 2.5 million cycles [197, 200, 359].

Although long-term creep effects (say 10 – 15 years) of the MaltaHip prosthesis were not studied experimentally in this work (as it would have required the testing regime to be prolonged by a considerable amount of time), it is postulated that the load bearing surfaces of the MaltaHip would not have exhibited any further creep deformations, than those already produced by the tested 5 million cycles. In fact, it should be noted that the surfaces which are intended to constrain the motion of the components were designed not to carry any loads (and thus behave as non-load bearing surfaces), as evident by their low stress values, as shown by the MaltaHip cup in Fig. 5.15 (p. 135) and rotator in Fig. 5.17 (p. 137).

Despite the relatively tight dimensional tolerances which were required to constrain the motion of the components, creep deformations were not observed to compromise the functionality of the prosthesis. In fact, no signs of any backlashes were experienced between any of the articulations. As outlined above, it is highly unlikely that creep effects would have compromised the uni-directional mechanisms of the prosthesis at extended wear testing regimes, as the creep deformations in the prosthesis are likely to be saturated at 5 million cycles. By eliminating stresses from the non-load bearing surfaces that constrain the motion of the prosthesis, the components are able to maintain their uni-directional sliding functionality for prolonged periods.

6.5.6. Lubrication

UHMWPE exhibits poor fluid adsorption due to its intrinsic low surface energy [243]. Hence, the boundary lubrication is achieved via the fluid which is adsorbed to the metal (or ceramic) bearing surface. Nonetheless, under the right conditions, hydrodynamic lubrication can still be achieved, causing the articulating surfaces to become distanced from each other. The lubricant acts as an interstitial fluid that can sustain the loads of the articulation and thus reduces the wear [249].

Hydrodynamic lubrication is achieved by using a large femoral head (to increase the velocity of the surface), smooth bearing surface, and tight radial clearance at the articulation [66]. Tight radial clearances are needed since the capability of the fluid to support normal loads

decreases with increasing film thickness. The observed worn surfaces of conventional ball-and-socket implants in literature (UHMWPE in Fig. 2.35, p. 50, and XPE in Fig. 2.36, p. 52) indicate the difficulty involved in recreating the conditions necessary to generate a full-fluid film during *in vivo* conditions. In fact, the type of wear exhibited by the articulations of such prostheses most often indicate that ball-and-socket implants undergo a combination of boundary and mixed lubrication regimes [66, 152].

The cup-flexor articulation developed in this work exhibits slightly higher sliding velocities, when compared to a 28 mm femoral head, due to its longer slide track distance (Fig. 5.33, p. 156). Frictional effects are also minimized over time due to the molecular orientation hardening effects. Furthermore, the radial clearances were designed to be relatively tight (Table 5.2, p. 120). This was necessary for minimizing the articular contact stresses and for engaging the components via the interlocking mechanism. Therefore, the tight radial clearance designed at this articulation is likely to have enabled the ingress of a full fluid film which was able to support the generated loads. The retention of machining marks on both the UHMWPE (Fig. 5.102, p. 222) and VEHXPE (Fig. 5.107, p. 229) MaltaHip cups corroborates with the low contact stress values that were produced in the FE results (Fig. 5.21, p. 141), as a result of its large contact area. Further data is required to establish whether hydrodynamic lubrication effects were produced. Nonetheless, the generation of low contact stress may have very likely promoted mixed boundary lubrication conditions, thus resulting in low amount of wear being generated.

6.5.7. Fluid Absorption

Fluid absorption by the polyethylene components should not be underestimated as it induces significant gains in weight, which may not provide the full-picture of the actual performance of the prosthesis. This becomes particularly more relevant with use of thick hemispherical cups which are able to absorb higher volumes of fluid [360, 361]. As the majority of the MaltaHip components (UHMWPE cup, VEHXPE cup and VEHXPE rotator) attained negative wear rate values (i.e. representing a net gain in weight) a discussion on the fluid absorption is warranted.

As discussed in Section 5.7.3 (p. 191), the resultant negative wear rates are produced due the rate of fluid absorption being higher than the rate of wear. Pre-soaking and loaded soak controls are standardised procedures in ISO 14242-1 to minimize the amount of fluid uptake during wear testing [310]. Nonetheless, negative wear values were still obtained in this work, despite the wear values were corrected for fluid uptake using the data that was obtained from the loaded soak controls. Bragdon *et al.* [310] has studied the cause for the increased fluid uptake

during wear testing and concluded that this was attributed to the sliding action of the articulation. Therefore, the negative wear rates obtained in the MaltaHip components represent the net mass result of the material removed due to wear, together with the fluid-uptake due to the sliding motion. As a consequence, it is not possible to isolate the contribution of each process, and thus the effect of sliding motion on the fluid absorption rate remains unquantified [53, 310, 362].

6.6. Wear Particle Analysis

6.6.1. Wear Particle Morphology

The wear particles liberated from the MaltaHip implant have been mostly released from the rotator components, rather than the MaltaHip cups, due to their higher wear rates. Furthermore, it can be noted that, in general, the two types of polymers used in this work produced particles with similar morphologies, as observed from wear debris analysis results produced in Tables 5.20 and 5.21 (p. 245). In fact, the mean ECD values of the UHMWPE and VEHXPE were noted to be very similar to each other, being 0.21 and 0.22 μm , respectively.

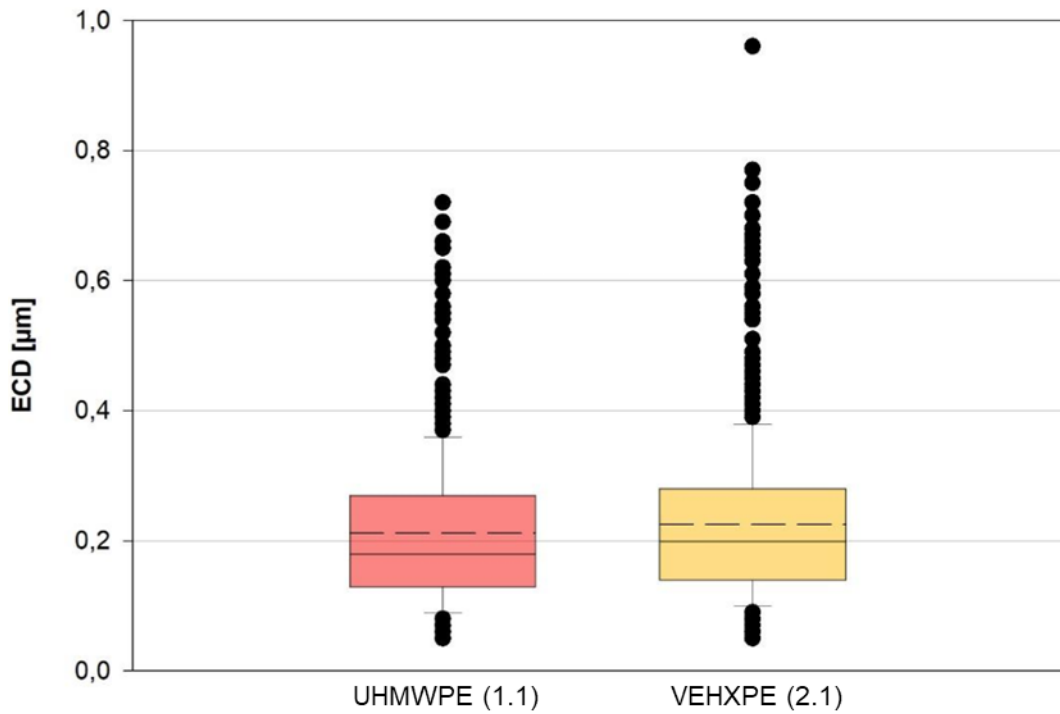
The box plots of the ECD values obtained for the MaltaHip and conventional ball-and-socket implants (provided by Endolab®) are shown in Fig. 6.11. However, these results cannot be directly compared, since the results produced by the MaltaHip implants (Fig. 6.11a) are each based on 1 sample, whereas those for the UHMWPE ball-and-socket implants (Fig. 6.11b) are based on 104 samples, and those for the XPE ball-and-socket implants (Fig. 6.11b) are based on 54 samples. Furthermore, the ball-and-socket ECD values represent the overall results of implants that are produced with different designs by different manufacturers. However, it can generally be observed that the majority of wear particles produced by the MaltaHip implant possess similar ECD values to those produced by the ball-and-socket implants for both materials investigated in this work.

Wear debris produced from UHMWPE hemispherical cups is usually observed to be fibrillar and elongated, as shown by the examples reported in literature (Fig. 2.41a and b, p. 60). The diameters of these particles were observed to be in the submicron range, whereas their fibrillar lengths were noted to range between 1 to 20 μm [15]. Their slightly elongated morphology is associated with extensive plastic flow as a result of adhesive wear mechanisms. The UHMWPE particles produced by the MaltaHip, shown in Fig. 5.123a (p. 248), have been observed to be less fibrillar, due to their shorter tails (Fig. 5.123a, p. 248). The fibrillar morphology of UHMWPE wear particles are usually associated with the multi-directional motion of the ball-and-socket implants [85]. Hence, this further supports the notion that the extent of

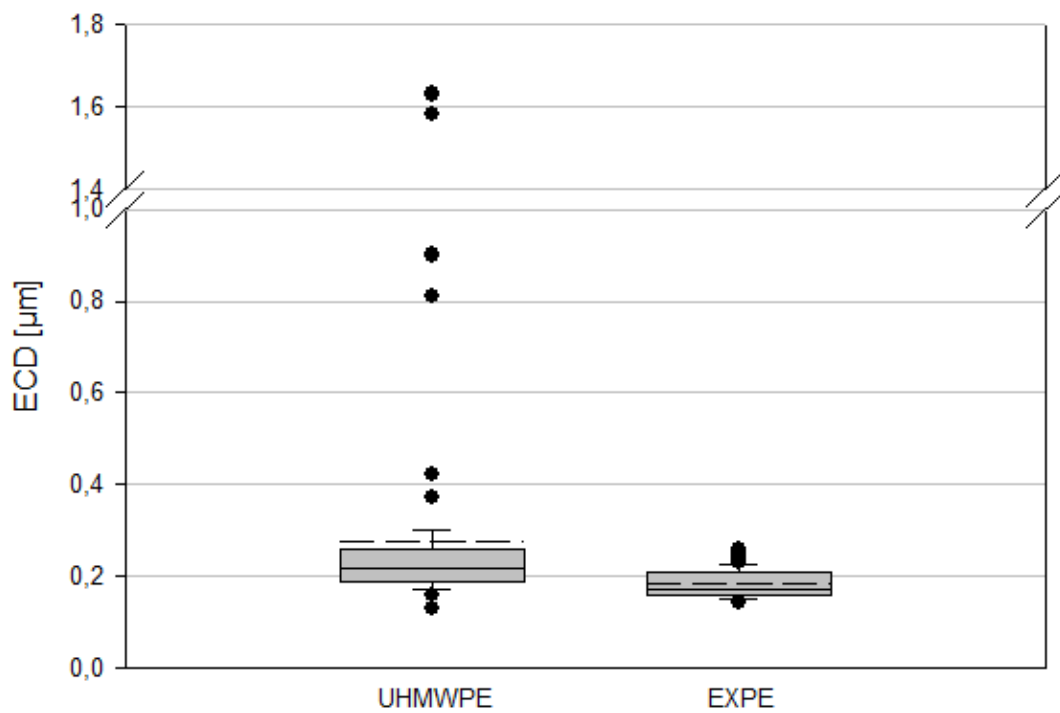
adhesive wear was reduced in the MaltaHip. In fact, the morphological characteristics of the UHMWPE particles have been observed to resemble closely to those which are usually produced in XPE hemispherical cups (Fig. 2.41c and d, p. 60), as a result of the orientation hardening effects induced via uni-directional sliding motion.

As discussed, XPE hemispherical cups have been reported to produce drastically reduced wear rates, when compared to their uncrosslinked counterparts [27, 76, 283, 284]. Despite their lower volumetric wear, this can often translate into higher quantities of wear particles being produced, as a result of their smaller volumetric size. As a consequence, this could potentially lead to increased osteolysis effects. In fact, this scenario is likely to occur with moderately crosslinked polyethylene hemispherical cups, which can result in the generation of high volumes of small-sized wear particles [308].

The FE-SEM images consisting of the VEXHPE particles, shown in Fig. 5.123a (p. 248) demonstrated that particles with smooth and flaked textures were generated. Flaked particles are a common by-product of hemispherical crosslinked polyethylene cups [363]. As discussed above, particles with smooth and rounded shape indicate the occurrence of adhesive wear. The small sizes of the flaked particles are likely to be attributed to increased levels of micro-fatigue wear occurring in the VEHXPE components, as a result of its lower ductility and fatigue resistance. It can be assumed that the majority of flaked particles have been produced from the VEHXPE rotator surface (Fig. 5.111, p. 233) which enables the abductor/adductor motion, due to its higher rate of wear. In fact, the lack of flaked particles produced in UHMWPE (Fig. 5.123, p. 248) indicates its superior fatigue resistance over VEHXPE.



(a) ECD of the UHMWPE ($n = 1$) and VEHXPE ($n = 1$) wear particles of the MaltaHip implant.



(b) ECD of the UHMWPE ($n = 104$) and EXPE ($n = 53$) wear particles of the ball-and-socket implant.

Fig. 6.11: Box plot illustrating the statistical data concerning the equivalent circle diameter (ECD) of the particles produced by the MaltaHip and the ball-and-socket design. See the representative boxplot in Fig. 5.120 (p. 246) for an explanation of the statistical mean, median and the different zones of the percentiles used in these box plots.

Source: Endolab® report (unpublished).

6.6.2. Functional Biological Activity

The specific biological activity (*SBA*) and the functional biological activity (*FBA*) values for the MaltaHip implant were computed using the method proposed by Fischer *et al.* [306], to provide an indication regarding the potential osteolytic effect produced by the prosthesis. The results for the MaltaHip UHMWPE and VEHXPE wear particles are shown in Table 6.1 (ref. MH1 and MH2).

It can be observed that both polymers produced wear particles with the smallest sizes, thus being the most biologically active (Fig. 2.42, p. 62), resulting in the highest *SBA* value (1.0). However, their functional biological activity (*FBA*), according to the wear rates generated in this work, resulted to be very low due to their limited volumetric wear rates. It should be noted that wear rate results produced in this work were compensated for fluid absorption due to loading (according to ISO 14242-1) only. Nonetheless, the wear rate results could not be compensated for fluid absorption due to sliding motion (as discussed in Section 6.5.7, p. 285). The MaltaHip with the UHMWPE components (Table 6.1, p. 62, ref. MH1) resulted in an *FBA* value of 6.4, whereas the *FBA* value for the MaltaHip with the VEHXPE components (Table 6.1, p. 62, ref. MH2) could not be predicted due to the negative volumetric wear rate that was produced. The produced *FBA* results are intended to provide a quantitative index which can be used to perform relative comparisons only, and cannot be used to perform comparisons with other implants unless tested under the same conditions and hip joint simulator. Even though accurate numerical values for the *FBA* cannot be produced, since fluid absorption due to sliding motion could not be compensated for both UHMWPE and VEHXPE MaltaHip implants, the analysis indicates that the VEHXPE MaltaHip implant is likely to induce lower osteolysis effects, when compared to the UHMWPE MaltaHip.

Table 6.1: Specific Biological Activity (*SBA*) and Functional Biological Activity (*FBA*). Source: [306].

Ref.	Implant	Material	Specific Biological Activity (<i>SBA</i>)	Functional Biological Activity (<i>FBA</i>)
			(particle specific)	(implant specific)
MH1	MaltaHip	GUR 1050, 0 kGy	1.00	6.4
MH2	MaltaHip	GUR 1020-e, 100 kGy	1.00	0*

* The *FBA* for the MaltaHip using VEHXPE components could not be predicted due to the resultant overall volumetric wear rate being negative.

6.7. Implant Overview and Potential Improvements

6.7.1. Implant Design and Materials

In the field of hip joint arthroplasty, various attempts have been made to modify the material properties of the polyethylene hemispherical cup to improve its tribological performance (e.g. carbon-reinforced polyethylene [22, 64, 65] and highly crystalline polyethylene [67, 70, 72]). However, limited work has been conducted with regards to altering the design of the standard ball-and-socket implant. Therefore, this work takes on a different approach by redesigning the structure of the hip implant, to make the best use of existing clinically approved materials, with the aim of enhancing its wear resistance. The use of these materials is highly beneficial as it could potentially reduce the lead time for introducing medical devices into the clinical market, due to the lower number of biocompatibility tests that would be required.

The benefits of the MaltaHip design can be best exploited by using polyethylene as the soft bearing components. The main reason being that the wear resistant mechanisms of the MaltaHip are reliant on two important features of the polyethylene material: its molecular reorientation mechanisms, and its low stiffness which improves the conformity of the articulations (thus reducing the extent of articular contact stress). Therefore, an all-metal MaltaHip implant will likely exhibit high concentrations of contact stress in the form of point contacts, due to the drastically high stiffness of the metallic components leading to stress concentrations. Hence, it is postulated that an all-metal MaltaHip implant would result in higher wear rates than those generated by the standard metal-on-metal ball-and-socket implants.

Lower wear rates in the MaltaHip prosthesis could hypothetically be achieved by substituting the metallic components with ceramic components. Nonetheless, the suitability of utilizing ceramic components must be studied with respect to their fracture toughness. Furthermore, it is likely that the critical dimensions of a ceramic flexor component (Fig. 3.10, p. 73) would need to be further optimised to ensure that the component does not fail due to fracture. Even though a ceramic abductor head can probably be used to improve the overall wettability of the articulation [71, 318, 364], it is likely that the high costs incurred by the ceramic material would compromise the benefits attained in the wear reductions, and thus would likely not be practical to implement.

Even though the MaltaHip implant with VEHXPE components resulted in the lowest wear rate (Fig. 5.69, p. 192), caution must be exerted in relation to its lower fatigue strength (both in resisting crack initiation and propagation) which could compromise the long-term survivorship of the prosthesis. In this regard, further studies may be required to analyse the specific fatigue

performance of the VEHXPE components in the MaltaHip configuration. Therefore, based on the assumption that the prosthesis may be subjected to abnormal loading conditions (e.g. tripping) which may cause high impact loads during in-service conditions, the lower fracture resistance of the VEHXPE components may compromise the long-term survivorship of the prosthesis.

Therefore, it is postulated that the ideal version of the MaltaHip is made of UHMWPE components or slightly crosslinked polyethylene to maintain the fatigue and fracture strength of the prosthesis. Nonetheless, minor improvements are still required to improve the contact area at the rotator-abductor interface, since the majority of wear was observed to be produced from the rotator component, due to its relatively high wear rate (Table 5.11, p. 196), when compared to the MaltaHip cup (Table 5.10, p. 195). This may be achieved by implementing minor design modifications on the existing MaltaHip design, which would require increasing the internal articulation area of the rotator component. This can be accomplished by increasing: the curvature radius of the filleted edge (A_f), abductor diameter (A_{t1}), and/or the width (A_{t2}), shown in Fig. 3.8 (p. 72).

A larger cylindrical component has demonstrated to result in reduced wear rates, as opposed to larger spherical head which leads to increased wear rates [54, 365]. Such implant design is postulated to be both fatigue and wear resistant, thus significantly prolonging its usability and lifespan.

Wear reductions attained in the MaltaHip are primarily attributed to the prosthesis' unique design. Hence, it is postulated that the MaltaHip implant would, in most cases, result in lower wear rates than the ball-and-socket implant for any type of polyethylene grade. This is attributed to the intrinsic affinity of the polyethylene material to undergo molecular reorientation under uni-directional sliding conditions (even at high levels of crosslinks). Therefore, the design of the MaltaHip could potentially remain applicable to newer polyethylene materials that are introduced on the clinical market.

6.7.2. Implant Interlocking Mechanism

Apart from enhancing the tribological performance of the prosthesis, it was also equally important to ensure that the implant is not susceptible to dislocation and impingement, as these may compromise the overall functionality of the prosthesis. Furthermore, practical factors of the new prosthesis regarding the ease of implantation were also taken into consideration.

As the components of the MaltaHip are based on the geometry of the cylinder, this provided a great design opportunity to integrate an interlocking mechanism to minimize the risk of dislocation. The principle behind the interlocking mechanism relies on the fact that assembly/disassembly of the components can only be achieved at joint angles which are not attainable during normal use by the implant-bearer. This was accomplished by designing an overhang feature which engages the components of the prosthesis.

Currently, the dual-mobility hip implant is the only type of prosthesis available on the market which offers a true mechanical interlock that minimizes hip dislocation [366, 367]. Therefore, a brief comparison of this mechanism to that of the MaltaHip is briefly discussed in this section. As the name suggests, the dual-mobility hip implant includes two articulations: the first articulation consisting of the femoral head and the polyethylene liner (Fig. 6.12a) and the second articulation consisting of the liner and the cup (Fig. 6.12b). The interlocking mechanism is provided by the captive design of the polyethylene liner, which is achieved via press-fitting (Fig. 6.13a) or impacting (Fig. 6.13b) the femoral head inside the polyethylene liner.

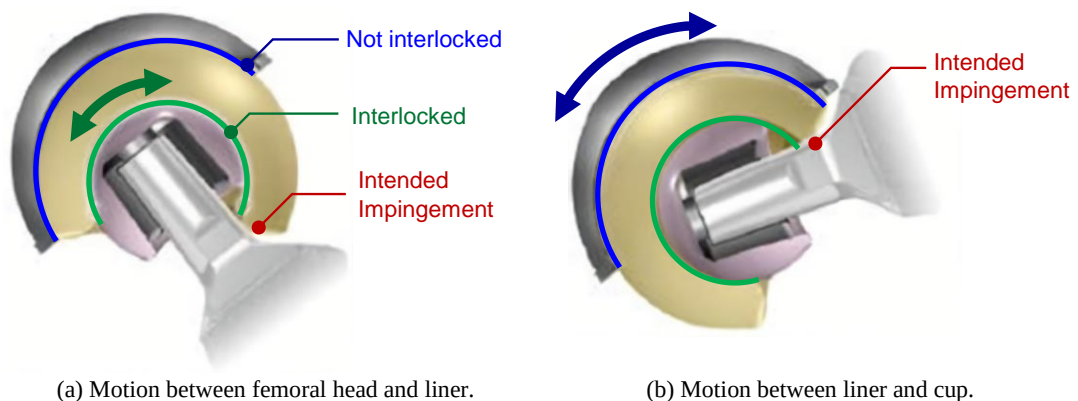


Fig. 6.12: Articulations of the dual-mobility hip implant. Adapted from: [368].

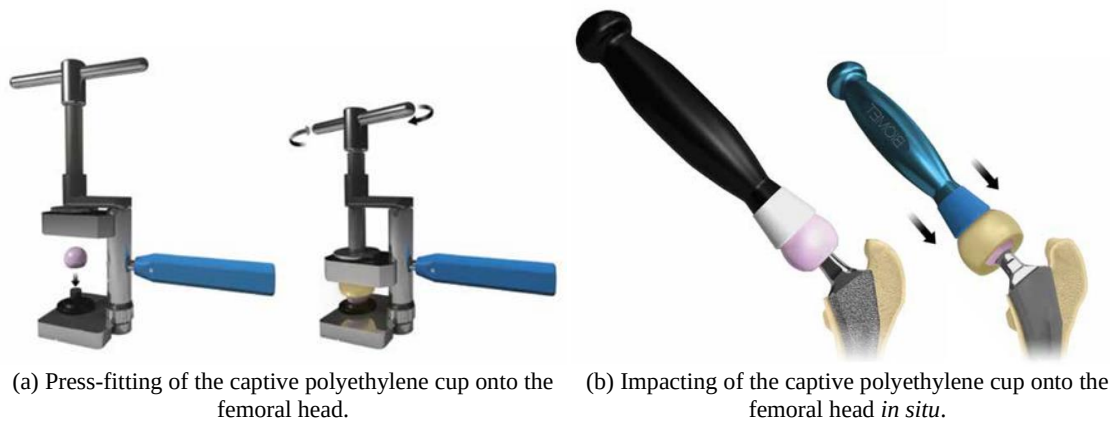


Fig. 6.13: Different assembly methods used of dual-mobility implant. Source: [369].

The main advantage of the MaltaHip interlocking mechanism is that the components do not require to be press-fitted together to engage with each other. Therefore, the MaltaHip avoids the need for additional surgical tools, as assembly of the MaltaHip prosthesis can be easily done by manually sliding the components into each other. In fact, the assembly of the MaltaHip cup, flexor and rotator can be done prior to its fixation to the pelvis. As a result, it was observed that no significant changes to the conventional surgical procedure are required. Apart from reducing the implantation time, it is also less susceptible to human errors. In fact, if the polyethylene liner of the dual-mobility implant is slightly misaligned during the press-fitting process, the prosthesis would need to be substituted with a new one, due to potential cracks that might have been generated. On the other hand, *in situ* errors may occur in case a non-compatible bearing impactor is used, which may cause severe damage to the dual mobility prosthesis [369].

Dual-mobility implants are intentionally designed to have the neck of the stem impinge on the polyethylene liner in order to achieve their extended range of motion [366, 370, 371]. As can be observed in Fig. 6.12, movement of the large articulation occurs when the neck impinges on the rim of the polyethylene liner. Although the impact during impingement is not severe (since the polyethylene liner is free to move), the impinged site is likely to act as a source of accelerated fatigue damage with increased use [20], particularly with the use of XPE as it exhibits poor resistance to crack propagation. On the other hand, the MaltaHip does not require any of the components to impinge on each other to achieve its extended range of motion.

The interlocking mechanism of the MaltaHip provides the implant-bearer the ability to achieve high flexion/extension angles with no risk for hip dislocation. This mechanism counteracts one of the most common types of dislocations that occurs in standard ball-and-socket implants during high flexion angles, as the femoral head is forced to disengage from the cup in the posterior direction. Furthermore, the MaltaHip interlocking mechanism also enables a wide range of medial/lateral rotation without any risk of hip dislocation along this direction.

An interlocking mechanism was intentionally excluded at the rotator-abductor articulation, which is responsible for the abduction/adduction motion of the prosthesis. Therefore, dislocations may occur at extreme abduction and adduction joint angles, which can cause the prosthesis to dislocate in the inferior and superior directions, respectively. The omission of the interlocking mechanism in rotator-abductor articulation serves an important two-fold purpose in the MaltaHip prosthesis. Firstly, it was necessary that the prosthesis possesses at least one articulation that could be easily assembled/disassembled, to facilitate the hip reduction process during surgery. Secondly, at least one articulation is required to disengage with relative ease to permit hip subluxation⁵⁹ during high impact actions (e.g. tripping). Although the occurrence of subluxation is not ideal, this prevents the excessive stresses from being transferred to the components, which could otherwise cause fracture of the polymeric components or failure of the bone-implant interface. This provides an element of safety for example in car crash involving a seated person with knee impact to the dashboard.

The interlocking mechanism of the MaltaHip could potentially provide the implant-bearer the ability to achieve manoeuvres and postures which are usually associated with high risks of dislocation when using the standard ball-and-socket implant. Following the mock surgery on the cadaver, the orthopaedic surgeons noted that the hip implant enabled the squat (Fig. 6.14a) and figure of four (Fig. 6.14b) postures to be achieved with a high level of stability, with no risk of dislocation. Hence, such feature may provide the opportunity to tap into markets involving young and active individuals, as well as others which require kneeling and squatting as part of their cultural traditions (e.g. kneeling and squatting as daily routine activities in various Asian countries).

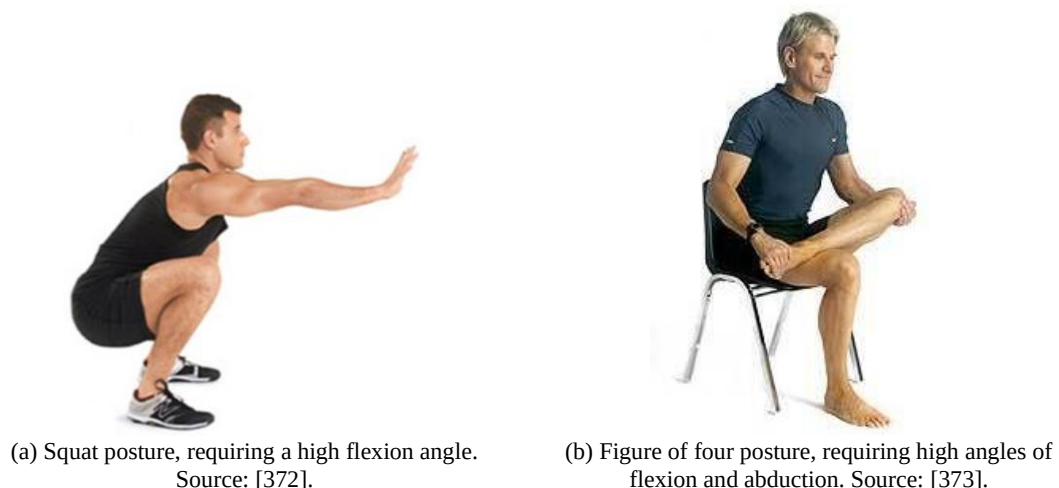


Fig. 6.14: Activities requiring extreme joint angles.

⁵⁹ Subluxation: Partial dislocation

6.8. Summary

This work has demonstrated that an artificial hip consisting of three uni-directional sliding articulations could result in lower wear rates than those produced by one multi-directional articulation. It was observed that both UHMWPE and VEHXPE benefitted from enhanced wear resistance when implemented in the MaltaHip design. The use of a uni-directional articulation does not only provide an increased surface area which effectively reduces the contact stresses, but also maximises the number of covalent bonds which are aligned along the direction of sliding motion, thus drastically increasing the wear resistance of the articulation. In fact, it was observed that the extent of adhesive wear was significantly reduced, as evident by the absence of fibrillar wear particles and preservation of the machining marks.

The largest articulation of the MaltaHip resulted in the lowest wear rate. This contrasts with the general behaviour of spherical femoral heads, which usually exhibit greater wear rates with increasing femoral head diameters. It is postulated that the uni-directional motion of the MaltaHip provided the right theoretical conditions for hydrodynamic lubrication to take place at the MaltaHip cup. In fact, it can be observed the MaltaHip cups resulted in the lowest wear rates and were able to preserve the machining marks in pristine condition. Furthermore, it was noticed that if the contact stress is low enough, an UHMWPE uni-directional articulation can potentially result in a lower wear rate than that produced by a VEHXPE articulation. This can be highly beneficial for artificial hips since UHMWPE possesses higher fatigue resistance than VEHXPE. The integration of the interlocking mechanism also proved to be beneficial in enhancing the stability of the prosthesis, minimizing the risk of dislocation, and providing an extended range of motion.

7. Conclusion

7.1. Work Contribution

In this work, the hypothesis that the new articulating mechanism of the MaltaHip provides a lower rate of wear, compared to the ball-and-socket articulation of conventional implants, was tested. The MaltaHip design is based on three cylindrical articulations that leverage the molecular orientation hardening mechanisms of the polyethylene, and the improved distribution of contact stresses due to the larger contact areas which are provided by the cylindrical surfaces. This work exploits the biomimetics of the ankle joint to provide a unique artificial articulation that is essentially based on a hinge joint that resembles a cylindrical articulation. The results of the study demonstrated statistically significant reductions in the wear rate obtained for the MaltaHip implant, thus supporting the research hypothesis formulated in this work.

The uni-directional mechanism has not only demonstrated to be beneficial in reducing the extent of wear, but also offers the opportunity to integrate an interlocking mechanism which can effectively provide the user with extended ranges of motion, that can be achieved with a high level of stability whilst minimizing the risk of dislocation.

Finite element studies using the elastic and the Three Network models were conducted on the MaltaHip implant. It was confirmed that the elastic model significantly overestimated the stresses induced in the components of the hip implants. In fact, it was observed that the Three Network model resulted in a reduction of 17 – 41 % in the maximum contact stress values when compared to the linear elastic model. Furthermore, it was noted that the Three Network model resulted in maximum von Mises stresses that are 11 – 21 % lower, compared to those predicted by the linear elastic model. Furthermore, both the ball-and-socket and the MaltaHip implants were simulated to reproduce the walking gait cycle using the Three Network model. In general, the MaltaHip implant produced higher average von Mises stress values than the ball-and-socket implant, ranging between 18 – 74 %. Nonetheless, the higher von Mises stress values did not exceed the distributed yield strength of the polyethylene material, and thus the bulk of the polyethylene components would still undergo elastic deformation during use. On the other hand, it was observed that in general, the average contact stresses produced by the MaltaHip articulation were lower than those exhibited by the ball-and-socket articulation, ranging between 12 – 62%. This is highly beneficial as it reduces the amount of wear debris that is released from the surfaces of the polyethylene components.

The theoretical wear rate of the ball-and-socket and MaltaHip implants were computed using the different wear models (Saikko, Liu, Kang and Petrella) available in literature. These predictions were based on the contact stress results and the various features of the slide tracks as produced by the different implant designs. The wear models have been observed to be indicative of the actual wear rates which are produced by the ball-and-socket implants. On the other hand, the wear models did not provide reliable predictions of the wear rates produced by the MaltaHip. Even though the Liu and Petrella wear models considered the cross-shear effects, both models overestimated the wear produced by the MaltaHip cup. Hence, this indicates the need for further studies to improve wear models to provide more reliable indications of the wear behaviour of polyethylene components when used in articulations with different designs.

The experimental wear tests that were conducted using the Endolab® hip joint simulator have demonstrated that the MaltaHip implants achieved lower rates of wear when compared to the ball-and-socket implants with a 28 mm femoral head diameter. The results of the study demonstrated statistically significant reductions in the wear rate obtained for the MaltaHip implant, at 99% confidence interval, thus supporting the research hypothesis formulated in this work. The MaltaHip implant with UHMWPE components resulted in a reduction of 75% in the gravimetric wear rate, when compared to the ball-and-socket prosthesis. The percentage decrease in the gravimetric wear rate for the VEHXPE components could not be computed since a negative rate of wear was obtained.

This indicated that the hypothesized theoretical principles were reproduced in the physical experiment, and thus the MaltaHip mechanism did in fact benefit from the orientation hardening mechanisms and the reduced levels of contact stress. This resulted in the greatest number of covalent bonds of the polymer chains to be aligned along the direction of sliding motion, thus increasing the threshold stress required to release a wear particle. Furthermore, the use of the large contacting areas has resulted in reducing contact stress values, thus minimizing the amount of wear being generated.

The uni-directional articulations of the MaltaHip induced different wear mechanisms than those which are exhibited by the ball-and-socket articulation, as evident by the different topographical surfaces observed from the optical microscopy images. It was interesting to note that the machining marks on the MaltaHip cups were retained on both the UHMWPE and VEHXPE components. This suggests that adhesive and surface fatigue wear mechanisms were minimal. Furthermore, it is likely that the MaltaHip cups permitted the formation of hydrodynamic lubrication. It has been deduced from this work that a uni-directional sliding articulation should opt for a large cylindrical diameter to minimize wear. Frictional effects at the cylindrical articulations are postulated to be minimal, due to the highly aligned polyethylene

structure as a result of the uni-directional sliding motion. This contradicts the principles of low-friction arthroplasty that states higher wear rates are produced with larger femoral head diameters.

Despite the highly-crosslinked nature of the VEHXPE material, which is primarily intended to produce an isotropic structure by limiting the mobility of the molecular chains, results produced from the wear tests and the optical microscopy images suggest that the surface molecules still underwent extensive molecular reorientation effects. This corroborates other results in literature that studied the molecular chain orientation on XPE. As a result, a highly anisotropic structure was formed at the surface which effectively limited the amount of wear particles that were produced. In fact, the characteristic scratches which are typically produced in crosslinked hemispherical cups were not observed in the MaltaHip VEHXPE cup.

Although both UHMWPE and VEHXPE components inside the MaltaHip have demonstrated lower wear rate results, it is postulated that the most robust and practical version of the MaltaHip would be one which is produced out of non-crosslinked polyethylene, or polyethylene components subjected to low levels of crosslinking to maintain its fatigue and fracture strength. Nonetheless, the implant version with UHMWPE components necessitates further design refinements since the rotator underwent a higher rate of wear. It is postulated that improving the contact area of the rotator-abductor interface is likely to significantly reduce the extent of wear that is generated.

The mock surgery exercise on the Thiel embalmed cadaver demonstrated that the new prosthesis design can be implanted using the standard surgical procedure. Only one surgical instrument (pusher) was required to conform to the geometry of the rotator component to press the cup against the bone cement inside the acetabulum. Furthermore, the orthopaedic surgeons noted that the hip reduction process was achieved with relative ease, and that the implant enabled a wide range of motion with minimal risk for dislocation due to the interlocking mechanism.

The particle analysis results demonstrated that the wear debris were classified within the smallest size range. The small sized particles have been classified as the most biologically reactive (i.e. inducing the greatest inflammation effects), as compared to larger sized particles. It is postulated that these wear particles have been mostly liberated from the rotator components, due to their higher rates of wear. Despite their high specific biological activity, the gravimetric wear rate results indicated that only small quantities of these particles were produced, therefore rendering the particles ineffective. Therefore, it is postulated that the overall osteolysis effects induced by MaltaHip implant would be lower than that produced by the ball-and-socket implant, thus potentially resulting in a prosthesis with a longer lifespan.

7.2. Future Work

Results produced from this study have demonstrated that the MaltaHip design could potentially offer a prosthesis design which exhibits lower wear rates than the ball-and-socket design, whilst at the same time enabling the hip to reproduce motions at extreme joint angles as a result of its interlocking mechanism.

As discussed, a large diameter cylindrical articulation produces less wear than a small diameter articulation (as opposed to the observations made with ball-and-socket articulations). Therefore, future studies are required to increase the contact area of the rotator-abductor interface (by increasing the diameter and width of the articulation). These increments can be achieved by reducing the substantially thick non-load bearing section (11.1 cm) of the MaltaHip cup. Such changes are postulated to improve the contact stress levels of the articulation and thus reduce the amount of wear that is generated by the UHMWPE component, whilst providing the prosthesis with superior fatigue resistance than one which is produced out of VEHXPE components.

In case the VEHXPE component demonstrates to be suitable for usage in this prosthesis configuration, it may be worth investigating if post-machining crosslinking processes would improve the wear resistance over a pre-crosslinked round bar. Post-machining crosslinking may be used to create crosslinks between the orientation hardened molecular chains generated from the machining processes. Therefore, the crosslinks may be used to enhance the molecular strength of the surface structure.

Another MaltaHip design feature which may require further refinement is the outer rim of the cup. Although the MaltaHip cup design has demonstrated that the cup is not susceptible to any impingement when aligned in its designated orientation, as shown in Fig. 5.67 (p. 188), further studies may be required to analyse the extent of impingement in cases when the MaltaHip cup is misaligned during implantation. Such study would require specific regions of the MaltaHip cups to be trimmed to prevent any potential impingement sites.

Once the dimensions of the abductor component would have been finalised, it would be worth investigating the feasibility of machining a monobloc stem which consists of an abductor head, due to its simpler design over the spherical femoral head. The use of a monobloc stem is highly appealing from a tribological point-of-view as it eliminates the risk of fretting at the neck of the stem.

The study of frictional torque produced at the different articulations of the MaltaHip would be of great interest. Such data could be obtained using specialised 3D frictional torque device or using the pendulum method. The individual contribution of each articulation of the

MaltaHip could be analysed using the described methods. Furthermore, this study would provide insight regarding the performance of the cylindrical articulations of the MaltaHip, as compared to the spherical articulations of the conventional ball-and-socket design.

Future studies may be also required to test and analyse the MaltaHip implant with respect to its resistance to third-body wear, to simulate the ingress of hard particles, such as bone fragments and/or bone cement. It would be interesting to compare the extent of abrasion wear that is produced under uni-directional sliding motion, as compared to that produced under multi-directional sliding motion due to the different slide tracks which are produced by the different articulations.

8. References

- [1] F. Pauwels, "Der schenkelhalsbruch ein mecha- nisches problem [The femoral neck fracture- A mechanical problem]", *Z Orthop Ihre Grenzgeb.* 63 (1935) 1–135.
- [2] R. Drake, A.W. Vogl, A.W.M. Mitchell, "Gray's Anatomy for Students", *Elsevier Health Sciences*, 2009.
- [3] P.E. Beaulé, "Hip Dysplasia: Understanding and Treating Instability of the Native Hip", *Springer International Publishing*, 2020.
- [4] C. Desai, H. Hirani, A. Chawla, "Life Estimation of Hip Joint Prosthesis", *J. Inst. Eng. Ser. C.* 96 (2015) 261–267.
- [5] C. Reyes, K.M. Leyland, G. Peat, C. Cooper, N.K. Arden, D. Prieto-Alhambra, "Association between overweight and obesity and risk of clinically diagnosed knee, hip, and hand osteoarthritis: a population-based cohort study", *Arthritis Rheumatol.* 68 (2016) 1869–1875.
- [6] T. Kendzerska, P. Jüni, L.K. King, R. Croxford, I. Stanaitis, G.A. Hawker, "The longitudinal relationship between hand, hip and knee osteoarthritis and cardiovascular events: a population-based cohort study", *Osteoarthr. Cartil.* 25 (2017) 1771–1780.
- [7] C. Charbonnier, N. Magnenat-Thalmann, C.D. Becker, P. Hoffmeyer, J. Menetrey, "An integrated platform for hip joint osteoarthritis analysis: Design, implementation and results", *Int. J. Comput. Assist. Radiol. Surg.* 5 (2010) 351–358.
- [8] R.M. Trommer, M.M. Maru, W.L. Oliveira Filho, V.P.S. Nykanen, C.P. Gouvea, B.S. Archanjo, E.H. Martins Ferreira, R.F. Silva, C.A. Achete, "Multi-Scale Evaluation of Wear in UHMWPE-Metal Hip Implants Tested in a hip Joint Simulator", *Biotribology.* 4 (2015) 1–11.
- [9] G. Grammatopoulos, G.E.R. Thomas, H. Pandit, D.J. Beard, H.S. Gill, D.W. Murray, "The effect of orientation of the acetabular component on outcome following total hip arthroplasty with small diameter hard-on-soft bearings", *Bone Joint J.* 97 (2015) 164–172.
- [10] M.S. Uddin, L.C. Zhang, "Predicting the wear of hard-on-hard hip joint prostheses", *Wear.* 301 (2013) 192–200.
- [11] OrthoInfo, "Total Hip Replacement", (2000). <https://orthoinfo.aaos.org/en/treatment/total-hip-replacement> (accessed May 12, 2010).
- [12] KBV Research, "Global Hip Replacement Implants Market By Application, By Product, By End Use (Orthopedic Clinics, Hospitals & Surgery Centers and Other End Use)", Delhi, India, 2019.
- [13] J.T. Evans, J.P. Evans, R.W. Walker, A.W. Blom, M.R. Whitehouse, A. Sayers, "How long does a hip replacement last? A systematic review and meta-analysis of case series and national registry reports with more than 15 years of follow-up", *Lancet.* 393 (2019) 647–654.
- [14] K.J. Bozic, S.M. Kurtz, E. Lau, K. Ong, T.P. Vail, D.J. Berry, "The Epidemiology of Revision Total Hip Arthroplasty in the United States", *J. Bone Jt. Surgery-American Vol.* 91 (2009) 128–133.
- [15] A. Wang, D.C. Sun, S.-S. Yau, B. Edwards, M. Sokol, A. Essner, V.K. Polineni, C. Stark, J.H. Dumbleton, "Orientation softening in the deformation and wear of ultra-high molecular weight polyethylene", *Wear.* 203 (1997) 230–241.
- [16] L.A. Korduba, A. Wang, "The effect of cross-shear on the wear of virgin and highly-crosslinked polyethylene", *Wear.* 271 (2011) 1220–1223.
- [17] F. Liu, J. Fisher, Z. Jin, "Effect of motion inputs on the wear prediction of artificial hip joints", *Tribol. Int.* 63 (2013) 105–114.
- [18] V. Saikko, O. Calonius, "An improved method of computing the wear factor for total hip prostheses involving the variation of relative motion and contact pressure with location on the bearing surface", *J. Biomech.* 36 (2003) 1819–1827.
- [19] A. Wang, A. Essner, R. Klein, "Effect of contact stress on friction and wear of ultra-high molecular weight polyethylene in total hip replacement", *Proc. Inst. Mech. Eng. Part H J. Eng. Med.* 215 (2001) 133–139.
- [20] D.A. Baker, A. Bellare, L. Pruitt, "The effects of degree of crosslinking on the fatigue crack initiation and propagation resistance of orthopedic-grade polyethylene", *J. Biomed. Mater. Res. - Part A.* 66 (2003) 146–154.

- [21] J. Jerosch, S. Fuchs, T. Schmidt, "Is Hylamer adequate for use in all arthroplasties?", *Arch. Orthop. Trauma Surg.* 117 (1998) 79–83.
- [22] G.M. Farling, "Human Body Implant of Graphitic Carbon Fibre Reinforced Ultra-High Molecular Weight Polyethylene", (n.d.).
- [23] J.E. Bischoff, J.C. Fryman, J. Parcell, D.A. Orozco Villaseñor, "Influence of crosslinking on the wear performance of polyethylene within total ankle arthroplasty", *Foot Ankle Int.* 36 (2015) 369–376.
- [24] A.L. Galvin, J.L. Tipper, L.M. Jennings, M.H. Stone, Z.M. Jin, E. Ingham, J. Fisher, "Wear and biological activity of highly crosslinked polyethylene in the hip under low serum protein concentrations", *Proc. Inst. Mech. Eng. Part H J. Eng. Med.* 221 (2007) 1–10.
- [25] M. Greaser, J.K. Ellington, "Ankle arthritis", *J Arthritis.* 3 (2014) 2.
- [26] J. Charnley, "Arthroplasty of the hip: a new operation", *Lancet.* 277 (1961) 1129–1132.
- [27] R. Sonntag, J.P. Kretzer, "Materials For Total Joint Arthroplasty: Biotribology Of Potential Bearings", *World Scientific Publishing Company*, 2015.
- [28] J. Charnley, "Low Friction Arthroplasty of the Hip: Theory and Practice", *Springer Berlin Heidelberg*, 2012.
- [29] M. Kothari, D.L. Bartel, J.F. Booker, "Surface geometry of retrieved McKee-Farrar total hip replacements", *Clin. Orthop. Relat. Res.* 329 (1996) S141–S147.
- [30] M. Winter, P. Griss, G. Scheller, T. Moser, "Ten-to 14-year results of a ceramic hip prosthesis.", *Clin. Orthop. Relat. Res.* (1992) 73–80.
- [31] J.S. Bergstrom, J.E. Bischoff, "An advanced thermomechanical constitutive model for UHMWPE", *Int. J. Struct. Chang. Solids.* 2 (2010) 31–39.
- [32] L. V. Wilches, J.A. Uribe, A. Toro, "Wear of materials used for artificial joints in total hip replacements", *Wear.* 265 (2008) 143–149.
- [33] V. Saikko, "Effect of contact pressure on wear and friction of ultra-high molecular weight polyethylene in multidirectional sliding", *Proc. Inst. Mech. Eng. Part H J. Eng. Med.* 220 (2006) 723–731.
- [34] S.-J. Park, M.-K. Seo, "Element and processing", in: *Interface Sci. Technol., Elsevier*, 2011: pp. 431–499.
- [35] J.A. Puértolas, F.J. Pascual, M.J. Martínez-Morlanes, "Impact resistance and fractography in ultra high molecular weight polyethylenes", *J. Mech. Behav. Biomed. Mater.* 30 (2014) 111–122.
- [36] M.N. Collins, D. Barron, C. Birkinshaw, "Ultra high molecular weight polyethylene (UHMWPE) for orthopaedic devices: structure/property relationships", *Polyethylene-Based Blends, Compos. Nanocomposites.* 1 (2015) 21–39.
- [37] R. Varadarajan, E.K. Dapp, C.M. Rimnac, "Static fracture resistance of ultra high molecular weight polyethylene using the single specimen normalization method", *Polym. Test.* 27 (2008) 260–268.
- [38] J. Fu, Z.M. Jin, J.W. Wang, "UHMWPE Biomaterials for Joint Implants: Structures, Properties and Clinical Performance", *Springer Singapore*, 2019.
- [39] National Joint Registry, "17th Annual Report", 2020.
- [40] P. Kinov, A. Tzoncheva, P. Tivchev, "Evidence linking elevated oxidative stress and aseptic loosening of hip arthroplasty", *Comptes Rendus L'Academie Bulg. Des Sci.* 63 (2010) 1231–1238.
- [41] S. Patil, A. Bergula, P.C. Chen, C.W. Colwell, D.D. D'Lima, "Polyethylene Wear and Acetabular Component Orientation", *J. Bone Jt. Surg.* 85 (2003) 56–63.
- [42] I. Milošev, S. Kovač, R. Trebše, V. Levašič, V. Pišot, "Comparison of ten-year survivorship of hip prostheses with use of conventional polyethylene, metal-on-metal, or ceramic-on-ceramic bearings", *J. Bone Jt. Surg. - Ser. A.* 94 (2012) 1756–1763.
- [43] E. Ingham, J. Fisher, "Biological reactions to wear debris in total joint replacement", *Proc. Inst. Mech. Eng. Part H J. Eng. Med.* 214 (2000) 21–37.
- [44] T.P. Schmalzried, K.H. Akizuki, A.N. Fedenko, J. Mirra, "The role of access of joint fluid to bone in periarticular osteolysis: a report of four cases", *JBJS.* 79 (1997) 447–452.

- [45] W.H. Harris, A.L. Schiller, J.M. Scholler, R.A. Freiberg, R. Scott, "Extensive localized bone resorption in the femur following total hip replacement", *JBJS*. 58 (1976) 612–618.
- [46] V. Saikko, T. Ahlroos, "Type of motion and lubricant in wear simulation of polyethylene acetabular cup", *Proc. Inst. Mech. Eng. Part H J. Eng. Med.* 213 (1999) 301–310.
- [47] L.A. Pruitt, A.M. Chakravartula, "Mechanics of biomaterials: fundamental principles for implant design", *Cambridge University Press*, 2011.
- [48] B.C. Carr, T. Goswami, "Knee implants--Review of models and biomechanics", *Mater. Des.* 30 (2009) 398–413.
- [49] A.S. Shanbhag, J.J. Jacobs, J. Black, J.O. Galante, T.T. Glant, "Macrophage/particle interactions: effect of size, composition and surface area", *J. Biomed. Mater. Res.* 28 (1994) 81–90.
- [50] T.D. Brown, J.M. Elkins, D.R. Pedersen, J.J. Callaghan, "Impingement and dislocation in total hip arthroplasty: mechanisms and consequences.", *Iowa Orthop. J.* 34 (2014) 1–15.
- [51] S.P. Singh, H.P. Bhalodiya, "Head size and dislocation rate in primary total hip arthroplasty", *Indian J. Orthop.* 47 (2013) 443.
- [52] J.F. Plate, T.M. Seyler, D.A. Stroh, K. Issa, M. Akbar, M.A. Mont, "Risk of dislocation using large- vs . small-diameter femoral heads in total hip arthroplasty", (2012) 2–7.
- [53] O.K. Muratoglu, C.R. Bragdon, D. O'Connor, R.S. Perinchief, D.M. Estok II, M. Jasty, W.H. Harris, "Larger diameter femoral heads used in conjunction with a highly cross-linked ultra--high molecular weight polyethylene: a new concept", *J. Arthroplasty.* 16 (2001) 24–30.
- [54] J.C. Hermida, A. Bergula, P. Chen, C.W. Colwell Jr, D.D. D'Lima, "Comparison of the wear rates of twenty-eight and thirty-two-millimeter femoral heads on cross-linked polyethylene acetabular cups in a wear simulator", *JBJS*. 85 (2003) 2325–2331.
- [55] K. Hirakawa, T.W. Bauer, Y. Hashimoto, B.N. Stulberg, A.H. Wilde, M. Secic, "Effect of femoral head diameter on tissue concentration of wear debris", (1997).
- [56] J.M. Kabo, J.S. Gebhard, G. Loren, H.C. Amstutz, J.M. Kabo, J.S. Gebhard, G. Loren, H.C. Amstutz, "the Journal of Bone and Joint Surgery in Vivo Wear of Polyethylene Acetabular Components", *J Bone Jt. Surg [Br]*. 75 (1993) 254–8.
- [57] C. Delaunay, M. Hamadouche, "What Are the Causes for Failures of Primary Hip Arthroplasties in France ?", (2013) 3863–3869.
- [58] P. Sadoghi, M. Liebensteiner, M. Agreiter, A. Leithner, N. Böhler, G. Labek, "Revision Surgery After Total Joint Arthroplasty : A Complication-Based Analysis Using Worldwide Arthroplasty Registers", *J. Arthroplasty.* 28 (2013) 1329–1332.
- [59] S.M. Jafari, C. Coyle, S.M.J. Mortazavi, P.F. Sharkey, J. Parvizi, "Revision hip arthroplasty: infection is the most common cause of failure", *Clin. Orthop. Relat. Res.* 468 (2010) 2046–2051.
- [60] M. Karadsheh, "OrthoBullets - THA Prosthesis Design", (n.d).
<https://www.orthobullets.com/recon/5033/tha-prosthesis-design> (accessed October 30, 2019).
- [61] Z.S. Bagheri, R. Zdero, E.H. Schemitsch, H. Bougherara, M. Rezaey, "The Biomechanical Effect of Loading Speed on Metal-on-UHMWPE Contact Mechanics", *Open Biomed. Eng. J.* 8 (2014) 28–34.
- [62] J.C. McCarthy, P.C. Noble, R.N. Villar, "Hip joint restoration : worldwide advances in arthroscopy, arthroplasty, osteotomy and joint preservation surgery", 2017.
- [63] K. Zhao, E. Lau, K.J. Bozic, M. Kelly, K. Ong, S.M. Kurtz, "Future Young Patient Demand for Primary and Revision Joint Replacement: National Projections from 2010 to 2030", *Clin. Orthop. Relat. Res.* 467 (2009) 2606–2612.
- [64] H. McKellop, I. Clarke, K. Markolf, H. Amstutz, "Friction and wear properties of polymer, metal, and ceramic prosthetic joint materials evaluated on a multichannel screening device", *J. Biomed. Mater. Res.* 15 (1981) 619–653.
- [65] J.H. Dumbleton, "Tribology of natural and artificial joints", *Elsevier*, 1981.
- [66] D.J. Berry, J.R. Lieberman, "Surgery of the Hip", *Elsevier/Saunders*, 2013.

- [67] M. Reggiani, A. Tinti, P. Taddei, M. Visentin, S. Stea, M. De Clerico, C. Fagnano, "Phase transformation in explanted highly crystalline UHMWPE acetabular cups and debris after in vivo wear", *J. Mol. Struct.* 785 (2006) 98–105.
- [68] M.J. Chmell, R. Poss, W.H. Thomas, C.B. Sledge, "Early failure of Hylamer acetabular inserts due to eccentric wear", *J. Arthroplasty.* 11 (1996) 351–353.
- [69] B. Reggiani, A. Leardini, F. Corazza, M. Taylor, "Finite element analysis of a total ankle replacement during the stance phase of gait", *J. Biomech.* 39 (2006) 1435–1443.
- [70] S.K. Sinha, "Polymer Tribology", *Imperial College Press*, 2009.
- [71] S.M. Kurtz, "UHMWPE Biomaterials Handbook: Ultra High Molecular Weight Polyethylene in Total Joint Replacement and Medical Devices: Third Edition", 2015.
- [72] J.P. Collier, L.S. Bargmann, B.H. Currier, M.B. Mayor, J.H. Currier, B.C. Bargmann, "An analysis of Hylamer and polyethylene bearings from retrieved acetabular components", *Orthopedics.* 21 (1998) 865–871.
- [73] L. Costa, M.P. Luda, L. Trossarelli, E.M.B. Del Prever, M. Crova, P. Gallinaro, "Oxidation in orthopaedic UHMWPE sterilized by gamma-radiation and ethylene oxide", *Biomaterials.* 19 (1998) 659–668.
- [74] J.J. Callaghan, H.E. Rubash, J.C. Clohisy, P.E. Beaulé, C.J. Della Valle, "The Adult Hip : Hip Arthroplasty Surgery", Third edit (2016).
- [75] J. Zhou, A. Chakravartula, L. Pruitt, K. Komvopoulos, "Tribological and Nanomechanical Properties of Unmodified and Crosslinked Ultra-High Molecular Weight Polyethylene for Total Joint Replacements", *J. Tribol.* 126 (2004) 386.
- [76] S.M. Kurtz, H.A. Gawel, J.D. Patel, "History and systematic review of wear and osteolysis outcomes for first-generation highly crosslinked polyethylene", *Clin. Orthop. Relat. Res.* 469 (2011) 2262–2277.
- [77] P.A. Devane, J.G. Home, A. Ashmore, F. Ortho, J. Mutimer, F. Ortho, W. Kim, J. Stanley, "Revision Rates in Total Hip Arthroplasty", (2017) 1703–1714.
- [78] V. Premnath, W.H. Harris, M. Jasty, E.W. Merrill, "Gamma sterilization of UHMWPE articular implants: an analysis of the oxidation problem", *Biomaterials.* 17 (1996) 1741–1753.
- [79] T.J.S. Puolakka, J.T. Keränen, K. a Juhola, K.J.J. Pajamäki, P.J. Halonen, J.K. Nevalainen, V. Saikko, M.U.K. Lehto, M. Järvinen, "Increased volumetric wear of polyethylene liners with more than 3 years of shelf-life time.", *Int. Orthop.* 27 (2003) 153–9.
- [80] B. Smaller, M.S. Matheson, "Paramagnetic species produced by gamma irradiation of organic compounds", *J. Chem. Phys.* 28 (1958) 1169–1178.
- [81] D.J. Carlsson, S. Chmela, J. Lacoste, "On the structures and yields of the first peroxy radicals in gamma-irradiated polyolefins", *Macromolecules.* 23 (1990) 4934–4938.
- [82] J. Lacoste, D.J. Carlsson, S. Falicki, D.M. Wiles, "Polyethylene hydroperoxide decomposition products", *Polym. Degrad. Stab.* 34 (1991) 309–323.
- [83] N. Tomita, T. Kitakura, N. Onmori, Y. Ikada, E. Aoyama, "Prevention of fatigue cracks in ultrahigh molecular weight polyethylene joint components by the addition of vitamin E", *J. Biomed. Mater. Res.* 48 (1999) 474–478.
- [84] E. Oral, K.K. Wannomae, N. Hawkins, W.H. Harris, O.K. Muratoglu, "α-Tocopherol-doped irradiated UHMWPE for high fatigue resistance and low wear", *Biomaterials.* 25 (2004) 5515–5522.
- [85] M.D. Ries, M.L. Scott, S. Jani, "Relationship between gravimetric wear and particle generation in hip simulators: conventional compared with cross-linked polyethylene", *JBJS.* 83 (2001) S116--122.
- [86] M.L. Harper, A. Dooris, P.E. Paré, "The fundamentals of biotribology and its application to spine arthroplasty", *SAS J.* 3 (2009) 125–132.
- [87] E.W. Paxton, M.C.S. Inacio, R.S. Namba, R. Love, S.M. Kurtz, "Metal-on-conventional Polyethylene Total Hip Arthroplasty Bearing Surfaces Have a Higher Risk of Revision Than Metal-on-highly Crosslinked Polyethylene: Results From a US Registry", *Clin. Orthop. Relat. Res.* 473 (2015) 1011–1021.
- [88] D.A. Bichara, E. Malchau, N.H. Sillesen, S. Cakmak, G.P. Nielsen, O.K. Muratoglu, "Vitamin E-Diffused Highly Cross-Linked UHMWPE Particles Induce Less Osteolysis Compared to Highly Cross-Linked Virgin UHMWPE Particles In Vivo", 2 (2014) 232–237.

- [89] R. De Steiger, M. Lorimer, S.E. Graves, "Cross-linked polyethylene for total hip arthroplasty markedly reduces revision surgery at 16 years", *JBJS*. 100 (2018) 1281–1288.
- [90] C. Shen, Z.H. Tang, J.Z. Hu, G.Y. Zou, R.C. Xiao, D.X. Yan, "Does cross-linked polyethylene decrease the revision rate of total hip arthroplasty compared with conventional polyethylene? A meta-analysis", *Orthop. Traumatol. Surg. Res.* 100 (2014) 745–750.
- [91] R.L. Illgen, T.M. Forsythe, J.W. Pike, M.P. Laurent, C.R. Blanchard, "Highly Crosslinked vs Conventional Polyethylene Particles-An In Vitro Comparison of Biologic Activities", *J. Arthroplasty*. 23 (2008) 721–731.
- [92] T.R. Green, J. Fisher, M. Stone, B.M. Wroblewski, E. Ingham, "Polyethylene particles of a 'critical size' are necessary for the induction of cytokines by macrophages in vitro", *Biomaterials*. 19 (1998) 2297–2302.
- [93] P. Bracco, A. Bellare, A. Bistolfi, S. Affatato, "Ultra-high molecular weight polyethylene: Influence of the chemical, physical and mechanical properties on the wear behavior. A review", *Materials (Basel)*. 10 (2017).
- [94] C.W. McBryde, P.B. Pynsent, "Birmingham hip resurfacing arthroplasty", 87 (2005) 167–170.
- [95] B.R.F. Spencer, "Evolution in Hip Resurfacing Design and", (2011) 84–88.
- [96] G. Bousquet, D.F. Gazielly, P. Girardin, J.L. Debieesse, M. Relave, A. Israeli, "The ceramic coated cementless total hip arthroplasty. Basic concepts and surgical technique", *J Orthop Surg Tech*. 1 (1985) 15–28.
- [97] J. Geringer, B. Boyer, F. Farizon, "Understanding the dual mobility concept for total hip arthroplasty. Investigations on a multiscale analysis-highlighting the role of arthrofibrosis", *Wear*. 271 (2011) 2379–2385.
- [98] Smith & Nephew, "Birmingham Hip Resurfacing System", (n.d.). <https://www.smith-nephew.com/professional/products/all-products/bhr-birmingham-hip-resurfacing/> (accessed October 30, 2019).
- [99] Corin Group, "Trinity", (n.d.). <https://www.coringroup.com/uk/solutions/trinity-2/> (accessed October 30, 2019).
- [100] W.H. Harris, P.G.J. Maquet, "Biomechanics of the Hip: As Applied to Osteoarthritis and Related Conditions", *Springer Berlin Heidelberg*, 2012.
- [101] B.F. Morrey, K.N. An, J.W. Sperling, "Joint Replacement Arthroplasty: Hip, knee, and ankle", *Wolters Kluwer Health/Lippincott Williams & Wilkins*, 2011.
- [102] M.O. Heller, J.H. Schröder, G. Matziolis, A. Sharenkov, W.R. Taylor, C. Perka, G.N. Duda, "Muskuloskeletale belastungsanalysen. Biomechanische erklärung klinischer resultate--Und mehr", *Orthopade*. 36 (2007) 188–194.
- [103] G. Németh, H. Ohlsén, "In vivo moment arm lengths for hip extensor muscles at different angles of hip flexion", *J. Biomech*. 18 (1985) 129–140.
- [104] D.T. Davy, G.M. Kotzar, R.H. Brown, K.G. Heiple, V.M. Goldberg, J.K.G. Heiple, J. Berilla, A.H. Burstein, "Telemetric force measurements across the hip after total arthroplasty.", *J. Bone Joint Surg. Am.* 70 (1988) 45–50.
- [105] G. Bergmann, G. Deuretzbacher, M. Heller, F. Graichen, A. Rohlmann, J. Strauss, G.N. Duda, "Hip contact forces and gait patterns from routine activities", *J. Biomech*. 34 (2001) 859–871.
- [106] M.O. Heller, G. Bergmann, G. Deuretzbacher, M. Pohl, L. Claes, N.P. Haas, G.N. Duda, "Musculo-skeletal loading conditions at the hip during walking and stair climbing", 34 (2001) 883–893.
- [107] C. Perka, U. Fischer, W.R. Taylor, G. Matziolis, "Developmental hip dysplasia treated with total hip arthroplasty with a straight stem and a threaded cup", *JBJS*. 86 (2004) 312–319.
- [108] M.O. Heller, G. Bergmann, G. Deuretzbacher, L. Claes, N.P. Haas, G.N. Duda, "Influence of femoral anteversion on proximal femoral loading: measurement and simulation in four patients", *Clin. Biomech*. 16 (2001) 644–649.
- [109] S.J. Breusch, H. Malchau, "The well-cemented total hip arthroplasty theory and practice", 2005.
- [110] R.N. Stauffer, E.Y. Chao, R.C. Brewster, "Force and motion analysis of the normal, diseased, and prosthetic ankle joint.", *Clin. Orthop. Relat. Res.* (1977) 189–196.

- [111] J.R. Williams, N.J. Wegner, B.J. Sangeorzan, M.E. Brage, "Intraoperative and perioperative complications during revision arthroplasty for salvage of a failed total ankle arthroplasty", *Foot Ankle Int.* 36 (2015) 135–142.
- [112] G. Labek, M. Thaler, W. Janda, M. Agreiter, B. Stöckl, "Revision rates after total joint replacement: cumulative results from worldwide joint register datasets", *J. Bone Joint Surg. Br.* 93 (2011) 293–297.
- [113] B. Jay Elliot, D. Gundapaneni, T. Goswami, "Finite element analysis of stress and wear characterization in total ankle replacements", *J. Mech. Behav. Biomed. Mater.* 34 (2014) 134–145.
- [114] M.R. McGuire, R.F. Kyle, R.B. Gustilo, R.F. Premer, "Comparative analysis of ankle arthroplasty versus ankle arthrodesis.", *Clin. Orthop. Relat. Res.* (1988) 174–181.
- [115] J.M. Michael, A. Golshani, S. Gargac, T. Goswami, "Biomechanics of the ankle joint and clinical outcomes of total ankle replacement", *J. Mech. Behav. Biomed. Mater.* 1 (2008) 276–294.
- [116] A. Seireg, R.J. Arvikar, "The prediction of muscular load sharing and joint forces in the lower extremities during walking", *J. Biomech.* 8 (1975) 89–102.
- [117] D. Gundapaneni, R.T. Laughlin, T. Goswami, "Characterization of retrieved total ankle replacement liners", *Eng. Fail. Anal.* 70 (2016) 237–254.
- [118] R.A. Brand, "Joint contact stress: a reasonable surrogate for biological processes?", *Iowa Orthop. J.* 25 (2005) 82.
- [119] MatOrtho, "BOX Total Ankle Replacement", (n.d.). <https://www.matortho.com/products/box-total-ankle-replacement/> (accessed October 30, 2019).
- [120] N. Martinelli, S. Baretta, J. Pagano, A. Bianchi, T. Villa, G. Casaroli, F. Galbusera, "Contact stresses, pressure and area in a fixed-bearing total ankle replacement: a finite element analysis", *BMC Musculoskelet. Disord.* 18 (2017) 493.
- [121] S. Lal, Isolation, Characterisation and Software Development for Polymeric Wear Particles from In Vitro Joint Simulators, Durham University, 2016.
- [122] O.N. Schipper, S.L. Haddad, S. Fullam, R. Pourzal, M.A. Wimmer, "Wear characteristics of conventional ultrahigh-molecular-weight polyethylene versus highly cross-linked polyethylene in total ankle arthroplasty", *Foot Ankle Int.* 39 (2018) 1335–1344.
- [123] L. Ombregt, "A System of Orthopaedic Medicine - E-Book", *Elsevier Health Sciences*, 2013.
- [124] OrthoInfo, "Osgood-Schlatter Disease (Knee Pain)", (2020). <https://orthoinfo.aaos.org/en/diseases--conditions/osgood-schlatter-disease-knee-pain/> (accessed May 25, 2020).
- [125] MicroPort Orthopedics, "Knee", (2020). <https://ortho.microport.com/index.cfm/products/knees/> (accessed November 7, 2020).
- [126] M. Ishikawa, S. Kuriyama, H. Ito, M. Furu, S. Nakamura, S. Matsuda, "Kinematic alignment produces near-normal knee motion but increases contact stress after total knee arthroplasty: a case study on a single implant design", *Knee.* 22 (2015) 206–212.
- [127] N.M.A. Azam, R. Daud, H.M. Ayu, J. Ramli, M.F.B. Hassan, A. Shah, M. Adib, "The effect of knee flexion angle on contact stress of total knee arthroplasty", in: MATEC Web Conf., 2018: p. 3009.
- [128] D. Tarnita, D.M. Calafeteanu, I.D. Geonea, A. Petcu, D.-N. Tarnita, "Effects of malalignment angle on the contact stress of knee prosthesis components, using finite element method", *Rom J Morphol Embryol.* 58 (2017) 831–836.
- [129] J. Zhang, D. Tian, Z. Ren, Y. Hu, X. Yu, "Influence of Congruency Design on the Contact Stress of a Novel Hinged Knee Prosthesis Using Finite Element Analysis", *Orthop. Surg.* 12 (2020) 631–638.
- [130] T.M. Grupp, D. Stulberg, C. Kaddick, A. Maas, B. Fritz, J. Schwiesau, W. Blömer, "Fixed bearing knee congruency--influence on contact mechanics, abrasive wear and kinematics", *Int. J. Artif. Organs.* 32 (2009) 213–223.
- [131] G.W. Blunn, P.S. Walker, A. Joshi, K. Hardinge, "The dominance of cyclic sliding in producing wear in total knee replacements.", *Clin. Orthop. Relat. Res.* (1991) 253–260.
- [132] H. McKellop, "What are the wear mechanisms and what controls them", *Implant Wear Total Jt. Replace. Clin. Biol. Issues, Mater. Des. Considerations. Rosemont, Illinois Am. Acad. Orthop. Surg.* (2001) 176–185.

- [133] J. Fisher, M. Stone, D. Shaw, D.D. Auger, T. Stewart, Z.M. Jin, "Experimental and Theoretical Study of the Contact Mechanics of Five Total Knee Joint Replacements", *Proc. Inst. Mech. Eng. Part H J. Eng. Med.* 209 (2007) 225–231.
- [134] Y.G. Koh, K.M. Park, H.Y. Lee, K.T. Kang, "Influence of tibiofemoral congruency design on the wear of patient-specific unicompartmental knee arthroplasty using finite element analysis", *Bone Joint Res.* 8 (2019) 156–164.
- [135] R. Pourzal, C.B. Knowlton, D.J. Hall, M.P. Laurent, R.M. Urban, M.A. Wimmer, "How does wear rate compare in well-functioning total hip and knee replacements? A postmortem polyethylene liner study", *Clin. Orthop. Relat. Res.* 474 (2016) 1867–1875.
- [136] M.C. Sobieraj, S.M. Kurtz, C.M. Rimnac, "Large deformation compression induced crystallinity degradation of conventional and highly crosslinked UHMWPEs", 26 (2005) 6430–6439.
- [137] M.C. Sobieraj, C.M. Rimnac, "Ultra high molecular weight polyethylene: Mechanics, morphology, and clinical behavior", *J. Mech. Behav. Biomed. Mater.* 2 (2009) 433–443.
- [138] L. Wang, W. Yang, X. Peng, D. Li, S. Dong, S. Zhang, J. Zhu, Z. Jin, "Effect of progressive wear on the contact mechanics of hip replacements - Does the realistic surface profile matter?", *J. Biomech.* 48 (2015) 1112–1118.
- [139] J. Ashok, P.L.H. Varaprasad, "Polyethylene (02H4) n", 1991.
- [140] M. Vrbka, D. Nečas, M. Hartl, I. Křupka, F. Urban, J. Gallo, "Visualization of lubricating films between artificial head and cup with respect to real geometry", *Biotribology.* 1–2 (2015) 61–65.
- [141] R.H. Partridge, "Vacuum-Ultraviolet Absorption Spectrum of Polyethylene", *J. Chem. Phys.* 45 (1966) 1685–1690.
- [142] L.E. Sutton, D. Phil, D.G. Jenkin, A.D. Mitchell, L.C. Cross, H.J.M. Bowen, J. Donohue, O. Kennard, P.J. Wheatley, D.H. Whiffen, "Tables of Interatomic Distances and Configuration in Molecules and Ions (Special Publication No. 11).", 1958.
- [143] L. Pauling, "The Nature of the Chemical Bond...", *Cornell university press Ithaca, NY*, 1960.
- [144] F. Rodriguez, C. Cohen, C.K. Ober, L. Archer, "Principles of Polymer Systems, Sixth Edition", *Taylor & Francis*, 2014.
- [145] Lumen Learning, "Hydrocarbons", (2017).
<https://courses.lumenlearning.com/chemistryformajors/chapter/hydrocarbons/> (accessed February 14, 2017).
- [146] S.M. Kurtz, O.K. Muratoglu, M. Evans, A.A. Edidin, "Advances in the processing, sterilization, and crosslinking of ultra-high molecular weight polyethylene for total joint arthroplasty", *Biomaterials.* 20 (1999) 1659–1688.
- [147] R.M. Gul, F.J. McGarry, C.R. Bragdon, O.K. Muratoglu, W.H. Harris, "Effect of consolidation on adhesive and abrasive wear of ultra high molecular weight polyethylene", *Biomaterials.* 24 (2003) 3193–3199.
- [148] S.L. Rowell, B.W. Ghali, E. Oral, O.K. Muratoglu, "Vitamin E-blended UHMWPE with a gradient vitamin E concentration", in: Las Vegas, NV Trans. 55th Annu. Meet. Orthop. Res. Soc., 2009.
- [149] J. Bellemans, M.D. Ries, J.M.K. Victor, "Total Knee Arthroplasty: A Guide to Get Better Performance", *Springer Berlin Heidelberg*, 2005.
- [150] P. Taddei, M. Di Foggia, S. Affatato, "Raman characterisation of conventional and cross-linked polyethylene in acetabular cups run on a hip joint simulator", *J. Raman Spectrosc.* 42 (2011) 1344–1352.
- [151] L. Lin, A.S. Argon, "Structure and plastic deformation of polyethylene", *J. Mater. Sci.* 29 (1994) 294–323.
- [152] A. Wang, A. Essner, V.K. Polineni, C. Stark, J.H. Dumbleton, "Lubrication and wear of ultra-high molecular weight polyethylene in total joint replacements", *Tribol. Int.* 31 (1998) 17–33.
- [153] A. Bellare, H. Schnablegger, R.E. Cohen, "A small-angle x-ray scattering study of high-density polyethylene and ultrahigh molecular weight polyethylene", *Macromolecules.* 28 (1995) 7585–7588.
- [154] D.F. Farrar, A.A. Brain, "The microstructure of ultra-high molecular weight polyethylene used in total joint replacements", *Biomaterials.* 18 (1997) 1677–1685.
- [155] R.M. Gul, F.J. McGarry, "Processing of ultra-high molecular weight polyethylene by hot isostatic pressing, and the effect of processing parameters on its microstructure", *Polym. Eng. Sci.* 44 (2004) 1848–1857.

- [156] L. Pruitt, L. Bailey, "Factors affecting the near-threshold fatigue behavior of surgical grade ultra high molecular weight polyethylene", *Polymer (Guildf)*. 39 (1998) 545–553.
- [157] B. Weightman, D. Light, "A comparison of RCH 1000 and Hi-Fax 1900 ultra-high molecular weight polyethylenes", *Biomaterials*. 6 (1985) 177–183.
- [158] M. Goldman, R. Gronsky, R. Ranganathan, L. Pruitt, "The effects of gamma radiation sterilization and ageing on the structure and morphology of medical grade ultra high molecular weight polyethylene", *Polymer (Guildf)*. 37 (1996) 2909–2913.
- [159] R.M. Gul, Improved UHMWPE for use in Total Joint Replacement, Massachusetts Institute of Technology, 1997.
- [160] S.M. Kurtz, M.L. Villarraga, M.P. Herr, J.S. Bergström, C.M. Rimnac, A.A. Edidin, "Thermomechanical behavior of virgin and highly crosslinked ultra-high molecular weight polyethylene used in total joint replacements", *Biomaterials*. 23 (2002) 3681–3697.
- [161] K. Chen, F. Lu, "Time-Dependent Uniaxial Ratchetting of Ultrahigh Molecular Weight Polyethylene Polymer : Viscoelastic – Viscoplastic Constitutive Model", 83 (2016).
- [162] L.A. Pruitt, "Deformation, yielding, fracture and fatigue behavior of conventional and highly cross-linked ultra high molecular weight polyethylene", *Biomaterials*. 26 (2005) 905–915.
- [163] I.H. Hall, "Structure of crystalline polymers", *Elsevier Applied Science Publishers*, 1984.
- [164] A. Wang, J.H. Dumbleton, "Ultra-High-Molecular-Weight Polyethylene (UHMWPE) as a Bearing Material in Hip Joint Replacements", in: Q.J. Wang, Y.-W. Chung (Eds.), *Encycl. Tribol., Springer US*, Boston, MA, 2013: pp. 3933–3939.
- [165] S.M. Kurtz, L. Pruitt, C.W. Jewett, R.P. Crawford, D.J. Crane, A.A. Edidin, "The yielding, plastic flow, and fracture behavior of ultra-high molecular weight polyethylene used in total joint replacements", *Biomaterials*. 19 (1998) 1989–2003.
- [166] M.C. Galetz, U. Glatzel, "Molecular deformation mechanisms in UHMWPE during tribological loading in artificial joints", *Tribol. Lett.* 38 (2010) 1–13.
- [167] P.J. Phillips, "Polymer morphology and crystallisation", *Mater. Sci. Technol.* 19 (2003) 1153–1160.
- [168] M.M. Shahin, R.H. Olley, M.J. Blissett, "Refinement of etching techniques to reveal lamellar profiles in polyethylene banded spherulites", *J. Polym. Sci. Part B Polym. Phys.* 37 (1999) 2279–2286.
- [169] J. Zhou, K. Komvopoulos, "Wear Mechanisms of Untreated and Gamma Irradiated Ultra-High Molecular Weight Polyethylene for Total Joint Replacements", *J. Tribol.* 127 (2005) 273.
- [170] M.C. Galetz, C. Goetz, P. Adam, U. Glatzel, "Hysteretic heating during cyclic loading of medical grade ultra high molecular weight polyethylene (UHMWPE)", *Adv. Eng. Mater.* 9 (2007) 1089–1096.
- [171] V.P. M, M.J.M. Morlanes, "Polyethylene-Based Blends, Composites and Nanocomposites", *Wiley*, 2015.
- [172] D.C. Bassett, "Principles of Polymer Morphology", *Cambridge University Press*, 1981.
- [173] M. Visentin, S. Stea, M. De Clerico, M. Reggiani, C. Fagnano, S. Squarzone, A. Toni, "Determination of crystallinity and crystal structure of Hylamer™ polyethylene after in vivo wear", *J. Biomater. Appl.* 21 (2006) 131–145.
- [174] L. Kurelec, S. Rastogi, R.J. Meier, P.J. Lemstra, "Chain mobility in polymer systems: On the borderline between solid and melt. 3. Phase transformations in nascent ultrahigh molecular weight polyethylene reactor powder at elevated pressure as revealed by in situ Raman spectroscopy", *Macromolecules*. 33 (2000) 5593–5601.
- [175] N.G. McCrum, C.P. Buckley, C.B. Bucknall, C.B. Bucknall, "Principles of Polymer Engineering", *Oxford University Press*, 1997.
- [176] J.S. Bergstrom, "Mechanics of Solid Polymers: Theory and Computational Modeling", *Elsevier Science*, 2015.
- [177] T.M. Wright, "Design considerations for an acetabular component made from an enhanced form of ultra high molecular weight polyethylene", in: 37th Annu. Meet. Orthop. Res. Soc. 1991, 1991: p. 248.
- [178] J.E.L. Pacheco, C.A. Bavastri, J.T. Pereira, "Viscoelastic relaxation modulus characterization using Prony series", *Lat. Am. J. Solids Struct.* 12 (2015) 420–445.

- [179] J.P. Davim, "Biotribology", Wiley, 2013.
- [180] P.B. Bowden, R.J. Young, "Deformation mechanisms in crystalline polymers", *J. Mater. Sci.* 9 (1974) 2034–2051.
- [181] J.M. Peterson, P.H. Lindenmeyer, "Screw dislocations in anisotropic media", *J. Appl. Phys.* 37 (1966) 4051–4053.
- [182] M.F. Butler, A.M. Donald, A.J. Ryan, "Time resolved simultaneous small-and wide-angle X-ray scattering during polyethylene deformation—II. Cold drawing of linear polyethylene", *Polymer (Guildf)*. 39 (1998) 39–52.
- [183] E.F. Oleinik, "Plasticity of Semicrystalline Flexible-Chain Polymers at the Microscopic and Mesoscopic Levels", *Polym. Sci. Ser. C.* 45 (2003) 2137–2264.
- [184] D.P. Pope, A. Keller, "Deformation of oriented polyethylene", *J. Polym. Sci. Polym. Phys. Ed.* 13 (1975) 533–566.
- [185] H.H. Kausch, "Advances in Polymer Science and Engineering", *Plenum Press. New York.* (1972) 207.
- [186] K. Friedrich, "Crazes and shear bands in semi-crystalline thermoplastics", in: *Crazing Polym.*, Springer, 1983: pp. 225–274.
- [187] J. V Hamilton, H.C. Wang, C. Sung, "The effect of fusion defects on the mechanical properties of UHMWPE", in: *Trans. 5th World Biomaterials Congr. Toronto*, 1996.
- [188] G.H. Isaac, D. Dowson, B.M. Wroblewski, "An investigation into the origins of time-dependent variation in penetration rates with Charnley acetabular cups-wear, creep or degradation?", *Proc. Inst. Mech. Eng. Part H J. Eng. Med.* 210 (1996) 209–216.
- [189] S.L. Bevill, G.R. Bevill, J.R. Penmetsa, A.J. Petrella, P.J. Rullkoetter, "Finite element simulation of early creep and wear in total hip arthroplasty", *J. Biomech.* 38 (2005) 2365–2374.
- [190] W. Wieleba, "The mechanism of tribological wear of thermoplastic materials", *Arch. Civ. Mech. Eng.* 7 (2007) 185–199.
- [191] K.Y. Lee, D. Pienkowski, "Compressive creep characteristics of extruded ultrahigh-molecular-weight polyethylene", *J. Biomed. Mater. Res.* 39 (1998) 261–265.
- [192] F. Quinci, M. Dressler, A.M. Strickland, G. Limbert, "Towards an accurate understanding of UHMWPE visco-dynamic behaviour for numerical modelling of implants", *J. Mech. Behav. Biomed. Mater.* 32 (2014) 62–75.
- [193] K.-Y. Lee, D. Pienkowski, "Viscoelastic recovery of creep-deformed ultra-high molecular weight polyethylene (UHMWPE)", in: *Charact. Prop. Ultra-High Mol. Weight Polyethyl.*, ASTM International, 1998.
- [194] F. Metin, M. Cengil, "Short-term creep and recovery behavior of medical grade ultra-high molecular weight polyethylene (UHMWPE)", *Manuf. Eng.* 78 (2016) 65–70.
- [195] M. Deng, R.A. Latour, A.A. Ogale, S.W. Shalaby, "Study of creep behavior of ultra-high-molecular-weight polyethylene systems", *J. Biomed. Mater. Res.* 40 (1998) 214–223.
- [196] O.K. Muratoglu, A. Mark, D.A. Vittetoe, W.H. Harris, H.E. Rubash, "Polyethylene damage in total knees and use of highly crosslinked polyethylene", *JBJS.* 85 (2003) S7--S13.
- [197] B.M. Wroblewski, P.D. Siney, P.A. Fleming, "Low-friction arthroplasty of the hip using alumina ceramic and cross-linked polyethylene: a ten-year follow-up report", *J. Bone Joint Surg. Br.* 81 (1999) 54–55.
- [198] S. Glyn-Jones, P. McLardy-Smith, H.S. Gill, D.W. Murray, "The creep and wear of highly cross-linked polyethylene: a three-year randomised, controlled trial using radiostereometric analysis", *J. Bone Joint Surg. Br.* 90 (2008) 556–561.
- [199] Y. Takahashi, T. Tateiwa, T. Shishido, T. Masaoka, K. Kubo, K. Yamamoto, "Post-deformation shape-recovery behavior of vitamin E-diffused, radiation crosslinked polyethylene acetabular components", *J. Mech. Behav. Biomed. Mater.* 63 (2016) 399–406.
- [200] D.M. Estok, C.R. Bragdon, G.R. Plank, A. Huang, O.K. Muratoglu, W.H. Harris, "The measurement of creep in ultrahigh molecular weight polyethylene: A comparison of conventional versus highly cross-linked polyethylene", *J. Arthroplasty.* 20 (2005) 239–243.

- [201] A. Wang, "A unified theory of wear for ultra-high molecular weight polyethylene in multi-directional sliding", *Wear*. 248 (2001) 38–47.
- [202] O. Ltd, "Crosslinking", (n.d.). <https://www.orthoplastics.com/products/crosslinking> (accessed October 30, 2019).
- [203] H. McKellop, F.W. Shen, W. DiMaio, J.G. Lancaster, "Wear of gamma-crosslinked polyethylene acetabular cups against roughened femoral balls", *Clin. Orthop. Relat. Res.* (1999) 73–82.
- [204] O.K. Muratoglu, C.R. Bragdon, D.O. O'Connor, M. Jasty, W.H. Harris, R. Gul, F. McGarry, "Unified wear model for highly crosslinked ultra-high molecular weight polyethylenes (UHMWPE)", *Biomaterials*. 20 (1999) 1463–1470.
- [205] L. Zhang, Y. Sawae, T. Yamaguchi, T. Murakami, H. Yang, "Investigation on oxidation of shelf-aged crosslinked Ultra-High Molecular Weight Polyethylene (UHMWPE) and its effects on wear characteristics", *Tribol. Online*. 10 (2015) 1–10.
- [206] M.D. Ries, K. Weaver, R.M. Rose, J. Gunther, W. Sauer, N. Beals, "Fatigue strength of polyethylene after sterilization by gamma irradiation or ethylene oxide.", *Clin. Orthop. Relat. Res.* (1996) 87–95.
- [207] R. Poggie, M. Takeuchi, R. Averill, S. Nasser, "Accelerated aging and associated changes in ultra-high molecular weight polyethylene (UHMWPE) microstructure as a function of resin type and consolidation variables", in: Charact. Prop. Ultra-High Mol. Weight Polyethyl., *ASTM International*, 1998.
- [208] S.M. Kurtz, M. Manley, A. Wang, S. Taylor, J. Dumbleton, others, "Comparison of the Properties of Annealed Crosslinked (Crossfire™) and Conventional Polyethylene as Hip Bearing Materials", *Bull. Jt. Dis.* 61 (2002) 17–26.
- [209] H. McKellop, F. Shen, B. Lu, P. Campbell, R. Salovey, "Development of an extremely wear-resistant ultra high molecular weight polyethylene for total hip replacements", *J. Orthop. Res.* 17 (1999) 157–167.
- [210] O.K. Muratoglu, C.R. Bragdon, D.O. O'Connor, M. Jasty, W.H. Harris, "A novel method of cross-linking ultra-high-molecular-weight polyethylene to improve wear, reduce oxidation, and retain mechanical properties: recipient of the 1999 HAP Paul Award", *J. Arthroplasty*. 16 (2001) 149–160.
- [211] E. Oral, A.S. Malhi, O.K. Muratoglu, "Mechanisms of decrease in fatigue crack propagation resistance in irradiated and melted UHMWPE", *Biomaterials*. 27 (2006) 917–925.
- [212] A.K. Radhakrishnan, D. Mahalingam, K.R. Selvaduray, K. Nesaretnam, "Supplementation with natural forms of vitamin E augments antigen-specific TH1-type immune response to tetanus toxoid", *Biomed Res. Int.* 2013 (2013).
- [213] E. Oral, S.D. Christensen, A.S. Malhi, K.K. Wannomae, O.K. Muratoglu, "Wear resistance and mechanical properties of highly cross-linked, ultrahigh--molecular weight polyethylene doped with vitamin E", *J. Arthroplasty*. 21 (2006) 580–591.
- [214] E. Oral, E.S. Greenbaum, A.S. Malhi, W.H. Harris, O.K. Muratoglu, "Characterization of irradiated blends of α -tocopherol and UHMWPE", *Biomaterials*. 26 (2005) 6657–6663.
- [215] E. Oral, C.G. Beckos, A.S. Malhi, O.K. Muratoglu, "The effects of high dose irradiation on the cross-linking of vitamin E-blended ultrahigh molecular weight polyethylene", *Biomaterials*. 29 (2008) 3557–3560.
- [216] T.M. Grupp, B. Fritz, I. Kutzner, C. Schilling, G. Bergmann, J. Schwiesau, "Vitamin E stabilised polyethylene for total knee arthroplasty evaluated under highly demanding activities wear simulation", *Acta Biomater.* 48 (2017) 415–422.
- [217] E.M. Flament, K.R. Berend, J.M. Hurst, M.J. Morris, J.B. Adams, A. V Lombardi Jr, "Early Experience with Vitamin E Antioxidant-Infused Highly Cross-Linked Polyethylene Inserts in Primary Total Knee Arthroplasty.", *Surg. Technol. Int.* 29 (2016) 334–340.
- [218] S.M. Kurtz, J.S. Bergström, C.M. Rimnac, A.A. Edidin, "Multiaxial validation of constitutive theories for UHMWPE", in: Trans. 27th Annu. Meet. Soc. Biomater., 2001: p. 310.
- [219] X. Hua, B.M. Wroblewski, Z. Jin, L. Wang, "The effect of cup inclination and wear on the contact mechanics and cement fixation for ultra high molecular weight polyethylene total hip replacements", *Med. Eng. Phys.* 34 (2012) 318–325.
- [220] F. Liu, I.J. Udofia, Z.M. Jin, F. Hirt, C. Rieker, P. Roberts, P. Grigoris, "Comparison of contact mechanics between a total hip replacement and a hip resurfacing with a metal-on-metal articulation", *Proc. Inst. Mech. Eng. Part C J. Mech. Eng. Sci.* 219 (2005) 727–732.

- [221] R.K. Korhonen, A. Koistinen, Y.T. Kontinen, S.S. Santavirta, R. Lappalainen, "The effect of geometry and abduction angle on the stresses in cemented UHMWPE acetabular cups - Finite element simulations and experimental tests", *Biomed. Eng. Online*. 4 (2005) 1–15.
- [222] X. Zhang, L. Wang, X. Peng, D. Li, J. He, Y. Liu, Q. Lian, Z. Jin, C. Liu, "The effect of asphericity of acetabular bearing surface on contact mechanics of UHMWPE total hip implants by finite element analysis", *J. Mech. Med. Biol.* 17 (2017) 1–14.
- [223] V. Pakhaliuk, A. Polyakov, M. Kalinin, V. Kramar, "Improving the finite element simulation of wear of total hip prosthesis' spherical joint with the polymeric component", *Procedia Eng.* 100 (2015) 539–548.
- [224] S. Affatato, M. Merola, A. Ruggiero, "Development of a novel in silico model to investigate the influence of radial clearance on the acetabular cup contact pressure in hip implants", *Materials (Basel)*. 11 (2018) 1–11.
- [225] M.F. Abd Manap, S. Shuib, A.Z. Romli, A.A. Shokri, "Finite element study of acetabular cup contact region for Total Hip Replacement (THR)", *J. Mech. Eng. SI 2* (2017) 71–82.
- [226] G. Matsoukas, R. Willing, I.Y. Kim, "Total hip wear assessment: A comparison between computational and in vitro wear assessment techniques using ISO 14242 loading and kinematics", *J. Biomech. Eng.* 131 (2009) 1–11.
- [227] F. Liu, J. Fisher, Z. Jin, "Computational modelling of polyethylene wear and creep in total hip joint replacements: Effect of the bearing clearance and diameter", *Proc. Inst. Mech. Eng. Part J J. Eng. Tribol.* 226 (2012) 552–563.
- [228] I.B. Anwar, E. Saputra, R. Ismail, J. Jamari, E. Van Der Heide, "Fixation strength analysis of cup to bone material using finite element simulation", in: *AIP Conf. Proc.*, 2016: p. 20006.
- [229] A.E. Bowden, E. Oneida, J. Bergström, "Computer Modeling and Simulation of UHMWPE", in: *UHMWPE Biomater. Handb.*, Elsevier, 2009: pp. 519–532.
- [230] Y. Zhou, L. Yang, Y. Huang, "Micro- and Macromechanical Properties of Materials", *Taylor & Francis*, 2013.
- [231] B.S. Mitchell, "An Introduction to Materials Engineering and Science for Chemical and Materials Engineers", *Wiley*, 2004.
- [232] G.C. Papanicolaou, S.P. Zaoutsos, "Viscoelastic constitutive modeling of creep and stress relaxation in polymers and polymer matrix composites", in: *Creep Fatigue Polym. Matrix Compos.*, Elsevier, 2019: pp. 3–59.
- [233] H.F. Brinson, L.C. Brinson, "Polymer engineering science and viscoelasticity", *An Introd.* (2008).
- [234] W. Flügge, "Viscoelasticity", *Springer Berlin Heidelberg*, 2013.
- [235] L. Veryst Engineering, "PolyUMod - A Library of Advanced User Materials", (n.d.).
- [236] N. Rull, A. Sánchez-Ferrer, P.M. Frontini, "Deformation behavior of crosslinked polyurea elastomers obtained via sol-gel chemistry: experimental determination and constitutive modelling.", *Express Polym. Lett.* 14 (2020).
- [237] E.M. Arruda, M.C. Boyce, "A three-dimensional constitutive model for the large stretch behavior of rubber elastic materials", *J. Mech. Phys. Solids*. 41 (1993) 389–412.
- [238] D. Pond, A.T. McBride, L.M. Davids, B.D. Reddy, G. Limbert, "Microstructurally-based constitutive modelling of the skin – Linking intrinsic ageing to microstructural parameters", *J. Theor. Biol.* 444 (2018) 108–123.
- [239] V.L. Popov, "Contact Mechanics and Friction: Physical Principles and Applications", *Springer Berlin Heidelberg*, 2010.
- [240] I.G. Goryacheva, "Contact Mechanics in Tribology", *Springer Netherlands*, 2013.
- [241] H. Hertz, "On the contact of solids—on the contact of rigid elastic solids and on hardness", *Misc. Pap.* (1896) 146–183.
- [242] C.M. Mate, R.W. Carpick, "Tribology on the Small Scale: A Modern Textbook on Friction, Lubrication, and Wear", *Oxford University Press*, 2019.

- [243] A. Wang, C. Stark, J.H. Dumbleton, "Mechanistic and morphological origins of ultra-high molecular weight polyethylene wear debris in total joint replacement prostheses", *Proc. Inst. Mech. Eng. Part H J. Eng. Med.* 210 (1996) 141–155.
- [244] K.L. Johnson, "Contact mechanics and the wear of metals", *Wear.* 190 (1995) 162–170.
- [245] S. Ge, S. Wang, N. Gitis, M. Vinogradov, J. Xiao, "Wear behavior and wear debris distribution of UHMWPE against Si₃N₄ ball in bi-directional sliding", *Wear.* 264 (2008) 571–578.
- [246] A. Wang, D.C. Sun, C. Stark, Dumbleton, JH, "Wear mechanisms of UHMWPE in total joint replacements", *Wear.* 181 (1995) 241–249.
- [247] A. Wang, V.K. Polineni, A. Essner, M. Sokol, D.C. Sun, C. Stark, J.H. Dumbleton, "The significance of nonlinear motion in the wear screening of orthopaedic implant materials", *J. Test. Eval.* 25 (1997) 239–245.
- [248] V. Saikko, J. Kostamo, "RandomPOD-A new method and device for advanced wear simulation of orthopaedic biomaterials", *J. Biomech.* 44 (2011) 810–814.
- [249] S. Flanagan, *Friction, Lubrication and Wear of Total Joint Replacements*, University of Limerick, 2010.
- [250] S.R. Simon, I.L. Paul, R.M. Rose, E.L. Radin, "'Stiction-friction' of total hip prostheses and its relationship to loosening", *J Bone Jt. Surg Am.* 57 (1975) 226–230.
- [251] G. Bergmann, F. Graichen, A. Rohlmann, N. Verdonschot, G.H. Van Lenthe, "Frictional heating of total hip implants. Part 2: finite element study", *J. Biomech.* 34 (2001) 429–435.
- [252] Z. Lu, H. McKellop, "Frictional heating of bearing materials tested in a hip joint wear simulator", *Proc. Inst. Mech. Eng. Part H J. Eng. Med.* 211 (1997) 101–108.
- [253] J.A. Davidson, G. Schwartz, G. Lynch, S. Gir, "Wear, creep, and frictional heating of femoral implant articulating surfaces and the effect on long-term performance--Part II, Friction, heating, and torque.", *J. Biomed. Mater. Res.* 22 (1988) 69–91.
- [254] S.M. Kurtz, J.L. Turner, M. Herr, A.A. Edidin, "Deconvolution of surface topology for quantification of initial wear in highly cross-linked acetabular components for THA", *J. Biomed. Mater. Res.* 63 (2002) 492–500.
- [255] O. Kayabasi, B. Ekici, "The effects of static, dynamic and fatigue behavior on three-dimensional shape optimization of hip prosthesis by finite element method", *Mater. Des.* 28 (2007) 2269–2277.
- [256] F. Bayata, C. Yildiz, "The effects of design parameters on mechanical failure of Ti-6Al-4V implants using finite element analysis", *Eng. Fail. Anal.* 110 (2020) 104445.
- [257] Z.M. Jin, D. Dowson, J. Fisher, "A parametric analysis of the contact stress in ultra-high molecular weight polyethylene acetabular cups.", *Med. Eng. Phys.* 16 (1994) 398–405.
- [258] P. Goebel, D. Klues, J. Wieding, R. Souffrant, H. Heyer, M. Sander, R. Bader, "The influence of head diameter and wall thickness on deformations of metallic acetabular press-fit cups and UHMWPE liners: a finite element analysis", *J. Orthop. Sci.* 18 (2013) 264–270.
- [259] A.J. Shimmin, W.L. Walter, C. Esposito, "The influence of the size of the component on the outcome of resurfacing arthroplasty of the hip: a review of the literature", *J. Bone Joint Surg. Br.* 92 (2010) 469–476.
- [260] D. Bennett, L. Humphreys, S. O'Brien, C. Kelly, J. Orr, D.E. Beverland, "The influence of wear paths produced by hip replacement patients during normal walking on wear rates", *J. Orthop. Res.* 26 (2008) 1210–1217.
- [261] C.R. Bragdon, D.O. O'Connor, J.D. Lowenstein, M. Jasty, W.D. Syniuta, "The importance of multidirectional motion on the wear of polyethylene", *Proc Inst Mech Eng H.* 210 (1996) 157–165.
- [262] T. Schwenke, M.A. Wimmer, "Cross-shear in metal-on-polyethylene articulation of orthopaedic implants and its relationship to wear", *Wear.* 301 (2013) 168–174.
- [263] V. Saikko, O. Caloni, J. Keränen, "Effect of extent of motion and type of load on the wear of polyethylene in a biaxial hip simulator", *J. Biomed. Mater. Res. Part B Appl. Biomater.* 65B (2003) 186–192.
- [264] M. Turell, A. Wang, A. Bellare, "Quantification of the effect of cross-path motion on the wear rate of ultra-high molecular weight polyethylene", *Wear.* 255 (2003) 1034–1039.

- [265] V. Saikko, S.M. Kurtz, R.S. Siskey, D. Baykal, H. Haider, T. Ahlroos, "Advances in tribological testing of artificial joint biomaterials using multidirectional pin-on-disk testers", *J. Mech. Behav. Biomed. Mater.* 31 (2013) 117–134.
- [266] C.C. Hsiao, "Flow orientation and fracture strength of a model linear hard polymer solid", *J. Polym. Sci.* 44 (1960) 71–79.
- [267] F. Liu, A. Galvin, Z. Jin, J. Fisher, "A new formulation for the prediction of polyethylene wear in artificial hip joints", *Proc. Inst. Mech. Eng. Part H J. Eng. Med.* 225 (2011) 16–24.
- [268] R.M. Hall, A. Unsworth, P. Siney, B.M. Wroblewski, "Wear in retrieved Charnley acetabular sockets", *Proc. Inst. Mech. Eng. Part H J. Eng. Med.* 210 (1996) 197–207.
- [269] A.A. Edidin, L. Pruitt, C.W. Jewett, D.J. Crane, D. Roberts, S.M. Kurtz, "Plasticity-induced damage layer is a precursor to wear in radiation-cross-linked UHMWPE acetabular components for total hip replacement", *J. Arthroplasty.* 14 (1999) 616–627.
- [270] M.C. Galetz, T. Uth, M.A. Wimmer, P. Adam, U. Glatzel, "Determination of the temperature rise within UHMWPE tibial components during tribological loading", *Acta Biomater.* 6 (2010) 552–562.
- [271] F. Bueche, "Physical properties of polymers. 1962", *New York Intersci.* (n.d.).
- [272] V. Saikko, O. Calonius, "Slide track analysis of the relative motion between femoral head and acetabular cup in walking and in hip simulators.pdf", 35 (2002) 455–464.
- [273] K. Kato, K. Adachi, "Chapter 7: Wear Mechanisms", in: B.E. Bhushan (Ed.), *Mod. Tribol. Handb.*, CRC press, n.d.: pp. 273–300.
- [274] K.J. Hamelynck, J.B. Stiehl, "LCS® Mobile Bearing Knee Arthroplasty: A 25 Years Worldwide Review", *Springer Science & Business Media*, 2013.
- [275] J.K. Lancaster, "Basic mechanisms of friction and wear of polymers", *Plast. Polym.* 41 (1973) 297–306.
- [276] A. Wang, C. Stark, J.H. Dumbleton, "Role of cyclic plastic deformation in the wear of UHMWPE acetabular cups", *J. Biomed. Mater. Res.* 29 (1995) 619–626.
- [277] H. McKellop, P. Campbell, S.H. Park, T. Schmalzried, H. Amstutz, A. Sarmiento, "Origins of Submicron UHMWPE Wear Debris in Total Hip Arthroplasty", *John Charnley Award Pap. Hip Soc.* (1994).
- [278] H.A. McKellop, T. Schmalzried, S.-H. Park, P. Campbell, "Evidence for the generation of sub-micron polyethylene wear particles by micro-adhesive wear in acetabular cups", *19th Ann. Mtg. Soc. Biomater. Birmingham, AL.* (1993) 184.
- [279] C.G. Figueiredo-Pina, A.A.M. Neves, B.M.B. das Neves, "Corrosion-wear evaluation of a UHMWPE/Co-Cr couple in sliding contact under relatively low contact stress in physiological saline solution", *Wear.* 271 (2011) 665–670.
- [280] K.E. Elbert, T.M. Wright, C.M. Rinnac, R.W. Klein, A.R. Ingrassia, K. Gunsallus, D.L. Bartel, "Fatigue crack propagation behavior of ultra high molecular weight polyethylene under mixed mode conditions", *J. Biomed. Mater. Res.* 28 (1994) 181–187.
- [281] O.K. Muratoglu, E.W. Merrill, C.R. Bragdon, D. O'Connor, D. Hoeffel, B. Burroughs, M. Jasty, W.H. Harris, "Effect of radiation, heat, and aging on in vitro wear resistance of polyethylene.", *Clin. Orthop. Relat. Res.* 417 (2003) 253–262.
- [282] L. Bradford, D. Baker, M.D. Ries, L.A. Pruitt, "Fatigue crack propagation resistance of highly crosslinked polyethylene", *Clin. Orthop. Relat. Res.* (2004) 68–72.
- [283] C.H. Geerdink, B. Grimm, R. Ramakrishnan, J. Rondhuis, A.J. Verburg, A.J. Tonino, "Crosslinked polyethylene compared to conventional polyethylene in total hip replacement: pre-clinical evaluation, in-vitro testing and prospective clinical follow-up study", *Acta Orthop.* 77 (2006) 719–725.
- [284] C.A. Engh, A.S. Stepniewski, S.D. Ginn, S.E. Beykirch, C.J. Sychterz-Terefenko, R.H. Hopper, C.A. Engh, "A Randomized Prospective Evaluation of Outcomes After Total Hip Arthroplasty Using Cross-linked Marathon and Non-cross-linked Enduron Polyethylene Liners", *J. Arthroplasty.* 21 (2006) 17–25.
- [285] L. Ambrosio, G. Carotenuto, G. Marletta, L. Nicolais, A. Scandurra, "Wear effects in retrieved acetabular UHMW-PE cups", *J. Mater. Sci. Mater. Med.* 7 (1996) 723–729.
- [286] B.M. Wroblewski, "Wear of high-density polyethylene on bone and cartilage", *J. Bone Joint Surg. Br.* 61 (1979) 498–500.

- [287] P. Gao, M.R. Mackley, "The structure and rheology of molten ultra-high-molecular-mass polyethylene", *Polymer (Guildf)*. 35 (1994) 5210–5216.
- [288] C. Vasile, M. Pascu, R.T. Limited, "Practical Guide to Polyethylene", *RAPRA Technology*, 2005.
- [289] O.K. Muratoglu, E.S. Greenbaum, C.R. Bragdon, M. Jasty, A.A. Freiberg, W.H. Harris, "Surface analysis of early retrieved acetabular polyethylene liners: a comparison of conventional and highly crosslinked polyethylenes", *J. Arthroplasty*. 19 (2004) 68–77.
- [290] T.R. Green, J. Fisher, J.B. Matthews, M.H. Stone, E. Ingham, "Effect of size and dose on bone resorption activity of macrophages by in vitro clinically relevant ultra high molecular weight polyethylene particles", *J. Biomed. Mater. Res. An Off. J. Soc. Biomater. Japanese Soc. Biomater. Aust. Soc. Biomater. Korean Soc. Biomater.* 53 (2000) 490–497.
- [291] M. Jasty, H.E. Rubash, O. Muratoglu, "Highly Cross-Linked Polyethylene The Debate Is Over — In the Affirmative", 20 (2005) 55–58.
- [292] L. Kang, A.L. Galvin, Z.M. Jin, J. Fisher, "A simple fully integrated contact-coupled wear prediction for ultra-high molecular weight polyethylene hip implants", *Proc. Inst. Mech. Eng. Part H J. Eng. Med.* 220 (2005) 33–46.
- [293] J.R. Atkinson, D. Dowson, J.H. Isaac, B.M. Wroblewski, "Laboratory wear tests and clinical observations of the penetration of femoral heads into acetabular cups in total replacement hip joints: III: The measurement of internal volume changes in explanted Charnley sockets after 2--16 years in vivo and the deter", *Wear*. 104 (1985) 225–244.
- [294] J.F. Archard, "Contact and rubbing of flat surfaces", *J. Appl. Phys.* 24 (1953) 981–988.
- [295] P.D.P.E. James C. Gerdeen, P.D.P.E. Ronald A. L. Rorrer, "Engineering Design with Polymers and Composites, Second Edition", *Taylor & Francis*, 2011.
- [296] J.J. Kauzlarich, J.A. Williams, "Archard wear and component geometry", 215 (n.d.) 387–403.
- [297] M.A. Hamilton, M.C. Sucec, B.J. Fregly, S.A. Banks, W.G. Sawyer, "Quantifying multidirectional sliding motions in total knee replacements", *J. Trib.* 127 (2005) 280–286.
- [298] A.J. Petrella, J.R. Armstrong, P.J. Laz, P.J. Rullkoetter, "A novel cross-shear metric for application in computer simulation of ultra-high molecular weight polyethylene wear", *Comput. Methods Biomech. Biomed. Engin.* 15 (2012) 1223–1232.
- [299] P.S.M. Barbour, D.C. Barton, J. Fisher, "The influence of contact stress on the wear of UHMWPE for total replacement hip prostheses", *Wear*. 181 (1995) 250–257.
- [300] R.M. Rose, H. V. Goldfarb, E. Ellis, A.M. Crugnola, "On the pressure dependence of the wear of ultrahigh molecular weight polyethylene", *Wear*. 92 (1983) 99–111.
- [301] W. Rostoker, J.O. Galante, "Contact pressure dependence of wear rates of ultra high molecular weight polyethylene", *J. Biomed. Mater. Res.* 13 (1979) 957–964.
- [302] J.F. Archard, W. Hirst, "The wear of metals under unlubricated conditions", *Proc. R. Soc. London. Ser. A. Math. Phys. Sci.* 236 (2006) 397–410.
- [303] L. Kang, A.L. Galvin, J. Fisher, Z. Jin, "Enhanced computational prediction of polyethylene wear in hip joints by incorporating cross-shear and contact pressure in addition to load and sliding distance: Effect of head diameter", *J. Biomech.* 42 (2009) 912–918.
- [304] M.K. Musib, S. Saha, "Fractionation and characterization of particles simulating wear of total joint replacement (TJR) following ASTM standards", *J. Long. Term. Eff. Med. Implants.* 21 (2011) 79–92.
- [305] M. Scott, M. Morrison, S.R. Mishra, S. Jani, "Particle analysis for the determination of UHMWPE wear", *J. Biomed. Mater. Res. - Part B Appl. Biomater.* 73 (2005) 325–337.
- [306] J. Fisher, J. Bell, P.S.M. Barbour, J.L. Tipper, J.B. Matthews, A.A. Besong, M.H. Stone, E. Ingham, "A novel method for the prediction of functional biological activity of polyethylene wear debris", *Proc. Inst. Mech. Eng. Part H J. Eng. Med.* 215 (2001) 127–132.
- [307] J.H. Ingram, M. Stone, J. Fisher, E. Ingham, "The influence of molecular weight, crosslinking and counterface roughness on TNF-alpha production by macrophages in response to ultra high molecular weight polyethylene particles", *Biomaterials.* 25 (2004) 3511–3522.

- [308] M. Endo, J.L. Tipper, D.C. Barton, M.H. Stone, E. Ingham, J. Fisher, "Comparison of wear, wear debris and functional biological activity of moderately crosslinked and non-crosslinked polyethylenes in hip prostheses", *Proc. Inst. Mech. Eng. Part H J. Eng. Med.* 216 (2002) 111–122.
- [309] J.Q. Yao, T.A. Blanchet, D.J. Murphy, M.P. Laurent, "Effect of fluid absorption on the wear resistance of UHMWPE orthopedic bearing surfaces", *Wear.* 255 (2003) 1113–1120.
- [310] C.R. Bragdon, D.O. O'Connor, E. Weinberg, "The effect of load plus motion versus load alone on fluid inhibition into UHMWPE", *Trans. Soc. Biomater.* 22 (1999) 1999.
- [311] T.A. Blanchet, S.L. Peterson, K.D. Rosenberg, "Serum lubricant absorption by UHMWPE orthopaedic bearing implants", *J. Trib.* 124 (2002) 1–4.
- [312] P. Schembri Wismayer, M.K. Bartolo, J. Buhagiar, P. Mollicone, "Development of a low-wearing novel metal on metal hip joint prosthesis for a longer lifespan", *Malta Counc. Sci. Technol. (MCST), FUSION R&I Technol. Dev. Voucher Appl.* (2016).
- [313] J.P. Paul, "Forces transmitted by joints in the human body", in: *Proc. Inst. Mech. Eng. Conf. Proc.*, 1966: pp. 8–15.
- [314] W. Pirker, R. Katzenschlager, "Gait disorders in adults and the elderly: A clinical guide", *Wien. Klin. Wochenschr.* 129 (2017) 81–95.
- [315] International Standard, "Implants for surgery -- Wear of total hip-joint prostheses --Part 1: Loading and displacement parameters for wear-testing machines and corresponding environmental conditions for test", Geneva, CH, 2014.
- [316] Dassault Systemes, "SolidWorks 2018", (2017).
- [317] ANSYS, "Workbench 19.2", (2018).
- [318] M.A. Wimmer, M.P. Laurent, D.J. Berry, J.R. Lieberman, "Chapter 3: Tribology of the Artificial Hip Joint", in: *Surg. Hip, Elsevier/Saunders*, 2013: pp. 35–53.
- [319] "Sandvik High-N Bar Datasheet", (2019).
- [320] Adendorff Machinery Mart, "MAC-AFRIC Bench Buffer & Polisher 200 mm", (2019). <https://www.adendorff.co.za/product/mac-afric-bench-buffer-polisher/> (accessed September 3, 2019).
- [321] Firm Salvatore Caruana, "Polishing/Brushing Accessories", (2019). <http://www.fscaruana.com/wp-content/uploads/2017/03/Polishing-Brushing-Accessories.pdf> (accessed September 15, 2019).
- [322] ATA Tools, Inc., "ST100 Oil Free Turbine Pencil Grinder", (2020). https://www.atagroup.com/assets/uploads/PDFs/Products/20181510_ST100_Synopsis_Sheet_Air_Tools.pdf (accessed January 5, 2020).
- [323] Meusburger Georg GmbH & Co KG, "Felt bob with shank, medium", (2019). <https://www.meusburger.com/EN/GB/workshop-equipment/surface-finishing-equipment/polishing-felt-products/v-76702> (accessed October 4, 2019).
- [324] S. Affatato, M. Spinelli, M. Zavalloni, C. Mazzega-Fabbro, M. Viceconti, "Tribology and total hip joint replacement: Current concepts in mechanical simulation", *Med. Eng. Phys.* 30 (2008) 1305–1317.
- [325] H. McKellop, B. Lu, P. Benya, "Friction, lubrication and wear of cobalt-chromium, alumina and zirconia hip prostheses compared on a joint simulator", *Trans Orthop Res Soc.* 17 (1992) 402.
- [326] M. Scott, H. Forster, S. Jani, K. Vadodaria, W. Sauer, M. Anthony, "Validation of an alternative method for isolating UHMWPE wear debris from joint simulator serum", in: *Sixth World Biomater. Congr.*, 2000: p. 2000.
- [327] M.A. Wirth, C.M. Agrawal, J.D. Mabrey, D.D. Dean, C.R. Blanchard, M.A. Miller, C.A. Rockwood, "Isolation and characterization of polyethylene wear debris associated with osteolysis following total shoulder arthroplasty", *JBJS.* 81 (1999) 29–37.
- [328] Sympatec GmbH, "Particle Shape Analysis", (2020). <https://www.sympatec.com/en/particle-measurement/glossary/particle-shape/#:~:text=In general it is defined,xFmax90 are used.> (accessed May 10, 2020).
- [329] R. Sonntag, S. Braun, L. Al-Salehi, J. Reinders, U. Mueller, J.P. Kretzer, "Three-dimensional friction measurement during hip simulation", *PLoS One.* 12 (2017) 1–20.

- [330] V. Saikko, "Adverse condition testing with hip simulators", *Biotribology*. 1–2 (2015) 2–10.
- [331] M. Ali, M. Al-Hajjar, S. Partridge, S. Williams, J. Fisher, L.M. Jennings, "Influence of hip joint simulator design and mechanics on the wear and creep of metal-on-polyethylene bearings", *Proc. Inst. Mech. Eng. Part H J. Eng. Med.* 230 (2016) 389–397.
- [332] S. Herrmann, D. Kluess, M. Kaehler, R. Grawe, R. Rachholz, R. Souffrant, J. Zierath, R. Bader, C. Woernle, "A novel approach for dynamic testing of total hip dislocation under physiological conditions", *PLoS One*. 10 (2015) 1–25.
- [333] G. Cheng, J.L. Yu, W. Gu, J.L. Liu, "Design features of a parallel testing platform for simulating kinematic characteristics of hip joint", *Instrum. Sci. Technol.* 40 (2012) 402–415.
- [334] N.I. Galanis, D.E. Manolakos, "Design of a hip joint simulator according to the ISO 14242", *Proc. World Congr. Eng. III* (2011) 2–7.
- [335] V. Saikko, "A 12-station anatomic hip joint simulator", *Proc. Inst. Mech. Eng. Part H J. Eng. Med.* 219 (2005) 437–448.
- [336] D.J.W. McMinn, "Modern Hip Resurfacing", *Springer London*, 2009.
- [337] X. Hua, J. Li, Z. Jin, J. Fisher, "The contact mechanics and occurrence of edge loading in modular metal-on-polyethylene total hip replacement during daily activities", *Med. Eng. Phys.* 38 (2016) 518–525.
- [338] X. Hua, J. Li, L. Wang, Z. Jin, R. Wilcox, J. Fisher, "Contact mechanics of modular metal-on-polyethylene total hip replacement under adverse edge loading conditions", *J. Biomech.* 47 (2014) 3303–3309.
- [339] A. Bellare, R.E. Cohen, "Morphology of rod stock and compression-moulded sheets of ultra-high-molecular-weight polyethylene used in orthopaedic implants", *Biomaterials*. 17 (1996) 2325–2333.
- [340] J.R. Cooper, D. Dowson, J. Fisher, "Macroscopic and microscopic wear mechanisms in ultra-high molecular weight polyethylene", *Wear*. 162 (1993) 378–384.
- [341] X. Hua, "Contact Mechanics of Metal on Polyethylene Hip Replacements", (2013).
- [342] V. Atreya, P. Agarwal, "Finite element analysis and comparative study on stresses induced on UHMWPE acetabular cup surface of the artificial hip implant during free walking and walking while carrying weights", *Trends Biomater. Artif. Organs*. 27 (2013) 62–66.
- [343] A.P. Sanders, R.M. Brannon, "Assessment of the applicability of the Hertzian contact theory to edge-loaded prosthetic hip bearings", *J. Biomech.* 44 (2011) 2802–2808.
- [344] Z.M. Jin, S.M. Heng, H.W. Ng, D.D. Auger, "An axisymmetric contact model of ultra high molecular weight polyethylene cups against metallic femoral heads for artificial hip joint replacements", *Proc. Inst. Mech. Eng. Part H-Journal Eng. Med.* 213 (1999) 317–327.
- [345] U.G. De Bellis, C. Legnani, G.M. Calori, "Acute total hip replacement for acetabular fractures: a systematic review of the literature", *Injury*. 45 (2014) 356–361.
- [346] S.T. Gomaa, "Predicting the effect of creep of UHMWPE on the femoral-tibial contact area and contact stresses following total knee arthroplasty", in: *Orthop. Res. Soc. Annu. Meet. San Fr.*, 2011.
- [347] S.T. Gomaa, S. Leisinger, "Testing and modeling the nonlinear behavior of uhmwpe used in orthopaedic implants", in: *Conf. Proc. Annu. Meet. Am. Soc.*, 2010: p. p7.
- [348] J.P. Davim, "Machining of Complex Sculptured Surfaces", *Springer London*, 2012.
- [349] A. Tabeshian, D. Persson, L. Arnberg, R. Aune, "Comparison of the electrochemical behavior of amorphous Zr55Cu30Ni5Al10, stainless steel (316LVM), and CoCrMo (F75) in simulated body fluid with and without addition of protein", *Mater. Corros.* 70 (2019) 652–660.
- [350] B.D. Ratner, B.D.R.F.J.S.J.E.L. Allan S. Hoffman, K. (Firm), S. for Biomaterials, A.S. Hoffman, F.J. Schoen, J.E. Lemons, "Biomaterials Science: An Introduction to Materials in Medicine", *Elsevier Science*, 2004.
- [351] G.R. Plank, D.M. Estok, O.K. Muratoglu, D.O. O'Connor, B.R. Burroughs, W.H. Harris, "Contact stress assessment of conventional and highly crosslinked ultra high molecular weight polyethylene acetabular liners with finite element analysis and pressure sensitive film", *J. Biomed. Mater. Res. Part B Appl. Biomater. An Off. J. Soc. Biomater. Japanese Soc. Biomater. Aust. Soc. Biomater. Korean Soc. Biomater.* 80 (2007) 1–10.

- [352] R.K. Korhonen, A. Koistinen, Y.T. Kontinen, S.S. Santavirta, R. Lappalainen, "The effect of geometry and abduction angle on the stresses in cemented UHMWPE acetabular cups - Finite element simulations and experimental tests", *Biomed. Eng. Online*. 4 (2005) 1–14.
- [353] C.C. Hu, J.J. Liao, C.Y. Lung, C.H. Huang, C.K. Cheng, "A two-dimensional finite element model for frictional heating analysis of total hip prosthesis", *Mater. Sci. Eng. C*. 17 (2001) 11–18.
- [354] J.S. Bergström, C.M. Rimnac, S.M. Kurtz, "Molecular chain stretch is a multiaxial failure criterion for conventional and highly crosslinked UHMWPE", *J. Orthop. Res.* 23 (2005) 367–375.
- [355] M.X. Wei, S.Q. Wang, L. Wang, X.H. Cui, "Wear and friction characteristics of a selected stainless steel", *Tribol. Trans.* 54 (2011) 840–848.
- [356] J. Zeman, M. Ranuša, M. Vrbka, J. Gallo, I. Křupka, M. Hartl, "UHMWPE acetabular cup creep deformation during the run-in phase of THA's life cycle", *J. Mech. Behav. Biomed. Mater.* 87 (2018) 30–39.
- [357] K.K. Wannomae, S.D. Christensen, B.R. Micheli, S.L. Rowell, D.W. Schroeder, O.K. Muratoglu, "Delamination and adhesive wear behavior of α -tocopherol-stabilized irradiated ultrahigh-molecular-weight polyethylene", *J. Arthroplasty*. 25 (2010) 635–643.
- [358] J.E. Dowd, C.J. Sychterz, A.M. Young, C.A. Engh, "Characterization of long-term femoral-head-penetration rates: association with and prediction of osteolysis", *JBJS*. 82 (2000) 1102.
- [359] A.L. Galvin, L.M. Jennings, J.L. Tipper, E. Ingham, J. Fisher, "Wear and creep of highly crosslinked polyethylene against cobalt chrome and ceramic femoral heads", *Proc. Inst. Mech. Eng. Part H J. Eng. Med.* 224 (2010) 1175–1183.
- [360] H.A. McKellop, P. Campbell, S.-H. Park, T.P. Schmalzried, P. Grigoris, H.C. Amstutz, A. Sarmiento, "The origin of submicron polyethylene wear debris in total hip arthroplasty.", *Clin. Orthop. Relat. Res.* (1995) 3–20.
- [361] D.D. D'Lima, J.C. Hermida, P.C. Chen, C.W. Colwell Jr, "Polyethylene cross-linking by two different methods reduces acetabular liner wear in a hip joint wear simulator", *J. Orthop. Res.* 21 (2003) 761–766.
- [362] V. Saikko, P. Paavolainen, M. Kleimola, P. Slätis, "A Five-Station Hip Joint Simulator for Wear Rate Studies", *Proc. Inst. Mech. Eng. Part H J. Eng. Med.* 206 (1992) 195–200.
- [363] S. Bhambri, M. Laurent, P. Campbell, L. Gilbertson, S. Lin, "Morphology of wear particles of heavily cross linked polyethylene", *Trans Orthop Res Soc.* 24 (1999) 838.
- [364] D. Dowson, "A comparative study of the performance of metallic and ceramic femoral head components in total replacement hip joints", *Wear*. 190 (1995) 171–183.
- [365] I.C. Clarke, A. Gustafson, H. Jung, A. Fujisawa, "Hip-simulator ranking of polyethylene wear: comparisons between ceramic heads of different sizes", *Acta Orthop. Scand.* 67 (1996) 128–132.
- [366] W.G. Blakeney, J.A. Epinette, P.A. Vendittoli, "Dual mobility total hip arthroplasty: Should everyone get one?", *EFORT Open Rev.* 4 (2019) 541–547.
- [367] B. Boyer, R. Philippot, J. Geringer, "Primary total hip arthroplasty with dual mobility socket to prevent dislocation : a 22-year follow-up of 240 hips", (2012) 511–518.
- [368] M. van Heumen, P.J.C. Heesterbeek, B.A. Swierstra, G.G. Van Hellemond, J.H.M. Goosen, "Dual mobility acetabular component in revision total hip arthroplasty for persistent dislocation: no dislocations in 50 hips after 1–5 years", *J. Orthop. Traumatol.* 16 (2015) 15–20.
- [369] Zimmer Biomet, "G7 Dual Mobility Construct - Surgical Technique", 2015.
- [370] A. Di Laura, H.S. Hothi, J. Henckel, A. Cerquiglini, M.H.L. Liow, Y.M. Kwon, J.A. Skinner, A.J. Hart, "Retrieval evidence of impingement at the third articulation in contemporary dual mobility cups for total hip arthroplasty", *Int. Orthop.* 41 (2017) 2495–2501.
- [371] T.P. Scott, L. Weitzler, A. Salvatore, T.M. Wright, G.H. Westrich, "A retrieval analysis of impingement in dual-mobility liners", *J. Arthroplasty*. 33 (2018) 2660–2665.
- [372] Doctorlib.info, "Bodyweight 8: Deep Squat", (2019). <https://doctorlib.info/sport/mens-health-body/8.html> (accessed September 30, 2018).
- [373] Solutions Northwest Inc., "Ergonomics Tips for Remote Workers", (2020). <https://www.solutionsnw.com/category/remote-workers/> (accessed June 15, 2020).

- [374] M.B. Cross, D. Nam, D.J. Mayman, "Ideal Femoral Head Size in Total Hip Arthroplasty Balances Stability and Volumetric Wear", *HSS J.* 8 (2012) 270–274.
- [375] F.W. Shen, Z. Lu, H.A. McKellop, "Wear versus thickness and other features of 5-mrad crosslinked UHMWPE acetabular liners", *Clin. Orthop. Relat. Res.* 469 (2011) 395–404.

Appendix A: Material Certificates

A1. UHMWPE GUR 1050, Ram Extruded Bar – Ø 80 mm



Accredited to
ISO/IEC 17025:2005

TEST CERTIFICATE



ORTHOPLASTICS
Science making a material difference

Orthoplastics GUR - 1050 Medical Grade UHMWPE

CERTIFICATE ACCORDING TO ISO 5834-2 2011 This material also meets the requirements of ASTM F648-14

Batch No **12730M** ISO Type **2** Powder Lot No **0000974957** Polymer Grade GUR **1050**
This Material Has Been Processed By **Ram Extrusion** Country of Origin - **UK**

Customer **MCL Components Ltd** Order Number **PO182562** Orthoplastics Ref **032907/1**
Address **BLB037, Bulebel Industrial Estate** Size **80mm dia x 500mm**
Zejtun Part Number **RDT0080S4/BAS**
Malta **ZTN 3000** Number off Rod/Slab ref. #'s
3 off. Rod #28.

MATERIAL SUPPLIED AGAINST THIS CERTIFICATE HAS BEEN ANNEALED IN ACCORDANCE WITH ORTHOPLASTICS QUALITY PROCEDURES SECTION WI-OMU 002, AND ULTRASONICALLY INSPECTED IN ACCORDANCE WITH ORTHOPLASTICS QUALITY PROCEDURES WI-EXT-08 & WI-FRD-031. ZERO UNCONSOLIDATED REGIONS DETECTED. NO NON-FUSED FLAKES (LIGHT PATCHES) OR PARTICLES >300 µm WERE FOUND ON TEST.

Certificate Number **032907/1-12730M-1** Date of Test / Manufacture **08.06.18**

Orthoplastics considers the batch testing to be the last step in the manufacturing process as every batch manufactured must be tested before release. Orthoplastics verifies that the manufacturing process of fabrication / annealing and testing will be completed within 30 days.

Property	ISO Standard (Test Method)	Units	Requirements	Test Result
Density	5834-2 2011 (1183-2)**	kg/m ³	927/944	932
▶ Ash*	3451-1 2008	mg/kg	≤ 150	45
▶ Particle Count <300 µm	5834-2 2011	Number	≤ 10	0
▶ Light Patch <300 µm	N/A	Number	≤ 10	0
Charpy Impact Strength	5834-2 2011 (11542-2)	kJ/m ²	≥ 90	120
Tensile Stress at Yield	5834-2 2011 (527-3)	MPa	≥ 19	23.5
Ultimate Tensile Strength	5834-2 2011 (527-3)	MPa	≥ 27	61
Elongation at Break	5834-2 2011 (527-3)	%	≥ 300	414
Morphology Index	5834-5 2005	Number		0
Customer specific tests - limits and methods per specification				
Izod Impact Strength	5834-2 2011	kJ/m ²	≥ 73	105

* Test carried out by external subcontractor not covered by Orthoplastics' accreditations
** Density test method ISO1183-2 supercedes 1183-1
▶ NOT UKAS ACCREDITED
Humidity - GUR UHMWPE resins are water repellent & do not swell. GUR properties are maintained in the finished part regardless of the environmental humidity, therefore humidity is not required to be controlled.

This certificate does not affect the obligation to perform an incoming goods inspection. This certificate relates to semi-finished material. Printed

11-Sep-18

Signed *A. Collier* Date *11-9-18*
ANTHONY COLLIER - INSPECTOR Version 1.54 for Orthoplastics

Orthoplastics Ltd., Unit A, Beech Industrial Estate, Bacup, Lancashire, OL13 9EL, England.
Telephone: +44 (0)1706 874171, Fax: +44 (0)1706 879826



Celanese Sales Germany GmbH
Am Unisys-Park 1
D-65843 SULZBACH

ORTHOPLASTICS LTD
BEECH INDUSTRIAL ESTATE
BACUP
Lancashire
OL13 9EL
UNITED KINGDOM

Inspection Certificate EN 10204-3.1

GUR 1050 - NATURAL R1 (O)

Customer No.:	1071897	Cert Issue Date:	16 Nov 2017
Material No.:	20004961	Qty Shipped:	1.250,000 KG
Customer Material:	XV101050S4	Order Item /date:	1915640 30 / 27 Oct 2017
Produced at:	Oberhausen	Delivery item/date:	85432627 30 / 23 Nov 2017
Tested at:	Oberhausen	Customer PO No.:	28294

Batch 0000974957

On the batch, of which the consignment is a part, the following values were determined.

Characteristic	(Method)	UoM	Value
Elongation Stress F150/10	(ISO 11542-2)	MPa	0,53
VN / C=0,0002 g/ml	(DIN ISO 1628-3)	mltr/gm	3660
Bulk density	(ISO 60)	g/cm ³	0,44
Density	(ISO 1183)	g/cm ³	0,926
Notched Impact Strength	(ISO 11542-2)	kJ/m ²	169
Ash Content	(ISO 3451)	ppm(m)	30
Titanium	(ICP)	ppm(m)	9
Aluminum	(ICP)	ppm(m)	3
Calcium	(ICP / AA)	ppm(m)	0
Chlorine	(XRF)	ppm(m)	10
Particle Size > 800µ	(Laser Diffraction)	%(m)	0,0
Particle Size > 250µ	(Laser Diffraction)	%(m)	8,3
Particle Size < 63µ	(Laser Diffraction)	%(m)	7,2
Particle Size (D50)	(Laser Diffraction)	µm	146
Contamination Mean Value	(DIN ISO 5834-1)		0,2
Contamination Single Value	(DIN ISO 5834-1)		2

The properties of our delivered GUR 1050 O fulfil the requirements for Type 2 of ISO 5834 Part 1 and ASTM F 648 at date of manufacture.

Quality Inspector

Page 1 of 2





Celanese Sales Germany GmbH
Am Unisys-Park 1
D-65843 SULZBACH

ORTHOPLASTICS LTD
BEECH INDUSTRIAL ESTATE
BACUP
Lancashire
OL13 9EL
UNITED KINGDOM

Inspection Certificate EN 10204-3.1

GUR 1050 - NATURAL R1 (O)

Customer No.:	1071897	Cert Issue Date:	16 Nov 2017
Material No.:	20004961	Qty Shipped:	1.250,000 KG
Customer Material:	XV101050S4	Order Item /date:	1915640 30 / 27 Oct 2017
Produced at:	Oberhausen	Delivery Item/date:	85432627 30 / 23 Nov 2017
Tested at:	Oberhausen	Customer PO No.:	28294

Elke Landgraf
Celanese Production Germany GmbH and Co.KG Site Oberhausen
Otto-Roelen Str. 3
D 46147 Oberhausen

This report is machine-printed and will not be signed.

A2. UHMWPE GUR 1050, Ram Extruded Bar – Ø 40 mm



Accredited to
ISO/IEC 17025:2005

TEST CERTIFICATE



ORTHOPLASTICS
Science making a material difference

Orthoplastics GUR - 1050 Medical Grade UHMWPE

CERTIFICATE ACCORDING TO ISO 5834-2 2011 This material also meets the requirements of ASTM F648-14

Batch No **12727M** ISO Type **2** Powder Lot No **0000974957** Polymer Grade GUR **1050**
This Material Has Been Processed By **Ram Extrusion** Country of Origin - **UK**

Customer **MCL Components Ltd** Order Number **PO182128** Orthoplastics Ref **032351/1**
Address **BLB037, Bulebel Industrial Estate** Size **40mm dia x 1000mm**
Zejtun Part Number **RDT0040S4/CUS**
Malta **ZTN 3000** Number off Rod/Slab ref. #'s
2 off. Rod #114.

MATERIAL SUPPLIED AGAINST THIS CERTIFICATE HAS BEEN ANNEALED IN ACCORDANCE WITH ORTHOPLASTICS QUALITY PROCEDURES SECTION WI-OMU 002, AND ULTRASONICALLY INSPECTED IN ACCORDANCE WITH ORTHOPLASTICS QUALITY PROCEDURES WI-EXT-08 & WI-PRD-031. ZERO UNCONSOLIDATED REGIONS DETECTED. NO NON-FUSED FLAKES (LIGHT PATCHES) OR PARTICLES >300 µm WERE FOUND ON TEST.

Certificate Number **032351/1-12727M-1** Date of Test / Manufacture **01.06.18**

Orthoplastics considers the batch testing to be the last step in the manufacturing process as every batch manufactured must be tested before release. Orthoplastics verifies that the manufacturing process of fabrication / annealing and testing will be completed within 30 days.

Property	ISO Standard (Test Method)	Units	Requirements	Test Result
Density	5834-2 2011 (1183-2)**	kg/m ³	927/944	932
▶ Ash*	3451-1 2008	mg/kg	≤ 150	45
▶ Particle Count <300 µm	5834-2 2011	Number	≤ 10	0
▶ Light Patch <300 µm	N/A	Number	≤ 10	0
Charpy Impact Strength	5834-2 2011 (11542-2)	kJ/m ²	≥ 90	125
Tensile Stress at Yield	5834-2 2011 (527-3)	MPa	≥ 19	23.6
Ultimate Tensile Strength	5834-2 2011 (527-3)	MPa	≥ 27	59
Elongation at Break	5834-2 2011 (527-3)	%	≥ 300	409
Morphology Index	5834-5 2005	Number		0
Customer specific tests - limits and methods per specification				
Izod Impact Strength	5834-2 2011	kJ/m ²	≥ 73	110
* Test carried out by external subcontractor not covered by Orthoplastics' accreditations				
** Density test method ISO1183-2 supercedes 1183-1				
▶ NOT UKAS ACCREDITED				
Humidity - GUR UHMWPE resins are water repellent & do not swell. GUR properties are maintained in the finished part regardless of the environmental humidity, therefore humidity is not required to be controlled.				

This certificate does not affect the obligation to perform an incoming goods inspection. This certificate relates to semi-finished material. Printed 13-Jul-18

Signed *A. Collier* Date **13-7-18**
ANTHONY COLLIER - INSPECTOR Version 1.53 for Orthoplastics

Orthoplastics Ltd., Grove Mill / Todmorden Rd, Bacup, Lancashire, OL13 9EF, England.
Telephone: +44 (0)1706 874171, Fax: +44 (0)1706 879826



Celanese Sales Germany GmbH
Am Unisys-Park 1
D-65843 SULZBACH

ORTHOPLASTICS LTD
BEECH INDUSTRIAL ESTATE
BACUP
Lancashire
OL13 9EL
UNITED KINGDOM

Inspection Certificate EN 10204-3.1

GUR 1050 - NATURAL R1 (O)

Customer No.:	1071897	Cert Issue Date:	16 Nov 2017
Material No.:	20004961	Qty Shipped:	1.250,000 KG
Customer Material:	XV101050S4	Order Item /date:	1915640 30 / 27 Oct 2017
Produced at:	Oberhausen	Delivery item/date:	85432627 30 / 23 Nov 2017
Tested at:	Oberhausen	Customer PO No.:	28294

Batch 0000974957

On the batch, of which the consignment is a part, the following values were determined.

Characteristic	(Method)	UoM	Value
Elongation Stress F150/10	(ISO 11542-2)	MPa	0,53
VN / C=0,0002 g/ml	(DIN ISO 1628-3)	milltr/gm	3660
Bulk density	(ISO 60)	g/cm ³	0,44
Density	(ISO 1183)	g/cm ³	0,926
Notched Impact Strength	(ISO 11542-2)	kJ/m ²	169
Ash Content	(ISO 3451)	ppm(m)	30
Titanium	(ICP)	ppm(m)	9
Aluminum	(ICP)	ppm(m)	3
Calcium	(ICP / AA)	ppm(m)	0
Chlorine	(XRF)	ppm(m)	10
Particle Size > 800µ	(Laser Diffraction)	%(m)	0,0
Particle Size > 250µ	(Laser Diffraction)	%(m)	8,3
Particle Size < 63µ	(Laser Diffraction)	%(m)	7,2
Particle Size (D50)	(Laser Diffraction)	µm	146
Contamination Mean Value	(DIN ISO 5834-1)		0,2
Contamination Single Value	(DIN ISO 5834-1)		2

The properties of our delivered GUR 1050 O fulfil the requirements for Type 2 of ISO 5834 Part 1 and ASTM F 648 at date of manufacture.

Quality Inspector

Page 1 of 2





Celanese Sales Germany GmbH
Am Unisys-Park 1
D-65843 SULZBACH

ORTHOPLASTICS LTD
BEECH INDUSTRIAL ESTATE
BACUP
Lancashire
OL13 9EL
UNITED KINGDOM

Inspection Certificate EN 10204-3.1

GUR 1050 - NATURAL R1 (O)

Customer No.:	1071897	Cert Issue Date:	16 Nov 2017
Material No.:	20004961	Qty Shipped:	1.250,000 KG
Customer Material:	XV101050S4	Order Item /date:	1915640 30 / 27 Oct 2017
Produced at:	Oberhausen	Delivery Item/date:	85432627 30 / 23 Nov 2017
Tested at:	Oberhausen	Customer PO No.:	28294

Elke Landgraf
Celanese Production Germany GmbH and Co.KG Site Oberhausen
Otto-Roelen Str. 3
D 46147 Oberhausen

This report is machine-printed and will not be signed.

A3. VEHXPE GUR 1020, Compression Moulding – Ø 60 mm

TEST CERTIFICATE

Orthoplastics GUR - 1020 Medical Grade UHMWPE Containing Alpha Tocopherol (Vit E)

CROSS LINKED TEST RESULTS

Customer	MCL Components Ltd	Order Number	PO191313	Orthoplastics Ref	034350/1
Size	60mm DIA x 1524mm	Number off ref no. #	1 of.	Date of XL Test	4/9/18
Powder Grade GUR	1020			XL Batch #	ORTHO 3588

This Material Has Been Processed By Compression Moulding - Type 1

Batch No	30917M	Powder Lot	909946CP76/77
----------	--------	------------	---------------

STATEMENT ACCORDING TO ASTM F2695 - NO STABILIZERS OR PROCESSING AIDS WERE ADDED TO THE VIRGIN POLYMER DURING MANUFACTURE OF THE FABRICATED FORMS. ALPHA-TOCOPHEROL WAS ADDED TO THE VIRGIN POLYMER PRIOR TO CONSOLIDATION.

PRE-IRRADIATED MATERIAL SUPPLIED AGAINST THIS CERTIFICATE HAS BEEN ANNEALED IN ACCORDANCE WITH ORTHOPLASTICS QUALITY PROCEDURES SECTION WI OMU 002. NO NON-FUSED FLAKES (LIGHT PATCHES) OR PARTICLES >300 µm WERE FOUND ON TEST.

Property	Units	Requirements	Test Result
Dosage Received	kGy	90-110	100.9
Notched Izod Impact Strength - ASTM F648	kJ/m ²	≥25	72
Density - ASTM D1505	kg/m ³	927-944	941
Tensile Stress at Yield 23 °C - ASTM D638	MPa	≥19	24.6
Ultimate Tensile Strength 23 °C - ASTM D638	MPa	≥27	57
Elongation at Break 23 °C - ASTM D638	%	≥250	326
Surface Oxidation Index - ASTM F2102	Number	≤0.1	0
Bulk Oxidation Index - ASTM F2102	Number	≤0.1	0

This certificate does not affect the obligation to perform an incoming goods inspection. This certificate relates to semi-finished material. Printed 03-Apr-19

Signed



03/4/19

Orthoplastics
A MedFast Company
science making a material difference

JORDAN MILLER - CCU OPERATIVE

CMCR Ver 1.76

Orthoplastics Ltd., Grove Mill / Todmorden Rd, Bacup, Lancashire, OL13 9EF, England.
Telephone: +44 (0)1706 874171, Fax: +44 (0)1706 879826

TEST CERTIFICATE

Orthoplastics GUR - 1020 Medical Grade UHMWPE

CERTIFICATE ACCORDING TO ASTM F2695 - 12

Customer	MCL Components Ltd	Order Number	PO191313	Orthoplastics Ref	034350/1
Size	60mm DIA x 1524mm	Number of Rod/Slab ref. #'s	1 of.	Date of Test	19-06-18
ASTM Type	1	Powder Lot No	909946CP76/77	Batch No	30917M
Powder Grade GUR	1020				

This Material Has Been Processed By Compression Moulding - Type 1

STATEMENT ACCORDING TO ASTM F2695 - NO STABILIZERS OR PROCESSING AIDS WERE ADDED TO THE VIRGIN POLYMER DURING MANUFACTURE OF THE FABRICATED FORMS. ALPHA-TOCOPHEROL WAS ADDED TO THE VIRGIN POLYMER PRIOR TO CONSOLIDATION.

MATERIAL SUPPLIED AGAINST THIS CERTIFICATE HAS BEEN ANNEALED IN ACCORDANCE WITH ORTHOPLASTICS QUALITY PROCEDURES SECTION WI OMU 002. NO NON-FUSED FLAKES (LIGHT PATCHES) OR PARTICLES >300 µm WERE FOUND ON TEST.

MATERIAL MANUFACTURED PRIOR TO 26-01-01, HAS BEEN TESTED TO ASTM F648-98, AND WILL NOT HAVE A MORPHOLOGY INDEX RESULT. THIS MATERIAL ALSO CONFORMS TO THE TEST REQUIREMENTS OF ASTM F648 AND ISO5834.

Property	Units	Requirements	Test Result
Density	kg/m ³	927/944	937
Particle Count <300 µm	Number	< 10	0
Light Patch <300 µm	Number	< 10	0
Izod Impact Strength - ASTM F648	kJ/m ²	≥ 126	139.3
Tensile Stress at Yield 23 °C	MPa	≥ 21	23.2
Ultimate Tensile Strength 23 °C	MPa	≥ 40	69
Elongation at Break 23 °C	%	≥ 380	466.6
Morphology Index	Number		0

This certificate does not affect the obligation to perform an incoming goods inspection. This certificate relates to semi-finished material. Printed

03-Apr-19

Signed		03/4/19
JORDAN MILLER - CCU OPERATIVE		for Orthoplastics

CMCR Ver 1.76

Orthoplastics Ltd., Grove Mill / Todmorden Rd, Bacup, Lancashire, OL13 9EF, England.
Telephone: +44 (0)1706 874171, Fax: +44 (0)1706 879826



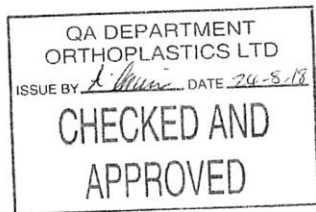
Certificate of Irradiation

Customer : ORTHOPLASTICS LTD., ENGLAND
Product : UHMWPE
Order Nr : 030206
Batch : ORTHO3588
Number of pallet(s) : 1
Minimum product dose (kGy) : 90.00
Maximum product dose (kGy) : 110.00

We herewith certify that all readings are within the specified range :

Irradiation Unit : Gamma **Validation Nr :** ORP10_Ae0
Process ID : G18.09169
Date of irradiation : 19.08.2018 **Date of reading :** 20.08.2018
Dosimeter Type: Alanine_TapeTab **Dosimeter Batch :** S5C_2018
Pallet ID : G18.09169.01 **To :** G18.09169.01
Minimum monitoring dose (kGy) : 93.6
Maximum monitoring dose (kGy) : 103.9

Dosimeter ID	Dose (kGy)	Dosimeter ID	Dose (kGy)
G18.09169.01	97.7		



These products have been treated, according to the following standards :
- ISO 9001, ISO 13485, ISO 11137, 21CFR Part 820 (FDA c GMP)

Issued and checked by QC (date/visa) : 20. AUG. 2018 Released by QC (date/visa) : 20.08.2018

Page : 1 / 1 Printed : 20.08.2018 09:38:31 Version: 1 This version replaces all previous certificates

Synergy Health Däniken AG · Hogenweidstrasse 6 · CH-4658 Däniken
UID CHE-114.783.567 MWST



Celanese Sales Germany GmbH
Am Unisys-Park 1
D-65843 SULZBACH

ORTHOPLASTICS LTD
BEECH INDUSTRIAL ESTATE
BACUP
Lancashire
OL13 9EL
UNITED KINGDOM

Inspection Certificate EN 10204-3.1

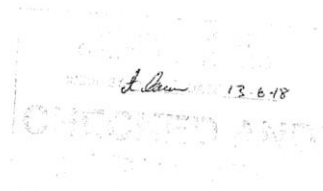
GUR 1020-E - NATURAL R11

Customer No.:	1071897	Cert Issue Date:	30 Apr 2018
Material No.:	21008789	Qty Shipped:	500.000 KG
Customer Material:	GUR 1020-E	Order Item /date:	1979752 10 / 28 Mar 2018
		Delivery item/date:	85637892 900005 / 02 May 2018
		Customer PO No.:	029392

Quality Inspector

Elke Landgraf
Celanese Production Germany GmbH and Co.KG Site Oberhausen
Otto-Roelen Str. 3
D 46147 Oberhausen

This report is machine-printed and will not be signed.





Celanese Sales Germany GmbH
Am Unisys-Park 1
D-65843 SULZBACH

ORTHOPLASTICS LTD
BEECH INDUSTRIAL ESTATE
BACUP
Lancashire
OL13 9EL
UNITED KINGDOM

Inspection Certificate EN 10204-3.1

GUR 1020-E - NATURAL R11

Customer No.:	1071897	Cert Issue Date:	30 Apr 2018
Material No.:	21008789	Qty Shipped:	500.000 KG
Customer Material:	GUR 1020-E	Order Item /date:	1979752 10 / 28 Mar 2018
		Delivery item/date:	85637892 900006 / 02 May 2018
		Customer PO No.:	029392

Batch 909946CP77

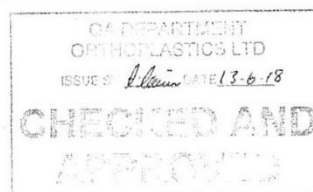
On the batch, of which the consignment is a part, the following values were determined.

Characteristic	(Method)	UoM	Value
Vitamine E	(HPLC)	ppm(m)	950
Vitamine E - distribution			0
Contamination Single Value	(DIN ISO 5834-1)		0
Additional Lot Data			
The following test results were determined on the original GUR 1020 lot:			
Elongation Stress F150/10	(ISO 11542-2)	MPa	0.24
VN / C=0,0002 g/ml	(DIN ISO 1628-3)	milltr/gm	2370
ASH CONTENT	(ISO 3451)	ppm(m)	35
Titanium	(ICP)	ppm(m)	8
Aluminum	(ICP)	ppm(m)	2
Calcium	(ICP / AA)	ppm(m)	0
Chlorine	(XRF)	ppm(m)	10
Particle Size < 63µm	(Laser Diffraction)	%(m)	3.9
Contamination Mean Value	(DIN ISO 5834-1)		0.2
Contamination Single Value	(DIN ISO 5834-1)		1

The properties of the original GUR 1020 O lot used as base fulfil the requirements for Type 1 of ISO 5834 Part 1 and ASTM F648 at date of manufacture.

The properties of the GUR 1020-E meet the requirements of ASTM F2695 at date of manufacture.

Page 1 of 2





Celanese Sales Germany GmbH
Am Unisys-Park 1
D-65843 SULZBACH

ORTHOPLASTICS LTD
BEECH INDUSTRIAL ESTATE
BACUP
Lancashire
OL13 9EL
UNITED KINGDOM

Inspection Certificate EN 10204-3.1

GUR 1020-E - NATURAL R11

Customer No.:	1071897	Cert Issue Date:	30 Apr 2018
Material No.:	21008789	Qty Shipped:	500.000 KG
Customer Material:	GUR 1020-E	Order Item /date:	1979752 10 / 28 Mar 2018
		Delivery item/date:	85637892 900006 / 02 May 2018
		Customer PO No.:	029392

Quality Inspector

Elke Landgraf
Celanese Production Germany GmbH and Co.KG Site Oberhausen
Otto-Roelen Str. 3
D 46147 Oberhausen

This report is machine-printed and will not be signed.

Elke Landgraf 13-6-18

A4. High-N Austenitic Stainless Steel – Ø 50 mm

NO 85644000

ABNAHMEPRÜFZEUGNIS
INSPECTION CERTIFICATE
CERTIFICAT DE RECEPTION

ISO 9001:2008 certification
EN ISO 14001:2004 certification



EN 10204-3.1

Cert. No.: 225082 / 2017.10.30
Blatt/Sheet/Page: 1 / 4

Bestell-Nr./Purchaser order No./No. de commande: 1291002759 / 2017.05.04	Empfängerref.-Nr./Receiver reference-No./Référence destinataire: -
Werksauftrags-Nr./Works order-No./No. de la commande de l'usine: 2113108 / 2017.05.04	Lieferschein-Nr./Delivery note-No./Avis d'expédition du client: 51459776 / 2017.10.12
Prüfgegenstand/Object of test/Objet d'examen: BÖHLER P504 W-Nr. 1.4472RN Stabstahl, gewalzt, lösungsgeglüht, abgeschreckt Barsteel, rolled, solution annealed, quenched ECOBANK ISO 286/2 ITh9 Rauheit / Roughness (Ra) = max. 3.2 µm	Anforderungen/Requirements/Exigence: Werkstoffdatenblatt Rohmaterial Nr.: 234N Rev.-Nr.: 6 Anhang / Annex WD-RM 234N Rev.-Nr.:6 ISO 5832-09 Second edition 2007-06-15 ASTM F1586-13 E1 TMP P504 0002 Rev.000

Umfang der Lieferung/Volume of delivery/liste descriptive

Pos./Los	Abmessung Dimensions Dimensions	Länge Length Longueur	Stückzahl No. of Pieces No. de Pieces	Gewicht kg Weight kgs Poids kg	Mat-ID	Prüf-Nr. Test No. Eprouvette	Schmelze-Nr. Heat No. No. de coulee
10/1	RD 50 MM	3.000 - 3.500 MM	-	1546,0	SYC7	1608817-3	C49508

Qualitätswärmebehandlung / Quality heat treatment

	Temperatur Temperature	Haltezeit Soak time	Abkühlung Cooling
Lösungsgeglüht / Solution annealed	970°C	0,5 h M	Wasser / Water

M...Haltezeit auf Zieltemperatur nachdem das Materialzentrum die Toleranzgrenze erreicht hat.
M...Holding time at nominal temperature after center of material has reached the tolerance limit.

approved
Zug 17.7.18
M. [Signature]

Chemische Zusammensetzung / Chemical Composition / Composition chimique (%)											
Schmelzanalyse / Chemical Composition Erschmelzungsart / Steelmaking Process: Almet+ESR										Schmelze-Nr. Heat No. No. de coulée	
C	Si	Mn	P	S	Cr	Mo	Ni	V	W	C49508	
0,034	0,33	4,01	0,016	0,0003	20,86	2,19	10,38	0,07	<0,05		
Cu	Co	Ti	Al	Nb	N	FL038*				C49508	
0,11	<0,05	<0,005	0,007	0,34	0,46	0,18					
*FL038 = V+W+Co+Ti+Al											
Mutterschmelze / Master melt = C13238											
Metallographische Prüfungen / Metallographic examination											
Nichtmetallische Einschlüsse / Non metallic inclusions											
Prüfnorm / Testing standard = ASTM E45-13 Methode A											
	A		B		C		D				
Stück Nr. Piece no.	dünn thin	dick heavy	dünn thin	dick heavy	dünn thin	dick heavy	dünn thin	dick heavy			
86	-	-	0.5	-	-	-	1.5	0.5			
87	-	-	0.5	-	-	-	1.0	0.5			
Entsprechend / Equivalent to ISO 4967:2013 Verfahren / method A											
Ferritgehaltbestimmung / Ferrite content evaluation											
Das Material ist frei von Delta-Ferrit / The material is free from Delta-Ferrite											
Korngrößenbestimmung / Grain size evaluation											
Prüfnorm / Testing standard = ASTM E112-13											
	Rand / Rim			1/2 Radius (1/4T)			Zentrum / Center				
Korngröße / Grain size	11			10			9				
Gefügeuntersuchung / Microstructural examination											
Austenitisches Gefüge / Austenitic structure											
Wir bestätigen folgende Vereinbarung Intermetallische Verbindungen (z.B. Chi- oder Sigma Phase) sind unzulässig. We confirm the following agreement Intermetallic compounds (e.g. Chi- or Sigma phases) are not acceptable.											



<u>Mechanische Eigenschaften / Mechanical Properties</u>									
Zugversuch im Lieferzustand/Tensile test in delivery condition									
Prüf-Nr. Test no.	*Stk.-Nr. *Piece no.	Prüfnorm Testing standard	Lage Location	Temp. grad C	Dehngrenze Yield Strength	Zugfestigkeit Ultimate Tensile Strength	Dehnung Elongation		Einschnürung Reduction of Area
					MPa	MPa	A4 %	A5 %	Z %
1608817-3	86	ISO 6892-1 01.02.2017	LA	23	>=430	>=740	>=35		>=30
					507	859	43		65
1608817-3	86	ASTM E 8/E8M- 16a 01.09.2016	L2	23	>=430	>=740	>=35		>=30
					483	869	45		68

Korrosionsprüfung / Corrosion examination

Interkristalline Korrosion / Intergranular corrosion
Prüfnorm / Testing standard = DIN EN ISO 3651-2 Verfahren / method A
Das Material erfüllt die Anforderungen / The material fulfils the requirements



REGISTERED OFFICE OF THE COMPANY: KAPFENBERG; REGISTER COURT LANDESGERICHT LEOBEN FN 294435v

ABNAHMEPRÜFZEUGNIS
INSPECTION CERTIFICATE
CERTIFICAT DE RECEPTION

ISO 9001:2008 certification
EN ISO 14001:2004 certification



EN 10204-3.1

Cert. No.: 225082 / 2017.10.30
Blatt/Sheet/Page: 3 / 4

Mechanische Eigenschaften / Mechanical Properties									
Zugversuch im Lieferzustand/Tensile test in delivery condition									
Prüf-Nr. Test no.	*Stk.-Nr. *Piece no.	Prüfnorm Testing standard	Lage Location	Temp. grad C	Dehngrenze Yield Strength	Zugfestigkeit Ultimate Tensile Strength	Dehnung Elongation		Einschnürung Reduction of Area
					MPa	MPa	A4 %	A5 %	Z %
1608817-3	86	ISO 6892-1 01.02.2017	LA	23	>=430	>=740	>=35		>=30
					507	859	43		65
1608817-3	86	ASTM E 8/E8M- 16a 01.09.2016	L2	23	>=430	>=740	>=35		>=30
					483	869	45		68

Korrosionsprüfung / Corrosion examination

Interkristalline Korrosion / Intergranular corrosion
Prüfnorm / Testing standard = DIN EN ISO 3651-2 Verfahren / method A
Das Material erfüllt die Anforderungen / The material fulfils the requirements



REGISTERED OFFICE OF THE COMPANY: KAPFENBERG; REGISTER COURT LANDESGERICHT LEOBEN FN 294435v

A5. High-N Austenitic Stainless Steel – Ø 30 mm

ABNAHMEPRÜFZEUGNIS
INSPECTION CERTIFICATE
CERTIFICAT DE RECEPTION

ISO 9001:2008 certification
EN ISO 14001:2004 certification



EN 10204-3.1

Cert. No.: 194416 / 2016.04.22
Blatt/Sheet/Page: 1 / 3

<u>Bestell-Nr./Purchaser order No./No. de commande:</u> 1291002425 / 2015.09.08		<u>Empfängerref.-Nr./Receiver reference-No./Référence destinataire:</u> -					
<u>Werkauftrags-Nr./Works order-No./No. de la commande de l'usine:</u> 2025740 / 2015.09.08		<u>Lieferschein-Nr./Delivery note-No./Avis d'expédition du client:</u> 51312659 / 2016.04.05					
<u>Prüfgegenstand/Object of test/Object d'examen:</u> BÖHLER P504 W-Nr. 1.4472RN Stabstahl, gewalzt, lösungsgeglüht, abgeschreckt ECOBLANK ISO 286/2 ITh9		<u>Anforderungen/Requirements/Exigence:</u> Werkstoffdatenblatt Rohmaterial Nr.: 234N Rev.-Nr.: 5 ISO 5832-09 Second edition 2007-06-15 ASTM F1586-13 E1					
<u>Umfang der Lieferung/Volume of delivery/liste descriptive</u>							
Pos./Los	Abmessung Dimensions	Länge Length Longueur	Stückzahl No. of Pieces No. de Pieces	Gewicht kg Weight kgs Poids kg	Mat.-ID	Prüf-Nr. Test No. Epreuve	Schmelze-Nr. Heat No. No. de coulée
10/1	RD 30 MM	3.000 - 3.500 MM	-	1582,0	LQ3Q	1490171-1	B50603
<u>Qualitätswärmebehandlung</u>							
		Temperatur	Haltezeit	Abkühlung			
	Lösungsgeglüht	970°C	0.5 h M	Wasser			
M...Haltezeit auf Zieltemperatur nachdem das Materialzentrum die Toleranzgrenze erreicht hat.							

approved
Zug, 17.7.18
M. J.

REGISTERED OFFICE OF THE COMPANY: KAPFENBERG; REGISTER COURT LANDESGERICHT LEOBEN FN 284435v

Chemische Zusammensetzung/Chemical Composition/Composition chimique (%)										
Schmelzanalyse/Chemical Composition Erschmelzungsart/Steelmaking Process: AImelt+ESR										Schmelze-Nr. Heat No. No. de coulée
C	Si	Mn	P	S	Cr	Mo	Ni	V	W	B50603
0,035	0,31	3,76	0,014	0,0005	20,83	2,18	10,30	0,09	<0,05	
Cu	Co	Ti	Al	Nb	N	FL038*				B50603
0,10	0,06	<0,005	0,009	0,34	0,45	0,21				

*FL038 = V+W+Co+Ti+Al

Mutterschmelze = B14710

Nichtmetallische Einschlüsse
Prüfnorm = ASTM E45-13 Methode A

Test Nr.	A		B		C		D	
	dünn	dick	dünn	dick	dünn	dick	dünn	dick
29	-	-	-	-	-	-	1.0	-
30	-	-	-	-	-	-	1.0	-

Feritgehaltbestimmung
Ergebnis = Frei von Delta-Ferit

Korngrößenbestimmung
Prüfnorm = ASTM E 112-13
ASTM No. = 11

Gefügeuntersuchung
Austenitisches Gefüge - Frei von Phasen und Ausscheidungen

Wir bestätigen folgende Vereinbarung:
Ti-Nb- Verbindungen ebenso wie alle Arten von Ausscheidungen oder intermetallischen Verbindungen
(z.B. Chi- oder Sigma-Phase) sind unzulässig.



ABNAHMEPRÜFZEUGNIS
INSPECTION CERTIFICATE
CERTIFICAT DE RECEPTION

ISO 9001:2008 certification
EN ISO 14001:2004 certification



EN 10204-3.1

Cert. No.: 194416 / 2016.04.22
Blatt/Sheet/Page: 3 / 3

Mechanische Eigenschaften/Mechanical Properties										
Zugversuch im Lieferzustand/Tensile test in delivery condition										
Legende / Key		S = Schopf / Top		Dehngrenze		Zugfestigkeit		Dehnung		Einschnürung
H = Härtester / hardest		M = Mitte / Middle		Yield Strength		Ultimate Tensile Strength		Elongation		Reduction of Area
W = Weichster / softest		B = Boden / Bottom		Rp0,2		Rm		A4		Z
Prüf-Nr.	*Stk.-Nr.	Prüfnorm	Lage	Temp.	MPa	MPa	%	%		
Test no.	Piece no.	Testing standard	Location	grd C						
1490171-1	29	EN ISO6892-1/09	LA	23	>=430	740 - 920	>=35	Info		
					537	888	40	66		
1490171-1	29	ASTM E8/E8M-15a	LZ	23	>=430	740 - 920	>=35	Info		
					526	899	44	67		
Härteprüfung im Lieferzustand/Hardness test in delivery condition										
					Methode					
Prüf-Nr.	Stk. Nr.	Prüfnorm	Prüfart	HBW 2.5/187.5						
Test no.	Piece no.	Testing standard	Location							
1490171-1	1	ASTM E10-15	Zentrum	240 - 290						
				248						
Korrosionsprüfung										
Interkristalline Korrosion nach ISO 3651-2 Methode A: Gutbefund										
Zerstörungsfreie Prüfung										
Verwechslungsprüfung : Positive Materialidentifikation										
100% Ultraschallprüfung nach AMS-STD-2154 Rev. A 2012-10 Type I mit Phased Array.										
Das Material entspricht der Qualitätsklasse AA.										
100% Ultraschallprüfung nach AMS 2630C mit Phased Array.										
Das Material entspricht der Klasse A1.										
100% Oberflächenprüfung nach DIN EN 10277-1.										
Das Material entspricht der Qualitätsklasse 4.										
Eine Wirbelstromprüfung wurde durchgeführt.										
Die Stäbe sind frei von unzulässigen Oberflächenfehlern.										
Rauheit: <1 µm										
Statements										
Das Material ist frei von Quecksilber Kontamination.										
Es wurden keine Schweißungen am Material durchgeführt.										
Herkunfts - und Erschmelzungsland = OESTERREICH										
Radioaktivitätskontrolle/Radioactivity inspection: Co-60 <0,1Bq/g										
Hiermit kleiner als Grenzwert in der anzuwendenden Spezifikation IAEA RS-G-1.7 für unbedenkliche Stoffe.										
Therefore smaller than upper limit required according to specification IAEA RS-G-1.7 for inoffensive material.										
Wir bestätigen hiermit, dass die obengenannten Erzeugnisse den Bestellvorschriften entsprechen.										
We hereby certify that the above mentioned products are consistent with the order prescriptions.										
Nous certifions que les produits énumérés ci-dessus sont conformes aux prescriptions de la commande.										
Zeichen des Lieferwerks:		Besichtigung und Nachmessung:				Zeichen des Prüfers:				
Brand of Manufacturer:		Keine Beanstandung				Symbol of Inspector:				
Marques de l'usine:		Inspection and Checking of Dimensions: Satisfactory				Symbole de l'inspecteur:				
		Inspection of Control des dimensions: Satisfaisant								
BOHLER Edelstahl GmbH & Co KG			Johann.Leodolter@bohler-edelstahl.at			Abnahmebeauftragter				
Mariazellersrasse 25			AUSSTELLER/			Inspection Representative				
8605 Kapfenberg, AUSTRIA			ORIGINATOR/AUTEUR			BOHLER Edelstahl GmbH & Co KG				
www.bohler-edelstahl.com										



REGISTERED OFFICE OF THE COMPANY: KAPFENBERG; REGISTER COURT LANDESGERICHT LEOBEN FN 294435v